

Donal M. Ragan

# STRUCTURAL GEOLOGY

An Introduction to  
Geometrical Techniques

FOURTH EDITION

CAMBRIDGE

CAMBRIDGE

[www.cambridge.org/9780521897587](http://www.cambridge.org/9780521897587)

This page intentionally left blank

**STRUCTURAL GEOLOGY**  
An Introduction to Geometrical Techniques  
FOURTH EDITION

Many textbooks describe information and theories about the Earth without training students to utilize real data to answer basic geological questions. This volume – a combination of text and lab book – presents an entirely different approach to structural geology. Designed for undergraduate laboratory classes, it is dedicated to helping students solve many of the geometrical problems that arise from field observations. The basic approach is to supply step-by-step instructions to guide students through the methods, which include well-established techniques as well as more cutting-edge approaches. Particular emphasis is given to graphical methods and visualization techniques, intended to support students in tackling traditionally challenging two- and three-dimensional problems. Exercises at the end of each chapter provide students with practice in using the techniques, and demonstrate how observations and measurements from the field can be converted into useful information about geological structures and the processes responsible for creating them.

Building on the success of previous editions, this fourth edition has been brought fully up-to-date and incorporates new material on stress, deformation, strain and flow. Also new to this edition are a chapter on the underlying mathematics and discussions of uncertainties associated with particular types of measurement. With stereonet plots and full solutions to the exercises available online at [www.cambridge.org/ragan](http://www.cambridge.org/ragan), this book is a key resource for undergraduate students as well as more advanced students and researchers wanting to improve their practical skills in structural geology.

DON RAGAN was educated at Occidental College, University of Southern California and at the University of Washington in Seattle, receiving his Ph.D. in 1960. He spent a year as a Fulbright Scholar at the University of Innsbruck, and later, with a National Science Foundation Fellowship, at Imperial College, London, where he received a Diploma of Membership in Geology (DIC). His teaching career at the University of Alaska, Fairbanks, and at Arizona State University has spanned a total of 34 years, and has focused on imbuing students with a thorough understanding of geometrical and analytical techniques in structural geology. His research interests center on the role of structural settings in structure-making processes, including studies of Alpine peridotites, glacial ice and welded tuffs.



# STRUCTURAL GEOLOGY

An Introduction to Geometrical Techniques

FOURTH EDITION

DONAL M. RAGAN

*Arizona State University, USA*



**CAMBRIDGE**  
UNIVERSITY PRESS

CAMBRIDGE UNIVERSITY PRESS  
Cambridge, New York, Melbourne, Madrid, Cape Town, Singapore,  
São Paulo, Delhi, Dubai, Tokyo

Cambridge University Press  
The Edinburgh Building, Cambridge CB2 8RU, UK

Published in the United States of America by Cambridge University Press, New York

[www.cambridge.org](http://www.cambridge.org)

Information on this title: [www.cambridge.org/9780521897587](http://www.cambridge.org/9780521897587)

© D. M. Ragan 2009

This publication is in copyright. Subject to statutory exception and to the provision of relevant collective licensing agreements, no reproduction of any part may take place without the written permission of Cambridge University Press.

First published in print format 2009

ISBN-13 978-0-511-64137-4 eBook (NetLibrary)

ISBN-13 978-0-521-89758-7 Hardback

ISBN-13 978-0-521-74583-3 Paperback

Cambridge University Press has no responsibility for the persistence or accuracy of urls for external or third-party internet websites referred to in this publication, and does not guarantee that any content on such websites is, or will remain, accurate or appropriate.

For  
Janne, Anneliese and Ásta





# Contents

<i>Preface</i>	<i>page xv</i>
<i>Acknowledgements</i>	<i>xvii</i>
<b>1 Structural planes</b>	<b>1</b>
1.1 Introduction	1
1.2 Definitions	1
1.3 Dip and strike	2
1.4 Accuracy of angle measurements	5
1.5 Graphic methods	10
1.6 Finding apparent dip	13
1.7 Analytical solutions	15
1.8 Cotangent method	17
1.9 True dip and strike	18
1.10 Dip vectors	20
1.11 Three-point problem	24
1.12 Observed apparent dips	25
1.13 Exercises	27
<b>2 Thickness and depth</b>	<b>30</b>
2.1 Definitions	30
2.2 Thickness determination	31
2.3 Thickness by direct measurement	31
2.4 Thickness from indirect measurements	32
2.5 Apparent thickness	36
2.6 Thickness between non-parallel planes	39
2.7 Thickness in drill holes	41
2.8 Depth to a plane	43
2.9 Distance to a plane	44
2.10 Error propagation	46
2.11 Exercises	54

---

<b>3</b>	<b>Lines and intersecting planes</b>	<b>57</b>
3.1	Definitions	57
3.2	Linear structures	57
3.3	Plunge of a line	59
3.4	Pitch of a line	61
3.5	Intersecting planes	64
3.6	Cotangent method	65
3.7	Structure contours	66
3.8	Line vectors	67
3.9	Accuracy of trend determinations	69
3.10	Exercises	71
<b>4</b>	<b>Planes and topography</b>	<b>72</b>
4.1	Exposures on horizontal surfaces	72
4.2	Effect of topography	74
4.3	Dip and strike from a geological map	76
4.4	Linear interpolation	77
4.5	Parallel lines	79
4.6	Three-point problem	80
4.7	Structure contours	82
4.8	Predicting outcrop patterns	84
4.9	Exercises	87
<b>5</b>	<b>Stereographic projection</b>	<b>88</b>
5.1	Introduction	88
5.2	Stereogram	88
5.3	Stereonet	92
5.4	Plotting techniques	93
5.5	Measuring angles	99
5.6	Attitude problems	101
5.7	Polar net	104
5.8	Dip and strike errors	105
5.9	Intersection errors	106
5.10	Exercises	107
<b>6</b>	<b>Rotations</b>	<b>109</b>
6.1	Introduction	109
6.2	Basic techniques	109
6.3	Sequential rotations	114
6.4	Rotations about inclined axes	116
6.5	Rotational problems	118
6.6	Tilting problems	119

---

6.7	Two tilts	121
6.8	Folding problems	122
6.9	Small circles	124
6.10	Exercises	128
<b>7</b>	<b>Vectors</b>	<b>130</b>
7.1	Introduction	130
7.2	Sum of vectors	134
7.3	Products of vectors	136
7.4	Circular distributions	143
7.5	Spherical distributions	147
7.6	Rotations	149
7.7	Rotational problems	154
7.8	Three-point problem	157
<b>8</b>	<b>Faults</b>	<b>165</b>
8.1	Definitions	165
8.2	Fault classification	166
8.3	Slip and separation	168
8.4	Faults in three dimensions	172
8.5	Slip and its determination	174
8.6	Overthrusts	179
8.7	Fault terminations	182
8.8	Faults and folds	184
8.9	Extension and contraction	185
8.10	Rotation	188
8.11	Facing on faults	194
8.12	Dilation of dikes	195
8.13	Exercises	197
<b>9</b>	<b>Stress</b>	<b>198</b>
9.1	Introduction	198
9.2	Traction	199
9.3	Stress components	201
9.4	Stress in two dimensions	204
9.5	Mohr Circle for stress	209
9.6	Superimposed stress states	215
9.7	Pole of the Mohr Circle	217
9.8	Role of pore pressure	222
9.9	Deviatoric and hydrostatic stress	223
9.10	Stress ellipse	224

---

9.11	Tractions versus forces	227
9.12	Stress tensor	229
9.13	Exercises	238
<b>10</b>	<b>Faulting</b>	<b>240</b>
10.1	Introduction	240
10.2	Experimental fractures	240
10.3	Role of friction	241
10.4	Coulomb criterion	247
10.5	Limitations	250
10.6	Classification of faults	251
10.7	Faults and stresses	251
10.8	States of stress at depth	254
10.9	Magnitudes of stress components	257
10.10	Open fractures	261
10.11	Stress drop	262
10.12	Faults in anisotropic rocks	263
10.13	Oblique faults	264
10.14	Other limitations	266
10.15	Earthquakes	266
10.16	Exercises	267
<b>11</b>	<b>Deformation</b>	<b>269</b>
11.1	Introduction	269
11.2	Continuum assumption	273
11.3	Homogeneous deformation	276
11.4	Analysis of simple shear	278
11.5	Superimposed deformations	284
11.6	Inhomogeneous deformation	287
11.7	Deformation and related tensors	290
11.8	Exercises	300
<b>12</b>	<b>Strain</b>	<b>302</b>
12.1	Introduction	302
12.2	Deformed grains	302
12.3	Deformed fossils	304
12.4	Deformed pebbles	306
12.5	Geometry of the strain ellipse	309
12.6	Mohr Circle for finite strain	313
12.7	Pole of the Mohr Circle	315
12.8	Strain from measured angles	316
12.9	Strain from measured stretches	321

---

12.10	Restoration	328
12.11	Strain and related tensors	331
12.12	Exercises	343
<b>13</b>	<b>Flow</b>	<b>346</b>
13.1	Introduction	346
13.2	Active tectonics	346
13.3	Ancient tectonics	349
13.4	Progressive deformation	350
13.5	Kinematics	356
13.6	Deformation rates from structures	365
13.7	Exercises	367
<b>14</b>	<b>Folds</b>	<b>369</b>
14.1	Introduction	369
14.2	Single surfaces	369
14.3	Relationships between surfaces	375
14.4	Associated structures	375
14.5	Fold orientation	379
14.6	Isogon classification	382
14.7	Thickness variation	385
14.8	Alternative graphs	386
14.9	Inverse thickness	388
14.10	Best-fit indicatrix	392
14.11	Determining the flattening index	397
14.12	Competence	399
14.13	Exercises	409
<b>15</b>	<b>Parallel folds</b>	<b>410</b>
15.1	Introduction	410
15.2	Rounded folds	410
15.3	Rounded folds in cross section	416
15.4	Balanced cross sections	426
15.5	Depth of folding	427
15.6	Non-parallel modifications	430
15.7	Angular folds	433
15.8	Angular folds in cross section	435
15.9	Faults in fold cores	438
15.10	Some problems	439
15.11	Exercises	439

---

<b>16</b>	<b>Similar folds</b>	<b>441</b>
16.1	Introduction	441
16.2	Geometry of shear folds	441
16.3	Single-sense shear	443
16.4	Shear folds in three dimensions	444
16.5	Superposed folds in two dimensions	445
16.6	Wild folds	449
16.7	Superposed folds in three dimensions	450
16.8	Exercises	452
<b>17</b>	<b>Folds and topography</b>	<b>454</b>
17.1	Map symbols	454
17.2	Outcrop patterns	454
17.3	Down-plunge view	456
17.4	Fold profile	459
17.5	Hinge and hinge plane	463
17.6	Computer graphs	463
17.7	Transformation of axes	464
17.8	Cautionary note	467
17.9	Exercises	467
<b>18</b>	<b>Structural analysis</b>	<b>468</b>
18.1	Introduction	468
18.2	S-pole and beta diagrams	468
18.3	Fold axis and axial plane	469
18.4	Equal-area projection	470
18.5	Polar net	473
18.6	Equal areas	473
18.7	Contoured diagrams	474
18.8	Statistics of scatter diagrams	478
18.9	Computer-generated diagrams	480
18.10	Interpretation of diagrams	482
18.11	Superimposed folds	484
18.12	Sampling problems	487
18.13	Engineering applications	489
18.14	Exercises	490
<b>19</b>	<b>Tectonites</b>	<b>493</b>
19.1	Introduction	493
19.2	Isotropy and homogeneity	493
19.3	Preferred orientation	494
19.4	Planar and linear fabrics	494
19.5	Complex structures	500

19.6	<i>LS</i> tectonites	502
19.7	Exercises	502
<b>20</b>	<b>Drill hole data</b>	<b>504</b>
20.1	Introduction	504
20.2	Oriented cores	505
20.3	Cores without orientation	507
20.4	Cores with a known plane	510
20.5	Two drill holes	511
20.6	Analytical solution	513
20.7	Three drill holes	515
20.8	Interpretation of folds	516
20.9	Exercises	517
<b>21</b>	<b>Maps and cross sections</b>	<b>518</b>
21.1	Geological maps	518
21.2	Other types of maps	521
21.3	Geological history	522
21.4	Structure sections	523
21.5	Other types of sections	527
21.6	Vertical exaggeration	527
21.7	Enlarged sections	532
21.8	Exercises	533
<b>22</b>	<b>Block diagrams</b>	<b>534</b>
22.1	Introduction	534
22.2	Isometric projection	534
22.3	Isometric cube as a strain problem	536
22.4	Orthographic projection	539
22.5	General cube	540
22.6	Computer plot of cube	541
22.7	Geological structure	543
22.8	Orthographic cube as a strain problem	544
22.9	Topography	547
22.10	Modified blocks	548
22.11	Exercises	550
<i>Appendices</i>		
A	Descriptive geometry	551
B	Spherical trigonometry	564
<i>References</i>		
578		
<i>Index</i>		
595		





# Preface

The first steps in the study of geological structures are largely geometrical. This is true in the historical development of our knowledge of such structures, in the initial stages of any field investigation, and in the education of a structural geologist. This concern for geometry includes the methods of describing and illustrating the form and orientation of geological structures, and the solution of various dimensional aspects of these structures.

This book attempts to fill a need for an introduction to the geometrical techniques used in structural geology. I have sought an approach which is basic yet modern. The topics covered include well-established techniques, newer approaches which hold promise and an introduction to certain fundamental mechanical concepts and methods. Students who go no further in structural geology should have a working knowledge of the basic geometrical techniques and at least some appreciation of where the field is headed. Those who do go on, either in advanced courses or on their own should have the necessary foundation.

The first few chapters apply the methods of orthographic projection to the solution of simple structural problems. An introduction or review of these methods is given in Appendix A. Application to geological and topographical maps are included and extensive use is made of Mackin's powerful method of visualization – the down-structure view of geological maps.

The method of stereographic projection and the stereonet, together with the methods of plotting and solving angular problems are introduced fairly early. Many of the same elementary problems as well as some more advanced ones are solved with their uses.

Faults are described and classified. Problems of displacement are solved by combining orthographic and stereographic methods. The geometry of states of stress in two dimensions is then given in some detail. With this as background the Coulomb criterion of shear failure is applied to the interpretation of shear and extensional fractures in rocks.

Folds are described and classified in a similar way. In particular, the orientation and geometry are treated thoroughly. The powerful isogon classification of the shape of a single folded layer is treated in some detail. The relationship of these shapes to deformation and strain is briefly outlined. Parallel and similar folds are the subject of separate chapters.

The subject has a mathematical side. It is a common observation that geology students, despite having been exposed to these matters in other courses, do not retain much of the material. As Vacher (1998, p. 292) put it, “Students leave that information in ‘that other building’ when they go to their geology classes.” An important part of the problem is that they do not have much opportunity, especially in introductory courses, to see how mathematics can be applied to geology. I have sought a variety of ways to address this deficiency by including a number of applications throughout the book. Most of this material has been placed in separate modules close to the areas to which they apply. Thus an instructor or reader can use them, or not, but they can not be easily ignored. With one exception, the mathematics will be recognized from introductory courses in physics and calculus. The exception is a brief introduction to matrix algebra, a powerful, natural language of vectors and tensors.

Even at these early stages it is important to realize that geometry is not the end. The final goal, however elusive, is a complete understanding of the processes responsible for the structure in as great detail as possible. This is a branch of applied mechanics (see Pollard & Fletcher, 2005). While an introductory course is not the place to treat these matters in any great detail, it most certainly is the place to set the stage for such a consideration. In particular, it is important to understand the core concepts of stress, deformation, strain and flow.

# Acknowledgements

There have been many bumps along the way, some small, some not so small. For their help over these, I thank Ray Arrowsmith, Declan De Paor, George Hilley, Richard Lisle, Win Means, Simon Peacock, Steve Semkin, Rick Stocker, Al Swimmer, Sue Treagus, Len Vacher, Frederick Vollmer, Dave Waltham, and Mark Zoback.

Special thanks to Ramón Arrowsmith who took over the introductory course when I retired. He made a number of suggestions which led to important improvements and helped in many other ways.

Finally I wish to acknowledge the many years of support and encouragement by the late Troy L. Péwé. By his own admission he regretted his lack of proficiency in mathematics. And yet, far better than most, he understood its important role in the teaching and practice of geology.



# 1

## Structural planes

### 1.1 Introduction

Especially in the early stages of an investigation of the geology of an area, much attention is paid to determining and recording the location and orientation of various structural elements. Planes are the most common of these. They are also a useful starting point in the introduction to the geometrical methods of structural geology.

### 1.2 Definitions

**Plane:** a flat surface; it has the property that a line joining any two points lies wholly on its surface. Two intersecting lines define a plane.

**Attitude:** the general term for the orientation of a plane or line in space, usually related to geographical coordinates and the horizontal (see Fig. 1.1). Both trend and inclination are components of attitude.

**Trend:** the direction of a horizontal line specified by its bearing or azimuth.

**Bearing:** the horizontal angle measured east or west from true north or south.

**Azimuth:** the horizontal angle measured clockwise from true north.

**Strike:** the trend of a horizontal line on an inclined plane. It is marked by the line of intersection with a horizontal plane.

**Structural bearing:** the horizontal angle measured from the strike direction to the line of interest.

**Inclination:** the vertical angle, usually measured downward, from the horizontal to a sloping plane or line.

**True dip:** the inclination of the steepest line on a plane; it is measured perpendicular to the strike direction.

**Apparent dip:** the inclination of an oblique line on a plane; it is always less than true dip.

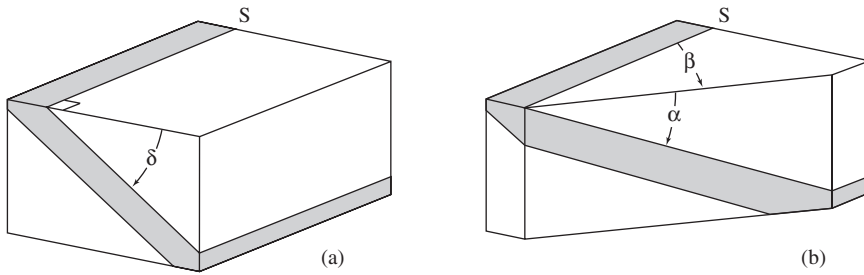


**Figure 1.1** Strike  $S$ , true dip  $\delta$  (delta), apparent dip  $\alpha$  (alpha) and structural bearing  $\beta$  (beta).

### 1.3 Dip and strike

The terms *dip* and *strike* apply to any structural plane and together constitute a statement of its *attitude*. The planar structure most frequently encountered is the bedding plane. Others include cleavage, schistosity, foliation and fractures including joints and faults. For inclined planes there are special *dip and strike map symbols*; in general each has three parts. The only exception is the special case of a horizontal plane which requires a special symbol.

1. A *strike line* plotted long enough so that its trend can be accurately measured on the map.
2. A short *dip mark* at the midpoint of one side of the strike line to indicate the direction of downward inclination of the plane.
3. A *dip angle* written near the dip mark and on the same side of the strike line.

The most common symbols are shown in Fig. 1.2 and their usage is fairly well established by convention. However, it is sometimes necessary to use these or other symbols in special circumstances, so that the exact meaning of all symbols must be explained in the map legend.

Attitude angles are also often referred to in text, although the usage is considerably less standard. There are two basic approaches. One involves the trend of the strike of the plane and the other the trend of the dip direction. Each of the four following forms refers to exactly the same attitude (for other examples see Fig. 1.3).

#### 1. Strike notation

- (a) N 65 W, 25 S: the bearing of the strike direction is  $65^\circ$  west of north and the dip is  $25^\circ$  in a southerly direction. For a given strike, there are only two possible dip directions, one on each side of the strike line, hence it is necessary only to identify which side by one or two letters. If the strike direction is nearly N-S or E-W then a single letter is appropriate; if the strike direction is close to the  $45^\circ$  directions (NE or NW) then two letters are preferred (see Fig. 1.3 for examples).
- (b) 295, 25 S: the azimuth of the strike direction is  $295^\circ$  measured clockwise from north and the dip is  $25^\circ$  in a southerly direction. Usually the trend of the north-

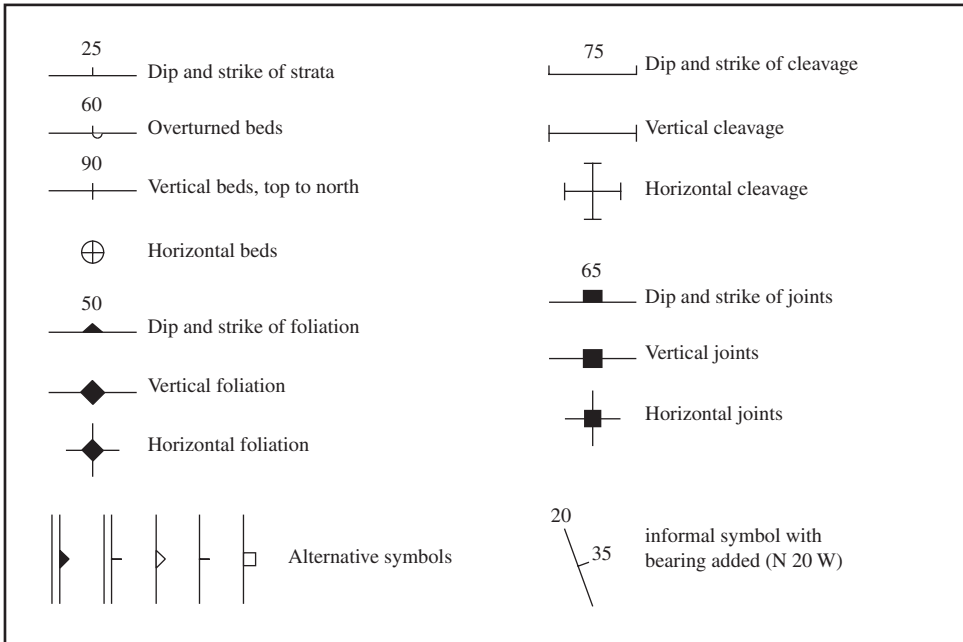


**Figure 1.2** Map symbols for structural planes.

ernmost end of the strike line is given, but the azimuth of the opposite end of the line may also be used, as in 115, 25 S.

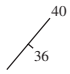
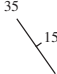
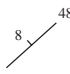
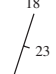
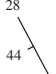
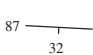
## 2. Dip notation

- (a) 25, S 25 W: the dip is  $25^\circ$  and the trend of the dip direction has a bearing of  $25^\circ$  west of south.
- (b) 25/205: the dip is  $25^\circ$  and the trend of the dip direction has an azimuth of  $205^\circ$  measured clockwise from north. The order of the two angles is sometimes reversed, as in 205/25. To avoid confusion, dip angles should always be given with two digits and the trend with three, even if this requires leading zeros.

As these dip and trend angles are written here, the degree symbol is not included and this is a common practice. However, this is entirely a matter of individual preference and taste.

The two forms of the strike notation are the most common, with the difference usually depending on whether the compass used to make the measurements is divided into quadrants or a full  $360^\circ$  and on personal preference. The advantage of the quadrant method of presentation is that most people find it easier to grasp a mental image of a trend more quickly with it.

The forms of the dip notation are more generally reserved for the inclination and trend of lines rather than planes, although when the line marks the direction of true dip, it may apply to both. The last method gives the attitude unambiguously without the need for letters and, therefore, is particularly useful for the computerized treatment of orientation

SYMBOL						
Strike (a)	N 40 E, 36 SE	N 35 W, 15 NE	N 48 E, 8 NW	N 18 E, 23 E	N 28 W, 44 SW	N 87 W, 32 S
Strike (b)	40, 36 SE	325, 15 NE	48, 8 NW	198, 23 E	332, 44 SW	273, 32 S
Dip (a)	36, S 50 E	15, N 55 E	8, N 42 W	23, S 72 E	44, S 62 W	32, S 3 W
Dip (b)	36/130	15/055	08/318	23/108	44/242	32/183

**Figure 1.3** Examples of the strike and dip notations.

data. For this reason it is becoming increasingly common to see the attitudes of planes written in this way.

It is essential to learn to read all these shorthand forms with confidence and to this end we will use them in examples and problems. However, they are not always the best way of recording attitude data in the field. It is a common mistake to read or record the wrong cardinal direction, especially for beginners. For example, it is easy to write E when W was intended for a strike or dip direction.

One way to avoid such errors is to adopt a convention such as the *right-hand rule*. There are two versions.

1. Face in the strike direction so that the plane dips to the right and report that trend in azimuth form.
2. Record the strike of your right index finger when the thumb points down dip (Barnes, 1995, p. 56).

Alternatively, record the attitude by sketching a dip and strike symbol in your field notebook and adding the measured bearing or azimuth of the strike direction (see the informal symbol in Fig. 1.2).<sup>1</sup> This permits a visual check at the outcrop – stand facing north and simply see that the structural plane and its symbolic representation are parallel. Recording attitudes in this way also reduces the chance of error when transferring the symbols to a base map.

Strike and dip measurements are commonly made with a compass and clinometer. A variety of instruments are available which combine both functions. In North America,

<sup>1</sup>It is not necessary to plot this strike line in your notebook using a protractor. With a little practice any trend line can be sketched with an accuracy of  $\pm 5^\circ$  or better. In combination with the labeled strike direction this is sufficient.



the Brunton compass is widely used. In Europe and elsewhere the Silva Ranger, Chaix and Freiberg compasses are favored (McClay, 1987, p. 18, 21). The methods of measuring attitudes in a variety of field situations are given in some detail by Barnes (1995, p. 7–9), Davis and Reynolds (1996, p. 662–669) and McClay (1987, p. 22–30).

The most direct method is to hold a compass directly against an exposed plane surface at the outcrop. We illustrate the procedure using the Brunton compass, but the methods with the other instruments are similar. The Freiberg compass is an exception because the dip and dip direction are measured in a single operation, and this has some advantages.

1. Strike is measured by placing one edge of the open case against the plane and the compass rotated until it is horizontal as indicated by the bull's eye bubble (Fig. 1.4a). The measured trend in this position is the strike direction.
2. Dip is determined by placing one side of the compass box and lid directly against the exposed plane perpendicular to the previously measured strike. The clinometer bubble is leveled and the dip angle read (Fig. 1.4b).

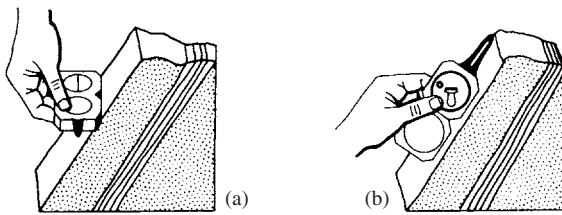


**Figure 1.4** Measurements with a Brunton compass (from Compton, 1985, p. 37 with permission of John Wiley): (a) strike; (b) dip.

## 1.4 Accuracy of angle measurements

The goal of making dip and strike measurements is to record an attitude which accurately represents the structural plane at a particular location. With reasonable care, horizontal angles may be read on the dial of the compass to the nearest degree, especially if the needle is equipped with damping. Vertical angles may also be read on the clinometer scale to the nearest degree, or better if a vernier is used.

There are two reasons why such accuracy does not automatically translate into accurately known attitudes. First, even if the plane is geometrically perfect it is not possible to place the compass in *exactly* the correct position when making a measurement. Second, the presence of local irregularities means that a result will depend on the precise placement of the instrument on the exposed surface. In everyday terms, the first is an error, while the second introduces an uncertainty. In practice, however, it is difficult or impossible to separate these two effects. Thus *error* and *uncertainty* are essentially synonymous when applied to any scientific measurement (Taylor, 1997, p. 3).

It is, of course, easy to make a *mistake* when measuring or recording an angle of dip or strike. Almost everyone has had the unfortunate experience of finding an attitude which

seems out of place in a notebook or on a map. If the mistake is small it may be difficult to identify, but then its presence may not make much difference. On the other hand, if the mistake is large, then some effort should be made to avoid or correct it. There are statistical methods for identifying *outliers* and discarding them, but the question always remains: is the exception real or not? A better approach is to identify them while it is still possible to correct them in the field. A good way to do this is to plot the attitude symbols on a sketch map as they are made. Then seemingly anomalous attitudes can be quickly confirmed or discarded by additional observations.

Because all measurements are subject to such errors or uncertainties there will generally be a *discrepancy* between any two angles measured on the same plane. There are two main types of errors: *random* and *systematic*.

The difference between these two may be illustrated with a simple “experiment” consisting of a series of shots fired at a target (Taylor, 1997, p. 95–96). Accurate “measurements” are represented by shots which cluster around the center of the bull’s eye: they may be tightly clustered (Fig. 1.5a) or not (Fig. 1.5b). An important cause of random errors is the marksman’s unsteady hand. In either case, if there is a sufficient number of shots and their distribution is truly random, the mean location of the shots will define the center of the target with acceptable accuracy.

Systematic errors are caused by any process by which the shots arrive off-center, such as misaligned sights. As before, the random component may be small (Fig. 1.5c) or large (Fig. 1.5d). In both cases, the mean will depart significantly from the center of the target.

While the pattern of shots is a good way of illustrating the difference between random and systematic errors, it is misleading in an important sense. Knowing the location of the bull’s eye is equivalent to knowing the true value of the measured quantity. In the real world we do not know this true value; indeed if we did we would not have to make any measurements. A more realistic illustration would be to examine the pattern without the target. Then the random errors would be easy to identify but systematic errors would not be.<sup>2</sup>

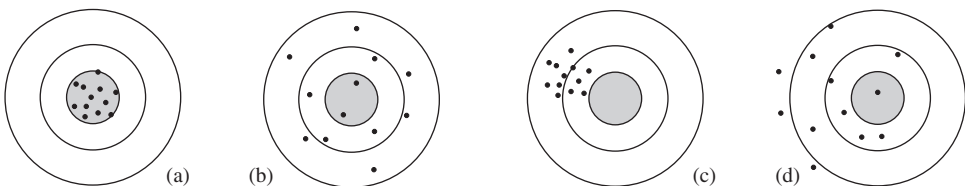


**Figure 1.5** Combinations of small and large random  $R$  and systematic  $S$  errors (after Taylor, 1997, p. 95): (a)  $R$  small,  $S$  small; (b)  $R$  small,  $S$  large; (c)  $R$  large,  $S$  small; (d)  $R$  large,  $S$  large.

<sup>2</sup>Then there is the *Texas Sharpshooter Fallacy*: a fabled marksman randomly sprays the side of a barn with bullets and then paints a circle around a cluster. Epidemiologists call this fallacy the *clustering illusion*, the intuition that random events which occur in clusters are not really random events at all. To such clusters politicians, lawyers and, regrettably, some scientists assign a causal relationship, such as a link of some environmental factor and a disease, when they are actually due to the laws of chance (Carroll, 2003, p. 375).

For horizontal trend angles measured in the field, systematic errors arise if the magnetic declination is improperly set on the compass or an incorrect angle is used to manually correct a reading. The compass needle may also be deflected by magnetic materials, such as magnetite, in the rock or a piece of magnetized iron, such as a rock hammer, near the compass. A similar effect may be produced by the electromagnetic fields associated with nearby power lines. The standard approach to controlling systematic errors is the use of equipment which has been tested and calibrated, but this has rather limited application for the field geologist. With awareness and care, these systematic errors may be minimized.

Random errors of both dip and trend arise from the actual process of making the measurements. Even for a geometrically perfect plane, it is never possible to align the compass and read the angles *exactly*. Further, inevitable natural irregularities on the surface of naturally occurring planes make this process even more difficult. Measuring the attitude of a stiff field notebook, map case or a small aluminum plate held tightly against the rock surface helps eliminate the effect of small-scaled features.

There is also a way to reduce the effect of such irregularities. Stand back from the outcrop several meters and determine the trend of a horizontal line of sight parallel to the bedding (Fig. 1.6a), and then measure the inclination of the bedding perpendicular to this line (Fig. 1.6b). Although it takes practice to become proficient, this is probably the most accurate field method of determining dip and strike at the scale of a single outcrop.

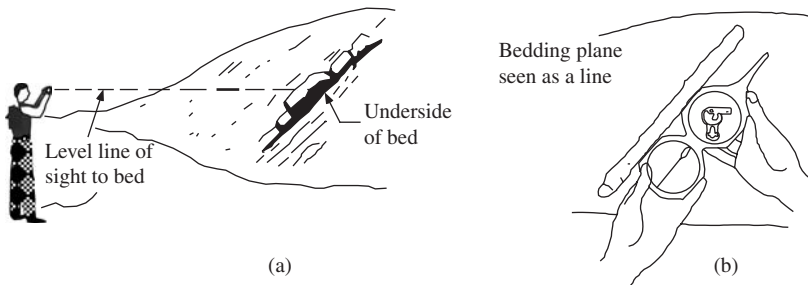


**Figure 1.6** Avoiding minor irregularities (Compton, 1985, p. 35 with permission of John Wiley): (a) sighting a level line; (b) dip measured perpendicular to this line.

Because of such inevitable random errors, there will generally be a *discrepancy* between any two measured values of the same angle on the same plane. To evaluate such random errors, the standard procedure is to make multiple measurements. For dip angles or any such measured quantities, the simple *arithmetic mean*  $\bar{x}$  of a series of  $N$  measurements  $x_1, x_2, \dots, x_N$  is found from

$$\bar{x} = \frac{x_1 + x_2 + \dots + x_N}{N} = \frac{1}{N} \sum_{i=1}^N x_i. \quad (1.1)$$

This mean is almost always the *best* estimate of the true value (Taylor, 1997, p. 10, 98, 137). That is,

$$x_{best} = \bar{x}.$$

The discrepancies  $d_i$  associated with a set of measurements  $x_i$  are then

$$d_i = x_i - \bar{x}, \quad (i = 1 \text{ to } N).$$

These are positive or negative, depending on whether the value of  $x_i$  is greater or less than  $\bar{x}$ .

These discrepancies give a valuable indication of the uncertainty associated with the measurements (Taylor, 1997, p. 10). The measure of this uncertainty is most simply approximated as the magnitude of the largest discrepancy:

$$\Delta x = |d_i|_{large}.$$

The positive number  $\Delta x$  is termed the *uncertainty*, or *error*, or *margin of error*. Then the result of any measurement is expressed in the *standard form* as

$$(\text{measured value of } x) = x_{best} \pm \Delta x.$$

This means that we can be confident that the correct value *probably* lies between  $x_{best} - \Delta x$  and  $x_{best} + \Delta x$ , though it is *possible* that it lies slightly outside this range, absent systematic errors, as we have been assuming.

While dip angles can be treated directly in this way, horizontal trend angles in general and strike angles in particular present special problems and a different method for calculating their mean direction must be used (see §7.4).

Rondeel and Storbeck (1978) performed a series of experiments to evaluate the magnitudes of the dip uncertainties. Multiple measurements were made on a  $10 \times 10$  cm single, slightly irregular bedding plane surface which was rotated into different inclinations ranging from  $5^\circ$  to  $88^\circ$ . For moderate to steep inclinations, they found that 90% of the angles were within  $2^\circ$  of the mean. For bedding planes with greater irregularities, Cruden and Charlesworth (1976) found that the uncertainties were also greater, and ranged up to about  $10^\circ$ . For more formal purposes, the *sample standard deviation* is used to express the uncertainty and is defined as

$$\sigma_x = \sqrt{\frac{1}{N-1} \sum_{i=1}^N (d_i)^2} = \sqrt{\frac{1}{N-1} \sum_{i=1}^N (x_i - \bar{x})^2}. \quad (1.2)$$

For large  $N$  the denominator  $N - 1$  can be replaced with  $N$  (Taylor, 1997, p. 97–101), and this equation then becomes the statement of the *root mean square* (commonly abbreviated RMS) of the deviations.<sup>3</sup>

In most general field-mapping projects, we probably can accept carefully made single measurements recorded to the nearest degree because the uncertainties are probably modest. However, if these attitude measurements are to be used for special purposes, greater care and possibly other methods may be required.

There are certain situations where the uncertainty may be much greater. The case of a gently dipping plane poses special problems.

If the dimension of the outcrop is sufficiently large, the inclination of a smooth plane as small as one degree, then both the dip and the dip direction can be visually identified and estimated. However, if the plane is irregular it is possible that one or more measurements might yield a result such that  $\Delta x > x$ , implying that the dip may be in the opposite of the observed direction, which would be a huge error.

Further, in the measurement of the strike direction on such a gently dipping plane, even a slightly incorrect placement of the compass may result in a large error. By definition, the strike is the trend of a horizontal line on an inclined plane. If the compass is not exactly horizontal then a direction other than the true strike will be recorded. The geometry of this situation is shown in Fig. 1.7a where a *maximum operator error*  $\varepsilon_o$ , the largest angular departure from horizontal, goes uncorrected. The result is that a trend  $OS'$  rather than the true strike  $OS$  is recorded. The angle between these two directions is the *maximum strike error*  $\varepsilon_s$  and its magnitude as a function of the dip angle  $\delta$  may be evaluated. The three right-triangles in this figure yield the trigonometric relationships

$$w = d / \tan \delta, \quad l = d / \tan \varepsilon_o, \quad \sin \varepsilon_s = w / l.$$

Substituting the first two into the third gives<sup>4</sup>

$$\sin \varepsilon_s = \frac{\tan \varepsilon_o}{\tan \delta}. \quad (1.3)$$

This result, first obtained by Müller (1933, p. 232; see also Woodcock, 1976), is solved for values of  $\varepsilon_s$  and the results displayed graphically for  $\varepsilon_o = 1\text{--}5^\circ$  in Fig. 1.7b. It is important to note that for very small dip angles, the maximum possible strike error is large and approaches  $90^\circ$  as  $\delta \rightarrow 0$ .

<sup>3</sup>For large  $N$ , dividing by  $N - 1$  or  $N$  makes almost no difference. The advantage of using  $N - 1$  is that it gives a larger estimate of the uncertainty, and especially for measurements made in the field environment this is a good thing.

<sup>4</sup>As we will see later, this equation is just a specialized version of a more general description of the relationship between dip  $\delta$ , apparent dip  $\alpha$  and structural bearing  $\beta$  (compare Eq. 1.7).

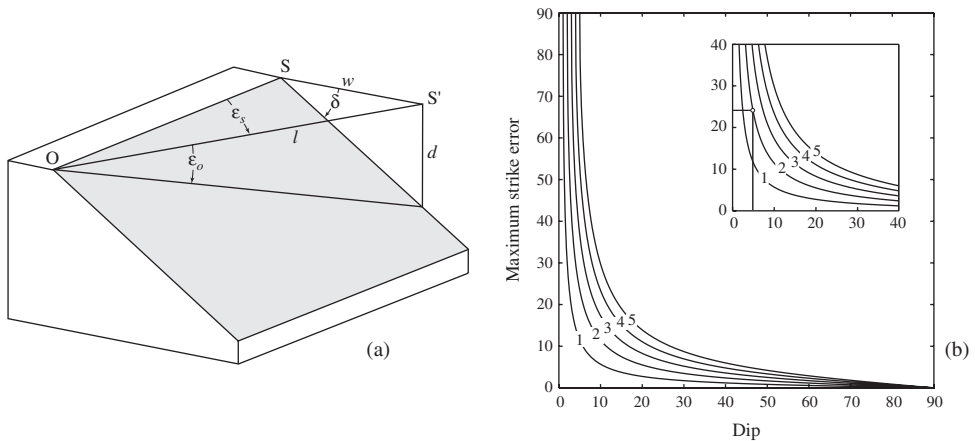


**Figure 1.7** Maximum strike error: (a) geometry; (b)  $\epsilon_s$  as a function of dip for values of  $\epsilon_o = 1\text{--}5^\circ$ . (The inset shows an example  $\epsilon_o = 2^\circ, \delta = 5^\circ$ , with the result that  $\epsilon_s \approx 24^\circ$ .)

## 1.5 Graphic methods

Indirect methods are also available for determining the various angles and these are the subject of the remainder of this chapter. All the techniques dealt with here are concerned with the relationships between the components of the attitude of planes – the angles of true and apparent dip, and the strike.

Of several possible approaches to solving these problems we choose at the outset an entirely graphical technique – the method of *orthographic projection* (see Appendix A). There are two reasons for this choice. First, with it we may readily and simply obtain solutions to a wide variety of problems. Second, it allows the various components of the problems to be visualized in a three-dimensional setting. This visualization is of crucial importance in developing the ability to solve geometrical problems in geology.

By way of introduction, consider a simple geological situation shown in the two block diagrams of Fig. 1.8.

### Problem

- The trace of an inclined plane is exposed on a flat, horizontal surface. The plane strikes east-west and dips  $36^\circ$  to the north. Construct a vertical section showing the angle of true dip. What is the depth to this plane at a map distance of  $w = 100$  m measured perpendicular to the strike line?

### Approach

- On the top of the block the trace of the inclined plane is a line of strike (Fig. 1.8a). The goal is to construct a vertical section showing the angle of true dip  $\delta$ . To do this we imagine standing at a point  $O$  on the surface trace of the plane and then walking a distance  $w = 100$  m due north to another surface point  $A$ . As we make this traverse, the

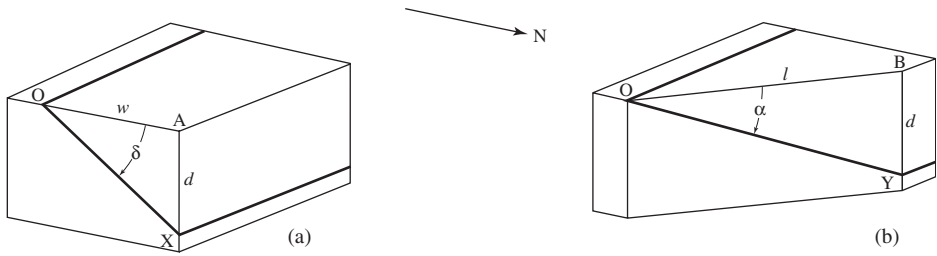


**Figure 1.8** Block diagrams: (a) true dip  $\delta$ ; (b) apparent dip  $\alpha$ .

vertical distance to the inclined plane steadily increases from zero to a depth  $d$  directly below  $A$ . With the dip angle and the traverse length known, we can easily make a scaled drawing of the top surface of the block showing its proper dimensions. To depict the vertical side, we imagine turning it upward as if it were hinged along edge  $OA$ . This hinge is called a *folding line*, abbreviated *FL* (see §A.2). We can now easily construct the required view.

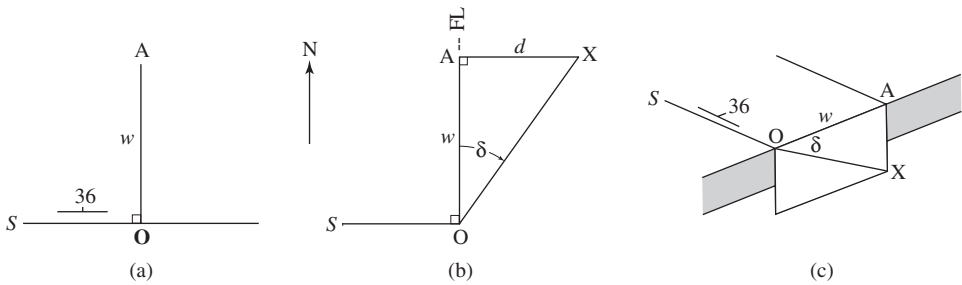


**Figure 1.9** True dip: (a) map; (b) section with  $OA$  as *FL*; (c) visualization.

**Construction**

1. On a map view draw an east-west line of strike  $S$  and locate point  $O$  on it. From  $O$  draw a line in the dip direction to locate point  $A$  at a distance of  $w = 100$  m using a convenient scale (Fig. 1.9a).
2. With  $OA$  as a *FL* draw a line on this now upturned section making angle  $\delta = 36^\circ$  with the horizontal. This is the required trace of the inclined structural plane (Fig. 1.9b).
3. At surface point  $A$  on this section, draw a vertical line downward to intersect the trace of the inclined plane at point  $X$ . Distance  $AX$  is the depth  $d = 73$  m to the plane at this point.

Accuracy is an important part of these constructions (see §A.3 for some general guidelines). It is particularly important that lines, such as  $OA$ , be long enough so that their orientations can be measured easily to within one degree. In the previous problem this can be accomplished by using a scale of  $10\text{ mm} = 10\text{ m}$ . As a general rule, a single diagram

should occupy the central part of a letter-size sheet of paper. Beginners commonly make their constructions too small.<sup>5</sup>

A very useful aid in this kind of problem is to actually bend the drawing along the folding line over the edge of a table top (Fig. 1.9c). You can then actually see the relationship between the map and the vertical section in three dimensions.

Once this three-dimensional visualization can be made with some confidence, we can, of course, relate the angle  $\delta$  and the lengths of sides  $w$  and  $d$  of the vertical right-triangle  $OAX$  with the simple formula

$$\tan \delta = d/w. \quad (1.4)$$

A closely related situation involves depicting the trace of an inclined structural plane on an oblique vertical section as illustrated in the block diagram of Fig. 1.8b.

### Problem

- Depict the same north-dipping structural plane on a vertical section whose trend is N 60 W. In this direction the apparent dip  $\alpha = 20^\circ$ . What is the depth to the plane at a horizontal distance of  $l = 200$  m from the strike line measured in this oblique direction?

### Approach

- In similar fashion, the goal now is to construct the vertical section showing the angle of apparent dip. As before, we imagine starting at a point  $O$  on the strike line and walking in this direction (Fig. 1.8b). As we do this the depth to the plane now increases from zero to the *same* depth  $d$  at point  $Y$  directly below surface point  $B$ . With the known apparent dip angle and the traverse length we draw the vertical section using as the folding line  $OB$ .

### Construction

1. Through surface point  $O$  on an east-west line of strike  $S$  draw a line in the direction N 60 W and on it locate point  $B$  at a distance  $l = 200$  m using a convenient scale (Fig. 1.10a).
2. With  $OB$  as  $FL$  draw a line inclined at the angle  $\alpha = 20^\circ$  (Fig. 1.10b). A vertical line downward at  $B$  then intersects this inclined line at point  $Y$ . Distance  $BY$  is the depth  $d = 73$  m to the plane.

<sup>5</sup>All of the figures here and throughout the book were originally constructed at such a scale, but they have been reduced to conserve space.



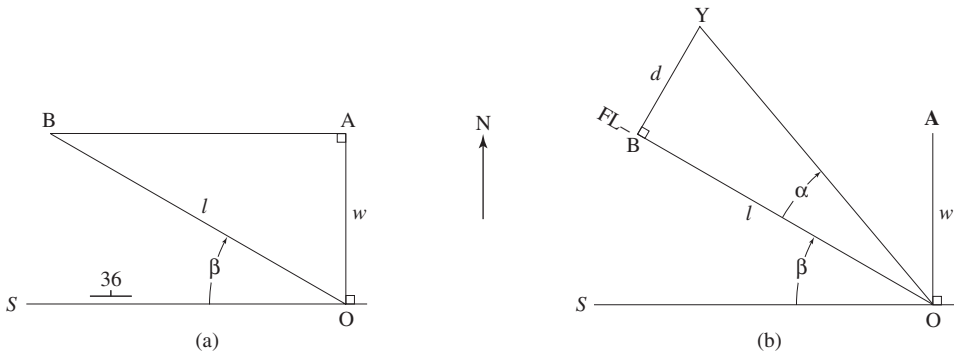


**Figure 1.10** Apparent dip: (a) map; (b) section with  $OB$  as  $FL$ .

Again, as an aid to visualization we may convert this drawing to a three-dimensional block diagram by folding the paper over the edge of a table top along the  $FL$ . We may also relate the three elements of the vertical right-triangle  $OBY$  with the formula

$$\tan \alpha = d/l. \quad (1.5)$$

Note that the essential features of these oblique sections remain the same no matter how the map is oriented. For this reason it is convenient to express the trend of the apparent dip relative to the strike direction. For this reason we refer to this angle  $\beta$  as the *structural bearing* of the line. The length  $l$  of the oblique traverse required to arrive at  $B$  can be obtained from the horizontal right-triangle  $OAB$  with

$$\sin \beta = w/l. \quad (1.6)$$

## 1.6 Finding apparent dip

In the previous problem, the apparent dip was given. However, this angle can not always be measured in the field. If inclined planes are to be depicted on such oblique sections we need a method for finding it.

### Problem

- If  $\delta = 36^\circ$  and  $\beta = 30^\circ$ , what is  $\alpha$ ?

### Approach

- The solution of this problem involves two steps: first draw the true-dip section (Fig. 1.10a); then draw the apparent-dip section (Fig. 1.10b). As is the general practice we combine the map and sections on a single diagram. This eliminates the need to replicate most angles and lengths and this reduces the chance of error.

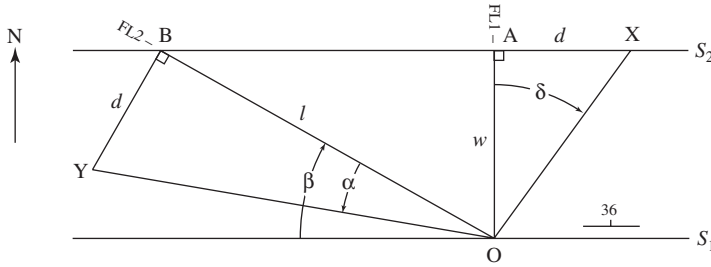


**Figure 1.11** Apparent dip from true dip and strike.

### Construction

1. Through a point  $O$  on strike line  $S_1$  draw a line in the dip direction (Fig. 1.11). On this line locate surface point  $A$  at an arbitrary but conveniently large distance  $w$ .
2. Construct a vertical section with  $OA$  as  $FL1$  showing the trace of the inclined plane at angle  $\delta = 36^\circ$  and thus determining the depth  $d$  of point  $X$  below  $A$ .
3. Through surface point  $A$ , draw a second strike line  $S_2$ .
4. A line from point  $O$  making angle  $\beta = 30^\circ$  with  $S_1$  intersects  $S_2$  at surface point  $B$ .
5. Construct a second vertical section with  $OB$  as  $FL2$  to locate point  $Y$  at the *same* depth  $d$  below  $B$ . Then  $OY$  represents the trace of the plane and its inclination is the angle of apparent dip.

### Answer

- The angle  $BOY$  is  $\alpha = 20^\circ$ .

Beginners are often confused by this jumping back and forth between map and section on the same drawing. Folding the drawing over the edge of a table top is a powerful aid in distinguishing the two distinct views. Using different colors for lines on the map and on the section also helps.

Several additional points should be noted. First, we need never know the actual depth  $d$ . Its scaled length may be transferred directly from sections  $OA$  to  $OB$  on the drawing with compass or divider. Second, in all such constructions, the direction of upward folding is immaterial, though it is usually best to choose it in the direction of the greatest open space on the drawing in order to avoid interfering lines.

As defined and used here, the angle of apparent dip is unambiguous and with reasonable care no difficulties should be encountered. There are, however, some situations where an “apparent” apparent dip may be observed (see §1.12) and this may be confusing. For this reason some prefer to speak of a *dip component* rather than an apparent dip, as we will do in §1.9.

## 1.7 Analytical solutions

By combining the two-dimensional views of maps and sections, the methods of orthographic projection are an invaluable tool in learning to visualize the geometry of structures in three dimensions.

Analytical solutions also have their place. A word of caution: both the calculator and computer do exactly what they are told and it is remarkably easy to enter the wrong number, use the wrong parameter or the wrong formula. The invariable result is the display of an impressive-looking number which is utterly wrong. Be careful!

The present problem involving  $\alpha$ ,  $\beta$  and  $\delta$  may be solved with the aid of a trigonometric equation (Herold, 1933). From Eq. 1.4  $w = d / \tan \delta$  and from Eq. 1.5  $l = d / \tan \alpha$ ; substituting these into Eq. 1.6 and rearranging yields

$$\boxed{\tan \alpha = \tan \delta \sin \beta.} \quad (1.7)$$

Obtaining an answer to this type of problem is a procedure called, fondly, *plug and chug*. Plugging in the values  $\delta = 36^\circ$  and  $\beta = 30^\circ$  gives

$$\tan \alpha = (0.726\ 54)(0.500\ 00).$$

Chugging out these values, your calculator displays

$$\tan \alpha = 0.363\ 27 \quad \text{or} \quad \alpha = 19.694\ 63.$$

Now what do we write down? For a proper answer we need two things: a way of identifying the figures which are significant, and then a way of eliminating the non-significant ones.<sup>6</sup>

As we have seen in §1.4, there is an inevitable uncertainty associated with any measured angle; we expressed such an angle together with its uncertainty in the form  $x \pm \Delta x$ . On the other hand, if we represent an angle by a single number, as we almost always do, there is an *implied uncertainty*. For example, consider the angle  $\delta = 36^\circ$ : As written, this is taken to mean that the angle which best represents  $\delta$  is probably closer to 36 than to 35 or 37, that is, it lies in the range  $36 \pm 0.5^\circ$ . This in turn means that the uncertainty is at least 0.5. This number is called the implied *absolute* uncertainty because it is expressed in the same units as the measured value.

We need a way of insuring that any calculated number we use takes advantage of the information content of the original measurement, while at the same time avoids any suggestion that it is more accurate than is justified. We do this by retaining only the significant figures and there are several convenient, well-established *Rules of Thumb* for accomplishing this.

<sup>6</sup>Vacher (1998) gives a good treatment of the use and abuse of significant figures.

1. When numbers are added or subtracted, the result should have the same number of decimal places as the number with the fewest decimal places.
2. When numbers are multiplied or divided, the result should have the same number of significant figures as the number with the fewest significant figures.
3. The presence of zeros requires special care. All these numbers have two significant figures: 20, 2.0, 0.20, 0.020, 0.0020.<sup>7</sup> Sometimes there is a question of just how many significant figures are there – how many are there in 320? A simple way of resolving this ambiguity is to write  $320 = 3.2 \times 10^2$  or  $320 = 3.20 \times 10^2$ , depending on what is intended.
4. Exact numbers are treated as if they have an infinite number of significant figures (2 and  $\pi$  in the expression  $2\pi r$  are examples).

Next, we need to have a systematic way of eliminating the non-significant figures. The process of doing this is called *rounding off*, which is simply a way of estimating or approximating the value of the final number as accurately as possible. First, we define the *rounding digit* as the rightmost significant number. Then the general rules are:

1. If the number just to the right of the rounding digit is *less* than 5, *round down* by dropping all the non-significant figures. The number is now slightly less than the calculated one.
2. If the number just to the right of the rounding digit is *greater* than 5, *round up* by adding 1 to the rounding digit and then dropping the non-significant figures. The number is now slightly greater than the calculated one. Note that rounding 9 up gives 10, not 0.
3. If the number just to the right is *equal* to 5 then there are two cases.
  - (a) If the numbers following the 5 are all zeros, or there are no numbers, round so that the rounding digit is even, that is, round up if it is odd and down if it is even. Zero is treated as even for this purpose. This practice insures that on average we round up or down half of the time.
  - (b) If there are any non-zero numbers to the right of the 5 this means that the total number is greater than 5, so always round up.

In our problem the specified values of  $\beta$  and  $\delta$  have only two significant figures, so the answer should also have only two significant figures. Rounding then gives  $\alpha = 20^\circ$ , which is the same as obtained graphically.

Unfortunately, these conventional rules sometimes gives misleading uncertainties. This is especially the case when numbers are multiplied or divided. An effort to improve

<sup>7</sup>We use the International System of Units (SI) throughout the book (for more details see <http://physics.nist.gov/cuu/>). Its application here is the rule that a zero should be placed in front of the decimal marker in decimal fractions (for example  $2/100$  is written as 0.02 *not* .02). By convention three-digit groups in numbers with more than four digits are separated by a thin space *not* a comma. This avoids any confusion with the comma sometimes used as a decimal marker.

the rounding rules is described by Mulliss and Lee (1998) and Lee *et al.* (2000).<sup>8</sup> A workable alternative is to simply accept the fact that these rules are, and were always meant to be, only approximate (Earl, 1988).

An additional complication occurs when numbers are combined: the uncertainties are propagated to the final answer. An investigation of such errors is a superior way of evaluating uncertainties, and we return to this important matter in §2.10.

## 1.8 Cotangent method

There is a useful short-cut method for determining the relationships between  $\alpha$ ,  $\beta$  and  $\delta$  which combines a simple geometrical construction with trigonometric data (Kitson, 1929).

### Problem

- If  $\delta = 36^\circ$  and  $\beta = 30^\circ$ , what is  $\alpha$ ?

### Construction

1. From point  $O$  on strike line  $S_1$  measure distance  $\cot \delta = 1/\tan \delta = 1.37638$  in the true dip direction using a convenient scale and plot point  $A$  (Fig. 1.12a).
2. Construct strike line  $S_2$  through point  $A$  parallel to  $S_1$ .
3. An oblique line through  $O$  making an angle  $\beta$  with  $S_1$  intersects  $S_2$  at point  $B$ .
4. Using the same scale, measure distance  $OB = \cot \alpha$ .

### Answer

- Length  $OB = \cot \alpha = 2.75$  and therefore  $\alpha = \arctan(1/2.75) = 20^\circ$ .

In problems such as these which involve lengths calculated from angles, the plots and measurements should generally be accurate to at least two decimal places so that angles can be determined to the nearest degree. There are, however, some situations where greater accuracy is desirable.

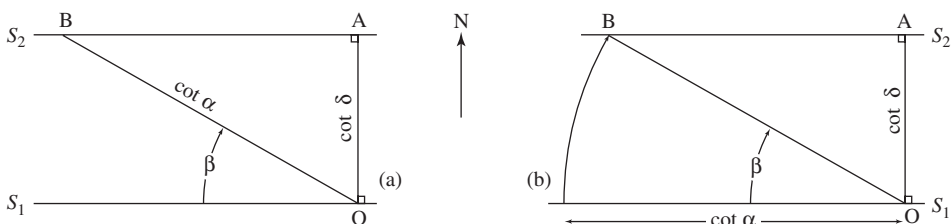


**Figure 1.12** Cotangent method: (a) apparent dip; (b) structural bearing.

<sup>8</sup>These two articles can be found at <http://www.angelfire.com/oh/cmulliss/index.html>.

In terms of the fully graphical technique with folding lines, the use of the cotangent function is equivalent to choosing depth  $d = 1$ . This short-cut gives a solution more quickly, while still retaining the visual advantages of the completely graphical approach. It is especially useful when dealing with small dip angles, which are difficult to construct accurately at any reasonable scale.

If an apparent dip is known, it is a simple matter to reverse this construction to find the angle of true dip. A closely related problem involves finding the structural bearing of a line whose apparent dip angle is specified.

### Problem

- If  $\delta = 36^\circ$  and  $\alpha = 20^\circ$ , what is  $\beta$ ?

### Approach

- To determine the structural bearing of a line we must construct the horizontal right-triangle  $OAB$  of Fig. 1.12a. We may easily find the length of side  $OB$  from the angle of apparent dip. The problem is then reduced to discovering its trend. This may be done simply with the cotangent method.

### Construction

1. On a map draw a strike line  $S_1$  and line  $OA$  in the direction of true dip (Fig. 1.12b).
2. In this dip direction measure a distance  $OA = \cot \delta$  using a convenient scale. Through  $A$  draw a second strike line  $S_2$ .
3. We now need a line whose length is equal to  $\cot \alpha$  using the same scale. It does not matter where we draw this line, but it is convenient to measure it along the existing line  $S_1$ .
4. With point  $O$  as center and length  $\cot \alpha$  as radius, swing an arc to locate point  $B$  on  $S_2$ . Line  $OB$  is then the trend of the line of apparent dip and the angle it makes with  $S_1$  and  $S_2$  is  $\beta$ .

### Answer

- The structural bearing  $\beta = 30^\circ$ . Note that two trends satisfy this angle, N 60 W and N 60 E.

## 1.9 True dip and strike

In some field situations it may not be possible to measure the true dip and strike directly. However, if apparent dips in two different directions are known, the attitude of the plane can be determined.

### Problem

- From the two apparent dips 20/296 and 30/046 determine the true dip and strike of the plane.

### Approach

- Two lines on the plane whose inclinations are the apparent dip angles  $\alpha_1$  and  $\alpha_2$  intersect at a point. Three points determine a plane, so two additional points must be found. A second point is located from a vertical triangle containing one of the apparent dips using a folding line. A third point, associated with the second apparent dip, could be found in like manner. However, it is advantageous to locate this third point at the same elevation as the second. A line joining these points of equal elevation is, by definition, a line of strike. The true dip is then measured perpendicular to this line.

### Construction

- From a local origin  $O$  plot the trends of the two apparent dip directions in map view (Fig. 1.13).
- Construct vertical sections in each of these apparent dip directions.
  - With the first line as  $FL1$  locate  $B_1$  at an arbitrary distance  $l_1$ . Construct the vertical triangle  $B_1 O Y_1$  using  $\alpha_1$  and thus determine the depth  $d$  to  $Y_1$  on the plane below surface point  $B_1$ .
  - With the second line as  $FL2$ , construct the vertical triangle  $B_2 O Y_2$  using  $\alpha_2$ . This time the traverse length  $l_2$  is determined by using the same depth  $d$  and this locates surface point  $B_2$ .
- Because  $Y_1$  and  $Y_2$  have identical depths below the common point  $O$  they also have equal elevations. A line through the two corresponding surface points  $B_1$  and  $B_2$  is then a line of strike.
- From  $O$  a line perpendicular to the strike and intersecting it at point  $A$  establishes the direction of true dip. At the same depth  $d$  below  $A$ , point  $X$  lies on the horizontal line  $Y_1 Y_2$ . With this true dip direction as  $FL3$  locate  $X$  at the same depth  $d$  below  $A$ . Angle  $AOX$  is the true dip angle.

### Answer

- The plane strikes east-west and dips  $40^\circ$  north.

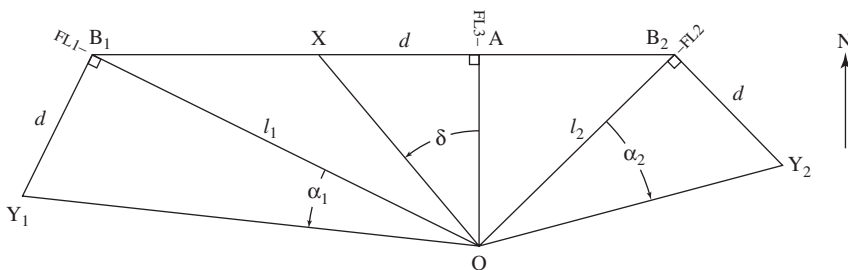


**Figure 1.13** True dip and strike from two apparent dips using folding lines.

This type of problem may be solved even more quickly by the cotangent method. This is particularly useful in situations where measurements have been made by tape because they do not have to be converted to degrees (Rich, 1932). For example, if the map distance  $l$  and the vertical distance  $d$  are measured then

$$\cot \alpha = l/d,$$

and this length can be used directly to construct a diagram. This is also a useful way of handling small dip angles, which are difficult to plot accurately at any reasonable scale.

### Problem

- From the two apparent dips 20/296 and 30/046 determine the true dip and strike of the plane using the cotangent method.

### Construction

1. In map view, plot rays from a single point  $O$  in each of the two apparent directions (Fig. 1.14).
2. Locate point  $B_1$  at a distance  $l_1 = \cot \alpha_1 = 2.74748$  and point  $B_2$  at a distance  $l_2 = \cot \alpha_2 = 1.73205$  along their respective rays using a convenient scale.
3. Line  $B_1B_2$  represents the strike direction.
4. The perpendicular distance  $OA$  to this strike line is  $\cot \delta = 1.19$  using the same scale.

### Answer

- The strike is east-west and the dip  $\delta = \arctan(1/1.19) = 40^\circ$  due north.

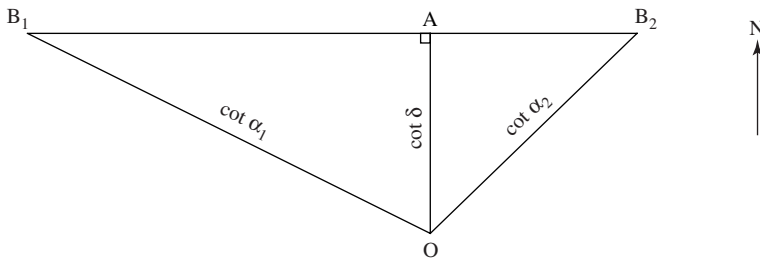


**Figure 1.14** Dip and strike from two apparent dips by the cotangent method.

## 1.10 Dip vectors

An alternative way of representing and manipulating angles of true and apparent dip is with vectors (Harker, 1884; Hubbert, 1931). Not only does this make use of the well-established concepts and methods of vector algebra, but it also opens up other possibilities which we explore in later chapters. Accordingly, we represent the attitude of a inclined



plane on a map with the *true dip vector*  $\mathbf{D}$ . This vector is horizontal and points in the direction of true dip. Its magnitude or length is equal to the slope of the dip angle:

$$D = \tan \delta. \quad (1.8a)$$

Similarly, we define the magnitude of the *apparent dip vector*  $\mathbf{A}$  as

$$A = \tan \alpha. \quad (1.8b)$$

These vectors, like the conventional dip and strike symbols, are two-dimensional representations of lines on an inclined plane.

We may now determine the angle of apparent dip in any direction specified by a unit vector  $\hat{\mathbf{u}}$  from the *scalar* or *dot product* of  $\mathbf{D}$  and  $\hat{\mathbf{u}}$ . By definition

$$\mathbf{A} = \mathbf{D} \cdot \hat{\mathbf{u}} = Du \cos \phi \quad (1.9)$$

where  $\phi$  is the angle between  $\mathbf{D}$  and  $\hat{\mathbf{u}}$ . Geometrically, the scalar product represents magnitude of the projection of one vector onto another (Halliday & Resnick, 1978, p. 22). Because  $D = \tan \delta$  and  $u = 1$ , Eq. 1.8 becomes

$$\boxed{\tan \alpha = \tan \delta \cos \phi.} \quad (1.10)$$

Because  $\phi = 90 - \beta$  this is equivalent to Eq. 1.6.

### Problem

- If  $\delta = 36$  and  $\phi = 90^\circ - \beta = 60^\circ$ , what is  $\alpha$ ?

### Construction

1. From a point  $O$  draw  $\mathbf{D}$  in the dip direction with scaled length  $\tan \delta = 0.72654$  (Fig. 1.15a).
2. Vector  $\hat{\mathbf{u}}$  from  $O$  with unit length and making an angle of  $\phi$  with  $\mathbf{D}$  represents the direction of  $\mathbf{A}$ .
3. The projection of  $\mathbf{D}$  onto  $\hat{\mathbf{u}}$  fixes the magnitude of  $\mathbf{A}$ .

### Answer

- $A = \tan \alpha = 0.36$  and therefore  $\alpha = 20^\circ$ . As this construction shows,  $\mathbf{A}$  is clearly a *component* of  $\mathbf{D}$ .

We can, of course, reverse this construction to determine the magnitude of  $\mathbf{D}$  and the angle it makes with  $\hat{\mathbf{u}}$  from a known apparent dip vector  $\mathbf{A}$  (Fig. 1.15b).

A straightforward extension of this construction then allows the true dip vector  $\mathbf{D}$  to be found from two apparent dip vectors  $\mathbf{A}_1$  and  $\mathbf{A}_2$ . The following procedure solves the problem of Fig. 1.13 or Fig. 1.14.

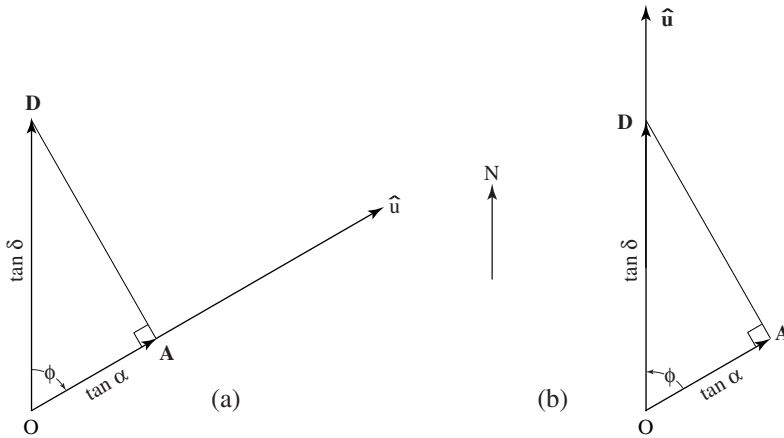


**Figure 1.15** Dip vectors: (a) **A** from **D**; (b) **D** from **A**.

**Problem**

- From apparent dip vectors **A**<sub>1</sub>(20/296) and **A**<sub>2</sub>(30/046) find the true dip vector **D**.

**Construction**

1. In map view draw vectors **A**<sub>1</sub> and **A**<sub>2</sub> radiating from point **O** with lengths  $A_1 = \tan \alpha_1 = 0.363\ 97$  and  $A_2 = \tan \alpha_2 = 0.577\ 35$  using a convenient scale (Fig. 1.10).
2. Draw perpendiculars from the tips of each of these apparent dip vectors.
3. These projection lines intersect to locate the tip of the dip vector **D** and its scaled length is  $\tan \delta = 0.84$ .

**Answer**

- The dip vector **D** makes an angle  $\phi_1 = 64^\circ$  with **A**<sub>1</sub> and  $\delta = \arctan(0.84) = 40^\circ$ .

This vector approach also leads to a simple analytical solution. Representing the two apparent dips by vectors **A**<sub>1</sub> and **A**<sub>2</sub> then

$$\tan \alpha_1 = \mathbf{D} \cdot \hat{\mathbf{u}}_1 \quad \text{and} \quad \tan \alpha_2 = \mathbf{D} \cdot \hat{\mathbf{u}}_2$$

where the unit vectors  $\hat{\mathbf{u}}_1$  and  $\hat{\mathbf{u}}_2$  represent the directions of the known apparent dips. Labeling the angles which the unknown vector **D** makes with each of these  $\phi_1$  and  $\phi_2$ , then with Eq. 1.9 we have

$$\tan \alpha_1 = \tan \delta \cos \phi_1 \quad \text{and} \quad \tan \alpha_2 = \tan \delta \cos \phi_2.$$

Solving each for  $\tan \delta$  and equating the two results gives

$$\frac{\tan \alpha_1}{\cos \phi_1} = \frac{\tan \alpha_2}{\cos \phi_2} \quad \text{or} \quad \tan \alpha_2 \cos \phi_1 = \tan \alpha_1 \cos \phi_2. \tag{1.11}$$

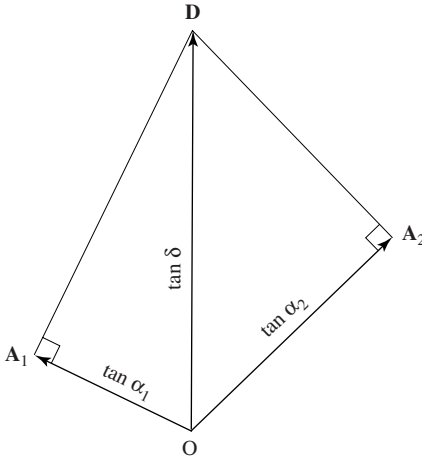


**Figure 1.16** Vector solution of true dip and strike.

Labeling the total angle between  $\hat{u}_1$  and  $\hat{u}_2$  as  $\phi$  we can express angle  $\phi_1$  in terms of  $\phi$  and  $\phi_2$ . There are two cases.

1. If  $D$  lies between  $A_1$  and  $A_2$  (Fig. 1.17a), then  $\phi = \phi_1 + \phi_2$  or  $\phi_2 = (\phi - \phi_1)$ .
2. If  $D$  lies outside  $A_1$  and  $A_2$  (Fig. 1.17b), then  $\phi = \phi_1 - \phi_2$  or  $\phi_2 = (\phi_1 - \phi)$ .

Using the identity for the cosine of the difference of two angles yields the identical results:

$$\cos \phi_2 = \cos(\phi - \phi_1) = \cos(\phi_1 - \phi) = \cos \phi \cos \phi_1 + \sin \phi \sin \phi_1.$$

Substituting this result, Eq. 1.11 becomes

$$\tan \alpha_2 \cos \phi_1 = \tan \alpha_1 (\cos \phi \cos \phi_1 + \sin \phi \sin \phi_1).$$

We solve this for  $\phi_1$  by expanding, dividing through by  $\cos \phi_1$  and rearranging. The result is

$$\boxed{\tan \phi_1 = \frac{\tan \alpha_2}{\tan \alpha_1 \sin \phi} - \frac{1}{\tan \phi}.}$$
 (1.12)

With both  $\phi_1$  and  $\alpha_1$  known, the true dip can be found from (see Eq. 1.10)

$$\boxed{\tan \delta = \frac{\tan \alpha_1}{\cos \phi_1}.}$$
 (1.13)

For Case 1 (Fig. 1.17a), from the previous problem,  $\alpha_1 = 20^\circ$ ,  $\alpha_2 = 30^\circ$  and  $\phi = 110^\circ$  and we find that  $\phi_1 = 64^\circ$  and  $\delta = 40^\circ$ .

For Case 2 (Fig. 1.17b),  $\alpha_1 = 20^\circ$ ,  $\alpha_2 = 30^\circ$  and  $\phi = 18^\circ$  and we find that  $\phi_1 = 64^\circ$  and  $\delta = 40^\circ$ . An ambiguity may arise in this case. By labeling the apparent dip angles so that  $\alpha_1 < \alpha_2$  the angle  $\phi_1$  is always measured from  $A_1$  toward  $A_2$  and this avoids any problem.

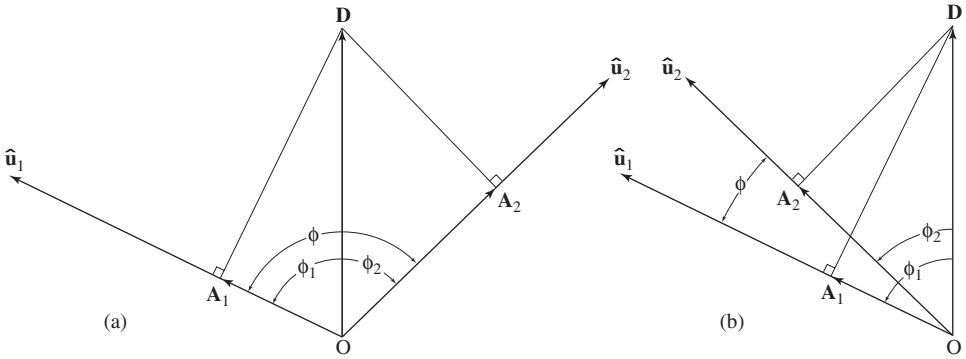


**Figure 1.17** Analytical solution of the problem of true dip and strike: (a) Case 1; (b) Case 2.

### 1.11 Three-point problem

These methods can also be used to determine the attitude of a plane if the location of *three* points on it are known.<sup>9</sup> It is convenient to label the highest point  $O$ . Then from the map distances  $l$  and elevation difference  $\Delta h$  to each of the other points, the apparent dip in each of these directions is calculated using

$$\tan \alpha = \Delta h/l \quad \text{or} \quad \alpha = \arctan(\Delta h/l). \tag{1.14}$$

With both  $\alpha_1$  and  $\alpha_2$  known, the procedure is then just as before.

In the special case of small elevation differences over large distances, a satisfactory solution requires that the locations of the three points be very accurately known. This can be accomplished with modern electronic surveying equipment.<sup>10</sup>

In these circumstances a graphical solution would require a very large drawing as well as large drafting tools and this is not practical.

<sup>9</sup>Additional details of this three-point problem are treated in Chapters 3 and 7.

<sup>10</sup>The electronic *total station* is a distance measurement device based on a phase comparison of reflected light from a semiconducting laser, and an electronic theodolite for measures angles, together with the attendant electronics to reduce and digitally record the data, as well as compute the coordinate geometry. It has wide application to mapping (see Philpots, *et al.*, 1997). For a typical instrument, the standard deviation of a length measurement is  $\pm 2$  mm + 2 parts per million of the measurement length, and the angular measurement has a standard deviation of  $\pm 3$  seconds of arc. For a 1 km measurement, the range has a standard deviation of  $\pm 4$  mm. Angles are less precisely determined:  $\pm 24.4$  mm in radial distance normal to the measurement direction. For more information see [www.leica-geosystems.com](http://www.leica-geosystems.com) and click on Products.

Table 1.1 Data for the three-point problem

	$l$	$\Delta h$	$t$
$P_1$	983.3 m	-24.7 m	23.8°
$P_2$	1563.6 m	-48.3 m	76.4°

### Problem

- Three points are located on a structural plane. From the base point  $O$ , map distances  $l_1$  and  $l_2$  and elevation differences  $\Delta h_1$  and  $\Delta h_2$  together with the trends  $t_1$  and  $t_2$  to points  $P_1$  and  $P_2$  are measured using an electronic surveying instrument (see Table 1.1 and Fig. 1.18a). Determine the dip and strike of the plane.

### Answer

- From the measured data calculate the magnitudes of the apparent dip vectors in the directions  $OP_1$  and  $OP_2$  using Eq. 1.12:  $\tan \alpha_1 = 24.7/983.3 = 0.0251$  ( $\alpha_1 = 1.4839$ ) and  $\tan \alpha_2 = 48.3/1563.6 = 0.0309$  ( $\alpha_2 = 1.8406$ ). The angle between these two apparent dip vectors  $\phi = t_2 - t_1 = 52.6^\circ$  (Fig. 1.18b). Using these values in Eq. 1.11 we find  $\phi_1 = 40.2255^\circ$ . Then Eq. 1.12 gives  $\delta = 1.88^\circ$  (with three significant figures in the input data, the three figures in this answer are also significant).

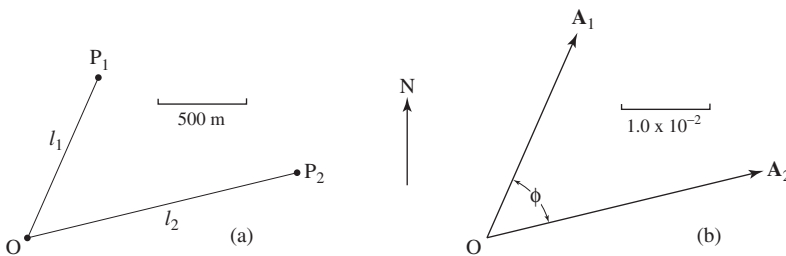


Figure 1.18 Three-point problem: (a) map of surveyed points; (b) apparent dip vectors.

## 1.12 Observed apparent dips

The attitude of a structural plane is based on field observation and there is a case that requires special care. Suppose that the trace of a dipping plane is exposed on a vertical plane. With a line of sight perpendicular to this exposure, the observed angle is, in general, an apparent dip. However, if the line of sight is oblique, either to the right or to the left, the observed angle is no longer the apparent dip but rather an “apparent” apparent dip. From Fig. 1.19 we have

$$h = l \tan \alpha, \quad w' = w \sin \beta, \quad \tan \alpha' = h/w',$$

where  $\alpha$  is the apparent dip,  $w$  is the outcrop width,  $h$  is the outcrop height,  $h'$  is the apparent height seen in the oblique view,  $\alpha'$  is the observed angle and  $\beta$  is the angle the line of sight makes with the exposure plane. Substituting the first two relationships into the third yields

$$\tan \alpha' = \frac{\tan \alpha}{\sin \beta}. \tag{1.15}$$

Figure 1.21a is a graph of this equation, where it can be seen that the observed angle  $\alpha'$  is always greater than  $\alpha$  and that small angles are distorted relatively more.

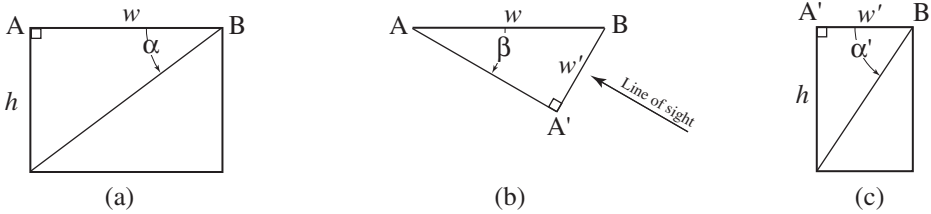


**Figure 1.19** Observed apparent dip: (a) direct view of vertical exposure plane; (b) top view of exposure and oblique line of sight in the horizontal plane; (c) observed angle of inclination.

Similarly, if the line of sight lies in a vertical plane perpendicular to the exposure but oblique to the plane of the exposure, the observed angle again is not the apparent dip. From Fig. 1.20 we have

$$w = h / \tan \alpha, \quad h' = h \sin \gamma, \quad \tan \alpha' = h' / w,$$

where  $\gamma$  is the angle the line of sight makes with the exposure plane and  $h'$  is the apparent height. Substituting the first two expressions into the third yields

$$\tan \alpha' = \tan \alpha \sin \gamma. \tag{1.16}$$

Figure 1.21b is a graph of this equation where it can be seen that the observed angle is always less than  $\alpha$  and large angles are distorted relatively more.

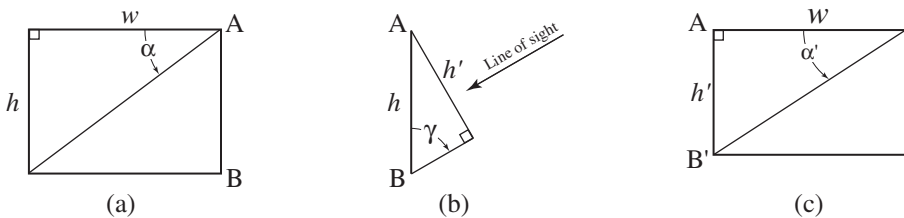


**Figure 1.20** Observed apparent dip: (a) direct view of vertical exposure plane; (b) side view of exposure plane with oblique line of sight in vertical plane; (c) observed angle.

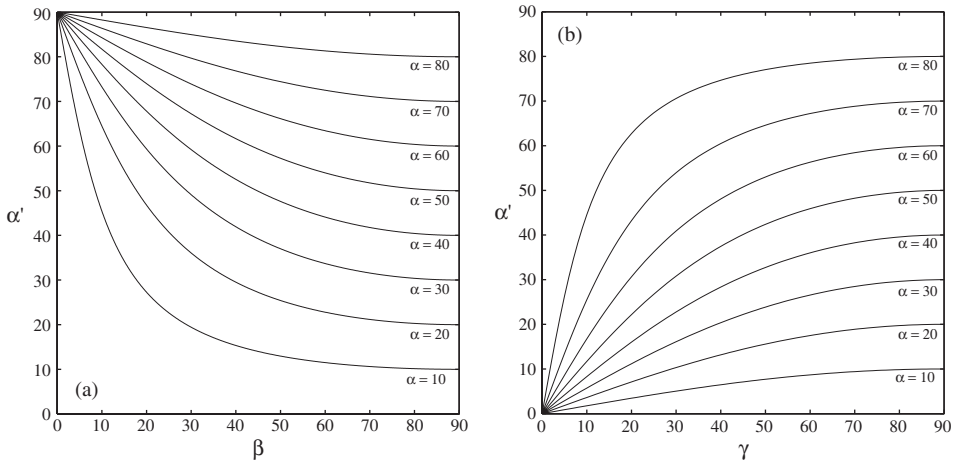


**Figure 1.21** Observed apparent dip: (a)  $\alpha'$  as a function of  $\beta$ ; (b) as a function of  $\gamma$ .

More generally, if the line of sight is neither horizontal nor in the plane perpendicular to the exposure the resulting observed angle is mixed – for some apparent dip angles and certain oblique lines of sight the observed angle may be either less or greater. The essential point is that if you find yourself making such observations be careful.

### 1.13 Exercises

These exercise problems are meant to introduce you to the power of graphical methods in geology and to help you learn the basic geometrical concepts of structural geology and “see” in 3D. Neatness in the constructions is important. Showing all your construction lines and writing a brief explanation of your steps will help make things clearer (such notes will also be an aid for future reference).

- Using the following data determine the unknown component graphically, and check your results trigonometrically. Each graphical result should be within  $1^\circ$  of the calculated value. If it is not then repeat your construction using greater care, making it larger, or both.
  - If the attitude of a plane is N 75 W, 22 N, what is the apparent dip in the direction N 50 E?
  - An apparent dip is 33, N 47 E, and the true strike is N 90 E. What is the true dip?
  - The true dip is  $40^\circ$  due north. In what direction will an apparent dip of  $30^\circ$  be found?
- A certain bed dips 40/000. In what direction will the apparent dip be exactly half as great. Will this same relationship hold if the bed dips  $10^\circ$ ,  $20^\circ$ ,  $50^\circ$ , or  $80^\circ$ ? If not, why not?

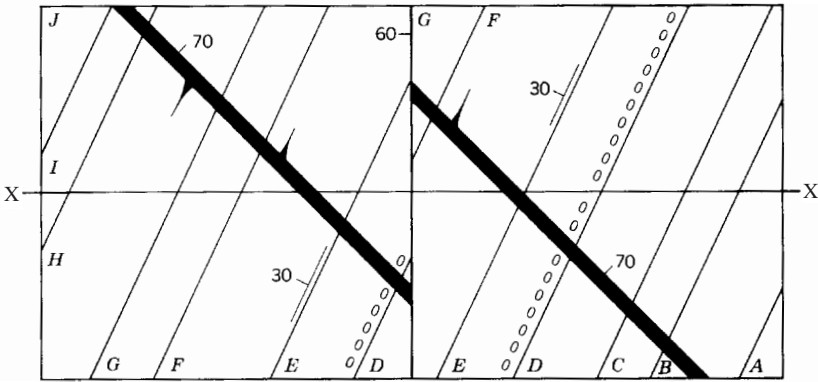


**Figure 1.22** Construction of a cross section from a simple map of dipping planes.

3. Three points *A*, *B* and *C* on an inclined plane have elevations of 150 m, 75 m and 100 m respectively. The map distance from *A* to *B* is 1100 m in a direction of N 10 W, and from *A* to *C* is 1560 in a direction of N 40 E. What is the attitude of the plane? (Hint: use Eq. 1.3 to determine two apparent dips.)
4. The most important need for the apparent dip arises during the construction of structure sections. Figure 1.22 is a simple geology map of an inclined sequence of sedimentary strata intruded by a basalt dike and the whole cut by a fault. Construct a vertical section along the line *XX'* showing the traces of the three structural planes with the correct inclination and proper position.
5. What is the maximum potential error in determining the strike direction if the dip is 5° and the maximum operator error is 2°?
6. Using the following data determine the unknown component graphically and check your results trigonometrically. Each graphical result should be within 1° of the calculated value. If it is not, then repeat your construction using greater care, making it larger, or both.
  - (a) If the attitude of a plane is N 85 E 25 NW, what is the apparent dip in the direction N 20 E?
  - (b) If the strike of a bed is 350 and the apparent dip 35 in the direction 300, what is the true dip.
  - (c) If the strike and dip of the bed are (N 45 E 30 SE) what is the apparent dip in the direction S 25 W.
7. A distinctive sandstone bed crops out at three localities in a corner of the Edmundsville Quadrangle. Outcrops *A* and *B* are on the 240 m contour line, and point *C* is on the 170 m contour line. Outcrop *B* is 500 m to the N 40 E of outcrop *A*, and outcrop *C* is 250 m to the N 20 W of outcrop *A*. Assuming that the sandstone is homoclinal (constant dip), what is its attitude? (1) Using the following data determine the unknown component graphically and check your results trigonometrically. Each graphical result



should be within  $1^\circ$  of the calculated value. If it is not, then repeat your construction using greater care, making it larger, or both. (a) If the attitude of a plane is N 85 W 19 NE, what is the apparent dip in the direction N 40 W? (b) Given the strike of a bed 350 and the apparent dip 25 in the direction 280, determine the true dip. (c) Given the strike and dip of the bed (N 85 W 30 SW) determine the apparent dip in the direction S 60 W. (2) A distinctive sandstone bed crops out at three localities in a corner of the Edmundsville Quadrangle. Outcrops A and B are on the 240 m contour line, and point C is on the 180 m contour line. Outcrop B is 400 m to the N 40 E of outcrop A, and outcrop C is 240 m to the N 20 W of outcrop A. Assuming that the sandstone is homoclinal (constant dip), what is its attitude?

# 2

## Thickness and depth

### 2.1 Definitions

**Thickness:** the perpendicular distance between the parallel planes bounding a tabular body, as displayed on any section perpendicular to these planes; also called the true or stratigraphic thickness (Fig. 2.1).

**Apparent thickness:** the distance between the bounding planes measured in some other direction, for example, the perpendicular distance between the traces of the bounding planes on an oblique section, or in some other specified direction, as in a drill hole. It is always greater than true thickness.

**Outcrop width:** the strike-normal distance between the traces of the parallel bounding planes measured at the earth's surface. It may be measured horizontally or on an incline.

**Depth:** the vertical distance from a specified level (commonly the earth's surface) downward to a point, line or plane.

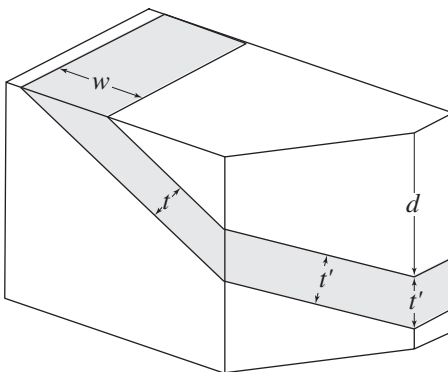


**Figure 2.1** True thickness  $t$ , apparent thickness  $t'$ , outcrop width  $w$  and depth  $d$ .

## 2.2 Thickness determination

Although geologists may determine the thickness of any stratiform body of rock, most often the concern is with the thickness of layers of sedimentary rocks. In this context “measuring a section” generally refers to a lithologic description of the rock strata as well as a determination of their thicknesses (Kottowski, 1965; Compton, 1985). Here, the concern is with thickness alone. The thickness of a layer may be determined in a number of ways. In special circumstances it may be possible to measure it directly, otherwise it must be determined from indirect measurements.

## 2.3 Thickness by direct measurement

Several examples will illustrate how thickness may be measured directly. In a simple case the thickness of a horizontal layer exposed on a vertical cliff face may be obtained by hanging a measuring tape over the edge of the cliff (Fig. 2.2a). Alternatively, if the elevations of the top and bottom of the horizontal layer can be determined accurately, the thickness is simply the difference of the two elevations regardless of slope angle. Another special case involves the exposure of a vertical layer on a horizontal surface; a tape measure extended perpendicular to the strike allows the thickness to be obtained directly (Fig. 2.2b).

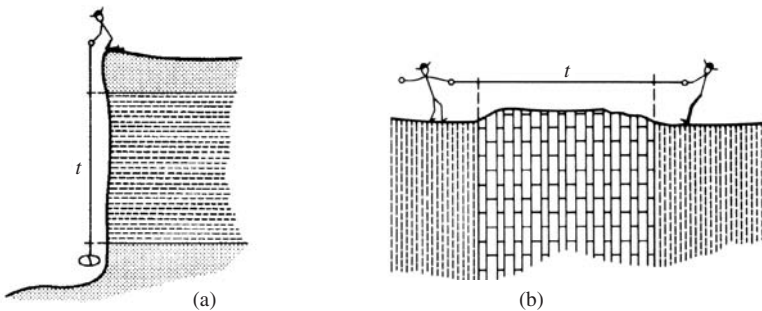


**Figure 2.2** Direct measurement of thickness: (a) horizontal layer; (b) vertical layer.

More generally, thickness may be measured directly regardless of the relationship between slope and dip with a Jacob’s staff (a light pole with gradations and clinometer or Brunton compass attached at the top; see Robinson, 1959; Hansen, 1960; Freeman, 1991, p. 25). The staff is tilted toward the dip direction through the dip angle (Fig. 2.3a) and a point on the ground is sighted in. The thickness of the layer or portion of the layer between the base of the staff and the sighted point is equal to the length of the staff (Fig. 2.3b). For layers less than staff height the gradations are used, and by occupying successive positions units of any thickness may be measured (Fig. 2.3c).

The principle common to each of these approaches is that if a line of sight can be obtained parallel to the dip direction, the layer appears in edge view, and the true thickness

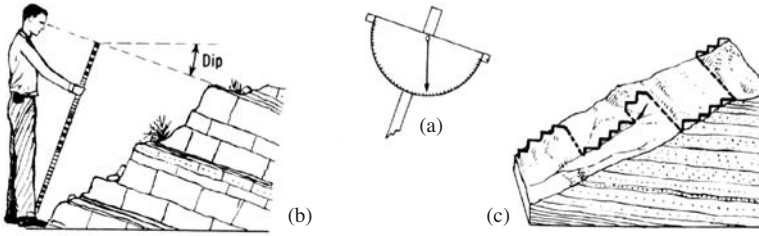


**Figure 2.3** Thickness with a Jacob's staff: (a) simple clinometer; (b) sighting down the dip; (c) stepwise course of measurements (from Compton, 1985, p. 230, with permission of John Wiley).

can be obtained by measuring across this view perpendicular to the two parallel bounding planes.

## 2.4 Thickness from indirect measurements

When direct measurement of thickness is not possible, there are several alternatives. Which of these is adopted depends on the field situation, on the equipment at hand, on the accuracy required, and finally on personal preference. Given a choice, it is always desirable to make the most nearly direct measurements possible.

All the solutions of true thickness require an edge view of the layer, that is, the image of the layer on a plane perpendicular to bedding. Of the many such planes one can always be readily found or constructed – it is the vertical plane parallel to the line of true dip.

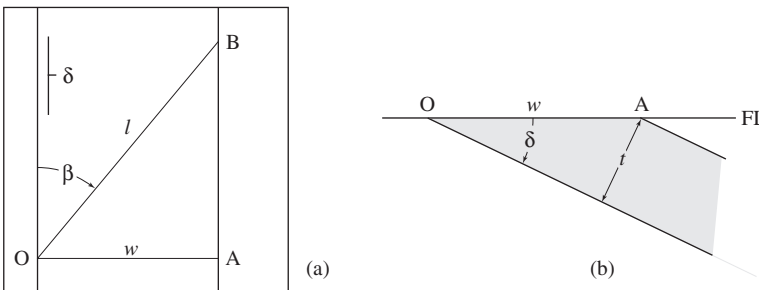


**Figure 2.4** Thickness from horizontal, strike-normal traverse of length  $w$ : (a) map; (b) strike-normal section.

The simplest of the indirect approaches is to measure the width of the exposed layer perpendicular to the strike direction on a horizontal plane ( $OA$  in Fig. 2.4a). Two measurements are required: the outcrop width  $w$  of the layer and the dip angle  $\delta$ . Then the thickness  $t$  can be determined graphically in either of two ways.

1. With the map, a folding line can be used to construct a strike-normal section, a procedure which is virtually identical to that used in problems of dip and strike in Chapter 1.
2. The field measurements can be used to plot the required section directly (Fig. 2.4b).

The thickness may also be calculated from

$$t = w \sin \delta. \quad (2.1)$$

Because of obstructions or lack of exposure it is not always possible to make measurements in the strike-normal direction. For an oblique horizontal traverse ( $OB$  in Fig. 2.4a), a correction is required.<sup>1</sup> In effect, the traverse length  $l$  is too long and must be reduced to the equivalent outcrop width  $w$ . This adjustment can be made with a scaled drawing of the horizontal right triangle  $OAB$ . Then just as in the previous case the thickness can be measured on the strike-normal section (Fig. 2.4b). The correction may also be calculated from

$$w = l \sin \beta,$$

where  $\beta$  is the structural bearing of the traverse. A complete analytical solution can be obtained by substituting this result into Eq. 2.1 giving

$$t = l \sin \beta \sin \delta. \quad (2.2)$$

In the more general case, thickness is determined from measurements made on sloping ground. We first consider the case where it is possible to measure the outcrop width directly. There are two alternatives.

1. Thickness can be determined from the slope distance and slope and dip angles along the measured strike-normal traverse.
2. It can also be found from the vertical and horizontal distances between the two ends of the traverse if the slope angle is known.

Each approach has advantages. The first method yields simpler relationships. The second is convenient when highly variable slopes are involved and it can also be used to obtain thickness from measurements made directly on a geological map.

When the outcrop width is measured directly, the approach is closely related to the result of Fig. 2.4, except that thickness is now a function of both dip angle  $\delta$  and slope angle  $\sigma$  (sigma). There are seven cases, and all are easily solved graphically from a simple scaled cross section based on the field measurements (see Fig. 2.5). Analytical solutions are also available for all cases.

1. Slope and dip are in the same direction,  $\delta < \sigma$  (Fig. 2.5a),

$$t = w \sin(\sigma - \delta). \quad (2.3a)$$

<sup>1</sup>Note that a vertical section constructed in the direction  $OB$  using the apparent dip angle would show the apparent thickness not the true thickness.

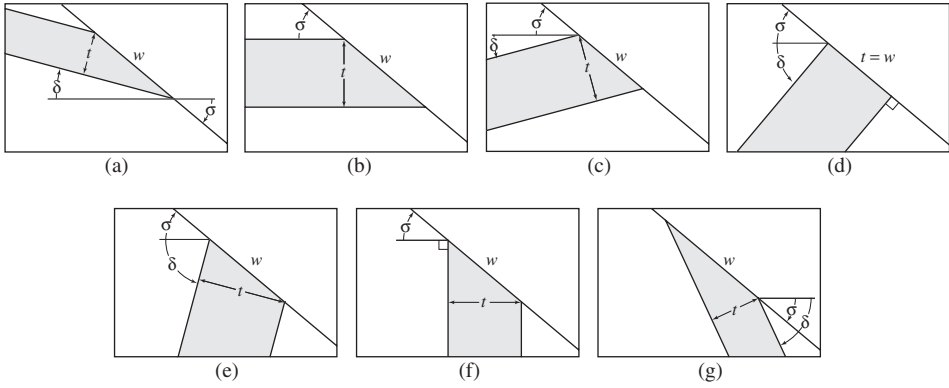


**Figure 2.5** Thickness determination from a strike-normal traverse on a slope.

2. The bed is horizontal,  $\delta = 0^\circ$  (Fig. 2.5b),

$$t = w \sin \sigma. \quad (2.3b)$$

3. Slope and dip are in the opposite directions,  $(\delta + \sigma) < 90^\circ$  (Fig. 2.5c),

$$t = w \sin(\delta + \sigma). \quad (2.3c)$$

4. Slope and dip are in the opposite directions,  $(\delta + \sigma) = 90^\circ$  (Fig. 2.5d),

$$t = w. \quad (2.3d)$$

5. Slope and dip are in the opposite directions,  $(\delta + \sigma) > 90^\circ$  (Fig. 2.5e),

$$t = w \sin [180 - (\delta + \sigma)] = w \sin(\delta + \sigma). \quad (2.3e)$$

6. The bed is vertical,  $\delta = 90^\circ$  (Fig. 2.5f),

$$t = w \sin(90 - \sigma) = w \sin(90 + \sigma). \quad (2.3f)$$

7. Slope and dip are in the same direction,  $\delta > \sigma$  (Fig. 2.5g),

$$t = w \sin(\delta - \sigma). \quad (2.3g)$$

All these separate cases can be expressed as a single equation by adopting a special sign convention.

1. If the slope and dip are in *opposite* directions the *sum*  $(\delta + \sigma)$  is used.
2. If the slope and dip are in the *same* direction the *difference*  $(\delta - \sigma)$  or  $(\sigma - \delta)$  is used.

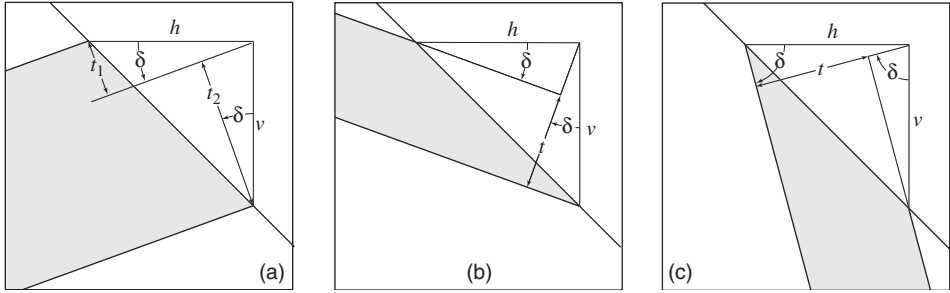


**Figure 2.6** Thickness from horizontal  $h$  and vertical  $v$  components.

The general equation is then

$$t = w \sin |\delta \pm \sigma| \tag{2.4}$$

where, because a negative thickness has no meaning, the absolute value of the angle is used.

The second approach involves determining the horizontal  $h$  and vertical  $v$  distances between two end points of a strike-normal traverse (Fig. 2.6). Again the stratum may be dipping in the same direction as the slope and/or the dip and slope directions may be opposite. In each case it is a simple matter to plot the field data on a scaled vertical section and measure the thickness. Thickness may also be computed. The general approach requires expressions for two partial thicknesses:

$$t_1 = h \sin \delta \quad \text{and} \quad t_2 = v \cos \delta.$$

There are two main cases.

1. If the slope and dip are in *opposite* directions then  $t = (t_1 + t_2)$  (Fig. 2.6a).
2. If the slope and dip are in the *same* directions the total thickness is the difference of the two partial thicknesses. There are two subcases:
  - (a) If  $(\delta < \sigma)$  then  $t = (t_1 - t_2)$  (Fig. 2.6b).
  - (b) If  $(\delta > \sigma)$  then  $t = (t_2 - t_1)$  (Fig. 2.6c).

Using the same sign convention as before all three cases can then be written as

$$t = |h \sin \delta \pm v \cos \delta|. \tag{2.5}$$

The more general case involves an oblique traverse (Fig. 11). From the horizontal right-triangle  $ABD$ , the horizontal distance  $h$  in the strike-normal direction between the two stations is given by

$$\sin \beta = h/h' \quad \text{or} \quad h = h' \sin \beta, \tag{2.6}$$

where  $h'$  is the horizontal distance in the oblique direction between the two stations. If a graphical solution is desired, first obtain the distance  $h$  from the map and then plot the data on a strike-normal section. The full analytical solution is obtained by substituting Eq. 2.6 into Eq. 2.5 to give

$$t = |h' \sin \beta \sin \delta \pm v \cos \delta|. \quad (2.7)$$

If the slope length and slope angle, rather than the horizontal and vertical distances, are measured in an oblique direction, it would seem to be a simple matter to introduce a similar correction, but there is no easy way of measuring the appropriate angle in the field ( $\angle BAC$  of Fig. 11). It is therefore necessary to take a different approach. From the vertical triangle  $ACD$

$$\cos \sigma = h'/l \quad \text{or} \quad h' = l \cos \sigma,$$

where  $l$  is the slope length and  $\sigma$  is now the slope angle in the direction of this oblique traverse. Combining this with Eq. 2.6 then gives

$$h = l \cos \sigma \sin \beta.$$

Again from the vertical triangle  $ACD$ ,

$$\sin \sigma = v/l \quad \text{or} \quad v = l \sin \sigma.$$

Using these expressions for  $h$  and  $v$  in Eq. 2.5 then yields the equation, first derived by Mertie (1922, p. 41),

$$t = l |\cos \sigma \sin \beta \sin \delta \pm \sin \sigma \cos \delta|. \quad (2.8)$$

This general equation for stratigraphic thickness is easily applied in the field. By identifying relatively uniform slope segments exposing strata with constant attitude, lay a tape measure along the surface and directly measure  $l$  for each lithologic unit. With a compass measure the slope  $\sigma$ , structural bearing  $\beta$ , and dip  $\delta$ . Computing the thickness of the individual beds using a spreadsheet on a laptop computer is then easy. By occupying successive slope segments one can rapidly construct a full stratigraphic column of the exposed rocks.

## 2.5 Apparent thickness

In all the previous cases, the true thickness was derived from a measured apparent thickness. In some situations is necessary to determine the apparent thickness from the true thickness, for example, as displayed on an oblique section.



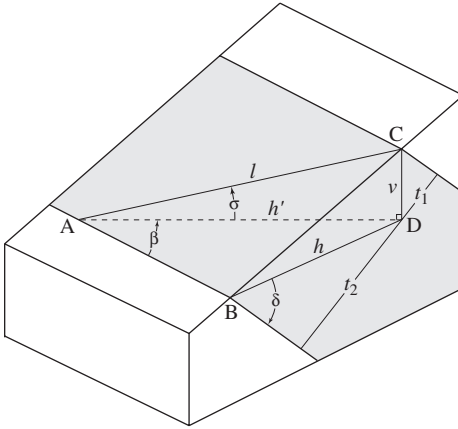


**Figure 2.7** Thickness from an oblique traverse on a slope.

**Problem**

- If the true thickness  $t = 50$  m and the dip  $\delta = 30^\circ$ , what will be the apparent thickness  $t'$  on a vertical section making an angle  $\phi = 40^\circ$  with the dip direction?

**Construction**

1. In a map view represent the outcrop trace of the lower boundary of the layer by strike line  $S_1$  (Fig. 2.8). From a local origin  $O$  on this line draw lines in the true dip direction and the required oblique section line.
2. With the dip line as  $FL1$  and using  $\delta = 30^\circ$  draw the trace of the lower boundary  $OX$ . With a convenient scale construct the trace of the upper boundary at a distance  $t = 50$  m from  $OX$ . This locates point  $A$  on the dip line and the outcrop width  $w = OA$ .
3. On the map draw a second strike line through  $A$  to represent the trace of the upper boundary, thus locating point  $B$  at the intersection of the oblique section. Now the traverse length  $l = OB$ .
4. Using Eq. 1.8 find the angle of apparent dip  $\alpha = 23.9^\circ$  in this direction. With  $OB$  as  $FL2$  draw the trace of the lower boundary inclined  $OY$  at this angle.
5. The perpendicular distance from this inclined trace to point  $B$  is the apparent thickness  $t'$ .

**Answer**

- The apparent thickness  $t' = 53$  m.

An analytical relationship between true and apparent thickness is also useful (Coates, 1945, p. 7; De Paor, 1988, p. 77; De Paor, 1997, personal communication). From Fig. 2.8 the vertical apparent thickness  $t'_v$ , which is the same in triangles  $OAX$  and  $OBY$ , we have

$$t = t'_v \cos \delta \quad \text{and} \quad t = t'_v \cos \alpha.$$

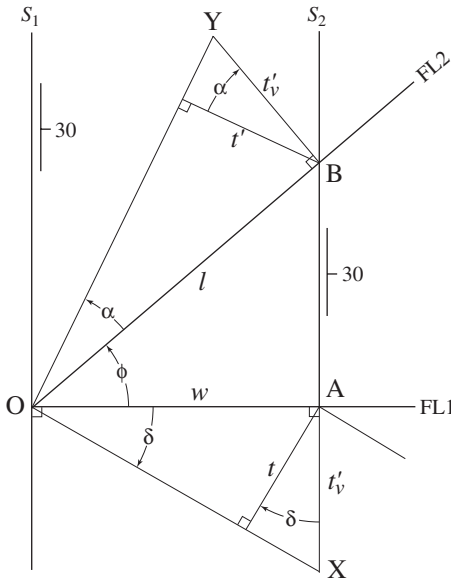


**Figure 2.8** Apparent thickness in an oblique section.

Solving both for  $t'_v$ , equating and rearranging gives

$$t' = \left[ \frac{\cos \alpha}{\cos \delta} \right] t.$$

Substituting the identities

$$\cos \alpha = 1 / \sec \alpha = 1 / \sqrt{1 + \tan^2 \alpha} \quad \text{and} \quad 1 / \cos \delta = 1 / \sqrt{\cos^2 \delta}$$

we then obtain

$$t' = \left[ \frac{1}{\sqrt{1 + \tan^2 \alpha}} \right] \left[ \frac{t}{\sqrt{\cos^2 \delta}} \right].$$

From Eq. 1.8

$$\tan \alpha = \tan \delta \cos \phi \quad \text{or} \quad \tan^2 \alpha = \tan^2 \delta \cos^2 \phi,$$

where  $\phi$  is the angle between the true and apparent dip directions. With this the expression for  $t'$  becomes

$$t' = \left[ \frac{1}{\sqrt{1 + \tan^2 \delta \cos^2 \phi}} \right] \left[ \frac{t}{\sqrt{\cos^2 \delta}} \right] \quad \text{or} \quad t' = \frac{t}{\sqrt{\cos^2 \delta + (\tan^2 \delta \cos^2 \delta) \cos^2 \phi}}.$$

Then with the identities  $\tan \delta \cos \delta = \sin \delta$  and  $\cos^2 \delta = (1 - \sin^2 \delta)$  this becomes

$$t' = \frac{t}{\sqrt{\cos^2 \delta + \sin^2 \delta \cos^2 \phi}} = \frac{t}{\sqrt{(1 - \sin^2 \delta) + \sin^2 \delta (1 - \sin^2 \phi)}}.$$

Expanding and combining terms we finally have

$$t' = \frac{t}{\sqrt{1 - \sin^2 \delta \sin^2 \phi}}. \quad (2.9)$$

From the example problem  $t = 50$  m,  $\delta = 30^\circ$  and  $\phi = 40^\circ$ , then  $t' = 52.8$  m, which is essentially the result obtained graphically.

## 2.6 Thickness between non-parallel planes

Previously the measured layer was taken to be strictly homoclinal, that is, the two bounding planes had identical attitudes. Often, however, the attitudes at the upper and lower ends of a traverse are different. Besides measurement error, which we treat later, there are two possible reasons for such divergencies: The bounding planes may not in fact be parallel because the rock body is wedge-shaped rather than tabular, or the layer may be folded.

If the departure from parallelism is small, thickness may be approximated by using the mean of the two dip angles and the mean of the two structural bearings

$$\delta = \frac{1}{2}(\delta_1 + \delta_2) \quad \text{and} \quad \beta = \frac{1}{2}(\beta_1 + \beta_2) \quad (2.10)$$

in Eqs. 2.2 or 2.8. If the deviation from parallelism is greater, shorter intervals with more nearly parallel boundaries can be treated separately, and the results summed to give an estimate of the total thickness.

If the beds are folded, then the boundaries are curved surfaces rather than planes and the matter is considerably more complicated. If it can be assumed that these bounding surfaces are still parallel, that is, the distance between the two surfaces measured perpendicular to them is constant, then the thickness can be estimated by a simple construction involving tangent arcs (Hewett, 1920).<sup>2</sup>

### Problem

- A strike-normal traverse is made on a slope. The measured strike directions at the upper and lower ends of the traverse are the same, but the dip angles are not. Estimate the thickness of the folded bed.

<sup>2</sup>Following Busk (1929) we use an extended version of this method in §15.3 to reconstruct folds in cross section.

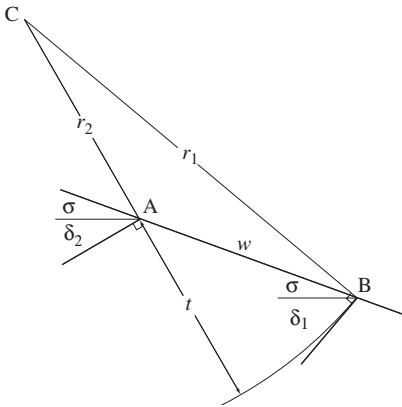


**Figure 2.9** Thickness of a folded layer.

### Construction

1. Draw a scaled cross section showing the slope angle  $\sigma$  along the traverse line and the two measured dip lines at stations  $A$  and  $B$ , where the measured slope distance  $w = AB$  (Fig. 2.9).
2. At each station construct the dip normals  $r_1$  and  $r_2$  to the dip lines to intersect at common point  $C$ .
3. With  $C$  as center, draw an arc with radius of  $BC$ . The thickness  $t$  is the distance between  $A$  and this arc measured in the direction of  $r_2$ .

The thickness in this case may also be obtained trigonometrically. Labeling the dip angles so that  $\delta_1 > \delta_2$  and the corresponding radii  $r_1 > r_2$ , then by the Law of Sines for the oblique triangle  $ABC$  we have

$$\frac{r_1}{\sin A} = \frac{r_2}{\sin B} = \frac{w}{\sin C}.$$

The lengths of the two radii are then

$$r_1 = \frac{w \sin A}{\sin C} \quad \text{and} \quad r_2 = \frac{w \sin B}{\sin C}.$$

Because the total thickness  $t = (r_1 - r_2)$  we have

$$t = w \left[ \frac{\sin A - \sin B}{\sin C} \right]. \quad (2.11)$$

With the angular relationships

$$\begin{aligned} \sin A &= \sin [90^\circ + (\delta_2 + \sigma)] = \cos(\delta_2 + \sigma), \\ \sin B &= \sin [90^\circ - (\delta_1 + \sigma)] = \cos(\delta_1 + \sigma), \\ \sin C &= \sin [180^\circ - A - B] = \sin(\delta_1 - \delta_2), \end{aligned}$$

and Eq. 2.11 becomes

$$t = w \left[ \frac{\cos(\delta_2 + \sigma) - \cos(\delta_1 + \sigma)}{\sin(\delta_1 - \delta_2)} \right]. \quad (2.12)$$

An important consequence of this construction is that if the dip angles at each end of the traverse are known, all intermediate dips are fixed. The dip at any intermediate point  $D$  can be found as the tangent of the concentric arc with  $C$  as center and  $CD$  as radius.

If the actual dip angles at intermediate points differ then the thickness determination using parallel arcs will be in error. One approach is to treat adjacent pairs of dips separately and sum the incremental thicknesses so determined. Mertie (1940) described the use of parallel curves of a more general nature, which takes into account additional dip measurements. This gives a better representation of the thickness of the layers, but constructing these curves is involved and the method is little used.

Another limitation is imposed if the two strike directions differ, a situation which suggests that the fold is not horizontal. True thickness then can no longer be represented in a vertical section. This and other matters related to fold geometry are considered in greater detail in later chapters.

## 2.7 Thickness in drill holes

In subsurface exploration by drilling it is important to determine the thickness of strata from measurements made in the drill holes or in recovered cores. This is especially important in the petroleum industry and Tearpock and Bischke (1991) give a comprehensive treatment.

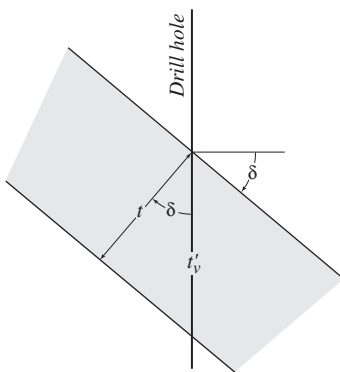


**Figure 2.10** Thickness in vertical drill hole.

If the hole is vertical then the determination of the thickness of a layer penetrated by the drill is particularly straightforward. From Fig. 2.10

$$t = t'_v \cos \delta, \quad (2.13)$$

where  $\delta$  is the dip of the bed and  $t'_v$  is the apparent thickness as measured in the vertical drill hole.

Holes which are exactly vertical are difficult to drill, especially if the beds are steeply dipping. The measure of the angular departure of a drill hole from vertical is termed *drift*, measured by the drift angle  $\psi$ . There are two cases. If the drift is exactly in the *down-dip* direction (Fig. 2.11a),

$$t = t'_m \cos(\delta + \psi),$$

where  $t'_m$  is the measured apparent thickness in the inclined hole. If the hole is exactly in the *up-dip* direction (Fig. 2.11b)

$$t = t'_m \cos |\delta - \psi|.$$

These two can be written as a single equation:

$$t = t'_m \cos |\delta \pm \psi| \quad (2.14)$$

where the positive sign is used if the drift has an down-dip component and the negative sign is used if it has a up-dip component.

If the drift is oblique to the true dip direction then the apparent dip in the vertical plane containing the drill hole is used giving

$$t = t'_m \cos |\psi \pm \alpha|. \quad (2.15)$$

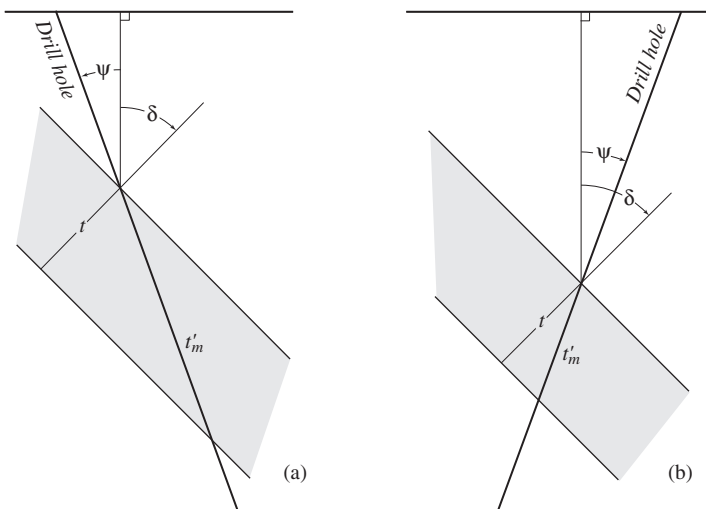


**Figure 2.11** Thickness in inclined drill hole: (a) down-dip drift; (b) up-dip drift.

### 2.8 Depth to a plane

Once the relationships involved in the determination of thickness can be visualized, problems of determining depth should present little additional difficulty for they follow closely same the methods.

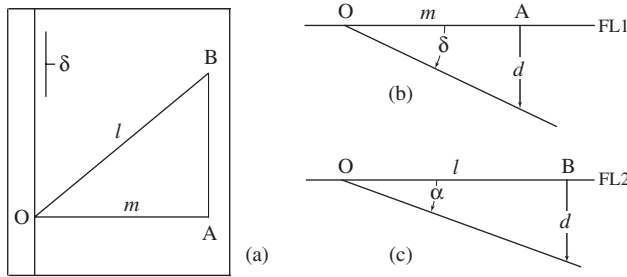


**Figure 2.12** Depth: (a) map; (b) strike-normal section; (c) oblique section.

As with thickness, the simplest case is the depth to an inclined plane from a horizontal surface at a distance  $m$  measured from a point on the outcrop trace of the plane in a strike-normal direction to the surface point where depth is required. The depth may be found by constructing a scaled triangle, as in the map of Fig. 2.12a, or by using the formula

$$d = m \tan \delta. \tag{2.16}$$

If distance  $l$  is measured oblique to the strike, the apparent dip in the traverse direction is used giving

$$d = l \tan \alpha. \tag{2.17}$$

From the previous result of Eq. 1.7

$$\tan \alpha = \sin \beta \tan \delta.$$

Using this in Eq. 2.17 we have an expression for the depth directly in terms of the true dip angle and structural bearing of the drill hole

$$d = l \sin \beta \tan \delta. \tag{2.18}$$

The next case involves the depth from a point on a slope. When slope and dip are in opposite directions (Fig. 2.13a)

$$d_1 = h \tan \delta \quad \text{and} \quad d_2 = m \sin \sigma.$$

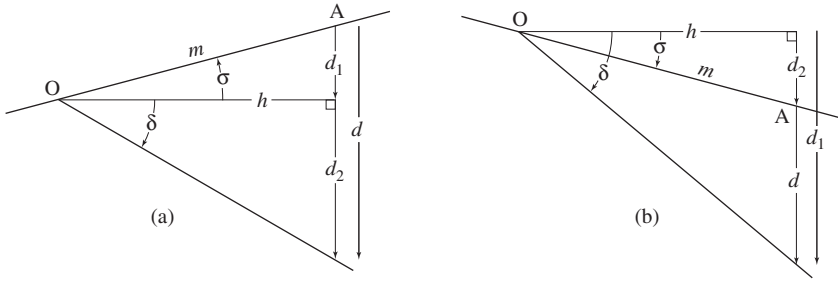


**Figure 2.13** Depth: (a) slope and dip in opposite directions; (b) slope and dip in same direction.

Because  $h = m \cos \sigma$  and the total depth  $d = (d_1 + d_2)$  we then have

$$d = m(\cos \sigma \tan \delta + \sin \sigma).$$

If the slope and dip are in the same direction and  $(\delta > \sigma)$  (Fig. 2.13b), the total depth  $d = (d_1 - d_2)$ . Then

$$d = m(\cos \sigma \tan \delta - \sin \sigma).$$

Combining gives

$$d = w |\cos \sigma \tan \delta \pm \sin \sigma|. \tag{2.19}$$

If  $(\delta < \sigma)$  then “depth” is measured upward, as might occur in a mine. This will be signaled by  $-d$ .

When the measurements are made oblique to the strike, Eq. 2.19 can be written in terms of the traverse length and the apparent dip

$$d = l |\cos \sigma \tan \alpha \pm \sin \sigma|,$$

and with Eq. 1.7 this becomes (after Mertie, 1922, p. 48)

$$d = l |\cos \sigma \tan \delta \sin \beta \pm \sin \sigma|. \tag{2.20}$$

### 2.9 Distance to a plane

A closely related measure is the distance to a plane in a direction other than vertical, as, for example, along an inclined drill hole. This distance may be found graphically by constructing a scaled section, or it may be calculated.

The simpler situation occurs when the trend of the inclined hole is normal to the strike of the plane at a known slope distance from the plane. We first express the depth of the



plane below the site of the drill hole (surface point  $A$  in Fig. 2.14) by the two partial depths

$$d_1 = h \tan p \quad \text{and} \quad d_2 = h \tan \delta$$

where  $h$  is the horizontal projection of the drill hole and  $p$  is its plunge angle.

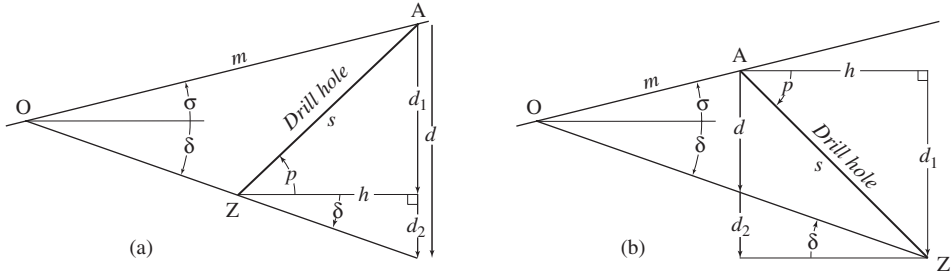


**Figure 2.14** Distance in vertical, strike-normal section: (a)  $\delta$  and  $p$  in opposite directions; (b)  $\delta$  and  $p$  in same direction.

There are two cases. In the vertical plane containing the drill hole the plunge and dip may be *opposite* in direction or the plunge and dip may be in the *same* direction.

1. In the first case, from Fig. 2.14a,  $h = s \cos p$  and  $d = d_1 + d_2 = h(\tan p + \tan \delta)$ . Combining these, using the identity  $\sin p = \cos p \tan p$ , and solving for the *inclined distance*  $s$  we have

$$s = \frac{d}{\sin p + \cos p \tan \delta}.$$

2. In the second case, from Fig. 2.14b, where  $d = d_1 - d_2$ , we obtain

$$s = \frac{d}{\sin p - \cos p \tan \delta}.$$

These two expressions can be combined into a single equation using the same sign convention for dip and plunge directions:

$$s = \frac{d}{\sin p \pm \cos p \tan \delta}. \tag{2.21}$$

If the vertical plane containing the drill hole is oblique to the strike, then the apparent dip in this direction can be used:

$$s = \frac{d}{\sin p \pm \cos p \tan \alpha},$$

or the correction of Eq. 1.4 can be incorporated directly (after Mertie, 1922, p. 48) giving

$$s = \frac{d}{\sin p \pm \cos p \sin \beta \tan \delta}. \quad (2.22)$$

Note that neither the slope angle nor the slope length enters into this equation. However, both are accounted for in the expression for  $d$  of Eq. 2.20 which, when used in conjunction with Eq. 2.22, gives the required inclined distance to the plane.

## 2.10 Error propagation

As we have seen in §1.4, any measured quantity  $x$  will be subject to an error or uncertainty  $\Delta x$ . It then follows that the calculation of any derived quantity – an angle, a depth, a thickness or a distance – will also be uncertain. In other words, the measurement errors will *propagate* through the calculations. We give a brief introduction to the methods of determining these propagated errors.<sup>3</sup>

There are several ways of representing the uncertainty associated with a given measurement (Taylor, 1997, p. 26–29). For example, if measured length  $l_{best} = 50$  m has an uncertainty  $\Delta l = 2$  m then:

1. The *absolute uncertainty* (or simply *uncertainty*) is expressed in the same units as the measurement

$$l_{best} \pm \Delta l = 50 \pm 2 \text{ m.}$$

2. The *fractional uncertainty*, also called the *relative uncertainty* or *precision*, is the dimensionless number

$$\frac{\Delta l}{|l_{best}|} = \frac{1 \text{ m}}{50 \text{ m}} = 0.02,$$

and this gives an estimate of the quality of the measurement.

3. The *percentage uncertainty* is just the fractional uncertainty expressed as a percentage

$$\frac{\Delta l}{|l_{best}|} \times 100\% = 2\%.$$

As a starting point we review some fundamental concepts of differential calculus. Given a function of a single variable

$$y = f(x), \quad (2.23)$$

<sup>3</sup>Taylor (1997, p. 45f) gives the basic theory in an easily accessible form and Vacher (2001b, 2001c) treats several geological applications.

an infinitesimally small change  $dx$  in the independent variable  $x$  results in an infinitesimally small change  $dy$  in the dependent variable  $y$ . The quantities  $dx$  and  $dy$  are *differentials*.

A *derivative* is a rate of change. The first derivative  $f'(x)$  is the ratio of these two infinitesimal changes. This derivative of  $f$  with respect to  $x$  is written as

$$f'(x) = dy/dx,$$

where the ratio of these infinitesimals describes the rate of change of  $y$  with respect to  $x$ . Geometrically this is the slope of the curve representing  $y = f(x)$ . Rearranging we have

$$\boxed{dy = f'(x) dx}, \tag{2.24}$$

which makes the distinction between differentials and the derivative clear. The official definition of a derivative is

$$f'(x) = \lim_{\Delta x \rightarrow 0} \frac{f(x + \Delta x) - f(x)}{\Delta x}.$$

If we remove the limit, this holds only approximately, that is,

$$f'(x) \approx \frac{f(x + \Delta x) - f(x)}{\Delta x}.$$

With  $\Delta y = f(x + \Delta x) - f(x)$  we write

$$\boxed{\Delta y \approx f'(x) \Delta x}. \tag{2.25}$$

Note the formal similarity of the exact version (Eq. 2.24) and the approximate version (Eq. 2.25). We can illustrate the relationship between these two versions graphically.

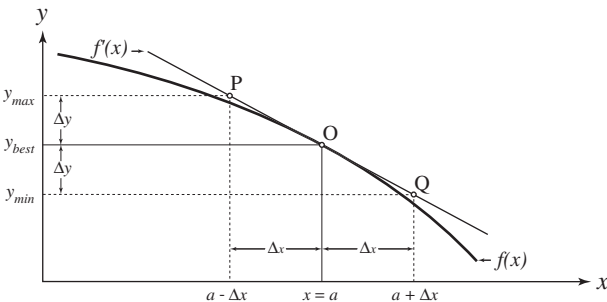


**Figure 2.15** Graph of  $y = f(x)$  vs.  $x$ .

Suppose we measure variable  $x$  and its value is  $a$ . This value of  $x$  and the corresponding best value of  $y$  are represented by the coordinates of point  $O$  on the curve representing the function  $f(x)$  (Fig. 2.15). Also suppose that this measured value has an uncertainty of  $\Delta x$ . This results in a propagated uncertainty  $\Delta y$ . We write this condition as

$$\Delta y \approx \left| \frac{dy}{dx} \right| \Delta x, \quad (2.26)$$

where the absolute value is used because the relationship is the same whether the slope is positive or negative. This says that for an uncertainty  $\Delta x$  in  $x$ , there will be a corresponding uncertainty  $\Delta y$  in  $y$ , and these two uncertainties are related by the slope  $dy/dx$  at point  $O$ .

Points  $P$  and  $Q$  on the line tangent to the curve at  $O$  approximate points on the curve itself, and the smaller  $\Delta x$  is, the closer these points will be to this curve, and therefore the better the approximation.

In our applications it will be useful to adopt the notation which explicitly recognizes that  $\Delta y$  and  $\Delta x$  are errors, as we have in §1.4 (see also Vacher, 2001b, p. 310). We express this as  $\varepsilon_x = \Delta x$  and  $\varepsilon_y = \Delta y$ . Then Eq. 2.26 becomes

$$\varepsilon_y = \left| \frac{dy}{dx} \right| \varepsilon_x. \quad (2.27)$$

Because angles play a prominent role in many situations, we start by examining how the uncertainty associated with a single measured angle is propagated.

### Problem

- If the measured angle  $\theta = 20 \pm 3^\circ$ , what is the best estimate of  $\cos \theta$  and what is the uncertainty (after Taylor, 1997, p. 65)?

### Solution

1. The best estimate is, of course,  $\cos \theta = \cos 20 = 0.93969$ .
2. Then according to Eq. 2.27

$$\varepsilon_{\cos \theta} = \left| \frac{d \cos \theta}{d \theta} \right| \varepsilon_\theta = |-\sin \theta| \varepsilon_\theta \quad (\varepsilon_\theta \text{ in radians}).$$

3. Because  $\varepsilon_\theta = 3^\circ = 0.05236$  rad we have  $\varepsilon_{\cos \theta} = (\sin 20)(0.05236) = 0.01791$ .<sup>4</sup>  
Rounding to significant figures gives  $\varepsilon_{\cos \theta} = 0.02$ .
4. For  $\theta = 20 \pm 3^\circ$ , we have  $\cos \theta = 0.94 \pm 0.02$ .

Measurement errors which are propagated to such trigonometric functions are, of course, also propagated to calculations which use these functions.

<sup>4</sup>Multiply by  $\pi/180 = 0.01745329252\dots$  to convert degrees to radians.

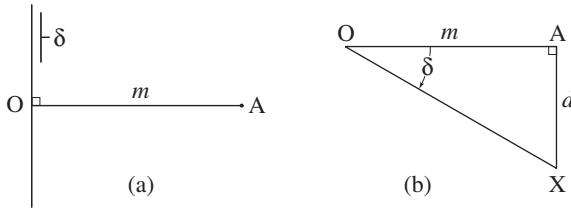


**Figure 2.16** Depth to a plane (after Vacher, 2001b, p. 312): (a) map; (b) true dip section.

### Problem

- How will the uncertainty in the measurement of the dip angle  $\varepsilon_\delta = 1^\circ$  influence the calculation of the depth to a plane at point A (Fig. 2.16a)?

### Solution

1. From the vertical section containing the true dip angle the depth  $d$  is given by (Fig. 2.16b)

$$d = m \tan \delta, \quad (2.28)$$

and assume that the horizontal strike-normal distance  $m = 100$  m exactly.

2. From Eq. 2.27

$$\frac{d(\tan \delta)}{d\delta} = \sec^2 \delta = \frac{1}{\cos^2 \delta}.$$

3. Then

$$d = m \left[ \tan \delta \pm \frac{\varepsilon_\delta}{\cos^2 \delta} \right]. \quad (2.29)$$

4. The fractional uncertainty is given by

$$\frac{\varepsilon_d}{d} = \frac{1}{\tan \delta \cos^2 \delta}.$$

5. The results for a range of dips are shown in Table 2.1.

For problems involving multiple variables there are several simple rules for the arithmetic involved (for details see Taylor, 1997, p. 49–53; Vacher, 2001c, p. 390–392). In the case of two variables these rules are:

1. If two quantities  $x$  and  $y$  are measured with uncertainties  $\Delta x$  and  $\Delta y$  and the measured values are used to compute a sum or difference

$$q = x + y \quad \text{or} \quad q = x - y,$$

Table 2.1 *Calculated depths for uncertainty  $\varepsilon_\delta = 1^\circ$* 

$\delta$	$d$	$\varepsilon_d$	$\varepsilon_\delta/d$
10	17.6	$\pm 1.8$	10%
30	58.0	$\pm 2.3$	4.0%
45	100	$\pm 3.5$	3.5%
60	173	$\pm 7$	4.0%
80	567	$\pm 58$	10%

then the uncertainty in the value of  $q$  is the sum of the original uncertainties

$$\Delta q = \Delta x + \Delta y,$$

that is, “the absolute propagated error for the sum and for the difference of two numbers is the sum of the absolute errors of those numbers” (Vacher, 2001c, p. 393).

- If two quantities  $x$  and  $y$  are measured with uncertainties  $\Delta x$  and  $\Delta y$  and the measured values are used to compute a product or quotient

$$q = xy \quad \text{or} \quad q = x/y,$$

then the uncertainty in the value of  $q$  is the sum of the original fractional uncertainties

$$\frac{\Delta q}{|q|} = \frac{\Delta x}{|x|} + \frac{\Delta y}{|y|},$$

that is, the relative propagated error for the product and for the quotient of two numbers is the sum of the relative errors for those numbers (Vacher, 2001c, p. 393).

To summarize, this means that the uncertainty in  $q(x, y)$  is

$$\Delta q = \left| \frac{\partial q}{\partial x} \right| \Delta x + \left| \frac{\partial q}{\partial y} \right| \Delta y. \quad (2.30)$$

### Problem

- What will the uncertainty in the depth to a plane be if the uncertainty in the dip is  $\delta \pm \varepsilon_\delta = 60 \pm 1^\circ$  and the uncertainty in the distance is  $m \pm \varepsilon_m = 100 \pm 2$  m.

### Solution

- Adapting Eq. 2.30 we have

$$\varepsilon_d = \left| \frac{\partial d}{\partial m} \right| \varepsilon_m + \left| \frac{\partial d}{\partial \delta} \right| \varepsilon_\delta.$$

2. Performing the partial differentiations on Eq. 2.28 yields

$$\frac{\partial d}{\partial m} = \tan \delta \quad \text{and} \quad \frac{\partial d}{\partial \delta} = \frac{m}{\cos^2 \delta}.$$

3. The uncertainty in the depth is then

$$\varepsilon_d = \varepsilon_m \tan \delta + \varepsilon_\delta \frac{m}{\cos^2 \delta} = 2(\tan 60) + \frac{\pi}{180} \left[ \frac{100}{\cos^2 60} \right] = 11 \text{ m}.$$

This pattern of combining uncertainties is easily extended to errors associated with more than two measurements. For three variables the formula is

$$\varepsilon_f = \left| \frac{\partial f}{\partial x} \right| \varepsilon_x + \left| \frac{\partial f}{\partial y} \right| \varepsilon_y + \left| \frac{\partial f}{\partial z} \right| \varepsilon_z. \tag{2.31}$$

**Problem**

1. If  $l = 125 \text{ m}$ ,  $\delta = 22^\circ$  and  $\beta = 15^\circ$ , what is the depth  $d$  to an inclined plane at point  $B$  (Fig. 2.17a)?
2. Now suppose that the uncertainty associated with each of these measures is  $l = 125 \pm 3 \text{ m}$ ,  $\delta = 22 \pm 3^\circ$  and  $\beta = 15 \pm 1^\circ$ , what now can be said about the depth  $d$  (after Vacher, 2001c, p. 394–395)?

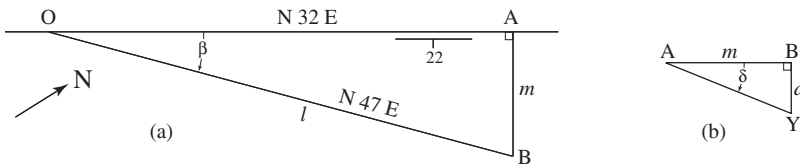


**Figure 2.17** Angles and distances (after Vacher, 2001c, p. 394): (a) map; (b) true dip section.

**Exact solution**

1. From the map view (Fig. 2.17a) and the dip section (Fig. 2.17b) we have the expressions

$$m = l \sin \beta \quad \text{and} \quad d = m \tan \delta.$$

2. Combining gives

$$d = l \sin \beta \tan \delta, \tag{2.32}$$

and we can calculate the depth using  $l = 125 \text{ m}$ ,  $\beta = 15^\circ$  and  $\delta = 22^\circ$ . The answer is  $d = 13.1 \text{ m}$ .

### Solution with uncertainties

1. From Eq. 2.31 the propagated error  $\varepsilon_d$  is given by

$$\varepsilon_d = \left| \frac{\partial d}{\partial l} \right| \varepsilon_l + \left| \frac{\partial d}{\partial \beta} \right| \varepsilon_\beta + \left| \frac{\partial d}{\partial \delta} \right| \varepsilon_\delta. \quad (2.33)$$

2. Using Eq. 2.32, form the three partial derivatives and plug in values of  $l$ ,  $\beta$  and  $\delta$  giving

$$\begin{aligned} \frac{\partial d}{\partial l} &= \sin \beta \tan \delta = 0.10457, & \frac{\partial d}{\partial \beta} &= l \cos \beta \tan \delta = 48.78642, \\ \frac{\partial d}{\partial \delta} &= \frac{l \sin \beta}{\cos^2 \delta} = 37.63349. \end{aligned}$$

3. Using these values in Eq. 2.33, together with

$$\varepsilon_l = 2 \text{ m}, \quad \varepsilon_\beta = \text{rad}(2^\circ) = 0.01349, \quad \varepsilon_\delta = \text{rad}(3^\circ) = 0.05236.$$

gives  $\varepsilon_d = 3.8 \text{ m}$ . Thus  $d = 13.1 \pm 3.8 \text{ m}$ , and the minimum and maximum estimates of the depth are

$$d_{min} = 13.1 - 3.8 = 9.3 \text{ m} \quad \text{and} \quad d_{max} = 13.1 + 3.8 = 16.9 \text{ m}.$$

Just how good are these calculated uncertainties? If they are *small* and *independent* and *random*, Eq. 2.30 is likely to overstate the total uncertainty, for there is a 50% chance that an underestimate of  $x$  will be accompanied by an overestimate of  $y$ , or vice versa. In such a case, the probability of underestimating or overestimating both  $x$  and  $y$  by the full amounts  $\Delta x$  and  $\Delta y$  is small, and therefore the calculated  $\Delta q$  overstates the probable total error.

Under these circumstances, is there a better estimate of  $\Delta q$ ? If both  $x$  and  $y$  are measured independently then an estimate of the uncertainty is given by

$$\Delta q = \sqrt{(\Delta x)^2 + (\Delta y)^2}. \quad (2.34)$$

This is called the *sum in quadrature* (Taylor, 1997, p. 57–62, 141–143), and it is widely used for calculating the uncertainties associated with careful measurements made under controlled conditions in the laboratory.

On the other hand, Vacher (2001c, p. 396) makes the important point that the uncertainties associated with measurements made by geologists in the field may not be sufficiently small for Eq. 2.34 to be valid.



Under these circumstances, there is an alternative approach (Courant & John, 1965, p. 490–492; Vacher, 2001b, 2001c): any function of a single variable  $f(x)$  can be represented by the Taylor series over some interval in the neighborhood of the specified point  $x = a$ . The resulting expression is

$$f(x) = f(a) + f'(a)(x - a) + \frac{f''(a)}{2!}(x - a)^2 + \dots + \frac{f^{(n)}(a)}{n!}(x - a)^n + \dots \quad (2.35)$$

The first term  $f(a)$  identifies the point on the curve. The second term  $f'(a)(x - a)$  represents the slope of the line tangent to the curve at this point. The addition of each of the higher order terms brings the sum into closer correspondence with  $f(x)$ . If  $\Delta x = (x - a)$  is small, then powers of  $\Delta x$  will be very much smaller and can be neglected. With  $\Delta y = f(x) - f(a)$ , Eq. 2.35 reduces to the approximation

$$\Delta y \approx f'(a)\Delta x,$$

which is the same as Eq. 2.25, and we now see that it is just an approximation of Eq. 2.35.

But if the uncertainty is *not* small, then the second-derivative term in the Taylor series may not be negligible. We then have

$$\Delta y \approx f'(a)\Delta x + \frac{1}{2}f''(a)(\Delta x)^2. \quad (2.36)$$

In an earlier example, we found that if  $\theta = 20 \pm 3^\circ$  then  $\cos \theta = 0.94 \pm 0.02$ . If instead there is a larger uncertainty, for example  $\theta = 20 \pm 6^\circ$ , what then is the propagated error for  $\cos \theta$ ? Using the earlier method, we obtain

$$\varepsilon_{\cos \theta} = |\sin \theta| \varepsilon_\theta = (0.342\,02)(0.104\,72) = 0.035\,82 \quad \text{or } \varepsilon_{\cos \theta} = 0.04,$$

and  $\cos \theta = 0.94 \pm 0.04$ . Note that for an uncertainty of  $6^\circ$  the error is just twice the uncertainty for  $3^\circ$  found earlier. The reason is that both use the same sloping tangent line.

Alternatively, adapting Eq. 2.36

$$\varepsilon_{\cos \theta} = | -\varepsilon_\theta \sin \theta + \frac{1}{2}\varepsilon_\theta^2 \cos \theta | = 0.030\,66,$$

that is,  $\cos \theta = 0.94 \pm 0.03$ . Note that this uncertainty is 25% less than that obtained by the use of only a single term.

This brief treatment together with the illustrative examples should make clear to geologists that the inevitable uncertainty associated with any calculation is important, and in particular that they have an obligation to make explicit such uncertainty, especially when the results of calculations have a bearing on the detailed understanding of the structural geometry.

## 2.11 Exercises

- A strike-normal traverse  $OA$  crosses an inclined layer  $\delta = 36^\circ$  of length  $w = 42$  m (Fig. 2.18a).
  - Graphically determine the thickness of the layer and check your result using Eq. 2.1.
  - Graphically determine the depth to the lower bounding plane at point  $A$  and check your results using Eq. 2.16.
  - If the uncertainty of the dip angle  $\Delta\delta = 2^\circ$  and the traverse is accurate enough to be considered exact, what is the uncertainty in the calculated thickness  $\Delta t$ ?
- An oblique traverse  $OB$   $\beta = 60^\circ$  crosses an inclined layer  $\delta = 23^\circ$  of length  $l = 54$  m (Fig. 2.18b).
  - Graphically determine the thickness and check your result using Eq. 2.3.
  - Graphically determine the depth to the lower bounding plane at point  $B$ . Check your result using Eq. 2.18.
  - If the uncertainties  $\Delta\delta = 2^\circ$ ,  $\Delta\beta = 1^\circ$  and  $\Delta l = 0.5\%$  what is the uncertainty in the calculated thickness  $\Delta t$ ?

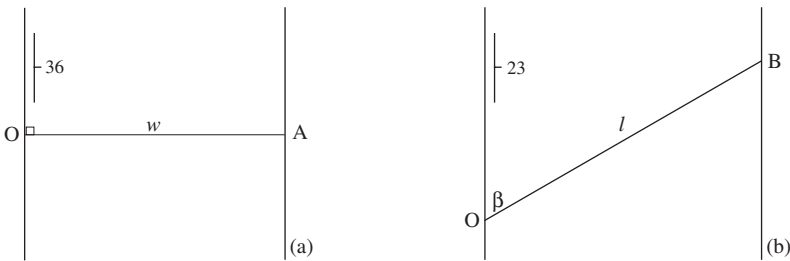


**Figure 2.18** Thickness from horizontal traverses: (a) strike-normal traverse; (b) oblique traverse.

- A south-to-north, strike-normal traverse made across a series of badland beds uniformly dipping  $50^\circ$  due north yielded the following data given in Table 2.2 (the setting is shown in Fig. 2.19). Determine the total thickness.

Table 2.2 *Total thickness*

Unit	Lithology	Slope distance	Slope angle
5	upper sandstone	6.7 m	$0^\circ$
4	upper red mudstone	17.7 m	$18^\circ$
3	lower sandstone	8.8 m	$-13^\circ$
2	pink claystone	8.0 m	$15^\circ$
1	lower purple mudstone	8.2 m	$10^\circ$

- The attitude of a sandstone unit is N  $65$  E,  $35$  N. A horizontal traverse with a bearing of N  $10$  E made from the bottom to the top measured  $125$  m.
  - Graphically determine the thickness.

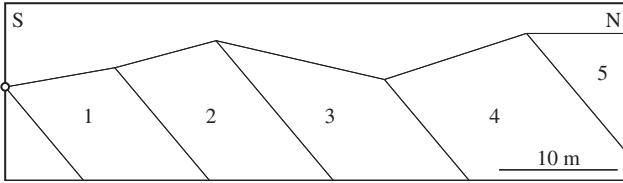


**Figure 2.19** Cross section.

- (b) Calculate the thickness using Eq. 2.3.
  - (c) If the uncertainty in the dip is  $2^\circ$ , the uncertainty of the traverse direction is  $1^\circ$  and the uncertainty in the measured length is 0.5%, what is the uncertainty in the thickness calculation?
5. The following information is from a geological map. The attitude of a basalt sill is N 5 W, 38 W. An eastern point on the lower contact has an elevation of 900 m, and a western point on the upper contact has an elevation of 1025 m. The line connecting these two points has a bearing of N 85 W. Determine the thickness of the sill graphically and check your result using Eq. 2.7.
  6. A mineralized vein with an attitude of N 37 W, 50 SW is exposed on a ridge crest. How far down a  $22^\circ$  slope in a N 82 W direction would it be necessary to go to find a point at which the vein lies at a depth of 100 m? At that point, what is the minimum inclination and length of a shaft to reach the vein?

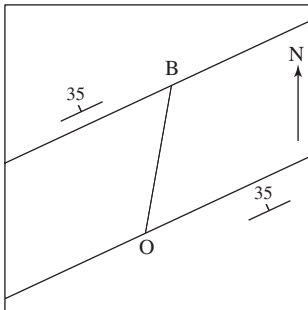


**Figure 2.20** Geological sketch map.

7. The geological sketch map of Fig. 2.20 shows a thick shale formation between two limestone units exposed on a south-facing slope. A trail angles up a brushy slope in a N 30 E direction at a nearly constant  $20^\circ$  angle. The traverse length in crossing the entire shale unit is 366 m. The beds have a consistent attitude of N 80 E, 35 N. If the shale–limestone contact lines are approximately horizontal how steep is the shale slope? What is the difference in elevation between the beginning and ending of the traverse? What is the thickness of the shale?

8. A 125 m long strike-normal traverse made up a  $15^\circ$  slope between the bottom and top of a limestone stratum gave the following information: the dip at the bottom of the unit is  $55^\circ$  and at the top it is  $65^\circ$ , both in a downslope direction. The strike directions at both points are the same. Using the method of tangent arcs estimate the thickness of the unit; check your result with Eq. 2.11. Compare this with the result obtained from Eq. 2.10 using the mean of the two dip angles.

# 3

## Lines and intersecting planes

### 3.1 Definitions

**Line:** the geometrical element generated by a moving point; it has only extension along the path of the point. Lines may be rectilinear (straight) or curvilinear (curved). Only straight lines are treated here.

**Plunge:** the vertical angle measured downward from the horizontal to a line (Fig. 3.1a).

**Pitch:** the angle between the strike direction and a line in a specified plane (Fig. 3.1b).  
Rake is synonymous.

**Trend:** the horizontal direction of the vertical plane containing the line, specified by its bearing or azimuth.

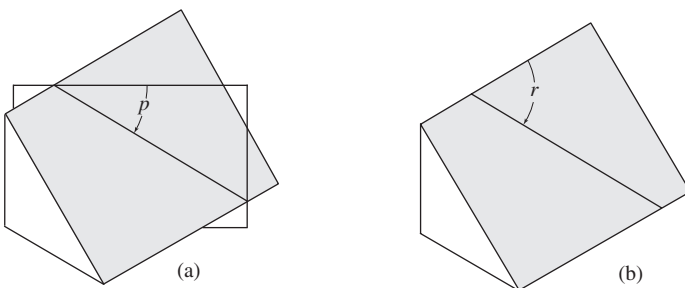


**Figure 3.1** Inclination of a line: (a) plunge  $p$ ; (b) pitch  $r$ .

### 3.2 Linear structures

There are two types of structural lines. They may exist in their own right, such as the long axes of mineral grains or streaks of mineral aggregates; elongate rock bodies and drill holes may also be considered linear for some purposes. Other lines occur in conjunction

with structural planes; examples include striations on fault surfaces, mineral lineation on foliation planes and lines formed by the intersection of planes.

The orientation of a line in space is specified by its trend and plunge. As with planes, there is a set of map symbols for structural lines, also with three parts.

1. A *trend line*.
2. An *arrowhead* giving the direction of downward inclination.
3. A *plunge angle* written near the arrowhead.

The arrow should be uniform in length and long enough so that its trend can be accurately measured on the map. Because its length is not scaled, this symbol is not a vector.

The most common symbols are shown in Fig. 3.2. Special symbols may be invented when needed, and all symbols used must be explained in the map legend.

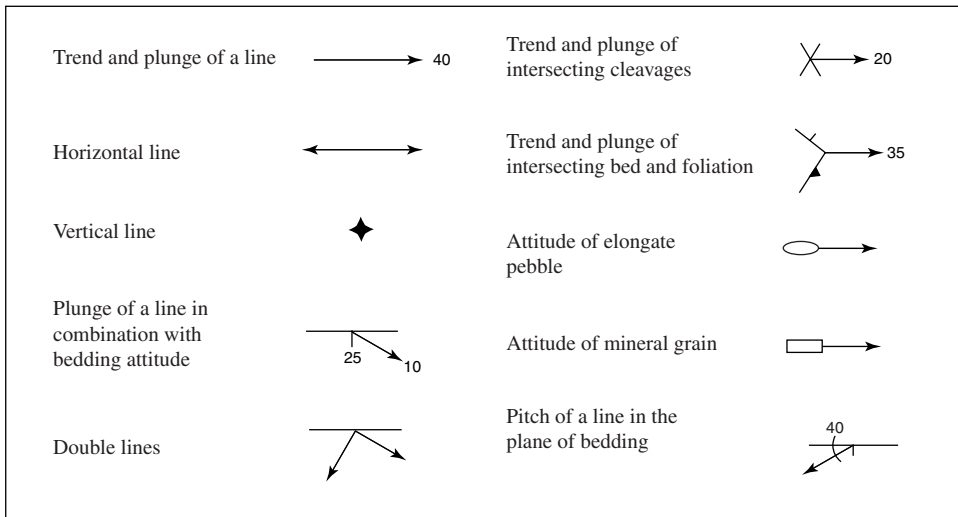


**Figure 3.2** Map symbols for structural lines.

The plunge and trend of a line may also be written out. The notation has two forms depending on whether the trend is expressed as a bearing or an azimuth.

1. The plunge angle is followed by the trend expressed as a bearing, as in 30, S 45 W, meaning that the line plunges 30° toward S 45 W.
2. The trend is given as an azimuth, as in 30/225. The order is sometimes reversed as 225/30 and expressing the azimuth with three digits even if this requires leading zeros avoids any possible confusion.

Again, the difference depends of the type of compass used and on personal preference. The azimuth form is particularly useful for computer processing of orientational data.

### 3.3 Plunge of a line

A plunging line is accurately depicted in the vertical section parallel to the trend of the line. If a line is to be depicted on any other section, the angle of *apparent plunge* must be used. The need for such an angle arises if an inclined drill hole and the rock units it penetrates are to be shown on a section oblique to the line of section (Fig. 3.3). Because such displays inevitably involve distortions, it is better to project over small distances and small angles if possible.

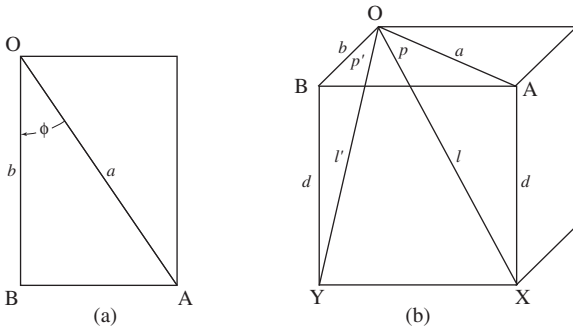


**Figure 3.3** Plunge  $p$  and apparent plunge  $p'$ .

This angle is analogous to apparent dip except that the apparent plunge  $p'$  is always greater than the true plunge  $p$ . When the section line is parallel to the trend of the line, the true plunge is shown and this is the minimum value. If the section is perpendicular to the trend of the line, then the apparent plunge is  $90^\circ$  and this is its maximum value.

#### Problem

- Project the inclined drill hole whose attitude is 30/150 onto a north-south section (Fig. 3.4a).

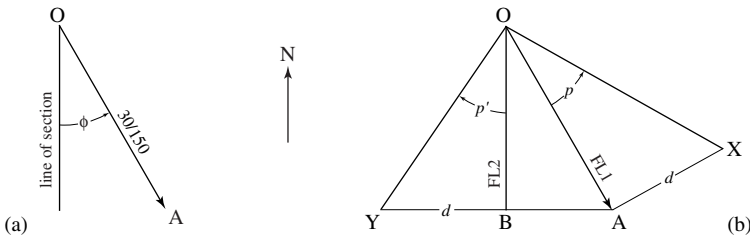


**Figure 3.4** Apparent plunge  $p'$ : (a) map; (b) construction.

#### Construction

1. In map view, draw a line of section parallel to the trend of the hole (Fig. 3.4b). With this line as  $FLI$  draw a section showing the true plunge.

2. With the angle of true plunge  $p$  find the depth  $d$  to point  $X$  at some convenient horizontal distance  $OA$ , or use the actual depth at the end of the hole to fix  $OA$ .
3. Project this surface point  $A$  back to the section line to locate point  $B$ .
4. With the line of the section as  $FL2$ , locate point  $Y$  at the same depth  $d$  below point  $B$ . The  $\angle BOY$  is the apparent plunge  $p'$ .

**Answer**

- The inclination of the drill hole to the vertical north-south section is  $p' = 35^\circ$ .

The trigonometric expressions for solving this same problem can be derived from the map of Fig. 3.3a,

$$b/a = \cos \phi,$$

and the block diagram of Fig. 3.3b,

$$a = d / \tan p, \quad b = d / \tan p'.$$

Substituting the expressions for  $a$  and  $b$  in the first equation and rearranging then gives

$$\boxed{\tan p' = \tan p / \cos \phi.} \quad (3.1)$$

From the previous problem  $p = 30^\circ$  and  $\phi = 35^\circ$ , and therefore  $p' = 35^\circ$ .

When projected to a vertical plane of section, any original length  $l$  measured along the plunging line is shortened to  $l'$ . Again from Fig. 3.3b

$$d = l / \sin p \quad \text{and} \quad d = l' / \sin p'.$$

Equating these two and rearranging yields

$$\boxed{l' = l(\sin p / \sin p').} \quad (3.2)$$

Our only concern in the remainder of this chapter is with lines lying in planes. For such lines the plunge angle is, in effect, an apparent dip. Therefore, all the graphical techniques of §1.5 are applicable with little modification to problems involving the relation of the plunge and trend of a line and the dip and strike of the plane. For the same reason, an expression for the plunge can be obtained directly from Eq. 1.4, which we rewrite as

$$\boxed{\tan p = \tan \delta \sin \beta} \quad (3.3)$$

where  $p$  is the plunge and, as before,  $\delta$  is the dip of the plane and  $\beta$  is the structural bearing measured from the strike direction.



### 3.4 Pitch of a line

The pitch is measured in a plane containing the line (Fig. 3.1b). Therefore it may range in value from  $r = 0^\circ$  when the line is horizontal, to  $r = 90^\circ$  when the line is in the dip direction. In describing pitch it is necessary only to give the angle and the direction in which the acute angle faces. For example, 35 N means that the pitch angle  $r = 35^\circ$  is measured downward from the northern end of the strike line.

In the field, the pitch of a line on an exposed plane is determined by first marking a horizontal line on the inclined plane and then measuring the angle between this line of strike and the linear structure with a protractor. If, however, the plane is not well exposed, the pitch angle may be determined from the dip of the plane and the structural bearing of the line. First, we treat the problem of determining the pitch from the known dip of the plane and a specified structural bearing. We do this by converting  $\beta$  to  $r$ .

#### Problem

- What is the pitch angle of a line with structural bearing  $\beta = 35^\circ$  on a plane with dip  $\delta = 40^\circ$ ?

#### Approach

- In the map view of an inclined plane containing a line we see directly the angle of the structural bearing  $\beta$ , which is the orthographic projection of the pitch angle  $r$  to the horizontal plane of the map (Fig. 3.5a). In order to determine this angle, we must obtain a direct view of the inclined plane and the line it contains. This is done by rotating the structural plane into a horizontal position using the strike direction as a folding line (Fig. 3.5b). This procedure can be usefully illustrated by unfolding a small paper model.

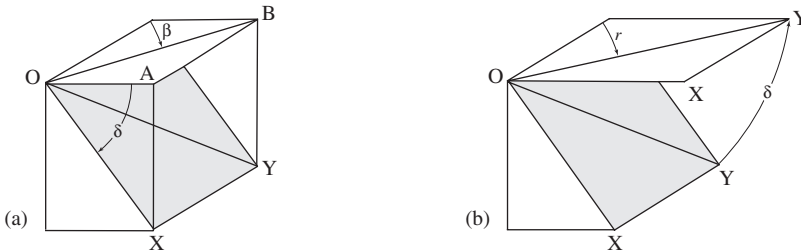


**Figure 3.5** Pitch: (a) projection of plane; (b) direct view of plane.

#### Construction

1. Draw a map showing a strike line, the trend of the inclined line and a line in the true dip direction. At a convenient distance  $OA$  draw a second line of strike  $AB$  (Fig. 3.6a).

2. With the dip line  $OA$  as  $FL1$ , construct a vertical section showing the angle of true dip and determine the depth  $d$  of point  $X$  directly beneath the surface point  $A$ .
3. With the strike line through  $O$  as  $FL2$ , using a compass rotate the inclined plane through the angle of dip thus locating points  $X$  and  $Y$  on the now horizontal structural plane.
4. In this upturned plane the angle line  $OY$  makes with the strike direction is the pitch angle  $r$ .

**Answer**

- The pitch of the line in the plane is  $r = 42^\circ$ .

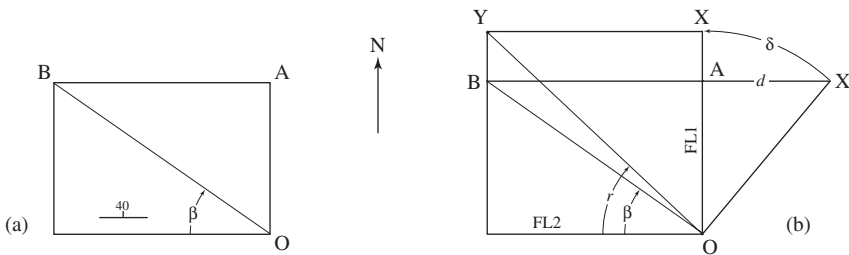


**Figure 3.6** Finding pitch: (a) map; (b) construction.

A more useful version of this problem is to determine the plunge of the line whose pitch has been measured and this requires the conversion of  $r$  to  $\beta$ . The construction is the reverse of that used in Fig. 3.6.

**Problem**

- What is the plunge of a line whose pitch  $r = 42^\circ$  on a plane with dip  $\delta = 40^\circ$ ?

**Construction**

1. Draw a direct view of the plane representing the pitch by the line  $OY$  which makes an angle of  $r = 42^\circ$  with the strike direction through  $O$  (Fig. 3.7a).
2. With the dip line as  $FL1$  construct a vertical section showing the angle of true dip.
3. In this section and using a compass, rotate point  $X$  downward to fix its location at depth  $d$  below point  $A$ . Draw the line  $AB$  as a second line of strike.
4. Construct two lines perpendicular to the dip line, the first through  $A$  to intersect the trend line at  $A'$ .
5. The angle between the strike line through  $O$  and line  $OB$  is the structural bearing  $\beta$ .
6. With  $\beta$  we can find the plunge using the same construction used to find the apparent dip (Fig. 3.7b).

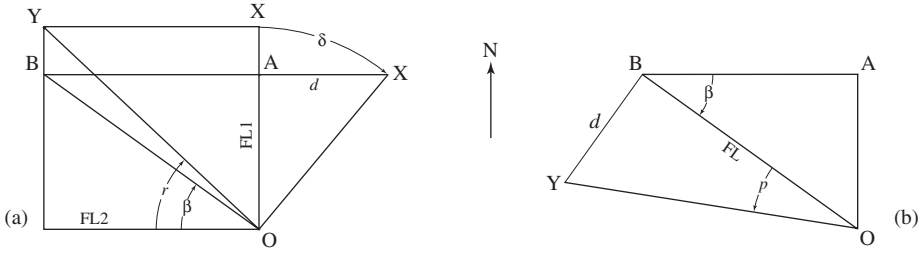


**Figure 3.7** Finding plunge from pitch.

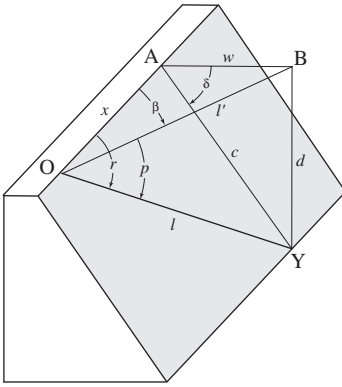


**Figure 3.8** Parameters used in expressions for the angle of pitch.

**Answer**

- The bearing of the line is  $\beta = 35^\circ$  and its plunge is  $p = 25^\circ$ .

There are two useful formulas which can be used to solve problems involving pitch angles. The first relates the pitch of a line to its structural bearing and the dip of the plane. From Fig. 3.8

$$w = c \cos \delta, \quad x = c / \tan r, \quad \tan \beta = w/x.$$

Substituting the first two of these in the third and rearranging gives

$$\boxed{\tan r = \tan \beta / \cos \delta.} \tag{3.4}$$

From the previous problem,  $r = 42^\circ$  and  $\delta = 40^\circ$ . Therefore  $\beta = 35^\circ$ . The second formula relates pitch to the structural bearing and plunge angle of the line. Again from Fig. 3.8

$$x = l' \cos \beta, \quad l = l' / \cos p, \quad \cos r = x/l.$$

Substituting the first two of these into the third gives

$$\boxed{\cos r = \cos p \cos \beta.} \tag{3.5}$$

### 3.5 Intersecting planes

Two non-parallel planes intersect in a line and in a number of situations it is important to determine the attitude of this line.

Before describing the construction, it is useful to visualize the geometry of intersecting planes and it helps to practice with the aid of flattened hands held parallel to the two planes. Folded paper models also can be used with advantage.

#### Problem

- What is the attitude of the intersection of Plane 1 (N 20 W, 36 E) with Plane 2 (N 42 E, 20 W)?

#### Approach

- A view of the map as if one were looking down a V-shaped trough indicates that the line of intersection trends in a northerly direction (Fig. 3.9a). From this view and the previously established relationship between true and apparent dip, we then see that the line of intersection, being common to both planes, can not have a plunge angle greater than the smaller of the two dip angles.

The trend of the line of intersection exactly bisects the angle between the strike directions only if the two dip angles are identical. Otherwise the trend of the line will be closer to the strike of the steeper plane. In this problem the plunge of the line of intersection must be less than the 20° dip of Plane 2 and its trend is closer to the strike of steeper Plane 1.

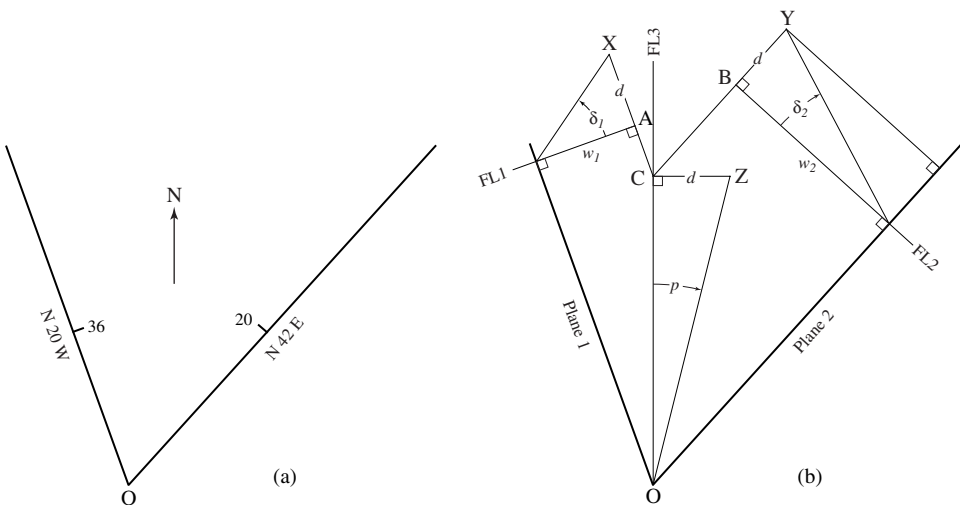


Figure 3.9 Line of intersection: (a) map; (b) construction.

**Construction**

1. In map view plot a strike line for each of the two planes and label their intersection  $O$  which represents one point common to both planes and therefore lies on the line of intersection (Fig. 3.9b).
2. To obtain another point on the line of intersection a second pair of intersecting strike lines at a known vertical distance below the intersecting first pair are needed.
  - (a) With  $FL1$  perpendicular to the strike of Plane 1, construct a vertical section showing the true dip  $\delta_1$ . Locate surface point  $A$  with a convenient distance  $w_1$  from the strike line. Then plot the trace of the inclined plane and determine the depth  $d$  to point  $X$  below surface point  $A$ .
  - (b) With  $FL2$  perpendicular to the strike of Plane 2, construct a second vertical section showing the true dip  $\delta_2$ . Using the same depth  $d$  to point  $Y$ , determine the length  $w_2$  and locate the surface point  $B$ .
3. Through both points  $A$  and  $B$  draw a second pair of lines parallel to the strike directions of the respective planes intersecting at point  $C$ . Direction  $OC$  represents the trend of the line of intersection which can be measured.
4. With  $FL3$  perpendicular to  $OC$ , construct a vertical section again using the same depth  $d$  to locate the point  $Z$  below at the surface point  $C$ . Vertical  $\angle COZ$  is the angle of plunge  $p$ .

**Answer**

- The attitude of the line of intersection is 14/000.

**3.6 Cotangent method**

This orthographic construction may be simplified by adapting the semi-graphical cotangent method used in §1.8. As before this is equivalent to choosing the depth  $d = 1$ .

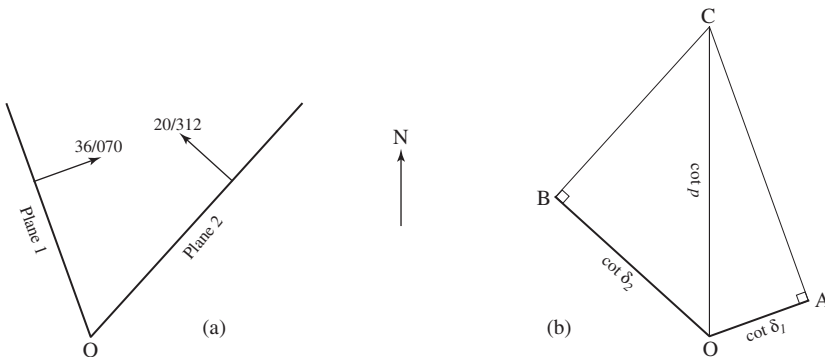


**Figure 3.10** Line of intersection by cotangent method.

**Problem**

- Find the intersection of the planes with dip lines  $D_1(36/070)$  and  $D_2(20/312)$  (Fig. 3.10a).

**Construction**

1. Plot rays from a common point  $O$  in each of the dip directions (Fig. 3.10b).
2. Using a convenient scale measure lengths  $OA = \cot \delta_1 = 1/\tan \delta_1 = 1.37638$  and  $OB = \cot \delta_2 = 1/\tan \delta_2 = 2.74748$  along the respective rays.
3. Through both  $A$  and  $B$  draw lines perpendicular to the respective rays. The point  $C$  at their intersection is a second point on the line of intersection. Line  $OC$  fixes its trend and its length is  $\cot p = 4.0$ .

**Answer**

- The line of intersection has a plunge of  $p = \arctan(1/4.0) = 14^\circ$  and its trend is 000. This is the same as found by the full graphic construction of Fig. 3.9b.

**3.7 Structure contours**

So far we have been concerned only with the *orientation* of a line of intersection. Its map *location* is an additional important property.

By definition points on a line of strike have the same elevations and there are an infinite number of such lines on any inclined plane. When the elevation is known or specified for a particular strike line then it becomes a *structure contour* on the plane. The map location of a point on a line of intersection requires two such contour lines, one on each plane.

If the elevations of the two strike lines are identical, then point  $O$  of the previous construction represents a point in space on the line. On the other hand, if the two structure contours do not have the same elevations then an auxiliary construction is needed to find a point which is exactly on the line.

**Problem**

- Given the map location of a point on plane  $A$  with attitude N 25 W, 20 W at an elevation of  $h_A = 200$  m and the location of point  $B$  on a second plane at an elevations of  $h_B = 150$  m with attitude N 48 E, 30 S, locate the line of intersections in space (Fig. 3.11).

**Approach**

- Because they have different elevations, structure contours through  $A$  and  $B$  cross on the map but do not intersect in space. We need to locate a second contour with the same elevation of one of these and there are two choices: locate the 150 m contour for plane  $A$ , or the 200 m contour for plane  $B$ .

**Construction**

1. To find an intersection we need a structure contour on one of the planes with the same elevation as the other. Our choice is to construct the structural contour on plane *B* at the same elevation as the plane at *A*.
2. With a *FL* perpendicular to the strike of plane through *B*, draw the inclined trace of the plane on the vertical section. Note that this trace must be projected *upward*, not downward.
3. On this trace locate a point at a scaled distance of 50 m higher than *B*, project this back to the map, and draw in the required structure contour. The intersection of this 200 m contour with the 200 m through *A* locates the required point *O*.
4. Using point *O*, we can then find the attitude of the line of intersection with the construction of Fig. 3.9 or Fig. 3.10.

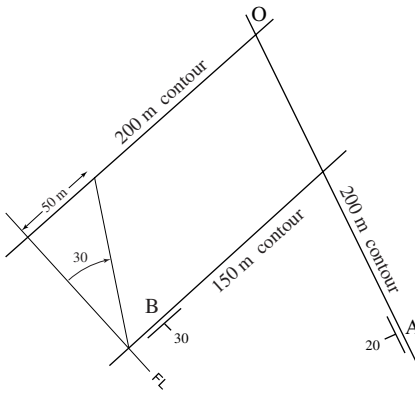


**Figure 3.11** Line of intersection when points have different elevations.

**3.8 Line vectors**

Just as we have represented the orientation of planes with two-dimensional vectors so too can we represent lines by such vectors (see §1.8). The direction of these vectors is established by trend of the line and the length is equal to  $\tan p$ . We can then obtain the orientation and length of the intersection vector **I** from dip vectors representing the two intersecting planes.

**Problem**

- From dip vectors  $\mathbf{D}_1(36/070)$  and  $\mathbf{D}_2(20/312)$  determine the intersection vector **I**.

**Construction**

1. Draw the dip vectors from a common point *O* with lengths  $\tan \delta_1 = 0.72654$  and  $\tan \delta_2 = 0.36397$  using a convenient scale (Fig. 3.12).

2. Draw a line connecting the end points of these two vectors.
3. The intersection vector **I** is established by drawing the perpendicular from *O* to this line. This gives its trend; its length is  $\tan p$ .

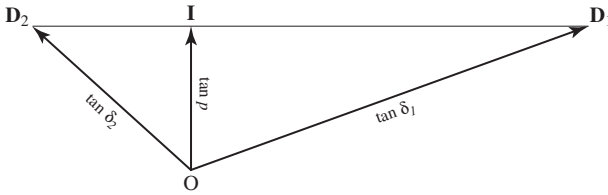


**Figure 3.12** Intersection vector from two dip vectors.

**Answer**

- The measured length of **I** is  $\tan p = 0.25$ , hence  $p = 14^\circ$  and its measured trend is 000.

From this vector method we may also obtain an analytical solution (Fig. 3.13). From the dot product of each of the two dip vectors **D**<sub>1</sub> and **D**<sub>2</sub> with the unit vector **u** in the direction of the unknown intersection vector **I** we have

$$\mathbf{D}_1 \cdot \hat{\mathbf{u}} = \mathbf{D}_2 \cdot \hat{\mathbf{u}}.$$

Using the form of the dot product from Eq. 1.9 gives

$$\tan \delta_1 \cos \phi_1 = \tan \delta_2 \cos \phi_2$$

where  $\phi_1$  and  $\phi_2$  are the angles each dip vector makes with **u**. Labeling the angle between **D**<sub>1</sub> and **D**<sub>2</sub>  $\phi$ , then  $\phi = \phi_1 + \phi_2$ , and we have

$$\phi_2 = (\phi - \phi_1).$$

Substituting this and using the identity for the cosine of the difference of two angles

$$\cos(\phi - \phi_1) = \cos \phi \cos \phi_1 + \sin \phi \sin \phi_1,$$

we obtain

$$\tan \delta_1 \cos \phi_1 = \tan \delta_2 (\cos \phi \cos \phi_1 + \sin \phi \sin \phi_1).$$

Rearranging then yields the expression for the trend of the line measured from **D**<sub>1</sub>

$$\boxed{\tan \phi_1 = \frac{\tan \delta_1}{\tan \delta_2 \sin \phi} - \frac{1}{\tan \phi}.} \tag{3.6}$$



The angle of plunge can then be obtained by recasting Eq. 1.11 into a more useful form. Substituting  $\beta = 90^\circ - \phi$  and  $\alpha = p$  we obtain

$$\boxed{\tan p = \tan \delta_1 \cos \phi_1.} \tag{3.7}$$

Using the values from the previous problem  $\delta_1 = 36^\circ$  and  $\delta_2 = 20^\circ$  and  $\phi = 118^\circ$  in Eq. 3.6 gives  $\phi_1 = 70.2974^\circ$ . Using this, Eq. 3.7 gives  $p = 13.7633^\circ$ . These results are essentially the same as found graphically in Figs. 3.9 and 3.12.

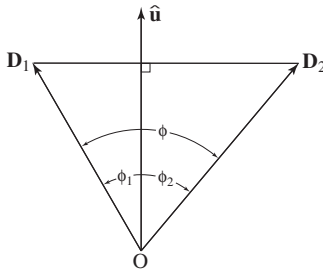


**Figure 3.13** Analytical solution of the line of intersection.

### 3.9 Accuracy of trend determinations

As with dip and strike, the angles of plunge and trend can not be measured without error, and as before, situations where small measurement errors may become magnified are of special concern.

In measuring the trend of a line on a structural plane it is common practice to align the compass in the direction of the horizontal projection of the line. As a result of an inevitable operator error, the measured trend as given by the angle  $\beta'$  will differ from the true trend given by the angle  $\beta$ . We seek an expression for the *maximum trend error*  $\epsilon_T$ ,

$$\epsilon_T = |\beta - \beta'|, \tag{3.8}$$

in terms of the angle  $\epsilon_O$  which the measured line makes with the true line as measured in the inclined plane which results from the maximum operator error. That is, we compare the true trend of a line as given by  $\beta$  with  $\beta'$  found from the pitch angle  $(r \pm \epsilon_O)$  on the same plane, where  $r$  is the true pitch angle.

There are two cases depending on whether the measured trend is on the down-dip ( $\beta' > \beta$ ) or on the up-dip ( $\beta' < \beta$ ) side of the line. The results are show graphically in Fig. 3.14.

1. If  $\beta' > \beta$ , to find an expression for this error we use Eq. 3.4, giving

$$\tan \beta = \tan r \cos \delta \quad \text{and} \quad \tan \beta' = \tan(r + \epsilon_O) \cos \delta.$$

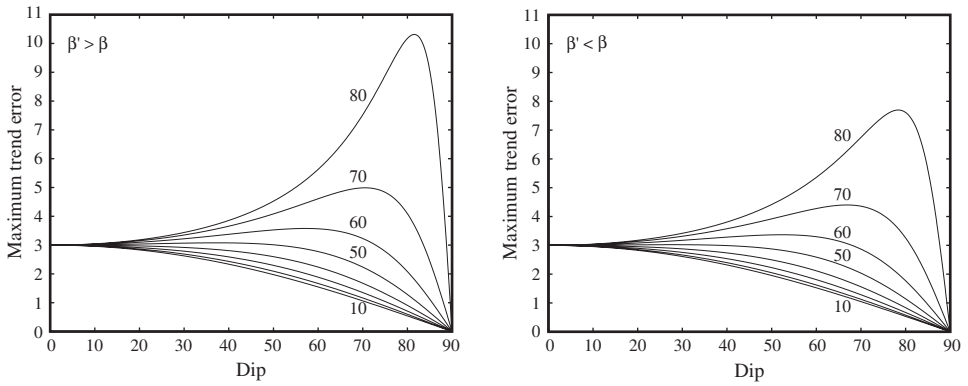


**Figure 3.14** Maximum trend error as a function of pitch and dip for  $\varepsilon_0 = 3^\circ$ .

Substituting these into the equation for the tangent of the difference of two angles

$$\tan(\beta' - \beta) = \frac{\tan \beta' - \tan \beta}{1 + \tan \beta \tan \beta'}$$

we have (after Woodcock, 1976, p. 352)

$$\tan \varepsilon_T = \frac{[\tan(r + \varepsilon_0) - \tan r] \cos \delta}{1 + [\tan(r + \varepsilon_0) \tan r] \cos^2 \delta} \quad (3.9)$$

The graph of this equation for  $\varepsilon_0 = 3^\circ$  shows that a combination of a steep plane and a large pitch angle may result in a large trend error.

- For the case  $\beta' < \beta$  we proceed in a similar way by expressing the maximum trend error associated with the smaller pitch angle ( $r - \varepsilon_0$ ). The resulting formula in this case is

$$\tan \varepsilon_T = \frac{[\tan r - \tan(r - \varepsilon_0)] \cos \delta}{1 + [\tan r \tan(r - \varepsilon_0)] \cos^2 \delta} \quad (3.10)$$

and the corresponding graph shows that, other things being equal, the maximum trend error in this case is less. This means that repeated measurements will not be symmetrically distributed about the true trend.

To avoid such errors it is advisable to measure the pitch of the line in the dipping plane directly and then determine its attitude either graphically or with the aid of Eq. 3.4.

A second type of error magnification occurs in determining the attitude of the line of intersection of two planes. Because the dip and strike measurements of both planes are subject to their own errors, the derived attitude of the line of intersection will also be in error and this error may be large if the angle between the two planes is small. This problem is treated in detail in Chapter 5.

### 3.10 Exercises

1. Determine the attitude of the line of intersection of the two planes  $A$  (N 66 E, 50 S) and  $B$  (N 22 W, 40 W). What is the pitch of this line in plane  $B$ ?
2. Plane  $A$  is a narrow shear zone and plane  $B$  is the top of a mineralized limestone bed. The locations of their outcrops are shown on the map of Fig. 3.15 and their elevations are  $h_A = 770$  m and  $h_B = 710$  m. Where in Boulder Creek would a drill hole encounter the vein system, and what would its depth be?

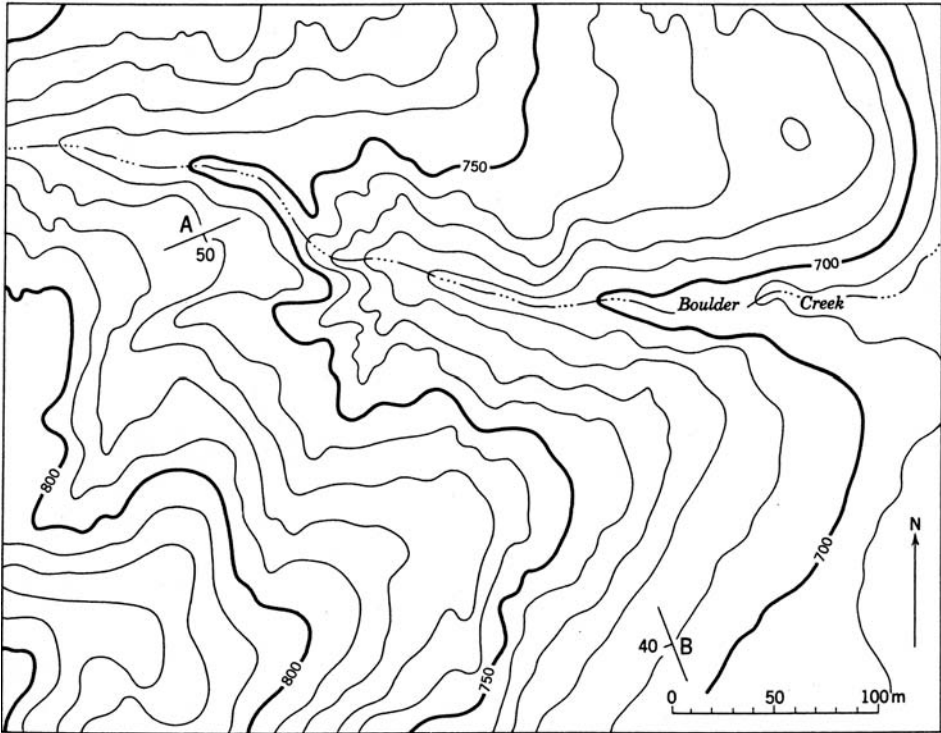


**Figure 3.15** Vein in Boulder Creek.

# 4

## Planes and topography

### 4.1 Exposures on horizontal surfaces

In Chapter 2 the simplest examples of the determination of thickness assumed that the earth's surface was a horizontal, geometrically perfect plane. The intersection of inclined layers with this surface results in an *outcrop pattern*. Represented in map view this pattern is a simple geological map.

In this case the width of the outcrop bands depends on two factors: the actual *thickness* of the layers and the angle of *dip* of each layer. The separate effect of each of these factors is shown in Fig. 4.1. In essence, these same relationships also apply to less-than-perfect real horizontal topographic surfaces.

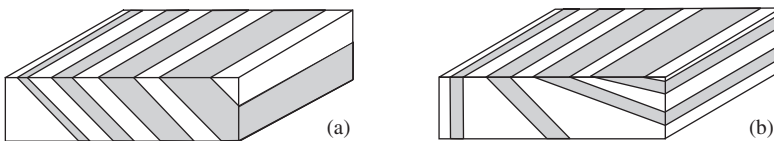


**Figure 4.1** Outcrop width: (a) varies with thickness; (b) varies with dip.

In the special case of a vertical layer, the outcrop width in map view is equal to the thickness of the layer. This unique relationship results from the fact that the map shows such a layer in edge view, that is, a line of sight in viewing the map coincides with a line which is parallel to the vertical layer. In estimating thickness of tabular objects, one instinctively seeks just such a view.

In the more general case of an inclined layer, one line of sight is always identifiable on a geological map; it is in the dip direction. For inclined layers an auxiliary view perpendicular to this line could easily be constructed that would show the layers in edge view and therefore in true thickness (Fig. 4.2a).

However, it is unnecessary to make this construction because the same information can be obtained directly from the map itself. Simply rotate the geological map so that

the dip direction is “north” and then view the map pattern along a line of sight inclined to the plane of the map at the dip angle. In this view the outcrop width, which is always greater than the thickness, is foreshortened by just the right amount to appear as true thickness (Fig. 4.2b). In adopting this oblique, down-dip view of the map it may help to reduce your depth perception by closing one eye. Clearly, this method of viewing the outcrop bands of inclined layers is limited to cases involving significant dip angles, for it is physically impossible to view horizontal strata in edge view along any line of sight of a map.

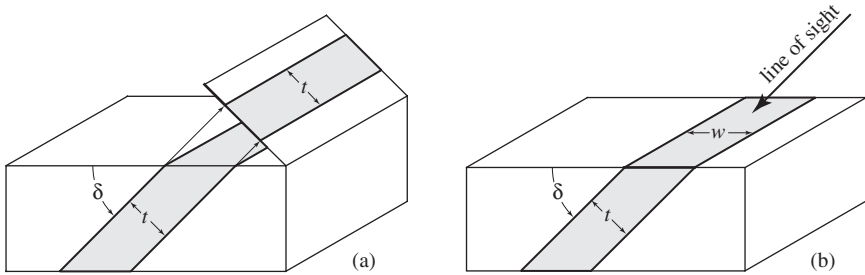


**Figure 4.2** True thickness: (a) plane normal to dip line; (b) down-dip view.

This principle is used in reverse for traffic signs painted on streets. By purposely distorting the letters as viewed vertically (map view) the foreshortening which accompanies the driver’s oblique view of the road surface exactly compensates for the distortion and the warnings appear in normal proportions and are perfectly readable (see Fig. 4.3).



**Figure 4.3** View from the left along a line inclined to the page.

In effect, twisting such simple geological maps so that the inclined strata are viewed in the down-dip direction restores the sedimentary beds to their original horizontal attitude. Contacts on the map then cease to be just lines separating stratigraphic units on the earth’s surface; they can be seen to come to life as the depositional and erosional surfaces which they once were. A map viewed down-dip represents a kind of cross section, such as might be seen in the walls of the Grand Canyon. As such, the important dimension of sequence of deposition in time is added to the map. Unconformities become buried landscapes, and this view facilitates comparisons with the present earth’s surface and the erosional processes responsible for its form. Certainly the possibility of completely overturned beds should be recognized, especially in areas of complex structure. In such cases, the

down-dip view yields a picture of the strata which is upside-down, but such a view may actually help the interpretation of overturning if other obvious evidence is lacking.

## 4.2 Effect of topography

In areas of sloping terrain, additional factors are involved in determining the character of outcrop patterns, and these include topographic slope angle and direction relative to the attitude of the strata, and variations in slope angle and direction. In other words, in addition to thickness and dip, the map pattern also depends on the details of the topography. The relationships between dip and topography have been formalized into a series of statements, collectively called the *Rule of Vs*, by which the direction of dip can be estimated directly from the outcrop patterns. Wherever the trace of a plane crosses a valley, the resulting pattern is characteristic of the attitude of the plane. There are several distinct types of patterns.

1. *Horizontal planes*: Topographic contour lines can be thought of as the surface traces of imaginary horizontal planes. The outcrop traces of real horizontal planes therefore exactly follow the topographic contours. Such patterns are completely controlled by the topography; the outcrop trace faithfully reflects the local contour lines in every detail. Therefore, the outcrop pattern Vs upstream, just as the contour lines do (Fig. 4.4a).
2. *Planes inclined upstream*: As the attitude departs from the horizontal, with the dip direction in the upstream direction, the pattern made by the traces of the structural planes is progressively modified into a blunter V, still pointing upstream (Fig. 4.4b). With steepening dip, the outcrop pattern is an increasingly subdued reflection of topographic detail.
3. *Vertical planes*: In the special case of a  $90^\circ$  dip, the outcrop traces are straight and parallel to the strike direction, regardless of topographic detail. There is no V at all, and thus no control on the pattern by the topography (Fig. 4.4c).
4. *Planes inclined downstream*: There are two general cases and one special boundary case.
  - (a) With dip greater than valley gradient, the pattern Vs downstream (Fig. 4.5a).
  - (b) If the dip angle and valley gradient are exactly equal, the outcrop trace will not cross the valley axis, and there is no V (Fig. 4.5b). However, streams generally steepen headward and a continuous planar structure will therefore cross somewhere upstream.
  - (c) If the dip is less than the valley gradient, but still in a downstream direction, the pattern will V upstream (Fig. 4.5c).

As stated, these rules assume that the strike direction is at a right angle to the valley axis. The result is that the V patterns are approximately symmetrical. With other strike

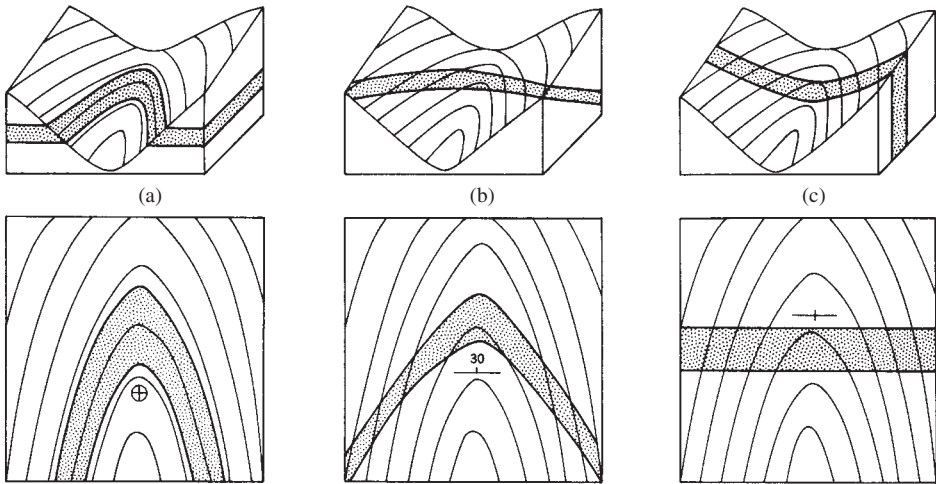


**Figure 4.4** Rule of Vs: (a) horizontal layer; (b) layer dipping upstream; (c) vertical layer.

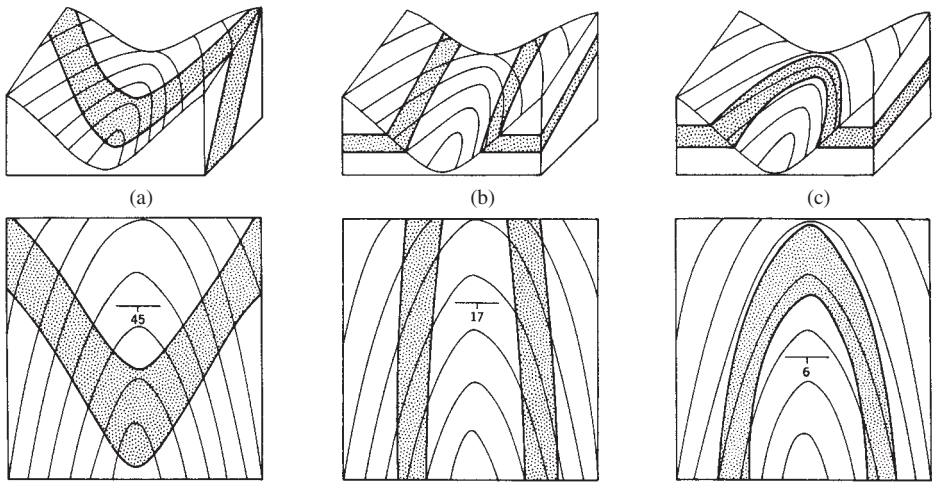


**Figure 4.5** Rule of Vs: (a) layer dipping downstream; (b) layer and valley axis with equal slopes; (c) layer dipping downstream at an angle less than valley gradient.

directions, asymmetrical Vs are produced, but in essence the rule still applies. In the limiting case when the valley and strike are parallel there is no V at all.

There is a simple, easily remembered statement which summarizes all these relationships: *the V of the outcrop trace points in the direction in which the formation underlies the stream* (Screven, 1963).

Better yet, however, is to visualize the geometrical relationship between the structural planes and topography in three dimensions. In an area of topographic relief the outcrop pattern of uniformly dipping beds is irregular, yet if these same beds were viewed from

an airplane in an oblique, down-dip direction, they would appear in edge view (the block diagram of Fig. 4.4b is very nearly in this orientation). The irregularities due to the topography are then eliminated and the traces of the inclined planes are straight; true thickness appears directly. This same relation would, of course, hold true for a scaled topographic relief model with the outcrop pattern included. By perceiving the earth's surface depicted by the topographic contour lines on the map as a relief model, the mind's eye can accommodate the influence of the topography of the outcrop pattern. This technique takes some effort to learn and practice is the key. Once the ability is attained, however, it is an enormously powerful aid in map interpretation, for even in areas of considerable and varied relief, and therefore of highly irregular map patterns, the structure can be viewed on the map in a down-dip direction with a great conceptual simplification.

### 4.3 Dip and strike from a geological map

In previous examples we treated the attitude of inclined planes in semi-quantitative terms only. However, the actual dip and strike can be found if the spatial locations of three points on the plane are known. In the simplest case, two of the points with the same elevation can often be recognized.

#### Problem

- In Fig. 4.6, the trace of the lower bounding plane of the inclined layer cuts the topographic contours at points  $A$ ,  $B$  and  $C$  with elevations  $h_A = h_B = 620$  m and  $h_C = 610$  m. What are the dip and strike?

#### Solution

1. Draw line  $AB$  connecting the two points of equal elevation. This is, by definition, a line of strike.
2. Draw a perpendicular line from  $AB$  to point  $C$ . This is the true dip direction. The true dip angle is measured in the vertical section containing this line.
3. Draw a line parallel to this dip direction as a horizontal  $FL$ . Extend the strike line  $AB$  and draw a second strike line through  $C$  to intersect this  $FL$ .
4. These two points on  $FL$  represent the map locations of the line  $AB$  and the point  $C$ .
5. At a vertical distance below the map point  $C$  of  $\Delta h = h_A - h_C = 10$  m plot the actual outcrop point  $C$  using the map scale. The inclined line of dip can be drawn and the dip angle measured.

#### Answer

- The attitude of the true dip is **D**(15/270).



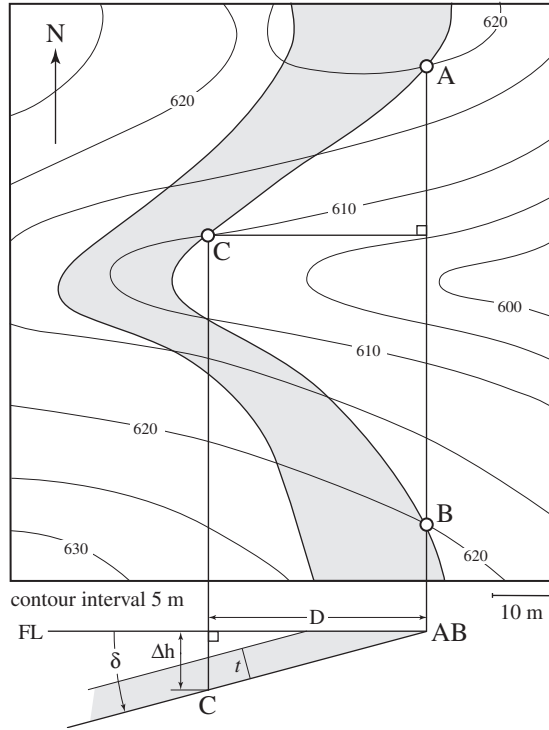


**Figure 4.6** Dip and strike from the outcrop pattern.

The dip angle can also be found from the map distance  $D$  from the strike line  $AB$  to  $C$  and the vertical distance  $\Delta h$  using

$$\tan \delta = \Delta h / D. \tag{4.1}$$

Either graphically or analytically, choosing as widely spaced points as possible improves accuracy.

### 4.4 Linear interpolation

More generally, the three points will have different elevations. We then need a way of locating a point with specified elevation lying on a line between two known ends. This involves *linear interpolation* and there are two complementary graphical approaches. The first uses previously established methods, while the second is simpler.

#### Problem

- Points  $O$  and  $A$  have elevations  $h_O = 296$  m and  $h_A = 178$  m. Map distance  $D_{OA} = 300$  m. Locate point  $B$  on  $OA$  with elevation  $h_B = 225$  m (Fig. 4.7a).

### Construction I

1. With horizontal line  $OA$  as  $FL$ , construct a section showing a vertical line directly below surface point  $A$  (Fig. 4.7a). Using the map scale locate two points on this line:
  - (a) Point  $X$  at a depth  $\Delta h_A = (h_O - h_A) = (296 - 178) = 118$  m.
  - (b) A point at an intermediate depth  $\Delta h_B = (h_O - h_B) = (296 - 225) = 71$  m.
2. Draw line  $OX$  to represent the inclination of the line between map points  $O$  and  $A$ .
3. A horizontal line from the intermediate point intersects this inclined line  $OX$  at  $Y$ .
4. Project  $Y$  vertically back to  $OA$  to locate point  $B$  on the map with the required elevation.

This construction is based on the fact that right triangles  $OAX$  and  $OBY$  are *similar* and a property of such triangles is that the lengths of corresponding pairs of sides have the same ratios – as  $Y$  divides  $AX$  in the ratio  $\Delta h_B/\Delta h_A = 71/118$ , so too  $B$  divides  $OA$  in this same ratio.

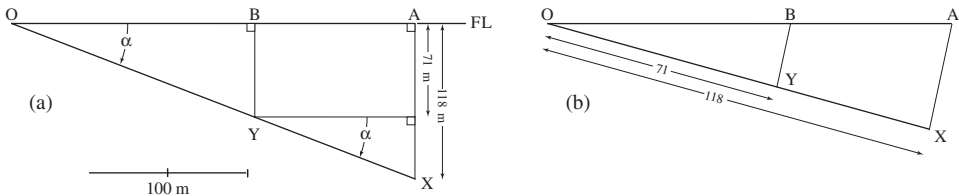


**Figure 4.7** Linear interpolation: (a) folding line; (b) scaled line.

In practice two problems arise with this construction. First, the map scale may be such that the depths to  $X$  and  $Y$  are difficult to plot accurately. Second, if the angle of dip, true or apparent, is small, locating point  $Y$  commonly involves a small angle intersection which is subject to a large error. An alternative method minimizes both these difficulties.

### Construction II

1. At a convenient but arbitrary angle draw a line from  $O$  oblique to the map line  $OA$  (Fig. 4.7b). The exact angle does not matter, but it should generally be modest (neither very small nor very large).
2. Locate two point on this line:
  - (a) Point  $X$  at a distance of  $\Delta h_A = 296 - 178 = 118$  units.
  - (b) Point  $Y$  at a distance of  $\Delta h_B = 296 - 225 = 71$  units.
3. Choose an arbitrary scale so that distance  $OX$  is roughly equal to  $OA$ . With a millimeter or engineers triangular scale this is easily accomplished. Using this scale plot point  $X$  at a distance of 118 units and point  $Y$  at a distance of 71 units.
4. Connect points  $A$  and  $X$  and then draw a parallel line through  $Y$  to locate point  $B$  on  $OA$ . With an appropriately chosen scale the angles at  $A$  and  $X$  will be approximately equal and they will be large if  $\alpha$  is small.

In this construction triangles  $OAX$  and  $OBY$  are similar. Therefore as  $Y$  divides  $OX$  in the ratio  $\Delta h_B/\Delta h_A = 71/118$ , so  $B$  divides  $OA$  in this same ratio.

The location of the intermediate point  $B$  on line  $OA$  can also be found by calculating the distance  $D_{OB}$  knowing the distance  $D_{OA}$ . In Fig. 4.7a  $OBY$  and  $OAX$  are right-triangles and therefore

$$\frac{\Delta h_B}{\Delta h_A} = \frac{D_{OB}}{D_{OA}} \quad \text{or} \quad D_{OB} = D_{OA} \left[ \frac{\Delta h_B}{\Delta h_A} \right]. \tag{4.2}$$

In the example problem, distance  $D_{OY}$  divides  $D_{OX}$  in the ratio  $\Delta h_B/\Delta h_A = 71/118$ , then  $B$  also divides  $OA$  in this same ratio. That is

$$D_{OB} = 300(71/118) = 181 \text{ m,}$$

and we can then locate point  $B$  on map line  $OA$  using the map scale.

There are two situations where such an analytical solution is useful. First, if the locations of points  $O$  and  $A$  have been determined using modern electronic surveying techniques and therefore are very accurately known *and* a similar accuracy for the location of point  $B$  is required, then the graphical methods are probably inappropriate.

Second, if several related interpolation problems have to be solved routinely then even if great accuracy is not needed an answer can be obtained quickly with a calculator.

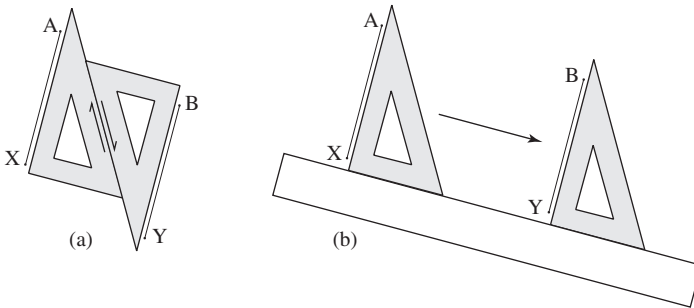


**Figure 4.8** Simple methods of drawing parallel lines.

### 4.5 Parallel lines

In several constructions we need to accurately draw parallel lines. Using a protractor to measure the orientation of the first line  $AX$  and then plotting the second line  $BY$  using this measured angle is not satisfactory because small errors are inevitable and the lines will not be exactly parallel. There are several alternative ways of drawing such lines more accurately.

1. The easiest way is to use a drafting machine.
2. A T-square and an adjustable triangle on a drafting board is almost as effective.

3. A specialized drafting tool called a *parallel glider* (essentially a straight edge attached to a pair of small wheels) can also be used. This device has the advantage of portability.
4. There are simple, serviceable alternatives.
  - (a) Using two identical triangles, place the side of one triangle along the line  $AX$ . With the second triangle in contact along their hypotenuses slide this triangle and draw the parallel line  $BY$  (Fig. 4.8a).
  - (b) Using a triangle and a straight edge, place one side of the triangle along the line  $AX$ . Then place a straight edge along the base of the triangle, and shift it along this base and draw the required parallel line  $BY$  (Fig. 4.8b).

#### 4.6 Three-point problem

With the accurate location of such an intermediate point with known elevation established by linear interpolation on a line with known end points, we are now prepared to determine the strike and dip of a plane from three general points whose map locations and elevations are known.

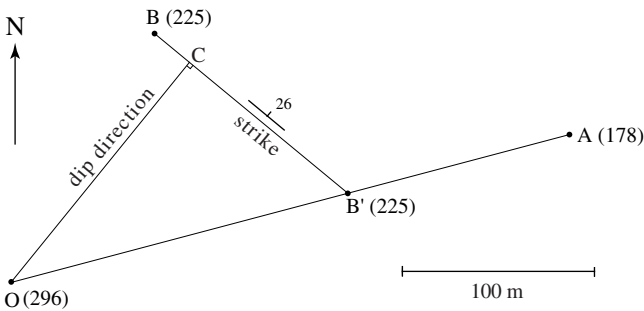


**Figure 4.9** Strike and dip from three points on a plane.

#### Problem

- From the map location of points  $O$ ,  $A$  and  $B$  on a plane and their elevations  $h_O = 296$  m,  $h_A = 178$  m and  $h_B = 225$  m, determine the attitude of the plane (Fig. 4.9).

#### Construction

1. Label the highest point  $O$  which serves as a local origin, the lowest point  $A$  and the intermediate point  $B$ . Draw line  $OA$ .
2. Locate point  $B'$  with elevation  $h_B = 296$  m between points  $O$  and  $A$  by linear interpolation (as in Fig. 4.7). Line  $BB'$  is then a line of strike.
3. From  $O$  a perpendicular line intersects  $BB'$  at point  $C$ . Line  $OC$  is then the dip direction. As in Fig. 4.5 a vertical section parallel to this direction can be constructed giving the dip of the plane, or Eq. 4.1 can be used to calculate it.

**Answer**

- The attitude of the plane is N 50 W, 26 N.

The three-point problem may also be viewed as an exercise in finding the true dip and strike from two apparent dips. First, the inclinations in directions  $OA$  and  $OB$  are found from the map distances  $D_{OA}$  and  $D_{OB}$  and elevation differences  $\Delta h_A$  and  $\Delta h_B$  either by the graphical construction of Figs. 1.11 or 1.12 or with

$$\alpha_A = \arctan(\Delta h_A/D_{OA}) \quad \text{and} \quad \alpha_B = \arctan(\Delta h_B/D_{OB}). \quad (4.3)$$

In the example problem

$$\alpha_A = \arctan(118/300) = 21.5^\circ \quad \text{and} \quad \alpha_B = \arctan(71/150) = 25.3^\circ.$$

If, as in this case, the distances are measured to the nearest meter, then the tenths of a degree are significant. The dip and strike can then be found with the constructions of Figs. 1.12, 1.13 or 1.15, or they may be calculated using Eqs. 1.10 and 1.11.

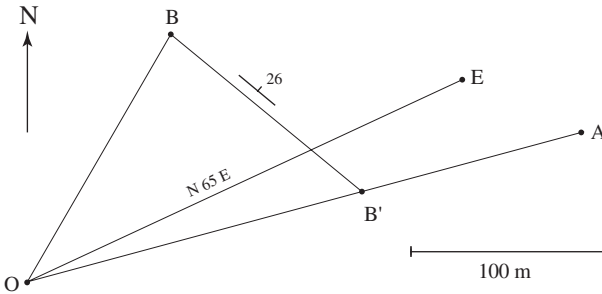


**Figure 4.10** Elevation of a fourth point on the plane.

A closely related problem is to determine the elevation of a fourth point on the plane with known dip and strike from its map location.

**Problem**

- What is the elevation of point  $E$  on the plane, where  $D_{OE} = 250$  m on a line bearing N 65 E (Fig. 4.10)?

**Construction**

1. From the known dip of the plane, determine the apparent dip in the direction  $OE$  graphically or with Eq. 1.5 or 1.8. The result is  $\alpha_E = 23.5^\circ$ .
2. With the apparent dip  $\alpha_E$  in the direction  $OE$ , the elevation difference between  $O$  and  $E$  can be found graphically or computed from

$$\Delta h_{OE} = D_{OE} \tan \alpha_E. \quad (4.4)$$

With  $D_{OE} = 250$  m, then  $\Delta h_{OE} = 109$  m.

3. The elevation of the fourth point  $E$  is

$$h_E = h_O - \Delta h_{OE} = 296 - 109 = 187 \text{ m.} \quad (4.5)$$

The three-point and related problems can also be solved analytically. As in the case of interpolation these may be used when greater accuracy is required or a number of similar problems have to be solved quickly. These are treated in some detail in §7.8.

#### 4.7 Structure contours

In some applications we need to depict an inclined plane on a map with *structure contours* (see §3.7), that is, by a series of parallel lines of equal elevation drawn on its surface at a fixed interval, each line representing a specified vertical distance from an established datum. To draw these contours a series of points must be interpolated corresponding to multiples of the contour interval. Again there are two ways of constructing such structure contours, corresponding to the two methods of graphic interpolation.

##### Problem

- Represent the inclined plane of Fig. 4.9 by structure contours with a contour interval of 20 m.

##### Construction I

1. As in Fig. 4.7a, construct a section with the horizontal line  $OA$  as  $FL$  and along the vertical line  $AX$  plot a series of points with elevations 280–160 m at intervals of 20 m using the map scale. Note that horizontal line  $OA$  has an elevation of 296 m so that the 280 m contour is just 16 m below it (Fig. 4.11a).
2. From these points draw a series of horizontal lines to intersect the inclined line  $OX$ .
3. Project these points back to  $OA$  to intersect it at  $90^\circ$ .
4. From these points add the structure contours parallel to the known strike direction.

In some cases structure contours may be required on both top and bottom of an inclined layer. Given that the contours of Fig. 4.11a represent the bottom of such a layer, we now require contours on its upper bounding plane (Fig. 4.11b). The construction proceeds exactly as before, except now the inclined line representing the top is used instead.

This method suffers from the same problems noted in Fig. 4.7a, and the use of the scaled line avoids small angle intersections. It also requires fewer steps. Further, contours above or below the two known points can also be easily established by *linear extrapolation*.

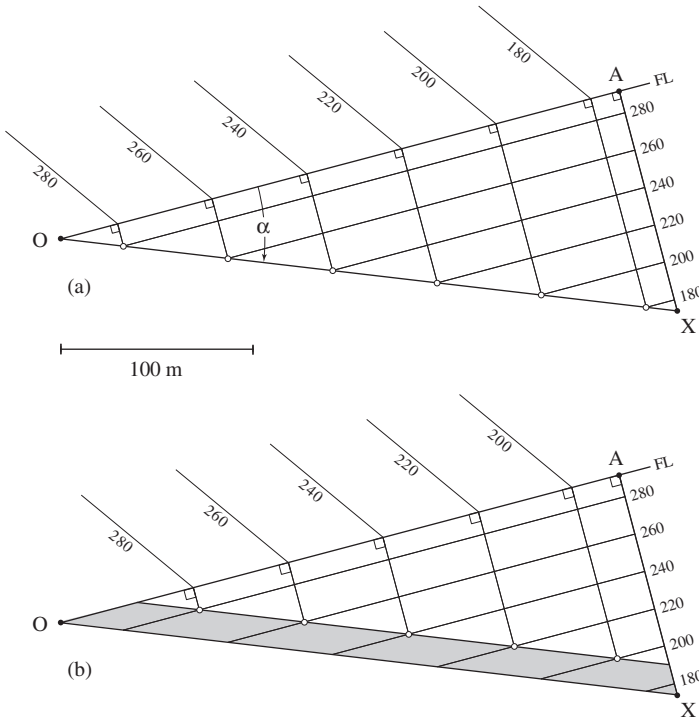


**Figure 4.11** Structure contours: (a) the scaled line; (b) structure contours.

**Construction II**

1. Draw a line at a convenient angle through point  $O$ , and locate point  $X$  on this line at a distance  $D_{OX} = h_O - h_X = 118$  units using a convenient scale (Fig. 4.12a).
2. As before locate a series of points along this line corresponding to the actual contour values. It is possible to start measuring from point  $O$ , but a useful strategy is to shift the scale so point  $O$  matches its elevation on the scale. In this example  $h_O = 296$ , so the scale is shifted 4 units to the left. Then all points at 20 unit increments can be easily marked. It is also easy to include contours beyond the end points  $O$  and  $A$ .
3. Project these points back to  $QA$  parallel to the line  $AX$ .
4. Then, as before, draw the contours parallel to the known strike.

Instead of locating these contours graphically, it may be easier and faster, especially for small dip angles, to calculate the map spacing  $\Delta D_{CI}$  between the contours along a line of true or apparent dip using

$$D_I = \Delta h_I / \tan \delta \quad \text{or} \quad D_I = \Delta h_I / \tan \alpha, \tag{4.6}$$

where  $\Delta h_I$  is the contour interval. One way of using this result is to set a pair of dividers to this calculated distance and to step off a series of points along a line in the true or

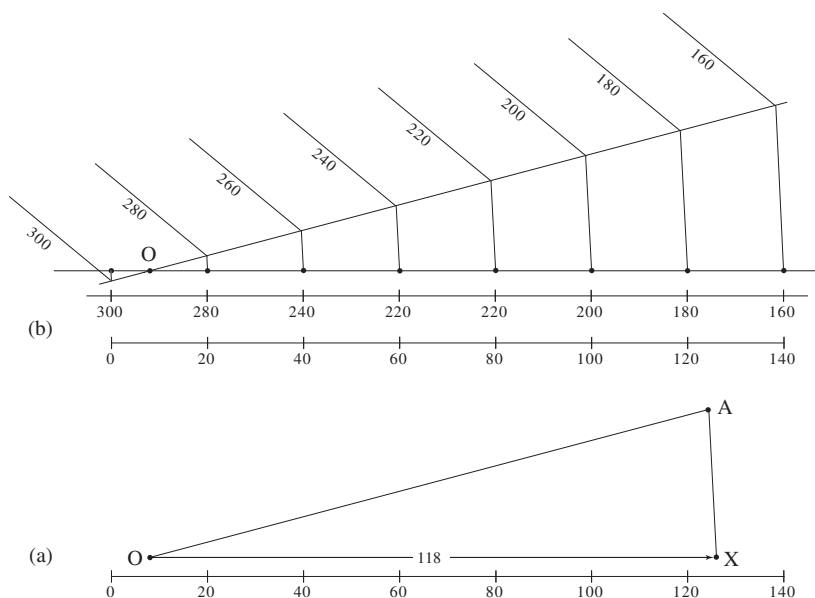


**Figure 4.12** Structure contours: (a) contours on lower surface; (b) contours on upper surface.

apparent dip direction. However, a small error in the original setting will be compounded as the number of contours increases. For example, if the setting has a 1% error, the tenth contour will be 10% in error. A better way is to determine multiples of  $\Delta DCI$  and plot these distances without moving the scale. There will inevitably be small plotting errors associated with each of these points but these errors will be independent.

#### 4.8 Predicting outcrop patterns

We may also reverse the processes of determining the attitude of a plane from known points and construct the outcrop trace of an inclined plane from its attitude at a single point. The earth's surface is represented on a map by topographic contours. As we have seen, structural surfaces can be similarly represented by structural contours. If both are represented by contours with the same interval and datum, points of intersection of corresponding contour lines represent points common to the topographic and structure contours, that is, outcrop points of the structural plane.

The technique for accomplishing this is illustrated with the block diagram (Fig. 4.13). Knowing the attitude of the structural plane at a single point  $O$ , a vertical section perpendicular to the strike direction is established and topographic contours are added to this section. Starting at the known point on this section, the trace of the dipping plane is then drawn. The intersection of this inclined line and the topographic contours fixes the locations of each structural contour (Points 1, 2, 3, 4).



Projecting these contours in the strike direction then locates points of intersection with the topographic contours on the earth's surface. The outcrop trace is completed by connecting these points. Note that not all of the structure contours are used; the contour associated with Point 4 remains totally underground. In other cases, the contours may be completely in the air.

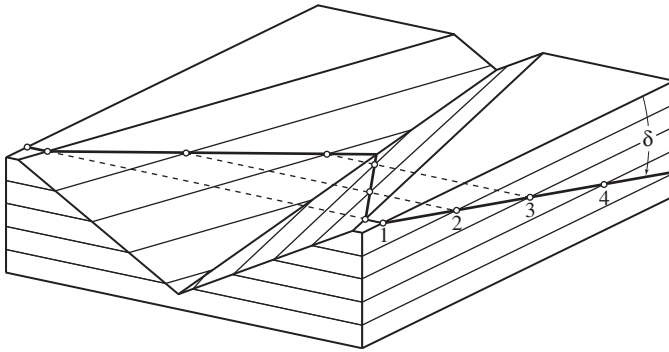


**Figure 4.13** Geometrical basis for predicting the outcrop trace of an inclined plane.

**Problem**

- Given a topographic map and a single outcrop point Z on a structural plane whose dip is  $20^\circ$  due north, construct the outcrop trace of the plane in the map area.

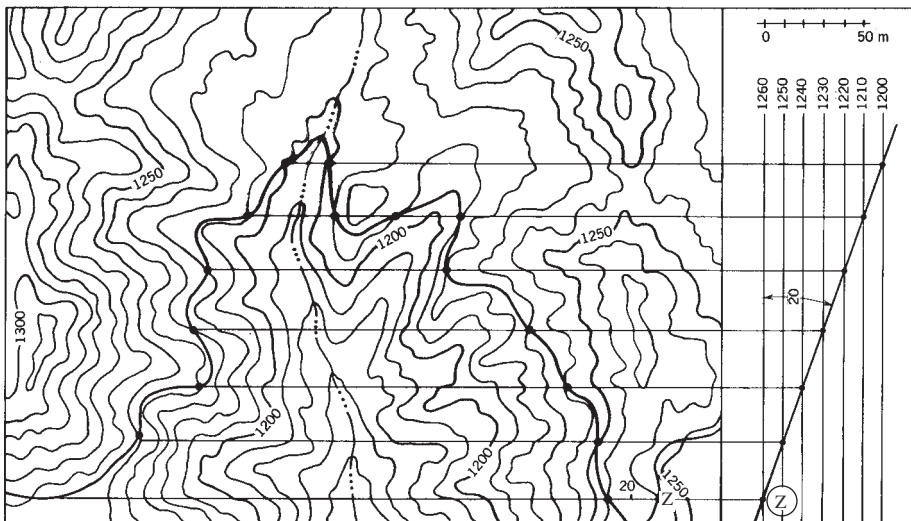


**Figure 4.14** Outcrop pattern of an inclined plane exposed at point Z (SE corner of map).

### Construction

1. As in Fig. 4.12 construct a series of structure contours representing the inclined plane on the section showing the true dip angle. The contour interval must be the same as on the topographic map, that is 10 m, and the 1260 m structure contour must pass through known point Z (Fig. 4.14).
2. Each intersection of a structure contour with its matching topographic contour is an outcrop point, and these should be marked distinctly. An easy way to avoid mismatching these contours is to start at the known point, drop down one structure contour and one topographic contour and mark the point. Repeat this until you run out of topographic contours and then reverse the direction and move up one contour at a time. Continue this up and down process until all points have been marked.
3. Complete the outcrop trace of the plane by joining successive outcrop points. This line must cross at and only at these marked points. If the contour spacing is wide, the outcrop trace can usually be sketched across the gap by visual interpolation.

Drawing the outcrop trace should be something more than an exercise in connecting points, as in a child's work book; they should certainly not be straight lines. Especially at breaks in slopes, in valley bottoms and on ridge crests it may be necessary to interpolate intermediate structure and the topographic contours, at least mentally, in order to achieve the desired sensitivity to the effects of topography on the outcrop pattern.

If both the upper and lower bounding planes of a layer are to be shown it is a simple matter to add the second boundary to the section using the thickness of the layer, then construct a second set of structure contours and repeat the procedure for the outcrop trace of this other boundary.

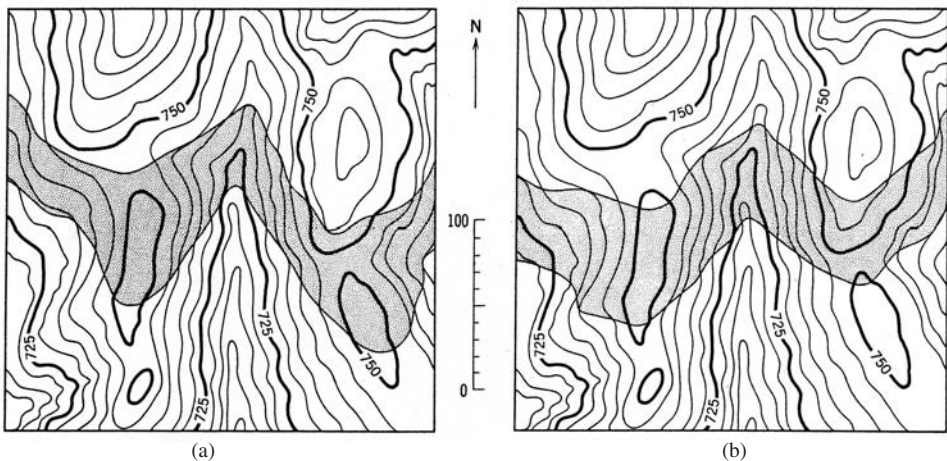


**Figure 4.15**

## 4.9 Exercises

1. Determine the attitude of the mapped unit of Fig. 4.15a. With this result view the map in a down-dip direction and, in combination with a visualization of the topography, try to see the unit as a layer in edge view. The topography of Fig. 4.15b is identical. With your visualization of the first map as a reference, now try to look down the dip of this layer, and estimate its different attitude and thickness. Check your results.
2. With the following information and the topographic map of Fig. 4.16, construct a geological map. The base of a 100 m thick sandstone unit of lower Triassic age is exposed at point *A*; its attitude is N 70 W, 25 S. Point *B* is on the east boundary of a 50 m thick, vertical diabase dike of Jurassic age; its trend is N 20 E. At point *C*, the base of a horizontal Cretaceous sequence is exposed and at point *D* the base of a conformable sequence of Tertiary rocks is present.

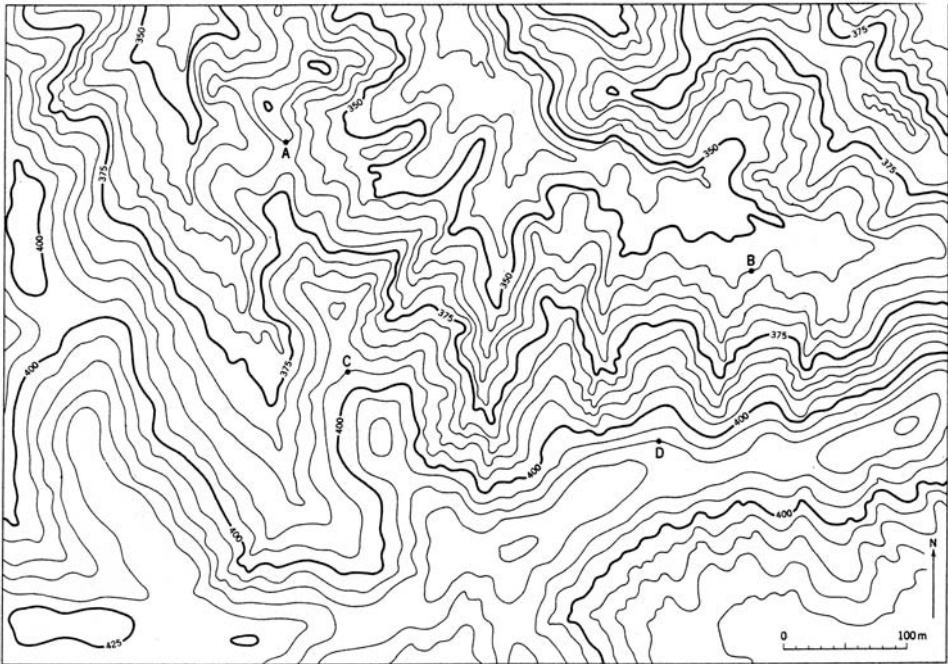


Figure 4.16

# 5

## Stereographic projection

### 5.1 Introduction

For any problem involving distances an orthographic construction is always required. For purely angular relationships, however, there is an alternative approach which is both quick and efficient. It also provides a means of solving more advanced problems which would otherwise be quite difficult.

Given an inclined plane containing a line (Fig. 5.1a), imagine a sphere of *unit* radius centered at a point *O* on the outcrop trace of an inclined structural plane containing a structural line (Fig. 5.1b). This plane passes through the center and therefore contains a diameter of the sphere and every such *diametral plane* intersects the sphere as a *great circle*. The line in this plane intersects the sphere as a point on this circle. This is called the *spherical projection* of the plane and line. We now require a way of reducing this three-dimensional representation to two dimensions. The choice is dictated by the desire to preserve angles and this is best accomplished with the method of *stereographic projection*.<sup>1</sup> It is treated in most introductory structural geology texts. The books by Phillips (1971) and Lisle and Leyshon (2004) are particularly useful.

### 5.2 Stereogram

The geometrical basis of this method involves the projection of a point on the sphere to the horizontal diametral plane. Consider the structural line whose attitude is 30/090. On the east-trending vertical diametral plane of the sphere the line is represented by the radius *OP* with plunge  $p = 30^\circ$  (Fig. 5.2a). Its spherical projection on the lower hemisphere is the point *P* and this is then projected to point *L* on the horizontal diameter using the *zenith point* *Z*. Point *L* then represents the inclined line in stereographic projection. We

<sup>1</sup>This method of projection was already known to Hipparchus of Nicaea [c. 190–220 BC], the great Greek astronomer of antiquity.

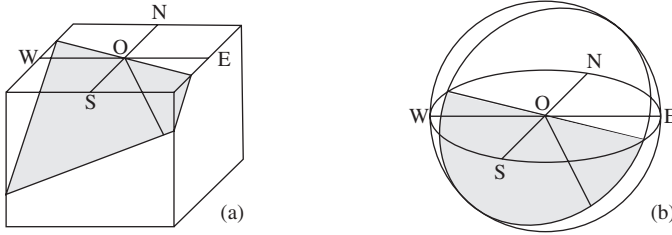


**Figure 5.1** Structural plane and line: (a) outcrop; (b) unit sphere.

can obtain an expression for the location of this point on the horizontal diametral plane (Fig. 5.2b). If the line  $OP$  makes angle  $\theta = 90^\circ - p$  with the vertical, then the line  $ZP$  makes angle  $\frac{1}{2}\theta$  with the same vertical.<sup>2</sup> Then the radial distance  $OL$  is

$$r = \tan \frac{1}{2}\theta = \tan \frac{1}{2}(90 - p). \tag{5.1}$$

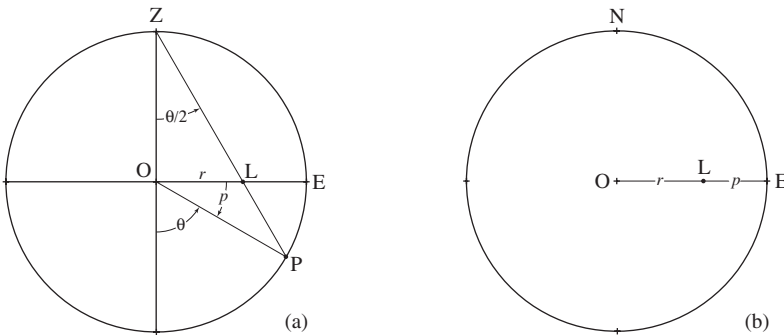


**Figure 5.2** Inclined line: (a) vertical section; (b) stereogram.

As this result shows we may now easily construct a view of the horizontal projection plane depicting the line as a point. This representation plotted inside the horizontal great circle, called the *primitive*, together with one or more of the cardinal compass directions constitutes a *stereogram* (Fig. 5.2b).

In this same way we may also easily represent a family of lines on a single structural plane as a series of points (Fig. 5.3a). These fall on a circular arc which represents a *great circle* on the sphere. An important property of the stereographic projection is that great circles on the sphere project as circles on the stereogram.

In a similar way we may represent lines of constant pitch on a series of inclined planes with common strike (Fig. 5.3b). These points fall on a *small circle* on the sphere. This also projects as the arc of a circle whose angular radius is the pitch angle.

<sup>2</sup>Here and elsewhere we make use of the fact that an inscribed angle is half the central angle when both intercept the same arc (see §9.7 for details).

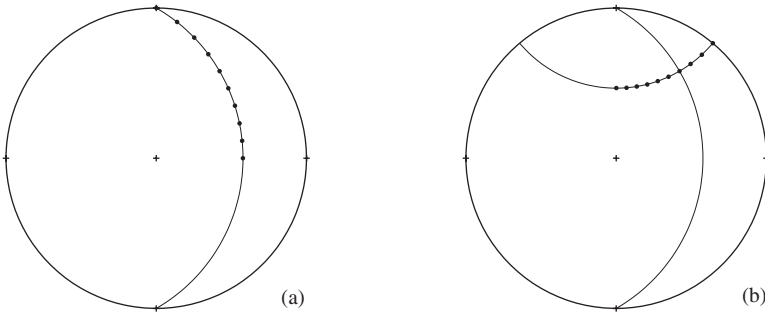


**Figure 5.3** Locus of points: (a) great circle; (b) small circle.

Because both great and small circles on the sphere are represented by circular arcs in projection it is especially easy to construct these on a stereogram. This permits the representation of any structural plane or line to be obtained quickly and easily. We now illustrate the techniques for doing this.

**Problem**

- Represent the plane dipping  $\delta = 30^\circ$  due east as a great circle on a stereogram.

**Construction**

1. On a circle of unit radius representing the vertical east-west diametral plane draw the radius  $OP$  representing the trace of the dipping plane inclined to the horizontal diameter at  $\delta = 30^\circ$  (Fig. 5.4a). Projection line  $PZ$  crosses the horizontal diameter at point  $D$  which represents the line of true dip on the horizontal projection plane.
2. On a second unit circle representing the horizontal projection plane, the required great circle must pass through  $D$  and points on the primitive representing both ends of the horizontal strike lines on the primitive (Fig. 5.4b). To locate its geometrical center  $C$  on the diameter through  $OD$ , draw a line from north making an angle  $\delta$  with the north-south diameter and with a compass complete the circular arc with  $CD$  as radius.

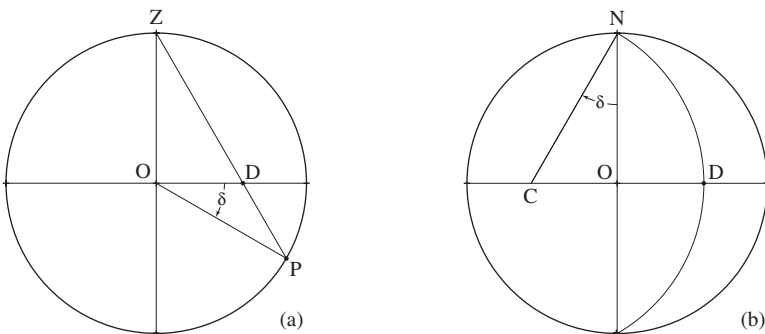


**Figure 5.4** Great circle construction: (a) inclined plane; (b) stereogram.

From this figure the expression for the radial distance  $r = OC$  is given by

$$r = \tan \delta. \quad (5.2)$$

In the special boundary case of  $\delta = 45^\circ$  the center lies on the primitive. If  $\delta < 45^\circ$  the center is inside the primitive and if  $\delta > 45^\circ$  it is outside.

### Problem

- Represent the locus of lines of constant pitch  $\rho = 30^\circ$  on a series of planes of variable dips which strike due east.

### Construction

1. On a unit circle representing the vertical diametral plane draw the radius  $OP$  representing the trace of the line at pitch angle  $\rho = 30^\circ$  and intersecting the lower hemisphere at  $P$  (Fig. 5.5a). Line  $ZP$  intersects the horizontal projection plane at  $L$ .
2. On a second unit circle representing the horizontal projection plane locate the trend points  $T_1$  and  $T_2$  on the primitive at horizontal angles  $\rho = 30^\circ$  on both sides of the east point (Fig. 5.5b).
3. The small circle passes through points  $T_1$ ,  $T_2$  and  $L$ . To locate its geometrical center  $C$  draw a line through either  $T_1$  or  $T_2$  tangent to the primitive circle to intersect the extended radius through  $OL$ . With a compass complete the circular arc with  $CL$  as radius.

From this figure the radial distance  $r = OC$  is given by

$$r = 1/\cos \rho. \quad (5.3)$$

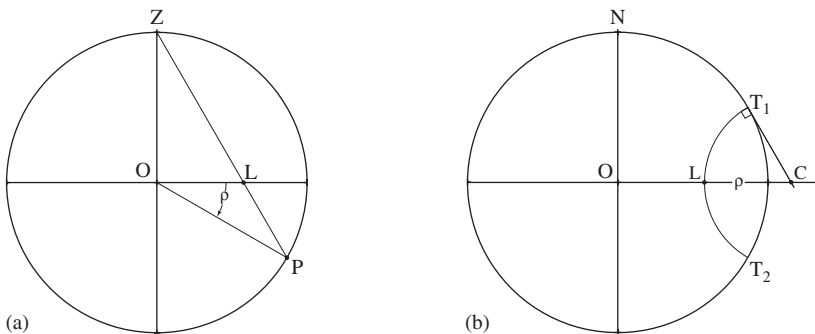


**Figure 5.5** Small circle construction: (a) vertical section; (b) stereogram.

In both of these constructions separate vertical and horizontal diametral circles were used in order to make the steps clearer. In practice, however, the entire construction may be completed quickly and efficiently on just one such circle. With their common

diameter as a folding line, a single circle is first viewed as a vertical section and then as the horizontal projection plane.

In all of these constructions only the lower hemisphere is used in order to maintain the correspondence between the representation of lines and planes and the previously established convention for giving their trend as the direction of *downward inclination*.

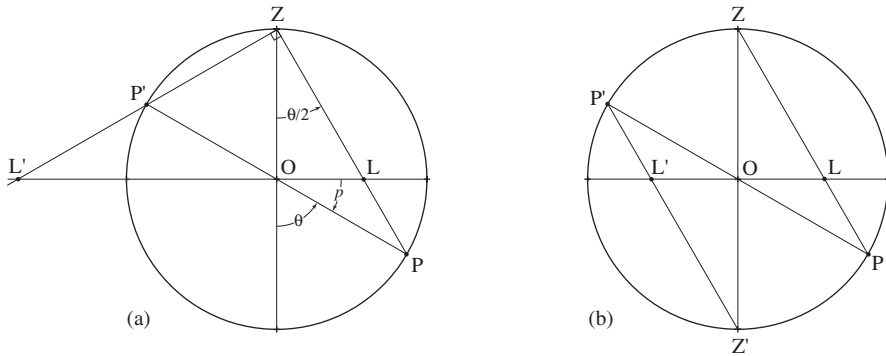


**Figure 5.6** Opposite of a line: (a) upper hemisphere; (b) lower hemisphere.

There are, however, some situations where the upper hemisphere must also be used. In Fig. 5.6a, the inclined radius  $OP$  is extended upward to intersect the upper hemisphere at  $P'$ , the *opposite* of  $P$ . As before we project  $P'$  to the projection plane using point  $Z$ . This locates point  $L'$ , the *opposite* of  $L$ , *outside* the primitive and this is the required representation of  $P'$ . Note that because  $PP'$  is a diameter of the circle  $\angle PZP' = 90^\circ$ . The radial distance  $OL'$  is given by

$$r' = \tan(90^\circ - \frac{1}{2}\theta) = 1/\tan \frac{1}{2}\theta. \quad (5.4)$$

As the angle of inclination of radius  $OP$  approaches  $90^\circ$ , the distance  $OL'$  approaches infinity. An alternative may then be used. This time we locate the projection of upper hemisphere point  $P'$  using the *nadir point*  $Z'$ , which is the opposite of  $Z$  (Fig. 5.6b). Note that  $L'$  now lies within the primitive and is symmetrical with  $L$ . With this second method it is essential to clearly label the upper hemisphere point  $L'$  in some special way to avoid confusion with points actually in the lower hemisphere. This is a particularly useful approach because the point  $L'$  can be treated and manipulated in a manner similar to  $L$ .

### 5.3 Stereonet

By constructing families of great and small circles we have the *equatorial stereographic net* (Fig. 5.7). This is also referred to as the *Wulff net*<sup>3</sup> or by the descriptive phrase *equal-angle net*, but more commonly it is simply called the *stereonet*.

<sup>3</sup>Named after the Russian mineralogist G.V. Wulff who first used it for these purposes in 1902.



It is useful to think of each great circle as a protractor. The primitive is a full-circular protractor with a range of trends expressed as azimuths from  $0$  to  $360^\circ$  measured clockwise. The great-circular arcs within the primitive are viewed as inclined semi-circular protractors and the small circle intersections are the gradations on these. There are two great circles which appear as mutually perpendicular diameters of the primitive.

1. One trends toward  $0^\circ$  (or  $180^\circ$ ) and represents the great circle trace of a diametral vertical plane.
2. The other trends toward  $90^\circ$  (or  $270^\circ$ ) and represents the special case of a small circle whose angular radius is  $90^\circ$ .

We will call these the *principal diameters* and one of them is used in almost all constructions. We will carefully identify which diameter and which end to use by its azimuth.

In practice the net is drawn large enough to be accurate and small enough to be portable. This is easily accomplished by multiplying the radial distances given in Eqs. 5.2 and 5.3 by the desired radius of the net. A net with a radius of 7.5 cm with great and small circles drawn every  $2^\circ$  meets these requirements.<sup>4</sup>

The printed net is a great aid in many constructions and greatest benefit is gained if one is always at hand. This is easily accomplished if the printed form is permanently mounted on a rigid backing and its surface protected with a sheet of clear plastic. In use structural data are plotted and problems solved on an overlay sheet of tracing paper. This overlay is affixed to the net by a single pin placed exactly at its center in order to allow the sheet to revolve freely. A small piece of clear plastic tape on the back of the tracing sheet to reinforce the pin hole prevents tearing or enlarging of this pivot point. Once the overlay sheet is in place, the north point on the primitive is marked *N* to coincide with the  $0^\circ$  point on the net. This starting point for all constructions is called the *home position*. It is also useful to add the primitive circle to the tracing sheet with a compass.

## 5.4 Plotting techniques

There are two techniques on which everything else is based: plotting lines and plotting planes. Especially when starting out, it is important to view the stereonet as a hemispherical-shaped bowl and to imagine the great and small circular arcs inscribed on its inner surface like the lines of latitude and longitude on a globe viewed from the inside. Structural elements can then be visualized as passing through the center of the sphere and intersecting its lower surface. Recording the results of this visualization with a quick sketch is also useful. This sketch makes the plotting easier and also serves as an important check on the proper location of the plots and on the general correctness of

<sup>4</sup>A full-scale printed stereonet can be found at the end of the book. It, and other plotting nets, can also be downloaded from the website [www.cambridge.org/ragan](http://www.cambridge.org/ragan).

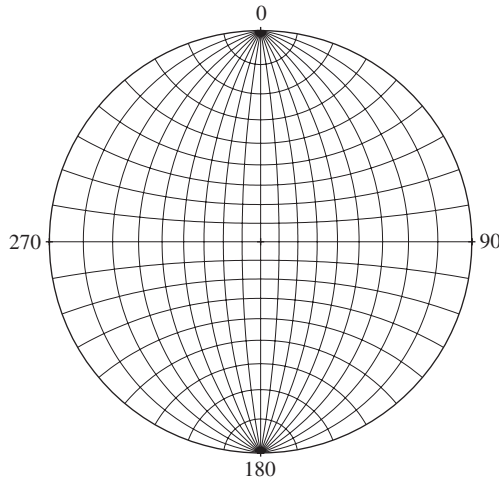


**Figure 5.7** Equatorial stereographic net.

the various manipulations. To actually plot structural lines and planes on the stereogram there are two ways of proceeding.

1. Rotate the underlying net while holding the tracing fixed. Although a little awkward, especially in the field, the important virtue of this method is that the representation of structural elements on the tracing sheet remains in constant orientation and this is especially useful for beginners. It also emphasizes the fact that the underlying net is simply a tool which facilitates plotting and measuring.
2. Alternatively, the underlying net is held fixed and the tracing sheet is rotated. Once a degree of competence and confidence in the plotting is attained there is not a great difference between these two methods and one may choose whichever seems most comfortable. We will illustrate the basic methods of plotting using both techniques.

### Problem

- On a stereogram represent the line whose attitude is 30/120.

### Visualization

- With the aid of a sketch map showing the attitude of the plunging line (Fig. 5.8a), and with the stereonet in front of you, hold a pencil over its center with the given attitude and visualize its intersection with the lower hemisphere in the southeast quadrant. Make a sketch of this visualization (Fig. 5.8b).

### Plotting a line I

1. With the overlay in the home position count off 120° clockwise from 0° on the net and make a tick mark on the primitive at this point to represent the trend of the line and label it *T* (Fig. 5.9a).

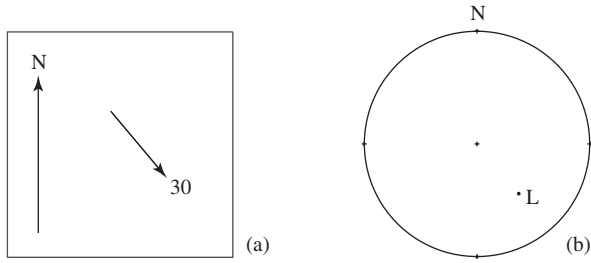


**Figure 5.8** Plunging line: (a) sketch map; (b) sketch stereogram.

2. Revolve the underlying net  $30^\circ$  clockwise so that  $T$  lies on the  $90^\circ$  principal diameter and count off  $p = 30^\circ$  inward from the primitive along this radius. Mark this point and label it  $L$  (Fig. 5.9b).
3. Compare your result with the sketch obtained by visualization.

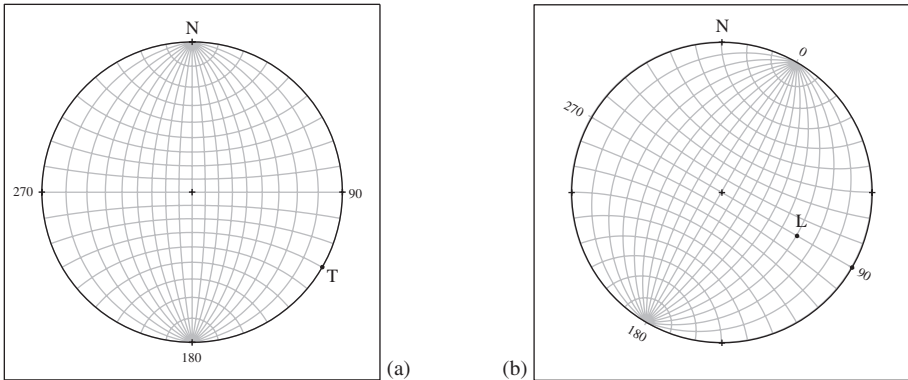


**Figure 5.9** Inclined line I: (a) mark trend; (b) revolve net.

**Plotting a line II**

1. As before, locate the trend of the line by counting off  $120^\circ$  clockwise from  $0^\circ$  and mark this  $T$  (Fig. 5.10a).
2. Revolve the overlay  $30^\circ$  anticlockwise so that  $T$  coincides with the  $90^\circ$  principal diameter and count off  $p = 30^\circ$  inward from the primitive. Mark this  $L$  (Fig. 5.10b).
3. Return to the home position and recheck by visualization (see Fig. 5.9b).

In both of these procedures the graduations along the  $90^\circ$  principal diameter were used for the plunge angle. However, either end of any principal diameter could just as easily have been used. Assure yourself that this is so by revolving  $L$  to any other principal diameter and checking that the plunge angle measured there is identical. Thus we see that there is a choice of plotting positions. This is sometimes a source of confusion for beginners and it is advisable to follow the listed steps closely until confidence develops.

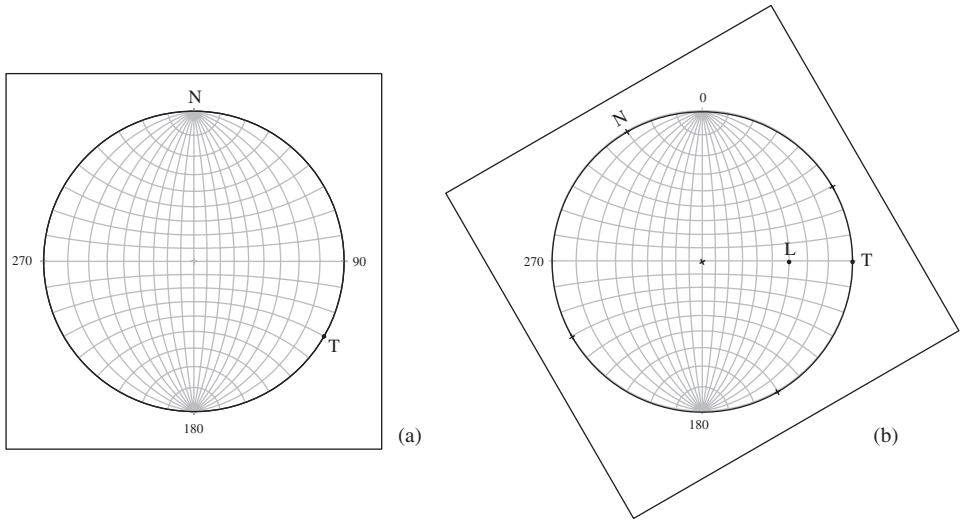


**Figure 5.10** Inclined line II: (a) mark trend; (b) revolve overlay.

Once the process becomes familiar, however, the use of such alternatives increases the ease and speed of plotting.

**Problem**

- Represent the plane whose strike and dip is N 30 E, 40 NW by a great circle on a stereogram.

**Visualization**

- With a sketch map showing the attitude of the plane line (Fig. 5.11a) and with the stereonet in front of you, hold your left hand, palm downward, over the center of the net with horizontal fingers pointing toward N 30 E and the plane of the hand inclined 40° toward the northwest. This plane can be imagined to intersect the lower hemisphere. Make a sketch of the great circle representation (Fig. 5.11b).

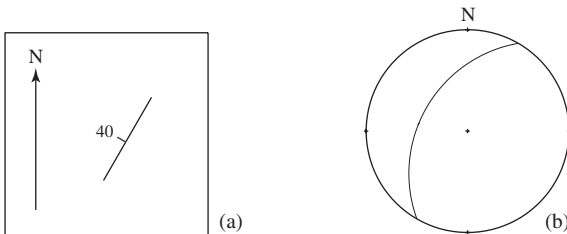


**Figure 5.11** Inclined plane: (a) sketch map; (b) sketch stereogram.

### Plotting a plane I

1. In the home position count off  $30^\circ$  clockwise from north and mark this strike direction  $S$  (Fig. 5.12a).
2. Revolve the underlying net so that  $0^\circ$  diameter coincides with  $S$ , that is, turn the net clockwise  $30^\circ$  (Fig. 5.12b).
3. Count off  $40^\circ$  from the primitive inward along the  $270^\circ$  diameter of the left side of the net and mark this point  $D$ , representing the line of true dip. Carefully trace in the arc of the great circle through  $D$ . If you are left handed you may find it easier to trace in this arc by turning the overlay  $180^\circ$  and using the curves on the right side of the net.
4. Compare this result with the sketch (Fig. 5.11b).

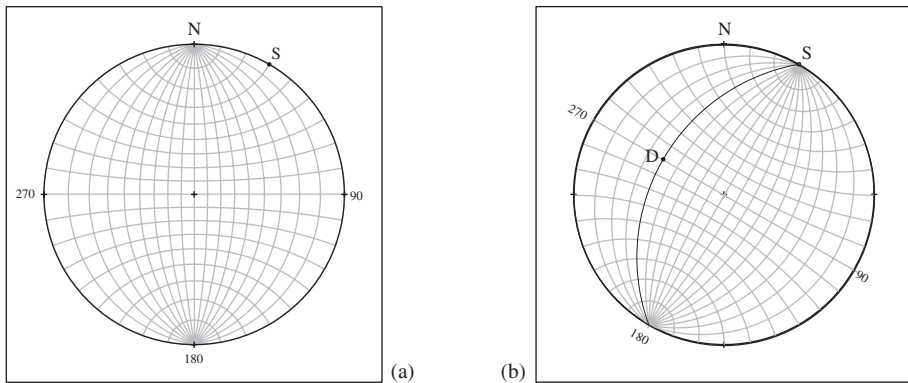


**Figure 5.12** Inclined plane I: (a) strike mark; (b) revolve net.

### Plotting a plane II

1. As before, in the home position count off  $30^\circ$  clockwise from north and mark this strike direction  $S$  (Fig. 5.13a).
2. Revolve the overlay  $30^\circ$  anticlockwise so that  $S$  coincides with  $0^\circ$  on the net (Fig. 5.13b).
3. Count off  $40^\circ$  from the primitive on the left side of the net inward along the  $90^\circ$  diameter of the net and mark this point  $D$ , representing the line of true dip. Carefully trace in the arc of the great circle through  $D$ .
4. Return the overlay to the home position and check the result by visualization (see Fig. 5.12b).

In common with other methods of projections, the dimensions of elements are reduced – the hemisphere is reduced to a plane, a plane to a curve and a line to a point. A further advantage of this projection is that a plane can be plotted as a point which represents the unique normal, called its *pole*.

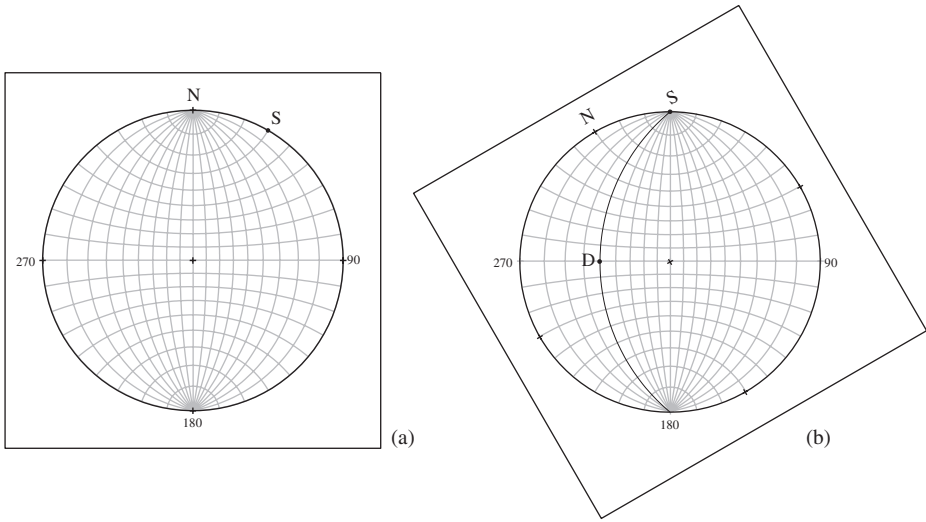


**Figure 5.13** Inclined plane II: (a) strike mark; (b) revolve overlay.

**Problem**

- Represent the plane whose attitude is N 30 E, 40 W by its pole.

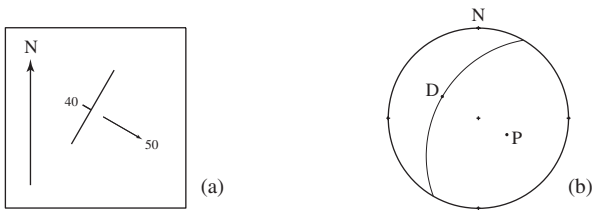


**Figure 5.14** Pole: (a) sketch map; (b) stereogram.

**Visualization**

- With the aid of a sketch map showing the dip and strike of the plane and its pole (Fig. 5.14a), and with the stereonet in front of you, hold your left hand oriented as before, but with a pencil between the fingers so that it is perpendicular to the plane of the hand. The line of the pencil will pierce the lower hemisphere at a point in the southeast quadrant. This point is 90° from the plane. Make a sketch stereogram (Fig. 5.14b).

**Plotting a pole**

1. Repeat the construction steps to plot the plane as a great circle (Fig. 5.15).
2. From the line of true dip *D* count off 90° inward from along the same principal and mark point *P*. Also mark *T* on the primitive representing the trend of the pole.

3. Check the result with your sketch obtained by visualization.

**Answer**

- Read off the plunge angle inward from the primitive along this same diameter. Return to the home position and read off the trend  $T$ . The attitude of the plane is  $P(50/120)$ .

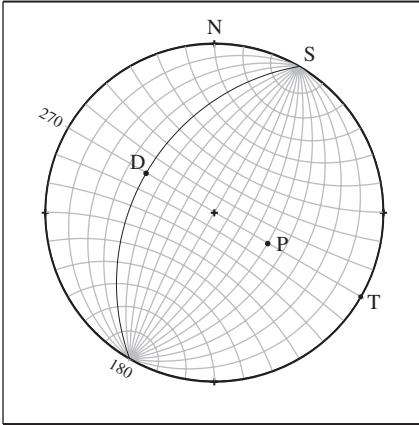


**Figure 5.15** Pole of a plane.

Note that we can easily find the great circle representation of a plane from its pole by reversing this procedure. With  $P$  on one of the principal diameters, count off  $90^\circ$  in the opposite direction to locate the dip direction  $D$  and then trace in the corresponding great circle.

**5.5 Measuring angles**

Each of these plotting techniques also makes clear that we can determine the attitude of a line, as represented by a point on a stereogram, and the attitude of a plane, as represented by a great circle, simply by returning them to their plotting positions and reading off the trends and inclinations.

Further, once the structural elements of a problem have been plotted, then the angles between these elements can be easily determined on the stereonet. The fundamental basis is the determination of the angle between two lines.

**Problem**

- What is the angle  $\theta$  between the line  $L_1(40/140)$  and line  $L_2(30/040)$ ?

**Method**

1. Plot points  $L_1$  and  $L_2$ .
2. Turn the net or overlay so that these points lie on the same great circle (Fig. 5.16a).
3. Count off the angle  $\theta$  between the points  $L_1$  and  $L_2$  along this arc.

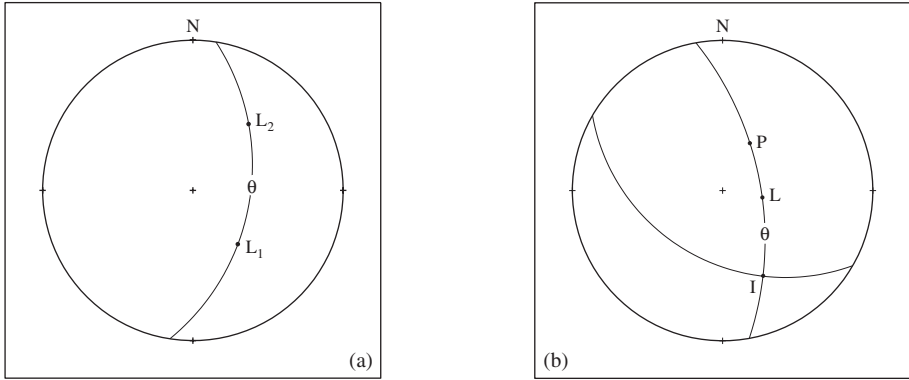


**Figure 5.16** Angles: (a) between two lines; (b) between line and plane.

### Answer

- The angle between  $L_1$  and  $L_2$  is  $\theta = 78^\circ$ .

This method may be extended to the angle between a line and a plane. By definition, this angle is measured in the plane containing the line which is perpendicular to the given plane. This is the smallest angle between the given line and any line in the given plane.

### Problem

- What is the angle  $\theta$  between line  $L(60/100)$  and plane whose pole is  $P(50/030)$ ?

### Method

1. Plot points  $L$ ,  $P$  and trace in the great circle representing the specified plane.
2. Turn the net or overlay so that  $L$  and  $P$  lie on the same great circle; this represents the plane on which  $\theta$  must be measured. Mark the point of intersection of this circular arc with the great circle representing the given plane and label it  $I$  (Fig. 5.16b).
3. Count off the angle along this arc between  $L$  and  $I$ .

### Answer

- The angle between the line and the plane is  $\theta = 51^\circ$ . Note that the angle between  $L$  and  $P$  is  $90^\circ - 51^\circ = 39^\circ$  so that this angle may be determined from a plot of the line and the pole of the plane alone.

### Problem

- Determine the angle  $\theta$  between the two planes whose dip directions are  $D_1(50/070)$  and  $D_2(60/290)$ . There are two ways to do this.



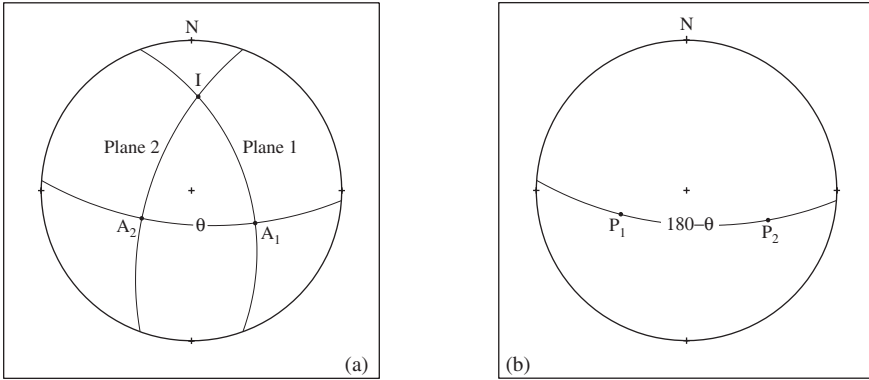


**Figure 5.17** Angle between two planes: (a) great circles; (b) poles.

**Method I**

1. Represent the two planes as great circles and label the point of intersection  $I$  (Fig. 5.17a).
2. Trace in the great circle whose pole is  $I$ .
3. Count off  $\theta$  between the points  $A_1$  and  $A_2$  where this arc cuts the great circles representing the two planes.

**Method II**

1. Represent the planes by their poles  $P_1(40/250)$  and  $P_2(30/110)$  (Fig. 5.17b).
2. Turn these two points so they lie on the same great circle and count off the angle between them.

**Answer**

- By the first method the angle between the planes is  $79^\circ$ . By the second method the angle between the poles is  $101^\circ$ . Note that  $79^\circ + 101^\circ = 180^\circ$  so that the results are interchangeable. By convention the *dihedral angle* is acute so the smaller angle is reported.

**5.6 Attitude problems**

With these basic plotting and measuring techniques, problems dealing with the orientation of lines and planes using orthographic methods in Chapters 1 and 3 can now be solved simply and directly on the stereonet.

**Problem**

- What is the apparent dip in the 080 direction on the plane N 40 E, 60 SE, and what is the pitch of this line?

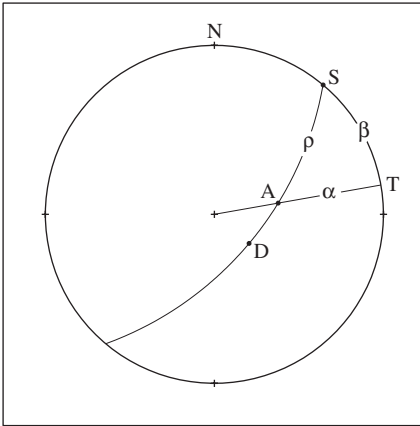


**Figure 5.18** Line of apparent dip and its pitch.

**Apparent dip and pitch**

1. In the home position, mark the strike  $S$  of the plane and the trend  $T$  of the apparent dip direction on the primitive (Fig. 5.18).
2. Revolve either the net or overlay so that  $S$  coincides with  $0^\circ$  on the net and trace the great circle representing the plane.
3. Similarly revolve  $T$  mark to the  $90^\circ$  point of the net and mark the point where the great circle crosses the east-west diameter and label it  $A$ . Read its angle of inclination by counting inward from the primitive.
4. Return the great circle to the plotting position and read off the pitch angle between  $S$  and  $A$  along the arc of the great circle.

**Answer**

- The angle of apparent dip in this direction is  $\alpha = 48^\circ$ . The pitch angle  $\rho = 59^\circ$ .

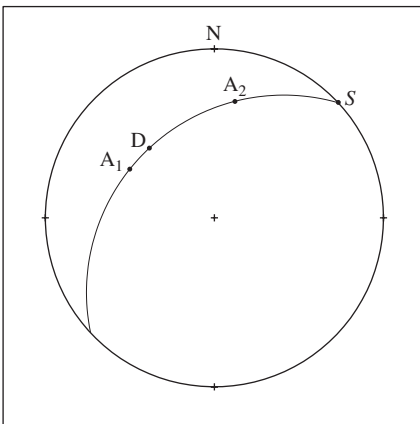


**Figure 5.19** True dip and strike.

**Problem**

- From the apparent dips  $A_1(30/300)$  and  $A_2(20/010)$  determine the attitude of the plane.

**True dip and strike**

1. Plot the points  $A_1$  and  $A_2$  representing the two known lines of apparent dip (Fig. 5.19).
2. Revolve the net or overlay so that these two points lie on the same great circle. Trace in this arc and mark its strike direction  $S$ . Without moving the overlay, mark the point  $D$  where this arc crosses the  $270^\circ$  diameter. Read the dip angle.
3. Return to the home position and read the angle  $S$  makes with  $N$ .

**Answer**

- The strike and dip of the plane is N 47 E, 31 N.

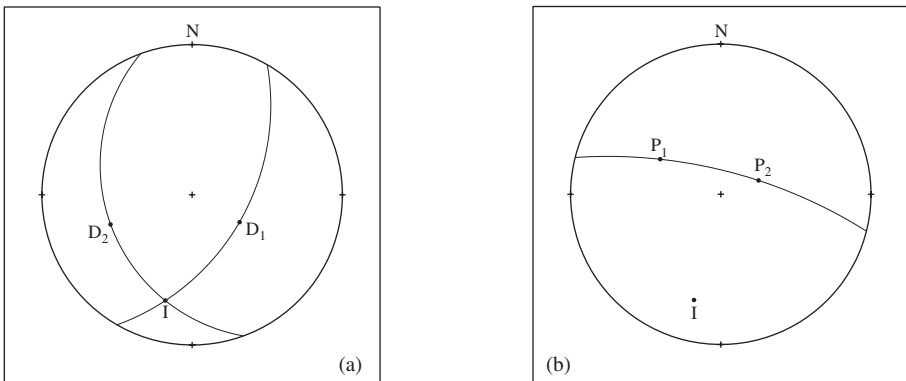


**Figure 5.20** Line of intersection: (a) great circles; (b) poles.

Problems involving the attitude of the line of intersection of two planes may be solved in two different ways. The first represents the planes as great circles and the second represents them by their poles.

**Problem**

- Given the planes N 30 E, 50 E and N 20 W, 30 W, find the attitude of the line of intersection.

**Intersection I**

1. Plot the lines of true dip  $D_1(50/120)$  and  $D_2(30/250)$  and through each trace in the corresponding great circles. Label the point of intersection  $I$  (Fig. 5.20a).
2. Read the plunge and trend of  $I$ .

### Intersection II

1. Plot the corresponding poles  $P_1(40/300)$  and  $P_2(60/070)$  (Fig. 5.20b).
2. Revolve the net or overlay so that these points lie on the same great circle. The pole of this circle is  $I$ .

### Answer

- Both constructions give the same attitude  $I(18/194)$ .

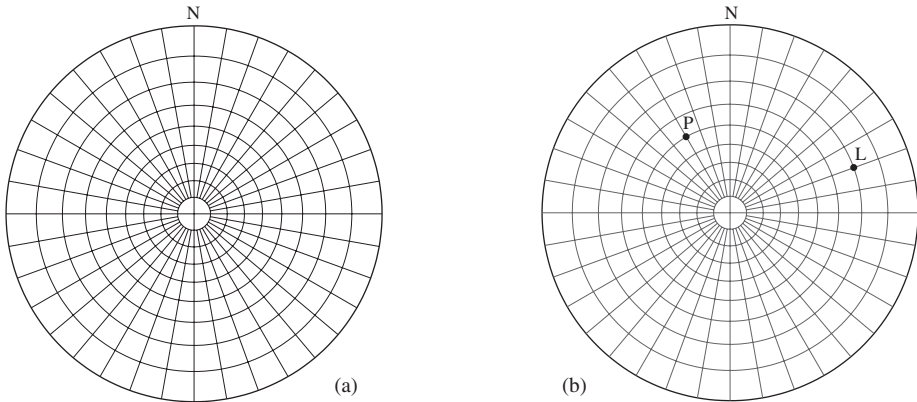


**Figure 5.21** Polar net: (a) basic graph; (b) plotting points  $L$  and  $P$ .

### 5.7 Polar net

There is an alternative to the equatorial net which is advantageous for display purposes (see also Lisle & Leyshon, 2004, p. 42). The planes represented by the great circles of the standard net are now vertical. Small circles are concentric about the center (Fig. 5.21a); their radii are given by Eq. 5.1. Lines and poles can be plotted directly without rotating the overlay and this makes the plotting of numerous data points more efficient. We will make special use of this property in later chapters.

### Problem

- Plot the line  $L(20/070)$  and the pole  $P(40/330)$  on the polar net (Fig. 5.21b).

### Procedure

1. For  $L(20/070)$  count off  $70^\circ$  clockwise from north and then  $20^\circ$  inward along the radius with this trend.
2. For  $P(40/330)$  count off  $330^\circ$  clockwise (or  $30^\circ$  anticlockwise) from north, and then  $40^\circ$  inward along the radius with this trend.

### 5.8 Dip and strike errors

Even on a geometrically perfect inclined plane, an error in placing the compass will result in a strike error (see §1.4). As a result, repeated measurements of the same plane will show a scatter which can be depicted by plotting the pole representing each measured attitude. There is another factor which also contributes to such a scatter – local irregularities on the plane which cause departures of the attitude from some mean value. Assuming that these measured poles are symmetrically distributed about this mean and that the probability of finding a pole of given angular distance from this mean pole decreases with increased angular distance, a simple expression for the *maximum strike error* can be obtained.

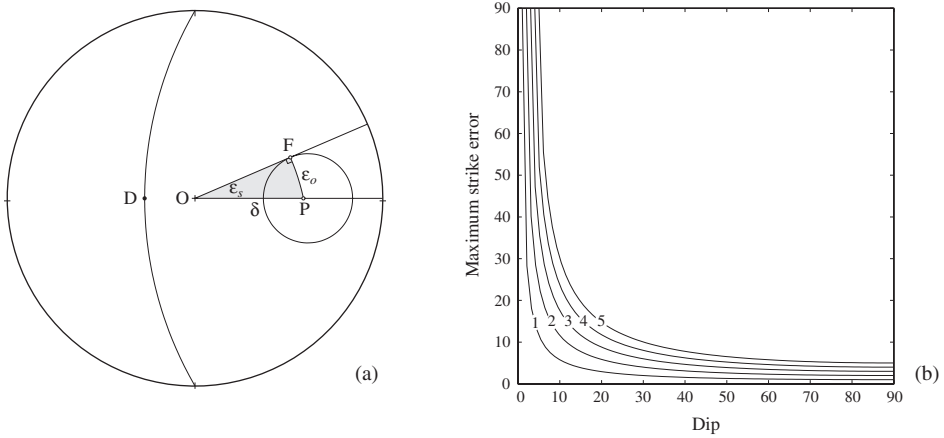


**Figure 5.22** Maximum strike errors  $\epsilon_s$ : (a) geometry; (b) graph.

Accordingly, the true position of the pole must lie within a small circle whose angular radius is the maximum operator error  $\epsilon_o$  about the mean pole  $P$ . In situations like this, the angular relations can be obtained from right-spherical triangle  $OPF$  shown in Fig. 5.22a. In this triangle (shown shaded) side  $OP$  is equal to the dip  $\delta$  of the plane, side  $PF$  is the angular radius of the error circle and this is the maximum observer error  $\epsilon_o$  and  $\angle POF$  is the maximum error in the trend of  $P$ , which is also the maximum strike error  $\epsilon_s$ . From this triangle (see details of the derivation in §B.4.4)

$$\sin \epsilon_s = \sin \epsilon_o / \sin \delta. \tag{5.5}$$

A graph of this equation, first obtained by Pronin (1949; see Vistelius, 1966, p. 51) is shown in Fig. 5.22b for values of the maximum operator error  $\epsilon_o = 1-5^\circ$ . Cruden and Charlesworth (1976) tested this result against field measurements. Making the reasonable assumption that  $\epsilon_o$  is small, they found that Eq. 5.5 gave better results than the Müller hypothesis (see Eq. 1.3), and that it can be considered an adequate description of the data. They also noted that lithology, and presumably the character of the surfaces of the structural planes, affected the scatter of the dip measurements more than the strike

measurements. They also found that for 10 measurements, at 95% confidence, the values of the total error in measuring a bedding pole ranged from  $\pm 3.4^\circ$  to  $\pm 9.5^\circ$ .

### 5.9 Intersection errors

Because errors are inevitable when determining the attitude of planes in the field, it follows that when two measured planes intersect the attitude determined for the line of intersection will also be in error. The basic construction of an intersection is illustrated in Fig. 5.23a. With perfect measurements of the orientations of the poles *A* and *B* of the two planes, the constructed point of intersection would be located at *I*.

However, because of measurement errors, each of these poles lies within a small circle whose angular radius is the *maximum observer error*  $\epsilon_o$ . Correspondingly, we know only that the line of intersection lies somewhere in the vicinity of the constructed point *I*. We now wish to find an expression for the *maximum trend error*  $\epsilon_t$  associated with this location.

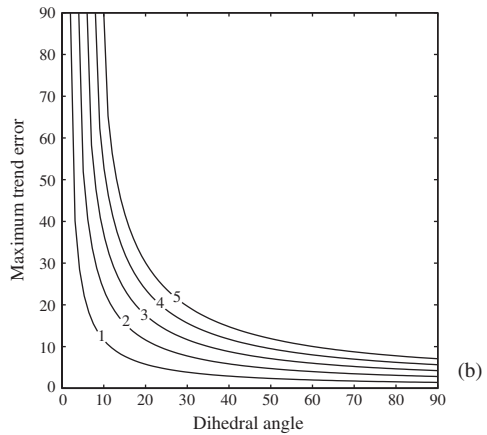
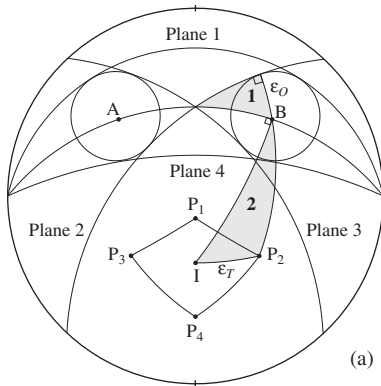


**Figure 5.23** Intersection errors: (a) geometry; (b) graph.

There are four limiting cases involving these two error circles and these are represented by the four great circles tangent to the two small error circles; these are labeled Planes 1, 2, 3 and 4. The poles of each of these planes *P*<sub>1</sub>, *P*<sub>2</sub>, *P*<sub>3</sub> and *P*<sub>4</sub> bound a diamond-shaped area within which the line of intersection actually lies and we wish to determine its size. To do this, we construct two right-spherical triangles at the common point *B* (shaded in Fig. 5.23a). For the angle *B*<sub>1</sub> (the angle at *B* in Triangle 1 with a 90° angle) and angle *B*<sub>2</sub> (the angle at *B* in Triangle 2 with a 90° side). From spherical trigonometry (see details of the derivation in §B.4.5)

$$\cos B_1 = \tan \epsilon_o / \tan \frac{1}{2}d \quad \text{and} \quad \cos B_2 = \cos \epsilon_t / \cos \epsilon_o,$$

where  $d$  is the angle between  $A$  and  $B$ . Because  $B_1 + B_2 = 90^\circ$ , then  $\cos B_2 = \sin B_1$  and we can eliminate  $B_2$  from the second equation. Then squaring each and summing the two equations and using the identity  $\sin^2 x + \cos^2 x = 1$  we have

$$\frac{\tan^2 \varepsilon_o}{\tan^2 \frac{1}{2}d} + \frac{\cos^2 \varepsilon_t}{\cos^2 \varepsilon_o} = 1,$$

or after rearranging

$$\cos^2 \varepsilon_t = \cos^2 \varepsilon_o - \frac{(\cos \varepsilon_o \tan \varepsilon_o)^2}{\tan^2 \frac{1}{2}d}.$$

Substituting the identities  $\sin x = \cos x \tan x$  and  $\cos^2 x = 1 - \sin^2 x$ , this becomes

$$\sin^2 \varepsilon_t = \sin^2 \varepsilon_o \left( 1 + \frac{1}{\tan^2 \frac{1}{2}d} \right).$$

Finally, with the identities  $1/\tan x = \cot x$  and  $1 + \cot^2 x = 1/\sin^2 x$ , and taking the square root we have

$$\boxed{\sin \varepsilon_t = \sin \varepsilon_o / \sin \frac{1}{2}d.} \quad (5.6)$$

A graph of this equation is given in Fig. 5.23b for values of  $\varepsilon_o = 1-5^\circ$  (see also Ramsay, 1967, p. 14). As can be seen the maximum trend error may be large for small dihedral angles. A common situation where this is a problem is the intersection of two gently dipping planes and a special effort is required to determine the attitudes of the planes as accurately as possible, perhaps with surveying instruments.

### 5.10 Exercises

- Construct a stereogram with a radius of 7.5 cm showing the  $45^\circ$  small and great circles. Compare your result with a printed net.
- Repeat the dip and strike problems of Chapter 1. Compare the methods of orthographic and stereographic projections for speed and accuracy.
  - If the attitude of a plane is N 75 W, 22 N, what is the apparent dip in the direction N 50 E?
  - An apparent dip is 33, N 47 E, and the true strike is N 90 E. What is the true dip?
  - The true dip is  $40^\circ$  due north. In what direction will an apparent dip of  $30^\circ$  be found?
- A plane contains two lines:  $L_1(30/320)$  and  $L_2(20/020)$ . What is the attitude of the plane, what is the pitch of each line in that plane and what is the angle between the two lines measured in the plane?

4. Two intersection planes have attitudes N 5 E, 15 W and N 15 E, 10 W. Determine the orientation of the line of intersection and the angle between the two planes. If the maximum operator error in measuring attitude is  $2^\circ$ , what is the maximum strike error for each of the planes, and what is the maximum  $\beta$  error for the line of intersection? How do these errors affect the calculated dihedral angle?



# 6

## Rotations

### 6.1 Introduction

In a number of geological situations structural lines and planes have been rotated from some initial orientation. One of our tasks is to describe such rotations and this can be done with the aid of the stereonet. Every *rigid rotation* can be defined by an angle and sense of rotation about a specified axis.

The most general case involves rotation about an inclined axis, but we start with the simpler cases of rotations about vertical and horizontal axes. We do this because it is a good way to introduce the techniques of rotations and because a sequence of such rotations is equivalent to a rotation about a single inclined axis. In all cases, the sense of rotation is described as clockwise or anticlockwise when looking along the rotation axis, whether horizontal, inclined or vertical.

### 6.2 Basic techniques

As an aid to visualization consider a turntable (Fig. 6.1). As the base rotates about its axis  $R$  through some angle  $\omega$  the locus of an oblique line  $L$  through its center  $O$  is a right-circular *cone of rotation*. Angle  $\phi$  between  $R$  and  $L$  is the semi-vertex angle of this cone. The intersection of this cone with the sphere will, in general, be a *small circle*, one in the lower and one in the upper hemisphere. There are, however, two limiting cases: if  $\phi = 0$  the surface degenerates to a line and if  $\phi = 90^\circ$  it becomes a plane.

Rotation about a vertical axis is the easiest to perform. To visualize imagine the turntable with its vertical axis downward as in Fig. 6.1a. The cone of rotation intersects the lower hemisphere as a small circle at the center of the net and the sense of rotation can be immediately and directly seen as either *clockwise* or *anticlockwise*.

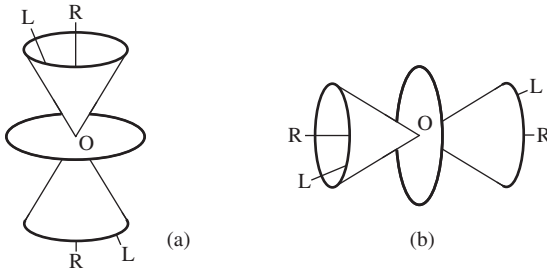


**Figure 6.1** Cone of rotation:  
vertical axis; (b) horizontal axis.

### Problem

- What is the orientation of the horizontal line  $L(00/150)$  after an anticlockwise rotation  $\omega = 70^\circ$  about a vertical axis?

### Construction

1. Mark  $R$  at the center of the net and plot point  $L$  on the primitive representing the line (Fig. 6.2a).
2. From  $L$  count off  $\omega = 70^\circ$  anticlockwise along the primitive to locate the point  $L'$  representing the rotated line.

### Answer

- After rotation the orientation of the line is  $L'(00/080)$ .

Because  $\phi = 90^\circ$ , in this special case the trace of the cone of rotation is a great circle. Note too that the trend changed but the line remained horizontal. The construction is only slightly more involved if an inclined line is rotated about vertical axis.

### Problem

- What is the orientation of inclined line  $L(30/150)$  after an anticlockwise rotation  $\omega = 70^\circ$  about a vertical axis?

### Construction

1. Mark  $R$  at the center of the net and plot point  $L$  representing the inclined line (Fig. 6.2b).
2. From the trend of  $L$  count off  $\omega = 70^\circ$  anticlockwise along the primitive to locate the trend of the rotated line. With the original plunge angle plot  $L'$  representing the rotated line.

**Answer**

- After rotation the orientation of the line is  $L'(30/080)$ .

Again, note that the trend changed but the plunge remained the same, that is, the initial  $L$  and final  $L'$  lie on the same small circle. Both  $L$  and  $L'$  lie on a small circle which represents the intersection of the vertical cone of revolution and the lower hemisphere. As a visual aid, this circle may be added to the stereogram; with a compass draw a circle about the center of the net with angular radius  $\phi = (90^\circ - p)$ ; in this example  $\phi = 60^\circ$ .

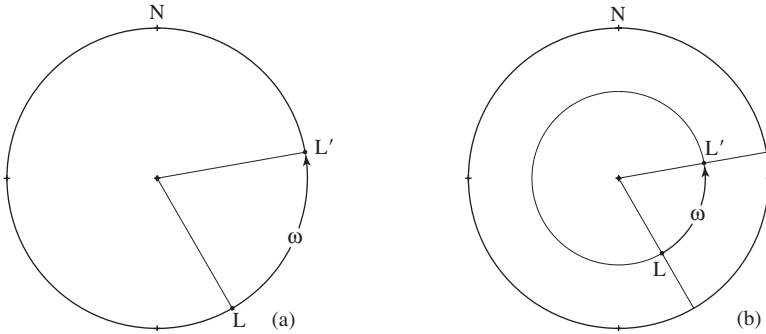


**Figure 6.2** Rotations about a vertical axis.

Rotation about a horizontal axis can also be performed readily on the stereonet (Fig. 6.1b). Unlike the case of the vertical axis, there are many possible horizontal axes. Rotations about such axes are always performed with  $R$  on the overlay coincident with the north or south point to take advantage of the *small circles* printed on the net. We illustrate with two examples.

**Problem**

- What is the attitude of the horizontal line  $L_1(00/030)$  after a  $110^\circ$  clockwise rotation about a horizontal axis which trends due north?

**Visualization**

- Looking north, a clockwise rotation about  $R$  moves  $L$  from right to left along its small circle.

**Construction**

1. Mark  $R(00/000)$  representing the rotation axis and plot point  $L_1(00/030)$  representing the horizontal line (Fig. 6.3a).
2. Along the small circle on which  $L_1$  lies count off  $\omega = 110^\circ$  from right to left to locate point  $L'_1$ .

**Answer**

- The attitude of the line after rotation is  $L'_1(28/349)$ .

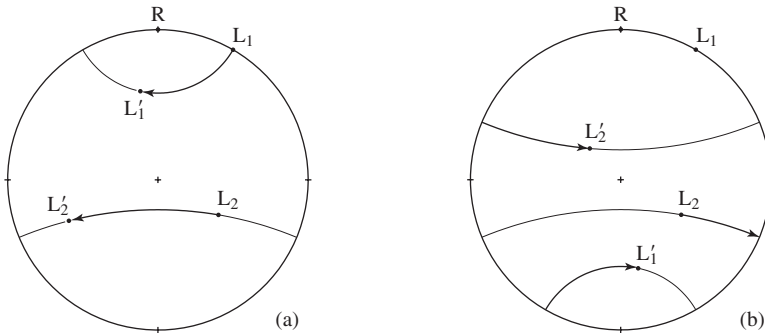


**Figure 6.3** Rotations about a horizontal axis: (a) clockwise; (b) anticlockwise.

Note that both the trend and plunge of the line changed as the result of this rotation. The second example involves the more general case of a rotation of an initially inclined line.

**Problem**

- What is the attitude of line  $L_2(40/120)$  after the same rotation  $\omega = 110^\circ$ ?

**Construction**

1. Again mark  $R(00/000)$  and plot point  $L_2(40/120)$ .
2. Along the small circle on which  $L_2$  lies count off  $110^\circ$  from right to left to locate point  $L'_2$  (Fig. 6.3a).

**Answer**

- The attitude of the rotated line is  $L'_2(24/245)$ .

In both these examples the lines remained in the lower hemisphere. Every such structural line has another end, called its *opposite*, which intersects the upper hemisphere and therefore normally remains out of sight. With other senses and angles of rotation, however, the initially downward end may move into the upper hemisphere. When this happens its opposite immediately moves into the lower hemisphere. Two closely related examples will illustrate the treatment (Fig. 6.3b).

1. If the horizontal line  $L_1(00/030)$  is rotated  $\omega = 110^\circ$  *anticlockwise* instead, it immediately moves into the upper hemisphere. At the same instant its opposite moves into the lower hemisphere diametrically opposite and thereafter along the same small circle. The final attitude is  $L'_1(28/169)$ .

- If the plunging line  $L_2(40/120)$  is similarly rotated  $\omega = 110^\circ$  anticlockwise it moves first along its small circle  $44^\circ$  to the primitive and then its opposite continues the rotation along the same small circle an additional  $66^\circ$ . The total rotation is thus made up of two parts. The final attitude is  $L'_2(57/315)$ .

In addition to lines, we can also rotate planes and there are two ways of doing this. First, several points along the great circle trace of the plane may be rotated individually to establish the great circle representation of the rotated plane.

### Problem

- Rotate the plane N 18 W, 50 W clockwise  $\omega = 40^\circ$  about a horizontal axis which trends N 30 E.

### Method I

- Trace in the great circle representing the given plane (Fig. 6.4a).
- Mark  $R(00/030)$  and revolve the overlay so that this point coincides with north on the net.
- In this position, arbitrarily locate three points  $L_1$ ,  $L_2$  and  $L_3$  on the arc of the great circle. These should be widely spaced and it simplifies things if each is located at the intersection of a small circle.
- Without moving the overlay count off  $\omega = 40^\circ$  from each of these points along the small circles in the direction given by the sense of rotation, that is, from right to left. Doing this for  $L_1$  and  $L_2$  locates the rotated points  $L'_1$  and  $L'_2$  directly. Point  $L_3$ , however, is carried to the primitive and beyond, which means that it moves into the upper hemisphere and its opposite  $L'_3$  into the lower hemisphere.
- Revolve the overlay so that  $L'_1$ ,  $L'_2$  and  $L'_3$  lie on a great circle which can then be traced in.

### Answer

- The strike and dip of the plane after rotation is N 62 W, 35 S. Note that two points would have sufficed to fix the great circle but the third serves as an important check.

With the second method, the plane is represented by its pole and this is rotated in a single step.

### Method II

- Mark  $R(00/030)$  and plot the pole of the plane  $P(40/072)$  (Fig. 6.4b).
- Revolve  $R$  to north and count off  $\omega = 40^\circ$  from  $P$  along its small circle to locate the rotated pole  $P'$ .
- Trace in the corresponding great circle representing the plane and read its attitude.

**Answer**

- The attitude of the pole of the rotated plane is  $P'(55/028)$  and this is the same attitude as before.

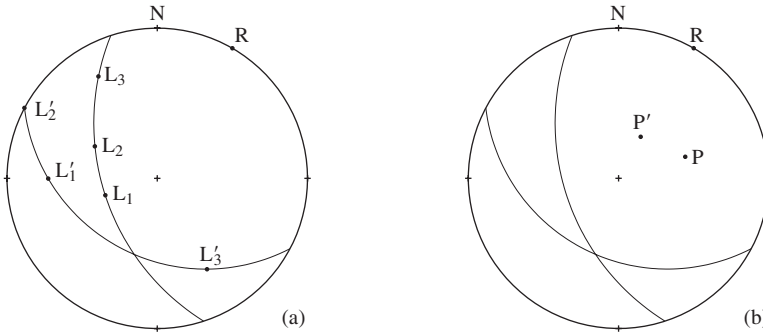


**Figure 6.4** Rotation of a plane: (a) points on plane; (b) poles.

Clearly, it is far easier to treat the single point representing the pole of the plane rather than several points on the great circle, although this requires that the dip and strike of the plane be converted to plunge and trend of the pole. Bengtson (1983) described an alternative plot which avoids even this step.

As emphasized by Phillips (1971, p. 5) these rotational techniques involve two closely related but geometrically different and distinct manipulations. The procedure of turning the overlay about its center to align a horizontal axis with north or south on the net is one of convenience, but the overlay always carries with it the  $N$  mark so that the original orientations never really changed. The term *revolve* is used specifically to describe this manoeuvre. On the other hand, as the result of a *rotation*, lines and planes have entirely new orientations relative to a fixed geographical direction.

### 6.3 Sequential rotations

A line of any initial orientation can be rotated into any final orientation by a sequence of these simple rotations. To illustrate we rotate an initially horizontal plane, represented by its vertical pole, containing a line in two steps: first about horizontal axis  $R_H$ , then about vertical axis  $R_V$ .

#### Problem

- A horizontal plane contains line  $L(00/320)$ . What is the attitude of the plane and line after a two-step rotation:
  1. rotate first about axis  $R_H$  which trends due south by a clockwise angle  $\omega_H = 60^\circ$ ,
  2. then rotate about axis  $R_V$  by an anticlockwise angle  $\omega_V = 40^\circ$ .

**Visualization**

- Looking due south in the direction of  $R_H$  we see that a *clockwise* rotation moves pole  $P$  and line  $L$  to the east (Fig. 6.5a). Alternatively, looking due north in the direction of the opposite of  $R_H$ , we see that this is equivalent to an *anticlockwise* rotation. This illustrates a general rule: a clockwise rotation about an axis produces the same results as an anticlockwise rotation about its opposite, and vice versa.

**Construction**

1. On the primitive, mark points  $R_H(00/180)$  and  $L(00/320)$ , and at the center the coincident points  $P(90/000)$  and  $R_V(90/000)$  (Fig. 6.5a).
2. There are two ways of performing the first rotation.
  - (a) Turn  $R_H$  to north. As the horizontal plane tilts clockwise about this axis, its pole  $P$  moves  $60^\circ$  to the left from the center along the east–west diameter of the net to  $P'$ , and line  $L$  moves  $60^\circ$  in the same sense along its small circle to  $L'$ .
  - (b) Leave  $R_H$  at the south point; its opposite is now at north. An anticlockwise tilt moves the pole and the line  $60^\circ$  to the right from the center along the east–west diameter of the net to  $P'$  and  $L$  by the same amount and sense to  $L'$ .
3. The second rotation about  $R_V$  changes the trends of both the once rotated pole  $P'$  and line  $L'$  by a anticlockwise angle of  $40^\circ$ , but their inclinations remain the same.

**Answer**

- After two rotations, the attitude of the pole is  $P''(30/050)$  and the attitude of the line is  $L''(34/297)$ . The corresponding dip and strike of the plane is N 40 W, 60 W and the line trends toward N 63 W.

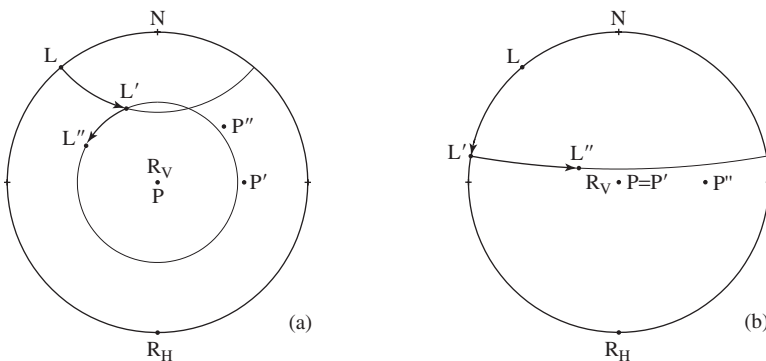


**Figure 6.5** Two rotations: (a) about  $R_H$  then  $R_V$ ; (b) about  $R_V$  then  $R_H$ .

If the order is reversed, that is, the rotation about  $R_V$  by  $\omega_V = 40^\circ$  is performed before the rotation about  $R_H$  by  $\omega_H = 60^\circ$ , the result is different (Fig. 6.5b). Because a rotation about a vertical axis does not change the orientation of a vertical line, the pole

has been, in effect, only rotated once. Its final attitude is  $P''(30/090)$ . The line has been rotated twice and its orientation is  $L''(59/289)$ . This demonstrates that in finite rotations the order of the steps is important, that is, they are not generally *commutative*.

#### 6.4 Rotations about inclined axes

The general case involves a rotation about an inclined axis. As before, the locus of a line rotated about such an axis is a small circle on the stereonet. We start with the basic geometry of the case in order to establish a visual picture of the process.

##### Problem

- Rotate the horizontal line  $L(00/050)$  about the inclined axis  $R(30/090)$  anticlockwise  $\omega = 90^\circ$ .

##### Construction

1. Plot inclined axis  $R$  and horizontal line  $L$ . The angle between these two points measured along the common great circle is  $\phi = 48^\circ$  (Fig. 6.6).
2. About  $R$  draw the small circle representing the cone of rotation with angular radius  $\phi$  (see §6.9).
3. As  $L$  rotates  $90^\circ$  about  $R$  it moves along this small circle to  $L'(63/033)$ .

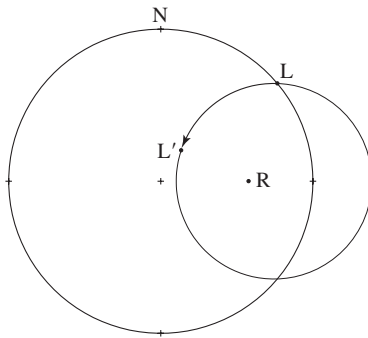


**Figure 6.6** Rotation about an inclined axis.

Besides requiring the extra effort of constructing this small circle, there is, unfortunately, no direct way of measuring the angle of rotation on it. This is not, therefore, a practical approach to performing rotations graphically. The diagram is, however, an important aid to visualizing the effects of a rotation about such an inclined axis. In practice, there are two alternative constructions.

The first depends on previous methods and consists of rotating the inclined axis  $R$  about a horizontal axis so that it is either horizontal or vertical. The advantage of adopting a vertical axis is that rotations into the upper hemisphere are commonly avoided. Then



the required rotation is performed as in the previous examples. Finally,  $R$  is returned to its original inclination by reversing the first rotation.

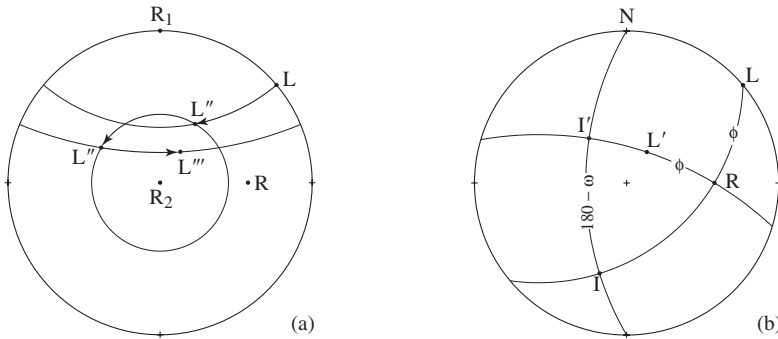


**Figure 6.7** Inclined axis: (a) sequential rotations; (b) direct rotation.

**Problem**

- Rotate the horizontal line  $L(00/050)$  anticlockwise  $\omega = 90^\circ$  about the inclined axis  $R(30/090)$ .

**Construction I**

1. Plot points  $R$  and  $L$  (Fig. 6.7a).
2. To bring  $R$  to the center of the net we need to rotate about an auxiliary horizontal axis whose trend is perpendicular to the trend of  $R$ , that is, due north. Mark this point  $R_1$ .
3. As  $R$  moves  $\omega = (90^\circ - 30^\circ) = 60^\circ$  to the center of the net,  $L$  moves by the same amount and sense along its small circles to  $L'$ .
4. Performing the  $\omega = 90^\circ$  anticlockwise rotation about the now vertical axis  $R_2$ , point  $L'$  moves to  $L''$  along a small circle concentric with the center of the net.
5. Reverse the rotation about  $R_1$  of Step 3 to return  $R$  to its original orientation and with it  $L''$  to  $L'''$ .

**Answer**

- The attitude of the line after this sequence of rotations is  $L'''(63/033)$ .

In serial constructions such as this, the potential errors increase with the number of steps, so this is not the preferred method. However, it is important because it forms the basis of methods which are treated in the next chapter.

The second method involves the direct rotation about the inclined axis using an auxiliary construction (Turner & Weiss, 1963, p. 69). An important advantage is that by reducing the number of steps the plotting errors are also reduced. Imagine the turntable with its axis pointing in the direction of inclined axis  $R$ . The plane of the turntable is now inclined and its great circle representation is easily drawn with  $R$  as its pole.

**Construction II**

1. As before plot  $R$  and  $L$ . Then trace in the great circle normal to  $R$  (Fig. 6.7b).
2. Revolve the overlay so that  $R$  and  $L$  lie on the same great circle on the net. Trace in this arc to intersect the first great circle whose pole is  $R$  at  $I$ .
3. The angle between  $L$  and  $R$  along this arc is  $\phi = 48^\circ$ .
4. As  $I$  rotates anticlockwise about  $R$  it moves first to the primitive and then its opposite to  $I'$ . Therefore count off  $\omega = 90^\circ$  from right to left in two increments. Alternatively, count  $180^\circ - 90^\circ = 90^\circ$  back from  $I$  to locate  $I'$ .
5. Revolve overlay so that  $I'$  and  $R$  lie on the same great circle and count off  $\phi = 48^\circ$  from  $R$  to locate  $L'$ .

**Answer**

- The attitude of the line after this single rotation is  $L'(68/033)$ , which is the same as before.

That the rotation of Fig. 6.7b about a single inclined axis produces the same results as the sequence of rotations of Fig. 6.7a illustrates an important fact. By a theorem due to the famous Swiss mathematician Leonard Euler [1707–1783] any sequence of rigid body rotations about a series of differently oriented axes can always be described by a single rotation by a single angle about a single axis.

**6.5 Rotational problems**

These several rotational techniques solve a class of *forward problems*. In each case, we started with a known initial state, applied a specified rotation, tracked the lines and poles along small circle paths to arrive at the final state. In effect, these model the rotations as they occur in nature.

In contrast, the geologist is faced with quite a different problem. In the field, we observe the orientation of planes and lines which have been rotated in the geological past. From measurements of such features we wish to determine the rotations which are responsible for these changes in orientation and thus to recover the initial state. These are examples of a class of *inverse problems*. Generally, these are commonly much more difficult to solve.

In particular, the fact that the rigid rotation of a body, no matter how complex, can always be described by a single Euler axis and Euler angle leaves us, in general, with only a description of the angular relation between the initial and final states. It could have been the result of a simple rotation about a single axis or the progressive rotation about a constantly shifting axis. There is no way to distinguish between these cases on the basis of the measurement of the orientation of line and planes alone. We take up some of these questions again in §7.5–7.6.

### 6.6 Tilting problems

A typical problem involves the restoration of tilted beds and sedimentary lineations which they contain to their pre-tilt orientation. For example, a solution of this problem would aid in the paleogeographical reconstruction of current directions in some past geological time. We can easily restore the plane to horizontality because it involves the rotation about a horizontal axis, but what about a possible rotation about a vertical axis? We could determine this rotation if we knew the pre-tilt trend of a line, but this is the very question that we are trying to answer.

Knowing only the final state, we usually do not have enough information to recover multiple rotations and the problem is therefore not solvable. What to do? As the construction using sequential rotations indicates, the horizontal component of rotation is parallel to the strike of the tilted beds. As a partial solution we therefore choose  $R$  in this direction and then proceed with the restoration on this basis. This is the *conventional tilt correction* (MacDonald, 1980).

#### Problem

- A dipping bed N 40 W, 60 W contains a sedimentary lineation which trends N 63 W. Restore the bed to horizontality and estimate the original trend of the lineation. Note that the attitude of this inclined plane and line are identical with the forward results obtained in Fig. 6.5a by a sequence of rotations.

#### Visualization

- Hold the right hand with palm upward and inclined to the west with fingers pointing toward the northwest over the net; also hold a pencil on the palm in the direction of the line. Now rotate the hand through an angle of  $60^\circ$  into a horizontal position and observe the final position of the line.

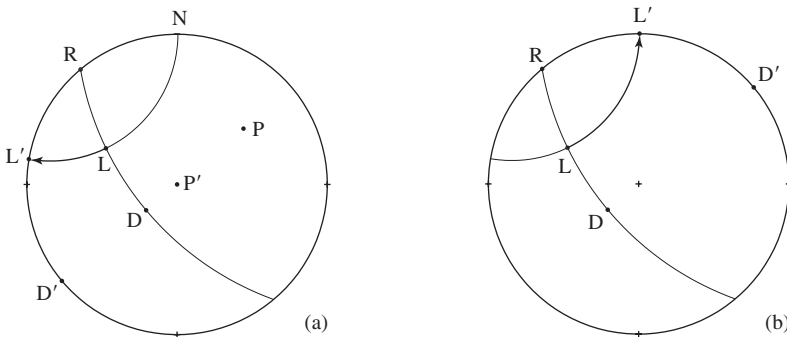


**Figure 6.8** Restoration of a plane and line: (a) upright; (b) overturned.

### Construction

1. Trace in the great circle representing the inclined plane and on it locate line  $L(34/297)$  (Fig. 6.8a).
2. Plot point  $P(30/050)$  representing the pole of the plane.
3. Label the strike direction  $R(00/340)$  and turn it to north.
4. As pole  $P$  moves  $60^\circ$  to the center of the net (and the bed to horizontality) line  $L$  moves along its small circle to  $L'$  on the primitive.

### Answer

- The restored orientation of the line is  $L'(00/280)$ .

As we have seen, the rotation of planes generally requires the use of poles. However, in cases such as this where the strike direction is taken as a rotation axis, the line of true dip remains fixed as the line of steepest inclination as if it were a physical line. In this case it is then simpler to rotate this line  $D(60/230)$  directly to the primitive, rather than plot and use the pole.<sup>1</sup> We will use this method in the next example.

Clearly, if the tilt correction is not made and the measured trend of the line on the inclined plane is used an error will result. In this example, the difference between the measured trend  $t$  and the restored trend  $t'$  is  $\Delta t = t - t' = 17^\circ$ . However, if the angle of dip is small and the line is close to the dip direction this trend error  $\Delta t$  may be negligible (Ten Haaf, 1959, p. 72; Ramsay, 1961). If this approximation is seriously considered it should always be tested with a plot on the stereonet.

Note carefully that this restoration using the conventional tilt correction is not the same as the starting state illustrated in Fig. 6.5. We have not recovered the trend of the line because we have not taken into account the component of rotation about a vertical axis.

Without additional information any such rotation about a vertical axis remains unknown. One way of obtaining such information is to compare the results of the restoration with undisturbed beds nearby. Ten Haaf (1959, p. 78) used this technique to demonstrate that kilometer-scale coherent slabs in the Apennines of northern Italy rotated about vertical axes through large angles during gravitational sliding. Another approach is to use paleomagnetic vectors to assist in identifying the axis of rotation which restores the tilted beds to their actual initial orientation (Tauxe & Watson, 1994; Weinberger, *et al.*, 1995).

There are certainly situations where beds have been tilted about axes which were horizontal or nearly so and this conventional approach will then produce acceptable results. In the face of the general uncertainties, however, it is prudent to remain cautious. All the remaining problems in this chapter involve these same uncertainties.

<sup>1</sup>That this is not true for rotations about other axes see Fig. 6.4 where point  $L_2$  is located on the line of true dip on its plane but the rotated point  $L'_2$  is *not* on the line of true dip of the rotated plane.

There is an additional special case. If the plane returned to horizontality was overturned, then the resulting orientation of the associated linear structure obtained using this method would be incorrect. An alternative construction must be used.

### Problem

- An overturned sedimentary bed N 40 W, 60 W contains a sedimentary lineation trending N 63 W. Restore the bed to horizontality and determine the original trend of the lineation using the conventional tilt correction.

### Visualization

- Hold the left hand, palm downward with a pencil in the proper orientation over the net. Now rotate the hand through an angle of  $120^\circ$  into a horizontal position with the palm upward and observe the position of the line.

### Construction

1. Trace in the great circle representing the inclined plane and on it locate the line of true dip  $D(60/230)$  and the line  $L(34/297)$  (Fig. 6.8b).
2. Label the strike direction  $R(00/340)$  and turn this mark to north.
3. As  $D$  moves  $120^\circ$ , first to center of the net and then to the primitive (and the bed to horizontal),  $L$  moves along its small circle to  $L'$  in the same sense and angle, also to the primitive.

### Answer

- The attitude of the restored line is  $L'(00/000)$ , that is, horizontal and due north. This is a quite different result from the restoration in the upright case.

## 6.7 Two tilts

A closely related situation involves the restoration of a structural plane that has been tilted twice, called the *problem of two tilts*. The goal is to determine the attitude of the plane after the first but before the second tilt.

### Problem

- The attitude of beds above an angular unconformity is N 20 E, 30 E and the attitude of the beds below the unconformity is N 70 E, 50 S. What was the attitude of the lower beds before the tilt of the upper beds?

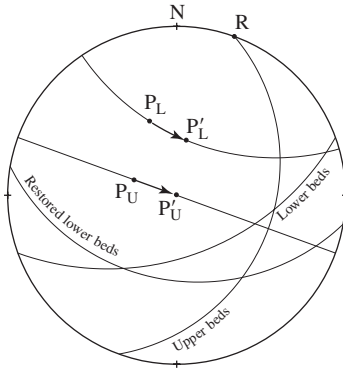


**Figure 6.9** Problem of two tilts.

### Method

- Because this correction of the tilt of the lower beds involves rotation about an axis which is oblique to the strike direction we can not use the line of true dip. The representation of the planes by their poles is required. Plotting the tilted planes by great circles is not necessary for a solution but they are helpful in visualizing the procedure and result.

### Construction

1. Plot the poles of the once tilted upper beds  $P_U(60/290)$  and the twice tilted lower beds  $P_L(40/340)$  (Fig. 6.9).
2. Mark the strike direction of the upper beds as the rotation axis  $R(00/020)$  and turn it to north.
3. In restoring the upper beds to horizontality, pole  $P_U$  moves  $30^\circ$  inward to the center of the net and pole  $P_L$  moves  $30^\circ$  in the same direction along its small circle to  $P'_L$ .

### Answer

- The restored pole  $P'_L(53/010)$  of the lower beds corresponds to an attitude of N 80 W, 37 S.

## 6.8 Folding problems

These same techniques can also be used to restore the attitude of folded beds. We describe the details of fold geometry in Chapter 13. Here it is sufficient to treat folds as two planes whose line of intersection represents the fold axis. In such applications there is an important caveat. If the folding is accompanied by distortion of the bedding planes, the angular relationships change and this requires a more involved treatment (see §12.9; also Ramsay, 1961). The following treatment assumes that such distortions are absent.

If the folds are horizontal, the conventional tilt correction suffices to return the beds to horizontality. If the folds plunge, the tilted beds can be considered to have two rotational axes: one of them is the fold axis and the other is a horizontal axis perpendicular to the trend of the fold axis (Ramsay, 1961). Reversing the rotations on both these then unrolls the folded beds to their original orientation. Using the previous approach, a sequence of rotations is used. First, the beds are unrolled about the plunging fold axis and then about the resulting strike direction to bring the beds back to horizontal.

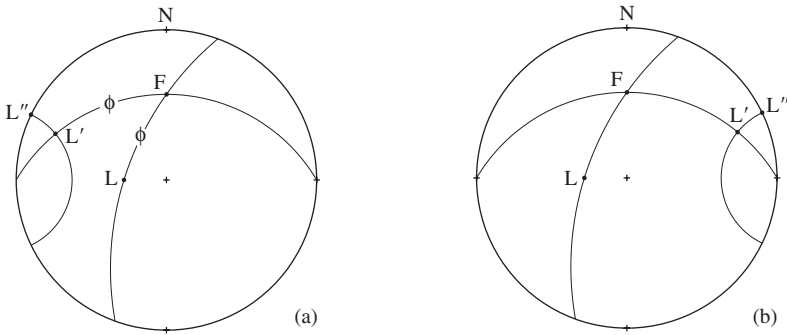


**Figure 6.10** Restoring folded beds: (a) upright limb; (b) overturned limb.

**Problem**

- The fold axis plunges  $31^\circ$  due north. On the west limb of an anticline, inclined beds whose attitude is N  $20^\circ$  E,  $60^\circ$  W contain sole markings which trend due west. Determine the prefolding orientation of this sedimentary lineation.

**Visualization**

- With the left hand represent the plane on the west limb with the index finger in the direction of the fold axis. Similarly, with the right hand represent a similarly oriented plane on the east limb. Now rotate both planes about your index fingers to bring the two planes into parallelism. Now perform the tilt correction to bring this plane into horizontality.

**Construction**

1. Plot the fold axis  $F(30/000)$  and draw in the great circle representing the inclined plane and locate the east-trend line  $L$  on its trace. Note that this great circle must pass through  $F$  (Fig. 6.10a).
2. Read off the angle  $\phi$  between  $L$  and  $F$ .
3. Unrolling the beds about the plunging fold axis results in a plane dipping  $30^\circ$  due north. The angle between  $F$  and  $L$ ,  $\phi = 55^\circ$ , remains constant. Thus, after unfolding,  $L'$  can be located at the same angle along the great circle representing this north-dipping plane.

4. The tilt correction then brings the plane to horizontal and the line to  $L''$  on the primitive.

### Answer

- The restored orientation of the sedimentary lineation is  $L''(00/056)$ .

If the beds are overturned this simple restoration will be in error and an adjustment must be made. With the same visualization as before, now rotate your hand about the fold axis so that the palm is downward. The angle  $\phi$  remains the same, but now  $L'$  is on the opposite side of  $F$ . The tilt correction then gives  $L'''$  with a trend of N 56 E (Fig. 6.10b).

## 6.9 Small circles

Throughout this chapter we have made use of small circles on the stereonet. It is a fundamental property of the stereographic projection that circles on the sphere project as circles (see §5.1). Here we show how to construct small circles about any inclined axis. We also prove that they are indeed circles.

As we have seen, a small circle is the intersection of the sphere and a right-circular cone. A vertical diametral plane of the sphere containing the inclined axis  $OP$  displays a section  $MON$  of this cone (Fig. 6.11a). The cone axis makes an angle  $\theta$  with the vertical and its vertex angle is  $2\phi$ . Line  $MN$  is the trace of the circular section of this cone.

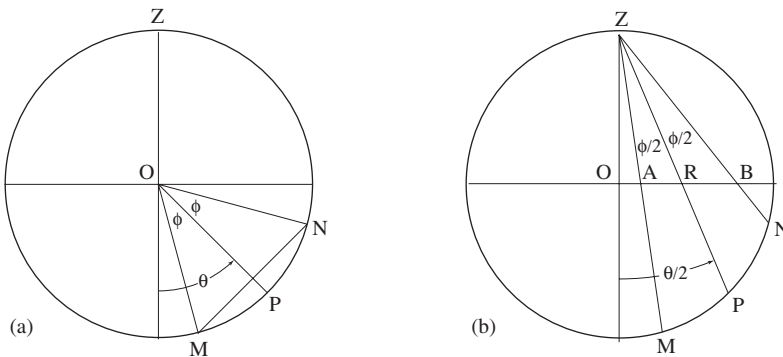


**Figure 6.11** Small circle: (a) on sphere; (b) in projection.

We project the small circle on the sphere to the horizontal projection plane using the zenith point  $Z$ . The center of the circle  $P$  projects to  $R$ , the lowest point  $M$  and highest point  $N$  on the circle project to points  $A$  and  $B$  (Fig. 6.11b). With these two points any small circle may be drawn on the stereonet. There are two important cases. The circle may be wholly within the lower hemisphere or it may be partially in the upper hemisphere. We start with the simpler case when the cone is entirely within the lower hemisphere.



**Problem**

- Construct the small circle whose angular radius  $\phi = 35^\circ$  about inclined axis  $R(45/140)$ .

**Construction**

1. Plot the axis  $R(45/160)$ . On a radius of the net through  $R$  plot points  $A$  downward and  $B$  upward from  $R$  at an angular distance of  $\phi = 35^\circ$ .
2. Bisect the linear distance  $AB$  to locate the center  $C$  and complete the circle with radius  $AC = BC$  using a compass. Note that  $C$  does not coincide with  $R$  (Fig. 6.12).

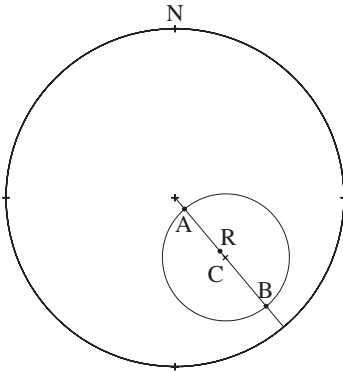


**Figure 6.12** Construction of a general small circle.

If the small circle overlaps the primitive, that is, if it extends partially into the upper hemisphere it is then necessary to construct the arc of its *opposite*. This requires additional steps because there is no direct way of plotting points outside the primitive.

On the vertical diametral section of the sphere, the trace of the cone is  $MON$  and its opposite is  $M'ON'$  (Fig. 6.13). Points  $M$  and  $N$  are projected using  $Z$  to points  $A$  and  $B$  on the projection plane in the usual way,  $A$  inside and  $B$  outside the primitive. In the same way the opposite points  $M'$  and  $N'$  are projected to  $A'$  outside and  $B'$  inside the primitive. Note that  $\angle NZN' = \angle MZM' = 90^\circ$ .

Just as before, segments  $AB$  and  $A'B'$  are bisected to locate centers  $C$  and  $C'$  and the two circles are completed with a compass. Although it is in two parts, the small circle is now complete in the lower hemisphere (and also in the upper hemisphere).

Expressions for the location of the center of the small circle and its radius can also be obtained. For a sphere of unit radius, and in the notation of Fig. 6.11b,

$$OA = \tan \frac{1}{2}(\theta - \phi) \quad \text{and} \quad OB = \tan \frac{1}{2}(\theta + \phi),$$

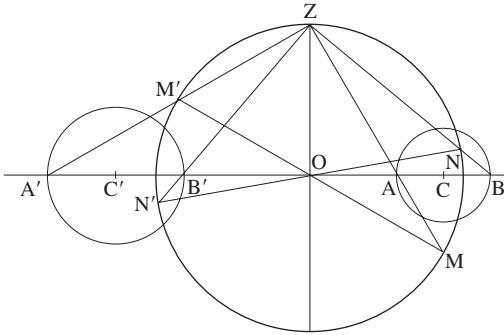


**Figure 6.13** Small circle and its opposite.

where  $\theta$  is the supplement of the plunge of the cone axis and  $\phi$  is the semi-vertex angle of the cone. With these the distance from  $O$  to the geometrical center of the small circle on the projection plane is then

$$c = \frac{1}{2}(OB + OA) = \frac{1}{2} \left[ \tan \frac{1}{2}(\theta + \phi) + \tan \frac{1}{2}(\theta - \phi) \right]$$

and its radius is

$$r = \frac{1}{2}(OB - OA) = \frac{1}{2} \left[ \tan \frac{1}{2}(\theta + \phi) - \tan \frac{1}{2}(\theta - \phi) \right].$$

Substituting the identities

$$\tan \frac{1}{2}(\theta + \phi) = \frac{\sin \theta + \sin \phi}{\cos \theta + \cos \phi} \quad \text{and} \quad \tan \frac{1}{2}(\theta - \phi) = \frac{\sin \theta - \sin \phi}{\cos \theta + \cos \phi}$$

and rearranging, these two expressions become

$$c = \frac{\sin \theta}{\cos \theta + \cos \phi} \quad \text{and} \quad r = \frac{\sin \phi}{\cos \theta + \cos \phi}.$$

These equations can also be used to locate earthquake epicenters (Garland, 1979, p. 54). Because  $\theta = (90^\circ - p)$  a more convenient form for our purposes is

$$c = \frac{\cos p}{\sin p + \cos \phi} \quad \text{and} \quad r = \frac{\sin \phi}{\sin p + \cos \phi}. \quad (6.1)$$

With these the location and size of a circle which is mostly in the lower hemisphere can be easily determined for a stereogram of any size. Just multiply the values of both  $c$  and  $r$  by the desired radius of the primitive.

These two parameters can also be used to calculate the location and size of the opposite small circle by using  $-p$  (indicating an upward inclination of the cone axis) in Eqs. 6.1, or by using

$$c = \frac{\cos p}{-\sin p + \cos \phi} \quad \text{and} \quad r = \frac{\sin \phi}{-\sin p + \cos \phi}. \tag{6.2}$$

Both the graphical and analytical methods illustrate two aspects of opposite small circles which have some practical importance.

1. As the opposite point  $M'$  approaches the projection point  $Z$  both  $c$  and  $r$  become very large and drawing the opposite arc is difficult or impossible.
2. Opposite small circles have two basic configurations:
  - (a) If  $(p + \phi) < 90^\circ$  its arc is convex toward the center of the net (Fig. 6.14a);
  - (b) If  $(p + \phi) > 90^\circ$  its arc is concave toward the center (Fig. 6.14c).

The boundary case occurs when the low point on the cone coincides with the center of the net, that is, when  $(p + \phi) = 90^\circ$  (Fig. 6.14b). In the graphical construction of its opposite  $A'$ , the projector from  $Z$  is parallel to the projection plane and both  $c$  and  $r$  are infinite. In Eqs. 6.2 this state is indicated when the denominator  $(-\sin p + \cos \phi) = 0$ . The representation of the opposite of such a circle is particularly easy to construct – it is a straight line.

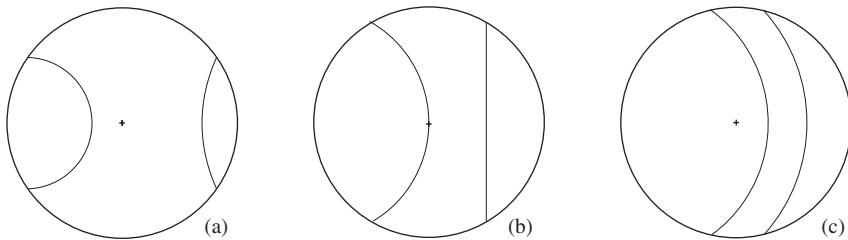


**Figure 6.14** Types of small circles.

We now demonstrate that circles on the sphere do, in fact, project as circles, following Phillips (1963, p. 24–25). As we have seen, any small circle is the intersection of a sphere and a right-circular cone with vertex at the center of the sphere (Fig. 6.11a). The axis of this cone  $OP$  makes angle  $\theta$  with the vertical and  $\angle MON = 2\phi$ . The small circle on the sphere has a diameter of  $MN$  and the point  $P$  is at its center.

The projection of points  $P$ ,  $M$  and  $N$  on the sphere to the projection plane uses the zenith point  $Z$ . The resulting three points  $A$ ,  $B$  and  $R$  define a second cone whose axis  $ZP$  makes an angle  $\frac{1}{2}\theta$  with the vertical and  $\angle MZN = \phi$  (Fig. 6.11b).

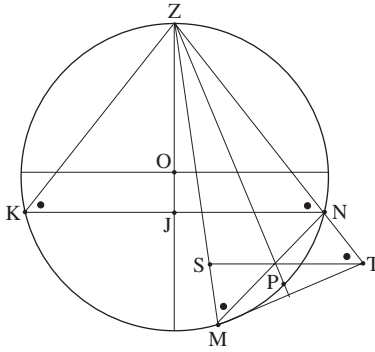


**Figure 6.15** A small circle and its projection.

### Proof

1. On the vertical plane containing the cone axis, chord  $KN$  is drawn parallel to the projection plane, hence also perpendicular to  $OZ$ . Right triangles  $ZKJ$  and  $ZNJ$  are congruent and so  $\angle ZKJ = \angle ZNJ$  (Fig. 6.15, where black dots mark equal angles).
2. Because they subtend these equal angles, the lengths of arcs  $ZK$  and  $ZN$  are equal. Then the inscribed angles which subtend these equal arcs are also equal, so  $\angle ZMN = \angle ZNJ$ .
3. Line  $MN$ , which is oblique to axis  $ZP$ , is the trace of a circular section of cone  $MZN$ . Therefore the right section of this cone  $MT$  is an ellipse.
4. By construction  $TS$  makes the same angle with axis  $ZP$  as the circular section  $MN$ . Therefore  $TS$  is a conjugate circular section.
5. Therefore  $\angle ZTS = \angle ZMN$ , and also  $\angle ZNJ = \angle ZTS$ . Lines  $TS$  and  $NJ$  are then parallel and also parallel to the projection plane.
6. Parallel sections of a cone are similar. Therefore the section in the projection plane is also a circle and the proof is complete.

### 6.10 Exercises

1. A horizontal plane contains a line whose trend is N 48 E.
  - (a) Rotate the plane and line about a vertical axis  $50^\circ$  anticlockwise.
  - (b) From the same starting position, rotate the plane and line about a north-trending horizontal axis  $60^\circ$  clockwise.
2. Sequence of rotations.
  - (a) Rotate the same horizontal plane and line first about a vertical axis  $50^\circ$  anticlockwise and then about a north-trending horizontal axis  $60^\circ$  clockwise.
  - (b) Rotate the horizontal plane and line first about a north-trending horizontal axis  $60^\circ$  clockwise and then about a vertical axis  $50^\circ$  anticlockwise.
3. Rotate the same plane and line about an axis whose plunge and trend is 30/200  $40^\circ$  clockwise.

4. The beds below an angular unconformity have an attitude of N 30 W, 40 W. The strata above the unconformity have an attitude of N 20 E, 30 E. What was the attitude of the lower beds before the tilting of the younger bed occurred?
5. An anticlinal fold axis plunges 24/040. On the east limb where the beds have an attitude of N 5 W, 32 E, the crest line of current ripple marks pitches 70 N in the plane of the bedding. What was the pre-tilt orientation of these marks? Compare your result with the assumption that the tilted orientation of the lineation adequately represents the original direction.
6. An anticline plunges 50/025. The eastern limb is overturned, and at one point the attitude is N 45 E, 50 W. At this same locality a sedimentary lineation plunges due west. What was the orientation of the lineation before folding?
7. Rotate the plane whose attitude is N 10 E, 30 E, fifty degrees anticlockwise as viewed down the plunge of an axis whose attitude is 30/340 in two ways: (1) as a series of steps involving rotation of the axis to the primitive, rotating the line about the now horizontal axis, and then returning the axis to its original orientation; (2) as a single rotation about the inclined axis.

# 7

## Vectors

### 7.1 Introduction

Vectors play a prominent role in many geometrical and physical applications. We have seen several simple examples in Chapters 1 and 3 where the attitudes of planes and lines were represented and manipulated using two-dimensional vectors. We now extend the treatment to three dimensions, and to several additional applications.

As we have seen, the stereonet is a useful way of displaying and manipulating structural lines and planes easily and directly in a three-dimensional setting. For the same reasons, we can use the stereonet to introduce an analytical approach involving vectors which is a powerful method for solving these same types of problems (see also Sprenke, 1992).

Because the orientations of planes are defined by their poles, we can represent all structural elements by lines. There are two types of such lines.

1. *Axes* have orientation but no sense. Lineations in metamorphic rocks, lines of intersection and poles of fracture planes are examples.
2. *Vectors* have both orientation and sense. Examples include some linear sedimentary structures and paleomagnetic directions.

Some structural lines may be treated in either way. For purely geometrical purposes the pole of sedimentary bedding is commonly treated as an axis, but for other purposes the pole in the direction of younging has sense and therefore is a true vector.

In many applications it is convenient to represent axes by vectors. In fact, we have already done this in Chapters 1 and 3 by choosing to represent lines of true and apparent dip as horizontal vectors which point in the direction of downward inclination. As before, the sense of these vectors is arbitrarily but conveniently chosen to point *downward*, thus we can always plot them on the lower hemisphere. If we encounter an upward pointing axis-as-vector we can immediately convert it to a downward pointing one.

These vectors can then be manipulated by taking advantage of the well-established vector formalism encountered in introductory courses in calculus and physics. Not only

is this a particularly powerful way of solving a number of structural problems but it also lays the groundwork for more advanced applications (Goodman, 1976, p. 217f; Priest, 1985; Wallbrecher, 1986).<sup>1</sup>

We need a coordinate system. For problems involving conditions within the earth, it is nearly universal to measure depth along a downward pointing  $z$  axis. Accordingly, we define a right-handed set of axes with  $+x$  = north,  $+y$  = east and  $+z$  = down (Fig. 7.1a).<sup>2</sup> The equation of the unit sphere is then

$$x^2 + y^2 + z^2 = 1, \quad (7.1)$$

and the directions of vectors can be represented by points on the surface of this sphere.

In many applications it is necessary to use vector components. Following common practice we take unit base vectors  $\mathbf{i}$ ,  $\mathbf{j}$  and  $\mathbf{k}$  to be parallel to the coordinate directions  $+x$ ,  $+y$  and  $+z$ , respectively. Then any vector  $\mathbf{V}$  is the sum of its components in each of these directions.<sup>3</sup> We write this sum as

$$\mathbf{V} = V_x\mathbf{i} + V_y\mathbf{j} + V_z\mathbf{k}. \quad (7.2)$$

Following common practice, we represent such a vector by its three scalar components  $(V_x, V_y, V_z)$ . The length or magnitude of vector  $\mathbf{V}$  is, from a three-dimensional version of the Pythagorean theorem,

$$|\mathbf{V}| = V = \sqrt{V_x^2 + V_y^2 + V_z^2}. \quad (7.3)$$

When used to represent the orientation of lines and poles we are interested in the directions not magnitudes of the associated vectors. It is then convenient to use only vectors of unit magnitudes. To find the unit vector with the same direction as a general vector, we *normalize* its components by dividing each by the magnitude. The three scalar components of this unit vector are called *direction cosines* and they are commonly given the symbols  $l$ ,  $m$  and  $n$ , where

$$l = V_x/V, \quad m = V_y/V, \quad n = V_z/V. \quad (7.4)$$

With these, Eq. 7.3 reduces to the useful identity

$$l^2 + m^2 + n^2 = 1. \quad (7.5)$$

<sup>1</sup>Wallbrecher's book contains the listing of a number of useful programs for structural geology. These are now available as the package Fabric8 at [www.geolsoft.com](http://www.geolsoft.com).

<sup>2</sup>In contrast, for problems involving surface or near surface features a geographical coordinate system with  $+x$  = east,  $+y$  = north and  $+z$  = up is generally used (see §7.8).

<sup>3</sup>We use the symbol  $\mathbf{V}$  to represent a generic vector. It should not be confused with the commonly used symbol for *volume*.

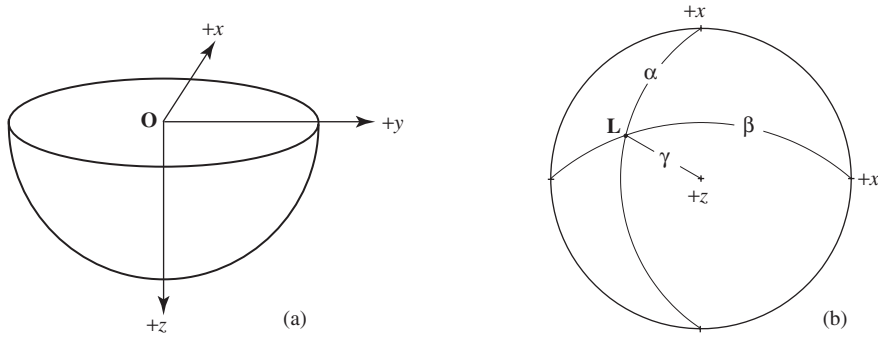


**Figure 7.1** Coordinate axes: (a) lower hemisphere; (b) stereogram and direction angles of line vector **L**.

With any two direction cosines this relationship yields the magnitude but not the sign of the third.

For use in plotting vectors as points on the stereonet, *direction angles* are more useful and these are defined as

$$\alpha = \arccos l, \quad \beta = \arccos m, \quad \gamma = \arccos n. \quad (7.6)$$

From the point plotted using its plunge and trend we can measure these three direction angles on a stereogram (Fig. 7.1b).

### Problem

- Find the direction angles of the vector **V**(30/300).

### Solution

1. Using its plunge and trend plot the point representing **V** in the usual way (Fig. 7.2a).
2. Measure  $\alpha$  from  $+x$ ,  $\beta$  from  $+y$ , and  $\gamma$  from  $+z$  to **V** along great circular arcs.

### Answer

- The direction angles are  $\alpha = 64^\circ$ ,  $\beta = 139^\circ$  and  $\gamma = 60^\circ$ .

These angles can be checked by using Eq. 7.5, but note that this identity will rarely be exactly satisfied because of inevitable errors in plotting the points and reading the angles. In the previous example the sum is 1.011 76, and this is about as close to confirmation as one can get when reading angles from the net to the nearest degree.

A closely related problem is to plot a vector on a stereogram given its direction angles.

### Problem

- Plot the point representing **V** using its direction cosines  $l = 0.433\ 01$ ,  $m = -0.750\ 00$ ,  $n = 0.500\ 00$ .



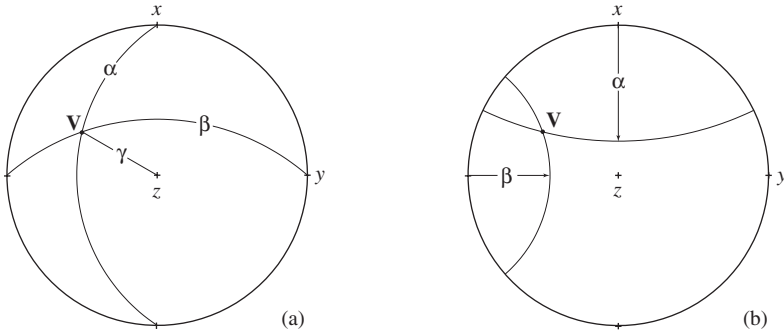


**Figure 7.2** Direction angles: (a) reading angles; (b) plotting angles.

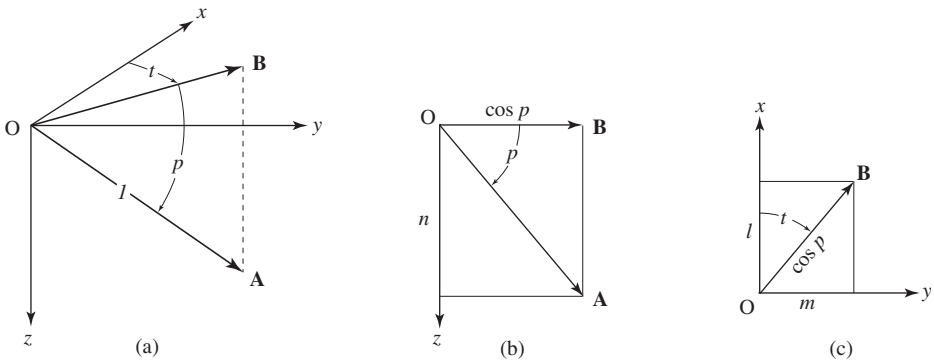


**Figure 7.3** Direction cosines from plunge and trend.

**Solution**

1. With Eqs. 7.6, the three direction angles are  $\alpha = 64.3^\circ$ ,  $\beta = 138.6^\circ$ ,  $\gamma = 60.0^\circ$ .
2. About the point on the primitive representing the  $+x$  axis trace in the small circle with angular radius  $\alpha = 64.3^\circ$  (Fig. 7.2b).
3. About the point representing the  $+y$  axis trace in the small circle with angular radius  $\beta = 138.6^\circ$ . Alternatively, this small circle can be located  $180^\circ - 138.6^\circ = 41.4^\circ$  from  $-y$ . Even simpler, just change the sign of  $m$  and then  $\arccos(+0.75000) = 41.4^\circ$ .
4. The small circle for  $\gamma = 60.0^\circ$  about  $+z$  can be added to the diagram with a compass but it is usually unnecessary. It is, however, a good idea to check that angle  $\gamma$  between  $+z$  and the intersection of the other two small circles is correct.

As with structural lines generally, we may also express the orientation of vectors by their plunge  $p$  and trend  $t$ . Note that in our adopted coordinate system *positive trend angles* are measured clockwise from  $+x =$  north and *positive plunge angles* are measured downward from the horizontal  $xy$  plane, as is standard. On the stereonet these angles are closely related to spherical coordinates:  $\theta = t$ ,  $\phi = 90^\circ - p$  and  $r = 1$ .

From plunge and trend we can also compute the direction cosines (Fig. 7.3a). The horizontal component of the inclined unit vector  $\mathbf{A}$  with length  $OA = 1$  is vector  $\mathbf{B}$  where  $B = \cos p$ . From Figs. 7.3b and 7.3c, the direction cosines of  $\mathbf{A}$  are

$$l = \cos p \cos t, \quad m = \cos p \sin t, \quad n = \sin p. \quad (7.7)$$

These may also be converted back to plunge and trend with

$$p = \arcsin n, \quad t = \arctan m/l. \quad (7.8)$$

The *arctan* function on hand-held calculators and in most programming languages returns angles in the range  $-90^\circ < t < 90^\circ$ , that is, only trend angles in the NE and NW quadrants are reported. If  $l < 0$  then the actual angle is in the range  $90^\circ < t < 270^\circ$  and it is necessary to add or subtract  $180^\circ$  to get the correct trend. In most programming languages and spreadsheet programs, the alternative function  $\text{atan2}(m, l)$  gives the trend without need for this correction.

## 7.2 Sum of vectors

There are many physical and geometrical situations where two or more vectors must be combined by addition, as we will see later. The equation expressing the addition of two vectors to give a third is

$$\mathbf{A} + \mathbf{B} = \mathbf{C}. \quad (7.9)$$

Given vectors  $\mathbf{A}$  and  $\mathbf{B}$  we can determine their sum  $\mathbf{C}$  either geometrically or analytically. The geometrical method uses the *parallelogram rule*: Place the tail of  $\mathbf{B}$  at the head of  $\mathbf{A}$ . Then draw the vector from the tail of  $\mathbf{A}$  to the head of  $\mathbf{B}$ ; this is  $\mathbf{C}$  (Fig. 7.4a). Note that  $\mathbf{B} + \mathbf{A}$  gives the same result – vector addition is commutative. Note too that  $\mathbf{C}$  is the diagonal of the parallelogram with sides parallel to  $\mathbf{A}$  and  $\mathbf{B}$ , hence the name of the rule.

The difference of two vectors can also be found. The solution of Eq. 7.9 for  $\mathbf{A}$  can be written in two ways

$$\mathbf{A} = \mathbf{C} - \mathbf{B} \quad \text{or} \quad \mathbf{A} = \mathbf{C} + (-\mathbf{B}).$$

The vector  $-\mathbf{B}$  has the same length as  $\mathbf{B}$  but points in the opposite direction. The graphical solution proceeds just as before (Fig. 7.4b).

The analytical method involves representing vectors as matrices. This enumerates the components and at the same time emphasizes that they represent a single entity. Even more important is that such matrices can be manipulated directly using matrix algebra.<sup>4</sup>

<sup>4</sup>Good geologically oriented introductions to matrix algebra are given by Ferguson (1994) and Davis (2002, p. 123–158).

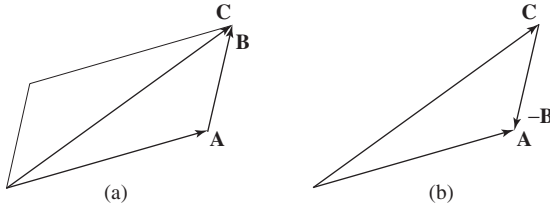


**Figure 7.4** Parallelogram rule: (a) addition; (b) subtraction.

In a simple example we represent them as *column matrices*. Then we form the sum of two vectors by adding components (Fig. 7.5). This is expressed by the matrix equation

$$\mathbf{A} + \mathbf{B} = \mathbf{C} = \begin{bmatrix} A_x \\ A_y \end{bmatrix} + \begin{bmatrix} B_x \\ B_y \end{bmatrix} = \begin{bmatrix} A_x + B_x \\ A_y + B_y \end{bmatrix} = \begin{bmatrix} C_x \\ C_y \end{bmatrix}. \tag{7.10}$$

The extension to three dimensions is straightforward.

$$\begin{bmatrix} C_x \\ C_y \\ C_z \end{bmatrix} = \begin{bmatrix} A_x + B_x \\ A_y + B_y \\ A_z + B_z \end{bmatrix}. \tag{7.11}$$

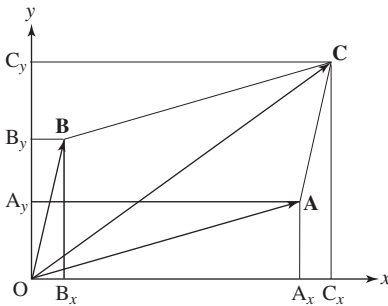


**Figure 7.5** Vector addition using components.

A useful application involves finding the vector which bisects the angle between two given vectors. If  $A = B$  then  $C$  divides the parallelogram whose sides are  $A$  and  $B$  into two congruent triangles. Therefore the angles between  $A$  and  $C$  and between  $B$  and  $C$  are equal (Fig. 7.6a).

**Problem**

- Bisect the angle between vectors  $A(30/310)$  and  $B(60/030)$  (Fig. 7.6b).

**Solution**

1. From plunge and trend of each vector, the direction cosines are  $A(0.556\ 67, -0.663\ 41, 0.500\ 00)$  and  $B(0.433\ 01, 0.250\ 00, 0.866\ 03)$ .

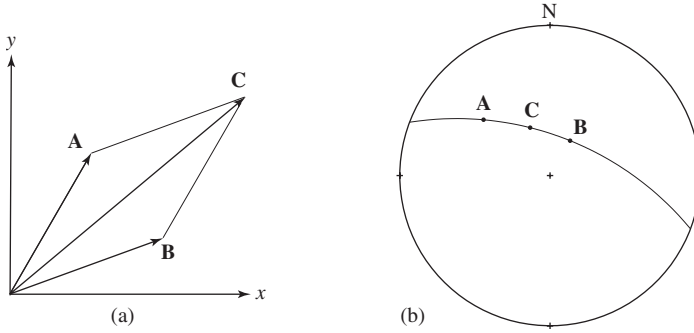


**Figure 7.6** Bisector of two vectors: (a) two dimensions; (b) three dimensions.

2. From Eq. 7.11 we then have

$$\begin{bmatrix} C_x \\ C_y \\ C_z \end{bmatrix} = \begin{bmatrix} 0.989\ 68 \\ -0.413\ 41 \\ 1.366\ 03 \end{bmatrix}. \quad (7.12)$$

3. Normalizing these components of  $\mathbf{C}$  we obtain the direction cosines  $\mathbf{C}(0.569\ 84, -0.238\ 03, 0.786\ 53)$ .

#### Answer

- The plunge and trend of the bisector is  $\mathbf{C}(52/337)$ . If vectors  $\mathbf{A}$  and  $\mathbf{B}$  represent the poles of planes, then vector  $\mathbf{C}$  bisects the angle between the two planes.

### 7.3 Products of vectors

Important relationships between two vectors can be found by forming the *scalar* or *dot product* and the *vector* or *cross product*.

#### Dot product

The first and simpler product of two vectors  $\mathbf{A}$  and  $\mathbf{B}$  is defined in terms of their magnitudes  $A$  and  $B$  and the angle  $\phi$  between them as

$$\mathbf{A} \cdot \mathbf{B} = AB \cos \phi, \quad (7.13)$$

where  $0 \leq \phi \leq 90^\circ$ . This has a useful geometrical interpretation:  $B \cos \phi$  is the projection of  $\mathbf{B}$  onto  $\mathbf{A}$  and  $A \cos \phi$  is the projection of  $\mathbf{A}$  onto  $\mathbf{B}$ . The dot product can also be expressed in component form as

$$\mathbf{A} \cdot \mathbf{B} = A_x B_x + A_y B_y + A_z B_z. \quad (7.14)$$

From these two versions it should be apparent that the order in which the vectors are taken makes no difference, that is,  $\mathbf{A} \cdot \mathbf{B} = \mathbf{B} \cdot \mathbf{A}$ . The dot product, like the sum, is commutative.

As before, it is convenient to write such expressions as matrix equations. Here  $\mathbf{A}$  is represented by a *row matrix* and  $\mathbf{B}$  by a *column matrix*. Thus

$$\mathbf{A} \cdot \mathbf{B} = [A_x \quad A_y \quad A_z] \begin{bmatrix} B_x \\ B_y \\ B_z \end{bmatrix} = A_x B_x + A_y B_y + A_z B_z. \quad (7.15)$$

In this easily remembered form the resulting scalar quantity is obtained by summing the products of the corresponding elements of the row and the column matrices. This is an example of *row times column multiplication* (Boas, 1983, p. 115–116), and we will use it repeatedly.

If both vectors have unit magnitudes then Eqs. 7.13 and 7.14 combine to give the useful formula for finding the angle between them

$$\hat{\mathbf{u}}_1 \cdot \hat{\mathbf{u}}_2 = \cos \phi = l_1 l_2 + m_1 m_2 + n_1 n_2, \quad (7.16)$$

where  $(l_1, m_1, n_1)$  and  $(l_2, m_2, n_2)$  are the two sets of direction cosines. With this formula the angle between any two directions represented by unit vectors may be easily found. If  $\theta = 90^\circ$ , that is the two vectors are mutually perpendicular, this equation reduces to

$$l_1 l_2 + m_1 m_2 + n_1 n_2 = 0 \quad (7.17)$$

and this can be used as a test for orthogonality.

The dot product can also be used if the two unit vectors lie in one of the coordinate planes. For example, in the  $xy$  plane, the direction angles measured from  $+z$  are  $\gamma_1 = \gamma_2 = 90^\circ$  and therefore  $n_1 = n_2 = 0$ . Then Eq. 7.16 reduces to

$$\cos \phi = l_1 l_2 + m_1 m_2, \quad (7.18)$$

and similar results can be obtained for vectors in the  $yz$  and  $zx$  coordinate planes.

### Problem

- What is the angle between the pole vectors  $\mathbf{P}_1(30/310)$  and  $\mathbf{P}_2(60/030)$ ?

### Solution

1. From each plunge and trend, using Eqs. 7.7, the direction cosines are

$$\mathbf{P}_1(0.556\ 67, -0.663\ 41, 0.500\ 00) \quad \text{and} \quad \mathbf{P}_2(0.433\ 01, 0.250\ 00, 0.866\ 03)$$

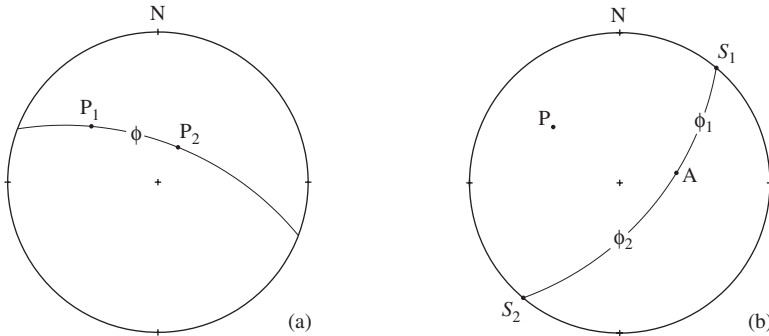


**Figure 7.7** Dot product: (a) angle between vectors; (b) pitch of a line.

2. With Eq. 7.16  $\cos \phi = 0.59820$  or  $\phi = 59^\circ$ . This angle may be acute or obtuse; if acute, as here, it is the dihedral angle between the two planes (Fig. 7.7a).

In exactly the same way the angle between two lines  $\mathbf{L}_1$  and  $\mathbf{L}_2$  or between a line  $\mathbf{L}$  and a pole  $\mathbf{P}$  may also be found from the dot product.

This technique can also be used to calculate the pitch of a line in a specified plane. There are several ways of doing this but the one which corresponds most closely with the previous graphical method requires the direction of the strike of the plane – it is perpendicular to the trend of the pole vector or, equivalently, perpendicular to the trend of the dip vector. The orientation of this strike vector can be obtained in either of two ways.

1. From the trend  $t$  of either the pole or the dip vector, the strike direction is simply  $t + 90^\circ$  or  $t - 90^\circ$ .
2. The direction of the strike may also be determined from the direction cosines  $(l, m, n)$  of either the pole or dip vector. From Eqs. 7.8, trend depends on  $m/l$ . The strike is then obtained from the negative reciprocal  $-(l/m)$ . This horizontal strike vector has two forms corresponding to its two equivalent ends

$$\mathbf{S}_1(-m, l, 0) \quad \text{and} \quad \mathbf{S}_2(m, -l, 0). \quad (7.19)$$

### Problem

- The orientation of a plane is given by its pole vector  $\mathbf{P}(30/310)$ . Determine the pitch of the apparent dip vector  $\mathbf{A}(48/080)$  (Fig. 7.7b).

### Solution

1. The two possible strikes of the plane are  $\mathbf{S}_1(00/040)$  and  $\mathbf{S}_2(00/220)$ . From Eqs. 7.7, the components of the unit strike vectors are  $\mathbf{S}_1(0.76604, 0.64279, 0.00000)$  and  $\mathbf{S}_2(-0.76604, -0.64279, 0.00000)$ .

2. From its plunge and trend, the components of the apparent dip vector are  $\mathbf{A}(0.116\ 19, 0.658\ 97, 0.743\ 14)$ .
3. Equation 7.16 gives  $\cos \phi_1 = 0.512\ 58$  or  $\phi_1 = 59^\circ$  measured from  $\mathbf{S}_1$  and  $\cos \phi_2 = -0.521\ 58$  or  $\theta_2 = 121^\circ$  measured from  $\mathbf{S}_2$ . Note that  $\phi_1 + \phi_2 = 180^\circ$ . By convention the pitch angle is acute.

### Cross product

The second way of forming the product of two vectors is written

$$\mathbf{C} = \mathbf{A} \times \mathbf{B}. \quad (7.20)$$

The product vector  $\mathbf{C}$  is perpendicular to the plane of  $\mathbf{A}$  and  $\mathbf{B}$  and its direction is determined by the *right-hand rule*: if the fingers of the right hand point from  $\mathbf{A}$  toward  $\mathbf{B}$  through the smaller angle, the thumb points in the direction of  $\mathbf{C}$ . If the order is reversed, the direction of  $\mathbf{C}$  is also reversed, hence the order does make a difference. This condition can be expressed as  $\mathbf{A} \times \mathbf{B} = -(\mathbf{B} \times \mathbf{A})$ . In other words, the cross product is not commutative.

The magnitude of the cross product vector is defined as

$$C = AB \sin \phi, \quad (7.21)$$

where, as before,  $\phi$  is the smaller angle between the two vectors.

In component form, the cross product may be expressed as the easily remembered determinant

$$\mathbf{A} \times \mathbf{B} = \begin{vmatrix} \mathbf{i} & \mathbf{j} & \mathbf{k} \\ A_x & A_y & A_z \\ B_x & B_y & B_z \end{vmatrix}.$$

For computational purposes this  $3 \times 3$  determinant can be reduced to the sum of three  $2 \times 2$  determinants by the *method of expansion by cofactors*, which follows a simple rule: for each scalar coefficient cross out in turn the row and column containing the unit base vectors  $\mathbf{i}$ ,  $\mathbf{j}$  or  $\mathbf{k}$  and in each case form the determinant of the remaining four elements. For example, crossing out the first row and first column gives the  $2 \times 2$  determinant composed of the four remaining elements times  $\mathbf{i}$  (Fig. 7.8a). The other cofactors are found in similar fashion. The full result is

$$\mathbf{A} \times \mathbf{B} = \begin{vmatrix} A_y & A_z \\ B_y & B_z \end{vmatrix} \mathbf{i} - \begin{vmatrix} A_x & A_z \\ B_x & B_z \end{vmatrix} \mathbf{j} + \begin{vmatrix} A_x & A_y \\ B_x & B_y \end{vmatrix} \mathbf{k}. \quad (7.22)$$

Note that the way the signs alternate follows a simple pattern: if the sum of the row number and the column number is *even* the sign is positive and if *odd* the sign is negative.

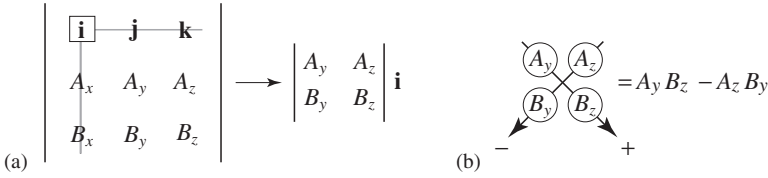


**Figure 7.8** Cofactors and determinants.

Expanding these three separate  $2 \times 2$  determinants also follows an easily remembered pattern: form the product of the upper-left and lower-right elements and subtract the product of the upper-right and lower-left elements (Fig. 7.8b). Applying this rule we then obtain

$$\mathbf{C} = \mathbf{A} \times \mathbf{B} = (A_y B_z - A_z B_y)\mathbf{i} - (A_x B_z - A_z B_x)\mathbf{j} + (A_x B_y - A_y B_x)\mathbf{k}. \quad (7.23)$$

Thus

$$C_x = A_y B_z - A_z B_y, \quad C_y = A_z B_x - A_x B_z, \quad C_z = A_x B_y - A_y B_x. \quad (7.24)$$

These expressions apply fully to any set of coordinate axes. As is often the case a special set of axes brings out some important aspects simply and clearly. Thus it is convenient to choose axes so that the plane of the two vectors  $\mathbf{A}$  and  $\mathbf{B}$  coincides with the  $xy$  coordinate plane. We can then see that the cross product has an important geometrical interpretation: in Fig. 7.9a the magnitude of vector  $\mathbf{C}$  represents the area of the *parallelogram* with sides parallel to  $\mathbf{A}$  and  $\mathbf{B}$ , that is

$$C = Ah = AB \sin \phi.$$

This is identical with the definition of Eq. 7.21. Thus the vector  $\mathbf{C}$  represents the orientation of the plane of the parallelogram and its magnitude  $C$  represents its area.

It is also of some interest to express this area in terms of the components of the vectors  $\mathbf{A}$  and  $\mathbf{B}$ . Dividing the parallelogram into two parts by a diagonal gives two congruent isosceles triangles which have identical areas (Fig. 7.9b). The area of these identical triangles is found from the sum of a right triangle (Fig. 7.9c) and a trapezoid (Fig. 7.9e) less the area of a second right triangle (Fig. 7.9d). From these three figures:

1. Area of the first sub-triangle is equal to half the base times the height  $+\frac{1}{2}(B_x B_y)$  (Fig. 7.9c).
2. Area of the trapezoid is equal to the base times the mean height  $+\frac{1}{2}(A_x - B_x)(A_y + B_y)$  (Fig. 7.9e).
3. Area of the second sub-triangle is  $-\frac{1}{2}(A_x A_y)$  (Fig. 7.9d).



After summing these three expressions, multiplying by 2, expanding and collecting terms, the total area of the parallelogram is then given by

$$B_x B_y + (A_x - B_x)(A_y + B_y) - A_x A_y = A_x B_y - A_y B_x, \tag{7.25}$$

and this is just the determinant for  $C_z$  given in Eqs. 7.24.

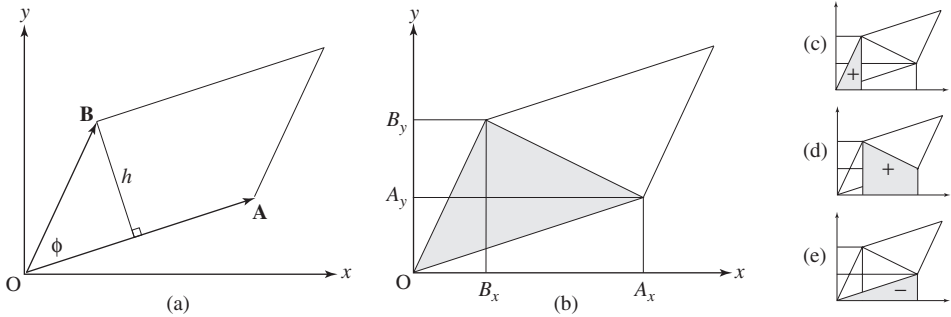


**Figure 7.9** Area of the parallelogram from  $\mathbf{A} \times \mathbf{B}$ .

Several important problems are easily solved using the cross product. The attitude of a plane, as represented by its pole vector  $\mathbf{P}$ , can be obtained directly from two apparent dip vectors  $\mathbf{A}_1$  and  $\mathbf{A}_2$ . This is written as

$$\mathbf{P} = \mathbf{A}_1 \times \mathbf{A}_2. \tag{7.26}$$

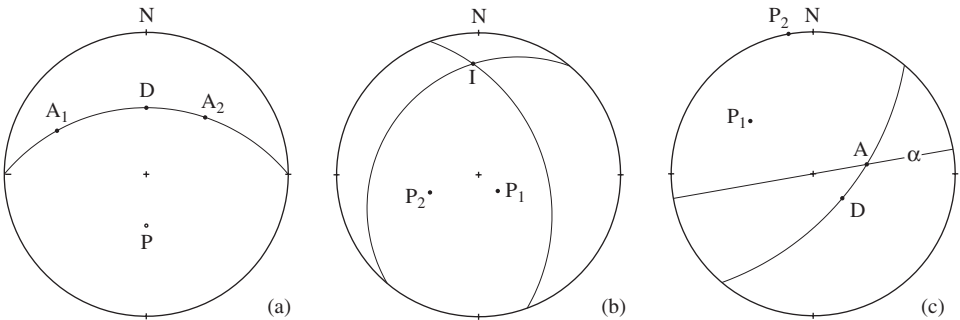


**Figure 7.10** Cross product: (a) pole of a plane  $\mathbf{P}$ ; (b) line of intersection  $\mathbf{I}$ ; (c) apparent dip  $\alpha$ .

**Problem**

- From apparent dip vectors  $\mathbf{A}_1(20/286)$  and  $\mathbf{A}_2(30/036)$  determine the attitude of the plane (Fig. 7.10a).

**Solution**

1. From the plunge and trend of each apparent dip vector, the two sets of direction cosines are

$$\mathbf{A}_1(0.305\ 93, -0.888\ 50, 0.342\ 02) \quad \text{and} \quad \mathbf{A}_2(0.700\ 63, 0.509\ 04, 0.500\ 00).$$

2. Perform the multiplication and then the normalized components of the resulting pole vector are  $\mathbf{P}(-0.618\ 35, -0.086\ 66, 0.778\ 24)$ .

**Answer**

- The plunge and trend of the pole is  $\mathbf{P}(50/170)$ ; the attitude of the dip vector is therefore  $\mathbf{D}(40/350)$ .

In these types of problems it is convenient to choose the order, as we have here, so that the product vector points downward. If the reverse order is taken it will be immediately signaled by  $P_z < 0$  or  $n < 0$ . This upward-pointing vector can be converted to the equivalent downward-pointing one by changing the signs of all three direction cosines or by changing the sign of the plunge and adding  $180^\circ$  to the trend.

The same procedure can be used to determine the orientation of the line of intersection of two planes. The intersection vector is given by

$$\mathbf{I} = \mathbf{P}_1 \times \mathbf{P}_2. \quad (7.27)$$

**Problem**

- From two pole vectors  $\mathbf{P}_1(70/146)$  and  $\mathbf{P}_2(50/262)$  determine the line of intersection of the two planes (Fig. 7.10b).

**Solution**

1. The components are  $\mathbf{P}_1(-0.262\ 00, 0.219\ 85, 0.939\ 69)$  and  $\mathbf{P}_2(-0.089\ 46, -0.636\ 53, 0.766\ 04)$ .
2. The normalized components of the intersection vector are  $\mathbf{I}(0.961\ 22, -0.146\ 26, 0.233\ 79)$ .

**Answer**

- The attitude of the line of intersection is  $\mathbf{I}(14/009)$ .

The cross product can also be used to find the apparent dip in a specified direction. The line of apparent dip is the intersection of the inclined plane and the vertical plane whose trend is in the apparent dip direction. From the poles of these two planes

$$\mathbf{A} = \mathbf{P}_1 \times \mathbf{P}_2, \quad (7.28)$$

where one of the poles is that of a vertical plane which contains the required direction.

**Problem**

- Find the apparent dip  $\mathbf{A}$  in the direction 080 from the dip vector  $\mathbf{D}(60/130)$  (Fig. 7.10c).

**Solution**

1. The pole of the inclined plane is  $\mathbf{P}_1(30/310)$ , and the pole of the vertical plane containing  $\mathbf{A}$  is  $\mathbf{P}_2(00/350)$ . The two sets of direction cosines are then

$$\mathbf{P}_1(0.556\ 67, -0.663\ 41, 0.500\ 00) \quad \text{and} \quad \mathbf{P}_2(0.984\ 81, -0.173\ 65, 0.000\ 00).$$

2. From the cross product, after normalization, we have  $\mathbf{A}(0.116\ 04, 0.658\ 07, 0.743\ 96)$ .

**Answer**

- The plunge and trend is  $\mathbf{A}(48/080)$  and the plunge angle is the required apparent dip.

**7.4 Circular distributions**

The statistical treatment of orientation data relies heavily on vector methods. We first treat the two-dimensional case. Cheeney (1983, p. 22–26, 93f), Middleton (2000, p. 161–167) and Borradaile (2003, Chapter 9) give good introductions to the subject and the book by Fisher (1993) contains a comprehensive treatment. The use of a spreadsheet is a convenient way to manipulate such data (Tolson & Correa-Mora, 1996).

By way of introduction, we illustrate several problems associated with determining the mean direction of measured strike lines. To do this we use a small invented data set (see Table 7.1).

1. The northeast trending strike lines (Column A of Table 7.1) are represented by points on the circumference of a unit circle (Fig. 7.11a). A straightforward calculation of the arithmetic mean gives the correct value of 025, that is, N 25 E (shown by the filled circle).
2. Because strike lines are axes, the trend of either end is an equally valid statement of orientation. Column B of Table 7.1 gives the same data with one trend reversed (Fig. 7.11b). Now the calculated mean of 061 is not correct.
3. The five strike lines are rotated 30° anticlockwise (30° subtracted from each strike direction (Column C of Table 7.1), and plotted as vectors (Fig. 7.11c). Again, the arithmetic mean of –005, that is N 5 W, is correct.
4. Trends are not commonly given by negative angles; azimuths are more appropriate (Column D of Table 7.1). The mean of these gives the wildly erroneous trend of 221.

The representing of horizontal vectors by points on the circumference of a circle of unit radius may display a wide variety of forms, including uniform, unimodal, bimodal and multimodal patterns. Here we confine our treatment to the simple but important case

Table 7.1 *The mean direction of measured strike lines*

	A	B	C	D
1	005	005	-025	335
2	015	015	-015	354
3	025	205	-005	355
4	035	035	005	005
5	045	045	015	015
Mean	025	061	-005	211

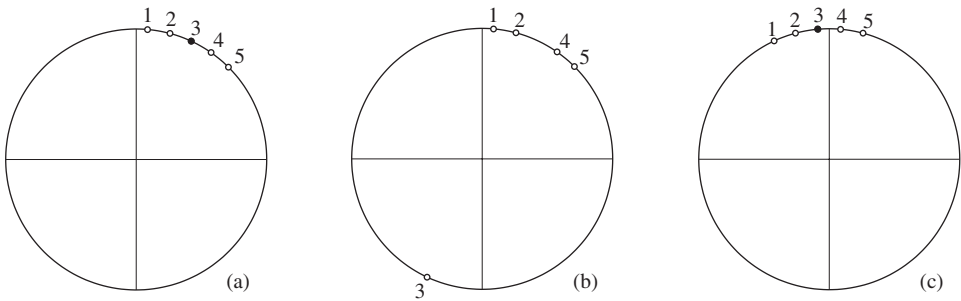


Figure 7.11 Strike Lines: (a) lines as vectors; (b) lines as axes; (c) lines rotated anticlockwise 30°.

of a single cluster, that is with a *unimodal* distribution, and the determination of its mean direction.

As we have seen the arithmetic mean of trend angles expressed as azimuths generally gives erroneous results. The reason is simple: consider two vectors with trends of 350 and 010. Clearly, the true mean direction is due north, but their arithmetic mean is 180° or due south.

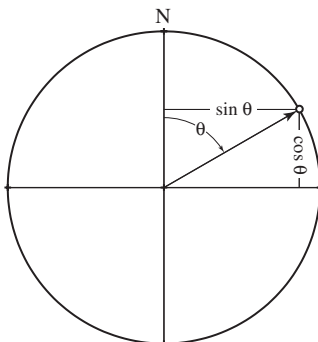


Figure 7.12 Components of trend vectors.

The correct way to combine a collection of  $N$  unit vectors is by vector addition, and we do this by summing their components (Fig. 7.12).

$$C = \sum_{i=1}^N \cos \theta_i \quad \text{and} \quad S = \sum_{i=1}^N \sin \theta_i, \tag{7.29}$$

where the  $\theta_i$  ( $i = 1, 2, \dots, N$ ) are the orientation angles of the individual vectors. The magnitude of the *resultant vector*  $\mathbf{R}$  is given by

$$R = \sqrt{C^2 + S^2}, \quad (0 \leq R \leq N). \tag{7.30}$$

Alternatively, the mean resultant length  $\bar{R}$  is

$$\bar{R} = R/N, \quad (0 \leq \bar{R} \leq 1). \tag{7.31}$$

$\bar{R} = 1$  implies that all points are coincident and  $\bar{R} = 0$  implies a uniform distribution, but only if the data make up a single group. The orientation of  $\mathbf{R}$ , which is the *mean direction*, is given by

$$\bar{\theta} = \arctan S/C. \tag{7.32}$$

As we have also seen, axial data present another problem: because the ends of axes are interchangeable there is an inherent ambiguity. The solution is to convert the axes to true vectors by doubling the orientation angles (Krumbein, 1939; Pincus, 1956), which are now given by  $2\theta \pmod{360}$  (Fisher, 1993, p. 37).<sup>5</sup>

Table 7.2 Calculation of the mean of the trends of two-dimensional vectors

$i$	$\theta$	$\sin \theta_i$	$\cos \theta_i$
1	245	-0.906 31	-0.422 62
2	254	-0.961 26	-0.275 64
3	272	-0.999 39	0.034 90
4	277	-0.992 55	0.121 87
5	281	-0.981 63	0.190 81
6	294	-0.913 55	0.406 74
7	301	-0.857 17	0.515 04
8	315	-0.707 11	0.707 11
9	329	-0.515 04	0.857 17
10	334	-0.438 37	0.898 79
Sums		-8.272 36	3.034 17

<sup>5</sup>In modular arithmetic the expression  $m \pmod{n}$  gives the remainder after integer division of  $m$  by the modulus  $n$ ; for example,  $466 \pmod{360} = 106$ . This is sometimes called *clock arithmetic* by analogy with arithmetic on a clock face which has a modulus of  $n = 12$ .

### Problem

- From 10 measured azimuths of the long axes of beach pebbles, determine the mean trend (Table 7.2).

### Method

1. A plot using azimuths in the range  $0\text{--}360^\circ$  shows that the trend angles lie in two distinct groups: seven in the NE quadrant and three in the SW quadrant (Fig. 7.13a).
2. By doubling the orientation angles and representing each resulting vector as a point on the circumference of a unit circle they now form a single group with a range  $0\text{--}180^\circ$  (Fig. 7.13b).
3. From each transformed trend angle  $2\theta_i$ , compute the values of  $\cos 2\theta$  and  $\sin 2\theta$  for each vector. The sums are then  $C = 8.25738$  and  $S = 3.29817$ .
4. From Eq. 7.29 we then have components of the resultant vector  $\mathbf{R}(0.26515, 0.81756)$ . Then from Eqs. 7.30, 7.31,  $\bar{R} = 0.86$ , which also indicates a fairly strong concentration.
5. With Eq. 7.32 we have  $2\bar{\theta} = 72.03113^\circ$  or  $\bar{\theta} = 36^\circ$ , and this is the mean orientation of the axes.

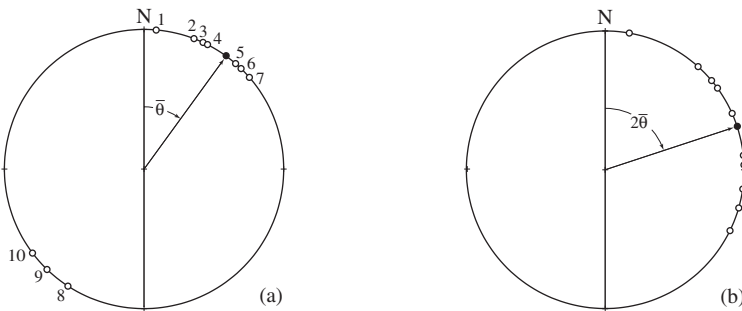


**Figure 7.13** Circular distributions of axes: (a) plot; (b) conversion to vectors.

The size of the samples in this illustrative problem is small; even a single additional point might be expected to change the mean direction, possibly significantly. In practice, more measurements are needed for greater confidence.

If the analysis of problems such as these is to be extended to other statistical attributes and tests we need to take into account the entire population from which the sample was taken and in particular the way the data points representing this population are distributed on the circle. The *circular normal* or *von Mises distribution*<sup>6</sup> is the most useful way of treating points which tend to cluster symmetrically about a single point. With this, a number of useful properties of such unimodal distributions can be found, but these

<sup>6</sup>This distribution is named for its formulator, the Austrian mathematician Richard von Mises [1883–1953], younger brother of the respected economist Ludwig von Mises.

matters would take us well beyond the level of this book. Cheeney (1983, p. 98–106) gives an easily followed discussion.

## 7.5 Spherical distributions

The extension to three dimensions is straightforward. Cheeney (1983, p. 107f), Middleton (2000, p. 167–180) and Borradaile (2003, Chapter 10) give good introductions and the books by Mardia (1972), Watson (1983), Fisher, *et al.* (1987) and Mardia and Jupp (2000) contain advanced treatments.

Three-dimensional orientation data are represented by points on a unit sphere. As in the two-dimensional case, such a collection of points can display uniform, unimodal, bimodal and girdle patterns (Mardia, 1972, p. 222; Mardia & Jupp, 2000, p. 161). We return to some related matters in Chapter 18.

As in the two-dimensional case, we treat a simple but important problem involving the distribution of points in a single cluster to illustrate the basic approach. If the cluster is approximately equidimensional it is said to be *unimodal* and the mean direction is given by the *resultant vector*  $\mathbf{R}$  of the  $N$  unit vectors. Its components are

$$R_x = \sum_{i=1}^N l_i, \quad R_y = \sum_{i=1}^N m_i, \quad R_z = \sum_{i=1}^N n_i, \quad (7.33)$$

where the  $(l_i, m_i, n_i)$ ,  $i = 1, 2, \dots, N$  are the direction cosines of the individual vectors. The *resultant length* or magnitude of this vector is

$$R = \sqrt{R_x^2 + R_y^2 + R_z^2}, \quad (7.34)$$

and its direction cosines are

$$\bar{l} = R_x/R, \quad \bar{m} = R_y/R, \quad \bar{n} = R_z/R. \quad (7.35)$$

$R$  is also a measure of the concentration of the points about the mean. It will be nearly as large as  $N$  if the points are tightly clustered and will be smaller if they are dispersed. If data sets with different numbers of measurements are to be compared, the *mean resultant length*  $\bar{R}$  is a more useful measure. This is defined as

$$\bar{R} = R/N, \quad \text{where } 0 \leq R \leq N \text{ and } 0 \leq \bar{R} \leq 1. \quad (7.36)$$

### Problem

- From 10 measured poles of bedding, determine the mean attitude (Table 7.4.

### Method

1. Convert the plunge  $p$  and trend  $t$  of each pole to direction cosines  $(l, m, n)$  and calculate the totals. From Eq. 7.33 we then have vector  $\mathbf{R}(-6.388\ 09, -3.673\ 84, 6.249\ 20)$ ,
2. From Eq. 7.34,  $R = 9.662\ 16$  and from Eqs. 7.35 the direction cosines of  $\mathbf{R}$  are then

$$\bar{l} = -0.661\ 15, \quad \bar{m} = -0.380\ 23, \quad \bar{n} = 0.646\ 77.$$

3. The attitude of the mean is  $\mathbf{R}(40/210)$  (shown as an open diamond in Fig. 7.14).
4. With  $R = 9.7$  and  $\bar{R} = 0.97$  the points are tightly clustered about the mean, as can be seen.

Table 7.3 Calculation of the mean of three-dimensional vectors

$i$	$p$	$t$	$l_i$	$m_i$	$n_i$
1	32	206	-0.762 22	-0.371 76	0.529 92
2	30	220	-0.663 41	-0.556 67	0.500 00
3	46	204	-0.634 60	-0.282 54	0.719 34
4	40	198	-0.728 55	-0.236 72	0.642 79
5	20	200	-0.883 02	-0.321 39	0.342 02
6	32	188	-0.839 79	-0.118 03	0.529 92
7	54	192	-0.574 94	-0.122 21	0.809 02
8	56	228	-0.374 17	-0.415 56	0.829 04
9	36	236	-0.452 40	-0.670 71	0.587 79
10	44	218	-0.566 85	-0.442 87	0.694 66
Sums			-6.388 09	-3.673 84	6.249 20

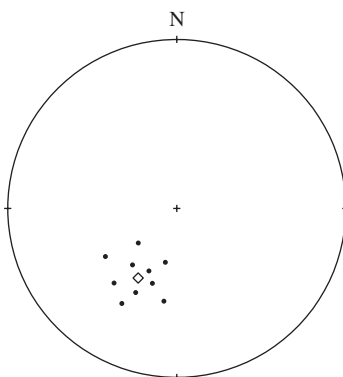


Figure 7.14 Unimodal distribution of poles and its mean.

As in the previous example problem of a circular distribution, in practice a larger number of measurements will increase confidence.



It should also be noted that the mean direction of any collection of points on the sphere may be calculated with this method, but in many situations this direction will have little or no geometrical meaning. For example, if the data are approximately uniformly distributed on the sphere, the mean vector may have almost any orientation.

If the analysis of this problem is to be extended to other statistical attributes, such as confidence limits, we need to take into account the entire population from which the sample was taken and in particular on the way the data points representing this population are distributed on the sphere. Because poles of bedding can be considered to be true vectors, the *spherical normal* or *Fisher distribution*<sup>7</sup> is the most useful way of treating points which tend to cluster symmetrically about a single point. With this, a number of useful properties of such unimodal distributions can be found, but to pursue these matters would take us well beyond the level of this book. Cheeney (1983, p. 112) and Middleton (2000, p. 167–180) give easily followed discussions.<sup>8</sup>

## 7.6 Rotations

The rotations performed graphically on the stereonet can also be accomplished analytically. To do this we need expressions which relate the initial vector  $\mathbf{r}(x, y, z)$  and final vector  $\mathbf{r}'(x', y', z')$  in terms of an axis and angle of rotation.

Just as rotations on the stereonet may be performed simply and easily about horizontal and vertical axes, so too is it easy to describe rotations about the three axes of our coordinate system. With these descriptions we may then develop procedures for the more general cases.

Before starting we need a sign convention for the sense of a rotation about an axis and we use the *right-hand rule* – when the thumb of the right hand points in the positive direction of an axis, the fingers indicate the sense of a positive rotation.

Expressions for the rotation of a position vector  $\mathbf{r}$  about the  $+x$  axis are obtained from a view of the vertical  $yz$  plane looking north, that is, in the direction of  $+x$  (Fig. 7.15a). Rotating about this axis, the  $x$  component remains unchanged, that is,  $x' = x$ , but the  $y$  and  $z$  components do change. In this plane, the orientation of  $\mathbf{r}$  is given by the angle  $\theta$  measured from  $+y$  and the orientation of  $\mathbf{r}'$  is given by the angle  $\theta + \omega_x$  also measured from  $+y$ . Note that the length of the vector is unchanged by rotation, that is,  $r = r'$ . Then

$$\begin{aligned} \cos \theta &= y/r & \text{and} & & \cos(\theta + \omega_x) &= y'/r, \\ \sin \theta &= z/r & \text{and} & & \sin(\theta + \omega_x) &= z'/r. \end{aligned}$$

<sup>7</sup>This distribution is named for its originator, the celebrated English statistician Ronald A. Fisher [1890–1962]. He published the description of this distribution in response to the needs of paleomagnetic studies which were then in their infancy, and it has been used extensively for this purpose ever since (see Fisher, 1953).

<sup>8</sup>Smith (1994) describes an interesting way of using the sphere as a tool to teach some additional and important statistical concepts to geology students.

Substituting these into the identities for the cosine and sine of the sum of two angles

$$\cos(\theta + \omega) = \cos \theta \cos \omega - \sin \theta \sin \omega \quad \text{and} \quad \sin(\theta + \omega) = \sin \theta \cos \omega + \cos \theta \sin \omega \quad (7.37)$$

and multiplying through by  $r$  yields expressions for  $y'$  and  $z'$ . These, plus the equality  $x = x'$ , are

$$\begin{aligned} x' &= x, \\ y' &= y \cos \omega_x - z \sin \omega_x, \\ z' &= y \sin \omega_x + z \cos \omega_x. \end{aligned}$$

With these equations we may obtain the components of the rotated vector from initial components  $x, y, z$  and  $\omega_x$  by simple substitution. We may also represent the rotation represented by these three equations with the matrix equation

$$\begin{bmatrix} x' \\ y' \\ z' \end{bmatrix} = \begin{bmatrix} 1 & 0 & 0 \\ 0 & \cos \omega_x & -\sin \omega_x \\ 0 & \sin \omega_x & \cos \omega_x \end{bmatrix} \begin{bmatrix} x \\ y \\ z \end{bmatrix} \quad (7.38)$$

where the vectors  $\mathbf{r}(x, y, z)$  and  $\mathbf{r}'(x', y', z')$  are represented by column matrices and the rotation by the  $3 \times 3$  square matrix. An important advantage of this type representation is that we can now think of the square matrix as a vector processor which changes one vector into another, and this focuses our attention on the entities rather than on their components. Such representations and their manipulation by matrix algebra have compelling advantages for many closely related problems in structural geology. The book by Ferguson (1994) gives a good introductory treatment for geology students. We illustrate a few simple applications here and in several later chapters.

The three algebraic equations can be obtained directly from the matrix equation of Eq. 7.38. To do this, we think of each row of the square matrix as a vector. Then *row times column multiplication* corresponds to finding the dot product of each row and the column vector (see Eq. 7.15). The basic method follows an easily remembered pattern. Consider the first row of the square matrix and ignore the other two. We then have

$$\begin{bmatrix} a & b & c \\ \cdot & \cdot & \cdot \\ \cdot & \cdot & \cdot \end{bmatrix} \begin{bmatrix} u \\ v \\ w \end{bmatrix} = \begin{bmatrix} au + bv + cw \\ \cdot \\ \cdot \end{bmatrix}. \quad (7.39a)$$

The second element of the resulting column vector is obtained in the same way by forming the dot product using the second row of the square matrix

$$\begin{bmatrix} \cdot & \cdot & \cdot \\ d & e & f \\ \cdot & \cdot & \cdot \end{bmatrix} \begin{bmatrix} u \\ v \\ w \end{bmatrix} = \begin{bmatrix} \cdot \\ du + ev + fw \\ \cdot \end{bmatrix}, \quad (7.39b)$$

and finally, the third element of the resulting column vector is the dot product using the third row

$$\begin{bmatrix} \cdot & \cdot & \cdot \\ \cdot & \cdot & \cdot \\ g & h & i \end{bmatrix} \begin{bmatrix} u \\ v \\ w \end{bmatrix} = \begin{bmatrix} \cdot \\ \cdot \\ gu + hv + iw \end{bmatrix}. \tag{7.39c}$$

With a little practice the pattern of making each of these combinations becomes automatic. In forming the three dot products it helps to keep track of each product by stepping along each of the rows with the left index finger while stepping down the column with the right index finger.

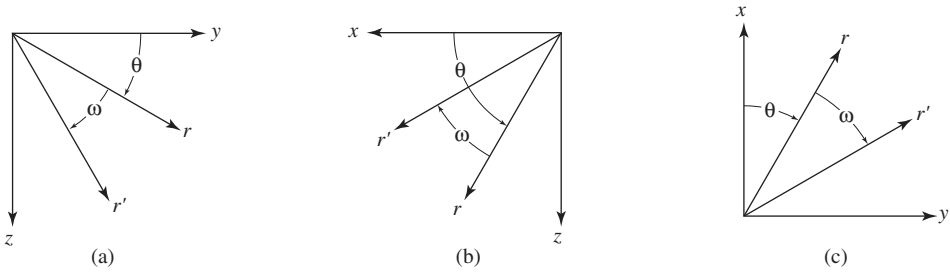


**Figure 7.15** Positive rotations: (a) about +  $x$ ; (b) about +  $y$ ; (c) about +  $z$ .

For a rotation about the  $y$  axis we obtain expressions for the changes in the  $x$  and  $z$  components on the vertical  $xz$  plane looking east, that is, in the  $+y$  direction (Fig. 7.15b). In this plane the orientation of  $\mathbf{r}$  is given by the angle  $\theta$  it makes with the  $+x$  axis and the orientation of  $\mathbf{r}'$  by the angle  $\omega_y$  it makes with  $\mathbf{r}$ . Then

$$\begin{aligned} \cos \theta &= x/r & \text{and} & & \cos(\theta - \omega_z) &= x'/r, \\ \sin \theta &= z/r & \text{and} & & \sin(\theta - \omega_z) &= z'/r. \end{aligned}$$

Using these expressions in the identities for the cosine and sine of the difference of two angles,

$$\cos(\theta - \omega) = \cos \theta \cos \omega + \sin \theta \sin \omega \quad \text{and} \quad \sin(\theta - \omega) = \sin \theta \cos \omega - \cos \theta \sin \omega, \tag{7.40}$$

yields the three equations

$$\begin{aligned} x' &= x \cos \omega_y + z \sin \omega_y, \\ y' &= y, \\ z' &= -x \sin \omega_y + z \cos \omega_y. \end{aligned}$$

In matrix form this rotation is given by

$$\begin{bmatrix} x' \\ y' \\ z' \end{bmatrix} = \begin{bmatrix} \cos \omega_y & 0 & \sin \omega_y \\ 0 & 1 & 0 \\ -\sin \omega_y & 0 & \cos \omega_y \end{bmatrix} \begin{bmatrix} x \\ y \\ z \end{bmatrix}. \quad (7.41)$$

Finally, the rotation about the  $z$  axis is described on the horizontal  $xy$  plane looking down (Fig. 7.15c). In this plane the orientation of  $\mathbf{r}$  is given by the angle  $\theta$  it makes with the  $+x$  axis and the orientation of  $\mathbf{r}'$  by the angle  $\omega_z$  it makes with  $\mathbf{r}$ . Then

$$\begin{aligned} \cos \theta &= x/r & \text{and} & \quad \cos(\theta + \omega_z) = x'/r, \\ \sin \theta &= y/r & \text{and} & \quad \sin(\theta + \omega_z) = y'/r. \end{aligned}$$

From the identities of Eqs. 7.37 we have the three equations

$$\begin{aligned} x' &= x \cos \omega_z - y \sin \omega_z, \\ y' &= x \sin \omega_z + y \cos \omega_z, \\ z' &= z, \end{aligned}$$

or the single matrix equation

$$\begin{bmatrix} x' \\ y' \\ z' \end{bmatrix} = \begin{bmatrix} \cos \omega_z & -\sin \omega_z & 0 \\ \sin \omega_z & \cos \omega_z & 0 \\ 0 & 0 & 1 \end{bmatrix} \begin{bmatrix} x \\ y \\ z \end{bmatrix}. \quad (7.42)$$

These results are fully general in the sense that they apply to the rotation of vectors of any magnitude. In all our examples, however, we treat only unit vectors as represented by direction cosines.

We represent each of the three square rotational matrices of Eqs. 7.38, 7.41 and 7.42 by the symbols  $\mathbf{R}_x(\omega_x)$ ,  $\mathbf{R}_y(\omega_y)$  and  $\mathbf{R}_z(\omega_z)$ .<sup>9</sup> Each of these rotations represents a corresponding graphical procedure used to rotate about vertical and horizontal axes on the stereonet. As we have indicated, each of these may be treated either as a set of three equations which can be manipulated by simple substitution or as a matrix multiplication.

We may also combine several separate rotation matrices into a single rotation matrix  $\mathbf{R}$ . For example, the sequence of rotations, first about  $+z$  and then about  $+x$ , may be written in this notation as

$$\mathbf{R} = \mathbf{R}_x(\omega_x)\mathbf{R}_z(\omega_z),$$

<sup>9</sup>The symbol  $\mathbf{R}$  here should not be confused with the resultant vector of the previous sections.

where  $\mathbf{R}_z$  is applied first and then  $\mathbf{R}_x$ , that is, the order is taken from *right to left*. Adhering to this order is important because finite rotations are not commutative.

The product matrix  $\mathbf{R}$  represents the single equivalent rotation. With the square matrices of Eqs. 7.38 and 7.42, representing rotations about the  $x$  and  $z$  axes, we then have

$$\begin{aligned} & \begin{bmatrix} 1 & 0 & 0 \\ 0 & \cos \omega_x & -\sin \omega_x \\ 0 & \sin \omega_x & \cos \omega_x \end{bmatrix} \begin{bmatrix} \cos \omega_z & -\sin \omega_z & 0 \\ \sin \omega_z & \cos \omega_z & 0 \\ 0 & 0 & 1 \end{bmatrix} \\ &= \begin{bmatrix} \cos \omega_z & -\sin \omega_z & 0 \\ \cos \omega_x \sin \omega_z & \cos \omega_x \cos \omega_z & -\sin \omega_x \\ \sin \omega_x \sin \omega_z & \sin \omega_x \cos \omega_z & \cos \omega_x \end{bmatrix}. \end{aligned}$$

The elements of this resulting  $3 \times 3$  product matrix are obtained by an extension of the pattern of Eqs. 7.39 again using *row times column multiplication*. To see this more clearly focus on the first row of the left-hand matrix and the first column of the right-hand matrix, disregarding all the others. We then see only

$$\begin{bmatrix} a & b & c \\ \cdot & \cdot & \cdot \\ \cdot & \cdot & \cdot \end{bmatrix} \begin{bmatrix} p & \cdot & \cdot \\ q & \cdot & \cdot \\ r & \cdot & \cdot \end{bmatrix} = \begin{bmatrix} ap + bq + cr & \cdot & \cdot \\ \cdot & \cdot & \cdot \\ \cdot & \cdot & \cdot \end{bmatrix}.$$

The resulting element in the product matrix is the *dot product* of this row and this column. Note that this element is located in the position common to the row and column, that is, in the first row and first column.

All the elements of the product matrix are obtained in this same way: put your left index finger against any row of the square matrix on the left and your right index finger against any column of the square matrix on the right; the three pairs of elements so identified appear in a single element of the product matrix as the sum of the products of corresponding elements. The position of each product element is the one common to the selected row and column.

### Problem

- Rotate line  $\mathbf{L}(00/320)$ , first with  $\mathbf{R}_z(-60^\circ)$  then with  $\mathbf{R}_x(-40^\circ)$  (see Fig. 6.5b).

### Solution

1. First, convert the plunge and trend of  $\mathbf{L}$  into direction cosines expressed as a column matrix.
2. Then substitute the rotational angles into the single product matrix of Eq. 7.43.
3. The full equation is then

$$\begin{bmatrix} x' \\ y' \\ z' \end{bmatrix} = \begin{bmatrix} 0.76604 & 0.64279 & 0.00000 \\ -0.32139 & 0.38302 & 0.86603 \\ 0.55667 & -0.66341 & 0.50000 \end{bmatrix} \begin{bmatrix} 0.76604 \\ -0.64279 \\ 0.00000 \end{bmatrix} = \begin{bmatrix} -0.17365 \\ -0.49240 \\ 0.85287 \end{bmatrix}.$$

**Answer**

- After the combined rotations, the attitude is  $L'(59/289)$  and this is the same result obtained graphically.

This same procedure can be extended to any number of rotations. By hand such multiple rotations require a tedious series of computations but the sequence can be easily programmed.

**7.7 Rotational problems**

With these matrix representations of rotations about the coordinate axes we can solve all the rotational problems of the previous chapter. As we have just seen any sequence of rotations can be combined by matrix multiplication into an equivalent single rotation matrix that produces the same result.

A simple but important geological problem is the restoration of the pre-tilt orientation of a line in an inclined plane by the conventional tilt correction. Following the procedure used in Fig. 6.8, we specify the attitude of the plane by the plunge and trend of the dip vector  $\mathbf{D}$ . To form the rotation matrix which restores the plane to horizontality by rotation about the strike direction then requires three steps.

**Steps**

1. Rotate vector  $\mathbf{D}$  about  $+z$  into the vertical  $xz$  plane by  $\mathbf{R}_z(-t)$ .
2. Rotate  $\mathbf{D}$  about  $+y$  to horizontal by  $\mathbf{R}_y(\delta)$ .
3. Return  $\mathbf{D}$  its original trend by  $\mathbf{R}_z(+t)$ .

This sequence can be represented by the equation

$$\mathbf{R}(\omega) = \mathbf{R}_z(+t) \mathbf{R}_y(\delta) \mathbf{R}_z(-t), \quad (7.43)$$

where again the order is taken from right to left. If the bed is overturned then the rotation about  $y$  is given by  $\mathbf{R}_y(\delta - 180^\circ)$ .

**Problem**

- A plane whose attitude is given by  $\mathbf{D}(60/230)$  contains line  $\mathbf{L}$  with  $t = 297^\circ$ . What was the pre-tilt trend of the line? (Fig. 7.16a; see also Fig. 6.8a).

**Solution**

1. The single equivalent rotation is found from the sequence of rotations

$$\mathbf{R} = \mathbf{R}_z(-230^\circ) \mathbf{R}_y(+60^\circ) \mathbf{R}_z(+230^\circ).$$

2. Using Eq. 1.8, the angle the trend of  $\mathbf{L}$  makes with the dip direction is  $\phi = 297 - 230 = 67^\circ$ . Then the plunge of this line is  $\alpha = 34.08881^\circ$ .

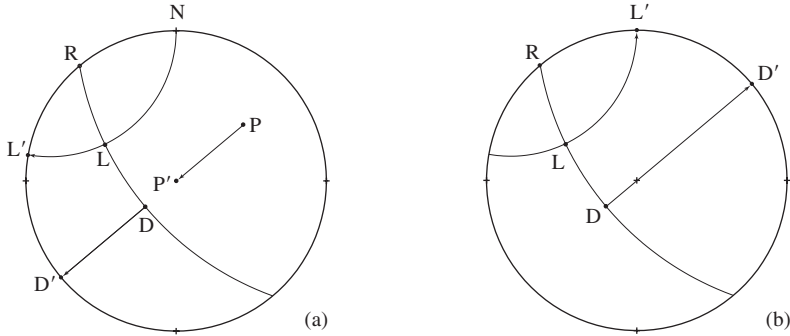


**Figure 7.16** Conventional tilt correction: (a) upright; (b) overturned.

3. Its plunge and trend give  $\mathbf{L}(0.375\ 98, -0.737\ 90, 0.560\ 48)$ .
4. The full rotation matrix equation is then

$$\begin{bmatrix} x' \\ y' \\ z' \end{bmatrix} = \begin{bmatrix} 0.793\ 41 & -0.246\ 20 & -0.556\ 67 \\ -0.246\ 20 & 0.706\ 59 & -0.663\ 41 \\ 0.556\ 67 & 0.663\ 41 & 0.500\ 00 \end{bmatrix} \begin{bmatrix} 0.375\ 98 \\ -0.737\ 90 \\ 0.560\ 48 \end{bmatrix} = \begin{bmatrix} 0.515\ 93 \\ -0.856\ 63 \\ 0.000\ 00 \end{bmatrix}.$$

**Answer**

- The estimated pre-tilt attitude of the line is  $\mathbf{L}'(00/280)$ .

**Problem**

- If the beds in the previous problem are overturned what was the pre-tilt trend of the line? (Fig. 7.16b; see also Fig. 6.8b).

**Solution**

1. The single equivalent rotation is found from the sequence

$$\mathbf{R} = \mathbf{R}_z(-230^\circ) \mathbf{R}_y(-120^\circ) \mathbf{R}_z(+230^\circ).$$

2. As before, using the given trend and Eq. 1.8, determine the plunge of the line in the plane and then its direction cosines.
3. In matrix form the set of equations representing the single rotation is then

$$\begin{bmatrix} x' \\ y' \\ z' \end{bmatrix} = \begin{bmatrix} 0.380\ 24 & -0.738\ 61 & 0.556\ 67 \\ -0.738\ 61 & 0.119\ 76 & 0.663\ 41 \\ -0.556\ 67 & -0.663\ 41 & -0.500\ 00 \end{bmatrix} \begin{bmatrix} 0.375\ 98 \\ -0.737\ 90 \\ 0.560\ 48 \end{bmatrix} = \begin{bmatrix} 0.999\ 98 \\ 0.005\ 75 \\ 0.000\ 00 \end{bmatrix}.$$

**Answer**

- The estimated pre-tilt attitude was  $L'(00/000)$ , that is, horizontal and trending due north.

In both these solutions the plunge of the line in the inclined plane was calculated from its trend using the apparent dip formula. If a measured plunge angle is used or its value is read from a plot it may not lie exactly in the plane and this may result in the corrected attitude departing slightly from horizontal. Even if the plunge is accurately calculated, a tiny round-off error may produce the same result. If, because of these errors, the restored line ends up in the upper hemisphere and it is reversed into the lower hemisphere the trend will be  $180^\circ$  in error. In such cases, some care is required when interpreting the results.

The case of a rotation about an inclined axis requires a sequence of five coordinate rotations. There are several equivalent ways of ordering these and the one we choose is closely related to the procedure used graphically in the previous chapter.

**Steps**

1. Rotate axis  $R$  about the  $+z$  axis by angle  $-t$  to bring it into the vertical  $xz$  plane.
2. Rotate this  $R$  about the  $+y$  axis by angle  $(p - 90^\circ)$  to bring it into coincidence with the  $+z$  axis.
3. Rotate about the  $+z$  axis by the specified angle  $\omega$  to perform the required rotation.
4. Rotate  $R$  about the  $+y$  axis by angle  $(90^\circ - p)$  as the first step in returning it to its original orientation.
5. Finally, rotate  $R$  about the  $+z$  axis by angle  $+t$  to return it to its initial orientation.

We may also express this sequence of five rotations in short-hand as

$$\mathbf{R}(\omega) = \mathbf{R}_z(+t) \mathbf{R}_y(90^\circ - p) \mathbf{R}_z(\omega) \mathbf{R}_y(p - 90^\circ) \mathbf{R}_z(-t). \tag{7.44}$$

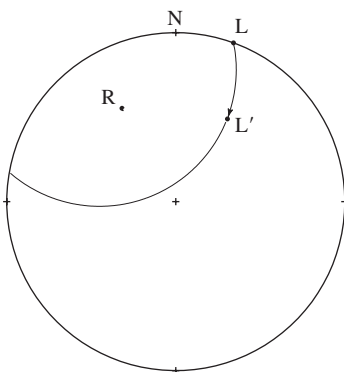


**Figure 7.17** Single rotation equivalent to a sequence of rotations.



**Problem**

- Rotate line  $L(00/020)$  about the inclined axis  $R(25/330)$  by  $\omega = +40^\circ$  (Fig. 7.17; see also Fig. 6.8).

**Solution**

1. The complete sequence of rotations is given by

$$\mathbf{R}(\omega) = \mathbf{R}_z(330^\circ) \mathbf{R}_y(65^\circ) \mathbf{R}_z(40^\circ) \mathbf{R}_y(-65^\circ) \mathbf{R}_z(-330^\circ). \quad (7.45)$$

2. Performing the multiplication of the five matrices, together with the direction cosines of the line, yields

$$\begin{bmatrix} x' \\ y' \\ z' \end{bmatrix} = \begin{bmatrix} 0.91017 & -0.35487 & -0.21368 \\ 0.18844 & 0.81409 & -0.54932 \\ 0.36889 & 0.45971 & 0.80783 \end{bmatrix} \begin{bmatrix} 0.93969 \\ 0.34202 \\ 0.00000 \end{bmatrix} = \begin{bmatrix} 0.73391 \\ 0.45551 \\ 0.50387 \end{bmatrix}.$$

**Answer**

- From these direction cosines, the plunge and trend of the line after rotation is  $L'(30/032)$ .

**7.8 Three-point problem**

The three-point problem may be solved analytically in several ways. Haneberg (1990) described a technique involving Lagrangian interpolation and De Paor (1991) used barycentric coordinates. Here we illustrate two additional, vector-related ways.

*Coordinate geometry*

The first method uses coordinate geometry to determine the components of the vector normal to the plane. Because elevations on land are almost always positive numbers it is convenient, and universal, to adopt the right-handed system of geographical coordinate axes with  $+x = \text{east}$ ,  $+y = \text{north}$  and  $+z = \text{up}$ . Note that in contrast to our previous coordinate system *positive* vertical angles are now measured upward and *positive* horizontal angles are measured anticlockwise from  $+x$ .

We need the equation of the plane passing through three non-collinear points  $P_1(x_1, y_1, z_1)$ ,  $P_2(x_2, y_2, z_2)$  and  $P_3(x_3, y_3, z_3)$ , and this requires the solution of the system of homogeneous equations (see Vacher, 2000)

$$\begin{aligned} Ax + By + Cz + D &= 0, \\ Ax_1 + By_1 + Cz_1 + D &= 0, \\ Ax_2 + By_2 + Cz_2 + D &= 0, \\ Ax_3 + By_3 + Cz_3 + D &= 0. \end{aligned}$$

The first of these is the general form of the equation of the plane. The other three express the conditions that the three points lie on this plane. We may also write these in the form of a matrix equation

$$\begin{bmatrix} x & y & z & 1 \\ x_1 & y_1 & z_1 & 1 \\ x_2 & y_2 & z_2 & 1 \\ x_3 & y_3 & z_3 & 1 \end{bmatrix} \begin{bmatrix} A \\ B \\ C \\ D \end{bmatrix} = \begin{bmatrix} 0 \\ 0 \\ 0 \\ 0 \end{bmatrix}.$$

This equation always has the trivial solution  $A = B = C = D = 0$ , but this case has no physical meaning. A non-trivial solution exists if and only if the determinant of the  $4 \times 4$  matrix is equal to zero

$$\begin{vmatrix} x & y & z & 1 \\ x_1 & y_1 & z_1 & 1 \\ x_2 & y_2 & z_2 & 1 \\ x_3 & y_3 & z_3 & 1 \end{vmatrix} = 0.$$

Expanding by the method of cofactors gives the required equation of the plane

$$\begin{vmatrix} y_1 & z_1 & 1 \\ y_2 & z_2 & 1 \\ y_3 & z_3 & 1 \end{vmatrix} x - \begin{vmatrix} x_1 & z_1 & 1 \\ x_2 & z_2 & 1 \\ x_3 & z_3 & 1 \end{vmatrix} y + \begin{vmatrix} x_1 & y_1 & 1 \\ x_2 & y_2 & 1 \\ x_3 & y_3 & 1 \end{vmatrix} z - \begin{vmatrix} x_1 & y_1 & z_1 \\ x_2 & y_2 & z_2 \\ x_3 & y_3 & z_3 \end{vmatrix} = 0.$$

There are two ways of expanding these  $3 \times 3$  determinants.

1. If there are all 1s in any column, as in the first three terms, the method of cofactors is particularly easy to apply.
2. In the more general case a simple extension of the method used for a  $2 \times 2$  determinant is perhaps the easiest approach. Copy the first two columns to the right. Then the three triple products from the upper left to lower right are positive (Fig. 7.18a) and the three triple products from upper right to lower left are negative (Fig. 7.18b).

Applying these yields

$$A = + \begin{vmatrix} y_1 & z_1 & 1 \\ y_2 & z_2 & 1 \\ y_3 & z_3 & 1 \end{vmatrix} = +[(y_2 z_3 - z_2 y_3) - (y_1 z_3 - z_1 y_3) + (y_1 z_2 - z_1 y_2)], \quad (7.46a)$$

$$B = - \begin{vmatrix} x_1 & z_1 & 1 \\ x_2 & z_2 & 1 \\ x_3 & z_3 & 1 \end{vmatrix} = -[(x_2 z_3 - z_2 x_3) - (x_1 z_3 - z_1 x_3) + (x_1 z_2 - z_1 x_2)], \quad (7.46b)$$

$$C = + \begin{vmatrix} x_1 & y_1 & 1 \\ x_2 & y_2 & 1 \\ x_3 & y_3 & 1 \end{vmatrix} = +[(x_2 y_3 - y_2 x_3) - (x_1 y_3 - y_1 x_3) + (x_1 y_2 - y_1 x_2)], \quad (7.46c)$$

$$D = - \begin{vmatrix} x_1 & y_1 & z_1 \\ x_2 & y_2 & z_2 \\ x_3 & y_3 & z_3 \end{vmatrix} = -[(x_1y_2z_3 + y_1z_2x_3 + z_1x_2y_3) - (z_1y_2x_3 + x_1z_2y_3 + y_1x_2z_3)]. \tag{7.46d}$$

Geometrically, the coefficients  $A$ ,  $B$  and  $C$  are the components of a vector  $\mathbf{N}$  normal to the plane. The constant  $D$  is related to the distance from the origin to the plane in this direction (which we don't need in this application). With  $A$ ,  $B$  and  $C$  evaluated, the equation of the normal vector is then

$$\mathbf{N} = A \mathbf{i} + B \mathbf{j} + C \mathbf{k}. \tag{7.47}$$

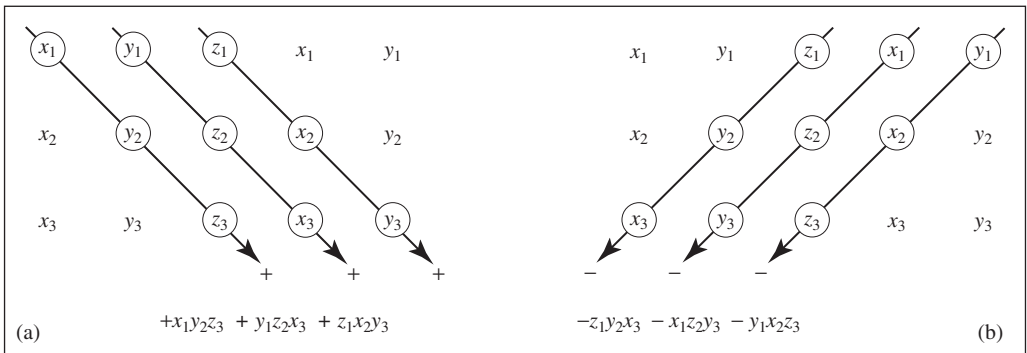


**Figure 7.18** Evaluating a  $3 \times 3$  determinant.

**Problem**

- From points  $P_1$ ,  $P_2$  and  $P_3$  on a plane, determine its attitude (see Fig. 7.19 and Table 7.4).

Table 7.4 *Dip and strike from coordinate geometry*

	$x$	$y$	$z$
$P_1$	100 m	60 m	535 m
$P_2$	350 m	16 m	415 m
$P_3$	156 m	214 m	440 m

**Solution**

1. From Eqs. 7.47 the values of the coefficients are  $A = 226\ 60$ ,  $B = 170\ 30$  and  $C = 409\ 64$ . These are direction numbers of the vector  $\mathbf{N}$  normal to the plane.
2. Normalizing these numbers, the direction cosines are  $\mathbf{N}(0.454\ 88, 0.341\ 86, 0.822\ 32)$ . Note that because the direction of  $+z$  is taken *upward*, these represent an *upward* pointing vector which is plotted in the upper hemisphere in Fig. 7.20a.

3. The opposite of  $\mathbf{N}$  is the downward pointing pole vector  $\mathbf{P}$ , that is,  $\mathbf{P} = -\mathbf{N}$ . This vector is plotted in the lower hemisphere in Fig. 7.20b.
4. The trend of the dip vector  $\mathbf{D}$  and the trend of  $\mathbf{N}$  are the same.

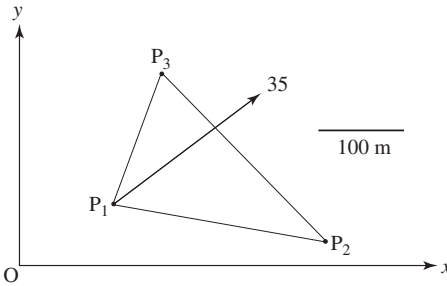


**Figure 7.19** Three-point problem by coordinate geometry.

### Answer

- Using Eqs. 7.8 gives the correct plunge of the dip vector but its trend is measured from  $+x = \text{east}$ . We need its complement and we thus have  $\mathbf{D}(35/053)$ .

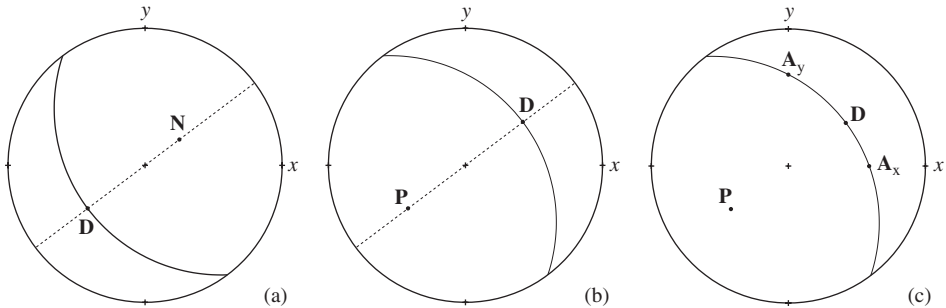


**Figure 7.20** Three-point problem: (a)  $\mathbf{N}$  and  $\mathbf{D}$  in the upper hemisphere; (b)  $\mathbf{P}$  and  $\mathbf{D}$  in the lower hemisphere; (c) true dip  $\mathbf{D}$  from apparent dips  $\mathbf{A}_x$  and  $\mathbf{A}_y$ .

Fielen (2005) extended this treatment to the case of more than three points using a least-squares technique to find the best-fit plane.

### Vector analysis

The second method uses elementary vector analysis. Not only does this provide a simple solution but the basic approach is directly applicable to a wide variety of other physical problems. The treatment closely follows Vacher (1989).

Associated with every point on a map depicting an inclined plane is a number representing its height  $h$ . The functional relationship between the elevation and these geographical points is written  $h(x, y)$ .

In mathematical terms  $h(x, y)$  is a *two-dimensional scalar field*. At every point in this field the rate of change of  $h$  with distance  $s$  depends on direction. This is the *directional derivative* and it is denoted  $dh/ds$ . The difference  $\Delta h$  in the heights between any two points on the inclined plane is found from the slope and map distance between the points, that is,

$$\Delta h = (dh/ds)s.$$

There is a direction in which  $dh/ds$  has a maximum value, and this direction of maximum slope is represented by a vector called the *gradient* of  $h$ , written  $\text{grad } h$  or  $\nabla h$ .<sup>10</sup> In component form this gradient vector is given by the sum of the vector components in each of the coordinate directions.

$$\nabla h = \frac{\partial h}{\partial x} \mathbf{i} + \frac{\partial h}{\partial y} \mathbf{j},$$

where  $\mathbf{i}$  and  $\mathbf{j}$  are the unit base vectors in the  $+x$  and  $+y$  directions and the partial derivatives  $\partial h/\partial x$  and  $\partial h/\partial y$  are the slopes of the plane in each of these directions. We can now express the *directional derivative* in any direction as the dot product

$$\nabla h \cdot \hat{\mathbf{u}} = \frac{dh}{ds},$$

where  $\hat{\mathbf{u}}$  is the unit vector in the required direction.

This gradient vector exists at every point in the field, expressed as  $\nabla h(x, y)$ , and this is the description of a *vector field*.<sup>11</sup>

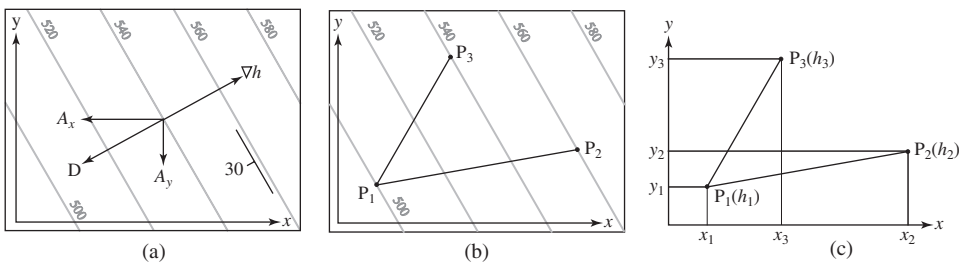


**Figure 7.21** Structure contours and the gradient vector  $\nabla h$ .

<sup>10</sup>The vector operator symbol  $\nabla$  was introduced by the Irish mathematician and physicist William Rowan Hamilton [1805–1865], and called *nabla* after a Hebrew harp of similar shape. It is now commonly termed *del*, but do not confuse the name or symbol with the Greek *delta*.

<sup>11</sup>In this application the scalar field  $h(x, y)$  describes an inclined plane and therefore the vector  $\nabla h$  has constant magnitude and direction everywhere in the field. But the analysis also applies to more general situations where  $h(x, y)$  describes a curvilinear surface;  $\nabla h$  still exists at every point, but both its magnitude and direction will vary.

Because vector  $\nabla h$  is the steepest direction its magnitude is also the slope of the line of true dip. The dip direction is given by  $-\nabla h$ , that is, opposite the direction of  $\nabla h$ . The reason for the change of sign is that  $\nabla h$  refers to the maximum *increase* while the dip refers to the maximum *decrease* of  $h$ . We can avoid this minus sign by defining the dip vector as

$$\mathbf{D} = -\nabla h. \quad (7.48)$$

The components of this vector in each of the coordinate directions give the magnitudes of the apparent dip vectors  $\mathbf{A}_x$  and  $\mathbf{A}_y$  (Fig. 7.21a). Thus

$$A_x = -\partial h / \partial x \quad \text{and} \quad A_y = -\partial h / \partial y. \quad (7.49)$$

The magnitude of the dip vector is then

$$D = \sqrt{A_x^2 + A_y^2}, \quad (7.50)$$

and the angle of true dip is

$$\delta = \arctan D. \quad (7.51)$$

The angle vector  $\mathbf{D}$  makes with  $+x$  is given by

$$\theta_x = \arctan(A_y/A_x). \quad (7.52)$$

In order to find the gradient vector  $\nabla h$  we need to express its components in terms of the coordinates of the three known points  $P_1(x_1, y_1, h_1)$ ,  $P_2(x_2, y_2, h_2)$  and  $P_3(x_3, y_3, h_3)$  on the plane. We may relate these components to the horizontal and vertical distances between pairs of these known points, and we do this for lines  $P_1P_2$  and  $P_1P_3$  (Fig. 7.21b).

1. The vertical distance between points  $P_1$  and  $P_2$  is  $\Delta h_{12} = (h_2 - h_1)$ . This is made up of two parts:  $\Delta h_x$  is associated with line parallel to the  $x$  axis and  $\Delta h_y$  is associated with line parallel to the  $y$  axis (Fig. 7.21c). In terms of the coordinates of points  $P_1$  and  $P_2$  these are

$$\Delta h_x = \frac{\partial h}{\partial x}(x_2 - x_1) \quad \text{and} \quad \Delta h_y = \frac{\partial h}{\partial y}(y_2 - y_1).$$

The total  $\Delta h$  is the sum of these two parts

$$\Delta h_{12} = \frac{\partial h}{\partial x}(x_2 - x_1) + \frac{\partial h}{\partial y}(y_1 - y_2) = (h_2 - h_1). \quad (7.53a)$$

Table 7.5 Dip vector from  $\nabla h$

	$x$	$y$	$h$
$P_1$	100 m	60 m	535 m
$P_2$	350 m	16 m	415 m
$P_3$	156 m	214 m	440 m

2. Similarly, the vertical distance between points  $P_1$  and  $P_3$  is  $\Delta h_{13} = (h_3 - h_1)$ . It too is made up of two parts and the sum of these parts is

$$\Delta h_{13} = \frac{\partial h}{\partial x}(x_3 - x_1) + \frac{\partial h}{\partial y}(y_3 - y_1) = (h_3 - h_1). \tag{7.53b}$$

We now have two equations for the two unknown slopes  $\partial h/\partial x$  and  $\partial h/\partial y$ . Solving for these using Cramer’s rule<sup>12</sup> gives

$$\frac{\partial h}{\partial x} = \frac{\begin{vmatrix} (h_2 - h_1) & (y_2 - y_1) \\ (h_3 - h_1) & (y_3 - y_1) \end{vmatrix}}{\begin{vmatrix} (x_2 - x_1) & (y_2 - y_1) \\ (x_3 - x_1) & (y_3 - y_1) \end{vmatrix}} \quad \text{and} \quad \frac{\partial h}{\partial y} = \frac{\begin{vmatrix} (x_2 - x_1) & (h_2 - h_1) \\ (x_3 - x_1) & (h_3 - h_1) \end{vmatrix}}{\begin{vmatrix} (x_2 - x_1) & (y_2 - y_1) \\ (x_3 - x_1) & (y_3 - y_1) \end{vmatrix}}.$$

Expanding these determinants we have

$$\frac{\partial h}{\partial x} = \frac{(h_2 - h_1)(y_3 - y_1) - (h_3 - h_1)(y_2 - y_1)}{(x_2 - x_1)(y_3 - y_1) - (x_3 - x_1)(y_2 - y_1)}, \tag{7.54a}$$

$$\frac{\partial h}{\partial y} = \frac{(h_3 - h_1)(x_2 - x_1) - (h_2 - h_1)(x_3 - x_1)}{(x_2 - x_1)(y_3 - y_1) - (x_3 - x_1)(y_2 - y_1)}. \tag{7.54b}$$

**Problem**

- Solve the same three-point problem using this vector approach (see Fig. 7.21 and Table 7.5).

**Solution**

1. With coordinates  $(x, y)$  and heights  $h$  (Table 7.5) Eqs. 7.55 yield the slopes in each coordinate direction  $\partial h/\partial x$  and  $\partial h/\partial y$ .
2. Eqs. 7.50 yield the corresponding downward slopes  $A_x(0.553\ 17)$  and  $A_y(0.415\ 73)$ . The apparent dip angles are then  $\alpha_x = 28.95^\circ$  and  $\alpha_y = 22.57^\circ$ .
3. From Eqs. 7.51 and 7.52,  $D = 0.691\ 97$ , hence the dip of the plane  $\delta = 34.68^\circ$ .

<sup>12</sup>Named after the Swiss mathematician Gabriel Cramer [1704–1752], a contemporary of Leonard Euler.

4. From Eq. 7.53,  $\theta_x = 36.93^\circ$  and this is the trend of the direction of true dip measured from east.

**Answer**

- The attitude of the dip vector is **D**(35/053), which is the same as obtained by coordinate geometry (see Fig. 7.20c).



# 8

## Faults

### 8.1 Definitions

**Fault:** a surface along which appreciable displacement has taken place; this surface may be planar or curvilinear.

**Fault zone:** a zone containing a number of parallel or anastomosing faults.

**Echelon faults:** relatively short, parallel faults of a zone which display an overlapping or staggered pattern.

**Shear zone:** a zone across which two blocks have been displaced in fault-like manner, but without development of visible fractures.

**Footwall:** the surface bounding the body of rock immediately below a non-vertical fault. The body of rock itself is called the footwall block.

**Hangingwall:** the surface bounding the body of rock immediately above a non-vertical fault. The body of rock itself is called the hangingwall block.

**Cut-off line:** the trace of a displaced plane on the fault surface; these lines occur in pairs, one on the footwall and one on the hangingwall.

**Slip:** the relative displacement of formerly adjacent points (Fig. 8.1a); also called the net slip. It is represented by the *relative slip vector*, usually of the hangingwall block relative to the footwall block. *Dip slip* and *strike slip* are components. This total displacement is the result of the accumulation of a number of small *slip events*, which are not necessarily parallel to the slip vector.

**Separation:** the distance between two displaced planes. It may be measured on the fault perpendicular to the cut-off lines, but more commonly in the strike or dip directions (Fig. 8.1b). On the other hand, *stratigraphic separation* is measured perpendicular to the displaced strata, not in the plane of the fault.

**Contractional fault:** a fault which produces horizontal shortening as measured across the trace of the fault.

**Extensional fault:** a fault which produces horizontal lengthening as measured across the trace of the fault.

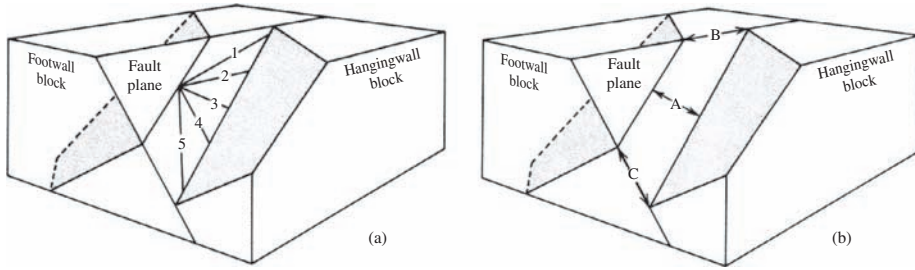


**Figure 8.1** Fault and displaced marker plane: (a) possible slip vectors 1–5; (b)  $A$  = separation,  $B$  = strike separation;  $C$  = dip separation (after Hill, 1959, 1963).

## 8.2 Fault classification

Although we will treat faults as surfaces along which slip has taken place, many faults are accompanied by comminuted rock material which may or may not be chemically altered or recrystallized (Wise, *et al.*, 1984). Although we do not consider these products further, their character gives important information on the processes of faulting and the environments in which it occurs.

The most important aspect of fault geometry is slip. We treat first *translational faults* where the relative slip vector has a constant magnitude and orientation everywhere on the fault plane or a specific portion of it. There are two important special cases: slip parallel to the dip of the fault or slip parallel to the strike of the fault. Combined with the two possible senses of displacement for each, this leads to a fourfold classification of slip.

### 1. Dip slip

- (a) Normal slip: hangingwall block has moved down relative to the footwall block.<sup>1</sup>
- (b) Reverse slip: hangingwall block has moved up relative to the footwall block.

### 2. Strike slip

- (a) Right slip: standing facing the fault, the opposite block has move relatively to the right.
- (b) Left slip: the opposite block has moved relatively to the left.

The names of the two corresponding types of dip-slip faults are usually shortened to *normal faults* and *reverse faults*.

*Right-slip* faults are also called *right-lateral* or *dextral* faults and *left-slip* faults are also called *left-lateral* or *sinistral* faults. Note that vertical and horizontal faults require special treatment. It is important to emphasize that all four of these special types and combinations are slip-based names (Table 8.1).

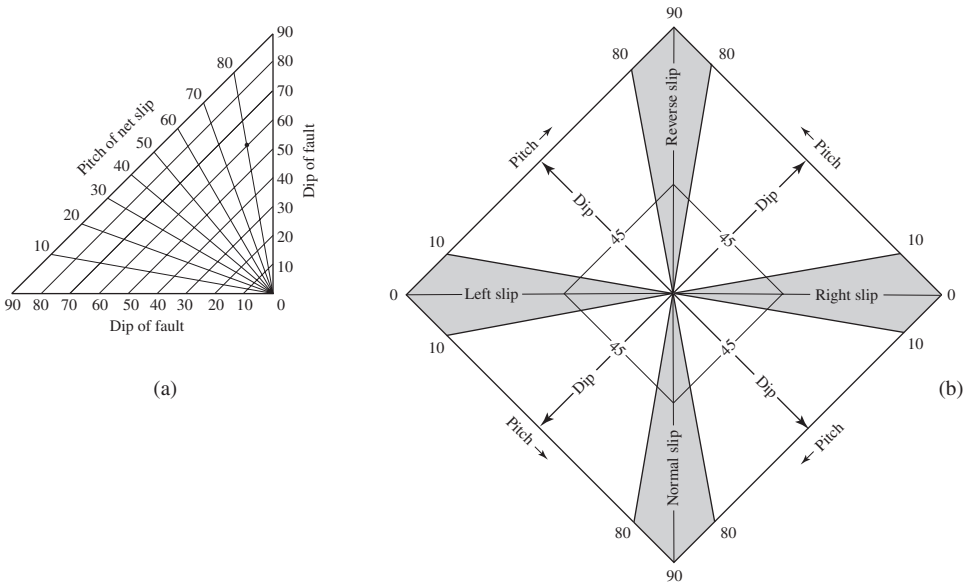
<sup>1</sup>An extended glossary of terms applied to various aspects of normal faults is given by Peacock, *et al.*, (2000).

Table 8.1 *Types of translational faults*

Dip slip	Normal-slip fault Reverse-slip fault
Strike slip	Right-slip fault Left-slip fault
Oblique slip	Dip- and strike-slip terms combined

The attitude of the fault plane is an important second factor in describing the relative displacement of the two fault-bounded blocks. For example, the dominantly horizontal displacement associated with a reverse fault with a dip of 20° differs considerably from that associated with the dominantly vertical displacement associated with a reverse fault with a dip of 70°. It is, therefore, useful to introduce dip into the classification of fault displacements.

Several ways of graphically depicting fault classes have been proposed (Rickard, 1972; Threet, 1973a). Rickard’s approach combines the fault dip with the pitch of the net slip on a triangular diagram, and this leads to a graphical classification scheme. Each possible dip-pitch pair is assigned a unique index; for example, for a fault dipping 60° on which the net slip pitches 80° the index symbol would be  $D_{60}R_{80}$  ( $R$  for rake, to avoid confusion with plunge). This is then represented by a point on the triangular grid (see plot, Fig. 8.2a). Four separate triangles are necessary to represent normal and reverse slips, and right and left slips (Fig. 8.2b).



**Figure 8.2** Translational fault: (a) dip-pitch grid; (b) categories: dip- and strike-slip faults (shaded), and oblique-slip faults (blank) (after Rickard, 1972).

In this way all possible translational faults can be plotted. Further, the main categories of faults can be added to the full diagram as an aid to classification. Rickard also suggests that the special cases of dip slip and strike slip be restricted to faults with pitch angles of  $80\text{--}90^\circ$  and  $0\text{--}10^\circ$ , respectively.

By including the dip of the fault plane in the classification, several additional categories are needed. It is useful and common to distinguish *high-angle faults* and *low-angle faults*, depending on whether the dip is greater or less than  $45^\circ$ . A low-angle reverse fault is called a *thrust*. The term *overthrust* is commonly used for a thrust with dip  $\delta = 0\text{--}10^\circ$ . The prefix *over* is used to emphasize the dominantly horizontal component of the relative displacement of the hangingwall block, and not to imply a direction of absolute movement. Low-angle normal faults also exist but there is no agreed special name.

To depict the various faults and their slip directions on geological maps, special symbols are used. Figure 8.3 shows a number of such symbols for the combinations of slip and dip which cover most situations.

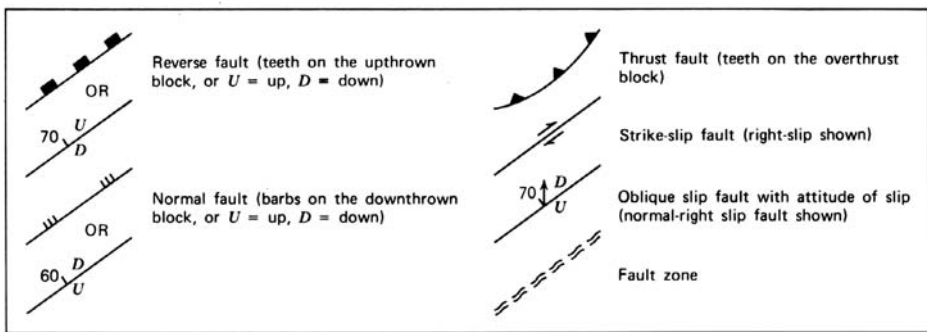


**Figure 8.3** Map symbols for faults (after Hill, 1963).

### 8.3 Slip and separation

Unfortunately, slip can not always be determined. It is separation which is more often measurable, and, in fact, observed separation is commonly the field evidence for the existence of a fault. However, a clear distinction must be maintained between these two terms because an observed separation may result from many possible orientations of the slip vector (see Fig. 8.1b). In order to emphasize this important distinction, two parallel classifications have evolved; one based on slip and the other on separation (Hill, 1959, 1963). Table 8.2 gives the terms for describing the sense of separation.

Because of these two ways of describing aspects of fault displacement it is crucially important to develop a clear understanding of the geometry of slip and separation and especially the relationships between them. A good way of doing this is by constructing a

Table 8.2 *Types of separation*

Right separation	Standing on a displaced marker plane on one block and facing the fault, the trace of the marker plane is to the right across the fault.
Left separation	The trace of the marker plane is to the left on the opposite block.
Normal separation	In a vertical section, the cut-off line of a marker plane on the hangingwall is below the cut-off line of the same marker on the footwall.
Reverse separation	The cut-off line on the hangingwall is above the cut-off line on the footwall.

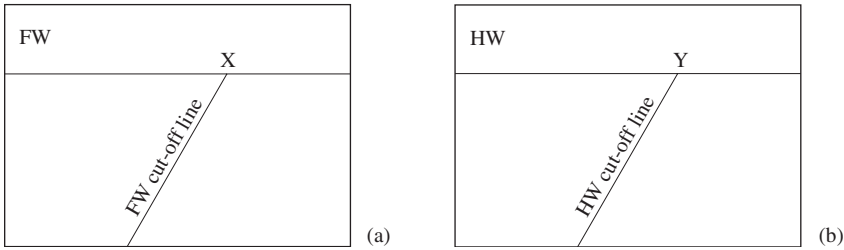


**Figure 8.4** Direct view of fault plane: (a) FW = footwall side; (b) HW = hangingwall side.

*direct view* of a fault plane in order to describe the geometrical effects of the displacement. With such a view, slip and separation can be modeled in a simple way.

### Procedure

1. On a sheet of paper representing the footwall side of the fault draw a horizontal line of strike and a cut-off line inclined to the left. Label the intersection of these lines X (Fig. 8.4a).
2. On a sheet of tracing paper representing the hangingwall side of the fault make a copy and label the point of intersection Y (Fig. 8.4b).
3. Place the hangingwall sheet on the footwall sheet with the lines and points coinciding. Possible slips are modeled simply by translating the tracing sheet. Line XY represents the relative slip vector **D**.
4. Two sets of experiments will illustrate the method.
  - (a) Move the hangingwall sheet directly downward to model normal slip (Fig. 8.5a). Note the normal separation (the HW cut-off line is below the FW cut-off line) and the left separation (the FW cut-off line is to the left of the HW cut-off line).
  - (b) Returning to the initial position now move the hangingwall sheet to the right to model left slip. Note the normal separation and left separation (Fig. 8.5b).
5. Make a second set of drawings, but this time with the cut-off lines inclined to the right.

- (a) Normal slip produces normal separation (as before the HW cut-off line below the FW cut-off line), but right separation (the FW cut-off line to the right of the FW cut-off line) (Fig. 8.6a).
- (b) Left slip produces left separation and reverse separation (Fig. 8.6b).

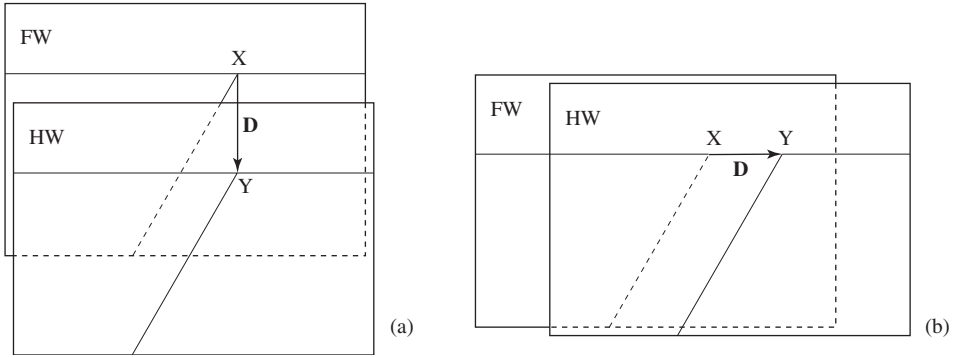


**Figure 8.5** Model I: (a) normal slip; (b) left slip.

Depending on the orientation of the cut-off lines, pure dip slip produces left separation (Fig. 8.5a) or right separation (Fig. 8.6a), and pure strike slip produces normal separation (Fig. 8.6b) or reverse separation (Fig. 8.6b). These results show that the sense of dip and strike separation may *agree* or *disagree* with the sense of the dip and strike slip. Similar experiments may be repeated for a variety of differently oriented slips, including oblique slip. In this way, three general rules can be confirmed (Threeth, 1973b).

1. If the slip vector pitches in a direction opposite to that of the cut-off lines the sense of each component of slip will agree with the respective senses of separation.
2. If the slip pitches in the same direction but at a smaller angle than the cut-off lines the sense of dip separation will disagree with the sense of dip-slip component, while the sense of the strike separation will agree with the sense of the strike-slip component.
3. If the slip pitches in the same direction but at a greater angle than cut-off lines the sense of strike separation will disagree with the sense of strike-slip component while the sense of dip separation will agree with the sense of dip-slip component.

While it is important to understand the implications of these rules it is not necessary to memorize them because the same information can be obtained directly from observations of a geological map. We show how to do this in the next section.

Because of these ambiguities a separation-based scheme is not really a description of displacement at all and any classification based on it is inherently misleading (see also Gill, 1935, 1941, 1971). If the separation is to be described it must be spelled out in terms of the attitude of the disrupted plane and the direction in which it is measured and its sense.

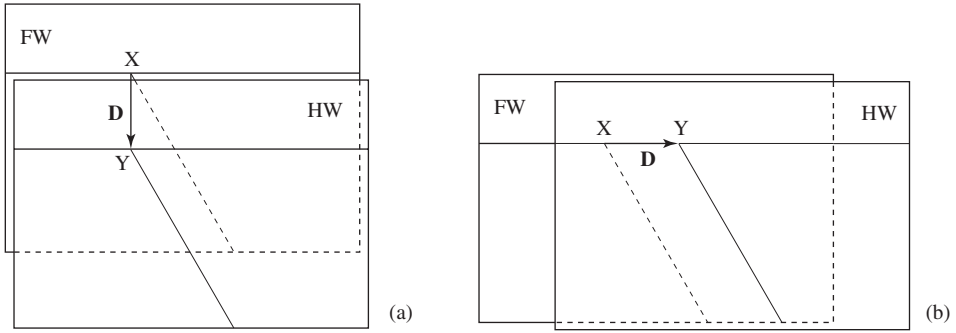


**Figure 8.6** Model II: (a) normal slip; (b) left slip.

There is another difficulty – the discrepancy between the amounts of slip and separation. This problem is particularly clear if the slip vector and cut-off lines are parallel (Fig. 8.7). There is no separation at all. The geometrical factors which lead to this situation are termed the *null combination* (Redmond, 1972). A potentially important case is a strike-slip fault cutting horizontal beds.

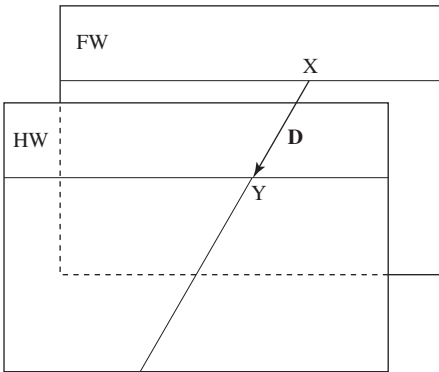


**Figure 8.7** Model of slip with zero separation.

At the opposite extreme, there are conditions where the measured separation is very much larger than the slip. For a unit of strike slip, the dip separation  $S_D$  is, from Fig. 8.8a,

$$S_D = \tan r, \tag{8.1}$$

where  $r$  is the pitch of the cut-off lines on the fault plane. Similarly, for a unit of dip slip the strike separation  $S_S$  is, from Fig. 8.8b,

$$S_S = 1 / \tan r. \tag{8.2}$$

For a pure strike-slip fault, the dip separation  $S_D$  becomes very large as the pitch angle approaches  $90^\circ$  (Eq. 8.1), and for a pure dip-slip fault, the strike separation  $S_S$  becomes very large as the pitch angle approaches  $0^\circ$  (Eq. 8.2).

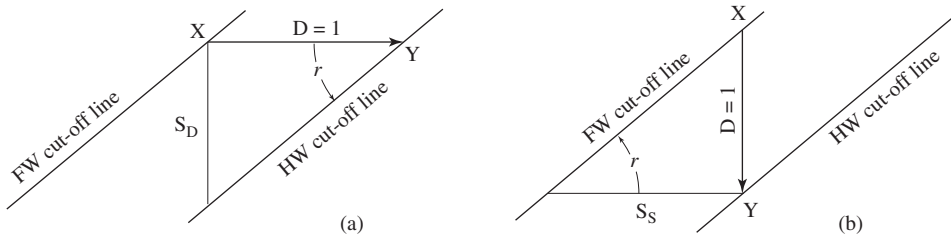


**Figure 8.8** Magnitude of separation: (a) unit strike slip; (b) unit dip slip.

While the accurate observation and description of separation is important, we see that the sense and amount of the separation are unreliable guides to interpreting the sense and magnitude of slip.

### 8.4 Faults in three dimensions

The down-structure method of viewing geological maps allows one to see some of these same relationships in a three-dimensional setting (Mackin, 1950; Threet, 1973b). The geological map of Fig. 8.9 shows three vertical faults displacing inclined strata. From the map the senses of strike separation can be immediately determined. Fault *L* shows right separation, and Faults *M* and *N* show left separation. But what about the sense of dip separation?

Adopting a down-dip view of the beds in the vicinity of Fault *L* reveals that Bed 2 is higher on the west side of the fault. Therefore, the sense of dip separation is up on the west (the terms reverse or normal do not apply here because the fault is vertical).

As an aid to this visualization, it is useful, especially for beginners, to represent the two sides of the fault by holding the two flattened hands with the fingers in the dip direction of the beds. Starting with the hands together move one hand parallel to the plane of the fault to reproduce the observed separation in two special ways.

1. Move the left hand representing the west block upward in pure dip-slip displacement.
2. Move the left hand northward in pure strike-slip displacement.

It can then also be seen that many differently oriented oblique slips are also possible, all of which can be easily modeled.

For Fault *M* the sense of dip separation can also be seen in a down-dip view; in contrast, it is up on the east. There is, however, a better way of viewing the map of such a fault, and it is in the direction of the line of intersection of the fault and the displaced plane. For Fault *M* the trend of the cut-off line is parallel to the strike of the vertical fault and its plunge is the apparent dip of the bed in this direction, that is, 28/350.

For Fault *N* the attitude of the line of intersection is 18/295, and looking in this direction gives quite a different picture but with essentially the same meaning.



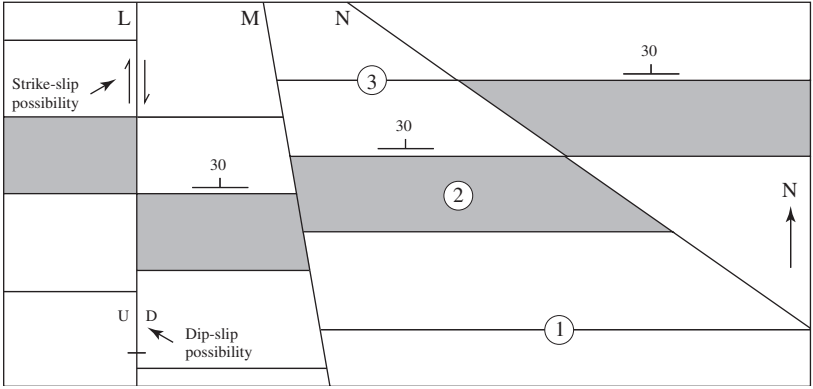


**Figure 8.9** Down-structure view of faults (after Mackin, 1950).

The utility of this down-plunge view is illustrated even better when the fault plane is inclined. Figure 8.10a shows a map of an east-dipping fault which obliquely cuts a bed inclined at  $40^\circ$ . As shown in the stereogram (Fig. 8.10b), the intersection  $I$  of the bed and fault is parallel to the line of dip on the fault, that is, the pitch of the cut-off lines  $l_{HW}$  and  $l_{FW}$  is  $90^\circ$ . The map clearly shows left separation. The dip separation, however, is infinite and we can see this clearly in a down-dip view of the fault plane (see also Fig. 8.10c).

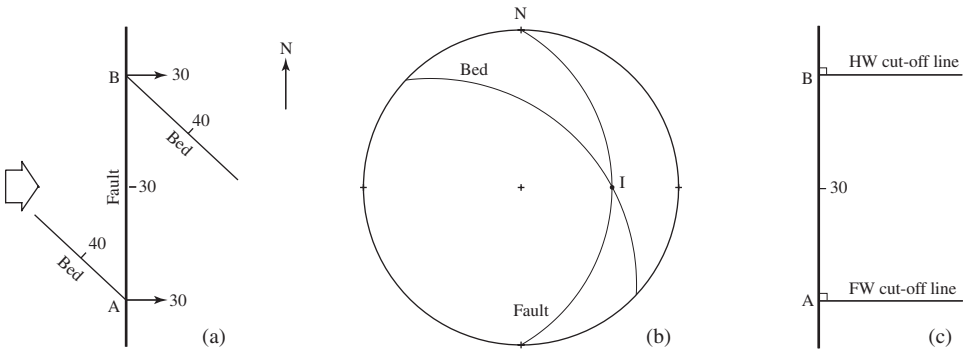


**Figure 8.10** Case  $r = 90^\circ$ : (a) map; (b) stereogram; (c) direct view.

In this example the attitude of the bed is such that the line of intersection is exactly parallel to the dip of the fault, and this illustrates the boundary between two general cases.

1. If the dip of the beds is less than  $40^\circ$  then the cut-off lines pitch to the north and the dip separation is reverse (Fig. 8.11a).
2. If the dip of the beds is greater than  $40^\circ$  the cut-off lines pitch to the south and the dip separation is normal (Fig. 8.11b).

In such cases the down-plunge view immediately reveals two important aspects of fault geometry.

1. The hangingwall block is seen to be above the footwall block, that is, they are in their correct vertical relationships.
2. The cut-off lines on the hangingwall and footwall sides are also seen to be in their correct vertical relationships. If the hangingwall cut-off line is below the footwall cut-off line the dip separation is normal, and if it is above the dip separation is reverse.

Thus in all cases a down-plunge view of the cut-off lines shows the correct sense of dip separation.

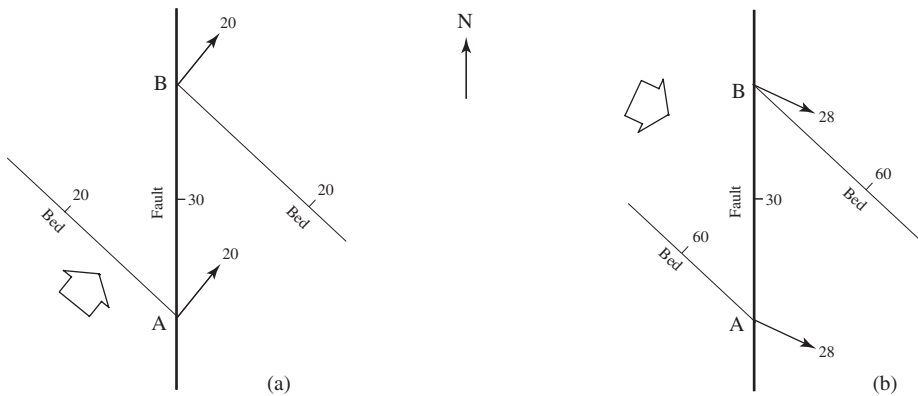


**Figure 8.11** Down-plunge views: (a) reverse separation; (b) normal separation.

Clearly it is *slip*, not separation, which most fundamentally describes the displacement on a fault, and a classification based on it is the only meaningful way of categorizing this information.

### 8.5 Slip and its determination

Because of its importance, we need to be able to deal with the geometry of slip. In order to introduce the approach used in the analysis of fault displacement, we start with the simpler situation where the direction and amount of the slip on a fault are given.

#### Problem

- A normal fault dips  $60^\circ$  due east (Fig. 8.12a). It cuts a vein whose attitude is N 50 E, 40 N which is exposed only on the west side. The slip is 100 m. Locate the vein on the opposite side of the fault.

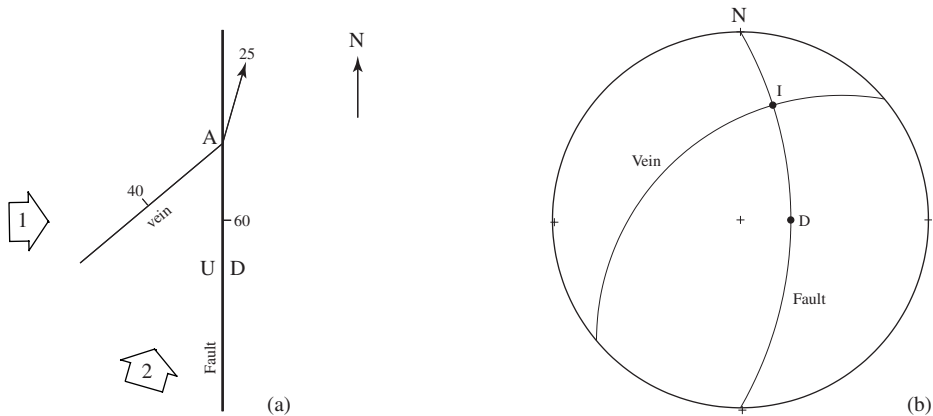


**Figure 8.12** Displaced vein: (a) map; (b) stereogram.

### Approach

- As always, visualize the elements of the problem. First, view the map by looking down the dip of the fault. See that the east side overlies the west side and is, therefore, the hangingwall block. Second, estimate the attitude of the line of intersection of the fault and the vein: it trends somewhat east of north and plunges less than dip of the vein. Now view the map in this direction and imagine the continuation of the map trace of the vein before faulting. Normal slip brings the hangingwall block directly down the dip of the fault. Therefore the vein will show normal separation, and its cut-off line on the hangingwall will appear below the cut-off line on the footwall side. This also means that the vein will show right separation.

### Construction

- On a stereogram plot the plane of the fault and the vein as great circles (Fig. 8.12b). Their intersection  $I$  (25/016) gives the attitude of the cut-off line and its pitch  $r = 29^\circ$  on the plane of the fault.
- To construct a direct view of the fault plane from the FW side, draw a line of strike, plot point  $A$  representing the surface point common to the fault and vein. With the pitch angle draw in the cut-off line on the footwall (Fig. 8.13a).
- Draw a slip vector  $D$  perpendicular to the strike line through  $A$ . From point  $A$  scale off 100 m along this line to locate a point on the hangingwall cut-off line. Through this point draw a parallel cut-off line to intersect the strike line at point  $B$  which is to the left on the hangingwall.
- $AB$  is the strike separation. Measure its scaled length to locate point  $B$  on the map trace of the fault and complete the outcrop trace of the vein on the hangingwall block (Fig. 8.13b).

Answer

- The measured strike separation is 180.4 m.

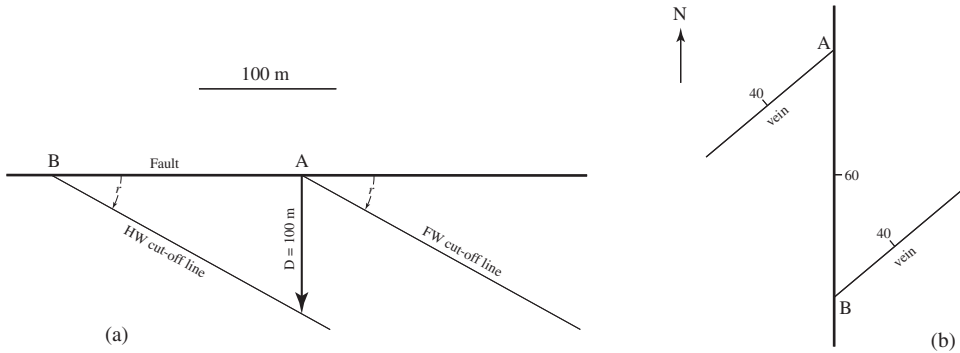


Figure 8.13 Known slip: (a) direct view of fault from the HW side; (b) map of fault and vein.

This problem is not very realistic because the direction and amount of slip was given. We need to determine its orientation, sense and amount from field observations and there are several ways of doing this.

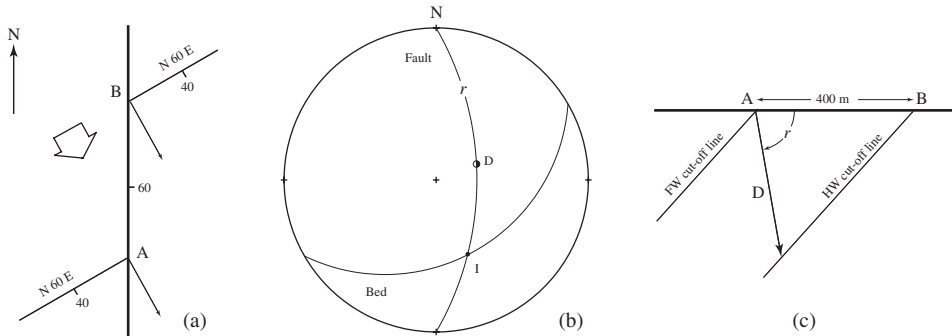
There may be features on the plane of the fault called *slickenstructures* (Fleuty, 1974, 1987b; see Table 8.3), which include *slickenplanes* and *slickenlines*. These are formed by abrasional or depositional processes acting during slip. In detail, these may take a variety of forms (Means, 1987).

Table 8.3 *Slickenstructures*

	Generic term	Abrasion	Growth
Planar feature	Slickenplane	Slickenside	Slickenzone
Linear feature	Slickenline	Slickenstriae	Slickenfiber

Polished fault surfaces produced by wear during slip are called *slickensides*. If present, grooves or scratches on these surfaces are *slickenstriae* (Weaver, 1975) and these give the direction of slip, although if there have been several differently oriented episodes of movement, only the last will be recorded. There also may be minute step-like features on these polished planes called *slickensteps*, which are approximately perpendicular to the slickenlines. The direction in which these steps face has been used as an indication of the sense of slip, but counter examples are known (Hobbs, *et al.*, 1976, p. 303–305).

Thin fibrous coatings or *slickenzones* are found on some movement planes. These are formed by the deposition, commonly of calcite or quartz, from aqueous solutions during sliding, and the orientation of the *slickenfibers* identifies the latest slip direction and in some cases also the sense of slip.



**Figure 8.14** Known slip direction: (a) map; (b) stereogram; (c) fault plane.

### Problem

- A fault dips  $60^\circ$  due east (Fig. 8.14a). A displaced bed with attitude N 60 E, 40 S shows 400 m of left separation. Slickensides on the fault plane plunge toward N 75 E. Determine the amount and sense of slip.

### Visualization

- The attitude of the line of intersection  $I$  of the fault and the bed is 40/151. A down-plunge view in this direction shows that the cut-off line on the hangingwall side is below the cut-off line on the footwall side, that is, the dip separation is normal.

### Construction

1. On a stereogram plot the planes of the fault and bed as great circles, and the slickensides as point  $D$  on the fault. The two planes intersect at  $I$  giving the pitch of the bed in the fault plane as  $r_B = 40$  S. Measure the pitch of  $D$  as  $r_D = 80$  N (Fig. 8.14b).
2. Using pitch angle  $r_B$ , construct a direct view of the fault plane from the hangingwall side showing the scaled separation  $AB$ . Draw the FW cut-off line through point  $A$  and the HW cut-off line through point  $B$  (Fig. 8.14c). Note that these two lines show normal separation thus confirming the results of the down-plunge view.
3. With its pitch angle  $r_D$ , draw the slip vector  $D$  through point  $A$  to intersect the hangingwall cut-off line. Measure its scaled length.

### Answer

- The amount of the slip is 377 m, and its sense is dominantly normal. This sense can be indicated on the stereogram by a small split circle with the dark half on the down side.

Without such direct information of its direction, determining the slip requires the recognition of two originally adjacent points on the fault surface or the equivalent. Strictly, geological examples of such points do not exist, and, therefore, other features from which points may be derived must be found. In practice, displaced lines may be recognized in

several situations. These lines intersect or pierce the fault plane, one on the footwall and one on the hangingwall, to give the required points. These are called *piercing points*. In Fig. 8.15, *X* is the piercing point of line *WX* and *Y* is the piercing point of line *YZ*.

Such lines may be represented by a variety of physical structures, including intersecting planes, the trace of one plane on another (e.g., beds truncated against an unconformity), linear geological bodies (shoe-string sands, linear ore veins, etc.), and stratigraphic lines (pinch-out lines, ancient shorelines, etc.). Or the required lines may be constructed from field data, such as isopachous or isochore lines, lithofacies lines, or hinge lines of folds.

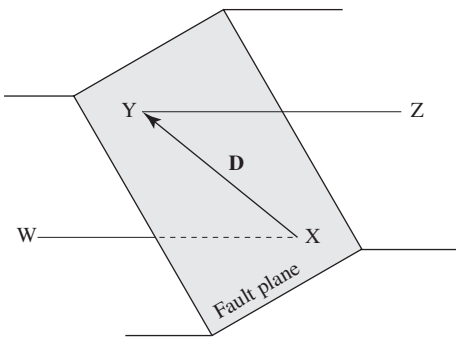


**Figure 8.15** Piercing points *X* and *Y*; segment *XY* represents the slip vector **D** (after Crowell, 1959).

**Problem**

- A fault dips 30/090 and displaces both a bed and a vein (Fig. 8.16a). The distances  $A_1A_2 = 120$  m,  $A_2B_1 = 180$  m, and  $B_1B_2 = 105$  m. Find the slip vector.

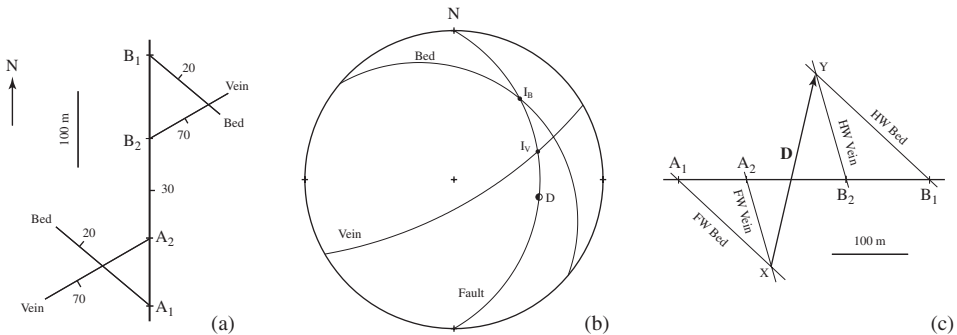


**Figure 8.16** Displaced planes: (a) map; (b) stereogram; (c) direct view of fault.

**Construction**

1. A stereogram of the three planes yields the intersection of the bed with the fault  $I_B$  and the intersection of the vein with the fault  $I_V$ . From these we measure the pitch of the bed  $I_B(33$  N) and of the vein  $I_V(60$  N) in the plane of the fault (Fig. 8.16b).

2. Using these pitch angles and the measured strike separations, the cut-off lines are then drawn on a direct view of the fault, first on the footwall side giving the piercing point  $X$  and then on the hangingwall side giving piercing point  $Y$  (Fig. 8.16c). Note that locating point  $Y$  requires that the cut-off lines be projected upward.
3. The line  $XY$  is the slip vector  $\mathbf{D}$  and its length and pitch angle are easily measured.

### Answer

- The net slip is 330 m, and the pitch of the slip vector on the fault is 82 S. The fault is a thrust with a small right-slip component.

## 8.6 Overthrusts

Low-angle thrusts have a number of special and important features which deserve additional treatment. There are also some special problems – because of their flat-lying nature, structures below the thrust sheet are usually concealed. Slips of tens of kilometers are not uncommon and such large displacements compound the problem of trying to match features above and below the fault plane.

Because of the low angle, the outcrop pattern of the thrust plane is strongly influenced by erosion. One result is that an erosional outlier, called a *klippe*, may be produced. Similarly, erosion may also expose the footwall block in a *window*. These two features are illustrated in Fig. 8.17.

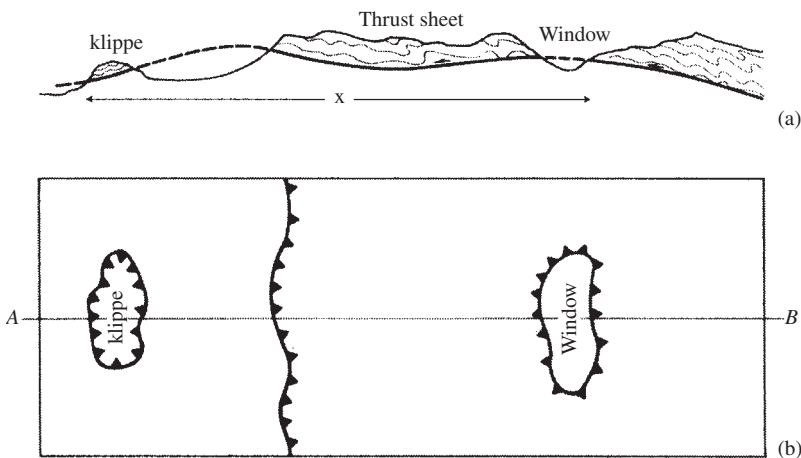


**Figure 8.17** Klippe and window: (a) cross section; (b) map showing both features depicted by closed curves (after Ramsay, 1969, p.63).

The determination of the slip for an overthrust sheet is often difficult. In principle, the methods used for other types of faults are also applicable to overthrusts. For example, the slip could be obtained from two originally adjacent points. Unfortunately, such a situation where this method could be used has apparently not yet been found.

One guide is that thrust sheets commonly move approximately up the dip direction in their central parts. This direction can be established by an application of the *bow and arrow rule* (Elliott, 1976, p. 298). A straight line is drawn connecting the two ends of the outcrop trace of a single thrust. The perpendicular bisector of this line then gives an estimate of the slip direction, and the length of the line is an estimate of its magnitude (Fig. 8.18). If possible, this determination should be tested by independent evidence.

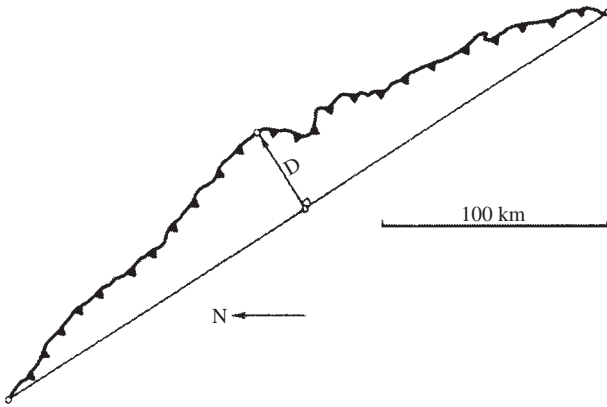


**Figure 8.18** Bow and arrow rule (after Elliott, 1976, p. 298).

Additional techniques for estimating the slip direction use the orientation of folds and slaty cleavage in the thrust sheet (Piffner, 1981), and the orientation of the foliation and lamination in mylonites (Butler, 1982a,b). The basis for some of these methods is treated in later chapters.

Knowing the slip direction, the total displacement may then be estimated in several ways. A simple approach is to draw a cross section parallel to this direction along a line across the exposed thrust plane, intersecting a klippe and a window. The maximum width of the exposure of the thrust then gives a measure of the minimum displacement (see distance  $X$  in Fig. 8.17).

The window-to-klippe method of putting a limit on thrust displacement breaks down entirely if rocks beneath the thrust are older than those above it, or if stratigraphic inversion occurred prior to thrusting by recumbent folding, or if a line drawn from window to klippe is not at least approximately parallel to the direction of displacement.

If a single displaced plane can be identified in both the footwall and hangingwall, the amount of slip can be determined using the previous methods.

### Problem

- An overthrust sheet was emplaced by slip due west (Fig. 8.19a). A displaced marker plane is found in two places: at points  $A$  on the hangingwall block, and  $B$  on the footwall block. Find the slip.



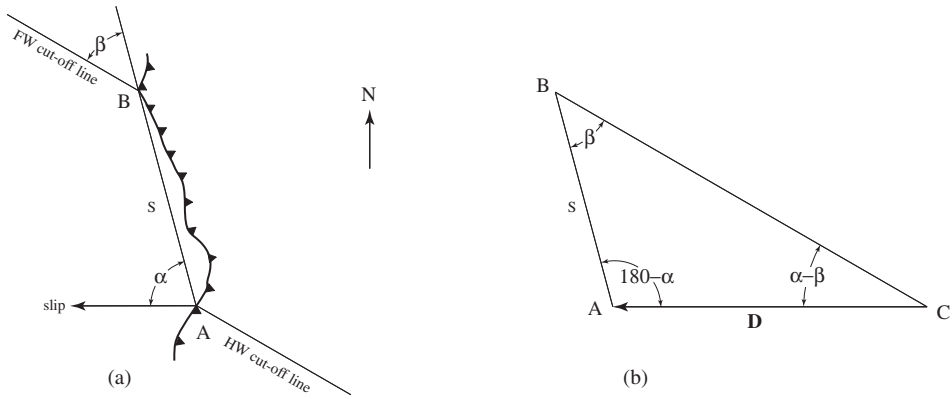


**Figure 8.19** Slip from separation on an overthrust (after Elliott & Johnson, 1980).

### Construction

1. In a plan view of the thrust plane (not the plane of the map), determine the orientation of the cut-off line on the thrust plane from both the hangingwall and footwall sides (Fig. 8.19b).
2. From  $B$  on the footwall side draw a line parallel to this trace to intersect the slip vector at  $C$ .
3. The length  $AC$  represents the magnitude of the slip.

The magnitude of the slip can also be calculated from these same measured quantities. From the map, the line  $AB$  is the oblique separation  $S$ . This line makes an angle  $\alpha$  with the slip vector  $D$ , and an angle  $\beta$  with the cut-off line of the displaced plane. Then

$$A = 180 - \alpha, \quad B = \beta, \quad C = 180 - (A + B) = |\alpha - \beta|.$$

From the oblique triangle  $ABC$  and the Law of Sines

$$D = S \frac{\sin \beta}{\sin |\alpha - \beta|}. \quad (8.3)$$

There may also be a number of major or minor thrusts on the hangingwall side. Such additional faults commonly display two distinct styles. One of these involves the presence of minor thrusts which root in the main basal thrust and curve upward to the surface; these shovel-shaped faults are called *listric thrusts*. If a number of such thrusts are present, the effect is to break the hangingwall block into a series of curved slabs, and this is described as *imbricate* structure (Fig. 8.20).

In the more complicated case, a body of rock bounded on all sides by minor faults is termed a *horse*. A *duplex* is an imbricate family of horses – “a herd of horses” (Boyer & Elliott, 1982, p. 1202). The faults bounding a thrust duplex top and bottom are called *roof* and *floor* thrusts (Fig. 8.21). The lowest thrust of the group is commonly referred



**Figure 8.20** Imbricate thrusts in the Canadian Rocky Mountains.

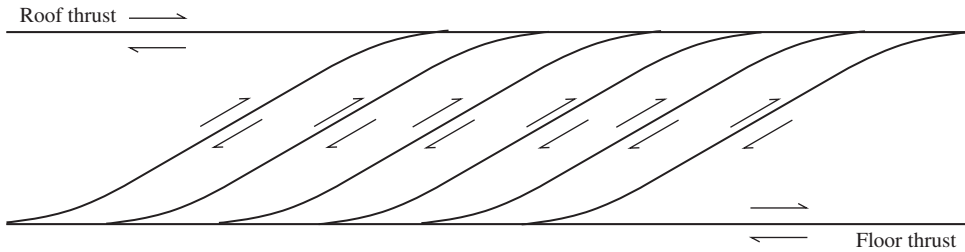


**Figure 8.21** Thrust duplex.

to as the *sole* thrust. One way of determining the total displacement is to sum the slips on each member fault, but this may be difficult.

**8.7 Fault terminations**

The slip which accompanies the first increment of movement on a new fault, or the renewed slip on an established fault has only finite extent. The region of slip can be pictured as an area inside a closed curve on the fault surface which may or may not intersect the earth’s surface. Figure 8.22a shows such a patch associated with an increment of slip on a normal fault. Along line *AB* the motion is perpendicular to the edge (see Fig. 8.22b) and along line *CD* the motion is parallel to the edge (see Fig. 8.22c). In these places a small slip over a large area is accommodated by small distortions.

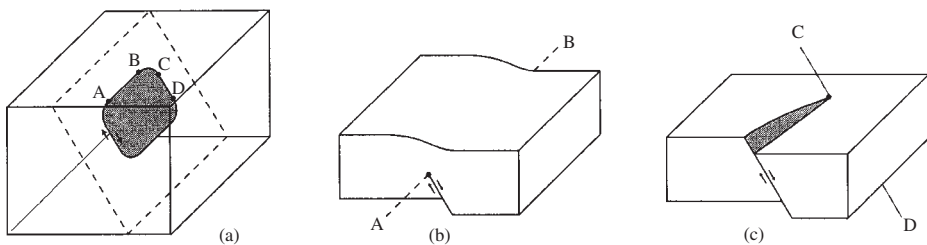


**Figure 8.22** Normal fault: (a) dislocation; (b) edge dislocation *AB*; (c) screw dislocation *CD*.

Another way of accommodating misfits is by developing branch faults at the termination of the main fault (Fig. 8.23a). For large displacements, subsidiary structures develop

by secondary faults or folds or both. A strike-slip fault may end by transverse normal faulting (Fig. 8.23b) or by transverse folds and thrusts (Fig. 8.23c). Note, however, that in such cases which structure developed to accommodate the movement on the other may not be clear.

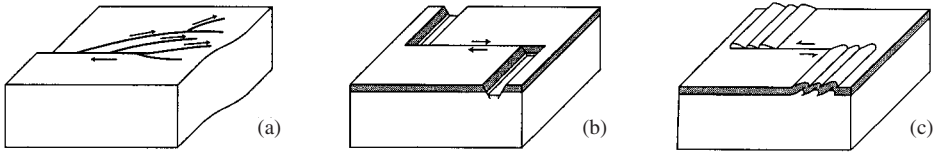


**Figure 8.23** Terminations on a strike-slip fault: (a) splay strike-slip faults; (b) normal faults; (c) folds and thrusts.

Another type of terminations occurs in fault zones made up of *echelon* faults. The displacement on one, relatively short fault is picked up by a similar fault nearby. These are commonly observed in zones of strike-slip faulting, such as the San Andreas of California. The description of such faults involves both the sense of slip and the relationship between adjacent faults. Standing on one of the faults facing in the strike direction the next fault is seen to step to either the right or left. In combination with the two possible senses of slip, this leads to four cases (Fig. 8.24). The inevitable distortions associated with such terminations requires distortion in the area of overlap: extension resulting in an irregular basin (Fig. 8.24a,d), or contraction resulting in a domal structure (Fig. 8.24b,c).

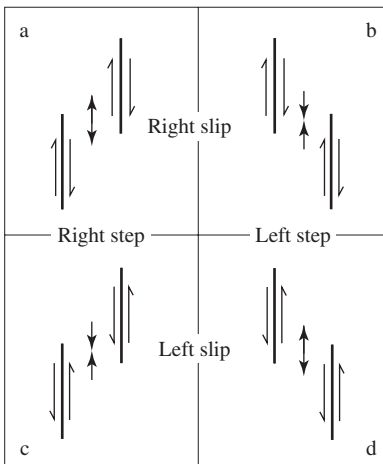


**Figure 8.24** Four patterns of echelon faults.

The mode of termination gives important information on the nature of the faulting mechanism, including the slip rate (Williams & Chapman, 1983) and should be examined carefully wherever possible.

Unfortunately, the ends of faults are not always seen in the field. Sometimes the trace of the fault extends well beyond the particular area being mapped. Other times the exposure, lithologic contrasts or geomorphic expressions are insufficient to permit the faults to be traced onward. This presents the field geologist with a dilemma (Gage, 1979). On one hand, it is not desirable to show a fault where it can not be found. On the other hand, it is equally undesirable to suggest that the fault termination was observed at the place where the mapped trace ends. One way of resolving the matter is with the use of question marks in the general locality where the fault “disappears”, together with an appropriate comment in the map legend.

## 8.8 Faults and folds

Faults and folds are often found together. Of particularly interest here are situations where there is a genetic relationship between faulting and folding, and there are two important cases.

First, the folds may result directly from the fault movement. During slippage of one block past the other, frictional drag on the fault plane may produce certain effects in the blocks themselves. One of these is the dragging of preexisting layers into folds, called *fault-drag folds*. Where present, they represent a displacement along the fault zone in addition to the slip. The total displacement, measured outside the zone of disturbance associated with the fault is termed *shift*.

The presence of such drag folds gives slightly more information concerning the fault movement than in cases where they are absent; the sense of fault separation can be determined from observations made on only one side of the fault.

Caution is, however, necessary. The presence of fault-drag folds tends to encourage an impulse to read into the pattern something more than the limited measurement of separation. For example, the map patterns shown in Fig. 8.25 have been mistakenly used as an indication of strike slip. While this is certainly one possibility, there is no more evidence of such slip than if the folds were absent. This fact can be verified by a down-plunge view of the line of intersection of the fault and the fold.

Further, considerable care is needed in interpreting the genesis of such folds. Similar final results can be obtained from an initial flexure which developed into a fault at a late stage, and the simultaneous development of folds and faults has been demonstrated experimentally (Dubey, 1980).

The second association occurs when the fault surface is curved. As a result of movement on a generally curved fault, at least one of the blocks must deform in order to maintain contact across the fault. These are *fault-bend folds* (Suppe, 1983).

An instructive special case involves structures which develop during slip on a listric normal fault. As a result of slip on the detachment part of the surface, the hangingwall block tends to be pulled away from the steeper, near-surface portion of the fault. If the block was completely rigid a crevasse-like gap would form (Fig. 8.26a), but because

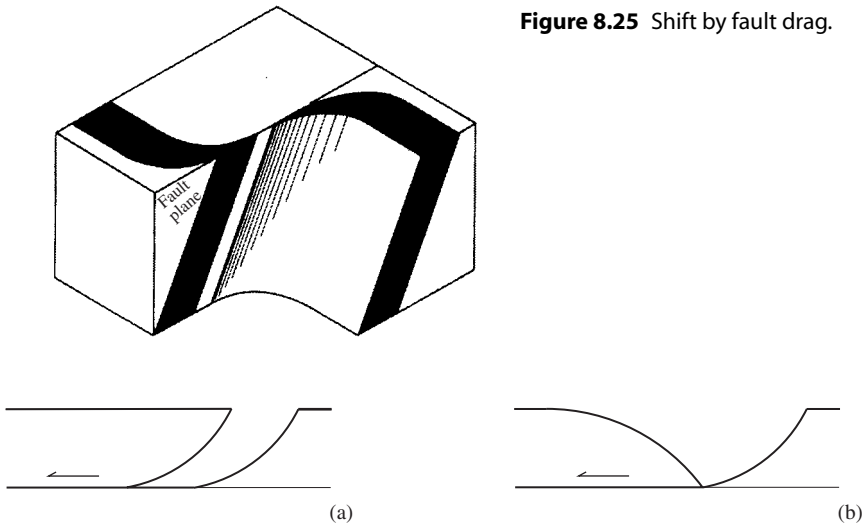


Figure 8.25 Shift by fault drag.

Figure 8.26 Rollover anticline.

rocks are weak the block sags into the potential opening and the resulting fold is called a *rollover anticline* (Fig. 8.26b).

An even more important example is the association of folds with changes in dip on thrust faults. It is common for thrust in bedded rocks to have alternating *flats* and *ramps*. A consequence is that a *ramp anticline* develops in the hangingwall block (Fig. 8.27). Ramsay (1992) makes the important point that both blocks may be involved in deformation.

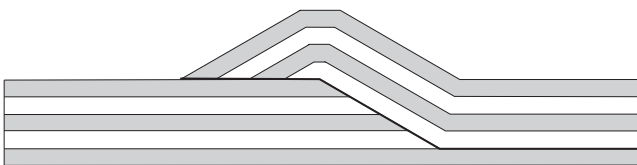


Figure 8.27 Ramp anticline.

### 8.9 Extension and contraction

Slip vectors also have *horizontal* components. This component, together with the slip sense, is a measure of the *extension* or *contraction* associated with the fault. Determination of this component requires a view of the vertical plane containing the slip vector. Examples for pure dip slip will illustrate the method.

1. Extension associated with a normal fault ( $\delta = 60^\circ$ ), assuming unit slip ( $D = 1$ ) is 0.50 (Fig. 8.28a).

2. Contraction associated with the thrust fault ( $\delta = 30^\circ$ ) with unit slip is 0.87 (Fig. 8.28b).

More generally, the magnitude of the horizontal component  $D_H$  of slip may also be calculated from

$$D_H = D \cos \delta, \quad (8.4)$$

where  $D$  is the magnitude of the slip vector and  $\delta$  is its dip. If the fault has an oblique component, the apparent dip  $\alpha$  of the slip vector in the fault plane should be used in this formula.

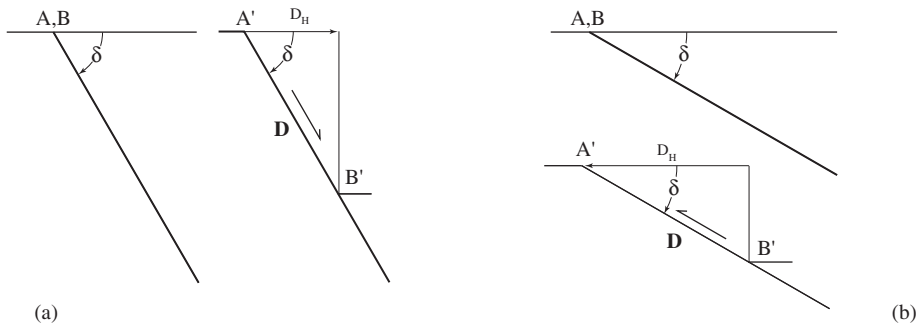


**Figure 8.28** Extension and contraction: (a) normal fault; (b) reverse fault.

Both horizontal extension and contraction are associated with strike-slip faults. A good example is the Jura Mountains of France and Switzerland (Fig. 8.29): faults which trend in a northerly direction are left-slip faults and those trending in a westerly direction are right-slip faults. Both indicate that there is an increase in length parallel to the arcuate fold belt.

In several situations when dealing with the displacement on faults it is convenient to introduce a parameter of change in overall length. The *extension*  $e$  is defined as the fractional change in length or

$$e = (l' - l)/l. \quad (8.5a)$$

Note that *extension* now has two meanings. In the narrow sense, as in ordinary English, it means an increase in length. In the broader technical sense it means a change in length, whether a decrease or increase. It is important to make clear which is meant explicitly or by context. A closely related measure is the *stretch*  $S$  defined as

$$S = l'/l = e + 1. \quad (8.5b)$$

With these measures the cases of decrease and increase in length are:

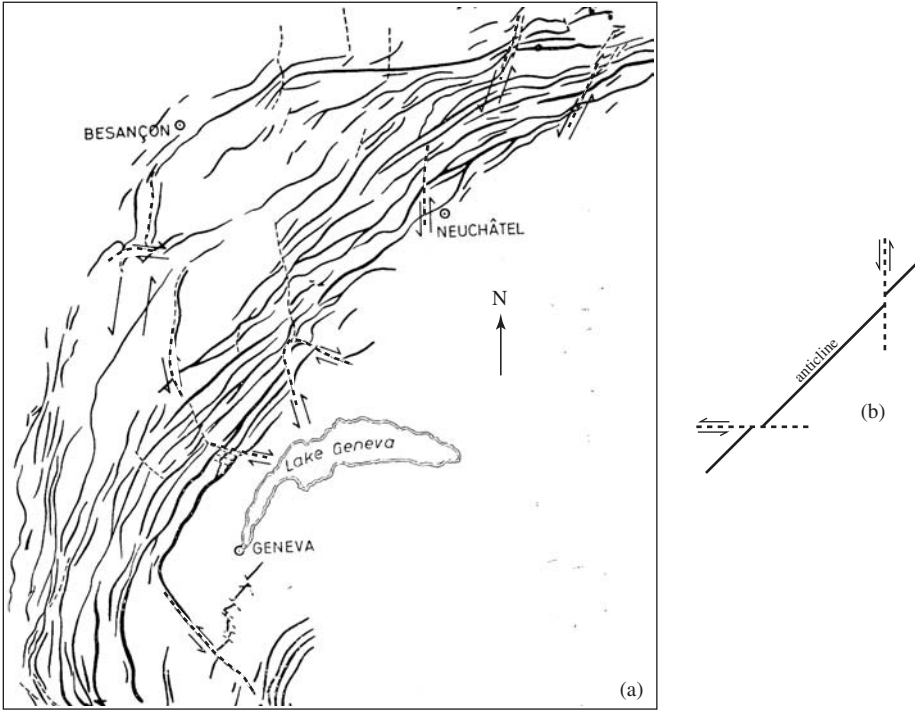


**Figure 8.29** Horizontal extension and contraction with strike-slip faults: (a) Jura fold-thrust belt; (b) schematic extension parallel to folds.

1. If the line is contracted ( $l' > l$ ), then  $e < 0$  and  $S < 1$ . For example, if  $e = -0.3$  the line has been reduced by 30% of its original length. Correspondingly,  $S = 0.7$  means that the length of the shortened line is 70% of its original length. Figure 8.30 shows the extension associated with a series of normal faults.
2. If the line is elongated ( $l' < l$ ), then  $e > 0$  and  $S > 1$ . For example, if  $e = 0.3$  the line is 30% longer than its original length. Correspondingly,  $S = 1.3$  means that the line is now 130% of its original length. Although it is usually much more difficult to evaluate, Fig. 8.20 is an example where such an approach is applied.

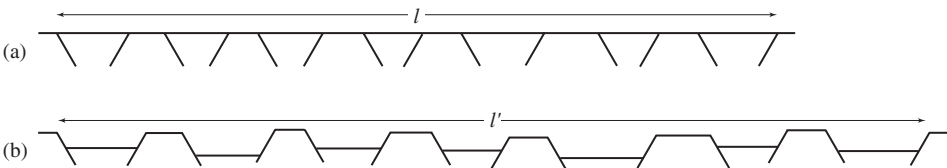


**Figure 8.30** Extension associated with a group of normal faults: (a) horizontal length  $l$  before faulting; (b) horizontal length  $l'$  after faulting.

## 8.10 Rotation

Rotation of one or both fault blocks may also occur and there are two important classes. The first involves rotation about an axis perpendicular to the plane of the fault. Such *rotational faults* include *hinge* and *pivotal* faults (Donath, 1963); Fig. 8.31 illustrates both of these types of rotation. Some care is required to distinguish between these two cases if exposures are not complete. Such ideally rigid rotations can not characterize a whole or even a significant part of a fault because the displacement away from the rotation axis would rapidly become excessive.

Further a rotational component must be present on all translational faults where they die out. Table 8.4 gives the terminology for describing the sense of rotation.

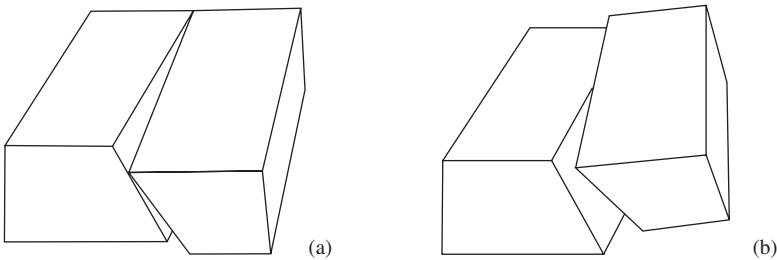


**Figure 8.31** Rotational faults: (a) hinge fault; (b) pivotal fault.

**Table 8.4** *Types of rotation on planar faults*

Clockwise rotation	Clockwise rotational fault (opposite block rotated relatively clockwise).
Anticlockwise rotation	Anticlockwise rotational fault (opposite block rotated relatively anticlockwise).

The rotational component can be determined if a plane has been displaced across the fault. The paper models used to illustrate the relationships between slip and separation can also be useful for showing the effects of a rotational component. As before, make separate drawings depicting the footwall and hangingwall sides of a fault each with a single cut-off line. From the starting position simply use a pin to act as an axis and rotate the hangingwall sheet (Fig. 8.32a). Such a rotation can also be combined with a translation (Fig. 8.32b), but note that the order of rotation and translation makes a difference.

### Problem

- Determine the angle and sense of rotation for the planar fault shown in the map of Fig. 8.33a.



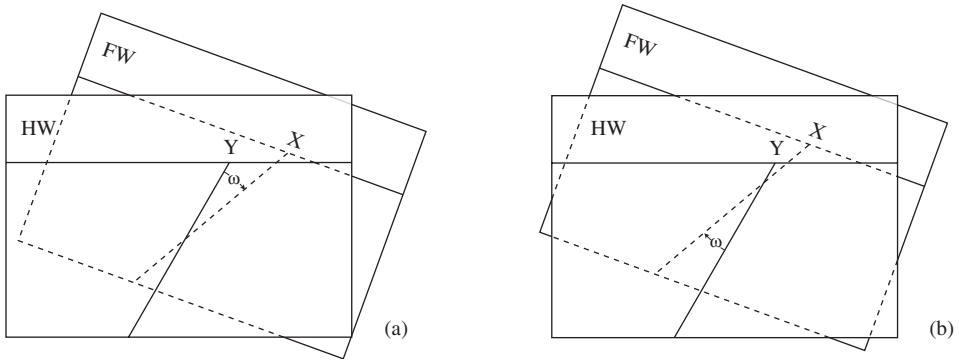


**Figure 8.32** Model of rotation: (a) pure rotation; (b) rotation plus translation.

**Method**

- The cut-off lines on the footwall and hangingwall sides of the fault can be plotted from their pitch determined on the stereonet and the angle between them is the angle of rotation. More directly, the rotation angle is simply the difference of the two pitch angles.

**Answer**

- The fault displays clockwise rotation through an angle of  $\omega = 30^\circ$ .

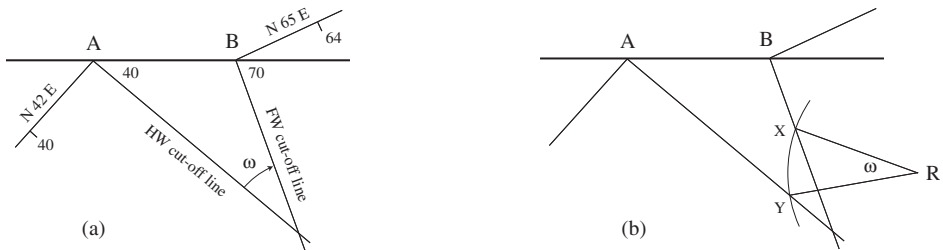


**Figure 8.33** Rotational fault: (a) map and direct view; (b) center of rotation.

If two piercing points can also be located ( $X$  and  $Y$  of Fig. 8.33b), a center of rotation  $R$  can also be found. It lies at the apex of the isosceles triangle whose base is  $XY$  and apex angle is the rotational angle. If rotation and translation are combined, this construction always locates a center, which would account for the displacement by rotation alone. Thus if a rotational component is present, and only two piercing points are known, the translational component remains indeterminate.

Despite this limitation, the construction of the rotation center  $R$  of Fig. 8.33b can be used to locate any structure on the opposite block. If sets of points could be found at two

different locations, and the angle of rotation is constant, the rotational centers will coincide in the case of rotation only, but will differ if a component of translation is involved. It should then be possible to separate the rotational and translational components.

In the second class, rotation occurs about an axis which is parallel to the fault surface, and the conditions under which it can occur are fairly restrictive.

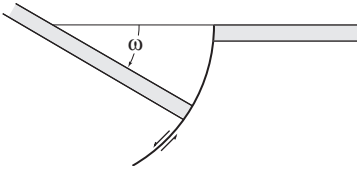


**Figure 8.34** Rotation on a curved fault.

One situation where rotation as a rigid body can occur is when the fault surface has the form of a cylinder of circular cross-sectional shape. Any other shaped curve requires that one or both of the blocks deform during slip, and we treat this case in the next section.

Figure 8.34 illustrates a normal faulting with a curved fault, and the result is a *tilted fault block*. Note that the fault has a high angle at the surface and a lower angle at depth. Probably no fault has such an ideal shape but it may be closely approximated, especially near the surface. Such rotation is described by the angle  $\omega$  between an initial and final line in the plane perpendicular to the rotation axis. If the fault displaces horizontal beds it is then just the final dip angle.

The geometry of rotation on near-circular faults has two important implications. The first is that the tilted block must be fault-bounded, otherwise the displacement will be excessive and a consequence is that such faults occur in sets. The second implication is that there must be a change in the shape of the fault at depth, and the presence of a flat or gently dipping *detachment fault* is implied. The result is then a *listric normal fault*.

The importance of recognizing the true shape of listric faults in estimating slip is shown in the geological sketch map and accompanying cross section of Fig. 8.35, which shows a low-angle normal fault dipping  $5^\circ$  due east displacing Tertiary volcanic rocks and underlying Precambrian basement rocks. Point *Y* at depth represents one piercing point. We need a second. Because the exposed fault is planar and the bedding in the two blocks has the same attitude, it is attractive to project the fault as a straight line to find the point *X*; the distance *XY* is then an estimate of the slip. However, if the exposed fault is actually the flat portion of a listric fault which originally steepened above the cross section, the slip is considerably less.

A second important type of rotation involves both the fault and the fault-bounded blocks (Fig. 8.36). It should be noted that the rotation of the fault significantly increases the horizontal component of the slip. As before, such faults tend to occur in groups, and the geometrical problems at depth imply the existence of a detachment surface at depth.

If a tabular body is extended in this way, rotation of the faults or beds will occur. Two separate cases arise. In the first, planar faults, together with the displaced beds, rotate.

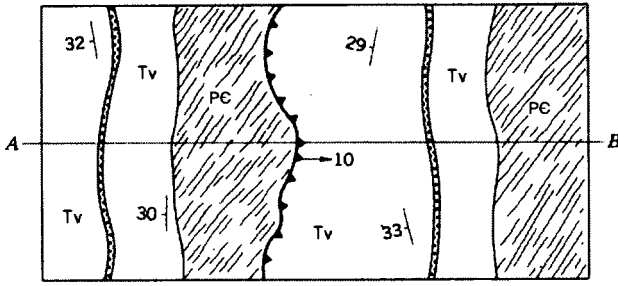


**Figure 8.35** Low-angle normal fault (after Wernicke & Burchfiel, 1982).

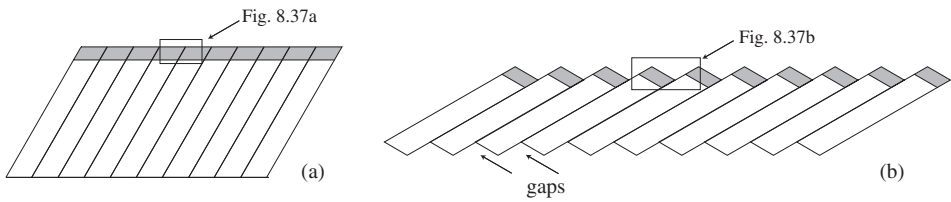
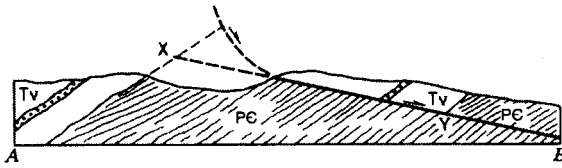


**Figure 8.36** Rotation on multiple planar normal faults.

This geometry is shown in Fig. 8.36. Following Thompson (1960) we may obtain an expression for the combined effects of slip and rotation. From Fig. 8.37b,  $\omega$  is the angle of rotation of the originally horizontal bedding,  $\delta$  is the dip of the fault before and  $\delta'$  is the dip of the fault after rotation. Then from the Law of Sines applied to triangle  $A'B'C'$

$$l' / \sin \theta = l / \sin \delta' \quad \text{or} \quad l' / l = \sin \theta / \sin \delta'.$$

Also from this figure  $\theta = 180^\circ - (\omega + \delta')$ , hence  $\sin \theta = \sin(\omega + \delta')$ . Then

$$l' / l = \sin(\omega + \delta') / \sin \delta'. \tag{8.6}$$

With the definitions of Eq. 8.5a we have

$$e = \frac{\sin(\delta' + \omega)}{\sin \delta'} - 1. \tag{8.7}$$

Figure 8.37c is a graph of this equation.

In the second case, we model a listric normal fault by assuming that the traces of both the fault and folded bedding in cross section are represented by circular arcs (Fig. 8.38a).

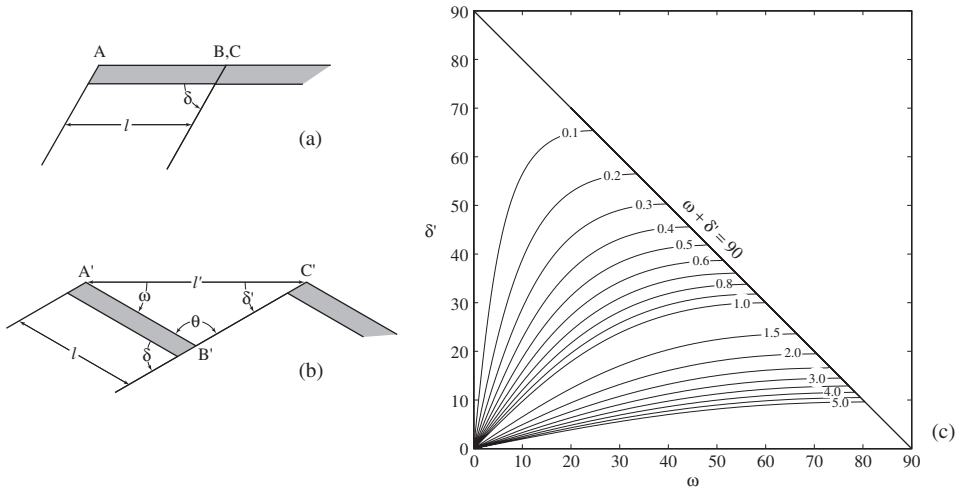


**Figure 8.37** Slip and rotation: (a) initial geometry; (b) final geometry; (c) values of  $e = 0.1$ – $5.0$  (note that the limiting case occurs when  $\omega + \delta' = 90^\circ$ ).

If the original length  $l$  is represented by the length of arc  $BQ$  with radius of curvature  $r_2$  and

$$l = \omega r_2 \quad (\omega \text{ in radians}),$$

the extended equivalent  $l'$  is represented by the straight line segment  $AB$ . From right Triangle I in Fig. 8.38b, and noting that point  $Q$  is the midpoint of the segment  $AB$  hence  $AQ = QB$ ,

$$l' = 2r_1 \sin \delta_S,$$

where  $\delta_S$  is the dip of the fault at surface point  $A$ . With both  $l$  and  $l'$  known, the horizontal extension due to the listric fault is

$$e = \frac{2r_1 \sin \delta_S}{\omega r_2} - 1 \quad (\omega \text{ in radians}). \tag{8.8}$$

We can also express radius  $r_2$  in terms of radius  $r_1$  and use the result to eliminate from this expression  $r_2$ . From right Triangle II

$$b = r_1 \cos \delta_S \tan \frac{1}{2}\omega$$

and from right Triangle III

$$c = r_2 \tan \frac{1}{2}\omega.$$

Because  $AB = 2(b + c)$

$$2r_1 \sin \delta_S = 2 \left[ r_1 \cos \delta_S \tan \frac{1}{2} \omega + r_2 \tan \frac{1}{2} \omega \right]. \tag{8.9}$$

Solving this for  $r_2$  gives

$$r_2 = r_1 \left[ \frac{\sin \delta - \cos \delta \tan \frac{1}{2} \omega}{\tan \frac{1}{2} \omega} \right]. \tag{8.10}$$

Using this in Eq. 8.8 and noting that  $\omega = \delta_S - \delta_D$ , where  $\delta_D$  is the dip of the fault at point  $D$ , we finally obtain

$$e = \frac{2}{\omega \left[ \cot \frac{1}{2} \omega - \cot(\omega + \delta) \right]} \quad (\omega \text{ in radians}). \tag{8.11}$$

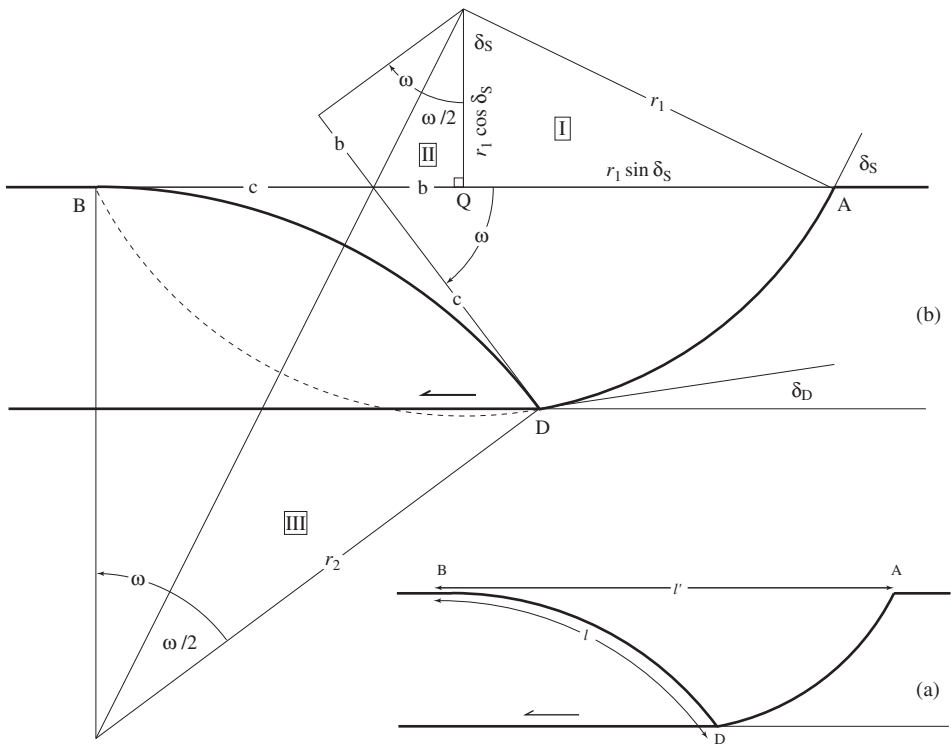


**Figure 8.38** Model listric normal fault (after Wernicke & Burchfiel, 1982, p. 107).

Figure 8.39 graphically illustrates the difference between the extension associated with rotated planar faults (Eq. 8.7) and listric normal faults (Eq. 8.11) in otherwise similar situations. Note that the rotation of the faults greatly increases the overall extension.

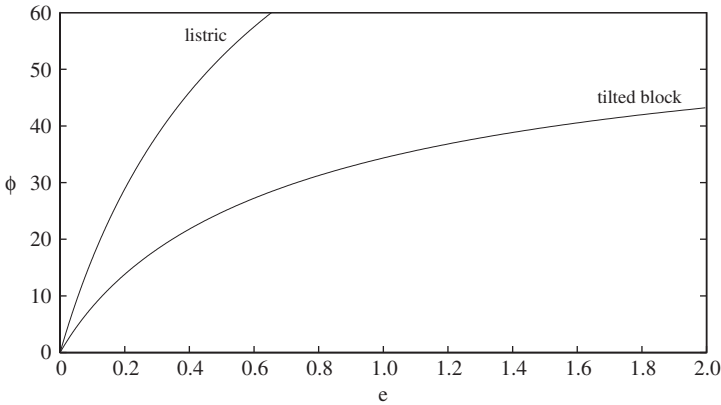


**Figure 8.39** Extension for listric and planar normal faults (after Wernicke & Burchfiel, 1982, p. 108).

**8.11 Facing on faults**

Measures of slip and separation are purely geometrical aspects of the description of fault displacement. Where possible additional geological information should be incorporated into such descriptions. One of these is the facing on the fault. A fault is said to *face* in the direction in the fault plane which is at right angles to the trace of the bedding and towards the younger beds (Lisle, 1985b; also Holdsworth, 1988). The two faults illustrated in Fig. 8.40 are geometrically identical but they face in opposite directions and therefore they are geologically distinct.

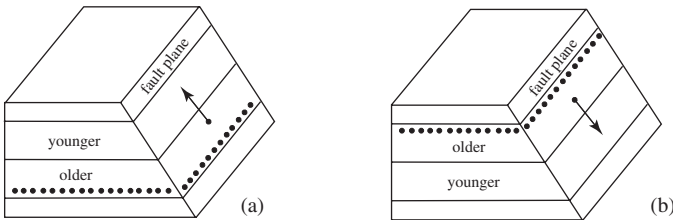


**Figure 8.40** Facing on faults: (a) upward facing; (b) downward facing.

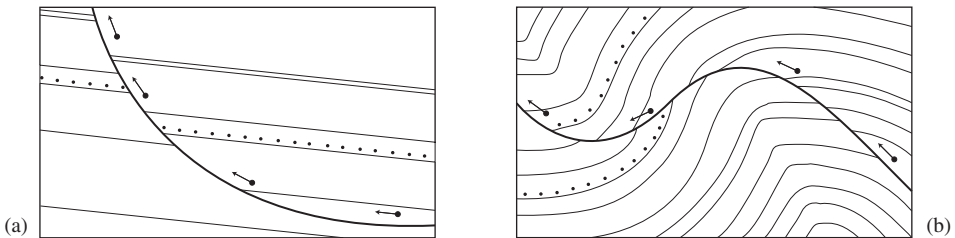


**Figure 8.41** Continuous change in facing directions (after Lisle, 1985b).

There are two general patterns exhibited by changes in facing directions. First, the changes may be *continuous*.

1. If a curved fault cuts individual beds in a particular section just once, the facing directions along the fault will change continuously (Fig. 8.41a).
2. A fault which cuts beds which are folded has a continuously changing facing direction which indicates that the fault has been folded (Fig. 8.41b).

On the other hand the changes in the facing direction on a fault may be *discontinuous*, and this may arise in several ways.

1. A curved fault may cut individual beds more than once and show discontinuous changes in facing direction (Fig. 8.42a).
2. A fault which cuts folded beds with discontinuous facing direction implies that the folding preceded the faulting (Fig. 8.42b).

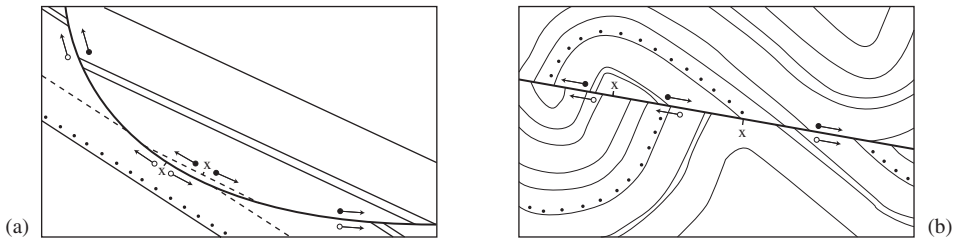


**Figure 8.42** Discontinuous change in facing directions (after Lisle, 1985b).

## 8.12 Dilation of dikes

A closely related problem concerns the direction and amount of the displacement of the emplacement of a dike (Bussell, 1989; Kretz, 1991). This is described by the orientation and length of a *relative dilation vector*  $\mathbf{D}$ . Like the relative slip vector, this gives the displacement of one wall relative to the other. Also like slip,  $\mathbf{D}$  is the line joining two formerly adjacent points on opposite walls of the dike.

This problem is easily solved if the dike cuts two intersecting planes. A line joining corresponding points at the intersection of the dike and such a plane across the dike is an *offset line* (which need not be horizontal). The dilation vector  $\mathbf{D}$  is parallel to the plane containing an offset line and the trace of the plane on the wall of the dike. The line of intersection of two such planes then fixes the angle  $\phi$   $\mathbf{D}$  makes with the pole of the wall. If  $\phi = 0$ , then  $\mathbf{D}$  coincides with the pole vector  $\mathbf{P}$  and the dike made space for itself by simple widening.

### Problem

- A dike with outcrop width  $w = 10$  m strikes due north and dips  $70^\circ$ . Plane A (N  $40^\circ$  W,  $60^\circ$  S) and Plane B (N  $60^\circ$  E,  $50^\circ$  N) are offset across the dike (Fig. 8.43a). Determine the orientation and length of the dilation vector associated with the dike.

### Solution

1. Plot the trace of the parallel walls of the dike as a great circle on a stereogram and add its pole  $P$  (Fig. 8.43b).
2. Also plot the great circles representing the offset planes A and B. These intersect the two offset planes at points  $I_A$  and  $I_B$  to give the orientation of the cut-off lines on both the hangingwall and the footwall.
3. Plot the orientation of offset line  $a$  (here horizontal) as a point and trace in the great circle through  $a$  and A. Repeat for offset line  $b$  (also horizontal).
4. The intersection of these two arcs fixes the orientation of the dilation line  $D$  and its plunge and trend can be read. Also measure the angle  $\phi$  between Dike pole  $P$  and line  $D$ .

### Answer

- The orientation is **D(09/116)** and  $\phi = 26^\circ$ . There are two possible interpretations: emplacement of the dike was accomplished by oblique dilation or the fracture into which the dike intruded was a fault.

The magnitude of the vector is found by combining  $t = w \sin \delta$  (Eq. 2.1) and  $t = D \cos \phi$  to give

$$D = \frac{w \sin \delta}{\cos \phi}. \quad (8.12)$$

With  $w = 10.0$  m, this gives  $D = 10.5$  m.

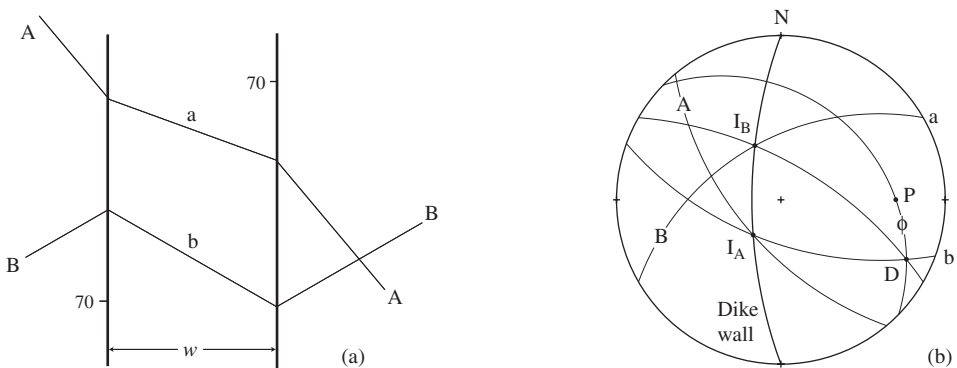


**Figure 8.43** Dilational dike: (a) geological map; (b) stereogram.



**8.13 Exercises**

1. The plane of a normal slip fault strikes due north and dips  $60^\circ$  to the west. The fault displaces a structural plane whose attitude is N 90 W, 30 N and which shows 100 m of left separation. What is the slip?
2. A fault whose attitude is N 90 W, 60 N cuts two structural planes: Plane 1 has an attitude of N 45 W, 30 NE, and Plane 2 has an attitude of N 50 E, 45 NW. The amounts and senses of separation are shown in Fig. 8.44a. What is the orientation and magnitude of the relative slip vector, and what is the slip-based name of the fault?
3. A fault whose attitude is N 30 E, 60 W displaces two planes as shown in Fig. 8.44b. What is the angle and sense of rotation? Locate the center of rotation which will account for the observed displacements.

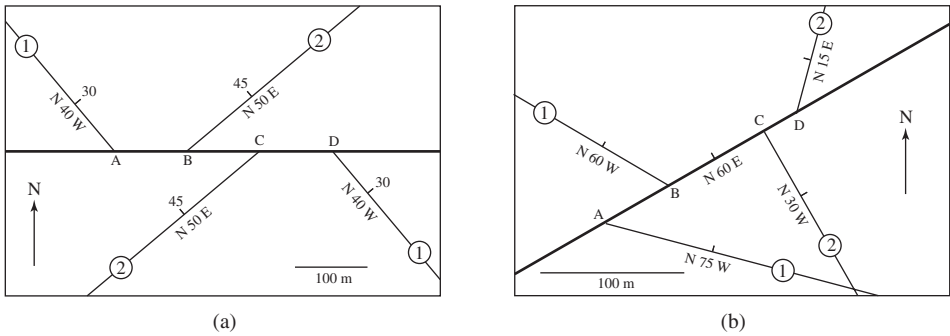


**Figure 8.44**

# 9

## Stress

### 9.1 Introduction

By Newton's Second Law *force*  $\mathbf{F}$  is the product of mass  $m$  and acceleration  $\mathbf{a}$ . With both magnitude and direction, it is a vector quantity. If a mass of one kilogram is given a linear acceleration of one meter per second per second, the magnitude of the force is one newton ( $1 \text{ N} = 1 \text{ kg} \cdot \text{m/s}^2$ ).<sup>1</sup>

The moment of a force or *torque*  $\mathbf{M}$  is also a vector quantity. If a force of one newton acts perpendicular to a moment arm one meter long, the torque is one newton meter ( $1 \text{ N m}$ ). As vectors, forces and torques can be manipulated according to the rules of vector algebra.

If the surface and body forces acting on a material body are balanced in such a way that it is at rest, the body is said to be in a state of *static equilibrium*. Two conditions must prevail for this state to exist. The first is that the total force must vanish, or in other words, the vector sum of all the  $N$  forces must be zero. This condition is expressed by the vector equation

$$\mathbf{F}_1 + \mathbf{F}_2 + \mathbf{F}_3 + \cdots + \mathbf{F}_N = \mathbf{0}.$$

Resolving each force into its components in each coordinate direction we have a necessary condition for equilibrium in the form of three scalar equations in terms of the magnitudes of these force components

$$\sum F_x = 0, \quad \sum F_y = 0, \quad \sum F_z = 0. \quad (9.1)$$

<sup>1</sup>The *newton* is named after the English physicist and mathematician Isaac Newton [1642–1727] who established the modern concept of force and used it in formulating the laws of motion. He also confounded the calculus with the German philosopher, mathematician and logician Gottfried Wilhelm Leibniz [1646–1716].

The second condition is that the total torque must also vanish, that is, the vector sum of all the  $N$  moments of the forces must be zero, or

$$\mathbf{M}_1 + \mathbf{M}_2 + \mathbf{M}_3 + \cdots + \mathbf{M}_N = \mathbf{0}.$$

This leads to a second necessary condition in the form of three scalar equations for the magnitudes of the torque components

$$\sum M_x = 0, \quad \sum M_y = 0, \quad \sum M_z = 0. \quad (9.2)$$

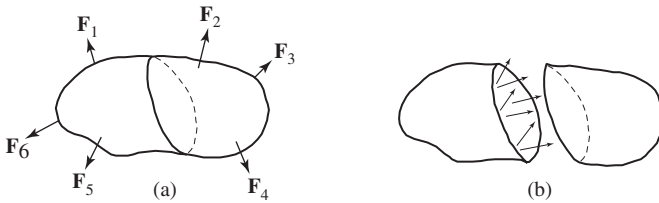


**Figure 9.1** Applied forces: (a) static equilibrium; (b) forces acting on a plane.

## 9.2 Traction

Consider a body subjected to several forces and in a state of static equilibrium (Fig. 9.1a). Due to these *external forces*, there will be *internal forces* acting between various parts of the body. We wish to determine the nature of these internal forces, and we start by examining the effect on a plane, real or imagined, within the body.

Across any such plane there will exist a field of forces equivalent to the loads exerted by the material on one side of the plane onto the material on the other (Fig. 9.1b). In general, these forces will not be uniform in either direction or magnitude. However, if we consider smaller and smaller areas in the vicinity of some point  $O$  the variation in direction and magnitude will also be smaller. Then, as the area in the neighborhood of this point becomes very small, the ratio of force  $\Delta\mathbf{F}$  to area  $\Delta A$  tends to a finite limit called the *traction*  $\mathbf{T}$  at that point, that is,

$$\mathbf{T} = \lim_{\Delta A \rightarrow 0} \frac{\Delta\mathbf{F}}{\Delta A} = \frac{d\mathbf{F}}{dA}. \quad (9.3)$$

In this context “at a point” means on the infinitesimal area  $dA$  surrounding the point. The traction may, of course, be homogeneous over a larger area. The equation simply insures that  $\mathbf{T}$  can always be defined.<sup>2</sup>

<sup>2</sup>This definition is an idealization. In reality, if the area is so small that the adjacent volume of material contains only a few individual atoms it is the attractive and repulsive atomic forces that are important. The analysis of such forces is much more complicated. Thus the area  $dA$  should be small but not too small. We return to this important matter in §11.3.

Traction has the dimensions of force per unit area. A force of one newton acting on one square meter is one pascal ( $1 \text{ N/m}^2 = 1 \text{ Pa}$ ).<sup>3</sup> A pascal is very small, so it is convenient in geology and geotechnical engineering to use kilopascals ( $1 \text{ kPa} = 10^3 \text{ Pa}$ ) or megapascals ( $1 \text{ MPa} = 10^6 \text{ Pa}$ ). A megapascal is equivalent to  $1 \text{ N/mm}^2$  making this a particularly useful multiple. In geophysical studies of the deeper parts of the earth, gigapascals are appropriate ( $1 \text{ GPa} = 10^9 \text{ Pa}$ ). In the past much of the geological literature has expressed tractions in bars and kilobars. The factors for converting these to pascals are easily remembered:

$$1 \text{ bar} = 10^5 \text{ Pa} = 0.1 \text{ MPa} \quad \text{and} \quad 1 \text{ kilobar} = 100 \text{ MPa}.$$

The orientation of  $dA$  is specified by the unit vector  $\hat{\mathbf{n}}$  normal to its plane. To distinguish the two sides of this plane  $\hat{\mathbf{n}}$  is chosen to point toward either part. Once this choice is made, the part toward which  $\hat{\mathbf{n}}$  points is identified as the positive side and the traction which the material on this side exerts on the opposite side is  $\mathbf{T}$ . Equilibrium requires that there be an equal and opposite traction  $-\mathbf{T}$  acting on the other side of  $dA$  whose orientation is given by the unit vector  $-\hat{\mathbf{n}}$ .

Generally the directions of  $\mathbf{T}$  and  $\hat{\mathbf{n}}$  do not coincide (Fig. 9.2a), and it is then convenient to resolve  $\mathbf{T}$  into a *normal* component  $\mathbf{T}_N$  perpendicular to the plane, and a *shearing* component  $\mathbf{T}_S$  tangential to the plane (Fig. 9.2b). These two components are also called, loosely, the *normal stress* and *shearing stress* acting on the plane. In much of the engineering and geological literature the symbol for the magnitude of the normal component is  $\sigma$  (sigma) and for the magnitude of the shearing component it is  $\tau$  (tau), and we will follow this usage.

Similarly,  $-\mathbf{T}$  also has equal and opposite normal and shearing components. If the normal components of  $\mathbf{T}$  and  $-\mathbf{T}$  are directed away from each other the material across the plane is in *tension* and if they are directed toward each other the material across the plane is in *compression*.

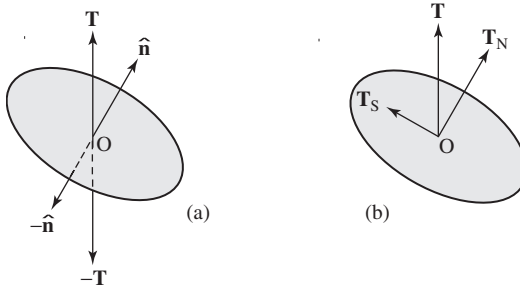


**Figure 9.2** Element  $dA$ : (a)  $\mathbf{T}$  and  $-\mathbf{T}$ ; (b)  $\mathbf{T}_N$  and  $\mathbf{T}_S$ .

<sup>3</sup>The *pascal* is named after the French polymath Blaise Pascal [1622–1662] whose experiments led to the invention of the barometer, which he then used to demonstrate that atmospheric pressure decreases as elevation increases.

### 9.3 Stress components

For a given set of applied forces, the traction  $\mathbf{T}$  at a point depends on the orientation of  $\hat{\mathbf{n}}$  and thus for different orientations the traction will, in general, also be different. The totality of the tractions for all orientations constitutes the *stress* in the material at that point.

If the tractions on three mutually perpendicular planes are known, the traction acting on any other plane can then be found. For these it is convenient to adopt planes which are related to our chosen coordinate system. Thus we represent these three planes by the faces of a volume element  $dx\,dy\,dz$  whose edges are parallel to the  $x$ ,  $y$  and  $z$  axes of a Cartesian coordinate system (Fig. 9.3).

On each of the three visible faces of this volume element the components of each traction act in a coordinate direction. The corresponding components acting on the three concealed faces are antiparallel. In all there are nine pairs of these, called the *Cartesian stress components*, which may be written as the ordered array or matrix

$$\begin{bmatrix} \sigma_{xx} & \tau_{xy} & \tau_{xz} \\ \tau_{yx} & \sigma_{yy} & \tau_{yz} \\ \tau_{zx} & \tau_{zy} & \sigma_{zz} \end{bmatrix}.$$

This is the *stress matrix*. Writing the components in this way it is easy to keep track of them. It also emphasizes the important fact that stress is a single entity, albeit with nine components.

In this notation, the first subscript identifies the coordinate direction in which the component acts and second identifies the plane by giving the coordinate direction of its outward normal (Nye, 1985, p. 82; Oertel, 1996, p. 46).<sup>4</sup>

As can be seen, each column contains the components which act on a single face and each row of the matrix contains the components which act in a single coordinate direction. Note too that the subscripts for the normal components are the same and the subscripts for the shearing components are different, hence it is not really necessary to use separate symbols for the normal and shearing components. In most of this chapter we will continue to use them, however, in order to maintain continuity with the previously established symbols for the traction components.

Because each of these components may act in either of two directions, signs are used to distinguish their sense. The most widely used convention throughout mechanics assigns a *positive* sign to a component which acts in a positive coordinate direction on a face whose outward normal is in a positive coordinate direction or which acts in a negative coordinate direction on a face whose outward normal is in a negative coordinate direction. Accordingly, all the nine components on the three visible faces of Fig. 9.3 are

<sup>4</sup>Others reverse the meaning of these subscripts (e.g., Johnson, 1970, p. 182; Jaeger & Cook, 1979, p. 18; Middleton & Wilcock, 1994, p. 119; Davis & Selvadurai, 1996, p. 19), but this causes some difficulties later (see §9.12).

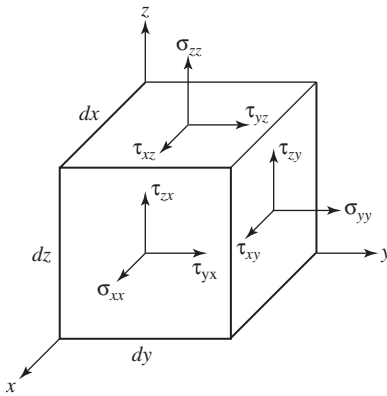


**Figure 9.3** Volume element  $dx\ dy\ dz$  and the stress components.

positive, as are the corresponding nine components on the three concealed faces. This sign convention is required for a variety of purposes, including computing the traction acting on a specified plane from the stress matrix (see §9.12) and in more advanced applications for describing the relationship between stress and strain or strain rate.

For the volume element to be in a state of static equilibrium certain restrictions must be placed on the shearing components. Equilibrium is expressed in terms of forces (Eq. 9.1) and moments (Eq. 9.2). To apply these conditions it is necessary to convert each traction component to a force and this is accomplished by multiplying each by the corresponding area on which it acts. To convert back to tractions, the forces are then divided by this area. We will use both of these conversions repeatedly in the following derivations.

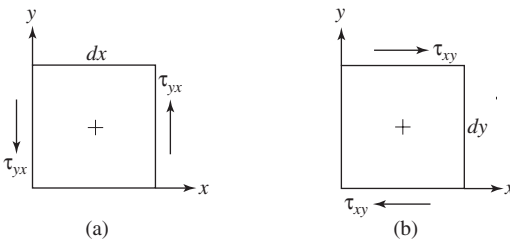


**Figure 9.4** Shearing components: (a)  $\tau_{yx}$ ; (b)  $\tau_{xy}$ .

Only two pairs of traction components contribute to the moment about a line parallel to any coordinate axis. For example, the moment about a line through the center of the volume element in the  $z$  direction is due to the shearing components  $\tau_{yx}$  and  $\tau_{xy}$ . The tangential force in the  $y$  direction on the front face is  $\tau_{yx}\ dy\ dz$ , and a tangential force of equal magnitude acts in the opposite direction on the rear face. The moments due to these tangential forces are found by multiplying each by the length of the moment arm  $\frac{1}{2}dx$  (Fig. 9.4a). The magnitude of the moment due to these two tangential forces is then

$$M_z = 2\tau_{yx}\ dy\ dz(dx/2) = \tau_{yx}\ dx\ dy\ dz.$$

By the right-hand rule, the moment vector associated with this pair of forces points in the  $+z$  direction.

In a similar way, the force in the  $x$  direction associated with the pair of shearing tractions  $\tau_{xy}$  on the right face is  $\tau_{xy} dx dz$ , and a force with equal magnitude acts in the opposite direction on the left face. The lengths of the moment arms are  $\frac{1}{2}dy$  (Fig. 9.4b). The magnitude of the moment due to these two forces is then

$$M_z = 2\tau_{xy} dx dz(dy/2) = \tau_{xy} dx dy dz$$

and the associated moment vector points in the  $-z$  direction. Equilibrium requires that the magnitudes of these two oppositely directed vectors be equal. That is

$$\tau_{yx} dx dy dz = \tau_{xy} dx dy dz,$$

and this reduces to

$$\tau_{yx} = \tau_{xy}.$$

Similar relationships hold for the shearing components acting on the two other pairs of parallel faces. Thus

$$\tau_{xz} = \tau_{zx} \quad \text{and} \quad \tau_{yz} = \tau_{zy}.$$

A matrix for which these three equalities hold is *symmetric* and only six of the elements are independent.

The choice of coordinates is a matter of convenience only. If a different set of axes are chosen the stress components will be different. For example, in the  $x'y'z'$  system axes the components are

$$\begin{bmatrix} \sigma_{x'x'} & \tau_{x'y'} & \tau_{x'z'} \\ \tau_{y'x'} & \sigma_{y'y'} & \tau_{y'z'} \\ \tau_{z'x'} & \tau_{z'y'} & \sigma_{z'z'} \end{bmatrix}$$

but the state of stress in the material will be identical. Of particular interest is the fact that there is a special set of axes which results in an important simplification – only normal components act on the corresponding faces of the volume element. In this system the stress matrix is then reduced to

$$\begin{bmatrix} \sigma_{x'x'} & 0 & 0 \\ 0 & \sigma_{y'y'} & 0 \\ 0 & 0 & \sigma_{z'z'} \end{bmatrix}.$$

These non-zero components are the *principal stresses* and the three mutually perpendicular directions in which they act are the *principal directions*. Such a matrix is said to be

in *diagonal* form. These principal stresses are also the greatest, intermediate and least normal stresses and they are labeled

$$\sigma_1 \geq \sigma_2 \geq \sigma_3.$$

With only three components there is a great advantage in adopting this system with coordinate axes in the principal directions wherever possible. We now show how to do this for the two-dimensional case.

### 9.4 Stress in two dimensions

If the stress components in one of the coordinate directions vanish, the body is said to be in a state of *plane stress*. Strictly, this condition holds for thin plates only, but it is a convenient way to introduce the geometry of the stress state and, as we will see later, the formulation has a more general meaning which makes it particularly useful. Following the usual practice we take all the components in the  $z$  direction to be zero (Fig. 9.5a). This reduces the total number of components from nine to four. This two-dimensional state of stress is represented by the matrix

$$\begin{bmatrix} \sigma_{xx} & \tau_{xy} \\ \tau_{yx} & \sigma_{yy} \end{bmatrix}.$$

Because  $\tau_{xy} = \tau_{yx}$  this matrix is also symmetric and only three of these components are independent. Though the magnitudes of the two shearing components are equal, they are geometrically distinct and we will, in general, retain their separate identities.

We now wish to determine the normal and shearing components of the traction acting on an inclined plane  $AB$  whose orientation is given by the angle  $\theta$  the normal vector  $\hat{n}$  makes with the  $x$  axis (Fig. 9.5b). To do this, we first imagine a wedge-shaped *free body*

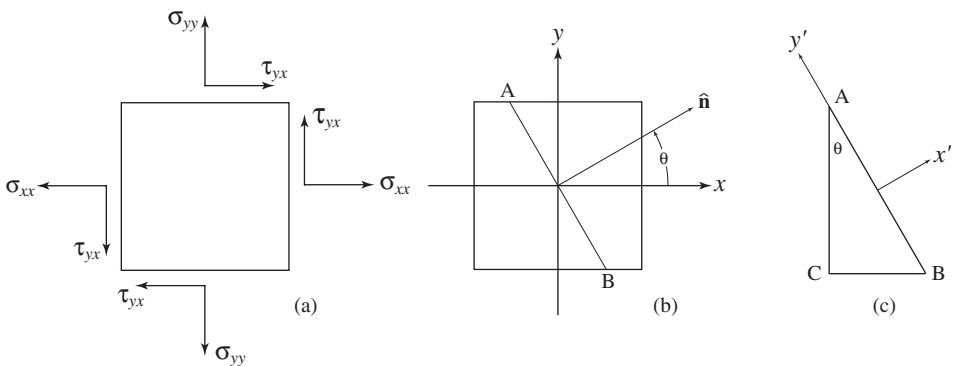


**Figure 9.5** Plane stress: (a) positive components; (b) inclined plane; (c) free body.



cut and isolated from the element (Fig. 9.5c). To restore this body to equilibrium we must replace the action of the material originally adjacent to the inclined plane with equivalent forces. To describe these forces it is convenient to adopt an auxiliary right-handed coordinate system with  $+x'$  in the direction of  $\hat{\mathbf{n}}$  and  $+y'$  parallel to the trace of the plane. We specify the orientation of these axes by the angle  $\theta$  which  $+x'$  makes with the  $+x$  axis. As in coordinate geometry this angle is *positive* if measured in an anticlockwise sense and *negative* if measured in a clockwise sense.

Our approach will be to derive expressions for  $\sigma$  and  $\tau$  in several simple situations separately. Then the total traction acting on the inclined plane is the sum of these separate tractions. Except that it fills out many of the steps, our approach closely follow that generally found in books in the first course on the mechanics of materials (e.g., see Gere, 2001, p. 479f).<sup>5</sup>

### Uniaxial stress

In the first case, the element is subjected to only one principal stress, and we choose this to be in the  $x$  direction (Fig. 9.6a). This state is *uniaxial* and the stress matrix is

$$\begin{bmatrix} \sigma_{xx} & 0 \\ 0 & 0 \end{bmatrix}.$$

If the area of the inclined plane  $AB$  is  $a$ , the corresponding area of side  $AC$  is  $a \cos \theta$  (Fig. 9.6b). The magnitude of the force  $F_x$  acting on side  $AC$  is then equal to the product of the normal component and this area, or

$$F_x = \sigma_{xx}(a \cos \theta), \quad (9.4)$$

and an opposite force of equal magnitude must also act on the inclined plane. We are especially interested in the magnitudes of the normal component  $F_{x'}$  and tangential component  $F_{y'}$  of this force. From the triangle involving these force components (Fig. 9.6b), we have

$$F_{x'} = F_x(a \cos \theta) \quad \text{and} \quad F_{y'} = -F_x(a \sin \theta).$$

Note that for a positive  $\sigma_{xx}$  and a positive  $\theta$ , the component  $F_{y'}$  acts in the  $-y'$  direction, hence the minus sign in the second of these equations. Substituting the expression for  $F_x$  from Eq. 9.4 and converting back to tractions by dividing by area  $a$  we obtain expressions for the magnitudes of the normal and shearing components of the traction acting on this

<sup>5</sup>On a first reading you may wish to skip the derivations and go directly to the results in §9.5. There is, however, much to be learned by working through the details.

inclined plane in terms of the applied uniaxial normal stress and the orientational angle. These are

$$\sigma_{x'x'} = \sigma_{xx} \cos^2 \theta \quad \text{and} \quad \tau_{x'y'} = -\sigma_{xx} \sin \theta \cos \theta. \quad (9.5)$$

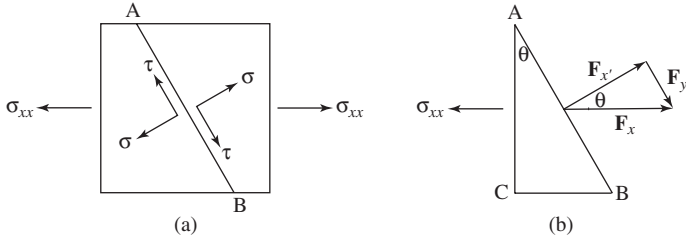


**Figure 9.6** Uniaxial Case 1: (a) component  $\sigma_{xx}$ ; (b) free body and forces.

*Biaxial stress*

If only normal components act in the coordinate directions the state is *biaxial* and the corresponding stress matrix is

$$\begin{bmatrix} \sigma_{xx} & 0 \\ 0 & \sigma_{yy} \end{bmatrix}.$$

To find the traction on the inclined plane in this case we determine the effects of a pair of uniaxial states in the  $x$  and  $y$  directions separately. Already having obtained the results for the first, we now consider the second (Fig. 9.7a). Proceeding as before, the magnitude of the force  $F_y$  on side  $BC$  of the free body is

$$F_y = \sigma_{yy}(a \sin \theta) \quad (9.6)$$

and an equal and opposite force must act on the inclined plane  $AB$  (Fig. 9.7b). From the triangle of forces, the normal and shearing components of the traction due to this force are

$$F_{x'} = F_y(a \sin \theta) \quad \text{and} \quad F_{y'} = F_y(a \cos \theta).$$

Substituting the expression for  $F_y$  from Eq. 9.6 and dividing by area  $a$  gives the corresponding traction components

$$\sigma_{x'x'} = \sigma_{yy} \sin^2 \theta \quad \text{and} \quad \tau_{x'y'} = \sigma_{yy} \cos \theta \sin \theta. \quad (9.7)$$

On summing corresponding pairs in Eqs. 9.5 and 9.7 the combined components are

$$\sigma_{x'x'} = \sigma_{xx} \cos^2 \theta + \sigma_{yy} \sin^2 \theta \quad \text{and} \quad \tau_{x'y'} = (\sigma_{yy} - \sigma_{xx}) \cos \theta \sin \theta. \quad (9.8)$$

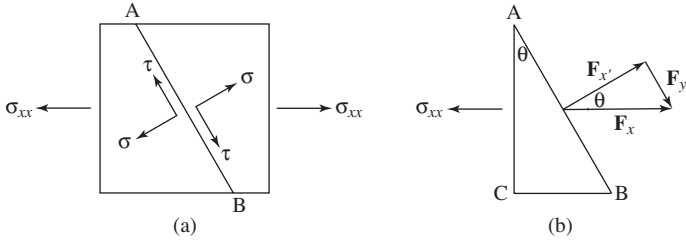


**Figure 9.7** Uniaxial Case 2: (a) component  $\sigma_{yy}$ ; (b) free body and forces.

*Pure shear stress*

Finally, we seek the effects of shearing components acting alone, a condition called *pure shear* (Fig. 9.8a). The stress matrix is now

$$\begin{bmatrix} 0 & \tau_{xy} \\ \tau_{yx} & 0 \end{bmatrix}.$$

Considering each pair of tractions acting on the free body separately, triangles of forces are constructed. First, from Fig. 9.8b the magnitude of  $F_x$  which balances the force due to the shearing component  $\tau_{xy}$  is

$$F_x = \tau_{xy}(a \sin \theta).$$

Second, from the triangle of forces involving this force the normal and tangential components acting on side  $AB$  are

$$F_{x'} = F_x(a \cos \theta) \quad \text{and} \quad F_{y'} = -F_x(a \sin \theta).$$

Again,  $F_{y'}$  acts in the  $-y'$  direction, hence the minus sign. Combining these and dividing by area  $a$ , the corresponding traction components are then

$$\sigma_{x'x'} = \tau_{xy} \sin \theta \cos \theta \quad \text{and} \quad \tau_{x'y'} = -\tau_{xy} \sin^2 \theta. \tag{9.9}$$

Second, from Fig. 9.8c, the magnitude of  $F_y$  which balances the force due to the shearing component  $\tau_{yx}$  is

$$F_y = \tau_{yx}(a \cos \theta),$$

and its normal and tangential components are

$$F_{x'} = F_y(a \sin \theta) \quad \text{and} \quad F_{y'} = F_y(a \cos \theta).$$

The traction components are then

$$\sigma_{x'x'} = \tau_{yx} \cos \theta \sin \theta \quad \text{and} \quad \tau_{x'y'} = \tau_{yx} \cos^2 \theta. \tag{9.10}$$

Combining Eqs. 9.9 and 9.10 and utilizing the equality of the two shear components, we have

$$\sigma_{x'x'} = 2\tau_{xy} \cos \theta \sin \theta \quad \text{and} \quad \tau_{x'y'} = \tau_{xy}(\cos^2\theta - \sin^2\theta). \quad (9.11)$$

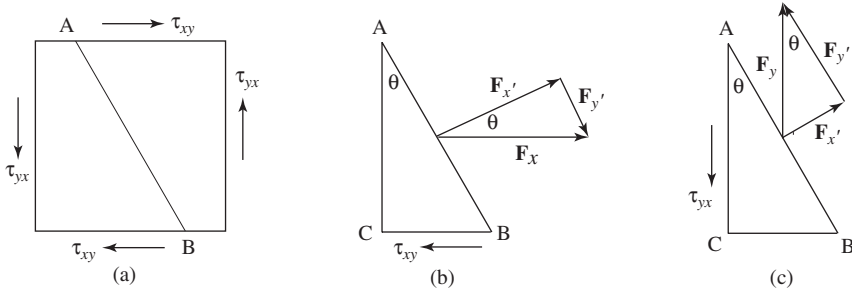


**Figure 9.8** Pure shear: (a)  $\tau_{xy}$  and  $\tau_{yx}$ ; (b)  $F_x$ ; (c)  $F_y$ .

### General two-dimensional stress

The contribution of the full complement of applied stress components to the normal and shearing tractions acting on the inclined plane can now be found by summing the expressions for the biaxial case of Eqs. 9.8 and pure shear case of Eqs. 9.11, giving

$$\sigma_{x'x'} = \sigma_{xx} \cos^2\theta + \sigma_{yy} \sin^2\theta + 2\tau_{xy} \cos \theta \sin \theta, \quad (9.12a)$$

$$\tau_{x'y'} = (\sigma_{yy} - \sigma_{xx}) \cos \theta \sin \theta + \tau_{xy}(\cos^2\theta - \sin^2\theta). \quad (9.12b)$$

Of special interest are the extreme values of the normal component  $\sigma_{x'x'}$  as a function of the orientation angle  $\theta$  and these are found by setting

$$\frac{d\sigma_{x'x'}}{d\theta} = 0.$$

Differentiating Eq. 9.12a with respect to  $\theta$ , setting the result equal to zero and dividing by 2 gives

$$(\sigma_{yy} - \sigma_{xx}) \cos \theta \sin \theta + \tau_{xy}(\cos^2\theta - \sin^2\theta) = 0. \quad (9.13)$$

Comparing this result with Eq. 9.12b we see that when the normal component  $\sigma_{x'x'}$  has an extreme value the shear components  $\tau_{x'y'} = \tau_{y'x'} = 0$ , that is, when the plane is oriented such that the normal component  $\sigma_{x'x'}$  has a maximum or minimum value, the shearing traction is zero. We can find the orientation of the normals to the planes on which these extreme normal tractions act by using the identities

$$\cos \theta \sin \theta = \frac{1}{2} \sin 2\theta, \quad \cos^2\theta - \sin^2\theta = \cos 2\theta, \quad \sin 2\theta / \cos 2\theta = \tan 2\theta,$$

in Eq. 9.13. After some manipulation we obtain

$$\tan 2\theta = \frac{2\tau_{xy}}{\sigma_{xx} - \sigma_{yy}}. \quad (9.14)$$

Two angles  $\theta$  and  $\theta + 90^\circ$  satisfy this expression, hence the maximum and minimum values occur on two mutually perpendicular planes. These extreme normal tractions are the *principal stresses*. We label them  $\sigma_1 \geq \sigma_3$  for two reasons. First, we wish to emphasize that in reality we always deal with a three-dimensional setting. Second, we are especially interested in the greatest and least principal values.

We now choose our coordinate axes to coincide with these two principal directions,  $x$  parallel to  $\sigma_1$  and  $y$  parallel to  $\sigma_3$ . We may then make the following replacement of symbols

$$\sigma_{xx} = \sigma_1, \quad \sigma_{yy} = \sigma_3, \quad \tau_{xy} = \tau_{yx} = 0.$$

When referred to these principal axes the stress matrix has the diagonal form

$$\begin{bmatrix} \sigma_{xx} & 0 \\ 0 & \sigma_{yy} \end{bmatrix} = \begin{bmatrix} \sigma_1 & 0 \\ 0 & \sigma_3 \end{bmatrix}.$$

Also, reverting to the earlier notation  $\sigma = \sigma_{x'x'}$  and  $\tau = \tau_{x'y'}$  Eqs. 9.12 become

$$\sigma = \sigma_1 \cos^2\theta + \sigma_3 \sin^2\theta \quad (9.15a)$$

$$\tau = -(\sigma_1 - \sigma_3) \cos\theta \sin\theta. \quad (9.15b)$$

When using the symbols  $\sigma$  and  $\tau$  for the traction components it must be understood that they act on the plane whose normal is specified by the angle  $\theta$ , otherwise the symbols have no meaning.

## 9.5 Mohr Circle for stress

Before we show how these final results can be put into a special form which leads directly to a graphical representation, we introduce two adjustments of the sign convention to be used in conjunction with this construction.

1. Because normal stresses are predominantly compressive within the earth, the common (but not universal) practice in geology and geotechnical engineering is to reckon compression *positive* and tension *negative*, thus avoiding the minus sign in most cases (Jaeger & Cook, 1979, p. 10). Adopting this convention reverses the labels given to the principal stresses:  $\sigma_1$  is now the greatest compressive or least tensile stress and  $\sigma_3$  is the least compressive or the greatest tensile stress. This also reverses the sign in the expression for  $\tau$  in Eq. 9.15b.

2. For use with the graphical representation we need a special sign convention for the shear components. We now define the sense of shear as *positive* if a pair of shearing tractions act in an anticlockwise sense and as *negative* if they act in a clockwise sense. Accordingly, the magnitudes of  $\tau_{xy}$  and  $\tau_{yx}$  are the same but their signs are different.

We now cast Eqs. 9.15 (using the new signs) into a more useful form. By substituting the double angle identities

$$\cos^2\theta = \frac{1}{2}(1 + \cos 2\theta), \quad \sin^2\theta = \frac{1}{2}(1 - \cos 2\theta), \quad \cos\theta \sin\theta = \frac{1}{2} \sin 2\theta, \quad (9.16)$$

and rearranging we obtain the important results

$$\sigma = \frac{1}{2}(\sigma_1 + \sigma_3) + \frac{1}{2}(\sigma_1 - \sigma_3) \cos 2\theta, \quad (9.17a)$$

$$\tau = \frac{1}{2}(\sigma_1 - \sigma_3) \sin 2\theta. \quad (9.17b)$$

These have the form

$$x = c + r \cos \alpha \quad \text{and} \quad y = r \sin \alpha,$$

which are the parametric equations of a circle of radius  $r$ , centered on the  $x$  axis at a distance  $c$  from the origin (Fig. 9.9a). The angle  $\alpha$  which a radius of this circle makes with the  $+x$  axis locates a point  $P(x, y)$  on the circumference. This property of Eqs. 9.17 allows a variety of problems involving  $\sigma$  and  $\tau$  to be solved graphically with a *Mohr Circle for stress* (Fig. 9.9b). For this circle the location of its center and its radius are given by

$$c = \frac{1}{2}(\sigma_1 + \sigma_3) \quad \text{and} \quad r = \frac{1}{2}(\sigma_1 - \sigma_3). \quad (9.18)$$

The coordinates of each point  $P$  on this circle associated with any radius  $CP$  which makes an angle  $2\theta$  with the  $\sigma_1$  direction represent the normal and shearing components of the traction acting on a plane whose normal makes angle  $\theta$  with the  $\sigma_1$  direction.

The Mohr Circle and the equations from which it is derived represent a transformation of the *physical plane* to the *Mohr Circle plane*. To go to the Mohr Circle plane the orientation angle  $\theta$  is doubled. To return to the physical plane the angle  $2\theta$  is halved. This simple rule is an important key to understanding the Mohr Circle construction.

Representing the orientation of the inclined plane by its unit normal vector is fundamental. Often, however, it is the orientation of the plane itself which is of interest and there is a shortcut which gives the angle  $\beta$  this plane makes with the  $\sigma_1$  direction. On the physical plane  $\theta + \beta = 90^\circ$  (Fig. 9.10a) and on the Mohr Circle plane  $2\theta + 2\beta = 180^\circ$  (Fig. 9.10b). Thus angle  $\beta$  which the plane makes with the  $\sigma_1$  direction can be obtained directly from the diagram. Note, however, that  $\beta$  is measured on the physical plane from  $\sigma_1$ , not from  $\sigma_3$  as the Mohr Circle diagram might suggest, and that  $\beta$  is measured in a sense which is opposite to that of  $\theta$ .

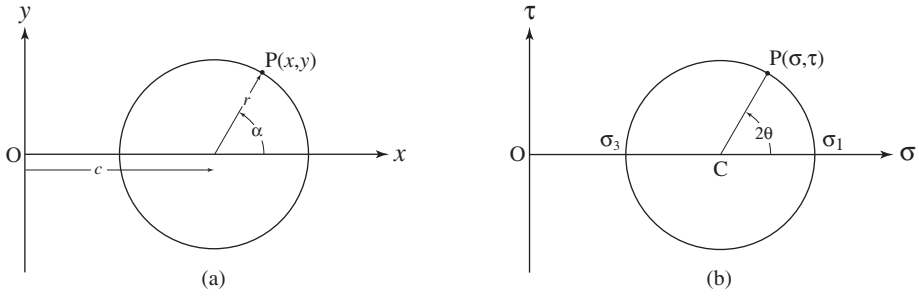


**Figure 9.9** Mohr Circle: (a) basic features; (b) traction components.

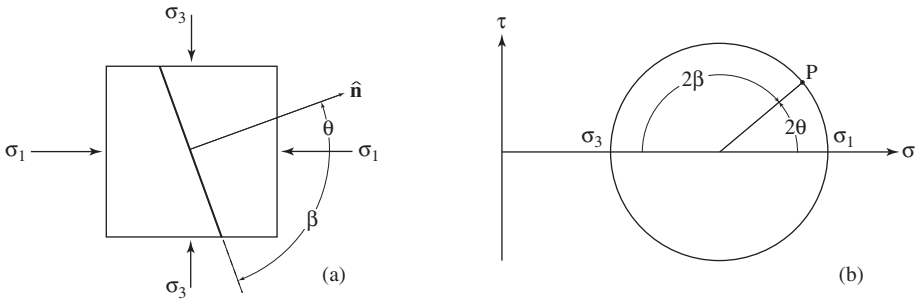


**Figure 9.10** Angle  $\beta$ : (a) physical plane; (b) Mohr Circle plane.

Solving two-dimensional stress problems graphically involves constructing the Mohr Circle and then extracting the required information from it. The simplest case involves first drawing the circle from given principal stresses. The traction components on any inclined plane are obtained by plotting the radius with slope angle  $2\theta$ .

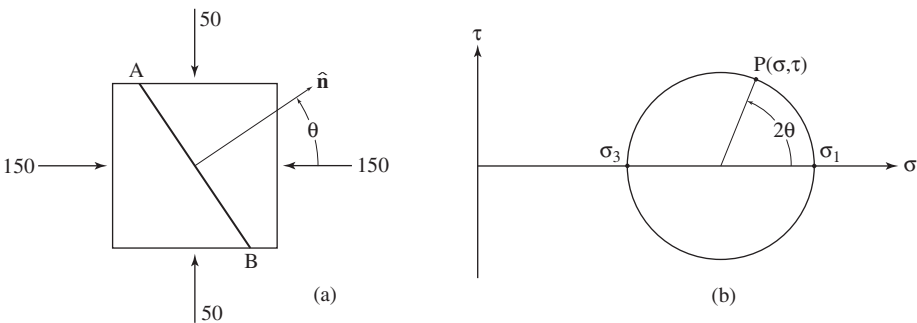


**Figure 9.11** Traction: (a) physical plane; (b) Mohr Circle plane.

**Problem**

- If  $\sigma_1 = 150$  MPa and  $\sigma_3 = 50$  MPa (Fig. 9.11a), what are the traction components on a plane whose normal makes angle  $\theta = +34^\circ$  with the  $\sigma_1$  direction?

### Construction

1. Draw a pair of axes with  $\sigma$  horizontal and  $\tau$  vertical (Fig. 9.11b).
2. Plot the points  $(\sigma_1, 0) = (150, 0)$  and  $(\sigma_3, 0) = (50, 0)$  using a convenient scale. Bisect the distance between these points to locate the center  $C$  and draw the circle with radius  $C\sigma_1 = C\sigma_3$ . Alternatively, with Eqs. 9.18  $c = \frac{1}{2}(\sigma_1 + \sigma_3) = 100$  and  $r = \frac{1}{2}(\sigma_1 - \sigma_3) = 50$ , which can then be used to draw the circle directly.
3. Locate point  $P$  on the circumference of the circle by drawing a radius making an angle of  $2\theta = +68^\circ$  measured in the same sense as  $\theta$  from  $\sigma_1$ , that is, anticlockwise.
4. The coordinates of  $P$  are the values of the normal and shearing tractions acting on the specified plane.

### Answer

- Measuring the coordinate of  $P$  using the same scale gives  $\sigma = 119$  MPa and  $\tau = +46$  MPa. The shearing traction is positive and therefore acts in an anticlockwise sense on the specified plane.

It is useful to check these results by using Eqs. 9.17 to assure yourself that the diagram gives the correct answer. Doing this gives  $\sigma = 118.73033$  and  $\tau = 46.35920$ . Because the decimal parts are not significant, these results are the same as found graphically.

In constructing these diagrams, the scale should be chosen so that the circle is large enough to plot and read the values of the stress components accurately to the appropriate significant figures. In this example, a scale of 1 mm = 1 MPa satisfies this requirement.

If the plotting conventions are correctly and consistently applied, the Mohr Circle gives the proper signs unambiguously. However, the sense of the shear can also be obtained by inspection and this serves as a useful check. To do this imagine that the inclined plane of interest is a frictionless cut. The force equivalent to the maximum principal stress  $\sigma_1$  will then cause the two pieces of the block to slip in the correct sense.

The Mohr Circle may also be constructed from the general stress components. From this circle we may then find the magnitude of the principal stresses and their orientations.

### Problem

- Determine the values of  $\sigma_1$  and  $\sigma_3$ , and their orientations from the stress components (Fig. 9.12a).

### Construction

1. Pair the components so that  $P_x(\sigma_{xx}, \tau_{yx}) = (+310, +100)$  and  $P_y(\sigma_{yy}, \tau_{xy}) = (+150, -100)$ , where  $P_x$  and  $P_y$  represent, respectively, the traction components on the planes whose normals are in the  $x$  and the  $y$  coordinate directions.
2. Plot  $P_x$  and  $P_y$  as a pair of points on a set of  $\sigma\tau$  axes using a convenient scale (Fig. 9.12b).



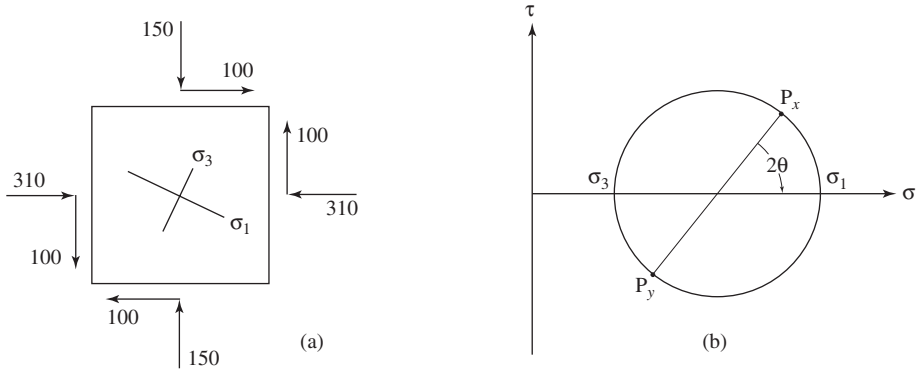


**Figure 9.12** Principal stresses: (a) physical plane; (b) Mohr Circle plane.

3. Because  $x$  and  $y$  are orthogonal, line  $P_x P_y$  is a diameter of the circle and its intersection with the horizontal  $\sigma$  axis marks its center  $C$ . With radius  $P_x C = P_y C$  complete the circle.
4. The two intercepts on the  $\sigma$  axis represent the principal stresses. The orientation of  $\sigma_1$  is found by measuring  $2\theta = -52^\circ$  from  $P_x$  toward  $\sigma_1$ , that is, clockwise.

**Answer**

- The principal stresses are  $\sigma_1 = 358$  MPa and  $\sigma_3 = 102$  MPa and the  $\sigma_1$  direction makes an angle of  $\theta = -26^\circ$  measured in the same sense, that is, clockwise from the  $x$  axis. Note that both  $\theta$  and  $2\theta$  are measured from a *known* coordinate direction toward the *unknown* principal direction.

These principal directions can also be estimated by inspection. This is done by considering separately the normal and shearing components. Without the shearing tractions,  $\sigma_{xx}$  is  $\sigma_1$  and  $\sigma_{yy}$  is  $\sigma_3$  (Fig. 9.13a). With only the shearing tractions, two principal stresses make angles of  $45^\circ$  with the coordinate axes (Fig. 9.13b). These two separate sets of principal stresses can not be combined directly because they act on different planes, but the orientation of  $\sigma_1$  for the total stress will lie between them (cf. Fig. 9.12a).

It is sometimes useful to express the stress components in a differently oriented coordinate system. The change from one set of mutually perpendicular axes to another set with the same origin is a *transformation of axes* (see §7.8). Expressing the stress components relative to transformed axes is easily accomplished with the aid of a Mohr Circle. Indeed, this is the underlying basis of the diagram.

**Problem**

- Starting with the stress components expressed in the  $xy$  coordinates of Fig. 9.12a, find the components in the  $x'y'$  axes rotated anticlockwise  $\phi = +50^\circ$  (Figure 9.14a).

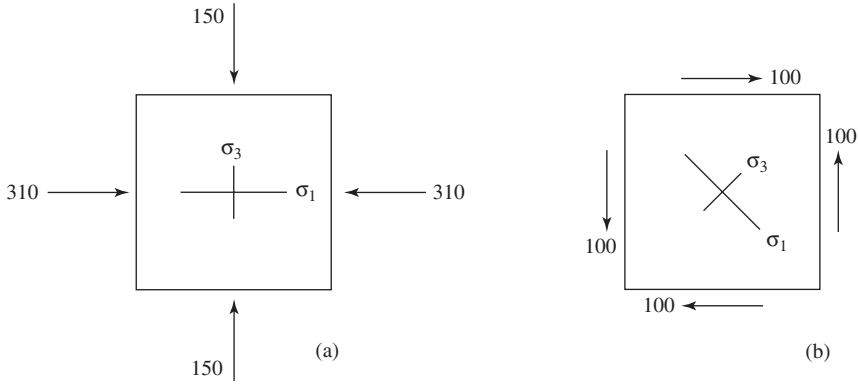


**Figure 9.13** Inspection: (a) normal components; (b) shear components.

**Construction**

1. As before plot points  $P_x(310, 100)$  and  $P_y(150, -100)$  and draw a line connecting them as a diameter (Fig. 9.14b), and draw the Mohr Circle passing through these two points.
2. Draw a second diameter  $P_{x'}P_{y'}$  at an angle  $2\phi = +100^\circ$  measured anticlockwise from the first.
3. The coordinates of the points  $P_{x'}$  and  $P_{y'}$  are the stress components relative to the new axes.

**Answer**

- The new components are  $P_{x'}(66, 23)$  and  $P_{y'}(84, -23)$ .

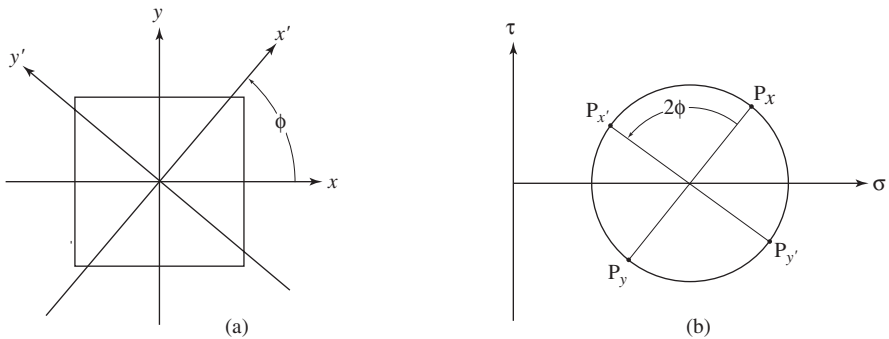


**Figure 9.14** Transformed axes: (a) physical plane; (b) Mohr Circle plane.

Note carefully that the components have changed because they are now referred to a different set of axes; the state of stress they describe has not – the Mohr Circle is the

same. In particular, the principal stresses have the same magnitudes and orientations in the fixed element on the physical plane.

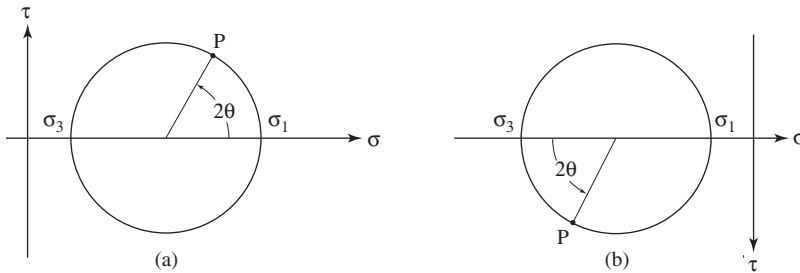


**Figure 9.15** Alternative circles: (a) compression positive; (b) tension positive.

Because the *tension positive* sign convention is used throughout the literature of mechanical engineering (e.g., Drucker, 1967, p. 226), it is useful to compare and contrast these results with the *compression positive* convention adopted here. With compression positive we find, as we have throughout this section, point  $P(\sigma, \tau)$  by drawing a radius at angle  $2\theta$  measured anticlockwise from  $\sigma_1$  (Fig. 9.15a).

With tension positive, the labels are reversed –  $-\sigma_1$  is the greatest tensile or least compressive stress and  $\sigma_3$  is the least tensile or greatest compressive stress. So that angles can be measured in the same sense on both the physical and Mohr Circle planes, negative or clockwise shears are plotted upward. Then point  $P(\sigma, \tau)$  is located by drawing a radius at angle  $2\theta$  measured anticlockwise from  $\sigma_3$  (Fig. 9.15b). Except for these two changes the basic construction is the same, as are the results.

## 9.6 Superimposed stress states

Traction vectors, hence also their normal and shearing components, can be added vectorially *only* if they act on the same plane, or equivalently, if the components are expressed in a common coordinate frame.

### Problem

- Combine the given gravitational and tectonic states of stress, each referred to different coordinate system, to determine the total state (Fig. 9.16). Find the magnitude and orientation of the principal stresses for the combined state.

### Approach

- To superimpose the two states of stress, both must be expressed in a common coordinate system, and there are three choices. We can use either of the given coordinates and express the other stress state in it, or we can choose a third independent set of axes and express both states in it. Here we choose to transform the tectonic stress components into the gravitational frame.

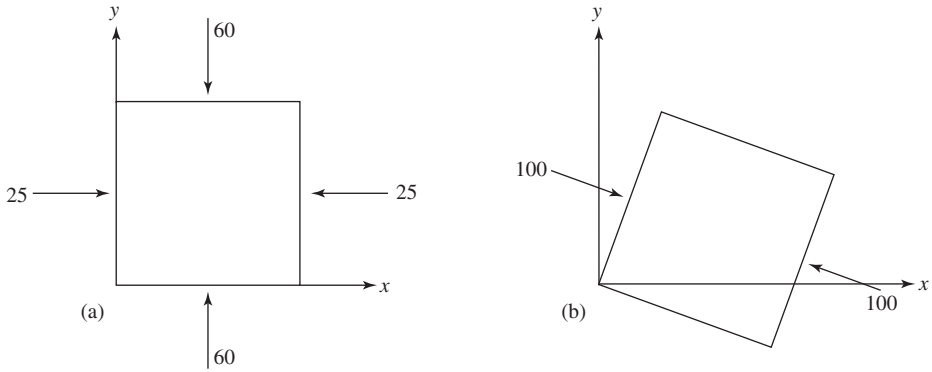


**Figure 9.16** Superimposed states: (a) gravitational stress; (b) tectonic stress.

**Construction**

1. Construct a Mohr Circle for the tectonic stresses  $\sigma'_1 = 100$  and  $\sigma'_3 = 0$  in the usual way (Fig. 9.17).
2. Draw a diameter of this circle making an angle of  $+40^\circ$  with the tectonic  $\sigma_1$  direction. This locates points  $P'_x$  and  $P'_y$ , which are the components in the gravitational frame.
3. To  $P'_x$  add the gravitational  $\sigma_3 = 20$  and to  $P'_y$  add the gravitational  $\sigma_1 = 60$ , giving two new points  $P_x$  and  $P_y$  on the circle for the total stress.
4. Draw a second circle through  $P_x$  and  $P_y$  and determine the principal stresses and their orientation.

**Answer**

- The principal stresses due to the combined states are  $\sigma_1 = 127$  MPa and  $\sigma_3 = 54$  MPa, and the  $\sigma_1$  direction makes an angle of  $\theta = -30.5^\circ$  with the horizontal.

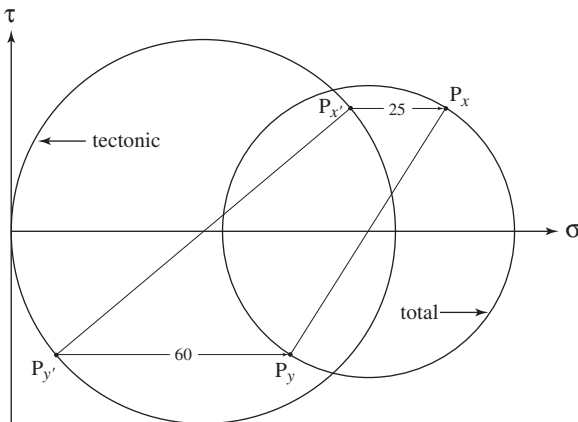


**Figure 9.17** Mohr Circles for superimposed stress states.

### 9.7 Pole of the Mohr Circle

The role of the double angles in relating the physical and Mohr Circle planes is fundamental because it allows the terms in the basic equations to be displayed in a simple way. There is, however, an auxiliary construction which bypasses their use with the advantage of a closer correspondence between the two representations.

An elementary property of a circle is that a central angle is exactly twice the inscribed angle when both subtend the same arc.<sup>6</sup> There are three cases (Gelfand & Saul, 2001, p. 62–63).

1. One side of the inscribed angle is a diameter (Fig. 9.18a). The inscribed angle  $\angle PAB$  and the corresponding central angle  $\angle POB$  subtend the same arc. Because all radii have equal lengths, the triangle  $AOP$  is isosceles. Therefore, the two base angles are equal. The interior angle at  $O$  is therefore  $180 - 2\theta$  and the exterior angle is then  $180 - (180 - 2\theta) = 2\theta$ .
2. The center of the circle  $O$  is inside the inscribed angle  $\angle PAB$  (Fig. 9.18b). Diameter  $AC$  divides this angle into  $\angle PAC$  and  $\angle BAC$  each of which has a diameter as one side and these are covered by Case 1. Then  $\angle PAC = \frac{1}{2}\widehat{PC}$  and  $\angle CAB = \frac{1}{2}\widehat{CB}$  and we have

$$\angle PAB = \angle PAC + \angle CAB = \frac{1}{2}\widehat{PC} + \frac{1}{2}\widehat{CB} = \frac{1}{2}\widehat{PB}.$$

3. The center  $O$  is outside the inscribed angle  $\angle PAB$  (Fig. 9.18c). Diameter  $AC$  divides this angle into  $\angle PAC$  and  $\angle BAC$  each with a diameter as one side. Then  $\angle PAC = \frac{1}{2}\widehat{PC}$  and  $\angle CAB = \frac{1}{2}\widehat{CB}$  which yields

$$\angle PAB = \angle PAC - \angle CAB = \frac{1}{2}\widehat{PC} - \frac{1}{2}\widehat{CB} = \frac{1}{2}\widehat{PB}.$$

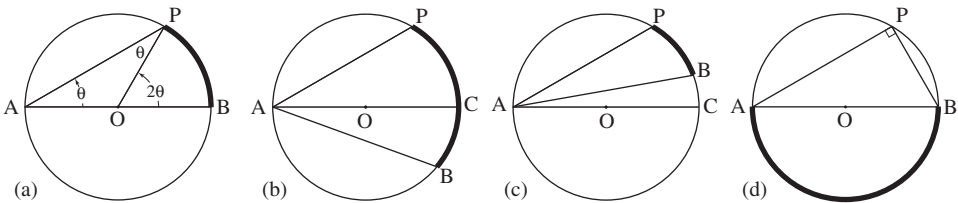


**Figure 9.18** Inscribed and central angles intercepting the same arc.

This fact can be used when plotting or measuring any angle. For example, the orientational angle  $\theta$  appears directly on the Mohr Circle (Fig. 9.18a). The angle  $\beta$  giving the

<sup>6</sup>This is Proposition 20 of Book III of Euclid’s *Elements*. That for a given circle all inscribed angles subtending the same arc are equal is Proposition 21.

orientation of the plane can be found in a similar way. In the important special case, an angle inscribed in a semicircle is always a right angle (Fig. 9.18d).<sup>7</sup>

Next, we use this geometrical fact to relate the orientations on the physical and Mohr Circle planes with the aid of a special point on the circumference of the circle. There are two versions.

1. One is the *pole for normals* (Drucker, 1967, p. 228–229). We refer to this point as the *origin of normals*, which is a useful short definition because the normals to all planes are drawn passing through it. Denoted  $O_N$  it has a useful property: A line through  $O_N$  and any point  $P$  on the circumference of the Mohr Circle is parallel to the normal of the plane on which the components of the traction given by the coordinates of  $P$  act.
2. The other, by analogy, is the *pole for planes*. This point is the *origin of planes* (Lambe & Whitman, 1979, p. 107) because the traces of all planes are drawn passing through it. Denoted  $O_P$  it has a useful property: A line through  $O_P$  and any point  $P$  on the circumference of the Mohr Circle is parallel to the trace of the plane on which the traction components given by the coordinates of  $P$  act.

Either of these poles can be used, but each has some advantages. The first is consistent with the established convention for identifying the orientation of a plane by its normal. The second emphasizes the plane itself. The two poles are diametrically opposite one another, so if the location of one is known the other can be found immediately. For problems involving principal directions it is advantageous to use pole  $O_N$ . For problems which require the traction components on a specified plane pole  $O_P$  is superior. We will illustrate both usages.

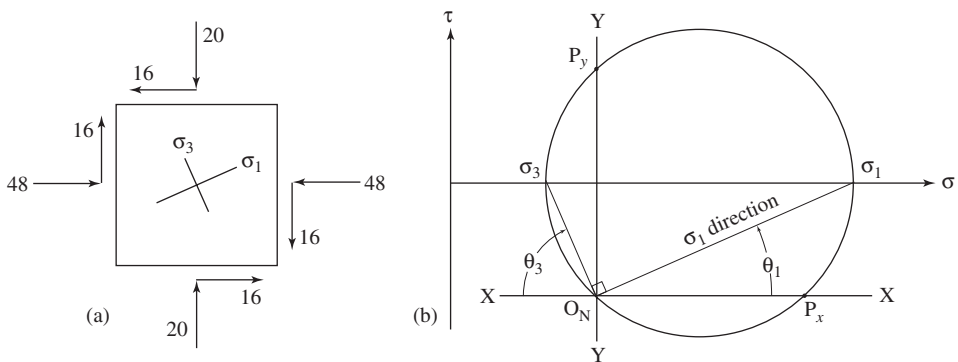


**Figure 9.19** Pole  $O_N$ : (a) physical plane; (b) Mohr Circle plane.

<sup>7</sup>The fact that inscribed angles subtending a diameter are right angles is said to have been proved by Thales of Miletus (ca. 625–546 BC), although it was already known to the Babylonians a thousand years earlier (Maor, 1998, p. 87).

### Problem

- Represent the state of stress of Fig. 9.19a by a Mohr Circle, and determine the principal stresses and their directions.

### Approach

- Because the principal directions are required, the pole for normals  $O_N$  is appropriate.

### Construction

1. Plot points  $P_x(+48, -16)$  and  $P_y(+20, +16)$ , construct a Mohr Circle through them and determine the values of  $\sigma_1$  and  $\sigma_3$  (Fig. 9.19b).
2. To locate  $O_N$  draw line  $XX$  through  $P_x$  parallel to the  $x$  axis or line  $YY$  through  $P_y$  parallel to the  $y$  axis (only one is needed).
3. Line  $O_N\sigma_1$  gives the  $\sigma_1$  direction and line  $O_N\sigma_3$  gives the  $\sigma_3$  direction and these can be transferred directly to the physical plane.

### Answer

- The principal stresses are  $\sigma_1 = 55$  MPa and  $\sigma_3 = 13$  MPa. The principal directions are given by the angles  $\theta_1 = +24^\circ$  and  $\theta_3 = -66^\circ$  measured from the  $x$  axis.

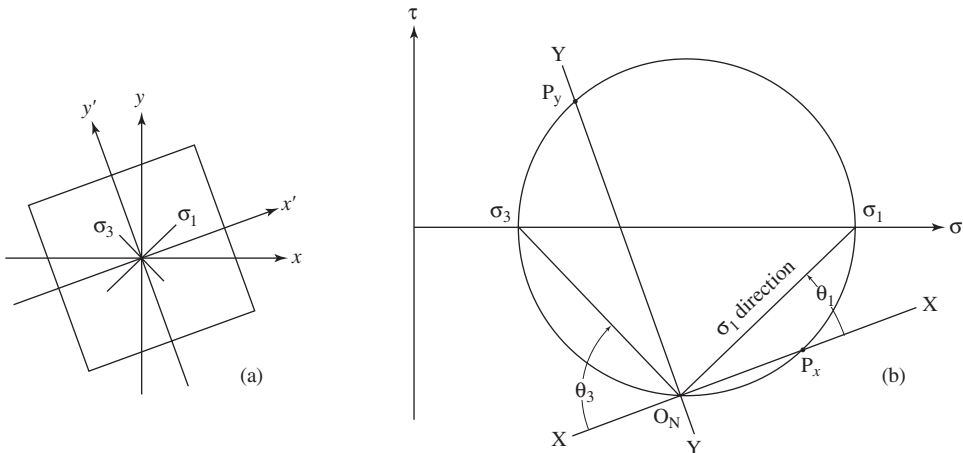


**Figure 9.20** Rotated body: (a) physical plane; (b) new pole  $O_N$ .

If this same physical body is rotated anticlockwise  $+20^\circ$  (Fig. 9.20a), the construction proceeds in exactly the same way (Fig. 9.20b). In the result, however, the pole is in a new place – it has rotated anticlockwise  $+40^\circ$ . We then see that the Mohr Circle itself represents the two-dimensional state of stress while the pole represents orientation of the axes to which the components are referred.

### Problem

- For the same state of stress (see Fig. 9.21a), determine the traction components on a plane making angle  $\beta = 60^\circ$  with the  $x$  direction using pole  $O_P$ .

### Approach

- Because the traction components on a plane are required, the pole for planes  $O_P$  is used.

### Construction

1. As before, plot points  $P_x(+48, -16)$  and  $P_y(+20, +16)$  and complete the Mohr Circle (Fig. 9.21b).
2. Locate  $O_P$  on the circumference by drawing line  $XX$  through  $P_x$  parallel to the *vertical* face or line  $YY$  through  $P_y$  parallel to the *horizontal* face (again only one is needed).
3. Through  $O_P$  draw a line parallel to the trace of the inclined plane  $AB$  to locate point  $P$  on the circle. The coordinates of  $P$  are the required traction components.

### Answer

- The traction components are  $\sigma = +27$  MPa and  $\tau = -20$  MPa.

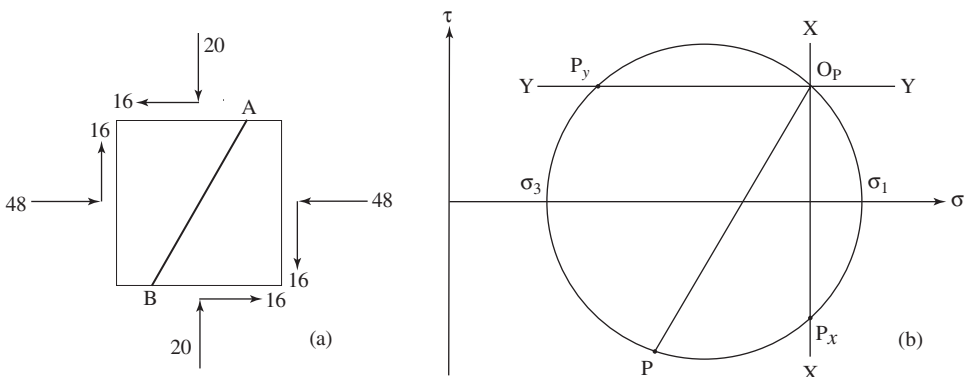


**Figure 9.21** Pole  $O_P$ : (a) physical plane; (b) Mohr Circle plane.

These methods of locating poles  $O_N$  and  $O_P$  work generally. There are, however, two special cases which deserve attention.

1. If  $\sigma_1$  is horizontal then  $O_N$  coincides with  $\sigma_3$  and  $O_P$  with  $\sigma_1$  (Fig. 9.22a).
2. If  $\sigma_3$  is horizontal then  $O_N$  coincides with  $\sigma_1$  and  $O_P$  coincides with  $\sigma_3$  (Fig. 9.22b).

We can use these special cases to simplify the construction of the Mohr Circle and its use in finding the traction components acting on a given plane (W.D. Means, 1996, personal communication). There are several possible variants but we will describe only one to illustrate the method.



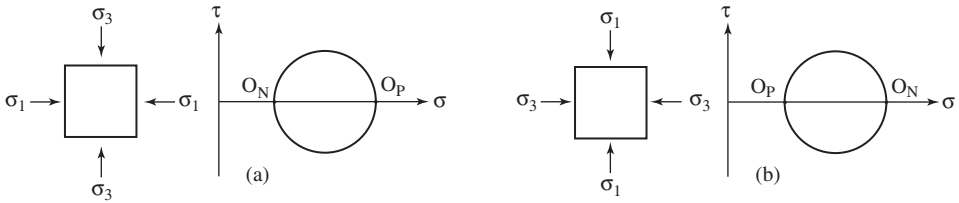


**Figure 9.22** Special cases: (a)  $\sigma_1$  horizontal; (b)  $\sigma_3$  horizontal.

**Problem**

- Given  $\sigma_1 = 80$  MPa and  $\sigma_3 = 20$  MPa and their orientation on the physical plane (Fig. 9.23a), determine the traction components acting on a fault making an angle of  $\beta = 25^\circ$  with the  $\sigma_1$  direction.

**Procedure**

1. Draw the  $\sigma$  axis parallel to the  $\sigma_1$  direction on the physical plane (Fig. 9.23b).
2. Using the principal stresses, construct the Mohr Circle in the usual way.
3. In this orientation, the pole for planes  $O_P$  automatically coincides with  $\sigma_1$ .
4. Draw a chord through  $O_P$  parallel to the trace of the fault on the physical plane to locate point  $P$  on the circle.

**Answer**

- The coordinates of  $P$  are the required components:  $\sigma = 31$  MPa and  $\sigma_3 = 23$  MPa, and the sense of shear on the fault is clockwise.

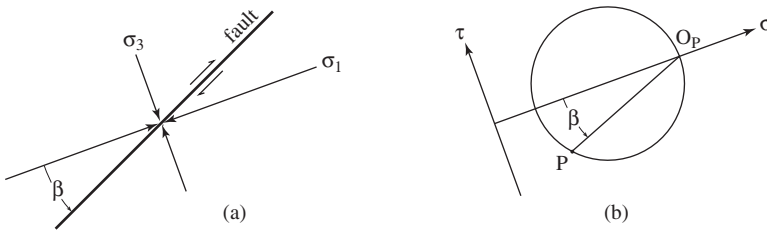


**Figure 9.23** Traction on plane from a special Mohr Circle.

Finally, having found the poles, we can now bring the representations on the physical and Mohr Circle planes into even closer correspondence. By centering the figure representing the physical plane on the pole of the circle we can immediately determine the components of the traction acting on any plane of interest. Again, there are two cases.

1. With the physical representation centered at the pole  $O_N$  the normal to the plane intersects the circle at point  $P$  which gives the components of the traction acting on the plane (Fig. 9.24a).

2. With the representation centered at the pole  $O_P$  the trace of the plane of interest extended intersects the circle at the same point  $P$  (Fig. 9.24b).

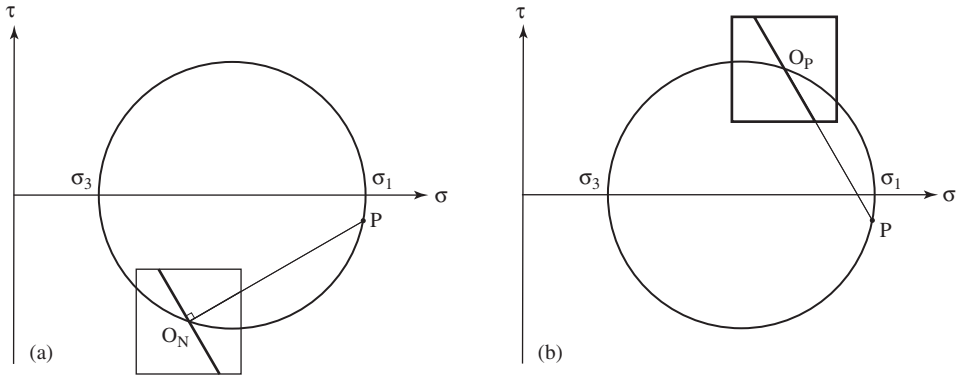


**Figure 9.24** Physical plane and Mohr Circle plane combined: (a) pole  $O_N$ ; (b) pole  $O_P$ .

### 9.8 Role of pore pressure

If a porous medium contains a fluid under hydrostatic pressure  $p$ , the state of stress is altered. As shown in Fig. 9.25a, this pressure in the pore fluid tends to counteract the effects of both principal stresses due to the applied loads. Hence

$$\sigma_1 = S_1 - p \quad \text{and} \quad \sigma_3 = S_3 - p,$$

where  $S_1$  and  $S_3$  are the principal stresses due to these external loads. Substituting these two expressions into Eqs. 9.17 yields

$$\sigma' = \frac{1}{2}(S_1 + S_3) + \frac{1}{2}(S_1 - S_3) \cos 2\theta - p, \tag{9.19a}$$

$$\tau' = \frac{1}{2}(S_1 - S_3) \sin 2\theta, \tag{9.19b}$$

where  $\sigma'$  and  $\tau'$  are the *effective stresses*, meaning that the pore pressure has been taken into account. In other words, the normal traction on any plane is reduced by the pressure  $p$ , while the shearing traction remains unchanged. We can write this relationship in the form of the matrix equations as

$$\begin{bmatrix} \sigma'_1 & 0 \\ 0 & \sigma'_3 \end{bmatrix} = \begin{bmatrix} \sigma_1 & 0 \\ 0 & \sigma_3 \end{bmatrix} - \begin{bmatrix} p & 0 \\ 0 & p \end{bmatrix}.$$

Because it applies to every normal component, we can express this even more simply as

$$\sigma' = \sigma - p. \tag{9.20}$$

This partitioning of applied stress and fluid pressure in porous solids is called *Terzaghi's relationship*.<sup>8</sup>

In terms of the Mohr Circle diagram, a change in the pore fluid pressure shifts the circle along the horizontal axis — to the left for an increase and to the right for a decrease by the amount of  $p$  without altering the size of the circle (Fig. 9.25b).

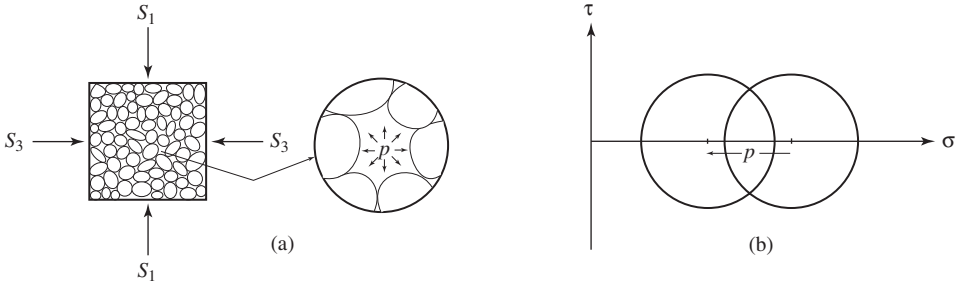


**Figure 9.25** Pore fluid pressure: (a) porous rock; (b) state of effective stress.

### 9.9 Deviatoric and hydrostatic stress

There is another way of partitioning a general state of stress which is useful in some applications (Engelder, 1993, p. 16, 80; 1993). First, the *mean normal stress*  $\sigma_m$  is defined as

$$\sigma_m = \frac{1}{3}(\sigma_1 + \sigma_2 + \sigma_3).$$

This part is viewed as causing a volume change and is commonly referred to as the *hydrostatic* component.

The other part or *deviatoric stress* is then defined as the difference between a normal component and this mean stress. That is,

$$\sigma_{dev} = \sigma - \sigma_m.$$

This part is viewed as causing distortion. Thus any general state of stress can then be factored into the sum of two stress matrices

$$\begin{bmatrix} \sigma_1 & 0 & 0 \\ 0 & \sigma_2 & 0 \\ 0 & 0 & \sigma_3 \end{bmatrix} = \begin{bmatrix} \sigma_1 - \sigma_m & 0 & 0 \\ 0 & \sigma_2 - \sigma_m & 0 \\ 0 & 0 & \sigma_3 - \sigma_m \end{bmatrix} + \begin{bmatrix} \sigma_m & 0 & 0 \\ 0 & \sigma_m & 0 \\ 0 & 0 & \sigma_m \end{bmatrix}. \quad (9.21)$$

<sup>8</sup>The celebrated civil engineer Karl Terzaghi [1883–1963] is widely considered to be *The Father of Soil Mechanics* (see Gretner, 1981).

Again, because it applies to every normal component we may express this simply as

$$\sigma = \sigma_{dev} + \sigma_m.$$

For the special case of plane stress, there is a simple graphical representation of these two parts: the Mohr Circle for a typical compressive state of stress (Fig. 9.26a). The center of this circle represents the mean stress. The deviatoric state is then represented by a circle centered at the origin (Fig. 9.26b).

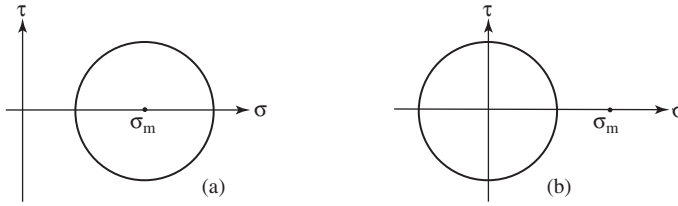


**Figure 9.26** Deviatoric stress: (a) standard circle; (b) deviatoric circle.

### 9.10 Stress ellipse

The Mohr Circle construction is indispensable for solving two-dimensional stress problems graphically in the simplest way. There is, however, an additional figure which aids the visualization of some two-dimensional states of stress.

The first step in constructing this figure is to express the  $x$  and  $y$  components of the traction vector acting on an inclined plane in terms of the orientational angle  $\theta$  and the principal stresses (Fig. 9.27). The procedure is identical to the one used before: convert applied stresses to forces, apply the condition of equilibrium and then convert forces back to traction components. The result is

$$\cos \theta = x/\sigma_1 \quad \text{and} \quad \sin \theta = y/\sigma_3. \quad (9.22)$$

Using these in the identity  $\cos^2\theta + \sin^2\theta = 1$  we then have

$$\frac{x^2}{\sigma_1^2} + \frac{y^2}{\sigma_3^2} = 1, \quad (9.23)$$

which is the equation of the *stress ellipse*. This figure represents the loci of the end points of all the possible traction vectors. These vectors point inward if the state is compressive and outward if it is tensile. The lengths of its semi-axes are the magnitudes of the principal stresses  $|\sigma_1|$  and  $|\sigma_3|$ .

There are several cases, but the geologically important one is when both principal stresses are compressive. Given a stress ellipse and a particular traction represented by

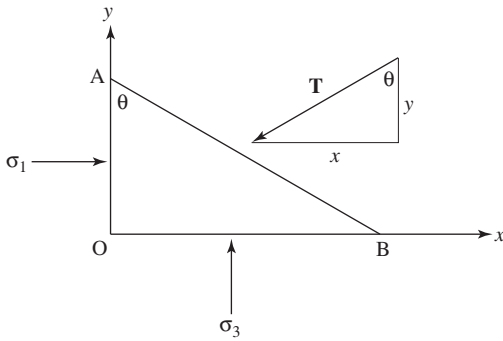


**Figure 9.27** Traction components  $x$  and  $y$  in terms of principal stresses.

the radius vector  $OP$  (Fig. 9.28a), what is the orientation of this vector on the physical plane?

We first show how the magnitude and orientation of a traction vector are represented directly on the Mohr Circle constructed from the principal stresses. With a compass, transfer length of radius  $OP$  on the stress ellipse to find point  $P$  on the circumference of the circle (Fig. 9.28b; note the scale change in this figure). Line  $OP$  on the Mohr Circle diagram then is equal to the magnitude of the traction vector and its normal and shear components are represented by the coordinates of  $P$ . Also from this diagram  $\mathbf{T}$  acts on the plane whose normal makes an angle  $\theta$  with the  $\sigma_1$  direction. The slope angle  $\psi$  is the angle between  $\mathbf{T}$  and  $\hat{\mathbf{n}}$ . From this diagram we obtain

$$T = \sqrt{\sigma^2 + \tau^2} \quad \text{and} \quad \psi = \arctan(\sigma/\tau).$$

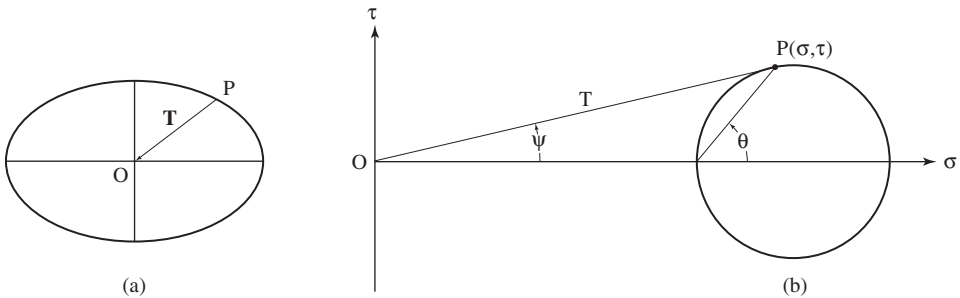


**Figure 9.28** Traction vector: (a) stress ellipse; (b) Mohr Circle (double size).

From these results it is clear that the stress ellipse does not directly give the orientation of the plane on which the traction acts. It can, however, be found with a simple construction (Durelli, *et al.*, 1958, p. 145; Means, 1976, p. 55).

### Problem

- For a given a stress ellipse and a radius vector  $OP$ , determine the orientation of the plane on which this traction acts.

### Construction

1. Draw either of the two auxiliary circles centered at the origin (only one is needed):
  - (a) a large circle with a radius equal to  $|\sigma_1|$  (Fig. 9.29a),
  - (b) a small circle with a radius equal to  $|\sigma_3|$  (Fig. 9.29b).
2. From the given point  $P$  on the ellipse draw a line parallel to the minor axis to intersect the larger circle at  $A$  and a line parallel to the major axis to intersect the smaller circle at  $B$ .
3. The identical slope angles of  $OA$  and  $OB$  represent the angle  $\theta$  which the traction vector makes with the  $\sigma_1$  direction. Further,  $\angle AOP = \angle BOP$  is the angle  $\psi$  which  $\mathbf{T}$  makes with  $\hat{\mathbf{n}}$ .

The validity of this construction is easily demonstrated. From Fig. 9.29

$$x_A = x_P = |\sigma_1| \cos \theta \quad \text{and} \quad y_B = y_P = |\sigma_3| \sin \theta, \quad (9.24)$$

where the subscripts  $A$ ,  $B$  and  $P$  identify the associated points. A comparison with Eqs. 9.22 shows that  $x_P$  and  $y_P$  are the components of the traction in the coordinate directions. These two are the *parametric equations* of an ellipse. By letting the *eccentric angle*  $\theta$  range from 0 to  $360^\circ$  the coordinates of a series of closely spaced points on the ellipse can be calculated. These coordinates can then be used to draw an ellipse on a computer screen or plot one on paper (see also De Paor, 1994).

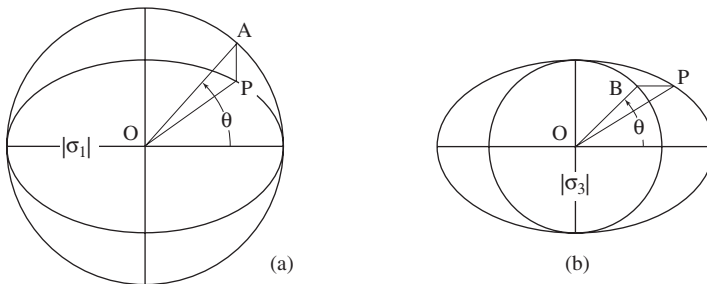


**Figure 9.29** Normal direction from the stress ellipse.

This construction can easily be reversed to find the traction acting on any plane as specified by the angle  $\theta$  its normal makes with the  $\sigma_1$  direction.

### Problem

- Given a stress ellipse, construct the traction vector acting on a plane whose normal makes an angle  $\theta$  measured from  $\sigma_1$  (as in Fig. 9.28).

**Construction**

1. Only one auxiliary circle is needed and the larger one is the easier to draw accurately.
2. A line with slope angle  $\theta$  intersects this circle at point  $A$ .
3. A line parallel to the minor axis through  $A$  locates point  $P$  on the ellipse.

**Answer**

- Radius vector  $OP$  represents the magnitude of the traction acting on this specified plane.

Depending on the signs of the two principal stresses there are two contrasting orientations of the stress ellipses.

1. If the principal stresses are both compressive then  $|\sigma_1| > |\sigma_3|$  and the major axis is parallel to  $x$  and the radius vectors point inward (Fig. 9.30a). This is the case we have treated.
2. If the principal stresses are both tensile then  $|\sigma_1| < |\sigma_3|$  and the major axis of the stress ellipse is parallel to  $y$  and the radius vectors point outward (Fig. 9.30b). This switch in orientation reduces its aid to visualization somewhat but otherwise its basic properties are the same.

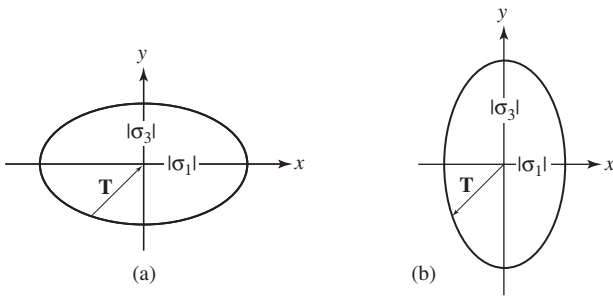


**Figure 9.30** Stress ellipses: (a) compression; (b) tension.

It is also possible to construct an ellipse if the signs of the principal stresses are mixed but the result is useless. Because the absolute magnitudes of the principal stresses are used, the construction can not distinguish between states when  $\sigma_3$  is positive or negative. Figure 9.31 shows two Mohr Circles with identical magnitudes of  $\sigma_1$  and  $\sigma_3$ . The corresponding stress ellipses representing these two quite different stress states are identical. Only for the case where  $\sigma_3 > 0$  does the ellipse describes the actual distribution of the traction vectors (Fig. 9.31a).

**9.11 Traction versus forces**

This description of stress was essentially established over 150 years ago by the celebrated French mathematician and physicist Augustine-Louis Cauchy [1789–1857]. Historically,

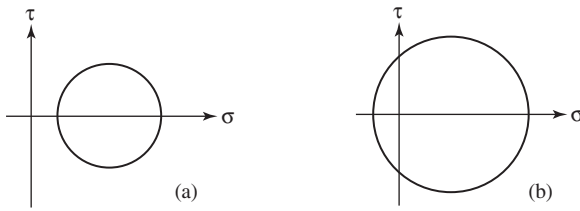


**Figure 9.31** Two stress states, one stress ellipse: (a)  $\sigma_3 > 0$ ; (b)  $\sigma_3 < 0$ .

however, it has not always been applied correctly to geological problems. The first clear statement in the geological literature was given by Anderson (1951) and reemphasized by Hubbert (1951) and by Hafner (1951).

Unfortunately, errors persist and they usually root in the manipulation of stress components as force vectors. An example from a structural geology text will illustrate how and why this approach goes wrong. Figure 9.32a shows a thrust fault with a dip of  $12^\circ$  and with  $\sigma_1$  horizontal and  $\sigma_3$  vertical (Badgley, 1965, p. 219). The principal stresses are treated as force vectors and the components of each in the plane of the fault are found. If  $\sigma_1 = 40$  and  $\sigma_3 = 28$  (scaled from Badgley's figure in arbitrary units) the magnitudes of the two opposed "tangential force vectors" on the fault plane are 39.1 and 5.8. The vector sum of these is equal to 33.3 and this, the author supposes, is the shearing force which drives the thrust.

Figure 9.32b shows the Mohr Circle for the same problem. For the given principal stresses, the shearing traction on the fault plane making an angle of  $\beta = 12^\circ$  with the  $\sigma_1$  direction is  $\tau = 2.4$  units. Not only is there a great discrepancy between these two results, but because  $\tau_{max} = 6.0$  units, the value obtained by the vector treatment is not possible for any orientation of the fault plane. Further, the vector treatment would give a net tangential force on the plane even if  $\sigma_1 = \sigma_3$ , in which case the circle shrinks to a point and then  $\tau = 0$  on all planes.

Stress components are *not* force vectors. To treat them as such is a serious error and any conclusion based on such a treatment is invalid.

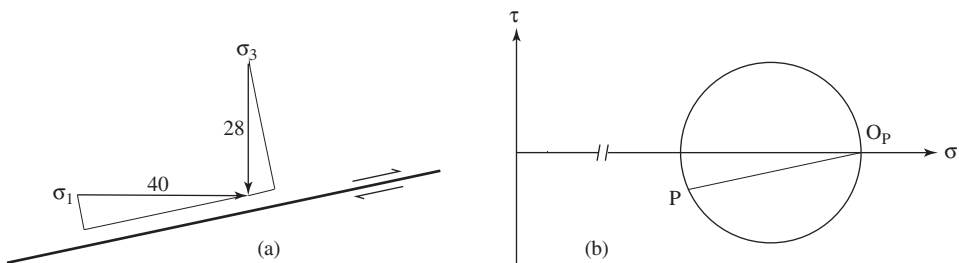


**Figure 9.32** Thrust fault: (a) tractions as force vectors; (b) Mohr Circle solution.



## 9.12 Stress tensor

The stress matrix represents a member of a class of entities called *tensors of second rank*.<sup>9</sup> We can think of such tensors as *vector processors* which operate on an input vector to produce an output vector (Means, 1996, p. 6). In the case of stress, these are the unit normal vector  $\hat{\mathbf{n}}$  and traction vector  $\mathbf{T}$ .

If we represent vectors  $\mathbf{T}$  and  $\hat{\mathbf{n}}$  by their components in each of the coordinate directions and write them as column matrices, we can then express this process by the matrix equation

$$\begin{bmatrix} T_x \\ T_y \end{bmatrix} = \begin{bmatrix} \sigma_{xx} & 0 \\ 0 & \sigma_{yy} \end{bmatrix} \begin{bmatrix} n_x \\ n_y \end{bmatrix}.$$

Writing in this way makes clear that the stress matrix operates on vector  $\hat{\mathbf{n}}$  to yield vector  $\mathbf{T}$ . Using the *row times column* rule of matrix multiplication (see §7.3) we then have

$$\begin{bmatrix} T_x \\ T_y \end{bmatrix} = \begin{bmatrix} \sigma_{xx}n_x \\ \sigma_{yy}n_y \end{bmatrix}. \quad (9.25)$$

With these components the magnitude of  $\mathbf{T}$  is

$$T = \sqrt{T_x^2 + T_y^2} \quad (9.26)$$

and its orientation is given by the angle  $\phi$  it makes with the  $x$  axis

$$\phi = \arctan(T_y/T_x). \quad (9.27)$$

The direction cosines of  $\mathbf{T}$  are obtained by normalizing its components, which are then  $(T_x/T, T_y/T)$ . With these the dot product yields the angle  $\psi$  between  $\mathbf{T}$  and  $\hat{\mathbf{n}}$ .

$$\cos \psi = (T_x/T)n_x + (T_y/T)n_y. \quad (9.28)$$

With this angle  $\psi$  the normal and shearing components are

$$\sigma = T \cos \psi \quad \text{and} \quad \tau = T \sin \psi. \quad (9.29)$$

When using these equations to find  $\mathbf{T}$  it is necessary to revert to the engineering sign convention with tension positive and compression negative. Otherwise the sense of the calculated traction vector will be reversed. This changes the labels of the principal stresses, but this affects neither the basic geometry nor physics of the problems.

<sup>9</sup>The terms *second order* is also used, but as Nye (1985, p. 5) observes this has another common meaning, as in second order effect, and so prefers rank. The number of subscripts denoting the components indicates the rank of a tensor.

**Problem**

- If  $\sigma_{xx} = 150$  MPa and  $\sigma_{yy} = 50$  MPa (see Fig. 9.11a), what are the traction components on a plane whose normal makes an angle of  $\theta = +34^\circ$  with the  $+x$  axis (Fig. 9.33a)?

**Solution**

1. The stress tensor is represented by the matrix

$$\begin{bmatrix} \sigma_{xx} & 0 \\ 0 & \sigma_{yy} \end{bmatrix} = \begin{bmatrix} -150 & 0 \\ 0 & -50 \end{bmatrix}.$$

(Note that the tensor sign convention is used.)

2. With Eq. 9.25, the components of the traction vector are

$$\begin{bmatrix} T_x \\ T_y \end{bmatrix} = \begin{bmatrix} -150 \cos 34^\circ \\ -50 \sin 34^\circ \end{bmatrix} = \begin{bmatrix} -124.355 \ 64 \\ -27.959 \ 65 \end{bmatrix}.$$

3. Then with Eq. 9.26 the magnitude of the traction vector is

$$T = \sqrt{T_x^2 + T_y^2} = 127.460 \ 06.$$

4. With Eq. 9.27 the angle the traction vector makes with the  $x$  axis is given by

$$\phi = \arctan(T_y/T_x) = -167.328 \ 55^\circ.$$

Note that it may be necessary to correct this angle by adding  $\pm 180^\circ$ , just as we did to calculate the trend of a vector from its direction cosines in §7.1.

5. With Eq. 9.28 the angle between  $\mathbf{T}$  and  $\hat{\mathbf{n}}$  is

$$\psi = \arccos \left[ (T_x/T) \cos 34^\circ + (T_y/T) \sin 34^\circ \right] = 158.671 \ 45^\circ.$$

Note that the dot product takes into account both the direction and sense of the two vectors (Fig. 9.33b).

6. With Eqs. 9.29 the normal and shearing components of the traction are

$$\sigma = T \cos \psi = -118.7 \text{ MPa} \quad \text{and} \quad \tau = T \sin \psi = +46.3 \text{ MPa}.$$

These results are identical to those found from the Mohr Circle equations.

This same approach can also be used to determine the traction when all stress components are present and the stress matrix is in its most general form (Fig. 9.34a). The matrix equation representing the process is then

$$\begin{bmatrix} T_x \\ T_y \end{bmatrix} = \begin{bmatrix} \sigma_{xx} & \tau_{xy} \\ \tau_{yx} & \sigma_{yy} \end{bmatrix} \begin{bmatrix} n_x \\ n_y \end{bmatrix}. \quad (9.30)$$

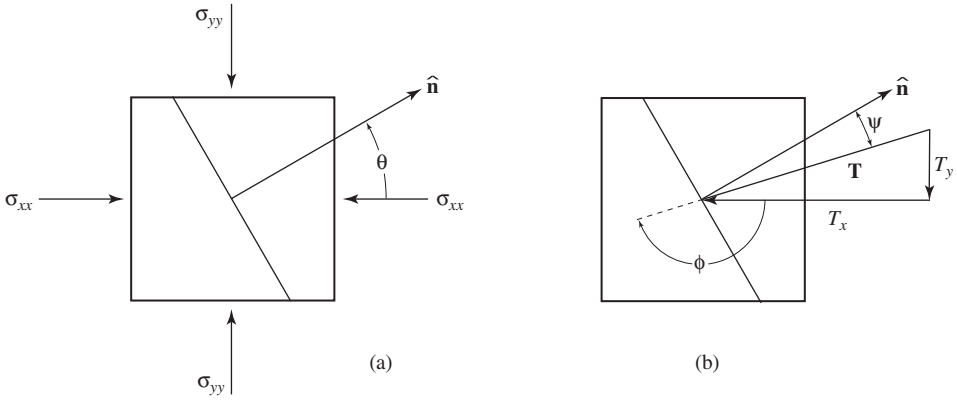


**Figure 9.33**  $\mathbf{T}$  and  $\hat{\mathbf{n}}$ : (a) biaxial stress; (b) traction vector and its components.

To evaluate the components of  $\mathbf{T}$  we balance the forces due to the stress components in each coordinate direction. The force in the  $x$  direction is due to components  $\sigma_{xx}$  and  $\tau_{xy}$  (Fig. 9.34b). Then

$$\sum F_x = T_x a - \sigma_{xx}(a \cos \theta) - \tau_{xy}(a \sin \theta) = 0. \tag{9.31}$$

The force in the  $y$  direction is due to components  $\sigma_{yy}$  and  $\tau_{yx}$  (Fig. 9.34c) and

$$\sum F_y = T_y a - \tau_{yx}(a \cos \theta) - \sigma_{yy}(a \sin \theta) = 0. \tag{9.32}$$

Dividing each of these by the area  $a$ , using  $n_x = \cos \theta$  and  $n_y = \sin \theta$ , rearranging and writing the results as two column vectors we have

$$\begin{bmatrix} T_x \\ T_y \end{bmatrix} = \begin{bmatrix} \sigma_{xx}n_x + \tau_{xy}n_y \\ \tau_{yx}n_x + \sigma_{yy}n_y \end{bmatrix}.$$

This result can also be obtained directly from Eq. 9.30 using, again, row times column multiplication.

As elsewhere in this chapter, these derivations employ the convention that the first subscript identifies the direction in which the stress component acts and the second identifies the direction of the normal to the plane on which it acts (see Fig. 9.35a). This is important for several reasons. First, it allows the standard rules of matrix multiplication to be applied. Second, the formula also makes no physical sense if the opposite convention is adopted. For example, if the reverse convention is adopted the component  $\sigma_{xy}$  then acts in the  $y$  direction and orthogonal forces can never balance each other (Means, 1996, p. 9).<sup>10</sup>

<sup>10</sup>Because  $\tau_{xy} = \tau_{yx}$ , the calculation gives the correct result but this does not make things any clearer.

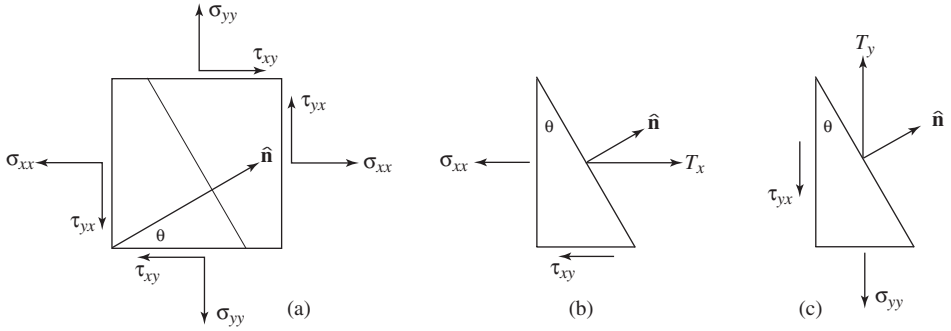


**Figure 9.34** Traction components: (a) stress components; (b)  $T_x$ ; (c)  $T_y$ .

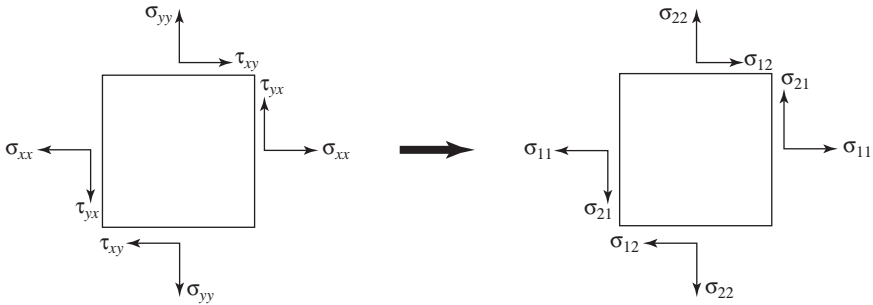


**Figure 9.35** Conversion to tensor notation.

By hand a solution is more easily obtained with a Mohr Circle construction so it is not generally practical to use the analytical expression. However, the relation between the components of the two vectors can be easily programmed. To do this, we relabel the coordinate axes  $x \rightarrow x_1$  and  $y \rightarrow x_2$ . We then also exchange letter subscripts  $x$  and  $y$  with numbers 1 and 2 in the vector and tensor components (Fig. 9.35b). This is commonly called the *tensor notation*. In this form we can now take advantage of arrays with subscripted variables which are part of all programming languages. Making this conversion to numerical subscripts Eq. 9.30 becomes

$$\begin{bmatrix} T_1 \\ T_2 \end{bmatrix} = \begin{bmatrix} \sigma_{11} & \sigma_{12} \\ \sigma_{21} & \sigma_{22} \end{bmatrix} \begin{bmatrix} n_1 \\ n_2 \end{bmatrix}. \tag{9.33}$$

Performing the multiplication then yields

$$\begin{bmatrix} T_1 \\ T_2 \end{bmatrix} = \begin{bmatrix} \sigma_{11}n_1 + \sigma_{12}n_2 \\ \sigma_{21}n_1 + \sigma_{22}n_2 \end{bmatrix}.$$

This result can also be written compactly using symbolic subscripts in two ways:

$$T_i = \sum_{j=1}^2 \sigma_{ij} n_j \quad (i = 1, 2) \quad \text{or} \quad T_i = \sigma_{ij} n_j \quad (i, j = 1, 2). \quad (9.34)$$

Each of these has identical meaning. The second, which often appears in the technical literature, uses the *Einstein summation convention*: when a letter subscript (here  $j$ ) is repeated twice (and only twice) in a single term, summation is automatically understood with respect to that subscript (Nye, 1985, p. 7).<sup>11</sup>

Both versions represent *Cauchy's formula* which is fundamental to the theory of stress. It is, in effect, also the definition of the stress tensor.

Finally, we can find the principal stresses, called *eigenvalues*, and their orientations, called *eigenvectors*, directly from the stress matrix. The condition that  $\mathbf{T}$  is a principal stress is that it acts in the same direction as  $\hat{\mathbf{n}}$ . That is,

$$\begin{bmatrix} T_1 \\ T_2 \end{bmatrix} = \lambda \begin{bmatrix} n_1 \\ n_2 \end{bmatrix} = \begin{bmatrix} \lambda n_1 \\ \lambda n_2 \end{bmatrix},$$

where  $\lambda$  is an as yet unknown scalar multiplier. We then write Eq. 9.33 as

$$\begin{bmatrix} \sigma_{11} & \sigma_{12} \\ \sigma_{21} & \sigma_{22} \end{bmatrix} \begin{bmatrix} n_1 \\ n_2 \end{bmatrix} = \begin{bmatrix} \lambda n_1 \\ \lambda n_2 \end{bmatrix}. \quad (9.35)$$

Performing the multiplication and collecting terms we have the pair of homogeneous equations

$$(\sigma_{11} - \lambda)n_1 + \sigma_{12}n_2 = 0, \quad (9.36a)$$

$$\sigma_{21}n_1 + (\sigma_{22} - \lambda)n_2 = 0. \quad (9.36b)$$

Such a system of equations has a solution other than the trivial solution  $n_1 = n_2 = 0$  if and only if the determinant of the coefficients is equal to zero. Applying this condition gives

$$\begin{vmatrix} \sigma_{11} - \lambda & \sigma_{12} \\ \sigma_{21} & \sigma_{22} - \lambda \end{vmatrix} = 0. \quad (9.37)$$

Expanding and collecting terms yields

$$\lambda^2 - (\sigma_{11} + \sigma_{22})\lambda + (\sigma_{11}\sigma_{22} - \sigma_{12}\sigma_{21}) = 0. \quad (9.38)$$

<sup>11</sup>This convention is named for the famous physicist Albert Einstein [1879–1955] who invented it.

This is the *characteristic equation* and its roots are called the *characteristic* or *latent* roots.<sup>12</sup> Forming this equation follows a simple, easily remembered recipe:

1. The coefficient of the  $\lambda^2$  term is always 1.
2. The coefficient of the  $\lambda$  term is the sum of the elements in the main diagonal, called the *trace*, with its sign changed.
3. The constant is the determinant of the stress matrix.

The characteristic equation and its roots are a property of the stress tensor and are independent of the coordinate axes to which the components of the stress matrix are referred. This means that the trace and determinant are *invariant* properties of the tensor.

We now write the pair of homogeneous equations of Eqs. 9.36 in the form of the matrix equation

$$\begin{bmatrix} \sigma_{11} - \lambda & \sigma_{12} \\ \sigma_{21} & \sigma_{22} - \lambda \end{bmatrix} \begin{bmatrix} v_1 \\ v_2 \end{bmatrix} = \begin{bmatrix} 0 \\ 0 \end{bmatrix}, \quad (9.39)$$

where  $(v_1, v_2)$  are the components of an eigenvector. We know that the determinant of the square matrix is equal to zero because this is exactly the condition which led to the eigenvalues. Homogeneous equations with a vanishing determinant are not independent; if one of the equations is satisfied the other will be also. Therefore, we may choose either the first (Eq. 9.36a) or second (Eq. 9.36b), that is, either

$$\frac{v_1}{v_2} = \frac{\sigma_{12}}{\lambda - \sigma_{11}} \quad \text{or} \quad \frac{v_1}{v_2} = \frac{\lambda - \sigma_{22}}{\sigma_{21}}. \quad (9.40)$$

We will illustrate the use of both.

An infinite number of vectors satisfy these equations – they are the vectors of all possible magnitudes parallel to a principal direction. However, we are interested only in the orientation of these vectors not their magnitudes. There are two simple ways of determining these.

1. Let the numerator and denominator of these fractions serve as representative values of  $v_1$  and  $v_2$

$$\begin{bmatrix} v_1 \\ v_2 \end{bmatrix} = \begin{bmatrix} \sigma_{12} \\ \lambda - \sigma_{11} \end{bmatrix} \quad \text{or} \quad \begin{bmatrix} v_1 \\ v_2 \end{bmatrix} = \begin{bmatrix} \lambda - \sigma_{22} \\ \sigma_{21} \end{bmatrix}. \quad (9.41)$$

These components can then be normalized to direction cosines by dividing each component by  $\sqrt{v_1^2 + v_2^2}$ .

2. Alternatively, the orientation angles can be determined directly from  $\theta = \arctan(v_2/v_1)$ .

<sup>12</sup>Hence the commonly used symbol  $\lambda$  (lambda).

**Problem**

- Determine the eigenvalues and the corresponding eigenvectors associated with the following matrix representing the stress tensor (Fig. 9.36a; this is the problem of Fig. 9.20a). Note that the tensor sign convention is required.

$$\begin{bmatrix} \sigma_{11} & \sigma_{12} \\ \sigma_{21} & \sigma_{22} \end{bmatrix} = \begin{bmatrix} -48 & -16 \\ -16 & -20 \end{bmatrix}.$$

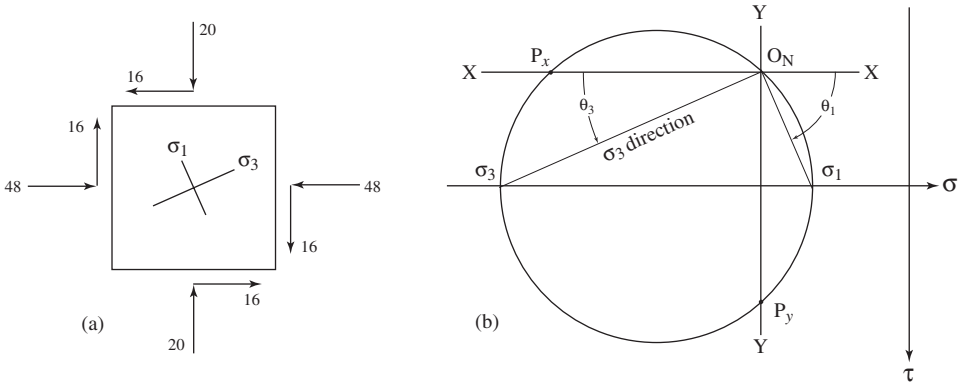


**Figure 9.36** Graphical solution: (a) physical plane; (b) Mohr Circle plane.

**Solution**

1. With these components  $\sigma_{ij}$  the characteristic equation is

$$\lambda^2 + 68\lambda + 704 = 0.$$

2. Using the quadratic formula its roots are  $\lambda_1 = -12.73971$  and  $\lambda_2 = -55.26029$  and these are the principal stresses.
3. Using the first of Eqs. 9.40, the components of the eigenvector associated with  $\lambda_1$  is

$$\begin{bmatrix} v_1 \\ v_2 \end{bmatrix} = \begin{bmatrix} \sigma_{12} \\ \lambda_1 - \sigma_{11} \end{bmatrix} = \begin{bmatrix} -16 \\ -12.73971 + 48 \end{bmatrix} = \begin{bmatrix} -16 \\ 35.26029 \end{bmatrix}.$$

Normalizing these gives the direction cosines  $v_1 = -0.41322$  and  $v_2 = 0.91063$ .

4. Using the second of Eqs. 9.40, the components of the eigenvector associated with  $\lambda_2$  are

$$\begin{bmatrix} v_1 \\ v_2 \end{bmatrix} = \begin{bmatrix} \lambda_2 - \sigma_{22} \\ \sigma_{21} \end{bmatrix} = \begin{bmatrix} -55.26029 + 20 \\ -16 \end{bmatrix} = \begin{bmatrix} -35.26029 \\ -16 \end{bmatrix}.$$

Normalizing these gives the direction cosines and  $v_1 = 0.41322$  and  $v_2 = 0.91063$ .

5. The principal stresses are  $\sigma_1 = -12.7$  MPa and  $\sigma_3 = -55.3$  MPa and the corresponding orientation angles are  $\theta_1 = -65.5^\circ$  and  $\theta_3 = 24.4^\circ$ . The reversal of labels of the principal stresses and change in measuring the orientation angles result from the use of the tensor sign convention.

The Mohr Circle solution of this same problem is shown in Fig. 9.36b. The basic method follows closely that of Fig. 9.20 but with two important differences (see Fig. 9.15b).

1. With the *tension positive* sign convention the circle plots to the left of the  $\tau$  axis and the positions of the principal stresses are reversed.
2. The *clockwise-up* convention for values of  $\tau$  is used for plotting the points  $P_x(-48, -16)$  and  $P_y(-20, 16)$ .

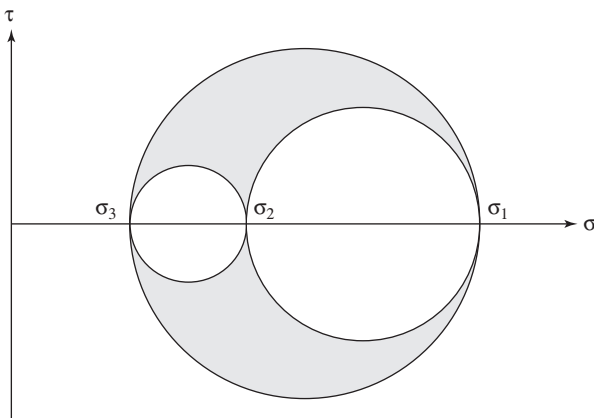


**Figure 9.37** Three-dimensional Mohr Circle diagram.

There is also a Mohr Circle construction for three-dimensional stress problems (Jaeger & Cook, 1979, p. 27f). It is especially useful for graphically presenting three-dimensional states of stress – points representing traction components plot on one of the three circles or in the area between them (shown shaded in Fig. 9.37). But as an analytical tool it is cumbersome.

The relation between the traction vector  $\mathbf{T}$  and the unit normal vector  $\hat{\mathbf{n}}$  can also be written as a matrix equation. For the simpler case of a stress matrix in diagonal form the equation has the form

$$\begin{bmatrix} T_1 \\ T_2 \\ T_3 \end{bmatrix} = \begin{bmatrix} \sigma_{11} & 0 & 0 \\ 0 & \sigma_{22} & 0 \\ 0 & 0 & \sigma_{33} \end{bmatrix} \begin{bmatrix} n_1 \\ n_2 \\ n_3 \end{bmatrix} = \begin{bmatrix} \sigma_{11}n_1 \\ \sigma_{22}n_2 \\ \sigma_{33}n_3 \end{bmatrix}. \quad (9.42)$$



For the stress matrix in its most general form it is

$$\begin{bmatrix} T_1 \\ T_2 \\ T_3 \end{bmatrix} = \begin{bmatrix} \sigma_{11} & \sigma_{12} & \sigma_{13} \\ \sigma_{21} & \sigma_{22} & \sigma_{23} \\ \sigma_{31} & \sigma_{32} & \sigma_{33} \end{bmatrix} \begin{bmatrix} n_1 \\ n_2 \\ n_3 \end{bmatrix} = \begin{bmatrix} \sigma_{11}n_1 + \sigma_{12}n_2 + \sigma_{13}n_3 \\ \sigma_{21}n_1 + \sigma_{22}n_2 + \sigma_{23}n_3 \\ \sigma_{31}n_1 + \sigma_{32}n_2 + \sigma_{33}n_3 \end{bmatrix}. \quad (9.43)$$

Cauchy’s formula for this completely general form is (cf. Eq. 9.34)

$$T_i = \sigma_{ij}n_j \quad (i, j = 1, 2, 3). \quad (9.44)$$

As before, performing the matrix multiplication gives the components of the traction vector. Its magnitude is then obtained from

$$T = \sqrt{T_1^2 + T_2^2 + T_3^2} \quad (9.45)$$

and its direction cosines are  $(T_1/T, T_2/T, T_3/T)$ . The angle  $\psi$  between  $\mathbf{T}$  and  $\hat{\mathbf{n}}$  can be obtained from the dot product (see Eq. 7.13). Then the normal and shearing components can be found using Eqs. 9.29.

**Problem**

- For principal stresses  $\sigma_{11} = -35$  MPa,  $\sigma_{22} = -15$  MPa and  $\sigma_{33} = -75$  MPa, what is the traction acting on a plane whose pole is  $P(35/065)$ , and in what direction does the shearing component act on this plane?

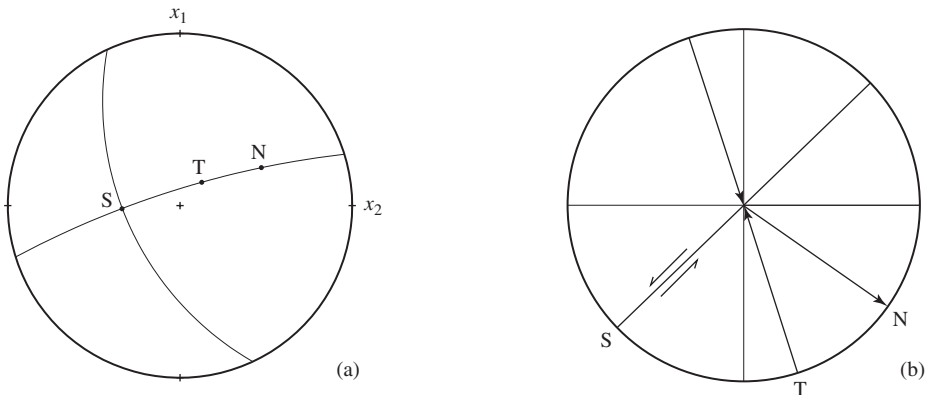


**Figure 9.38**  $\mathbf{T}$  and  $\hat{\mathbf{n}}$ : (a) stereogram; (b) inclined diametral plane containing  $NTS$ .

**Solution**

1. On a stereogram plot the pole to the specified plane and label it  $\hat{\mathbf{n}}$ ; by this choice the lower, or footwall is the positive side. Also trace in the great circle representing the plane (Fig. 9.38a).

2. With Eqs. 7.7 the direction cosines of  $N$  are  $n_1 = 0.34619$ ,  $n_2 = 0.74240$  and  $n_3 = 0.57358$ ,
3. With these and the principal stresses in Eqs. 9.26 the traction components are  $T_1 = -12.11660$ ,  $T_2 = -11.13606$  and  $T_3 = -43.01823$ . Then by Eq. 9.37,  $T = 46.05857$  MPa.
4. The direction cosines are  $T_1/T = -0.26307$ ,  $T_2/T = -0.24178$  and  $T_3/T = -0.93399$ . Because  $T_3$  is negative  $\mathbf{T}$  points upward below the plane (and downward above it).
5. To plot on the lower hemisphere, replace  $\mathbf{T}$  with its opposite by changing the signs of all these cosines. From Eqs. 7.8 its attitude is  $T(69/043)$  and we add this point to the stereogram.
6. Through  $N$  and  $T$  trace in the great circle to intersect the specified plane at  $S$ , which is the direction of the shearing component.
7. Now construct a direct view of the steeply inclined plane containing  $N$ ,  $T$  and  $S$  (Fig. 9.38b). Because the calculated  $\mathbf{T}$  below the plane points upward (and therefore above the plane points downward) the sense of shear on the plane is seen to be dominantly normal. Because  $S$  is close to the line of true dip, the fault is essentially a normal fault.

The procedure of obtaining the eigenvalues and eigenvectors from a  $3 \times 3$  stress matrix is essentially the same as used for the  $2 \times 2$  matrix, though more involved computationally. The characteristic equation is a cubic equation with three roots:

$$\sigma_p^3 - I_1\sigma_p^2 + I_2\sigma_p - I_3 = 0,$$

where the coefficients and the constant are the three *stress invariants*

$$I_1 = \sigma_{11} + \sigma_{22} + \sigma_{33},$$

$$I_2 = \sigma_{11}\sigma_{22} + \sigma_{22}\sigma_{33} + \sigma_{33}\sigma_{11} - \sigma_{12}^2 - \sigma_{23}^2 - \sigma_{13}^2,$$

$$I_3 = \sigma_{11}\sigma_{22}\sigma_{33} + 2\sigma_{12}\sigma_{23}\sigma_{13} - \sigma_{11}\sigma_{23}^2 - \sigma_{22}\sigma_{13}^2 - \sigma_{33}\sigma_{12}^2.$$

There is an algorithm for obtaining the roots of a cubic equation, but a much easier approach is to take advantage of the MATLAB command (see Middleton, 2000, p. 93):  $[V, D] = \text{eig}(S)$ , where  $S$  is the stress matrix;  $V$  contains the normalized components of the three eigenvectors and  $D$  is the diagonal matrix with the three eigenvalues.

### 9.13 Exercises

1. For  $\sigma_1 = 150$  MPa and  $\sigma_3 = 80$  MPa, use the following pair of equations to calculate the values of  $(\sigma, \tau)$  for  $\theta = 0-90^\circ$  at  $10^\circ$  intervals. Plot each of these pairs as point

on a set of axes  $x = \sigma$  and  $y = \tau$ . What is the form of the locus of these points?

$$\sigma = \sigma_1 \cos^2 \theta + \sigma_3 \sin^2 \theta,$$

$$\tau = (\sigma_1 - \sigma_3) \sin \theta \cos \theta.$$

2. Determine the principal stresses and their orientation (Fig. 9.39).

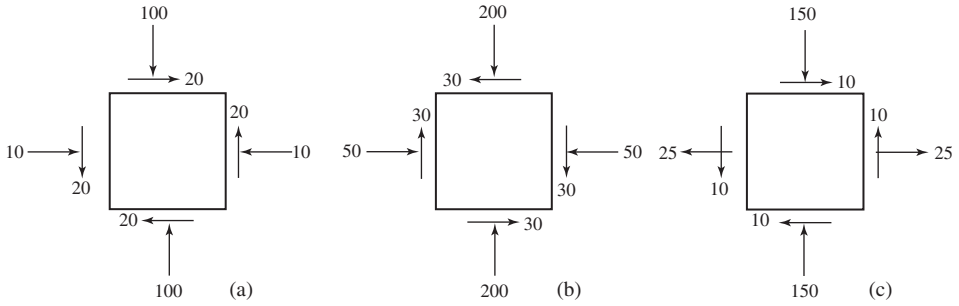


Figure 9.39

3. Determine the traction components acting on the oblique plane (Fig. 9.40).

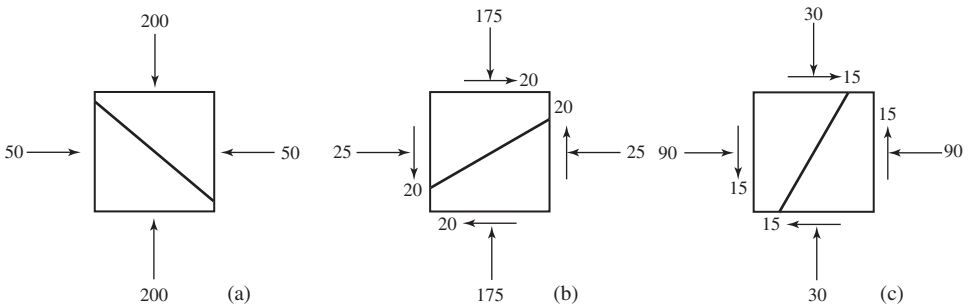


Figure 9.40

# 10

## Faulting

### 10.1 Introduction

An important goal of structural geology is to determine the nature of the stress field together with the mechanical properties of the rock material at the time of the formation of structures. In the case of faults, some of this information may be obtained by combining data obtained from experiments with a detailed field study of their geometrical features.<sup>1</sup>

### 10.2 Experimental fractures

To learn how rocks behave under various states of stress it is necessary to perform experiments which reproduce natural conditions as closely as possible. Ideally, the magnitudes of all three principal stresses should be independently controlled, but this is difficult to accomplish. In the *conventional triaxial test* a load is applied to the ends of a carefully prepared cylinder of rock jacketed with copper foil and immersed in a pressurized fluid. In this configuration,  $\sigma_1$  is parallel to the axis of the cylinder. The magnitudes of the other two principal stresses are equal to the pressure in the confining medium and this is commonly termed the *confining pressure*.

At low confining pressures the rock specimen fractures and there are two types: *extension fractures* perpendicular to  $\sigma_3$  (Fig. 10.1a) or *shear fractures* related to but not identical with the planes of maximum shearing stress. If fracture occurs before permanent distortion, the material is *brittle* (Fig. 10.1b); if a small permanent distortion ( $\leq 5\%$ ) precedes fracturing, it is *semi-brittle* (Fig. 10.1c). At higher confining pressures, the deformational mode is entirely *ductile* (Fig. 10.1d).

<sup>1</sup>The physical process of fault formation involves a complex sequence of nucleation, propagation and linkage of numerous diversely oriented microscopic flaws (see Reches & Lockner, 1994). We are concerned here only with the final macroscopic state.

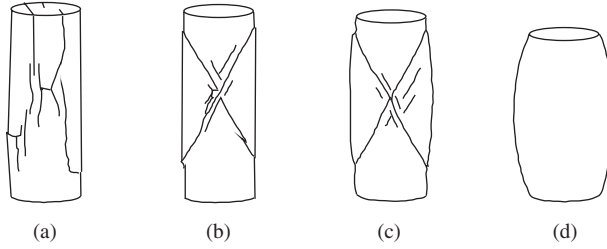


**Figure 10.1** Failure of limestone as a function of confining pressure (Verhoogen, *et al.*, 1970, p.458): (a) extension fractures (0.1 MPa); (b) brittle shear fractures (3.5 MPa); (c) semi-brittle shear fractures (30 MPa); (d) ductile failure (100 MPa).

### 10.3 Role of friction

What conditions must exist for a brittle rock to fail in shear? To approach this question we first consider the case of frictional sliding on a single preexisting plane in a rock mass. A simple model is a block on a table top (Fig. 10.2a). At rest, the forces acting on the block are its weight **W** which by Newton’s third law is balanced by an opposite normal force **N** of equal magnitude. If a small horizontal force **F** is applied to the block a frictional resistive force **f** arises which exactly equals this applied force.

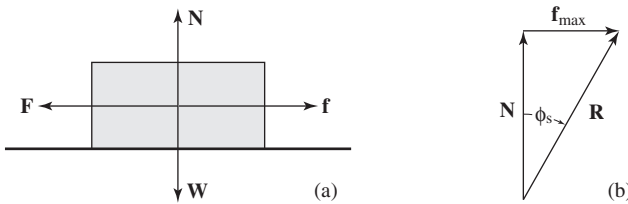


**Figure 10.2** Sliding block: (a) forces; (b) resultant.

With an increase in **F**, at a certain magnitude the block breaks contact and accelerates. At this instant the resistance **f** has its maximum magnitude which is proportional to **N**. Thus

$$f_{max} = \mu_s N, \tag{10.1}$$

where the constant of proportionality  $\mu_s$  is the *coefficient of static friction*. This is *Amon-ton’s law*, named for its modern formulator (Suppe, 1985, p. 289).

Once sliding is initiated the situation becomes more complicated. The *coefficient of dynamic friction* is less than  $\mu_s$  so that the resistance to sliding once in motion is less.<sup>2</sup> The result is a series of irregular slip-stick episodes which can be modeled with sliding blocks with springs attached (Turcotte, 1997, p. 245–255).<sup>3</sup> Our concern here is solely

<sup>2</sup>When trying to stop an automobile quickly, this is why it is desirable to avoid braking so hard that skidding results. The difficulty in doing this led to the development of automatic braking systems.

<sup>3</sup>The presence of gouge on the fault plane complicates this behavior (see Muhuri, *et al.*, 2003).

with the static case, but such detailed studies of fault motion are important because they lead to a deeper understanding of faulting and earthquakes.

Amontons's law also has a geometrical interpretation. From a triangle of forces, the angle the resultant vector  $\mathbf{R}$  makes with  $\mathbf{N}$  is called the *angle of static friction*  $\phi_s$  (Fig. 10.2b). Then

$$\mu_s = \tan \phi_s = f_{max}/N. \quad (10.2)$$

The value of  $\phi_s$  depends on the physical nature of the sliding surfaces and must be determined empirically. For sandpaper it is about  $45^\circ$  and for Teflon it is close to zero. In rocks, it is about  $30^\circ$  (Byerlee, 1978). If clay minerals are present on the fault plane it may be much lower. In most of our treatments it is convenient to assume that  $\phi_s = 30^\circ$  exactly.

An even more useful model is the familiar experiment of a block on a plane inclined at angle  $\alpha$  (Fig. 10.3a). With coordinate axes  $x$  parallel and  $y$  normal to the plane the force  $\mathbf{W}$  has scalar components in each of these direction which we obtain from the dot products of  $\mathbf{W}$  and the unit vectors  $\hat{\mathbf{u}}_x$  and  $\hat{\mathbf{u}}_y$  giving

$$W_x = \mathbf{W} \cdot \hat{\mathbf{u}}_x \quad \text{and} \quad W_y = \mathbf{W} \cdot \hat{\mathbf{u}}_y.$$

Thus

$$W_x = W \sin \alpha \quad \text{and} \quad W_y = W \cos \alpha.$$

At rest, equilibrium requires that the sum of all the forces is equal to zero (Fig. 10.3b). This in turn requires the sum of the components in the  $x$  direction to be

$$f - W_x = f - W \sin \alpha = 0 \quad \text{or} \quad f = W \sin \alpha, \quad (10.3)$$

and the sum of the components in the  $y$  direction to be

$$N - W_y = N - W \cos \alpha = 0 \quad \text{or} \quad N = W \cos \alpha. \quad (10.4)$$

With increasing slope a point is reached where the block breaks contact and, again, the frictional resistive force has its maximum value  $f_{max}$ . Dividing Eq. 10.3 by Eq. 10.4 gives

$$\frac{f_{max}}{N} = \frac{W \sin \alpha}{W \cos \alpha}.$$

From the definition of  $\mu_s$  in Eq. 10.2 we then have

$$\mu_s = \tan \alpha, \quad (10.5)$$

that is, the block starts to slide when the slope angle is equal to the angle of static friction. A natural counterpart of this simple experiment is the failure of a slope in dry rock by block sliding into a road cut (see Rahm, 1986, p. 172).

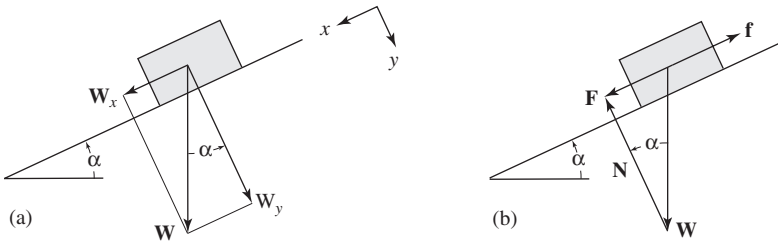


**Figure 10.3** Block on incline: (a) components of  $\mathbf{W}$ ; (b) forces at equilibrium.

In these examples we determined the condition which simultaneously satisfies both equilibrium and the criterion of sliding. This *limiting equilibrium analysis* is widely used in soil and rock mechanics and it also forms the basis of our treatment of faults.

For problems of faulting it is convenient to express Amontons’s law in terms of the normal and shearing components of the traction acting on the plane of sliding. Dividing Eq. 10.1 by the area of contact gives

$$\tau = \mu_s \sigma. \tag{10.6}$$

In this form it can be depicted on a Mohr Circle diagram (Fig. 10.4). Because slip depends on the magnitude, not sign of  $\tau$ , there are two conditions which satisfy Eq. 10.5 and these can be represented by a pair of lines passing through the origin with slope angles  $\pm\phi_s$ .

With this representation of Amontons’s law, we can now graphically determine the conditions which will cause slip. Consider a body of rock at depth containing a plane of weakness whose physical properties are determined solely by friction. As the *differential stress* ( $\sigma_1 - \sigma_3$ ) increases from some initial state, the traction on this plane will ultimately slip. The problem is to find the point on the Mohr Circle which simultaneously satisfies both the orientation of the plane and the slip condition.

The first possibility of slip occurs when the Mohr Circle is tangent to the two lines whose slope angles are  $\pm\phi_s$ . However, it will occur only on the planes making an angle  $\beta$  with the  $\sigma_1$  direction. From the two congruent right triangles  $OCP_1$  and  $OCP_2$  of Fig. 10.4

$$\phi_s = 90^\circ - 2\beta \quad \text{or} \quad \beta = 45^\circ - \frac{1}{2}\phi_s. \tag{10.7}$$

Because  $\beta = 90^\circ - \theta$  we also have

$$\theta = 45^\circ + \frac{1}{2}\phi_s. \tag{10.8}$$

Planes whose orientations are given by these angles are said to have the *optimum orientation*. Coincidentally, if  $\phi_s = 30^\circ$  then  $\beta = 30^\circ$ .

We now need a way of locating the point common to the circle and the line. The trick is to find a pole of the Mohr Circle using the known traction component and this usually requires that the representation on the physical plane be reoriented.

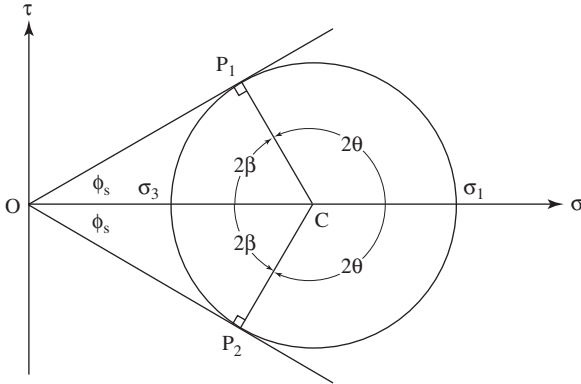


**Figure 10.4** Slip condition for optimally oriented planes.

**Problem**

- The physical property of an existing fault *AB* is given by  $\phi_s = 30^\circ$  (Fig. 10.5a). If  $\sigma_3 = 60$  MPa what will be the value of  $\sigma_1$  for slip if the orientation of the plane is given by  $\theta = +60^\circ$ ?

**Construction**

1. On a set of axes draw a line through the origin with slope angle  $+\phi_s$  (only this line is needed because  $\theta$  is positive). Using a convenient scale plot the point representing the known value of  $\sigma_3$  on the  $\sigma$  axis (Fig. 10.5b).
2. Because  $\sigma_3$  is known, the physical representation must be rotated so that the plane on which it acts is vertical (as shown). Then the pole  $O_P$  coincides with  $\sigma_3$  (see Fig. 9.22b).
3. A line through  $O_P$  parallel to the trace of the fault on the physical plane intersects the sloping  $\phi_s$  line at  $P$ . Line  $O_P P$  is a chord of the circle.
4. The perpendicular bisector of this chord intersects the  $\sigma$  axis at center  $C$  and the circle is drawn with  $CP$  as radius.

**Answer**

- For this circle  $\sigma_1 = 180$  MPa. The circle is tangent to the slip line, hence the plane is optimally oriented.



Under such conditions, the measure of the *strength* of the rock mass containing this plane of weakness is the differential stress  $\sigma_1 - \sigma_3 = 120$  MPa. Geometrically this is represented by the diameter of the limiting Mohr Circle.

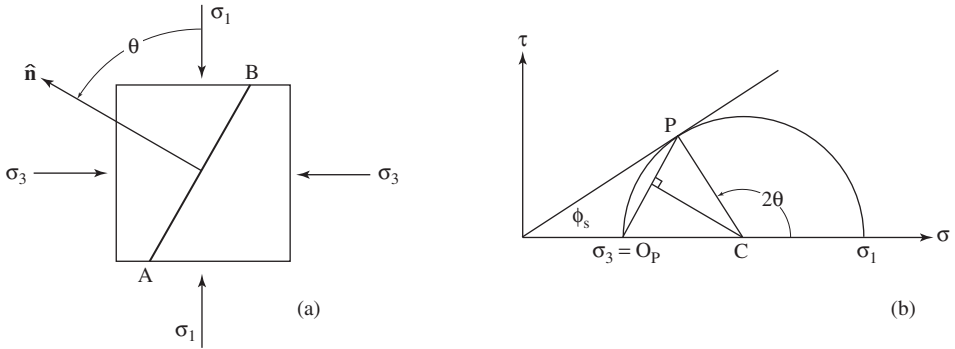


**Figure 10.5** Construction I: (a) physical plane; (b) Mohr Circle plane.

There is a simple analytical relationship between the two principal stresses for the case of renewed sliding on an optimum plane. From Fig. 10.4

$$\sin \phi_s = \frac{\frac{1}{2}(\sigma_1 - \sigma_3)}{\frac{1}{2}(\sigma_1 + \sigma_3)} \quad \text{or} \quad \frac{\sigma_1}{\sigma_3} = \frac{1 + \sin \phi_s}{1 - \sin \phi_s}. \tag{10.9}$$

If  $\phi_s = 30^\circ$  the minimum ratio of principal stresses for renewed sliding is

$$R_{min} = \sigma_1/\sigma_3 = 3.0. \tag{10.10}$$

This is a useful (and easy) number to remember. Other angles of friction will, of course, give different values of this ratio though they won't differ greatly.

If the preexisting plane of weakness has some other orientation, a further increase in the differential stress is required to produce slip.

**Problem**

- The property of an existing fault *AB* is given by  $\phi_s = 30^\circ$  (Fig. 10.6a). If  $\sigma_1 = 100$  MPa what will the required value of  $\sigma_3$  for slip be if the orientation of the plane of the fault is given by  $\theta_1 = -50^\circ$ ?

**Construction**

1. On a set of axes draw a line through the origin with slope angle  $-\phi_s$  (here  $\theta$  is negative). Plot the point representing  $\sigma_1$  on the  $\sigma$  axis using a convenient scale (Fig. 10.6b). For the pole  $O_P$  to coincide with this point the  $\sigma_1$  direction must be horizontal on the physical plane (see Fig. 9.22a).
2. A line parallel to the trace of plane *AB* through  $O_P$  intersects the  $\phi_s$  line at a point  $P_1$ .
3. The bisector of chord  $O_P P_1$  locates center *C* of the circle and its radius is  $C P_1$ .

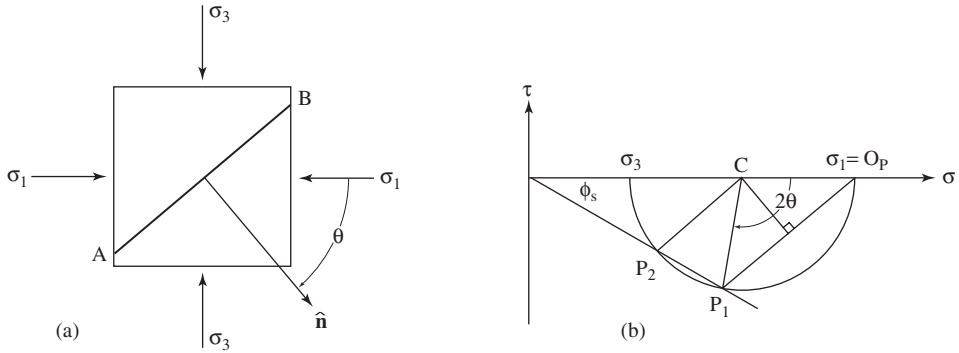


**Figure 10.6** Construction II: (a) physical plane; (b) Mohr Circle plane.

**Answer**

- From this circle  $\sigma_3 = 31$  MPa. Note that the second intersection  $P_2$  represents the slip on a second possible plane whose orientation is given by  $\theta_2 = -70^\circ$ .

Note carefully that the constructions for both these cases required that the pole be coincident with the point representing the known principal stress and this required the representation on the physical plane to be appropriately oriented.

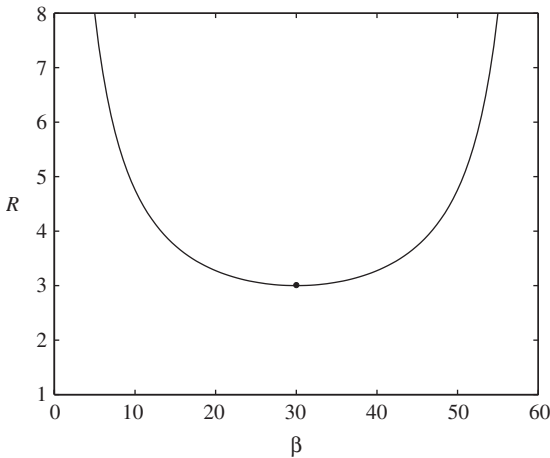


**Figure 10.7** Graph of  $FitR$  vs.  $\beta$  for  $\phi_s = 30^\circ$ .

We can also obtain an analytical expression for the stress required for slip on variously oriented planes. Substituting the expressions for  $\sigma$  and  $\tau$  of Eqs. 9.15 and using  $\theta = 90^\circ - \beta$ , Amontons's law of Eq. 10.6 becomes

$$(\sigma_1 - \sigma_3) \cos \beta \sin \beta = \mu_s(\sigma_1 \sin^2 \beta) + \mu_s(\sigma_3 \cos^2 \beta).$$

Dividing both sides by  $\cos \beta \sin \beta$ , using the identity  $\tan \beta = \sin \beta / \cos \beta$  and rearranging then yields

$$R = \frac{\sigma_1}{\sigma_3} = \frac{1 + \mu_s / \tan \beta}{1 - \mu_s \tan \beta}. \tag{10.11}$$

A graph of this equation for  $\phi_s = 30^\circ$  is shown in Fig. 10.7. Note that  $R = R_{min}$  when the plane is optimally oriented, that is, when  $\beta = 30^\circ$ . From the data of the previous problem  $\beta = 20^\circ$  and  $\beta = 40^\circ$ . Using both of these in Eq. 10.11 gives  $R = 3.27$ , which is the same result found graphically in Fig. 10.6b.

In some orientations of a preexisting plane of weakness the slip condition can be met only by very special states of stress. For example, if  $\phi_s = 30^\circ$  and  $\theta = 30^\circ$  then slip is possible only if  $\sigma_3 = 0$  (Fig. 10.8a). If  $\theta < 30^\circ$  then  $\sigma_3$  must be tensile for slip to occur (Fig. 10.8b).

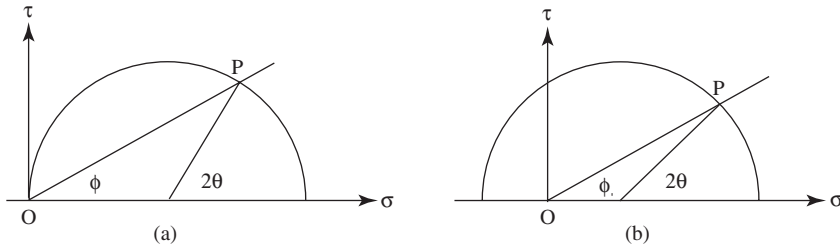


**Figure 10.8** Special conditions: (a)  $\theta = 30^\circ$ ; (b)  $\theta = 22^\circ$ .

### 10.4 Coulomb criterion

What if there is no preexisting plane of weakness? More than two hundred years ago, the French physicist Charles Augustin de Coulomb [1736–1806]<sup>4</sup> (see Handin, 1969) suggested that three factors resist the shearing traction which tends to cause failure in shear:

1. the friction on the potential shear plane,
2. the normal stress across the plane, and
3. the shear strength of the material parallel to the plane.

This is now known as the *Coulomb criterion of shear failure* and is usually written as

$$\tau = c + \mu_i \sigma \tag{10.12}$$

<sup>4</sup>Coulomb's name is also given to the law describing the force between two electric charges and to the unit of electric charge.

where  $c$  is the *cohesive shear strength* which is the resistance to shear when  $\sigma = 0$  and  $\mu_i = \tan \phi_i$  is the *coefficient of internal friction*, where  $\phi_i$  is the *angle of internal friction*. For most sedimentary rocks the cohesion is 10–20 MPa and for crystalline rocks it is about 50 MPa. The angle of internal friction is usually not identical to the angle of static friction, but typical values are still close to  $30^\circ$ .

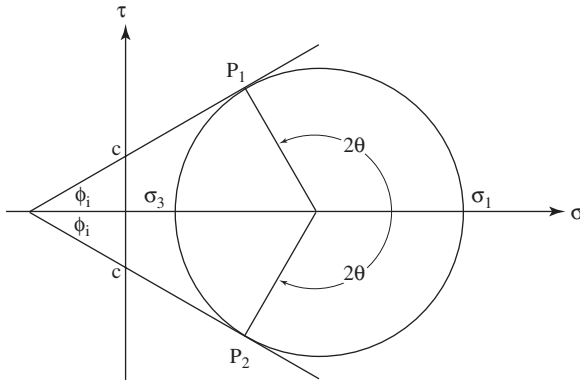


**Figure 10.9** Coulomb criterion of shear failure.

On a Mohr Circle diagram, this criterion of shear failure is represented by the lines with slope angles  $\pm\phi_i$  with intercepts on the  $\tau$  axis equal to the cohesion  $\pm c$  (Fig. 10.9). Tests made at moderate confining pressures confirm that this linear envelope describes the conditions of shear failure to a good approximation.

We can now determine the conditions for primary shear failure in rock. This condition is met when a Mohr Circle is tangent to the *failure envelopes*. In contrast to the previous case, no other possibility exists – no circle may extend beyond these two envelopes. In effect, newly formed fractures are always in the “optimum” orientation, hence the orientation of the new fault plane is, after Eqs. 10.6 and 10.7, given by

$$\theta = 45^\circ + \frac{1}{2}\phi_i \quad \text{or} \quad \beta = 45^\circ - \frac{1}{2}\phi_i. \tag{10.13}$$

**Problem**

- The rock properties are  $c = 25$  MPa and  $\phi_i = 30^\circ$ . If  $\sigma_3 = 60$  MPa what will  $\sigma_1$  be at failure?

**Construction**

1. From Eqs. 10.13 the orientation of one of the potential faults is given by  $\theta = +60^\circ$  and the trace  $AB$  of its plane can then be added to the representation on the physical plane (Fig. 10.10a).
2. On a Mohr Circle diagram draw a line with slope angle  $\phi_i = +30^\circ$  with intercept on the  $\tau$  axis at point  $(0, c) = (0, 25)$ . Plot the point representing  $\sigma_3$  at 60 units from  $O$  on the  $\sigma$  axis (Fig. 10.10b).

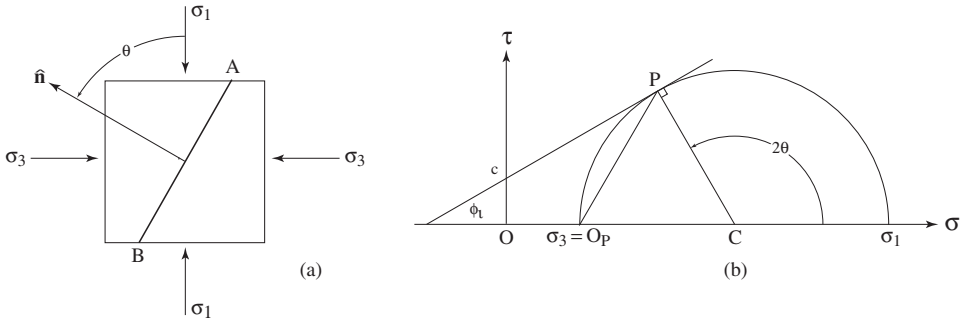


**Figure 10.10** Coulomb failure: (a) physical plane; (b) Mohr Circle.

3. In this orientation, the pole  $O_P$  coincides with  $\sigma_3$ . A line through  $O_P$  parallel to the potential fault intersects the sloping  $\phi_i$  line at P.
4. At point P a line perpendicular to the failure envelope locates center C and the circle can then be completed with radius CP.

**Answer**

- The second intercept of this circle with the  $\sigma$  axis gives  $\sigma_1 = 270$  MPa.

What controls whether failure is by renewed slip or the formation of a new fault? The answer can be found by constructing a Mohr Circle diagram for both criteria (Fig. 10.11). As we have seen, a new fault forms when the circle is tangent to the failure envelope (point  $P_2$ ). This same circle also satisfies the conditions for slip represented by points  $P_1$  and  $P_3$  on planes whose orientations are given by  $\theta_2 = 40^\circ$  and  $\theta_3 = 80^\circ$ . Under perfect conditions slip and fracture could occur simultaneously.

During the buildup of the differential stress the condition for slip would have been met on any preexisting plane whose orientation lies between  $\theta_2$  and  $\theta_3$ . For planes outside this range, fracture rather than renewed slip occurs.

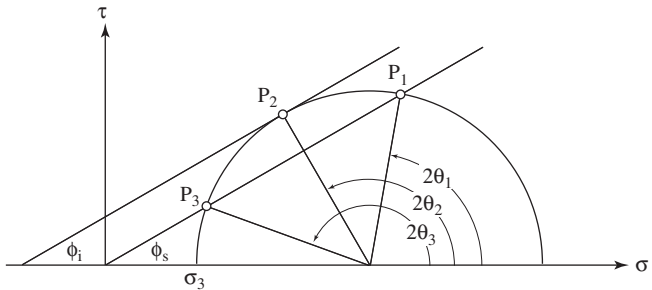


**Figure 10.11** Simultaneous fracture and renewed slip.

## 10.5 Limitations

The Coulomb criterion has two important limitations. First, the predicted tensile strength  $T$ , that is, when  $\tau = 0$ , as represented by the point of intersection of the sloping envelope and the  $\sigma$  axis is too great; commonly it is only about half the cohesion (Price, 1966, p. 27).

Therefore, the failure envelope must be modified to take this fact into account. The usual way is to adopt the *modified Griffith criterion*. This is based on the analysis of stressed microscopic elliptical *Griffith cracks*. Its basic form is a parabola (Fig. 10.12), and it predicts several different types of behavior.

The predicted tensile strength  $T$  is exactly half the cohesion. Further, the orientations of tensile fractures when  $\sigma_3 = -T$  are accurately predicted to be perpendicular to  $\sigma_3$ .

The part of the curve in the tensile field between the points  $(-T, 0)$  and  $(0, c)$  predicts the formation of fractures under hybrid conditions of tension and shear at high angles to  $\sigma_3$ . Unfortunately, these predicted fractures are not borne out by experience (Engelder, 1999).

1. Only a very few such naturally occurring fractures have been observed and they are open to alternative interpretations.
2. Laboratory experiments have failed to reproduce such fractures.
3. A more complete analysis involving *linear elastic fracture mechanics* predicts a different behavior.

In contrast, under conditions of  $\sigma > 0$ , the parabola does actually predict shear fractures with a range of orientations  $\beta = 45^\circ - 30^\circ$  and these have been confirmed by careful experiments.

Finally, at higher values of  $\sigma$ , the parabolic portion of the curve is replaced by the linear Coulomb criterion. Under these conditions the Griffith cracks close, at least partially, and resistance to further development is friction on the crack walls, and this gives a physical interpretation of the parameter “internal friction”. To avoid a discontinuity in the failure envelope it is convenient to join the sloping Coulomb line at the point where the slope angle on the parabola is equal to  $\phi_i$ .

The second important limitation is that at even higher confining pressures failure occurs not by fracture but by flow (see Fig. 10.1d). Within this ductile regime, flow is pressure insensitive and therefore the failure envelope is horizontal (Goetze & Evans, 1979, p. 471), and all the circles at failure are the same size (Fig. 10.12). For this reason the deviatoric stress is used to analyze such behavior. The sharp angle between the sloping Coulomb envelope and this horizontal failure line is suspect but the detailed characteristics of the transition are not clear.

The onset of ductile flow, that is, when the value of  $\tau$  reaches the *yield point*, depends on composition and on temperature – the higher the temperature the lower the yield point. The onset of plasticity in quartz occurs at about  $300^\circ\text{C}$  and in feldspar at about  $450^\circ\text{C}$  (Scholz, 2002). For rocks containing both these common minerals there is a range

of conditions over which ductile behavior appears, hence there will be a complicated *transition* from fully brittle to fully ductile behavior.<sup>5</sup>

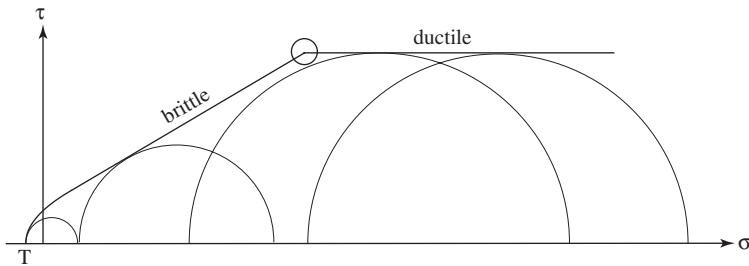


**Figure 10.12** Coulomb envelope modified for tensile and ductile failure.

## 10.6 Classification of faults

Clearly, no significant shearing traction acts along the air–earth interface, and therefore at shallow depths one of the principal stresses must be perpendicular to the earth’s surface. In areas of little or no relief this means that one of the principal stresses is essentially vertical. In combination with the geometrical relationship between fracture planes and principal stress directions, this leads to a three-fold classification of primary faults (Anderson, 1951, p. 15; see Fig. 10.13).

1. *Normal faults*:  $\sigma_1$  is vertical and the dip of the potential fault planes is  $\delta = 45^\circ + \frac{1}{2}\phi_i$ , or about  $60^\circ$ .
2. *Wrench faults*:  $\sigma_2$  is vertical and the potential fault planes are also vertical and the slip is horizontal.
3. *Thrust faults*:  $\sigma_3$  is vertical and the dip of the potential fault planes is  $\delta = 45^\circ - \frac{1}{2}\phi_i$ , or about  $30^\circ$ .

## 10.7 Faults and stresses

So far, our treatment started with known physical properties and then calculated the stress required to cause slip or fracture. This is a *forward problem*. In practice, however, we start with observed faults and then try to recover some information about the state of stress responsible for them. This is an *inverse problem* and a few simple examples will illustrate the general approach.

<sup>5</sup>Rutter (1986) makes the important point that some geologists associate *ductility* with a particular mechanism of rock deformation, namely intracrystalline plastic flow. It is better to reserve ductility for the capacity to strain by substantial amounts without any tendency for localized flow into bands (faults). Rather than *brittle–ductile* the term *brittle–plastic* avoids any confusion.

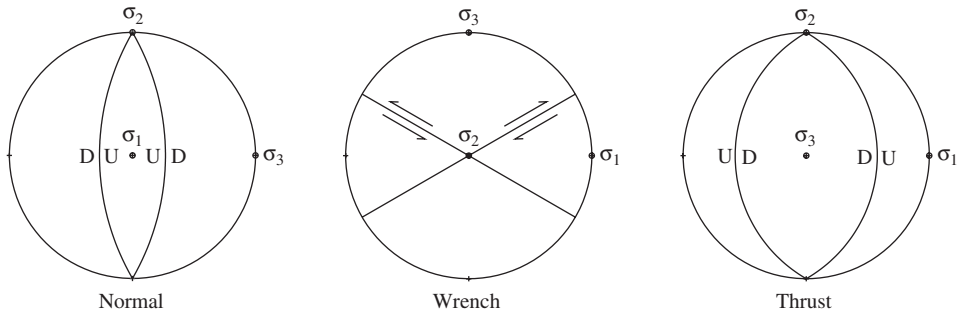


**Figure 10.13** Dynamic classification of faults.

If both of the two possible faults are present they are termed *conjugate shear fractures* (see Fig. 10.1b,c). From such pairs it is possible to determine the principal stress directions. These fractures are geometrically related to the stress in several ways.

1. The fractures intersect to fix the  $\sigma_2$  direction.
2. The dihedral angle between conjugate pairs is  $2\beta$ , and this angle is bisected by  $\sigma_1$ .
3. From  $\beta$  the angle of internal friction  $\phi_i$  is found from Eq. 10.13.
4. The slip direction is defined by the intersection of the fault plane and the  $\sigma_1\sigma_3$  plane.
5. The sense of slip is such that the wedge containing  $\sigma_1$  moves inward.

These relationships are sometimes collectively referred to as *Hartmann's rule* (Bucher, 1920, p. 709) and with them we can recover some important aspects of the orientation of the stress field and of some of the physical properties of the rock at the time of faulting. Note that if the pair of conjugate faults physically intersect, as in the experiments illustrated in Fig. 10.1, significant slip is possible on only one.

### Problem

- Given two conjugate faults with attitudes N 24 W, 50 W, and N 48 W, 76 NE (Fig. 10.14a), determine the orientation of the principal stresses, the direction and sense of slip and the angle of internal friction.

### Method

1. Represent the two faults as great circles on the stereonet (Fig. 10.14b). Their intersection defines the  $\sigma_2$  direction.
2. The great circle representing the plane whose pole is  $\sigma_2$  contains the  $\sigma_1$  and  $\sigma_3$  directions. The slip directions  $S_1$  and  $S_2$  are fixed by the intersection of this circle with the faults.
3. Bisect the acute segment of this great circle between the two faults to locate the orientation of  $\sigma_1$ . The  $\sigma_3$  direction is  $90^\circ$  along this same great circle.
4. The angle between  $\sigma_1$  and each of the slip directions is  $\beta$  and  $\phi_i$  can then be determined from Eq. 10.7.



**Answer**

- The principal stress directions are  $\sigma_1(65/173)$ ,  $\sigma_2(21/318)$  and  $\sigma_3(13/053)$ . Angle  $\beta = 29^\circ$ , hence  $\phi_i = 32^\circ$ . Because the  $\sigma_1$  direction is close to vertical, the sense of slip on both faults is dominantly normal. This sense can also be obtained by visualizing each fault with the flattened hand representing the plane of the fault and the index finger of the other hand representing the direction of  $\sigma_1$ .

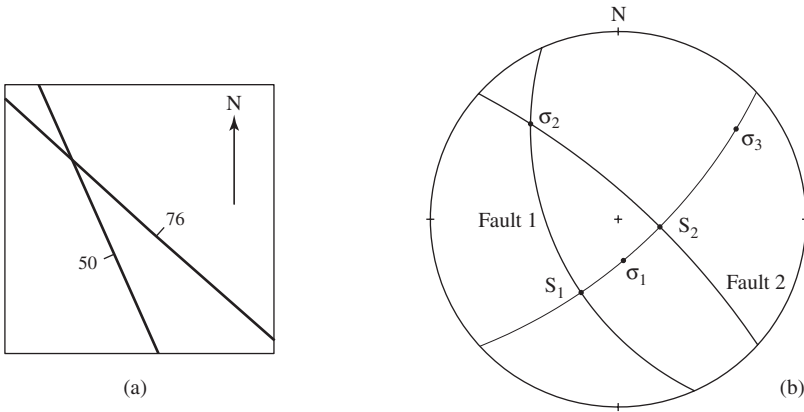


**Figure 10.14** Stress directions from conjugate faults: (a) map; (b) stereogram.

Extension fractures, commonly filled with quartz or calcite, are associated with some faults and these give additional information about the state of stress and the slip on a single fault.

**Problem**

- A fault (N 10 E, 25 W) has associated subhorizontal quartz veins (N 34 W, 6 E) (Fig. 10.15a). Determine the principal stress directions, the angle of internal friction, and the direction and sense of slip.

**Method**

- Plot the plane of the vein-filled fracture as a great circle (Fig. 10.15b). The pole of this plane is  $\sigma_3$ .
- Also plot the fault plane as a great circle. The plane of the vein intersects the fault to locate  $\sigma_2$ .
- With  $\sigma_2$  as the pole, the plane of  $\sigma_1$  and  $\sigma_3$  can be drawn. This great circle intersects the fault plane at the slip direction  $S$  and the plane of the vein at  $\sigma_1$ .
- The  $\sigma_3$  direction is  $90^\circ$  away from the  $\sigma_1$  direction. The angle between  $\sigma_1$  and the slip line is  $\beta$ .

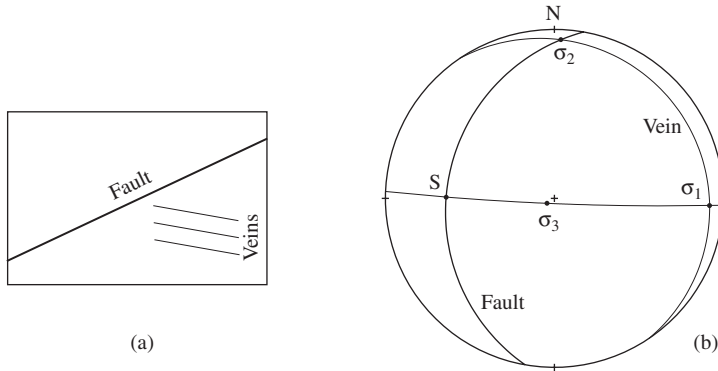


**Figure 10.15** Principal directions from fault and extension fractures: (a) section; (b) stereogram.

### Answer

- The orientations of the principal stresses are  $\sigma_1(05/093)$ ,  $\sigma_2(04/002)$ ,  $\sigma_3(84/236)$ . The measured angle between  $\sigma_1$  and the slip direction is  $150^\circ$ . This is the supplement of  $\beta$ , hence  $\phi_i = 30^\circ$ . Because  $\sigma_1$  is nearly horizontal the sense of slip is reverse and the fault is a thrust.

## 10.8 States of stress at depth

In the earth, the vertical component of stress, commonly called the *overburden pressure*, is a function of depth  $z$ , and its magnitude is given by

$$\sigma_{zz} = \rho g z, \quad (10.14)$$

where  $\rho$  is the rock density and  $g$  is the acceleration due to gravity. For example, assuming a mean density of  $2400 \text{ kg/m}^3$ , what is the vertical component of stress at a depth of 1 km?

$$\sigma_{zz} = (2400 \text{ kg/m}^3)(9.8 \text{ m/s}^2)(1000 \text{ m}) = 23.52 \times 10^6 \text{ Pa} = 23.52 \text{ MPa}.$$

Rounding this upward to 24 MPa introduces an error of only 2% (this is equivalent to the commonly used value  $g \approx 10 \text{ m/s}^2$ ). This is well within the accuracy of most *in situ* determinations of the density of crustal rocks, hence is acceptable for most purposes. With this approximation there is a close numerical relationship between the vertical component  $\sigma_{zz}$  and the density  $\rho$  which can be expressed in an easily remembered rule of thumb:

$$\sigma_{zz} = \rho / 100 \text{ MPa per kilometer}, \quad \rho \text{ in kg/m}^3.$$

What about the horizontal components of stress at depth? There are various observations and methods which are used to determine the orientation of the principal components in a horizontal plane (Zoback, *et al.*, 1989).

1. Geologic indicators (see §10.7).
2. Focal mechanisms (see §10.15).
3. Overcoring: a rock mass in a state of stress deforms elastically. If a part of such a mass is isolated by drilling a core the unstressed state will be recovered. The effects are small enough to be easily measured with sensitive strain gauges. From a knowledge of the physical properties of the rock, these strains are then converted back to the stress state before drilling (Turcotte & Schubert, 1982, p. 86). Such measurements are usually made at some distance from any free surface to avoid the perturbations which occur there.
4. Boreholes analyses: in an area subjected to a homogeneous compressive stress field with  $\sigma_{max}$  east-west and  $\sigma_{min}$  north-south (see Fig. 10.16a), the tractions tangential to the circumference of a vertical borehole, called *hoop stresses*, have a maximum value of  $3\sigma_{max} - \sigma_{min}$  at the north-south points and a minimum value of  $3\sigma_{min} - \sigma_{max}$  at the east-west points. This effect can be used in two ways to determine the orientation of the original principal stresses in the horizontal plane.
  - (a) Breakouts occur naturally in drill holes and are due to the compressive failure of the rock in the vicinity of the points of the maximum hoop stress with the result that the hole becomes enlarged (Fig. 10.16b).
  - (b) Hydraulic fractures are induced by pumping fluid into an isolated section of the drill hole. The result is tensile failure of the rock at the points of minimum hoop stress (Fig. 10.16c). Observing both features in the same well confirms that they are orthogonal.

Because the existing state of stress is important to a general understanding of the sources of lithospheric stresses and the nature of interplate tectonics there has been a concerted effort to make such measurements and, as part of *The World Stress Map* project, to compile the results in a uniform manner (Zoback, *et al.*, 1989; Zoback, 1992; Mueller, *et al.*, 2008).<sup>6</sup> As of 2008 more than 21 750 such measurements have been made. The North American portion of this map is shown in Fig. 10.17.

The broad or *first order* patterns are interpreted to be largely due to compressional forces applied at plate boundaries, primarily ridge push and continental collision, hence they are controlled by the geometry of the plate boundaries. Local perturbations or *second order* stresses are associated with specific geological or tectonic features (see Fig. 10.17).

Three independent lines of evidence indicate that in many places the stresses in the continental crust are in a state of *frictional equilibrium*, that is, the frictional resistive

<sup>6</sup>The maps, which are in color, are available on-line at <http://www-wsm.physik.uni-karlsruhe.de>

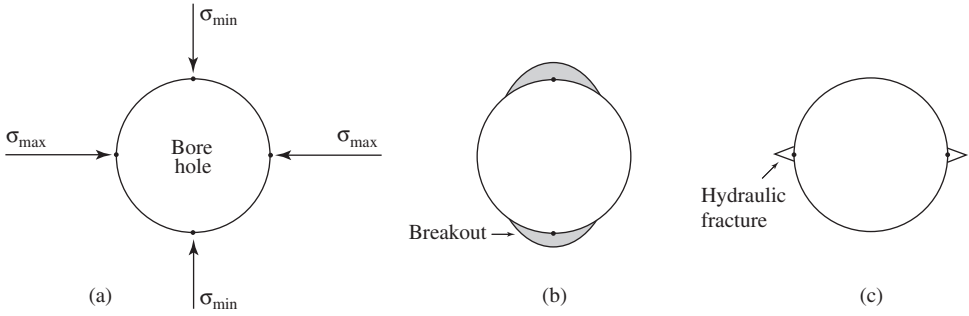


Figure 10.16 Stress orientation: (a) stresses before drilling; (b) breakouts; (c) hydraulic fractures.

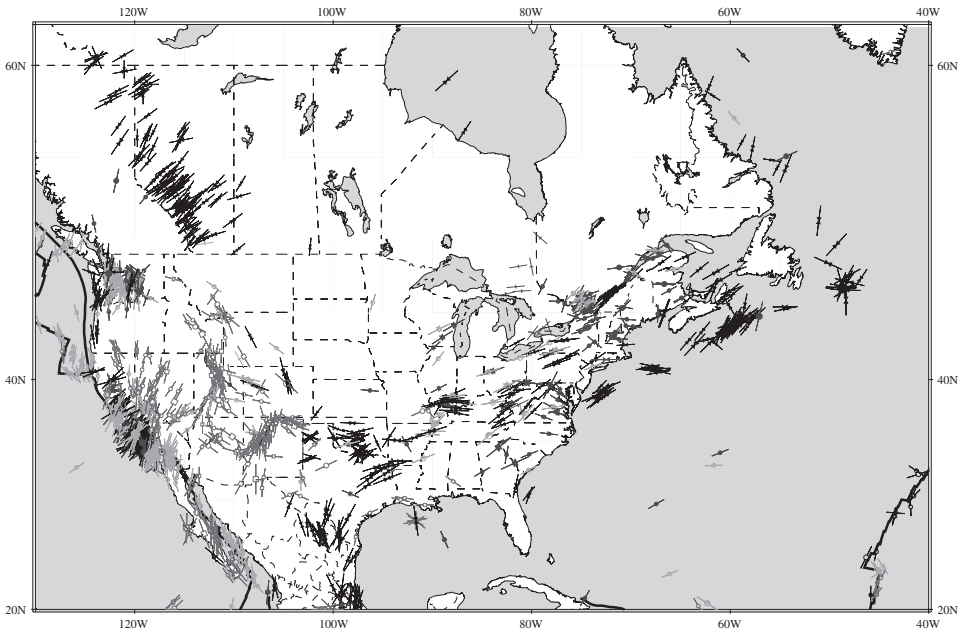


Figure 10.17 Stress Map of North America.

forces on existing faults and the tectonic and other forces are balanced (Townend & Zoback, 2000).

1. The widespread occurrence of seismicity induced by reservoir impoundment or fluid injection.
2. Earthquakes triggered by other earthquakes.
3. The measured stress states in the upper crust are consistent with the Coulomb criterion calculated using measured frictional coefficients.

Because it appears in the literature, there is one additional possibility that should be mentioned – the horizontal components may be equal to the overburden pressure, that

is, the state of stress is “hydrostatic”. This condition is expressed by

$$\sigma_{xx} = \sigma_{yy} = \sigma_{zz}.$$

In the solid earth, this state is termed *lithostatic* (Engelder, 1993, p. 4), and it is sometimes referred to as *Heim’s rule*. It is also the *standard state* used in the analytical description of the states of stress at depth (Anderson, 1951, p. 13). Here we use it only as a simple and convenient starting point. With the addition of tectonic forces, the state of stress at the point in question then becomes a more general and more interesting type.

### 10.9 Magnitudes of stress components

In order to get some feeling for the magnitudes of the principal stresses under conditions of frictional equilibrium we will analyze the conditions which must prevail at depth for renewed movement to occur. The following presentation is a graphical version of an analysis given by Sibson (1974).

For a normal fault,  $\sigma_1$  is vertical. If the bulk density is such that the vertical component of stress at a depth of 1 km is 24 MPa and  $\phi_s = 30^\circ$ , then with Eq. 10.9 the magnitude of  $\sigma_3$  is 8 MPa. This situation is illustrated in Fig. 10.18, where it can be seen that, assuming conditions were originally lithostatic and that the fault is in the optimum orientation, only a modest reduction of the horizontal stress is required for renewed slip. Note carefully that  $\sigma_3$  is *not* tensile for renewed normal faulting to occur under these conditions. In a similar way, we can determine the conditions for slip at depths of 2, 3, 4, 5 and 6 km.

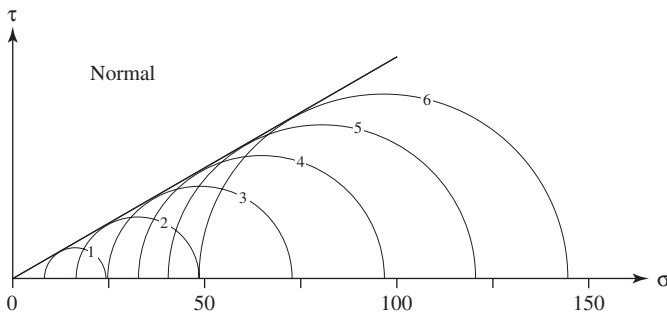


**Figure 10.18** Renewed slip on normal faults at 1–6 kilometers.

For thrust faults,  $\sigma_3$  is vertical and at a depth of 1 km its magnitude is the same 24 MPa. From Eq. 10.9, the magnitude of  $\sigma_1$  is then 72 MPa, and we see that a considerable increase in the horizontal stress component is required for renewed movement to occur. Similarly, we can find the stress conditions at greater depths (Fig. 10.19).

For a wrench fault  $\sigma_2$  is vertical, and there is a range of possibilities. All that is required is that  $\sigma_{zz}$  has a magnitude intermediate between  $\sigma_1$  and  $\sigma_3$ . That is,

$$\sigma_3 \leq \sigma_{zz} \leq \sigma_1.$$

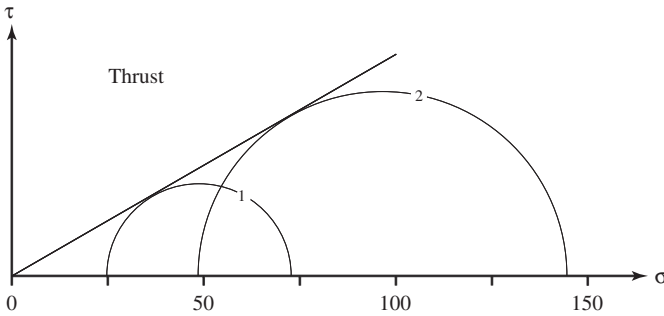


**Figure 10.19** Renewed slip on thrust faults at 1–2 kilometers.

We can express the relative value of  $\sigma_2$  by using

$$K = \frac{\sigma_2 - \sigma_3}{\sigma_1 - \sigma_3}. \tag{10.15}$$

Thus if  $\sigma_2 = \sigma_3$ ,  $K = 0$  and if  $\sigma_2 = \sigma_1$ ,  $K = 1$ . As an example, the conditions for slip are illustrated for  $K = 0.5$  in Fig. 10.20; in this special case the magnitude of  $\sigma_2$  coincides with the center of the Mohr Circle.

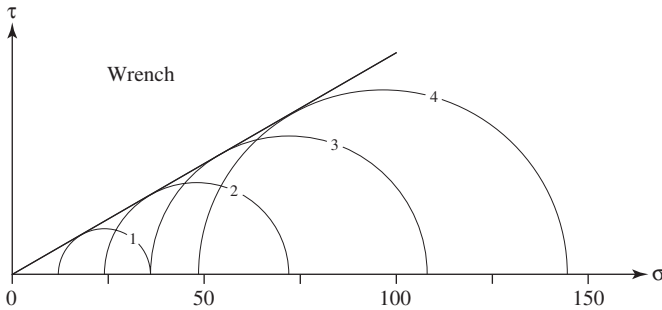


**Figure 10.20** Renewed slip on wrench faults ( $K=0.5$ ) at 1–4 kilometers.

These results clearly show that the resistance to slip increases with depth for all three types of faults, and that at any given depth it is the least for normal faults and the greatest for thrust faults.

An independent source of information concerning the magnitudes of the stress components comes from seismology. The probable maximum differential stress within the crust rarely exceeds about 100 MPa (Raleigh & Evernden, 1981) and for some faults it may be as small as 20 MPa. This immediately presents a problem. With 100 MPa as an upper limit, our analysis shows that normal faults can not slip below about 6 km, thrust faults below about 2 km, and wrench faults at intermediate depths. Yet it is known that deeper earthquakes are generated on all these types of faults. For geothermal gradients

typical of the continental crust, the *seismogenic zone* in quartz- and feldspar-bearing rocks extends to depths of about 12–15 km.

Admittedly, our analysis contains some approximations. In particular, the frictional sliding on rock surfaces is a good deal more complicated than a block sliding on an inclined plane. Still, it is unlikely that a more detailed approach would change our results by more than a small amount and therefore can not account for these large discrepancies.

Missing from our consideration so far is the role of the pressure  $p$  in the fluid in porous crustal rocks. Using Eq. 9.20 we can rewrite Amontons's law in terms of the effective normal stress as

$$\tau = \mu_s(\sigma - p) = \mu_s\sigma' \quad (10.16)$$

If the water in the pore spaces is connected to the atmosphere and if the groundwater table is at the earth's surface, then the hydrostatic pore pressure at any depth can be calculate from

$$p = \rho_w g z, \quad (10.17)$$

where  $\rho_w$  is the density of water. When the pore fluid pressure has this value it is said to be *normal*. At a depth of 1 km and using the same rule of thumb  $p \approx 10$  MPa. The ratio of the pore water pressure to the overburden pressure is given the symbol  $\lambda$ , defined as

$$\lambda = p/\sigma_{zz}. \quad (10.18)$$

This *pore fluid factor* expresses the fraction of the load borne by the fluid. If  $\lambda = 0$  the entire vertical load is supported by rock and if  $\lambda = 1.0$  it is entirely supported by fluid.

Hence in normal conditions  $\lambda \approx 10 \text{ MPa}/24 \text{ MPa} = 0.42$ , that is, almost half of the load is borne by the water. If the water table is not at the earth's surface a different depth  $z$  should be used. Also, the deep water may be brackish hence have a different density. Also, the density of crustal rocks is not uniform with depth. The actual value of  $\lambda$  may then differ from this figure in specific situations. If normal conditions prevail,  $\lambda$  will be approximately constant for all depths. The relationship between  $p$  and  $\sigma_{zz}$  can also be illustrated graphically (Fig. 10.21a).

However, *abnormal* pressures are regularly encountered in deep oil wells, where values of  $\lambda$  as high as 0.9 have been observed (Fig. 10.21b). Further, there is compelling geological evidence that values of  $\lambda = 1.0$  or greater are reached, at least briefly, with the result that faulting may be accompanied by tensile fractures (Sibson, 1981). Several mechanisms may contribute to such abnormal pressures but the main reason is that the permeability of clay shale is so low that the water escapes only very slowly and the pressure continues to rise during burial and compaction.

With elevated pore fluid pressures a differential stress of realistic magnitude can produce slip on a fault in the deeper parts of the seismogenic zone.

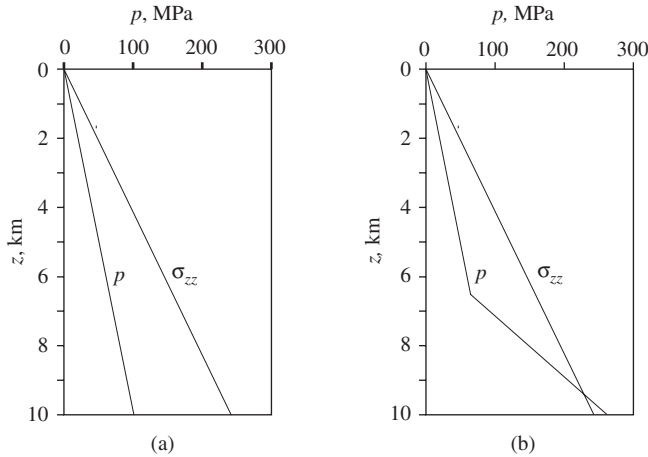


**Figure 10.21** Fluid pressure: (a) normal conditions; (b) abnormal conditions.

**Problem**

- For a maximum differential stress of 100 MPa and  $\phi_s = 30^\circ$  what are the conditions for slip on an optimally oriented thrust fault at a depth of 10 km?

**Construction**

1. For a thrust at this depth

$$\sigma_3 = (24 \text{ MPa/km})(10 \text{ km}) = 240 \text{ MPa} \quad \text{and} \quad \sigma_1 = (240+100) \text{ MPa} = 340 \text{ MPa}.$$

With these values, construct the corresponding Mohr Circle (Fig. 10.22).

2. Draw radius  $CP$  at angle  $2\theta = 120^\circ$  and add the failure line with slope angle  $\phi_s = 30^\circ$ .
3. Draw a line from  $P$  parallel to the  $\sigma$  axis to locate point  $P'$  on the failure line. Construct radius  $C'P'$  parallel to  $CP$  and draw a second Mohr Circle.

**Answer**

- This second circle represents the state of effective stress which will cause slip. The length of the line  $PP'$  represents the magnitude of the required pore pressure. Then  $p = 190 \text{ MPa}$  and  $\lambda = 0.79$ .

As this result shows, slip is possible under these conditions because the fault “thinks” that, in terms of its environment, it is at a much shallower depth.

We may also obtain an analytical solution for the required pore fluid pressure under such circumstances. The ratio  $R'$  of the effective principal stresses at failure can be written as

$$R' = \frac{\sigma'_1}{\sigma'_3} = \frac{\sigma_1 - p}{\sigma_3 - p} \quad \text{or} \quad p = \frac{R'\sigma_3 - \sigma_1}{R' - 1}. \tag{10.19}$$



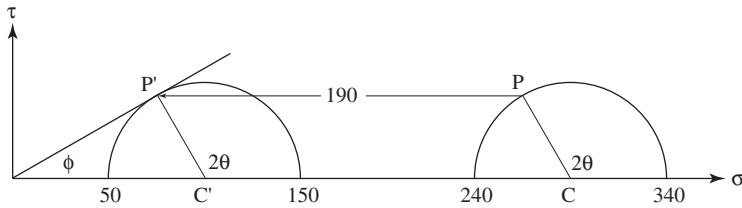


**Figure 10.22** Slip on a thrust at 10 km with elevated pore water pressure.

Using the values from the previous problem gives  $p = 190$  MPa, just as found graphically.

A similar problem is encountered in the formation of primary shear fractures at depth and the failure criterion must be modified to

$$\tau = c + \mu_i(\sigma - p) = c + \mu_i\sigma', \quad (10.20)$$

and this is called the *Coulomb–Terzaghi criterion*.

Finally, at high confining pressures ductile flow may dominate over fracture and mylonites may form. Conditions favorable for such flow occur below the base of the seismogenic zone and at a high differential stress. This suggests that mylonites should be found most commonly along deep thrust faults and rarely along normal faults, and this is just the case.

## 10.10 Open fractures

The presence of open fractures at depth has an important role in the emplacement of veins and dikes (Jolly & Sanderson, 1997). Open fractures require a tensile normal stress across their planes, and this may be illustrated in two equivalent ways with the aid of Mohr Circle diagrams.

1. The pore fluid pressure is greater than the normal traction acting across the fracture plane (Fig. 10.23a).

$$p \geq \sigma.$$

2. The effective normal traction across the plane is less than zero (Fig. 10.23b), or

$$\sigma' \leq 0.$$

The conditions which allow fractures to open are given by points on the Mohr Circle to the left of the lines defined by  $\sigma = p$  or  $\sigma' = 0$ . From these points the range of orientations of the potentially open fractures can also be determined.

Jolly and Sanderson (1997) have also extended this treatment to three dimensions in an application to two suites of dike swarms. In one, subhorizontal dikes are absent, indicating that  $\sigma_1$  was vertical at the time of emplacement. In the other, the dikes tend to be horizontal indicating that  $\sigma_1$  was horizontal. In both cases, they were also able to estimate the relative magnitudes of the principal stresses and the magmatic pressure at the time of emplacement.

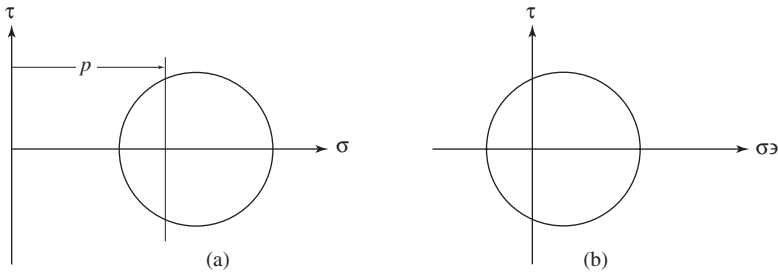


**Figure 10.23** Conditions for open fractures: (a)  $p > \sigma$ ; (b)  $\sigma' < 0$ .

### 10.11 Stress drop

Following a slip event, and with it the release of stored elastic strain energy in the form of earthquake waves, the state of stress adjacent to the fault is drastically altered. The value of  $\tau$  on the fault plane falls to some small value, possibly even zero, depending on whether slip halts with an episode of stick or not.

Consider the minimum conditions for the reactivation of a preexisting thrust fault. If the rocks are dry, then following a slip event the residual state of stress will be represented by a small Mohr Circle (Fig. 10.24a) with  $\sigma_3$  equal to the essentially constant overburden pressure. If the rocks are wet and there is a release of the pore water pressure, which is likely, then the post-slip residual state will be a small Mohr Circle with  $\sigma_3$  determined by both the overburden pressure and the normal value of  $\lambda$  (Fig. 10.24b). In a limiting case, both these small circles may degenerate to points.

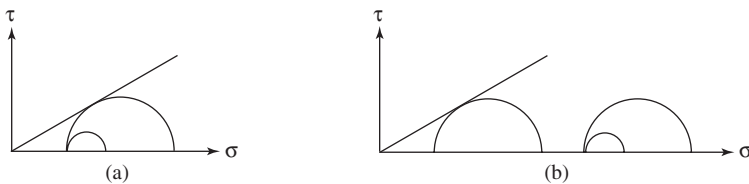


**Figure 10.24** Residual stress after slip on a thrust: (a)  $p = 0$ ; (b)  $p > 0$ .

### 10.12 Faults in anisotropic rocks

In anisotropic rocks, the relationship between the principal stress directions and shear fractures is more complicated. Donath (1961, 1964) experimentally investigated the role of cleavage in shear fracturing. By loading cylinders of slate cut at different angles, a varied relationship between the attitude of the plane of fracture and the cleavage was found (Fig. 10.25). If an isotropic rock had been used in these experiments, a conjugate pair of fractures inclined to  $\sigma_1$  at approximately  $30^\circ$  would have been expected. In the slate, such fractures were obtained in only two situations.

1. at higher confining pressure with the cleavage parallel to the long axis of the cylinder,
2. in all experiments with the cleavage perpendicular the cylinder axis and to  $\sigma_1$ .

In these two orientations, the slate is effectively isotropic. In all others, only one fracture developed and its attitude was controlled, directly or indirectly, by the cleavage. This is most clearly demonstrated by the essentially 1:1 relationship between cleavage and fracture attitude on the left side of the graph. Although for larger angles of cleavage inclination the fractures are no longer parallel to the cleavage, fracture angles greater than  $45^\circ$  also indicate a continuing influence by the planar weakness.

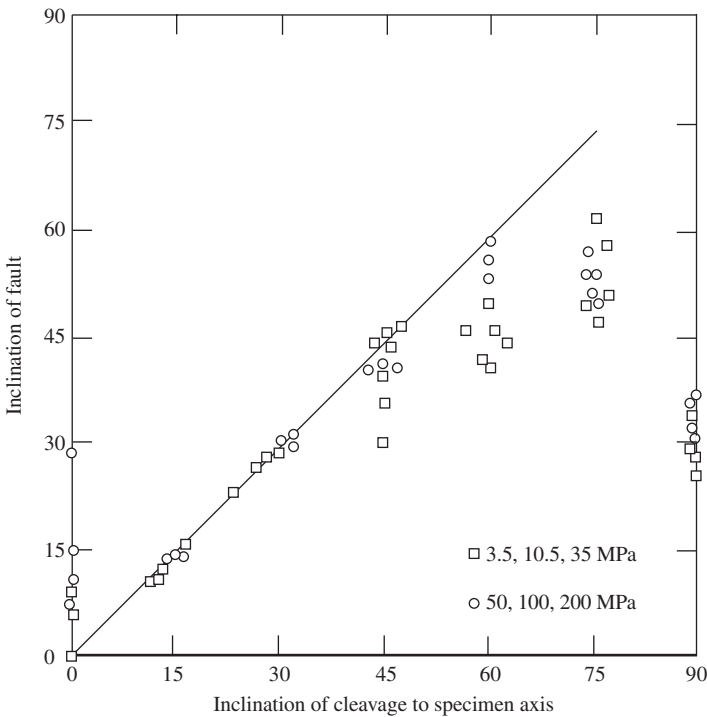


Figure 10.25 Fault orientation in slate (after Donath, 1963).

From the point of view of interpreting field examples, however, the uncertainties introduced by the effect of anisotropism make the determination of the principal stress directions from single or multiple fractures difficult.

### 10.13 Oblique faults

Neither Amontons's law nor the Coulomb criterion take into account the intermediate principal stress, which is, in effect, assumed to remain constant. There are, however, conditions where  $\sigma_2$  does play a role. As a result of the movement on a pair of conjugate faults the body of rock shortens in the  $\sigma_1$  direction, lengthens in the  $\sigma_3$  direction, and remains of constant length in the  $\sigma_2$  direction. If, however, extension occurs in the intermediate direction because of a decrease of  $\sigma_2$  then three or more intersecting faults may develop in order to accommodate the change in shape and the procedure used for two can not be applied (Reches, 1978; Aydin & Reches, 1982).

Another situation arises when there is a single plane of weakness oblique to all three principal directions. In three dimensions, the direction of the resolved shearing stress on such an inclined plane depends on the magnitude of all three principal stresses. From Bott (1959; see also Jaeger & Cook, 1979, p. 26, 430) the pitch  $r$  of the shear component in the plane is given by

$$\tan r = \frac{n}{lm} \left[ m^2 - (1 - n^2) \Phi \right] \quad (10.21)$$

where  $(l, m, n)$  are the direction cosines of the pole of the plane relative to principal stress directions and

$$\Phi = \frac{\sigma_{zz} - \sigma_{xx}}{\sigma_{yy} - \sigma_{xx}}, \quad (10.22)$$

where  $\sigma_{xx}$ ,  $\sigma_{yy}$  and  $\sigma_{zz}$  are principal stresses (this ratio describes the shape of the stress ellipsoid). In general, the value of the pitch given by Eq. 10.22 will be such that the maximum shear stress is not directly related to the principal stress directions. We now illustrate this fact.

#### Problem

- If the principal stresses are  $\sigma_{xx} = 35$  MPa,  $\sigma_{yy} = 15$  MPa and  $\sigma_{zz} = 75$  MPa, for a fault with pole  $P(35/065)$  what is the direction and sense of slip?

#### Answer

- With Eqs. 7.7 calculate the direction cosines of the pole of the fault. Then using these in Eq. 10.22, together with the values of the principal stresses, the pitch of the slip direction  $S$  is  $r = 77^\circ$  (Fig. 10.26a). Because  $\sigma_1 = \sigma_{zz}$ , the fault is dominantly normal. Note that this is the same result obtained in Fig. 9.35.

A slip direction on a single such oblique fault does not supply enough information to estimate the orientation of the stress tensor responsible for the renewed slip.

Observations on additional faults are needed. To convey the essence of a fruitful but advanced approach consider the case of three additional faults which are symmetrical with the coordinate axes (Fig. 10.26b). By symmetry the slip directions will also be symmetrical and it is then possible to determine the principal stress directions.

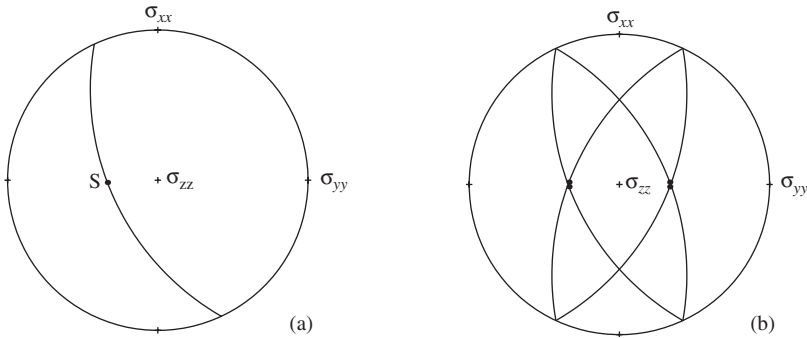


**Figure 10.26** Oblique faults: (a) single fault; (b) four symmetrical faults.

In practice, of course, such an ideal situation would be most unusual. However, there are situations where the stress orientation can still be estimated from a knowledge of renewed movement on a variety of preexisting planes. If a rock mass is cut by abundant, variously oriented fractures, renewed slip will occur on those planes with approximately the orientation of the conjugate pair that would have formed in intact rock. Given such a collection of fractures, the analytical procedure consists simply of plotting the poles of the preexisting planes which show evidence of movement. Barring a preferred orientation of these planes, the poles will form two clusters which are symmetrical to the principal stress directions as shown in Fig. 10.27 (Jaeger, 1969, p. 161; Compton, 1966, p. 1370).

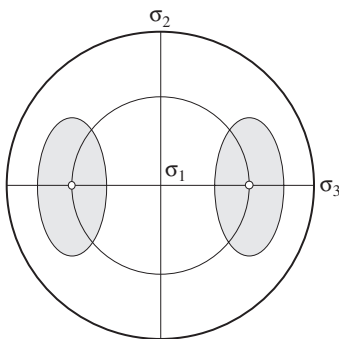


**Figure 10.27** Planes with poles within the shaded zones will show slip.

Estimating the state of stress from collections of faults is an active area of research and the literature is large and growing. Engelder (1993, p. 83f) and Angelier (1994) give good reviews.

This stress inversion technique is based on two assumptions. The first is that the regional stress is homogeneous. The second is that the direction of slip is parallel to the direction of maximum shear stress on the plane of the fault. These are acceptable in some situations, but not in others (Pollard, *et al.*, 1993).

### 10.14 Other limitations

The Coulomb criterion describes conditions at the instant of failure. As a result of the initial fracture and continued displacement on the fault, the magnitude and orientation of the principal stresses will not be the same as before failure. As the state of stress builds up for an additional increment of slip it will not return to the original state, though it is probably unlikely that any drastic changes in orientation will occur between small increments of slip.

For large displacements, not only may the state of stress change, but also the geometry of the fault may be altered. Thrusts, in particular, are subject to such changes. The 30° dip of a primary thrust can not be maintained for large displacements for an overhang at the earth's surface would result. A consequence of continued slip would be a flattening of the thrust plane. The state of stress during the continued motion of such an overthrust sheet would be different, and possibly quite different from that responsible for the initial fracture and early slip.

For large-scaled faults another difficulty arises. For example, regionally extensive wrench faults may well extend to depths beyond the zone of even semi-brittle fracture. The slip then may be related to deep crustal or subcrustal flow, and for such flow the relatively simple relationships on which the fracture analysis is based do not hold. Deep flow would, of course, set up stresses in the overlying brittle rocks, but these would not necessarily be uniform along the entire length of the fault. Such heterogeneity, as interpreted from local fracture and fold analysis, has been demonstrated along parts of the San Andreas fault of California (Dickinson, 1966). The picture which emerges is one of a series of irregular blocks or "tectonic rafts" along and adjacent to the fault. The stress states within adjacent rafts are, at least partly, local. This non-uniformity, together with the long history of movement, makes it difficult to interpret such faults in terms of a regionally developed homogeneous stress field. Probably all such major faults have a more complex origin and history.

### 10.15 Earthquakes

There are still other ways of determining important geometrical properties of active faults. From an analysis of seismograph records the site of an earthquake generated by fault slip can be located (Fowler, 1990, p. 85–86). There are two types of calculations.

Locating the epicenter involves determining the difference in the arrival times of the P- and S-waves at three or more seismograph stations. The depth to the earthquake focus, also called the *hypocenter*, can also be calculated from the difference of the arrival times of the direct P and reflected pP phases.

Further, the attitude and sense of slip on the fault can also be found (Fowler, 1990, p. 97–104, 149–151; Stein & Wysession, 2003, p. 219–222). This involves determining whether the arrival of the first pulse of the P-wave is compressive or tensile. Figure 10.28a shows a map of an east-west dextral strike-slip fault. For stations in the first and third quadrants the first motion will be *compressive* (by convention shown shaded) and in the second and fourth quadrants it will be *tensile* (shown blank). These four quadrants are separated by *nodal planes* one of which is the *fault plane* and the other is the *auxiliary plane*. Similarly Fig. 10.28b shows a north-south sinistral strike-slip fault which gives the same pattern of compression and tension. This ambiguity is usually resolved by comparing the orientations of the nodal planes with the known geology or with evidence on the ground of the orientation of the active fault.

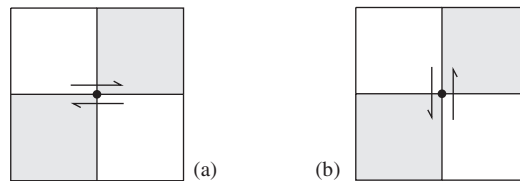


**Figure 10.28** First motion of P-wave: (a) dextral strike-slip; (b) sinistral strike-slip.

Of course, the earth closely approximates a sphere so that plotting the first-motions and the derived nodal planes on the lower hemisphere of a stereonet is appropriate. Figure 10.29 shows the distribution of compression and tension for the three basic fault types. Note that the line of intersection of the nodal planes lies in the plane of the fault and perpendicular to the slip direction. If the slip is oblique then the line of intersection of the two nodal planes will not be horizontal in the case of normal and thrust faults or vertical in the case of strike slip faults.<sup>7</sup>

## 10.16 Exercises

- Two faults have attitudes of N 10 W, 60 E and N 30 E, 70 W. What were the orientations of the principal stresses at the time of faulting, what is the angle of internal friction of the rock, and what are the senses of slip on the faults?
- The traces of two conjugate sets of shear planes are exposed in a quarry. Determine as many of the mechanical aspects at the time of fracture formation as possible.
  - Floor (horizontal): traces trend N 25 W and N 82 W.

<sup>7</sup>These stereographic diagrams are informally called “beach balls”.

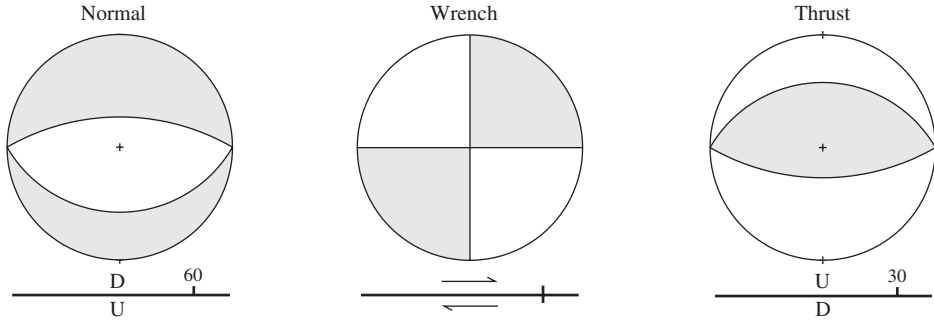


**Figure 10.29** Stereograms of first motion for the three types of faults.

- (b) Face 1 (N 10 E, 70 E): traces pitch 48 N and 18 S.
  - (c) Face 2 (N 76 E, 80 N): traces pitch 26 E and 30 W.
3. Vertical extension fractures are associated with a fault whose attitude is N 63 E, 70 S. Determine as many of the mechanical aspects of the fractures as possible.
  4. On a slickensided surface with attitude N 32 E, 60 SW, striations plunge 54 toward N 23 W. The associated fault shows normal separation. Estimate the orientations of the principal stresses at the time of faulting.
  5. Of a large number of fractures, those with the following orientations showed evidence of renewed slip. Estimate the orientations of the principal stresses, and for fracture No. 1 estimate the direction and sense of slip.
 

1. N 30 E, 50 E	7. N 5 W, 15 W
2. N 30 W, 30 W	8. N 54 E, 66 SE
3. N 84 E, 16 S	9. N 33 E, 63 SE
4. N 4 E, 43 E	10. N 80 E, 20 N
5. N 50 E, 49 SE	11. N 34 E, 28 NW
6. N 12 E, 30 SW	12. N 14 E, 56 E
  6. A rock has the following physical characteristics:  $c = 38$  MPa and  $\phi_i = 33^\circ$ .
    - (a) Assuming that  $\sigma_1$  remains a constant 100 MPa, what will the magnitude of  $\sigma_3$  be at failure?
    - (b) Under the same conditions, a preexisting cohesionless plane with angle of friction equal to  $30^\circ$  is inclined  $45^\circ$  to  $\sigma_1$ . Which will occur first, fracture or slip?
    - (c) Will slip or fracture occur first if this same plane is inclined  $55^\circ$  to the  $\sigma_1$  direction?
  7. Analyze the following situations for the principal stresses at the point of renewed slip.
    - (a) At a depth of 3.5 km, what would the magnitude of the horizontal component of stress be for renewed movement on a normal fault in the optimum orientation?
    - (b) At this same depth, what would the magnitude of the horizontal component of stress be for renewed slip on a thrust fault in the optimum orientation? If the maximum differential stress is 50 MPa, what pore fluid pressure is required to cause faulting in this case?



# 11

## Deformation

### 11.1 Introduction

Processes acting within the earth at various times and places cause bodies of rocks to be displaced from the sites of their origin. After such displacements the bodies have different locations and orientations, and also commonly different shapes and sizes. Such bodies are said to be *deformed*. Although it is ultimately necessary to treat these changes in a full three-dimensional setting, many situations can be approached from a consideration of just two, and this also serves as a useful way to introduce the subject.

Even in two dimensions, the complete geometrical description of the deformed state for a relatively simple structure may be quite involved. Imagine a rectangular block composed of sedimentary strata (Fig. 11.1a). As the result of a general deformation, original lines become curvilinear, original planes curvilinear and original parallel lines and planes are no longer parallel (Fig. 11.1b). Such a deformation is *inhomogeneous*.

The description of a deformation consists of comparing the initial and final configurations of the body with emphasis on the changes which have occurred. To facilitate this comparison we refer the body in its initial place, orientation, shape and size to *material coordinates*  $(x, y)$  and its final place, orientation, shape and size to *spatial coordinates*  $(x', y')$ . Every material point or *particle*  $P(x, y)$  in the body is displaced to spatial point  $P'(x', y')$ . Each point  $P'$  is related to its particle  $P$  by a *displacement vector*  $\mathbf{u}$ . This vector is *not* generally the path along which the particle moves, but simply identifies the final position  $P'$  of the particle initially at  $P$ . Every particle in the body has associated with it such a displacement vector and collectively these constitute the *displacement field*, an example of a vector field.

There are two different ways of relating the initial (undeformed) and final (deformed) configurations of the material body.

1. We may focus attention on the initial configuration and describe the changes represented by the final configuration. The independent variables are then the material

coordinates  $(x, y)$  of the particles in the initial configuration. This is the *material description*.

2. We may focus attention on the final configuration. The independent variables are then the spatial coordinates  $(x', y')$ . This is the *spatial description*.<sup>1</sup>

Each of these approaches has advantages and disadvantages. Nature always presents us with the final configuration, and so in the end we are forced to use the spatial description. On the other hand, the material description matches the way deformations occur, and it seems logical to think of the changes in this way. In this chapter we will concentrate on the material description and in the next we will emphasize the spatial description and show how to go from one to the other.

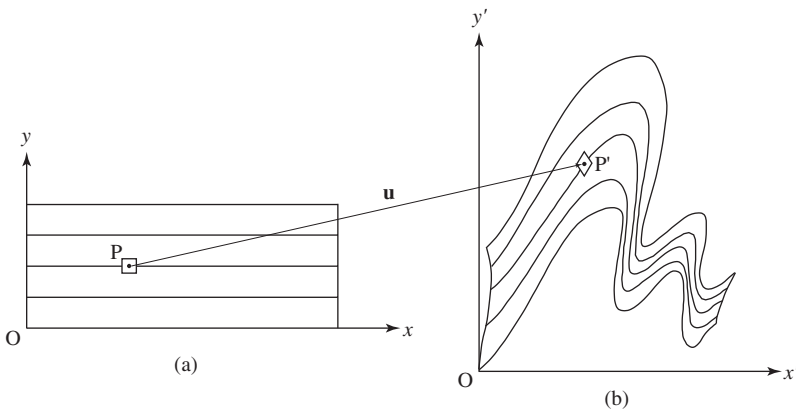


**Figure 11.1** Inhomogeneous deformation: (a) initial state; (b) final state.

In order to proceed with the description of such a deformed body, we consider the changes which have occurred. In §8.9 we introduced two measures of the change in the horizontal, straight-line distance across groups of associated faults. These are the *extension*  $e$  and the *stretch*  $S$  defined as

$$e = \frac{l' - l}{l} = \frac{l'}{l} - 1 \quad \text{and} \quad S = \frac{l'}{l} = 1 + e. \tag{11.1}$$

These measures do not apply directly in the present case because in a general deformation an initially straight line in the vicinity of  $P$  will be curved in the vicinity of  $P'$  and the changes in length along this curved line will not be uniform. As we consider a shorter line at  $P$  the deformed line at  $P'$  becomes straighter and its length more uniformly altered.

<sup>1</sup>Commonly “Lagrangian” is used for *material* and “Eulerian” is used for *spatial*, but the historical attributions are incorrect (Truesdell, 1954, p. 30): the material coordinates were introduced by Euler in 1762 and the spatial coordinates by d’Alembert in 1752. The terms Lagrangian and Eulerian are not used here. Clifford Ambrose Truesdell III [1919–2000] was an exceptional figure of twentieth-century science. In all of his work, he insisted that people get proper credit for their contributions, large or small.

Then, as the line becomes very short, the ratio of the final length  $\Delta l'$  to the initial length  $\Delta l$  tends to a finite limit which is the stretch  $S$  at  $P'$ , that is,

$$S = \lim_{\Delta l \rightarrow 0} \frac{\Delta l'}{\Delta l} = \frac{dl'}{dl}. \tag{11.2}$$

Of course, longer lines may be homogeneously deformed. The condition expressed by Eq. 11.2 simply insures that  $S$  (and  $e$ ) can always be defined.<sup>2</sup>

Because these parameters apply to all lines, a small rectangular volume element at  $P$  will, after deformation, have a high degree of regularity at  $P'$  (see Fig. 11.1). Original lines are still linear, original planes are still planar, and originally parallel lines and planes are still parallel. This state is *homogeneous*.

Accordingly, a fundamental mode of attack seeks such small parts which are effectively homogeneous and then builds up a picture of the overall pattern, either by comparing a number of closely spaced homogeneously deformed parts or by extrapolation based on the continuity of structures which develop as a consequence of the deformation.

A fundamental geometrical theorem is that a general homogeneous deformation may be regarded as resulting from the combination of three types of displacements (Truesdell & Toupin, 1960, p. 274).

1. *Translation* is a uniform rigid-body displacement of all particles (Fig. 11.2a).
2. *Rotation* is a uniform rigid-body change in the orientation of all lines (Fig. 11.2b).
3. *Stretch* involves a change in shape (distortion) and size (dilatation) of the body (Fig. 11.2c).

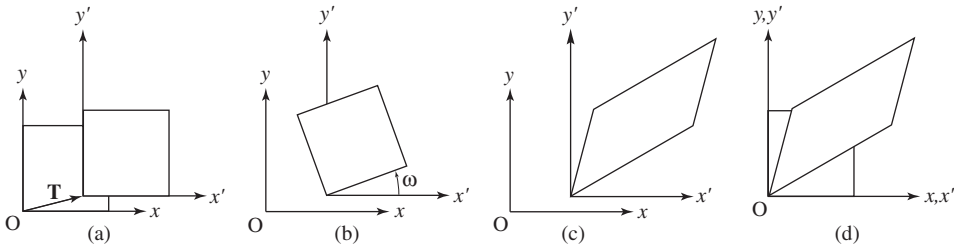


**Figure 11.2** Homogeneous deformation: (a) translation; (b) rotation; (c) stretch; (d) rotation and stretch without translation.

Our task then is to develop ways of evaluating the contribution of each of these in a geological structure of interest. Because there is generally little or no evidence preserved in the rocks which can be used to establish the initial location of a body it is particularly difficult to evaluate the translation. Because it does not affect on the geometry of the

<sup>2</sup>Note the formal similarity with the definition of traction in Eq. 9.3.

deformed body we therefore remove the translation from the complete deformation for separate consideration.

In effect, we now assume that the origin of the  $xy$  coordinate system is fixed to particle  $P(0, 0)$  and moves with the body to point  $P'(0, 0)$  which is then the origin of the  $x'y'$  coordinate system (Fig. 11.2d). Now the vector joining any particle  $P(x, y)$  and its corresponding point  $P'(x', y')$  is a *relative displacement vector*, which differs from the true displacement by the uniform translation.

We now need to develop an understanding of the geometrical roles of stretch and rotation in homogeneously deformed bodies. A particularly fruitful way of exploring this geometry is to draw or print a reference form on the edge of a reasonably thick deck of cards which is then sheared. In these card-deck models, the condition of homogeneity is met by insuring that the edge of the sheared deck is straight, then all straight lines remain straight and all parallel lines remain parallel. This is *simple shear*. In our illustrations of homogeneous simple shear we start with a known state, apply a particular deformation and observe the result. This process is known as *forward modeling*.

The easiest way to shear the deck is to gently flex it with one end held firmly and then release the deck with the other end held firmly. This procedure may be repeated a number of times until the deck has the desired shape. Alternatively, an accurately square box may be used and the deck deformed with a variety of shaped end pieces (Ragan, 1969a; Ramsay & Huber, 1983, p. 2).

A deck of any cards which are uniform in size, thin but sufficiently stiff will do.<sup>3</sup> Once sheared, the resulting patterns can then be analyzed directly on the cards or the patterns can be reproduced on a copy machine.

As an alternative, graphics software, now widely available, can be used to model these and many other changes (Bjørnerud, 1991; Tewksbury, 1996). Common objects, such as squares, rectangles, circles and ellipses, can be easily drawn on the screen. Although the command names may differ, these figure can be subjected to a stretch, slant, shear or rotation. The analysis can then be performed on a print-out.<sup>4</sup> Specially written computer programs are also now available which illustrate important aspects of other, more general types of two-dimensional deformations (Tikoff & Fossen, 1996).

Homogeneously deforming the card deck is easy to do with the flexing mechanism. The simple character of simple shear lies in the fact that a single parameter completely describes the deformation. This parameter is the *angle of shear*  $\psi$  (psi), defined as the *change of an original right angle* (see Fig. 11.3). This angle is easily measured by starting

<sup>3</sup>Combining two packs of index cards carefully shuffled to eliminate the curvature that single packs commonly exhibit is quite satisfactory. Curiously, some students resist experimenting with these models on the grounds that they are just 'games'. However, years of experience has demonstrated to us that for most students the act of manipulating the card-decks to produce these models enhances the understanding and retention of important geometrical facts.

<sup>4</sup>Card decks are an excellent way of modeling simple shear, but a word of caution is necessary. As we have noted, deformation involves a comparison of the initial and final states. In producing a model by incrementally shearing a card deck, it is inevitable that the progressive evolution of the final state is observed, but these changes are of no direct concern here. We return to this important matter in Chapter 13.

with a square-ended deck. The most basic experiment is to deform a reference circle into an ellipse. There are two cases:

1. the sense of shear may be *sinistral*:  $\psi$  is measured *anticlockwise* (Fig. 11.3a)
2. or the sense may be *dextral*:  $\psi$  is measured *clockwise* (Fig. 11.3b).

In most such experiments, the sense of shear is established by intent, otherwise it will be obvious by inspection, and since each result is the mirror image of the other, the basic geometrical features are identical, and only the details of the measurements differ.

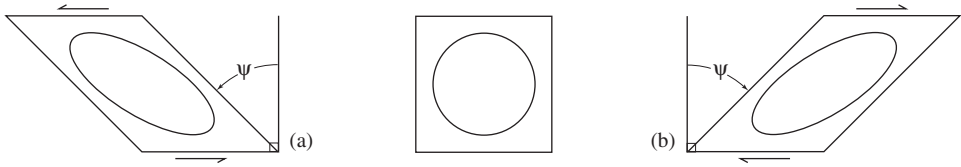


**Figure 11.3** Circle transformed into an ellipse: (a) sinistral shear; (b) dextral shear.

## 11.2 Continuum assumption

Strictly, a deformation involves displacements which vary continuously, whereas the deformation of the card deck is simulated by a series of small slips with each card remaining intact. However, the thinner the cards, the closer continuity is approached, and when forms of about one centimeter or larger are printed on a deck of thin cards, the distortions are for all practical purposes continuous. Because the images on a computer screen are composed of a series of discrete pixels about 0.25 mm in size, the forms are similarly discontinuous at this scale. However, from a normal viewing distance they too appear essentially continuous.

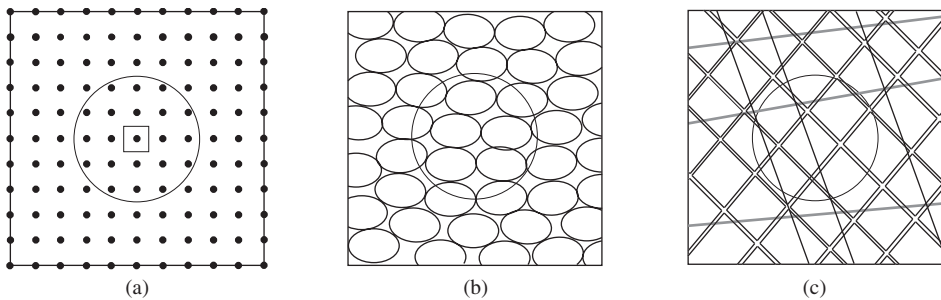


**Figure 11.4** Discontinuities: (a) crystal lattice; (b) granular rock; (c) fractured rock.

We face this same dependency on scale in all real-world situations. Consider the closely related problem of determining the density of a single plane of a simple cubic crystal, which we can illustrate using a simple graphical technique (R. L. Stocker, 1978, personal communication). Suppose we have a device for measuring the density of a portion of

this plane contained within a small circular area (Fig. 11.4a). What will be the results if different diameters are used? We may easily discover this relation between area and density by incrementally increasing the size of the circle and counting the number of point masses within it at each step and dividing by the area of the counter. For a lattice composed of unit point masses with a unit spacing the results are shown graphically in Fig. 11.5.

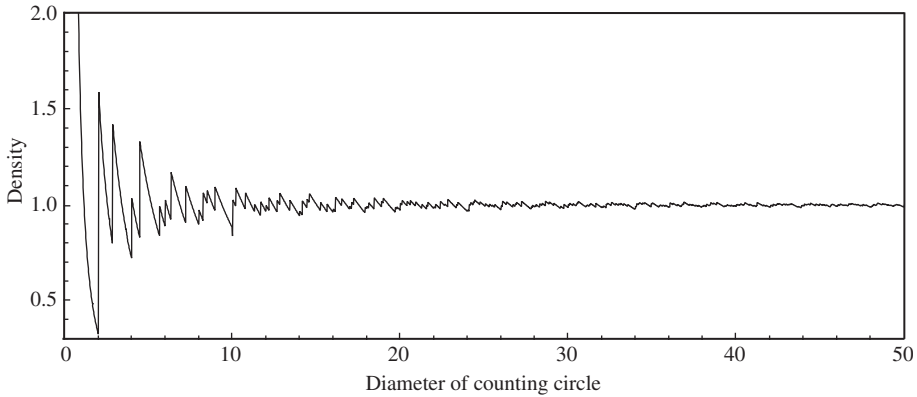


**Figure 11.5** Crystal density as a function of the size of the counting circle.

Clearly, the use of a measuring area which is small relative to the dimensions of the lattice results in great fluctuations in the density. The reason is that the distribution of mass is violently non-uniform when viewed on such a small scale as to reveal individual atoms.

It is only when larger measuring areas are used that a degree of uniformity is approached, that is, the *average* density becomes meaningful. For example, when the diameter of the measuring area is 10 units, the large fluctuations have vanished. When the diameter is 20 units, the fluctuations are quite small, and when the measuring circle approaches a diameter of 50 units the difference between the measured density and that of the unit cell is very small indeed.

On this basis we distinguish two distinctly different and physically important scales of observation. In the first, called the *microscopic* view, the properties of individual atoms and the discontinuities between them are important. In the second, essentially statistical in nature, called the *macroscopic* view, the average properties of the atoms, not the discontinuities, are important.

Conventionally, the mass density  $\rho$  of a body composed of a continuous medium is defined as

$$\rho = \lim_{\Delta V \rightarrow 0} \frac{\Delta M}{\Delta V} = \frac{dM}{dV} \quad (11.3)$$

where  $\Delta V$  is a volume and  $\Delta M$  is its mass. We now understand that the infinitesimal volume  $dV$  is not to be taken literally.

Because we are concerned with the behavior of matter on a scale which is much larger than the distances between atoms, that is, with macroscopic properties and behaviors, we will not often need to take the molecular nature of matter into account. We will then suppose that the physical behavior of these materials is the same as if they were perfectly continuous, and any physical quantities associated with a volume of matter will be regarded as being spread uniformly over that volume, instead of, as in strict reality, being concentrated within a small fraction of it (Batchelor, 1967, p. 4). Such an abstract material is called a *continuous medium* or a *continuum*, and the study of the physical behavior of such materials is called *continuum mechanics*.

All this should not be taken as a statement that a study of the microscopic properties of material is unimportant. Much experimental and theoretical work is being done in these directions and these studies offer much useful information (for a good introduction see Schedl & van der Pluijm, 1988). However, the microscopic scale is not the place to start a study of geological structures. Further, to be of use any microscopic results must be integrated into the macroscopic view.

We face a similar problem in dealing with soils and rocks, that is, material composed of heterogeneous aggregates of mineral grains. Now consider the analogous problem of determining the density of a sandstone (Fig. 11.4b). A small circular counter might lie wholly or partly within a single grain or pore space, and if we determined the density for increasing counter sizes, the results would be similar to those displayed in Fig. 11.5. It is only when the volume is large that continuity is closely approximated. This is called the *representative elementary volume*, abbreviated REV (Bear & Bachmat, 1984, p. 5).

For such granular materials we agree to replace the limit  $\Delta V \rightarrow 0$  with the limit  $\Delta V \rightarrow \Delta V_0$ , where  $\Delta V_0$ , called the *permissible volume*, is sufficiently large to contain a significant number of grains (Davis & Selvadurai, 1996, p. 5). In most rocks the size of this volume is measured in millimeters or centimeters, but would be considerably larger in a pegmatite or boulder conglomerate.

Finally, on an even larger scale, consider the similar problem involved in determining the properties of a fractured *rock mass* (Fig. 11.4c) (Hudson, 1989, p. 26). Here the size of the REV is commonly measured in meters, tens of meters or more.

In short, the body of material under consideration must be small enough so that the deformation is effectively homogeneous, yet not so small that it can not be taken as essentially continuous. Note carefully that the terms *microscopic* and *macroscopic* describing these two scales carry entirely different meanings from their common use in describing the scales of geological observation (Turner & Weiss, 1963, p. 15–16).

All heterogeneous materials contain discontinuities or jumps in physical properties at every scale from mineral grains to hand specimens, to outcrops, to map units. There are two ways of treating these.

1. If, at the chosen scale, the discontinuity is significant, then it must be treated as a *boundary* of a continuum. For example, the physical properties of quartz and feldspar are such that they behave quite differently during the formation of a mylonite. If the

concern is with understanding the processes responsible for the textures of such rocks, then the discrete grains must be treated as separate bodies with boundaries.

2. On the other hand, if the chosen scale is such that discontinuities are not significant, then their properties are included in the averaging process. If the concern is with the role mylonites play in thrust faulting, then it is the boundaries of the whole body, not the boundaries of individual grains, which are important.

### 11.3 Homogeneous deformation

The deformation modeled with card decks is *simple shear*. Simple shear is a very special type of deformation, yet despite this special character it portrays a number of important properties of more general types of deformation, including rotation.

In the models, the condition of homogeneity is met by insuring that the edge of the sheared deck is straight, then all straight lines remain straight and all parallel lines remain parallel. This is easy to do with the flexing mechanism. The most basic experiment is to deform a deck on which a circle has been drawn. The circle is transformed into an ellipse. If the original circle has a unit radius, the result is the *strain ellipse* although, as we will see, all the same information can be obtained from a circle of any known size. The term *strain* refers to the changes of lengths and angles as depicted by the strain ellipse.

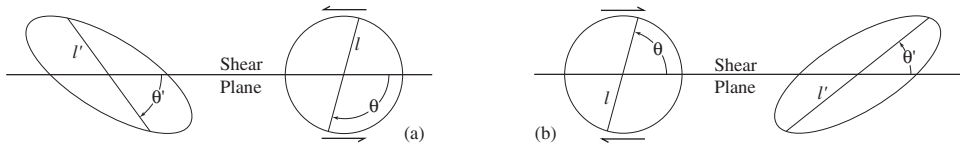


**Figure 11.6** Change in length and orientation of a line: (a) anticlockwise shear; (b) clockwise shear.

With a pronounced ellipse we can see that the geometrical properties of the initial circle have been systematically altered. We are particularly interested in the changes recorded by the deformation of material lines. The orientations of any line before and after deformation are given by the angles  $\theta$  and  $\theta'$  it makes with the shear plane (Fig. 11.6).

1. Generally, the lengths of lines change: some lengthen and some shorten. The measure of these changes is the stretch  $S = l'/l$ , which represents the corresponding radius of the strain ellipse.
2. Lines generally rotate: the sense may be anticlockwise (Fig. 11.6a), or clockwise (Fig. 11.6b). In both cases the magnitude of rotation is  $|\theta - \theta'|$  and its sense is the same as the shear.
3. The angle between any two lines also generally changes. In particular, if two lines are orthogonal before deformation they will generally not be orthogonal after deformation. The reason is that each line rotates by a different amount (Fig. 11.7).



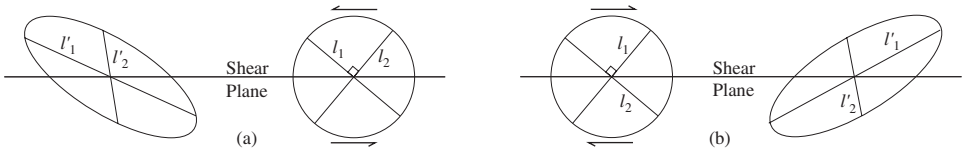


**Figure 11.7** Change in the angle between two initially orthogonal lines: (a) anticlockwise shear; (b) clockwise shear.

Again perform the circle-to-ellipse experiment and add the major and minor axes to the ellipse. These are the *principal axes* in the deformed state (Figs. 11.8a<sub>2</sub>, 11.8b<sub>2</sub>).<sup>5</sup> The semi-axes were both radii of the initial circle and therefore represent the directions of greatest increase and greatest decrease in length.

The corresponding lengths of the semi-axes of the strain ellipse are the *principal stretches*  $S_1$  and  $S_3$ , where

$$S_1 = 1 + e_1 \quad \text{and} \quad S_3 = 1 + e_3. \tag{11.4}$$

In simple shear, and two-dimensional deformations generally, the intermediate principal stretch is a direction of no change in length, hence  $S_2 = 1$ .

The orientation of these axes is given by the angles  $\phi$  and  $\phi'$  they make with the shear plane (a different symbol is used for angles involving these principal axes because of their importance as reference directions).

Returning the card deck to its starting position, the lines which marked the axes of the strain ellipse are also perpendicular in the initial circle. These are the *principal axes* in the undeformed state (Figs. 11.8a<sub>1</sub>, 11.8b<sub>1</sub>). No other pair of lines is orthogonal both before and after deformation.

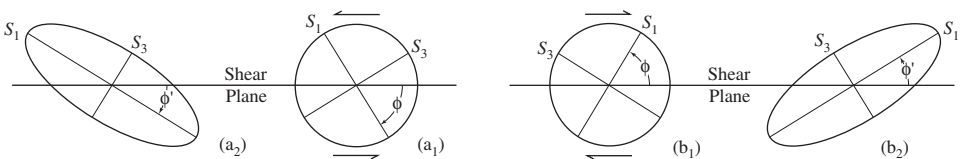


**Figure 11.8** Rotation of principal axes: (a) anticlockwise; (b) clockwise.

In a general deformation, as here, the pair of principal axes also rotate and in order to remain orthogonal they must both rotate by the same amount and this is measured by the *angle of rotation*  $\omega$  (omega), and is given by

$$\omega = \pm|\phi - \phi'|, \tag{11.5}$$

<sup>5</sup>The long axis can be located more accurately and should be drawn first. The short axis can then be constructed as its perpendicular bisector.

where  $\phi$  and  $\phi'$  identify the orientations of the axes before and after deformation. As with material lines generally, the sense of rotation may be anticlockwise or clockwise, according to the sense of shear.

The angle  $\omega$  measures the *internal rotation* associated with the deformation. We could subject the card deck to an *external rotation* simply by bodily turning the deck. We will see later that in certain types of folding, beds undergo layer-parallel shear while at the same time rotating bodily.

For many purposes it is convenient to express the shape of the strain ellipse by using the *strain ratio*, defined as

$$R_s = S_1/S_3. \tag{11.6}$$

Because  $S_1 \geq S_3$  by definition,  $R_s \geq 1$ . We can describe the shape of other elliptical objects in a similar way.

Superimposing a concentric circle on the final ellipse identical in size to the starting circle identifies two special lines which have undergone no net change in length, that is, lines for which  $S = 1$ . Diameters  $ab$  and  $cd$  of the circle (Fig. 11.9a) become diameters  $a'b'$  and  $c'd'$  of equal length in the ellipse (Fig. 11.9b). These are the *lines of no finite longitudinal strain*, or lines of NFLS for short. By symmetry, radii of equal lengths make equal angles with the ellipse axes, and the principal axes bisect these two lines.

Note too that all lines in the two sectors containing  $S_1$  increase in length and all lines in the two sectors containing  $S_3$  decrease in length.

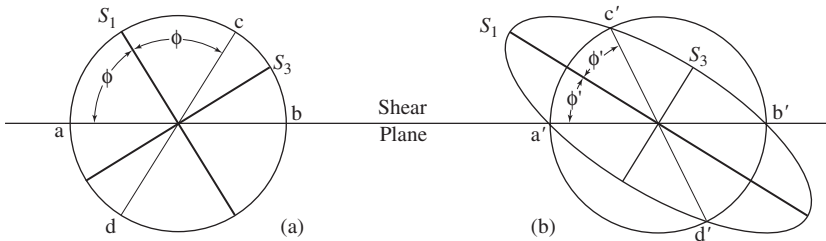


**Figure 11.9** Lines of no finite longitudinal strain: (a)  $ab$  and  $cd$ ; (b)  $a'b'$  and  $c'd'$ .

### 11.4 Analysis of simple shear

If we are to understand homogeneous simple shear more deeply we need to explore the various geometrical changes which occur quantitatively. To do this we need a coordinate system and we choose a set of Cartesian axes, oriented in the usual way with  $+x$  to the right and  $+y$  upward. Should the need arise, we are, of course, free to orient them in any other way.

If angles have sense, as the angles of shear and rotation do, this is specified by the standard sign convention: angles with an anticlockwise sense are *positive* and with a

clockwise sense are *negative*.<sup>6</sup> Accordingly, we specify  $\psi$  as *positive* for an anticlockwise sense (Fig. 11.10a) and *negative* for a clockwise sense (Fig. 11.10b).

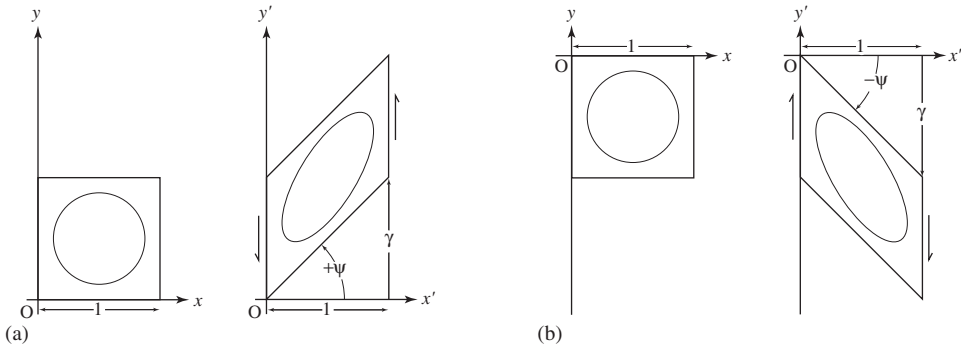


**Figure 11.10** Simple shear: (a) positive shear ( $+\psi$ ); (b) negative shear ( $-\psi$ ).

Before proceeding, we need an additional parameter. The *shear strain*  $\gamma$  (gamma) is defined as

$$\gamma = \tan \psi. \tag{11.7}$$

This is also called the *unit shear* because it is the maximum displacement on a card deck of unit thickness (see Fig. 11.10).

The angle of shear  $\psi$  can not be greater than  $90^\circ$  (Fig. 11.10a) nor less than  $-90^\circ$  (Fig. 11.10b), that is,

$$+90^\circ > \psi > -90^\circ.$$

By Eq. 11.7, the signs of  $\psi$  and  $\gamma$  must be the same. The simplest way to satisfy this condition and the sign convention is to measure  $\psi$  from the  $+x$  axis. This means that  $\psi$  is confined to the first and fourth quadrants of our coordinate system. In the first quadrant  $\gamma$  and  $\psi$  are both positive and in the fourth both are negative. As a consequence of this choice, the shear plane is parallel to the  $y$  axis (see Fig. 11.10).

Within this framework, the geometrical features associated with a homogeneous deformation by simple shear can be calculated using a method first set out by Thomson and Tait (1867, p. 106–107; 1962, p. 123–125; see also Truesdell & Toupin, 1960, p. 292–294; Treagus, 1981a).

As we have seen in Fig. 11.9, the one line of NFLS is always parallel to the shear direction. The orientation of the other depends on the angle of shear, and we can find

<sup>6</sup>This is just the right-hand rule applied to two dimensions. There is an implied  $+z$  axis pointing out from the page. If the thumb of the right hand points in this direction, the curled fingers indicate a positive sense on the  $xy$  plane. Ramsay (1967, p. 84) and others implicitly adopt the opposite convention. It seems preferable to retain the standard used throughout coordinate geometry.

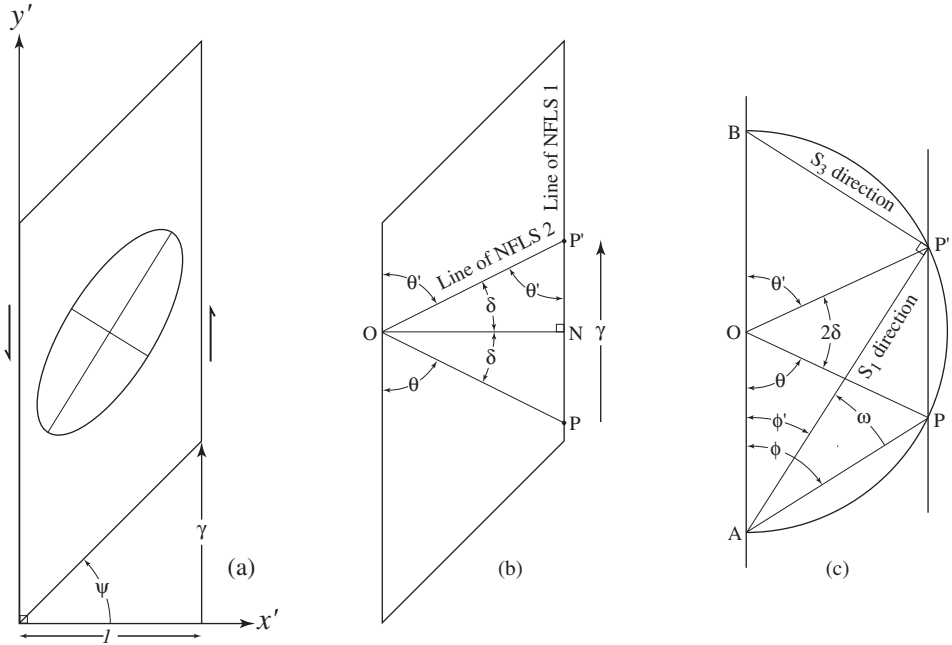


**Figure 11.11** Simple shear: (a) strain ellipse; (b) lines of NFLS; (c) principal axes.

its orientation with a simple construction. As a result of a deformation, particle  $P$  is displaced to point  $P'$  by the amount  $\gamma$  (Fig. 11.11b). Locate  $N$  at the mid-point of the segment  $PP'$  and then drop a perpendicular to the opposite side of the parallelogram to locate point  $O$ . Line  $OP$  before deformation has the same length as line  $OP'$  after deformation which is then the second line of NFLS. Both  $OP$  and  $OP'$  make equal angles with the shear plane, that is,  $\theta = \theta'$ .

The orientations of each of these lines are easily found. The angle  $\delta$  which each makes with the normal  $ON$  is related to  $\gamma$  by

$$\tan \delta = \frac{1}{2}|\gamma|. \tag{11.8}$$

Note that  $\delta$  is just the angle between two intersecting lines, and does not have sense and therefore its value depends on the magnitude of  $\gamma$ , not its sign. The angle which this second line of NFLS makes with the shear direction is then given by

$$\theta' = 90 - \delta = 90 - \arctan \frac{1}{2}\gamma. \tag{11.9}$$

With the orientation of the two lines of NFLS known, the principal axes can be found by bisecting the acute and obtuse angles line  $OP'$  makes with the shear direction at  $P'$  (Fig. 11.11b). This is easily accomplished with an elementary construction. First draw a semi-circle centered at  $O$  with  $OP = OP'$  as radius (Fig. 11.11c), and then add the

chord  $AP'$  to the diagram. Because inscribed angle  $AP'P$  and central angle  $AOP$  intercept the same arc  $AP$

$$\angle AP'P = \frac{1}{2}\theta = \frac{1}{2}\theta',$$

that is, chord  $AP'$  bisects the acute angle between the two lines of NFLS, which therefore marks the orientation of the  $S_1$  direction. Similarly, the chord  $BP'$  bisects the obtuse angle and marks the  $S_3$  direction.

The line  $AP$  marks the orientation of the  $S_1$  direction before deformation. It is then transformed into line  $AP'$ , which marks the  $S_1$  direction after deformation. The angle between these two is, therefore, the angle of rotation. The inscribed angle  $\omega$  and the central angle  $2\delta$  intercept the same arc  $PP'$  and we have  $\omega = \delta$ . Using this in Eq. 11.8 gives

$$\tan \omega = \frac{1}{2}\gamma. \quad (11.10)$$

Again, the signs of  $\omega$  and  $\gamma$  are the same, that is, the sense of rotation is the same as the sense of the angle of shear.

Expressions for the orientation of these two principal axes after deformation can also be obtained. From Fig. 11.10c, and because they intercept the same arc  $BP'$ ,  $\phi' = \frac{1}{2}\theta'$  or  $2\phi' = \theta'$ . With Eq. 11.9 we then have

$$2\phi' = 90 - \arctan \frac{1}{2}\gamma \quad \text{or} \quad \tan(90 - 2\phi') = \frac{1}{2}\gamma.$$

Using the identity  $\tan(90 - x) = 1/\tan x$  we then have

$$\tan 2\phi' = 2/\gamma. \quad (11.11)$$

Two angles satisfy this equation:  $\phi'$  gives the orientation of the  $S_1$  direction, and  $90 - \phi'$  gives of the orientation of the  $S_3$  direction. In a similar way the orientation of the principal axes before deformation can be found from

$$\tan 2\phi = 2/\gamma, \quad (11.12)$$

where  $\phi$  gives the orientation of the  $S_3$  direction and  $90 - \phi$  gives the orientation of the  $S_1$  direction.

The magnitudes of the principal stretches can also be found. In the  $S_1$  direction  $l = AP$  and  $l' = AP'$  (Fig. 11.10c). With the definition of stretch of Eqs. 11.1

$$S_1 = AP'/AP.$$

With this, and noting that  $AP = BP'$  we then have

$$\tan \phi' = BP'/AP' = AP/AP' = 1/S_1,$$

hence

$$S_1 = 1/\tan \phi'. \quad (11.13)$$

Two-dimensional deformations also generally change area. The *area strain*  $\Delta$  is defined as the *change in area per unit area*, or

$$\Delta = \frac{A' - A}{A} = \frac{A'}{A} - 1, \quad (11.14)$$

where  $A$  is the initial and  $A'$  is the final area; an increase in area is positive ( $A' > A$ ) and a decrease is negative ( $A' < A$ ). The ratio  $A'/A$  is sometimes called the *area stretch*. The area strain may be written in terms of the area of a circle and the area of an ellipse as

$$\Delta = \frac{\pi S_1 S_3 - \pi r^2}{\pi r^2}.$$

For our reference circle  $r = 1$  and this reduces to

$$\boxed{\Delta = S_1 S_3 - 1.} \quad (11.15)$$

In simple shear, area remains constant; the parallelogram of Fig. 11.11a has the same area as the original rectangle from which it was derived. Combined with the fact that no change in length occurs in the  $S_2$  direction simple shear also does not change volume. Deformations which preserve volume are termed *isochoric*.

With no area change  $\Delta = 0$ . With Eq. 11.15 we then have the necessary relationship between the principal stretches for the constant area condition

$$S_1 S_3 = 1 \quad \text{or} \quad S_3 = 1/S_1. \quad (11.16)$$

Be careful. Do not generalize to other types of deformation because constant area on the  $S_1 S_3$  plane does not necessarily imply constant volume nor does a change in area on this plane necessarily imply a change in volume. It all depends on the magnitude of the intermediate principal stretch  $S_2$ .

Substituting the expression for  $S_1$  from Eq. 11.13 into Eq. 11.16 then yields

$$S_3 = \tan \phi'. \quad (11.17)$$

From Eq. 11.6 we have

$$R_s = S_1/S_3 = 1/\tan^2 \phi'. \quad (11.18)$$

We can also express the shear strain in terms of the two principal stretches. From Eq. 11.11  $\gamma/2 = \cot 2\phi'$  and from Eq. 11.13  $S_1 = \cot \phi'$ . Substituting these two expressions into the double-angle identity

$$\cot 2\phi' = \frac{\cot^2 \phi' - 1}{2 \cot \phi'} = \frac{1}{2} \left[ \cot \phi' - \frac{1}{\cot \phi'} \right],$$

gives

$$\gamma = S_1 - 1/S_1 = S_1 - S_3. \quad (11.19)$$

As an example of the use of these expressions in the analysis of a simple shear deformation, consider the case  $\psi = 45^\circ$ . With Eq. 11.7,  $\gamma = 1$ . Using this in Eq. 11.11 gives  $\tan 2\phi' = 2$  and therefore  $\phi' = 31.71747^\circ$ . With this angle in Eq. 11.13 and Eq. 11.17, we then have<sup>7</sup>

$$S_1 = 1.61803\dots \quad \text{and} \quad S_3 = 0.61803\dots,$$

With Eq. 11.18, the strain ratio is

$$R_s = 1/\tan^2 \phi' = 2.61803\dots$$

Note the curious fact that the fractional parts of these three numbers are identical. With Eq. 11.19 the shear strain is

$$\gamma = S_1 - S_3 = 1.00000\dots,$$

which is just what we started with.

Finally, it is useful to observe how the orientation of any general line changes in simple shear (Ramsay, 1967, p. 87). If the line makes an angle  $\theta$  with the shear plane before (Fig. 11.12a) and angle  $\theta'$  after deformation (Fig. 11.12b), then

$$\cot \theta' = \gamma + \cot \theta. \quad (11.20)$$

The rotation of any general line is then given by  $|\theta - \theta'|$ , where, again, the sense of rotation and the sense of the angle of shear are the same (in this example it is anticlockwise or positive).

It is particularly instructive to examine the rotation of a pair of lines which make equal angles with the principal directions. In Fig. 11.13a, material lines  $l_1$  and  $l_2$  make

<sup>7</sup>These two numbers are the *golden ratio* and its *inverse*  $\frac{1}{2}(\sqrt{5} \pm 1)$ , and they have a long history (Livio, 2002). The ratio is mentioned by Euclid and was used in ancient Greek architecture (Devlin, 1994, p. 108). These numbers have many interesting properties (Graham, *et al.*, 1989, p. 285) and an astonishing variety of applications (Schroeder, 1991).

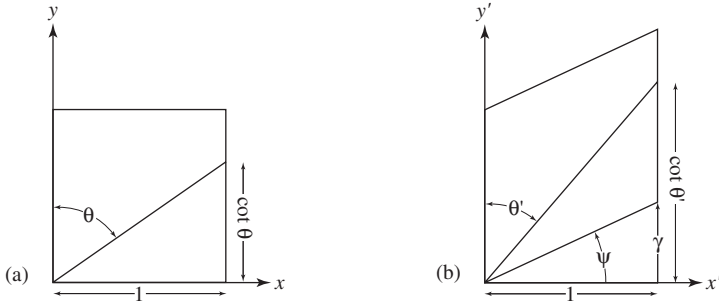


**Figure 11.12** Rotation of a general line in simple shear.

angles of  $\pm 20^\circ$  with the  $S_1$  axis before deformation. The same material lines  $l'_1$  and  $l'_2$  after simple shear ( $\gamma = 1$ ) now make equal angles of  $\pm 7.9^\circ$  with this same axis (Fig. 11.13b). Using Eq. 11.20 to determine the rotations of each of these lines we find that the rotation of the first line is  $38.63225^\circ$  and the rotation of the second line is  $14.47983^\circ$ . The mean of these two angles is  $\omega = 26.56505^\circ$  and this is just the angle found using Eq. 11.10. Since every line can be paired with its symmetric opposite in this way, we see that the rotation of the axes is just the average rotation of all radii of the strain ellipse.

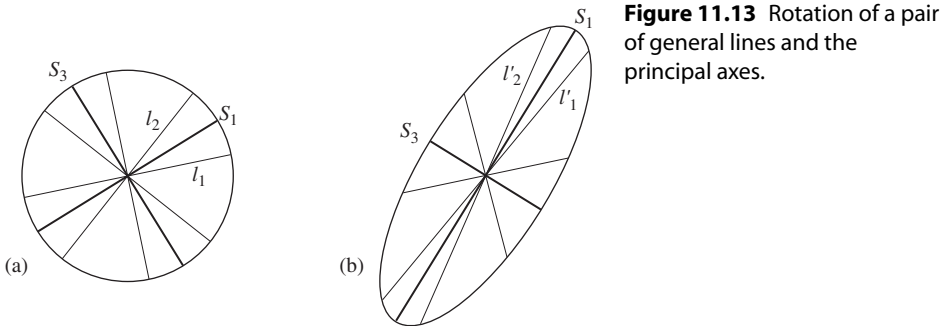


**Figure 11.13** Rotation of a pair of general lines and the principal axes.

### 11.5 Superimposed deformations

Models are also useful for illustrating the superposition of two or more homogeneous deformations. We now explore the range of geometrical possibilities of the ways such two-dimensional deformations combine.

A simple experiment consists of transforming a circle into an ellipse which represents the first deformation  $D_1$ . A second circle is sheared into an ellipse representing the second deformation  $D_2$ . The first circle, now twice deformed, represents the total deformation  $D_T$ .



We are not restricted to superimposed deformations by simple shear because any ellipse can represent the first deformation. For example, in Fig. 11.14a the first deformation  $\mathbf{D}_1$  is represented by an ellipse with an axial ratio  $R_1 = 2.0$  and oriented with its long axis perpendicular to the shear plane. It and a concentric circle are sheared to represent the second deformation  $\mathbf{D}_2$ , and the twice deformed ellipse represents the total deformation  $\mathbf{D}_T$  (Fig. 11.14b). Also, note that the  $\mathbf{D}_1$  ellipse rotates in the same sense as the simple shear ellipse but by a different angle because the axes of the two ellipses are not marked by the same material lines, and therefore this is only an *apparent rotation*. Note too that the axial ratios  $R_1$ ,  $R_2$  and  $R_T$  are not simply related.

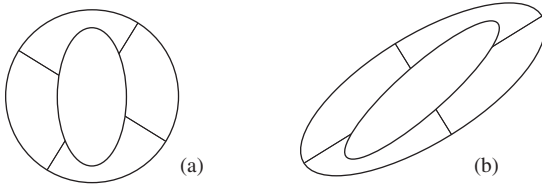


**Figure 11.14** Superposition: (a) after  $\mathbf{D}_1$ ; (b) after  $\mathbf{D}_2$ .

A second example illustrates an apparent rotation in an even more dramatic way. In Fig. 11.15a,  $\mathbf{D}_1$  is represented by an ellipse with axial ratio  $R_1 = 2.0$  and oriented with its long axis parallel to the shear plane. After shearing the deck we see that the  $\mathbf{D}_T$  ellipse has changed orientation in a sense counter to that of the simple shear rotation (Fig. 11.15b). This is quite obviously an apparent rotation.

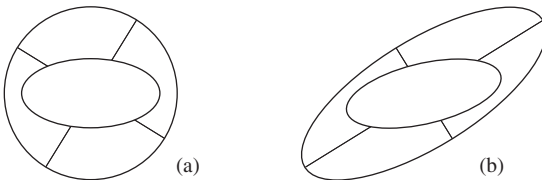


**Figure 11.15** Apparent rotation: (a) after  $\mathbf{D}_1$ ; (b) after  $\mathbf{D}_2$ .

Because the principal axes of  $\mathbf{D}_1$  and  $\mathbf{D}_2$  are differently oriented these two examples illustrate the general or *non-coaxial* superposition of homogeneous deformations. Superpositions which are *coaxial* may also be illustrated easily with card-deck models. There are two cases.

1. The  $\mathbf{D}_1$  ellipse is drawn with its principal axes *parallel* to the corresponding  $\mathbf{D}_2$  axes before deformation (Fig. 11.16a). After deformation, the two ellipses are also *coaxial* (Fig. 11.16b).
2. The  $\mathbf{D}_1$  ellipse is drawn with its axes *perpendicular* to the corresponding  $\mathbf{D}_2$  axes (Fig. 11.17a). Again, after deformation the two ellipses are *coaxial* (Fig. 11.17b).

There are four special types of coaxial superpositions and an understanding of each of these is important because they provide a series of reference points for describing

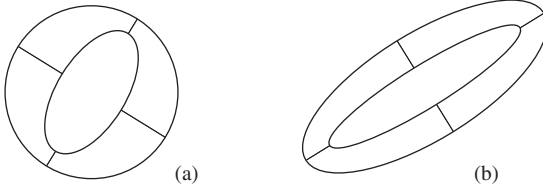


**Figure 11.16** Parallel superposition: (a) before  $\mathbf{D}_2$ ; (b) after  $\mathbf{D}_2$ .

superimposed homogeneous deformations generally. Because the same material lines mark the axes of the  $\mathbf{D}_1$  and  $\mathbf{D}_2$  ellipses, the rotation is the same for both and therefore plays no role in the final geometry. In order to concentrate on essentials it is therefore useful to eliminate it from consideration. This is easily accomplished by redrawing the results with axes parallel both before and after deformation.

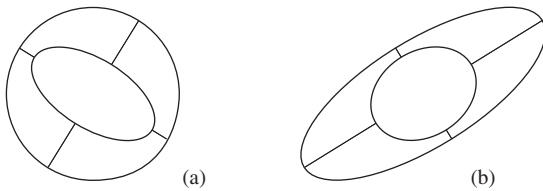


**Figure 11.17** Perpendicular superposition: (a) before  $\mathbf{D}_2$ ; (b) after  $\mathbf{D}_2$ .

1. If the pair of axes are parallel, that is, the angle between corresponding sets is  $0^\circ$ , the result always has a *narrow* form (Fig. 11.18a). For such coaxial deformations, the several axial ratios are related by

$$R_T = R_1 R_2. \tag{11.21}$$

In this example,  $R_1 = 1.71$ ,  $R_2 = 2.00$  and  $R_T = 3.42$ .

2. If the pair of axes are perpendicular, that is, the angle between corresponding sets is  $90^\circ$ , the results depend on the magnitudes of the ratios of the  $\mathbf{D}_1$  and  $\mathbf{D}_2$  ellipses. There are three sub-cases.

- (a) If  $R_1 > R_2$  the resulting ellipse has a *pre-circle broad form* (Fig. 11.18b), and the axes  $\mathbf{D}_2$  and  $\mathbf{D}_T$  are still perpendicular. The axial ratios are related by

$$R_T = R_1/R_2. \tag{11.22}$$

In this example  $R_1 = 2.56$ ,  $R_2 = 2.00$  and  $R_T = 1.28$ .

- (b) In the special case where  $R_1 = R_2$  then  $R_T = 1$  and the result is a *circle* (Fig. 11.18c).
- (c) If  $R_1 < R_2$  the result has a *post-circle broad form* (Fig. 11.18d), and the axes  $\mathbf{D}_2$  and  $\mathbf{D}_T$  are now parallel. The axial ratios are related by

$$R_T = R_2/R_1. \tag{11.23}$$

In this example  $R_1 = 1.56$ ,  $R_2 = 2.00$ , and  $R_T = 1.28$ .

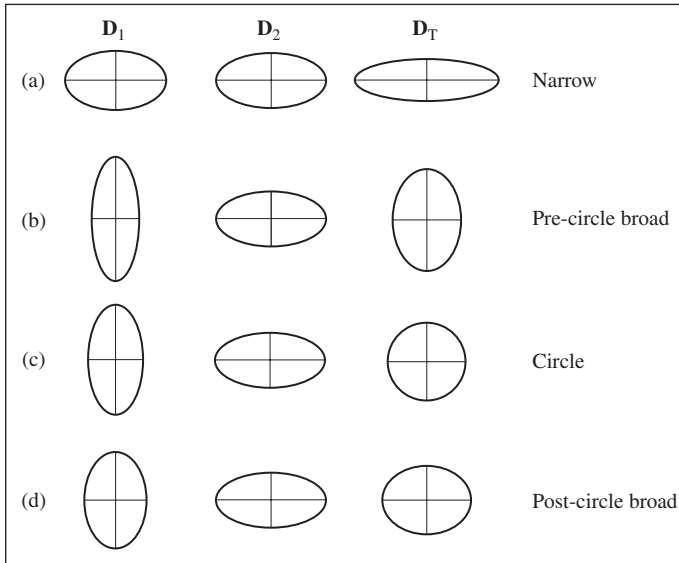


**Figure 11.18** Narrow, broad and circular forms.

## 11.6 Inhomogeneous deformation

Some important aspects of inhomogeneous deformations can also be illustrated with card-deck experiments. One simply deforms the deck so that the square end is transformed into a smooth curve. The structure modeled here is a *shear zone*, that is, a tabular body of sheared rock bounded on both sides by undeformed material.

We will approach the description of the deformation within a model zone in two different ways. First, we will generate a *forward model* by starting with a specified displacement curve and then examine the structure within the resulting zone. This will show clearly how the elements of the problem are related. Second, we will treat the shear zone as an *inverse problem* and show that we can recover the displacement curve solely from the geometry of the deformation within the shear zone.

### *Forward model*

The geometrical details of the resulting inhomogeneous deformation in the model can be followed closely if a number of small circles are stamped on the deck. This can be accomplished easily with a slip-on pencil eraser and an ink pad.

Because it roughly approximates the geometry of naturally occurring shear zones we choose as our displacement curve

$$y = A \sin mx.$$

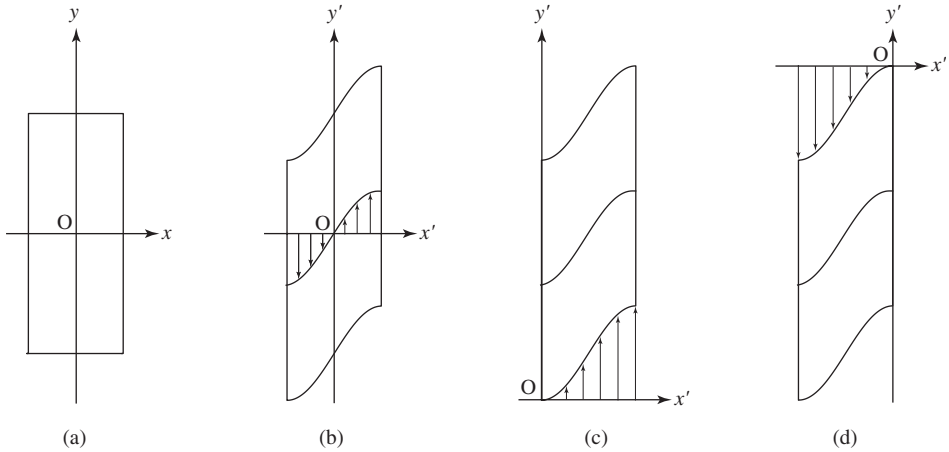


**Figure 11.19** Shear zone modeled with a card deck.

Accordingly, we establish the  $y$  direction of our coordinate system in the shear direction so that the equation describing the model zone will retain its familiar form (see Fig. 11.19a).

It is convenient to fix the origin of our coordinate system and to scale the dimensions of the model zone so that it is bounded by the parallel lines  $x = \pm 1$ , thus we choose  $m = \pi/2$ . We can also vary the amplitude of the sine curve; in the example we arbitrarily choose  $A = 1$  so that  $y_{max} = +1$  and  $y_{min} = -1$ . The equation of the displacement curve is then

$$y = \sin \frac{\pi x}{2}. \quad (11.24)$$

Accordingly, we displace a line along the  $x$  axis upward on the positive side of the origin and downward on the negative side (Fig. 11.19b). Note, however, that this pattern of displacements is not unique. We could have just as easily established the origin in a different place and displaced a line parallel to  $x$  entirely upward (Fig. 11.19c) or entirely downward (Fig. 11.19d) with identical results. This is the same ambiguity we faced in describing the displacement of the blocks bound by a fault. There, as here, we are forced to deal with the *relative* displacements.

Using this displacement curve to deform the deck the reference circles are converted into a series of small strain ellipses (Fig. 11.20a). A useful way of summarizing this information is to draw two sets of orthogonal curves, called *trajectories*, one set is everywhere tangent to the  $S_1$  direction and the other is everywhere tangent to the  $S_3$  direction (Fig. 11.20b).

The distribution of  $\gamma$  within the zone is just the slope  $dx/dy$  of the displacement curve  $D$ . To obtain the expression for this slope we differentiate Eq. 11.22 with respect to  $x$ , giving

$$\gamma = \frac{dy}{dx} = \frac{\pi}{2} \cos \frac{\pi x}{2}. \quad (11.25)$$

A plot of this equation is shown in Fig. 11.20c by the curve labeled  $\gamma$ .

The orientation angle the long axes make with the  $y$  direction is, from Eq. 11.11, given by

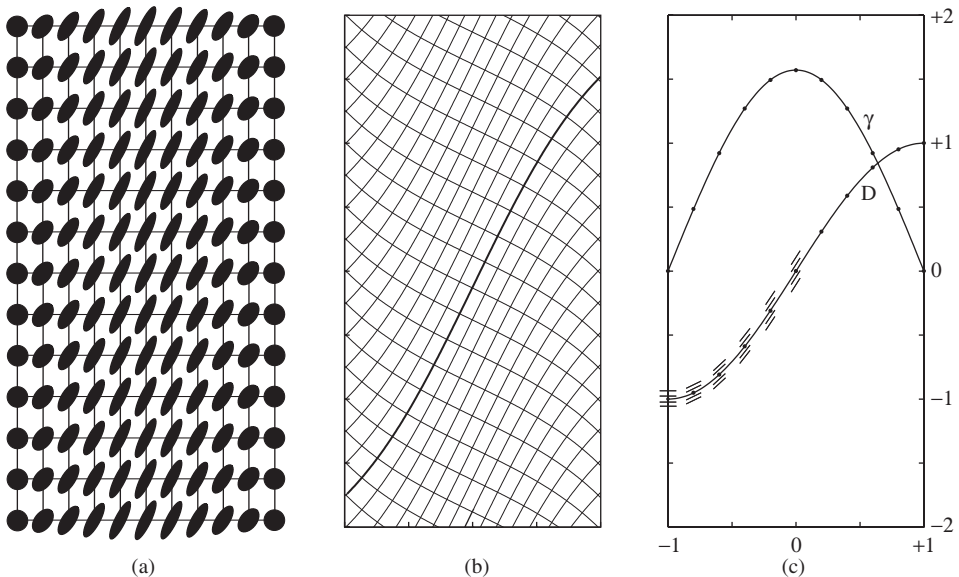
$$\phi' = \frac{1}{2} \arctan(2/\gamma). \quad (11.26)$$

Table 11.1 *Data for model shear zone*

$\pm x$	0	0.2	0.4	0.6	0.8	1.0
$\gamma$	1.5708	1.4939	1.2708	0.9233	0.4854	0
$\psi$	57.5184	56.2024	51.8006	42.7160	25.8921	0
$\phi'$	25.9270	26.6209	28.7841	32.6099	38.1790	45.0000

### *Inverse problem*

In real shear zones the curved  $S_1$  trajectories are commonly marked by aligned mineral grains, such as mica or amphibole; these are commonly referred to as  $S$  surfaces (from schistosity). In coarse-grained rocks, the shear planes may also be evident, and these are denoted  $C$  surfaces (from cisaillement, French for shear); in the model these are the planes of the cards themselves. In rocks with  $S$ - $C$  fabrics the sense of shear can be determined immediately from the monoclinic symmetry (Simpson & Schmid, 1983, p. 1284); in our model it is sinistral.



**Figure 11.20** Model shear zone: (a) structure; (b)  $S_1$  and  $S_3$  trajectories; (c) shear parameters.

This correspondence between the mineral foliation and  $S_1$  trajectories permits the strain distribution and the geometry of the displacements to be determined in naturally occurring zones formed by simple shear. The measured slope of the trace of the  $S$  surfaces at a series of points gives the distribution of angles  $\phi'$  across the zone and these define the orientations of the  $S_1$  axes. From the values of  $\phi'$  the value of  $\gamma$  at each point can be calculated from (see Eq. 11.11)

$$\gamma = 2 / \tan 2\phi'. \quad (11.27)$$

In the unlikely event that we could find an expression of the distribution of  $\gamma$  across a shear zone (such as Eq. 11.23), we might be able to integrate it to obtain the displacement curve responsible for the geometry of the curved  $S$  surfaces (such as Eq. 11.22). Without such an expression we need an alternative approach, and there are two ways to proceed.

1. The simplest method is to graphically integrate the distribution of  $\gamma$  obtained from the measured angles  $\phi'$  with Eq. 11.25. This is accomplished by plotting a series of short lines whose slope is given by the local value of  $\gamma$  and sketching a curve which is everywhere tangent to these lines (see the left half of the curve  $D$  in Fig. 11.20c).
2. The form of the displacement curve can also be determined by numerically integrating the distribution of the  $\gamma = dy/dx$ .<sup>8</sup>

Additional deformational patterns may be superimposed on simple shear in naturally occurring shear zones. For example, an inhomogeneous volume loss such that the zone boundaries move closer together. The shortening this produces may also be estimated from other structures found within some zones (Ramsay, 1980).

## 11.7 Deformation and related tensors

Homogeneous deformations can also be treated analytically. In much of the technical literature of continuum mechanics, a different notational scheme is used: variables in the material state are represented by capital letters (majuscules) and in the spatial state by lowercase letters (minuscules). Thus the material coordinates are  $X_1, X_2$  (Fig. 11.21a) and the spatial coordinates are  $x_1, x_2$  (Fig. 11.21b). Similarly, a typical material particle is  $P$  and its corresponding spatial location is  $p$ .

We now write the deformation as a pair of equations which describe an *affine transformation of the plane*.<sup>9</sup> In tensor notation (see §9.12), these are

$$x_1 = D_{11}X_1 + D_{12}X_2 + T_1, \quad (11.28a)$$

$$x_2 = D_{21}X_1 + D_{22}X_2 + T_2. \quad (11.28b)$$

<sup>8</sup>The  $S_1$  and  $S_3$  trajectories in Fig. 11.20b were calculated from the measured slopes of the principal directions at a series of points across the zone using Euler's finite-difference method (Ferziger, 1998, p. 87).

<sup>9</sup>An affine transformation preserves collinearity, hence also straightness and parallelism (Courant, 1936, p. 27).

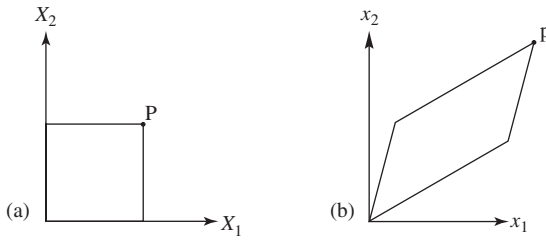


**Figure 11.21** Transformation: (a) material coordinates; (b) spatial coordinates.

In mathematical terms, this transformation *assigns* or *maps* each material particle  $P(X_1, X_2)$  to a spatial point  $p(x_1, x_2)$ . An important property is that as  $P$  moves along the circumference of a circle,  $p$  will, in general, trace out an ellipse. The coefficients  $D_{11}$ ,  $D_{12}$ ,  $D_{21}$  and  $D_{22}$  describe the rotation and stretch, and constants  $T_1$  and  $T_2$  describe the translation. For our purposes, it is useful to write this pair of expressions in the form of the single matrix equation

$$\begin{bmatrix} x_1 \\ x_2 \end{bmatrix} = \begin{bmatrix} D_{11} & D_{12} \\ D_{21} & D_{22} \end{bmatrix} \begin{bmatrix} X_1 \\ X_2 \end{bmatrix} + \begin{bmatrix} T_1 \\ T_2 \end{bmatrix}. \quad (11.29)$$

Accordingly, we now interpret  $\mathbf{X}(X_1, X_2)$  and  $\mathbf{x}(x_1, x_2)$  as position vectors of  $P$  and  $p$ , which we write as column matrices. This constitutes the *material description* of a homogeneous deformation.

We can also easily obtain an expression for the components of the total displacement vector which gives the position of  $p$  relative to  $P$ . It is

$$\begin{bmatrix} u_1 \\ u_2 \end{bmatrix} = \begin{bmatrix} x_1 - X_1 \\ x_2 - X_2 \end{bmatrix} + \begin{bmatrix} T_1 \\ T_2 \end{bmatrix} \quad (11.30)$$

and this makes clear that the total displacement is the sum of the *relative displacement vector* and the *uniform translation vector*. As before, we neglect the translation.

The essential part of the transformation of Eqs. 11.30 is the square matrix which represents the *deformation tensor*

$$\mathbf{D} = \begin{bmatrix} D_{11} & D_{12} \\ D_{21} & D_{22} \end{bmatrix}. \quad (11.31)$$

In general  $D_{12} \neq D_{21}$ , that is, the matrix is not symmetric. In common with all tensors of second rank, we can think of  $\mathbf{D}$  as a vector processor (see §9.12). The input is a vector before deformation and the output is the corresponding vector after deformation. Each of the four elements has a geometrical meaning. To see this, we process the two unit base

vectors using row times column multiplication. The results are

$$\begin{bmatrix} x_1 \\ x_2 \end{bmatrix} = \begin{bmatrix} D_{11} & D_{12} \\ D_{21} & D_{22} \end{bmatrix} \begin{bmatrix} 1 \\ 0 \end{bmatrix} = \begin{bmatrix} D_{11} \\ D_{21} \end{bmatrix} \quad \text{and} \quad \begin{bmatrix} x_1 \\ x_2 \end{bmatrix} = \begin{bmatrix} D_{11} & D_{12} \\ D_{21} & D_{22} \end{bmatrix} \begin{bmatrix} 0 \\ 1 \end{bmatrix} = \begin{bmatrix} D_{12} \\ D_{22} \end{bmatrix}.$$

Thus the first column contains the components of the unit vector initially in the  $X_1$  direction and the second column contains the components of the unit vector initially in the  $X_2$  direction. These vectors form two sides of a parallelogram (Fig. 11.22b).

We can also express the area strain associated with the homogeneous deformation in terms of these components. Before deformation, the reference square has unit area (Fig. 11.22a). After deformation the area  $A$  is obtained from the cross product in component form (Fig. 11.22b; also Fig. 7.9 and Eq. 7.27). Thus

$$A = D_{11}D_{22} - D_{12}D_{21}, \tag{11.32a}$$

and this is just the determinant of  $\mathbf{D}$ . With the definition of Eq. 11.14, the area stretch is then given by

$$\Delta + 1 = \left| \begin{matrix} D_{11} & D_{12} \\ D_{21} & D_{22} \end{matrix} \right|, \tag{11.32b}$$

that is, the determinant expresses the area of the unit reference square after transformation.

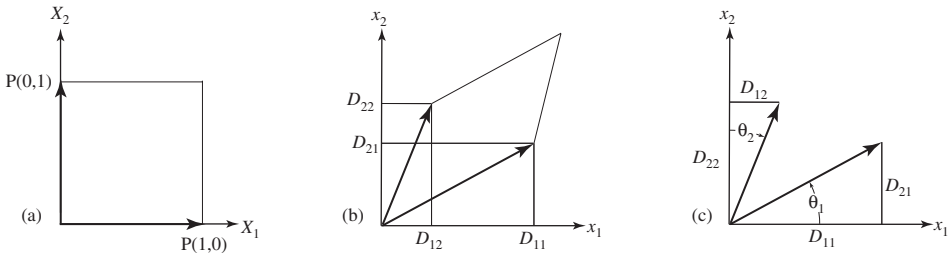


**Figure 11.22** Transformation: (a) unit base vectors; (b) after deformation; (c) orientations.

We can also find the stretches associated with the unit vectors initially in each coordinate direction. From Fig. 11.22c, the stretch of the line initially in the  $X_1$  direction is

$$S(X_1) = \sqrt{D_{11}^2 + D_{21}^2} \tag{11.33a}$$

and the stretch of the line initially in the  $X_2$  direction is

$$S(X_2) = \sqrt{D_{12}^2 + D_{22}^2}. \tag{11.33b}$$



Also from Fig. 11.22c the angles each of these stretched lines make with their respective axes after deformation are

$$\arctan \theta_1 = D_{21}/D_{11} \quad \text{and} \quad \arctan \theta_2 = D_{12}/D_{22}. \quad (11.34)$$

Finally, because these two vectors were initially orthogonal, the magnitude of the angle of shear associated with each is

$$|\psi| = \theta_1 + \theta_2. \quad (11.35)$$

### Problem

- With the following two closely related deformation tensors graphically deform the unit square with corner points  $P_1(1, 0)$  and  $P_2(0, 1)$  (Fig. 11.23a).<sup>10</sup> Determine the stretch associated with material lines initially in each coordinate direction, together with their final orientation, the angle of shear associated with each of these directions, and the area strain.

$$\mathbf{D}_1 = \begin{bmatrix} 1.4 & 0.2 \\ 0.6 & 0.8 \end{bmatrix} \quad \text{and} \quad \mathbf{D}_2 = \begin{bmatrix} 1.4 & 0.6 \\ 0.2 & 0.8 \end{bmatrix}.$$

### Procedure

1. On a pair of axes  $x_1 x_2$  plot points using a convenient scale:
  - (a)  $\mathbf{D}_1$ :  $p_1 = (D_{11}, D_{21}) = (1.4, 0.6)$  and  $p_2 = (D_{12}, D_{22}) = (0.2, 0.8)$ , (Fig. 11.23b),
  - (b)  $\mathbf{D}_2$ :  $p_1 = (D_{11}, D_{21}) = (1.4, 0.2)$  and  $p_2 = (D_{12}, D_{22}) = (0.6, 0.8)$  (Fig. 11.23c).
2. Lines  $Op_1$  and  $Op_2$  represent the deformed unit base vectors.
3. Complete the parallelograms by drawing the other two sides parallel to  $Op_1$  and  $Op_2$ .

### Results

1. The stretches associated with the pair of lines initially in each of the coordinate directions are
  - (a)  $\mathbf{D}_1$ :  $S(X_1) = 1.52$  and  $S(X_2) = 0.82$ ,
  - (b)  $\mathbf{D}_2$ :  $S(X_1) = 1.41$  and  $S(X_2) = 1.00$ .
2. The angles these lines make with the coordinate directions are
  - (a)  $\mathbf{D}_1$ :  $\theta_1 = 23^\circ$  and  $\theta_2 = 14^\circ$ ,
  - (b)  $\mathbf{D}_2$ :  $\theta_1 = 8^\circ$  and  $\theta_2 = 37^\circ$ .
3. The angles of shear associated with these initially orthogonal lines are
  - (a)  $\mathbf{D}_1$ :  $|\psi| = \theta_1 + \theta_2 = 37^\circ$ . For the line initially in the  $X_1$  direction  $\psi = -37^\circ$  and for the line initially in the  $X_2$  direction  $\psi = +37^\circ$ .

<sup>10</sup>These two representations differ only by positions of the off-diagonal elements; such *transpose* matrices have a role in later developments (see §12.12).

- (b)  $\mathbf{D}_2$ :  $|\psi| = \theta_1 + \theta_2 = 45^\circ$ . For the line initially in the  $X_1$  direction  $\psi = -45^\circ$  and for the line initially in the  $X_2$  direction  $\psi = +45^\circ$ .
4. In both deformations, the area strain  $\Delta = 0$ , that is, area is preserved.

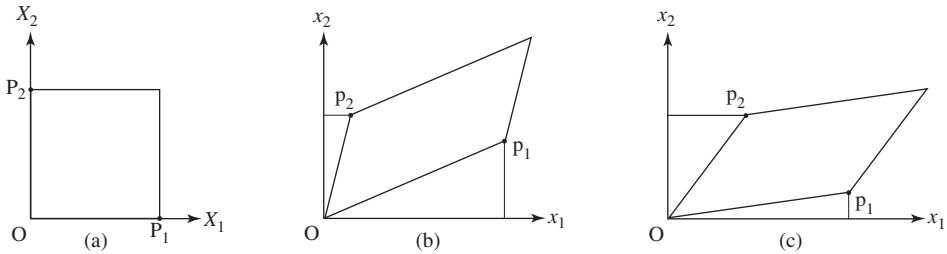


**Figure 11.23** Homogeneous deformations: (a) unit square; (b)  $\mathbf{D}_1$ ; (c)  $\mathbf{D}_2$ .

Additional features of the deformation, especially the principal stretches, their orientation and rotation are of fundamental interest, but this information is not easy to extract from the parallelogram. There is, however, an attractive alternative because we can represent two-dimensional deformation tensors graphically with the aid of a Mohr Circle diagram (Means, 1996, p. 16f).

**Problem**

- For the deformation tensor  $\mathbf{D}_1$  construct a Mohr Circle diagram. Determine the principal stretches, their orientation and the angle of their rotation.

**Construction**

1. Draw a pair of axes and label the horizontal axis ( $D_{11}, D_{22}$ ) and the vertical axis ( $D_{12}, D_{21}$ ) (Fig. 11.24a).
  - (a) Plot points  $p_1(D_{11}, -D_{21}) = p_1(1.4, -0.6)$  and  $p_2(D_{22}, D_{12}) = p_2(0.8, 0.2)$ .
  - (b) At the midpoint of the line segment  $p_1 p_2$  locate center  $C$  and draw a circle passing through both points.
2. The following features are important:
  - (a) The lengths of the segments  $Op_1$  and  $Op_2$  represent the stretches associated with the two initially orthogonal lines.
  - (b) These two lines make angles  $\theta_1$  and  $\theta_2$  with the horizontal axis, each measured toward this axis.
  - (c) The angles of shear with the two lines are  $\psi = \pm(\theta_1 + \theta_2)$ .
3. Draw the inclined line from the origin  $O$  through center  $C$  and beyond (Fig. 11.24b).
  - (a) The two intersections of this line with the circle represent the principal stretches  $S_1$  and  $S_3$ . Their magnitudes are equal to scaled lengths of  $OS_1$  and  $OS_3$ .
  - (b) The slope angle of this line represents the angle of rotation  $\omega$  measured from  $OC$  toward the horizontal axis.

(c) The angle  $2\phi$  between  $p_1$  and  $S_1$  on the Mohr Circle plane gives the angle  $\phi$  which the  $S_1$  direction makes with the  $X_1$  axis on the physical plane before deformation.

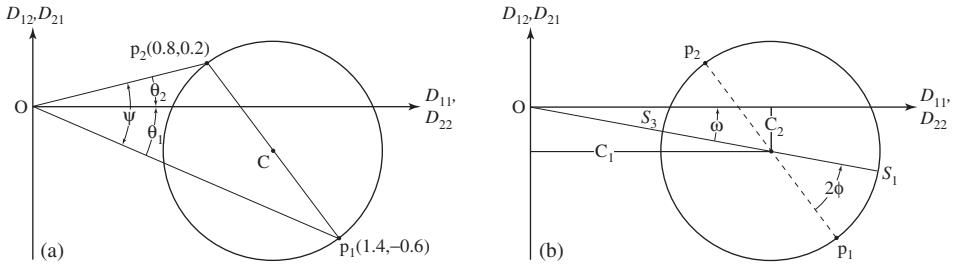


Figure 11.24 Mohr Circle for the deformation tensor  $D_1$ .

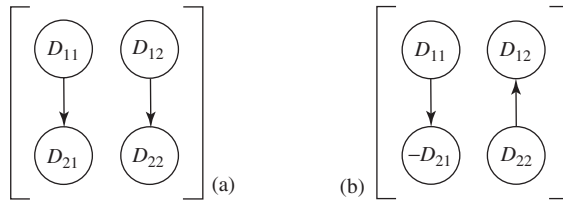


Figure 11.25 Plotting convention (after Means, 1996, p. 19): (a) physical plane; (b) Mohr Circle plane.

**Results**

- The rotation is anticlockwise and  $\omega = +10^\circ$ . The principal stretches are  $S_1 = 1.62$  and  $S_3 = 0.62$ . The angle the  $S_1$  direction makes with the  $X_1$  axis in the undeformed state is  $\phi = +22^\circ$ . In the deformed state the corresponding angle is  $\phi + \omega = 32^\circ$ .

Note carefully the two different ways of plotting points  $p_1$  and  $p_2$  for the parallelograms and the corresponding Mohr Circles. Figure 11.25 schematically displays these different patterns of combining the elements of the deformation matrix in an easily remembered form (Means, 1996, p. 19).

The construction of the Mohr Circle for  $D_2$  proceeds in exactly the same way (Fig. 11.26). The important difference is that the angle of rotation is the reverse of that for  $D_1$ .

Because rotation is an important part of a general deformation it is useful to pursue some related aspects in more detail. There are three cases, two general and one special.

1. If  $D_{12} < D_{21}$  then  $\omega > 0$ , that is, the center of the circle lies below the horizontal axis and the sense of rotation is anticlockwise (see Fig. 11.24b).
2. If  $D_{12} = D_{21}$ , then the center of the circle lies on the horizontal axis  $\omega = 0$  and there is no rotation.

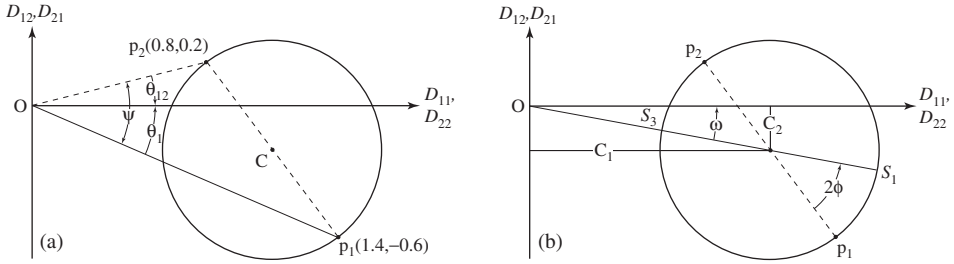


**Figure 11.26** Mohr Circle for the deformation tensor  $\mathbf{D}_2$ .

3. If  $D_{12} > D_{21}$  then  $\omega < 0$ , that is, the center lies above the horizontal axis and the sense of rotation is clockwise (see Fig. 11.26b).

There are several useful relationships which can be obtained directly from these Mohr Circle diagrams. In particular, we can obtain an expression for the angle of rotation (Fig. 11.24b). The coordinates of the center of the circle are

$$C_1 = \frac{1}{2}(D_{11} + D_{22}) \quad \text{and} \quad C_2 = \frac{1}{2}(D_{21} - D_{12}).$$

With these we have the slope of the line  $OC$

$$\tan \omega = C_2/C_1.$$

Substituting the expressions for  $C_1$  and  $C_2$  we then have

$$\boxed{\tan \omega = \frac{D_{21} - D_{12}}{D_{11} + D_{22}}}. \tag{11.36}$$

We can also find the magnitude of the principal stretches. The inclined distance  $c$  from the origin to the center of the circle and the radius  $r$  of the circle are given by

$$c = \frac{1}{2}\sqrt{(D_{11} + D_{22})^2 + (D_{12} - D_{21})^2} \quad \text{and} \quad r = \frac{1}{2}\sqrt{(D_{11} - D_{22})^2 + (D_{12} + D_{21})^2}.$$

The principal stretches are then

$$S_1 = c + r \quad \text{and} \quad S_3 = c - r.$$

This construction is valid for all two-dimensional deformation tensors, including the two special types we have already encountered. For simple shear the deformation matrix is

$$\mathbf{D} = \begin{bmatrix} D_{11} & D_{12} \\ D_{21} & D_{22} \end{bmatrix} = \begin{bmatrix} 1 & 0 \\ \gamma & 1 \end{bmatrix}. \tag{11.37}$$

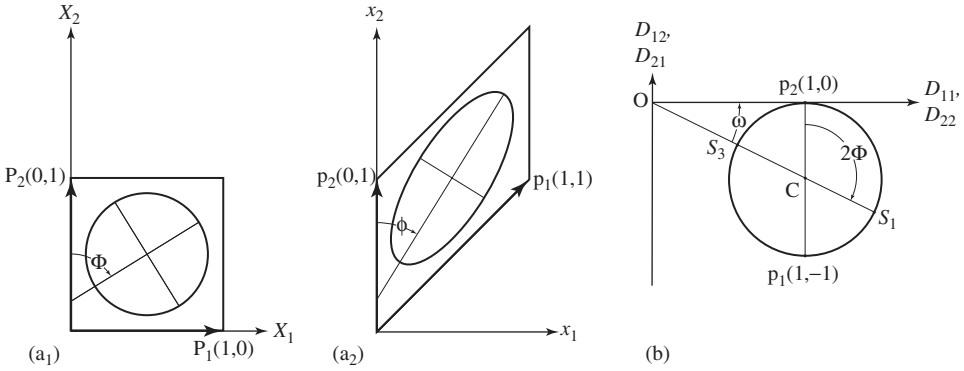


**Figure 11.27** Simple shear: (a) physical plane; (b) Mohr Circle plane.

For example, if  $\gamma = 1$ , the parallelogram derived from the unit square (Fig. 11.27a<sub>1</sub>) is constructed by plotting the corner points  $p_1(1, 1)$  and  $p_2(0, 1)$  and then adding the other two parallel sides (Fig. 11.27a<sub>2</sub>). The corresponding Mohr Circle is constructed using  $p_1(1, -1)$  and  $p_2(1, 0)$  (Fig. 11.27b).

For pure shear the deformation matrix, in diagonal form, is

$$\mathbf{D} = \begin{bmatrix} D_{11} & D_{12} \\ D_{21} & D_{22} \end{bmatrix} = \begin{bmatrix} S & 0 \\ 0 & 1/S \end{bmatrix}. \tag{11.38}$$

If  $S = 1.62$  and  $1/S = 0.62$  then the deformed equivalent of the unit square is a rectangle formed by plotting the corner points  $p_1(1.62, 0)$  and  $p_2(0, 0.62)$  (Fig. 11.28a). The Mohr Circle requires points  $p_1(1.62, 0)$  and  $p_2(0.62, 0)$  (Fig. 11.28b). The fact that this circle is centered on the horizontal axis is due to the fact that there is no rotation in pure shear (this is the meaning of *pure*).

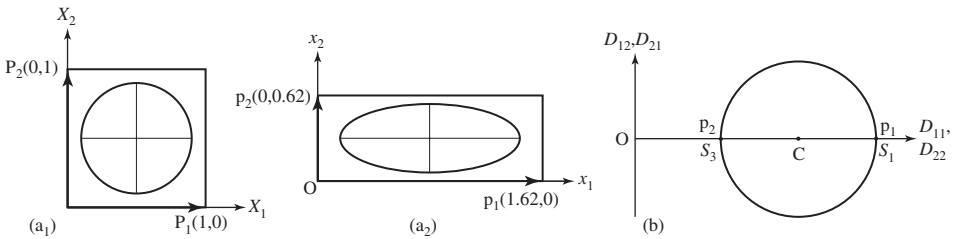


**Figure 11.28** Pure shear: (a) physical plane; (b) Mohr Circle plane.

With these methods we can easily explore the effects of superimposed deformations which we illustrated graphically in §11.5 by the matrix equation

$$\mathbf{D}_T = \mathbf{D}_2 \mathbf{D}_1 \tag{11.39}$$

where  $\mathbf{D}_T$  is the total deformation,  $\mathbf{D}_1$  is the first deformation and  $\mathbf{D}_2$  is the second deformation.

A simple shear deformation with the shear direction parallel to the  $X_2$  axis is given by the matrix of Eq. 11.38 and a pure shear deformation with the principal directions in the coordinate directions is given by the matrix equation of Eq. 11.39. With these, the result of simple shear  $\mathbf{D}_1$  followed by pure shear  $\mathbf{D}_2$  is then given by the matrix equation

$$\mathbf{D}_T = \mathbf{D}_2\mathbf{D}_1 = \begin{bmatrix} S & 0 \\ 0 & 1/S \end{bmatrix} \begin{bmatrix} 1 & 0 \\ \gamma & 1 \end{bmatrix} = \begin{bmatrix} S & 0 \\ \gamma/S & 1/S \end{bmatrix}. \tag{11.40}$$

Similarly, pure shear  $\mathbf{D}_1$  followed by simple shear  $\mathbf{D}_2$  is given by the matrix equation

$$\mathbf{D}_T = \mathbf{D}_2\mathbf{D}_1 = \begin{bmatrix} 1 & 0 \\ \gamma & 1 \end{bmatrix} \begin{bmatrix} S & 0 \\ 0 & 1/S \end{bmatrix} = \begin{bmatrix} S & 0 \\ \gamma S & 1/S \end{bmatrix}. \tag{11.41}$$

To illustrate these two cases, we will use the numerical examples of pure shear and simple shear

$$\begin{bmatrix} 1.62 & 0 \\ 0 & 0.62 \end{bmatrix} \quad \text{and} \quad \begin{bmatrix} 1 & 0 \\ 0.5 & 1 \end{bmatrix}.$$

Then pure shear superimposed on simple shear is shown in Fig. 11.29 and simple shear superimposed on pure shear is shown in Fig. 11.30.

Note carefully that the order of multiplication in Eq. 11.39 proceeds from  $\mathbf{D}_1$  on the right to  $\mathbf{D}_2$  on the left and that the resulting matrix representations of the two superimposed deformations  $\mathbf{D}_T$  are different. This difference is also seen clearly in the figures.

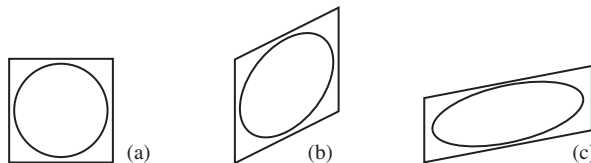


Figure 11.29 Superposition: (a) initial state; (b) simple shear  $\mathbf{D}_1$ ; (c) pure shear  $\mathbf{D}_2$ .

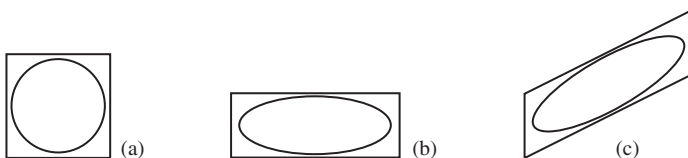


Figure 11.30 Superposition: (a) initial state; (b) pure shear  $\mathbf{D}_1$ ; (c) simple shear  $\mathbf{D}_2$ .

Finally, it is of some importance to understand that a homogeneous deformation represented by this tensor is closely related to the pattern of displacement vectors. In general,

these vectors will be neither parallel nor of equal magnitude for two adjacent material particles  $P$  and  $Q$  (Fig. 11.31a). If the distance between these is small then the displacement of  $Q$  relative to  $P$  is given by the vector  $d\mathbf{u}$  (Fig. 11.31b).

We can express the components of vector  $d\mathbf{u}$  in terms of the distance between the two points measured in the coordinate directions and the linear rates of change of these components in each of these directions (Fig. 11.31c). Thus

$$\begin{aligned} du_1 &= \frac{\partial u_1}{\partial X_1} dx_1 + \frac{\partial u_1}{\partial X_2} dx_2, \\ du_2 &= \frac{\partial u_2}{\partial X_1} dx_1 + \frac{\partial u_2}{\partial X_2} dx_2. \end{aligned}$$

We can also write these two as the matrix equation

$$\begin{bmatrix} du_1 \\ dx_2 \end{bmatrix} = \begin{bmatrix} \partial u_1/\partial X_1 & \partial u_1/\partial X_2 \\ \partial u_2/\partial X_1 & \partial u_2/\partial X_2 \end{bmatrix} \begin{bmatrix} dx_1 \\ dx_2 \end{bmatrix}. \tag{11.42}$$

This square matrix represents the *material displacement gradient tensor*.

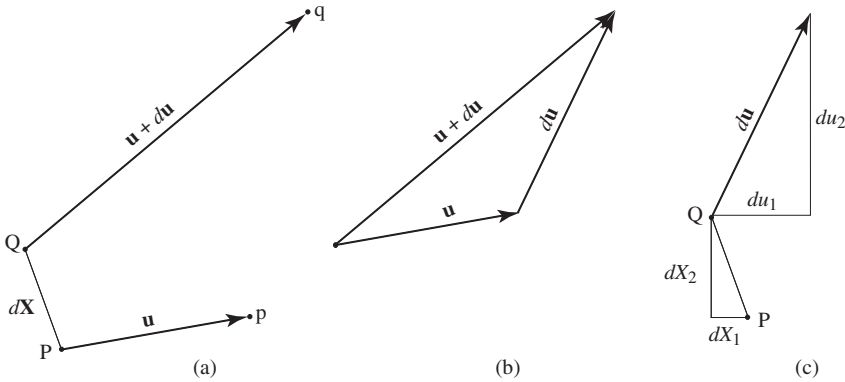


**Figure 11.31** Displacements: (a) adjacent particles  $P$  and  $Q$ ; (b) relative displacement vector  $d\mathbf{u}$ ; (c) displacement gradients.

We can obtain a closely related result in another way. Subtracting  $X_1$  from Eq. 11.28a and  $X_2$  from Eq. 11.28b gives (again neglecting the translation)

$$\begin{aligned} x_1 - X_1 &= D_{11}X_1 + D_{12}X_2 - X_1, \\ x_2 - X_2 &= D_{21}X_1 + D_{22}X_2 - X_2. \end{aligned}$$

Collecting terms and using Eq. 11.30 we have

$$u_1 = (D_{11} - 1)X_1 + D_{12}X_2, \tag{11.43a}$$

$$u_2 = D_{21}X_1 + (D_{22} - 1)X_2. \tag{11.43b}$$

Differentiating Eq. 11.43a partially once with respect to  $X_1$  and once with respect to  $x_2$  gives

$$\frac{\partial u_1}{\partial X_1} = D_{11} - 1 \quad \text{and} \quad \frac{\partial u_1}{\partial X_2} = D_{12}.$$

Similarly from Eq. 11.43b

$$\frac{\partial u_2}{\partial X_1} = D_{21} \quad \text{and} \quad \frac{\partial u_2}{\partial X_2} = D_{22} - 1.$$

We can write these results as the matrix equations

$$\begin{bmatrix} \partial u_1 / \partial X_1 & \partial u_1 / \partial X_2 \\ \partial u_2 / \partial X_1 & \partial u_2 / \partial X_2 \end{bmatrix} = \begin{bmatrix} D_{11} - 1 & D_{12} \\ D_{21} & D_{22} - 1 \end{bmatrix} \quad \text{or} \\ \begin{bmatrix} D_{11} & D_{12} \\ D_{21} & D_{22} \end{bmatrix} = \begin{bmatrix} 1 + \partial u_1 / \partial X_1 & \partial u_1 / \partial X_2 \\ \partial u_2 / \partial X_1 & 1 + \partial u_2 / \partial X_2 \end{bmatrix}$$

and these show the direct connection between the elements of the deformation tensor and the elements of the material displacement gradient tensor.

## 11.8 Exercises

- Using Fig. 11.32 showing the results of a circle-to-ellipse deformation make the necessary measurements to determine the values of  $\gamma$ ,  $S_1$ ,  $S_3$ ,  $\theta$ ,  $\theta'$  and  $\omega$ .<sup>11</sup>

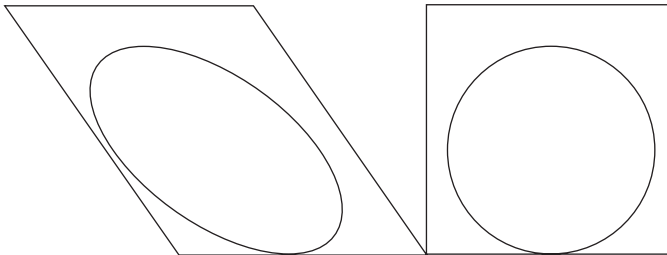


**Figure 11.32** Simple shear ellipse.

- With the angle  $\psi$  calculate the values of these same parameters.
- Using the example of a naturally occurring shear zone of Fig. 11.33, determine the displacements which are responsible for the structure – assume a unit width.

<sup>11</sup>An even better exercise is to analyze the results of a circle-to-ellipse experiment on a card deck.



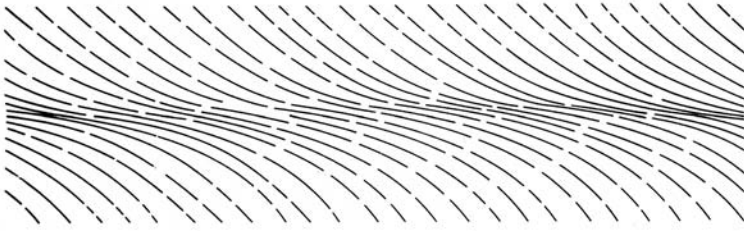


**Figure 11.33** Natural shear zone.

# 12

## Strain

### 12.1 Introduction

Deforming a circle into an ellipse clearly demonstrates that the orientations and lengths of lines and the angles between pairs of lines generally change. With suitable material the stretch and angle of shear associated with a line may be determined from measurements made on deformed objects whose original shape or size are known. It may then be possible to determine something of the shape, size and orientation of the strain ellipse. For example, measurement of the deformed shape of an originally spherical oolite yields the shape of the ellipse and its orientation directly. This chapter deals with some additional techniques for extracting two-dimensional strain information from deformed rocks. Many more examples, including some excellent photographs, can be found in the book by Ramsay and Huber (1983). Lisle (1994) gives a good review of more recent developments.

Before describing the full analytical method it will be useful to show that in some situations the shape and orientation of the strain ellipse can be obtained simply and directly using purely graphical means.

### 12.2 Deformed grains

The center points of individual grains in a section through a rock form a grid. In terms of the *center-to-center* distances the possible geometrical patterns have two end-members. If the distribution is random, the minimum distance between centers is zero and such pattern exhibits *clustering*. If all the grains are perfectly uniform circles and are closely packed then all distances between centers will be equal in the undeformed state (Fig. 12.1a), and thus are radii of a circle. After a homogeneous deformation these are systematically altered; they are now radii of an ellipse (Fig. 12.1b). Rocks commonly display patterns between these two and thus show degrees of *anticlustering*.

If the grain centers in the undeformed rock have a pronounced degree of anticlustering and the pattern is *isotropic*, that is, the spacing in all directions is the same, then the

shape and orientation of the strain ellipse can be recovered from the deformed grid (Fry, 1979a; 1979b; Hanna & Fry, 1979; also Ramsay & Huber, 1983, p. 111–113; Simpson, 1988, p. 352). The analysis is usually performed on the tracing of a photomicrograph.

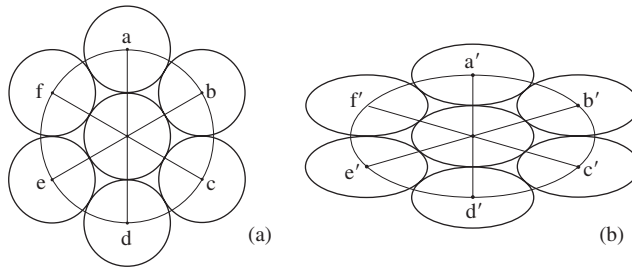


**Figure 12.1** Center-to-center distances: (a) before strain; (b) after strain.

### Problem

- From a section of deformed grains, determine the shape and orientation of the strain ellipse.

### Construction

1. Plot the centers of all individual grains, numbering each (Fig. 12.2a).
2. On an overlay sheet establish a reference mark representing the coordinate origin and position it over center No. 1. Mark all the other center points on this sheet.
3. Without rotating the overlay, translate the reference mark to center No. 2 and again mark all the other centers (Fig. 12.2b). Repeat this procedure for all grain centers.
4. After a few of these steps a vacancy about the reference mark should begin to take shape. Then grain centers at significantly greater distances need not be marked and this speeds the work considerably.

### Result

- The vacancy with the reference mark at its center defines the shape but not size of the strain ellipse and its orientation (Fig. 12.2c). Because we do not know the initial center-to-center distances the magnitude of the principal stretches can not be obtained, only their ratio.

Usually the recognizable pattern starts to emerge after about 25 points but, depending on the strength of the initial anticlustering, up to several hundred points may be required to adequately define the ellipse. If no such vacancy develops then the initial distribution was not sufficiently anticlustered and the determination of the strain is not possible.

This repetitive plotting procedure is an ideal computer application. The coordinates of each center can be recorded by hand using graph paper or better with the aid of a digitizing tablet. In some cases, such as deformed oolites, the centers may be clearly defined. In

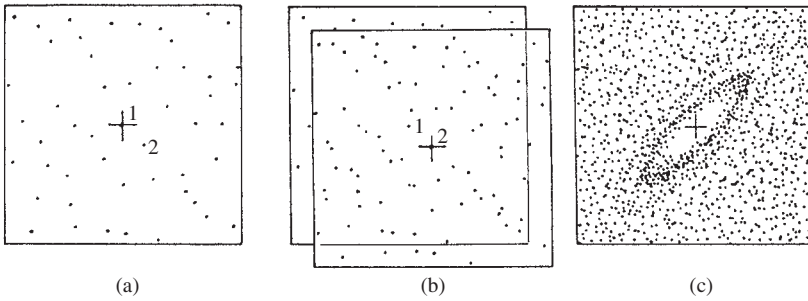


**Figure 12.2** Deformed grains: (a) centers; (b) plotting; (c) ellipse (from Ramsay & Huber, 1983, p. 113 with permission of Elsevier.)

other cases the locations of the centers may be estimated or calculated from points along the boundaries of the grains. Several programs are available to process this data file. De Paor (1989) lists a BASIC program which perform the necessary calculations and plots the results interactively.

Several refinements in the basic technique have been suggested. Crespi (1986) examined real and artificial patterns and discussed the sources of possible errors. Ghaleb and Fry (1995) describe a computer program to produce center-to-center models. The technique has been mostly used for grain aggregates whose shapes are the result of strain, but it has been extended to grain shapes due to pressure solution (Onasch, 1986a, b; Bhattacharyya & Longiaru, 1986).

Rocks are, of course, three-dimensional aggregates of grains, and a section through such an array will not pass through all grain centers. Erslev (1988) suggested a normalization procedure which improves the definition of the ellipse-shaped vacancy by compensating for this effect. McNaught (1994, 2002) described an alternative method and a way of estimating uncertainty. Erslev and Ge (1990) and Ailleres and Campenois (1994) described how to calculate a best-fit ellipse. Dunne, *et al.* (1990) noted that if the post-deformation grain centers do not coincide with their pre-deformation centers, the strain will be underestimated.

Recently, Waldron and Wallace (2007) described a method for objectively fitting ellipses to the center-to-center method.

Alternatives to the center-to-center approaches have also been suggested. Panozzo (1984, 1987) developed methods by treating the traces of grain boundaries as reoriented lines. Srivastava (1995) described a quick and easy way to estimate strain by counting the number of grains intersected along a series of radiating lines.

### 12.3 Deformed fossils

Fossils often possess planes of symmetry, known angular relationships, or proportions which are constant in individuals of a given species. They are, therefore, common objects

of known original shape. Wellman (1962) showed how the shape and orientation of the strain ellipse can be obtained from a collection of such forms in a simple way.

### Problem

- From a collection of deformed brachiopods on a plane, construct the strain ellipse (Fig. 12.3a).

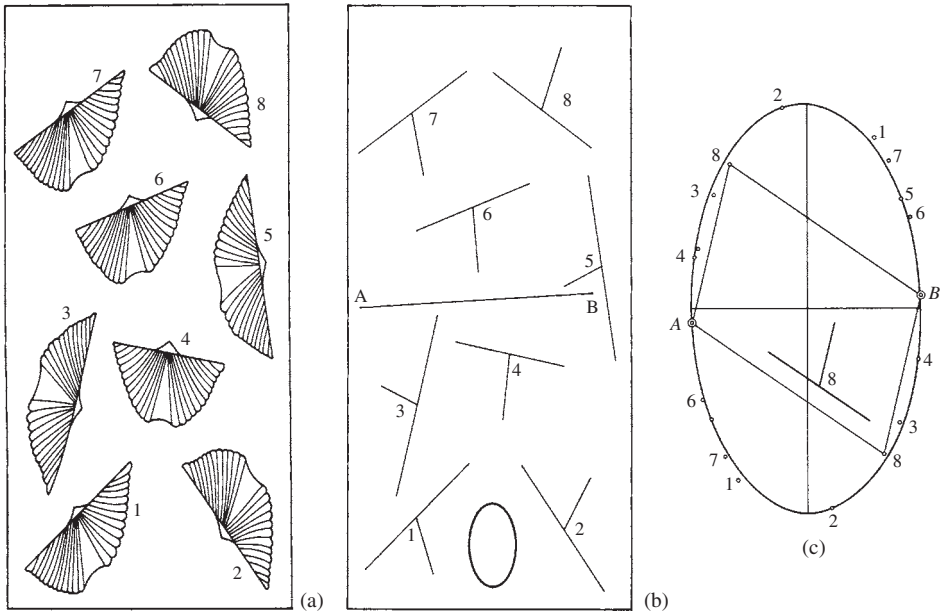


**Figure 12.3** Brachiopods: (a) slab of shells; (b) deformed lines; (c) strain ellipse.

### Construction

1. Transfer the hinge and symmetry lines of each deformed fossil to a tracing sheet (Fig. 12.3b).
2. On this tracing draw a line of arbitrary orientation and length; it should be at least 10 cm long and preferably not parallel to any fossil line (see line *AB* in Fig. 12.3b).
3. For each deformed shell in turn, draw a pair of lines parallel to the hinge and another pair parallel to the median line through the points *A* and *B* giving a parallelogram (see example drawn for Shell No. 8 in Fig. 12.3c).
4. Through all the pairs of fossil points determined in this way, including points *A* and *B*, sketch a best-fit ellipse and add the major and minor axes. This represents the strain ellipse.
5. Measure the orientation of the principal semi-axes, and their lengths.

### Answer

- Because the size of the constructed ellipse depends entirely on the arbitrary length of line  $AB$ , the absolute lengths of its semi-axes have no meaning. However, their ratio is independent of the size of the ellipse, and is found to be  $R_s = 1.7$ . The  $S_1$  direction makes an angle of  $10^\circ$  with the hinge of Shell No. 5. These results can be checked against the small ellipse, which was a circle before deformation.

In order to see why this method works, imagine having made the same construction before deformation. Because each pair of hinge and symmetry lines was originally perpendicular, rectangles rather than parallelograms would have resulted. Collectively, the corners of all these rectangles would have defined a circle with  $AB$  as diameter. This is the circle from which the constructed strain ellipse is derived.

Now reexamine the deformed brachiopods. The shape of each deformed shell is a function of orientation. Strictly, all right angles have been eliminated. However, Shell No. 3 is still nearly symmetrical; this is also the *narrow form*. Shell No. 4 also retains close to a  $90^\circ$  angle, but it is deformed into a *broad form*. Because the principal axes are the only pair of lines which remain perpendicular, the  $S_1$  direction must nearly coincide with the hinge line of Shell No. 3, and the median line of Shell No. 4. Thus one can estimate the orientation of the strain ellipse by inspection.

## 12.4 Deformed pebbles

Before deformation, the shapes of the constituent grains in many rocks are approximately elliptical. After a homogeneous deformation, these shapes are systematically changed and from these the state of strain can be determined. Because these situations are common, the methods that have been developed are widely used and reliable. Lisle (1985a) gives a comprehensive description.<sup>1</sup>

The way elliptical grains deform is geometrically similar to the results of superimposed deformations (see §11.6). The role of the strain ellipse after the first deformation is replaced by the shape of the elliptical grain.

Given a sufficient number of homogeneously deformed two-dimensional pebbles subject to the conditions that the initial shapes were identical and the pebbles were initially without preferred orientation, we may determine the orientation of the principal strain axes in the deformed state, the strain ratio  $R_s$  and the initial shape ratio  $R_i$ . The basic method relies on the fact that two of these pebbles will be oriented coaxially with the strain ellipse and these will be deformed into *narrow* and *broad* forms. There are two general cases.

<sup>1</sup>Mulchrone and Meere (2001) describe a computer program which performs the analysis of passively deformed elliptical markers. Meere and Mulchrone (2003) examine the role of sample size in several different analytical techniques.

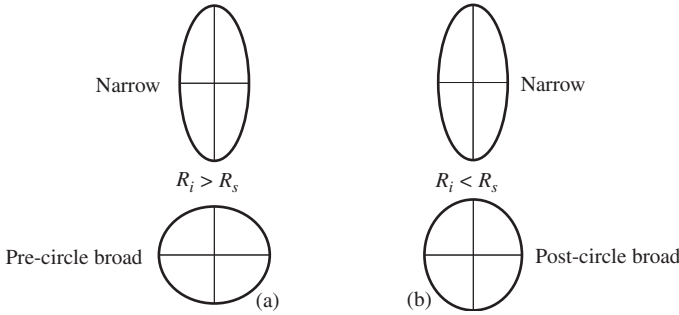


**Figure 12.4** Narrow and broad forms: (a)  $R_i > R_s$ ; (b)  $R_i < R_s$ .

1. If  $R_i > R_s$  the axes of the resulting two extreme shapes will be perpendicular and the deformed ellipses will have the *narrow* and *pre-circle broad* forms (Fig. 12.4a). The axial ratios of these are related by

$$R_{max} = R_s R_i \quad \text{and} \quad R_{min} = R_i / R_s.$$

Solving these two equations for the two unknown ratios gives

$$R_s = \sqrt{R_{max} / R_{min}} \quad \text{and} \quad R_i = \sqrt{R_{max} R_{min}}. \tag{12.1}$$

In the example  $R_{max} = 2.24$  and  $R_{min} = 1.14$ , then  $R_s = 1.4$  and  $R_i = 1.6$ .

2. If  $R_i < R_s$  the axes of the two extreme shapes will be parallel and the deformed ellipses will have the *narrow* and *post-circle broad* forms (Fig. 12.4b). The axial ratios

$$R_{max} = R_s R_i \quad \text{and} \quad R_{min} = R_s / R_i.$$

Solving these for the two unknown ratios gives

$$R_s = \sqrt{R_{max} R_{min}} \quad \text{and} \quad R_i = \sqrt{R_{max} / R_{min}}. \tag{12.2}$$

In the example,  $R_{max} = 2.24$  and  $R_{min} = 1.14$ , then  $R_s = 1.6$  and  $R_i = 1.4$ .

**Problem**

- From a section through a suite of deformed pebbles, determine the final shape ratios  $R_f$  of the narrow and broad forms, and from these determine  $R_i$ ,  $R_s$  and the orientation of the principal strain axes (Fig. 12.5a).

**Procedure**

1. Measure the orientational angle  $\theta'$  which the long axis of each pebble makes with arbitrary reference direction.
2. Measure the axial length of each pebble and calculate the final shape ratio  $R_f$ .
3. Plot each pair of values  $(\theta', R_f)$  as a point on a graph (Fig. 12.5b).

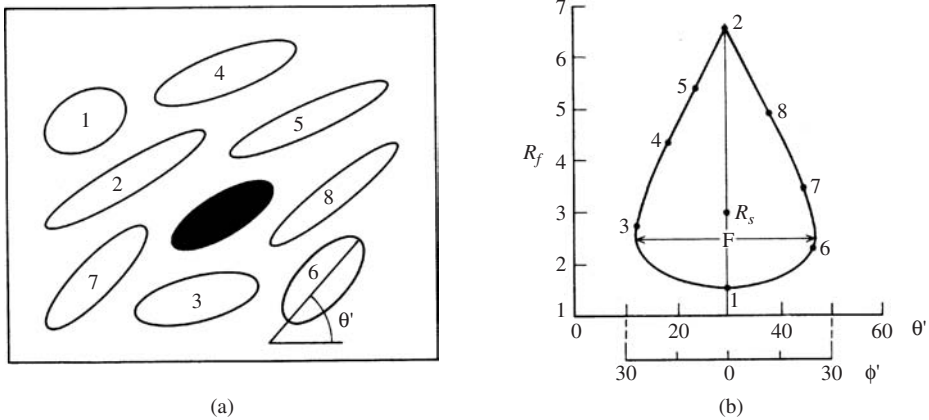


**Figure 12.5** Deformed pebbles: (a) angle  $\theta'$ ; (b)  $R_f$  vs.  $\theta'$ .

**Results**

1. These eight points lie on a closed tear-drop shaped curve, symmetrical about a fixed value of  $\theta'$ , which defines the  $S_1$  direction. Because both the narrow and broad forms have the same orientation, this is an example where  $R_i < R_s$  (see Fig. 12.5b). Having identified this direction, it is then convenient to adopt it as the reference direction and to relate the orientation of the deformed pebbles to it by the angles  $\pm\phi'$ .
2. The two points on the line  $\phi' = 0$  are  $R_{max} = 6.5$  and  $R_{min} = 1.5$ .

**Answer**

- Using these values of  $R_{max}$  and  $R_{min}$  in Eqs. 12.2 gives  $R_s = 3.12$  and  $R_i = 2.08$ .

In Fig. 12.5a, the black ellipse was initially a circle, and therefore represents the strain. Note that its ratio  $R_s$  plots near the center of the  $R_f/\phi'$  curve (Fig. 12.5b).

Suites of deformed elliptical grains have characteristic ranges of orientations, called the *fluctuation F* (Cloos, 1947, p. 861), and it can be determined from the  $R_f/\phi'$  curve as the angle between the extreme orientations. Depending on the relative values of  $R_i$  and  $R_s$  there are three characteristic types of fluctuation.

1. If  $R_i > R_s$  then  $F = 180^\circ$ .
2. If  $R_i = R_s$  then the “broad” form is a circle and  $F = 90^\circ$ .
3. If  $R_i < R_s$  then  $F < 90^\circ$  (in Fig. 12.5b,  $F = 56^\circ$ ).

The important feature of this evolving fluctuation is that  $F$  remains constant at  $180^\circ$  until  $R_s = R_i$  at which point a preferred orientation suddenly appears, and thereafter strengthens as  $R_s$  increases. In many deformed terranes, slaty cleavage appears quite abruptly and Elliott (1970, p. 2232) suggested that this *cleavage front* marks such a sudden onset of preferred orientation.



With a constant initial shape ratio this example is not very realistic. If a variety of distinct initial shapes are present, the  $R_f/\phi'$  graphs consist of a series of nested curves, one for each  $R_i$ .

More generally yet, real data will not plot on such distinct curves but will appear as a scatter of points, reflecting a continuous variation of initial shapes. Then a quasi-statistical graphical technique is usually used (see Lisle, 1985a). Several computer programs are available to accomplish this analysis (Peach & Lisle, 1979; Kutty & Joy, 1994; Mulchrone & Meere, 2001).

As described, this procedure needs a range of original orientations for a complete analysis, but Borradaile and McArthur (1991), following Yu and Zheng (1984), linearized the  $R_f/\phi'$  curves, thus facilitating the analysis of initially non-random fabrics.

In applying any of these techniques to naturally deformed materials, there are several factors which may limit their use. Most naturally occurring sedimentary fabrics show some degree of preferred orientation. In a study of the simulated deformation of such fabrics, Seymour and Boulter (1979) showed that large errors may result if it is mistakenly assumed that they were originally uniform. Also, if there is a ductility contrast between the elliptical objects and the matrix material, an additional component of rotation will be present which may invalidate the strain analysis (De Paor, 1980).

## 12.5 Geometry of the strain ellipse

With only a few strained objects we need a different approach and this requires a more fundamental description of the way lengths and angles change as the result of a deformation. To do this we refer the initial state to a set of  $xy$  axes which are parallel to the principal directions in the unstrained state (Fig. 12.6a). The equation of the reference circle of unit radius in these *material coordinates* is then

$$x^2 + y^2 = 1. \quad (12.3)$$

Similarly, we refer the strained state to a set of  $x'y'$  axes with the same orientation (Fig. 12.6b). The equation of the strain ellipse in these *spatial coordinates* is then

$$\frac{x'^2}{S_1^2} + \frac{y'^2}{S_3^2} = 1. \quad (12.4)$$

By this choice of axes and directions we have eliminated from consideration any translation or rotation and we do this to concentrate on the properties of the stretch component of the deformation.

Within this framework we now examine the geometrical changes associated with a particular material line. At a typical point  $P$  on the unit circle, we identify the direction of the *radius vector*  $\mathbf{r} = OP$  by the angle  $\phi$  it makes with the  $x$  axis (Fig. 12.6a). The components of this vector are  $(x, y)$  and its direction cosines are  $(\cos \phi, \sin \phi)$ .

The corresponding point on the ellipse is  $P'$  and we identify the direction of the radius vector  $\mathbf{r}' = OP'$  by the angle  $\phi'$  it makes with the  $x'$  axis (Fig. 12.6b). The components of this vector are  $(x', y')$  and its direction cosines are  $(\cos \phi', \sin \phi')$ .

As a result of strain, radius vector  $\mathbf{r}$  of the circle is transformed into radius vector  $\mathbf{r}'$  of the ellipse. Three separate geometrical features are associated with this transformation and all these changes can be observed within a circle-to-ellipse card-deck experiment.

1. Orientational angle  $\phi$  changes to  $\phi'$ .
2. The length of a radius of a circle  $r = 1$  changes to the radius of an ellipse  $r' = S$ .
3. The right angle between  $\mathbf{r}$  and the tangent  $T$  at point  $P(x, y)$  changes and the measure of this change is the angle of shear  $\psi$ . This is represented by the angle between the tangent  $T'$  and the line perpendicular to  $\mathbf{r}'$  at point  $P'(x', y')$ . Note that in the first and third quadrants the tangent rotates in an anticlockwise sense hence  $\psi$  is positive. In the two other quadrants  $\psi$  is negative.

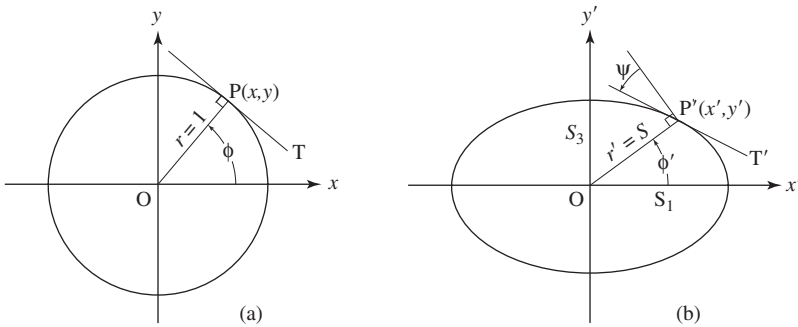


**Figure 12.6** Circle and ellipse: (a)  $xy$  coordinates; (b)  $x'y'$  coordinates.

We now need algebraic expressions for each of these changes associated with the material line in terms of its orientation and the principal stretches.<sup>2</sup>

*Change in orientation*

The relationship between vector  $\mathbf{r}(x, y)$  which marks a material line in the reference circle and the vector  $\mathbf{r}'(x', y')$  which marks the same material line in the strain ellipse is

$$x' = S_1x \quad \text{and} \quad y' = S_3y. \tag{12.5}$$

That is, the  $x$  component of  $\mathbf{r}$  is stretched to become the  $x'$  component of  $\mathbf{r}'$  and the  $y$  component is stretched to become  $y'$ . Dividing the second of these equations by the first gives

$$\frac{y'}{x'} = \frac{S_3 y}{S_1 x}. \tag{12.6}$$

<sup>2</sup>On a first reading you may wish to skip the details of the derivations and go directly to §12.6 for the results.

From Figs. 12.6a and 12.6b

$$\tan \phi = y/x \quad \text{and} \quad \tan \phi' = y'/x'.$$

Using these in Eq. 12.6 and using the definition of the strain ratio  $R_s = S_1/S_3$  we have the useful result, first obtained by Harker (1885, p. 822),

$$\tan \phi' = \frac{\tan \phi}{R_s} \quad \text{or} \quad R_s = \frac{\tan \phi}{\tan \phi'}. \tag{12.7}$$

This result may be used in two ways. The first version gives  $\phi'$  when  $\phi$  and  $R_s$  are known. By definition  $R_s > 1$  and therefore  $\phi' < \phi$ , that is, the angle a material line makes with the  $S_1$  direction is generally reduced. The only exceptions are when  $\phi = 0^\circ$  or  $\phi = 90^\circ$  and the orientation is unchanged. The second version can be used to determine the strain ratio  $R_s$  if both  $\phi$  and  $\phi'$  are known.

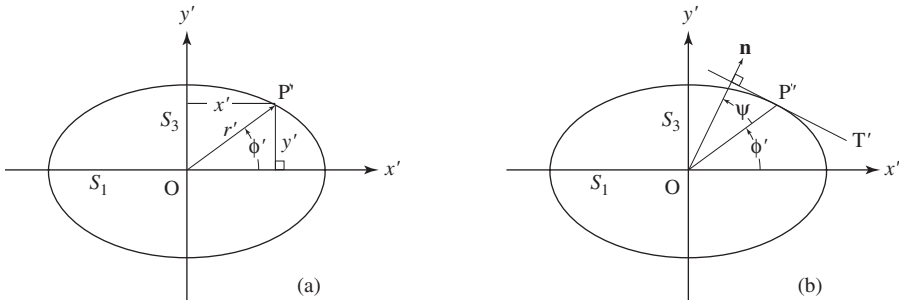


**Figure 12.7** Strain ellipse: (a) stretch; (b) angle of shear.

*Change in length*

Next we need an expression for the stretch associated with the transformation of  $\mathbf{r}$  into  $\mathbf{r}'$ . From Fig. 12.7a, where the magnitude of the radius vector  $\mathbf{r}'$  is the stretch  $S$ ,

$$x' = S \cos \phi' \quad \text{and} \quad y' = S \sin \phi'. \tag{12.8}$$

Using these expressions for  $x'$  and  $y'$  in the equation of the ellipse of Eq. 12.4 we have

$$\frac{S^2 \cos^2 \phi'}{S_1^2} + \frac{S^2 \sin^2 \phi'}{S_3^2} = 1 \quad \text{or} \quad \frac{1}{S^2} = \frac{\cos^2 \phi'}{S_1^2} + \frac{\sin^2 \phi'}{S_3^2}. \tag{12.9}$$

We now introduce a new parameter of longitudinal strain. The *reciprocal quadratic elongation*  $\lambda'$  is defined as the reciprocal of the square of the stretch

$$\boxed{\lambda' = 1/S^2}. \tag{12.10}$$

The *principal reciprocal quadratic elongations* are then  $\lambda'_1 = 1/S_1^2$  and  $\lambda'_3 = 1/S_3^2$  and Eq. 12.9 becomes

$$\boxed{\lambda' = \lambda'_1 \cos^2 \phi' + \lambda'_3 \sin^2 \phi'}. \quad (12.11)$$

and this is the desired result. The equation of the strain ellipse can now be written as (see Eq. 12.4)

$$\lambda'_1 x'^2 + \lambda'_3 y'^2 = 1. \quad (12.12)$$

### Change of a right angle

To find the angle of shear associated with the direction  $OP'$  graphically, draw vector  $\mathbf{n}$  normal to the line  $T'$  tangent to the ellipse at point  $P'$  (Fig. 12.7b). Then  $\psi$  is the angle between  $\mathbf{r}'$  and  $\mathbf{n}$ .

We can also find an expression for  $\psi$  from the dot product of vectors  $\mathbf{r}'$  and  $\mathbf{n}$  (see §7.3). This is simple in principle but unfortunately a little messy in execution because of the need to normalize the components of  $\mathbf{n}$  and to convert this angle to a strain parameter.

The equation of tangent  $T'$  can be written down directly from the equation of the ellipse using a simple recipe: replace one  $x'$  and one  $y'$  in Eq. 12.12 with the corresponding coordinates of the point of tangency  $P'(x', y')$  in the second of Eqs. 12.9. After dividing through by  $S$  the result is

$$(\lambda'_1 \cos \phi')x' + (\lambda'_3 \sin \phi')y' = 1/S.$$

The direction cosines of the normal vector  $\mathbf{n}$  are proportional to the coefficients of  $x'$  and  $y'$  in this equation. Normalizing both by dividing each by the square root of the sum of their squares gives

$$\frac{\lambda'_1 \cos \phi'}{\sqrt{\lambda_1'^2 \cos^2 \phi' + \lambda_3'^2 \sin^2 \phi'}} \quad \text{and} \quad \frac{\lambda'_3 \sin \phi'}{\sqrt{\lambda_1'^2 \cos^2 \phi' + \lambda_3'^2 \sin^2 \phi'}},$$

and these are the required direction cosines of  $\mathbf{n}$ . With these direction cosines of  $\mathbf{n}$  and the direction cosines of  $\mathbf{r}'$  from Eq. 12.8, the dot product gives an expression for  $\cos \psi$

$$\cos \psi = \frac{(\lambda'_1 \cos \phi')(\cos \phi') + (\lambda'_3 \sin \phi')(\sin \phi')}{\sqrt{\lambda_1'^2 \cos^2 \phi' + \lambda_3'^2 \sin^2 \phi'}},$$

which, after expanding and squaring, becomes

$$\cos^2 \psi = \frac{(\lambda'_1 \cos^2 \phi' + \lambda'_3 \sin^2 \phi')^2}{\lambda_1'^2 \cos^2 \phi' + \lambda_3'^2 \sin^2 \phi'}.$$

Substituting the identities  $\cos \psi = 1/\sec \psi$  and  $\sec^2 \psi = 1 + \tan^2 \psi$ , together with the definition  $\gamma = \tan \psi$ , this can be rearranged to give

$$\gamma^2 = \frac{\lambda_1'^2 \cos^2 \phi' + \lambda_3'^2 \sin^2 \phi'}{(\lambda_1' \cos^2 \phi' + \lambda_3' \sin^2 \phi')^2} - 1. \quad (12.13)$$

Observing that the denominator is equal to  $\lambda'^2$  (see Eq. 12.11), and defining a new measure of shear strain

$$\gamma' = \gamma \lambda' \quad \text{or} \quad \gamma = \gamma' / \lambda', \quad (12.14)$$

we then write Eq. 12.13 as

$$\gamma'^2 = \lambda_1'^2 \cos^2 \phi' + \lambda_3'^2 \sin^2 \phi' - (\lambda_1' \cos^2 \phi' + \lambda_3' \sin^2 \phi')^2.$$

Expanding and combining terms gives

$$\gamma'^2 = \lambda_1'^2 \cos^2 \phi' (1 - \cos^2 \phi') - 2\lambda_1' \lambda_3' \cos^2 \phi' \sin^2 \phi' + \lambda_3'^2 \sin^2 \phi' (1 - \sin^2 \phi'). \quad (12.15)$$

From the identity  $\cos^2 \phi' + \sin^2 \phi' = 1$  we obtain two relationships

$$\cos^2 \phi' = (1 - \sin^2 \phi') \quad \text{and} \quad \sin^2 \phi' = (1 - \cos^2 \phi').$$

Using these in Eq. 12.15 and again rearranging yields

$$\gamma'^2 = (\lambda_1'^2 - 2\lambda_1' \lambda_3' + \lambda_3'^2) \cos^2 \phi' \sin^2 \phi' = (\lambda_1' - \lambda_3')^2 \cos^2 \phi' \sin^2 \phi'.$$

Taking the square root we finally obtain the desired result

$$\boxed{\gamma' = (\lambda_1' - \lambda_3') \cos \phi' \sin \phi'}. \quad (12.16)$$

## 12.6 Mohr Circle for finite strain

The introduction of the new strain parameters  $\lambda'$  (Eq. 12.10) and  $\gamma'$  (Eq. 12.14) was aimed at obtaining Eq. 12.11 and Eq. 12.16 in these particular forms. It is useful to convert them by substituting the double angle identities

$$\cos^2 \phi' = \frac{1}{2}(1 + \cos 2\phi'), \quad \sin^2 \phi' = \frac{1}{2}(1 - \cos 2\phi'), \quad \cos \phi' \sin \phi' = \frac{1}{2} \sin 2\phi',$$

with the result

$$\lambda' = \frac{1}{2}(\lambda_1' + \lambda_3') + \frac{1}{2}(\lambda_1' - \lambda_3') \cos 2\phi', \quad (12.17a)$$

$$\gamma' = \frac{1}{2}(\lambda_1' - \lambda_3') \sin 2\phi'. \quad (12.17b)$$

These should look familiar. Their form is identical to the equations for the normal and shearing components of the traction vector (see Eqs. 9.17). Just as in that case, these expressions for  $\lambda'$  and  $\gamma'$  can be represented graphically by a *Mohr Circle for finite strain*. The main feature of this construction is a circle on the horizontal  $\lambda'$  axis (Fig. 12.8a). The distance to the center  $c$  and its radius  $r$  are given by

$$c = \frac{1}{2}(\lambda'_1 + \lambda'_3) \quad \text{and} \quad r = \frac{1}{2}(\lambda'_3 - \lambda'_1).$$

This circle has a number of features in common with the Mohr Circle for stress, but there are also some important differences. Because the lengths of the semi-axes of the strain ellipse are never negative, the circle lies wholly to the right of the origin.

Because  $S_1 > S_3$ , by definition  $\lambda'_1 < \lambda'_3$ . Therefore  $(\lambda'_1 - \lambda'_3)$ , which appears in both of these expressions, is always a negative quantity. This has two consequences.

1. By Eq. 2.17a, if  $\phi' = 0$  ( $2\phi' = 0$ ) then  $\lambda' = \lambda'_1$  and  $r \cos 2\phi' < 0$  so that  $\lambda'_1$  plots to the left of the center. If  $\phi' = 90^\circ$  ( $2\phi' = 180^\circ$ ) then  $\lambda' = \lambda'_3$  and  $r \cos 2\phi' > 0$  and  $\lambda'_3$  plots to the right of the center. This reversal arises from the definition  $\lambda' = 1/S^2$ .
2. As we have noted in Figs. 12.6 and 12.7, the angle of shear  $\psi$ , and therefore also the shear strain  $\gamma$ , is positive in the first and third quadrants ( $0 < \phi' < 90^\circ$  and  $180^\circ < \phi' < 270^\circ$ ) and negative in the other two. By Eq. 12.17b, however, the parameter  $\gamma'$  has the opposite sign in each of these quadrants. Because of this switch in signs, negative values of  $\gamma'$  are plotted above the horizontal axis and positive values are plotted below it. This is the important *clockwise-up* convention used for constructing this Mohr Circle (Treagus, 1987).<sup>3</sup> Now both  $2\phi'$  (Fig. 12.8a) and  $\phi'$  (Fig. 12.8b) are measured in the same sense on the Mohr Circle and physical planes.

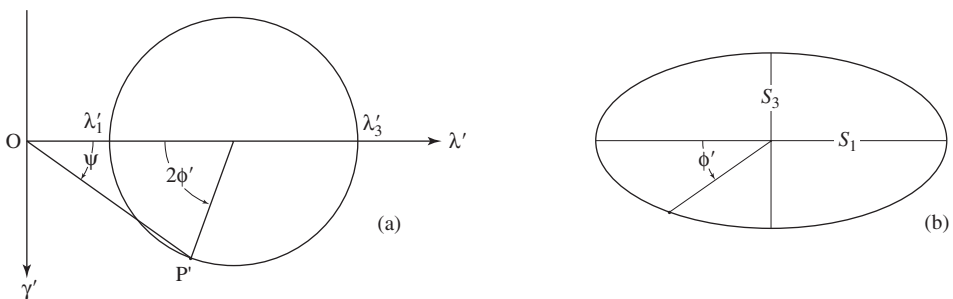


**Figure 12.8** Finite strain: (a) Mohr Circle plane; (b) physical plane.

There is an auxiliary construction which greatly increases the usefulness of this diagram. The slope angle of line  $OP'$  is the angle of shear  $\psi$  associated with this particular direction (Fig. 12.8a). This fact follows directly from the definition  $\tan \psi = \gamma'/\lambda'$  (see

<sup>3</sup>This same convention is used in the Mohr Circle for stress when tension is reckoned positive (see Fig. 9.15b).

Eq. 12.14), and it bypasses the mathematically convenient but otherwise obscure parameter  $\gamma'$ , which is therefore little used in graphical work.

### 12.7 Pole of the Mohr Circle

The geometry of the physical plane and Mohr Circle plane can be even more closely related with the aid of a special point on the circle called the *pole* or *origin of lines*. This point, here denoted  $O_L$ , has a very useful property: A line through  $O_L$  which intersects the circle at  $P'$  is parallel to the corresponding line on the physical plane whose strain parameters are given by the coordinates of point  $P'$ .

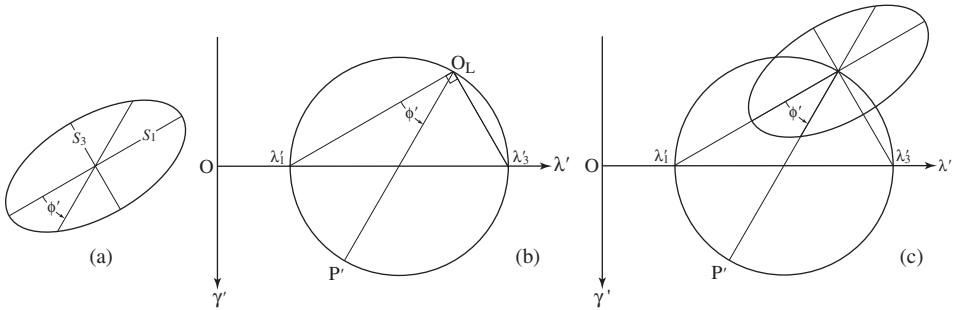


**Figure 12.9** Pole construction: (a) physical plane; (b) Mohr Circle plane; (c) combination.

The pole is the point on the Mohr Circle through which all lines parallel to the corresponding lines on the physical plane pass just as they radiate from the center of the ellipse (Fig. 12.9a). This is the meaning of the phrase *origin of lines* which is used here as a short definition. It is analogous to the *origin of normals* of the Mohr Circle for stress. The pole may be located in several ways, most simply by drawing either a line parallel to the  $S_1$  axis of the ellipse through the point  $\lambda'_1$  to intersect the circle at  $O_L$ , or a line parallel to the  $S_3$  axis of the ellipse through the point  $\lambda'_3$  to intersect the circle at  $O_L$  (Fig. 12.9b). Note that these two lines at  $O_L$  are orthogonal, as are the axes of the ellipse.

Having located the pole we may now combine the two representations of the state of finite strain by drawing the ellipse centered at  $O_L$  (Fig. 12.9c). Note that this construction would not be possible without the clockwise-up convention for shear. In practice it is not necessary to draw an accurate ellipse because all the quantitative information is contained on the circle, but a sketch is a useful aid, especially for beginners.

We now may easily determine the strain parameters associated with any general line. For example, the line through  $O_L$  parallel to any general radius in the strain ellipse making an angle  $\phi'$  with the  $S_1$  direction intersects the circle at  $P'$  and the coordinates of this point are the required strain parameters associated with this radius (Fig. 12.9c).

We can then see that the Mohr Circle represents the locus of all possible values of the two strain parameters for a given ellipse and the pole represents its particular orientation on the physical plane. As the ellipse rotates on the physical plane, the pole moves along

the circumference of the Mohr Circle. There are two special cases: If the  $S_1$  direction is vertical, pole  $O_L$  coincides with the point representing  $\lambda'_1$  (Fig. 12.10a), and if the  $S_3$  direction is vertical, pole  $O_L$  coincides with the point representing  $\lambda'_3$  (Fig. 12.10b).

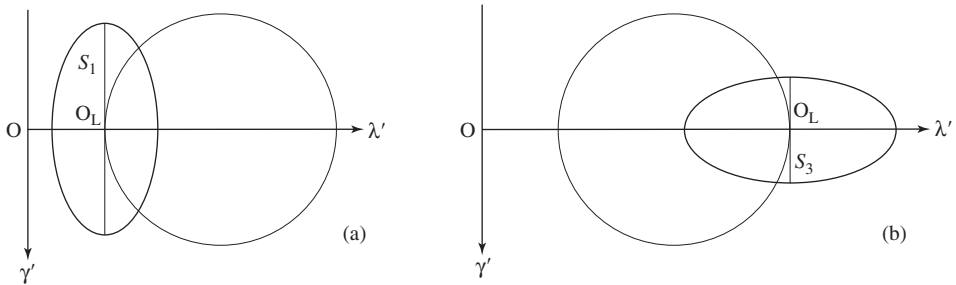


**Figure 12.10** Special cases: (a)  $O_L = \lambda'_1$ ; (b)  $O_L = \lambda'_3$ .

An even more important use of the Mohr Circle construction is to determine the principal stretches and their orientation from measurements of deformed angles or lines, and the pole plays a crucial role in this procedure.

The important first step is to form a *strain rosette* by drawing the stretched lines radiating from a single point, just as the radius vectors radiate from the center of the strain ellipse. In all these applications we are free to rotate the rosette into any orientation.

## 12.8 Strain from measured angles

Features from which angular changes can be determined are relatively common. As we have seen in the Wellman construction (Fig. 12.3), the angle of shear can be determined directly from a single deformed bilaterally symmetrical fossil. There are two main cases and both solutions utilize the pole and both follow closely the method described by Lisle (1991). The first involves one angle of shear associated with a line in known angular relation to the principal axes.

### Problem

- A deformed trilobite is exposed on the plane of slaty cleavage and its median line  $m$  makes an angle of  $\phi'_m = 20^\circ$  with a lineation marking the  $S_1$  direction. The angle of shear associated with this line is  $\psi_m = +36^\circ$  (Fig. 12.11a). Determine the shape of the strain ellipse.

### Construction

1. Form a rosette by assembling the strained median line  $m$  and the line representing the  $S_1$  direction radiating from a common point (Fig. 12.11b).
2. On a set of  $\lambda'\gamma'$  axes, draw a line through the origin with a slope angle  $\psi_m = +36^\circ$  (with the clockwise-up convention this line slopes downward).



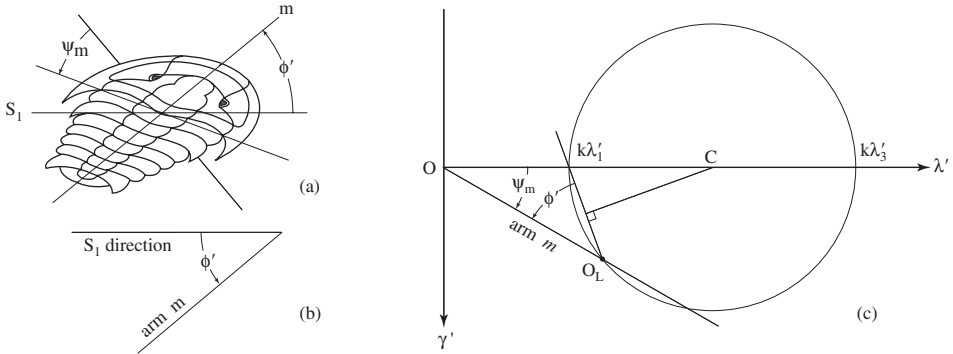


**Figure 12.11** Trilobite: (a) physical plane; (b) rosette; (c) Mohr Circle.

3. At a convenient but arbitrary distance along the sloping  $\psi_m$  line locate the pole  $O_L$ , which is then a first point on the circle.
4. At  $O_L$  construct the rosette with arm  $m$  along the  $\psi_m$  line. The arm representing the  $S_1$  direction then intersects the horizontal axis at  $\lambda'_1$ , which is a second point on the Mohr Circle.
5. The perpendicular bisector of the segment  $O_L\lambda'_1$  locates the center  $C$  on the horizontal axis.
6. Then with radius  $C\lambda'_1$  complete the circle (Fig. 12.11c).

**Answer**

- Because the pole  $O_L$  is arbitrarily located in this procedure, the two principal values can not be uniquely determined. We can, however, determine the strain ratio from

$$R_s = \sqrt{k\lambda'_3/k\lambda'_1}, \tag{12.18}$$

where  $k$  is an unknown scale factor. This calculation, based on measurement of the two intercepts, yields  $R_s = 2.0$ . An analytical solution for this problem is given by Ramsay (1967, p. 234).

For some purposes it is convenient to represent the strain derived from such angular measurements by a specific ellipse, and the ellipse with the same area as the unit circle is the most appropriate. From the definition of the strain ratio (Eq. 11.4)

$$R_s = S_1/S_3,$$

and from the condition for no area change  $\Delta = 0$  (Eq. 11.15)

$$S_3 = 1/S_1,$$

we can express the principal stretches  $\tilde{S}_1$  and  $\tilde{S}_3$  of the constant-area ellipse as

$$\tilde{S}_1 = \sqrt{R_s} \quad \text{and} \quad \tilde{S}_3 = 1/\sqrt{R_s}. \tag{12.19}$$

The second problem involves known angles of shear associated with two lines and the angle between these two lines. Then both the shape of the ellipse and its orientation can be found.

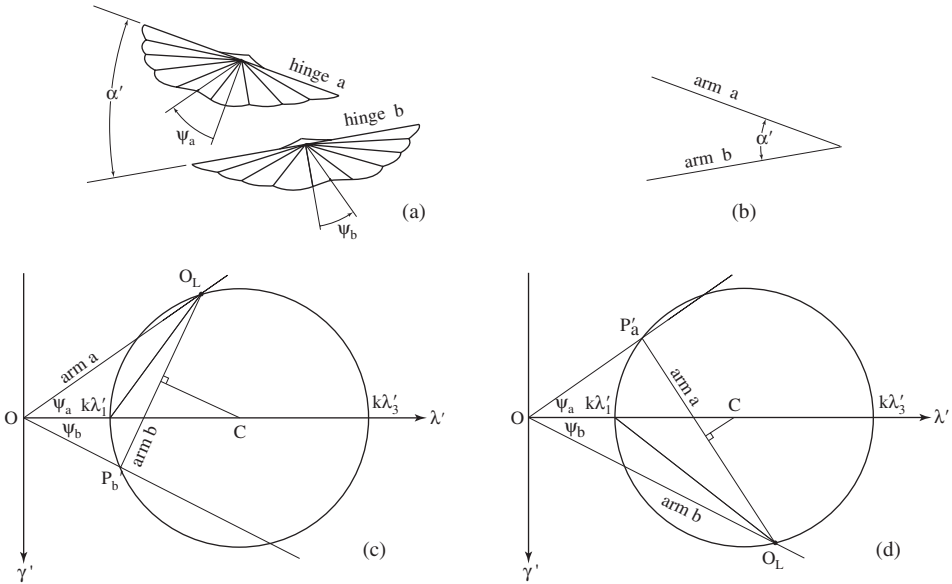


**Figure 12.12** Brachiopods: (a) physical plane; (b) rosette; (c) Mohr Circle 1; (d) Mohr Circle 2.

**Problem**

- The angle between the hinge lines of two deformed brachiopods is  $\alpha' = 30^\circ$ . The angles of shear associated with these lines are  $\psi_a = -35^\circ$  and  $\psi_b = +27^\circ$  (Fig. 12.12a). Determine the ratio of the principal stretches and their orientation.

**Construction**

1. Construct a strain rosette from hinge lines  $a$  and  $b$  (Figs. 12.12a and 12.12b).
2. On a pair of  $\lambda'\gamma'$  axes draw lines making angles of  $\psi_a$  and  $\psi_b$  with the horizontal  $\lambda'$  axis and passing through the origin (Fig. 12.12c), paying attention to their signs and the clockwise-up convention.
3. Arbitrarily locate  $O_L$  on either of these lines.
  - (a) If the  $\psi_a$  line is used, then position the rosette at that point with arm  $a$  along the  $\psi_a$  line (Fig. 12.12c). Arm  $b$  then intersects the  $\psi_b$  line at  $P'_b$ .

- (b) If the  $\psi_b$  line is used, then position the rosette at that point with arm  $b$  along the  $\psi_b$  line. Arm  $a$  then intersects the  $\psi_b$  line at  $P'_a$  (Fig. 12.12d).
- 4. The perpendicular bisector of either chords  $O_L P'_b$  or  $O_L P'_a$  locates the center  $C$  on the  $\lambda'$  axis. With radius  $O_L C = C P'_b$  complete the circle.
- 5. Chords  $O_L \lambda'_1$  and  $O_L \lambda'_3$  fix the orientations of the principal directions relative to arms  $a$  and  $b$  on the physical plane.

**Answer**

- Measure the distances to the two intercepts and calculate  $R_s = \sqrt{k\lambda'_3/k\lambda'_1} = 2.0$ . The  $S_1$  direction makes an angle of  $\phi'_a = 11^\circ$  with the arm  $c$ .

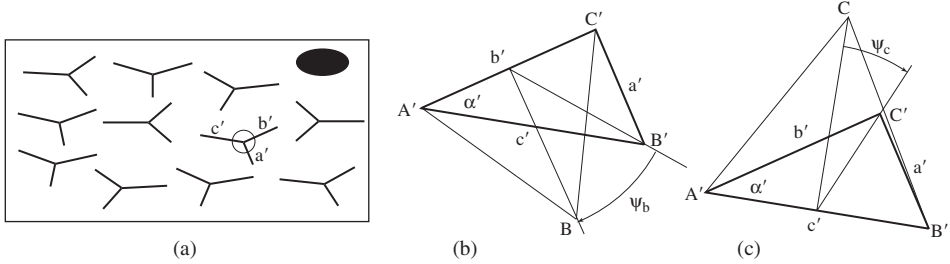


**Figure 12.13** Welded tuff: (a) model strain: (b) angle of shear  $\psi_b$ ; (c) angle of shear  $\psi_c$ .

In some situations angles of shear may be constructed from angles that are not initially right angles. The case of the deformed shards in welded tuff is one of these. Typically welded tuff display a strong foliation marked by the planar alignment of flattened pumice and glass shards. Some of these shards have a distinctive Y-shape. These originate between gas bubbles in the original flow and the angles between the three arms of these shards are approximately  $120^\circ$  (Ragan & Sheridan, 1972; Sheridan & Ragan, 1976). After deformation these angles are systematically changed (Fig. 12.13a) and these changes can be converted into angles of shear.

**Problem**

- For the deformed shard circled in Fig. 12.13a, determine the strain ratio and the orientation of the  $S_1$  direction.

**Construction**

1. Reassemble the three shard limbs  $a'$ ,  $b'$  and  $c$  into scalene triangle  $A'B'C'$  (Fig. 12.13b,c).
2. On two sides of this triangle construct an equilateral triangle (sides  $b'$  and  $c'$  are used here). These represent the shape, but not size, of the triangle before deformation.
3. The perpendicular bisector on each of the two base sides is the height of the triangles. As a result of a shear component parallel to these two sides apex point  $B$  is transformed to point  $B'$  (Fig. 12.13b) and apex point  $C$  is transformed to point  $C'$  (Fig. 12.13c).

4. As a result of these transformations we have measures of the two shear components:  $\psi_b = +36^\circ$  and  $\psi_c = -25^\circ$ . The angle between sides  $b'$  and  $c'$  is  $\alpha' = 34^\circ$ .
5. With these angles we can now construct the Mohr Circle just as before (Fig. 12.14).
  - (a) Plot the line with slope  $\psi_b$  below and the line with slope  $\psi_c$  above the  $\lambda'$  axis.
  - (b) Locate the pole  $O_L$  on either of these lines (we chose the  $\psi_b$  line).
  - (c) Plot arm along the  $\psi_b$  line. The arm  $c$  then intersects the  $\psi_c$  at point  $P_c$  which is a second point on the circle.
  - (d) Line  $O_L P_c$  is a chord of the circle and its perpendicular bisection locates the center  $C$  of the circle on the  $\lambda'$  axis. The circle can then be completed using as radius  $O_L C = P_c C$ .
  - (e) The line connecting points  $O_L$  and  $\lambda'_1$  gives the orientation of the  $S_1$  direction relative to the arms  $b$  and  $c$ .

### Answer

- $R_s = \sqrt{k\lambda'_3/k\lambda'_1} = 2.0$  and the  $S_1$  direction makes an angle  $\phi' = 11^\circ$  with arm  $c$  and this is parallel to the foliation. Similar results are obtained in any foliation-normal section. This foliation is essentially horizontal over great distances and  $R_s$  increases downward. This implies that the measured strain is due to the compaction of the tuff and that  $S_1 = S_2 = 1.0$  and  $S_3 = 0.5$ .

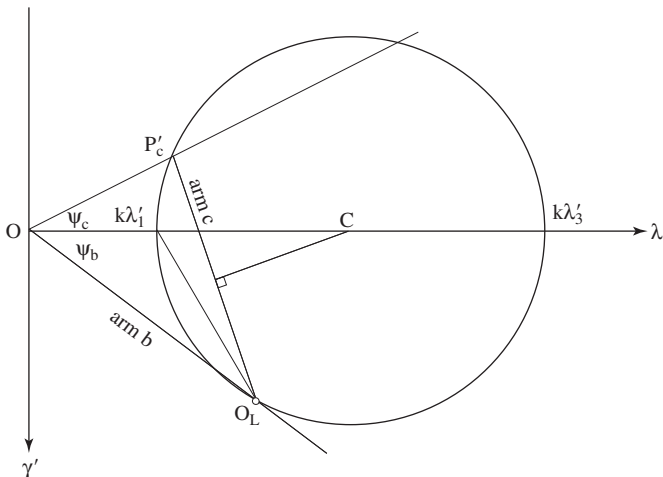


**Figure 12.14** Mohr Circle for deformed shard.

An analytical solution for the problem of determining the strain from two angles of shear is also available (Ragan & Groshong, 1993).

If the two measured angles of shear both have the same sign, the accuracy of the Mohr Circle construction can be improved by reversing the sign of one of them. This is easily accomplished by changing the line of reference. In the reference circle (Fig. 12.15a),

radius vectors  $\mathbf{r}_1 = OP_1$  and  $\mathbf{r}_2 = OP_2$  are orthogonal. Then tangent  $T_1$  at point  $P_1$  is parallel to  $\mathbf{r}_2$  and  $T_2$  at  $P_2$  is parallel to  $\mathbf{r}_1$ . These are *conjugate radii* in the circle.

In the strain ellipse (Fig. 12.15b), the corresponding vectors  $\mathbf{r}'_1 = OP'_1$  and  $\mathbf{r}'_2 = OP'_2$  are no longer orthogonal but the tangent  $T'_1$  at point  $P'_1$  is still parallel to  $\mathbf{r}'_2$  and the tangent  $T'_2$  at  $P'_2$  is parallel to  $\mathbf{r}'_1$ . These are conjugate radii in the ellipse; thus any pair of radii derived from conjugate radii are themselves conjugate. The measure of this change is  $\psi$  and the magnitude of the angle is the same for each radius vector, but of opposite sign.

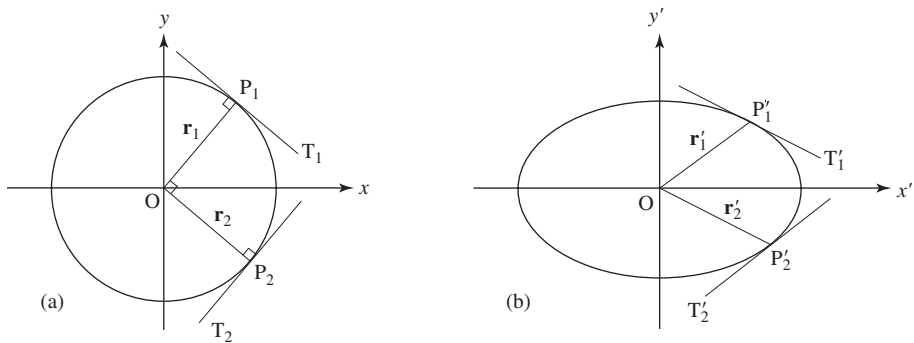


**Figure 12.15** Conjugate radii: (a) circle; (b) ellipse.

## 12.9 Strain from measured stretches

The strain ellipse can also be obtained from measured stretches. The deformed length of a passive line of known initial length would yield an exact value of a stretch. Unfortunately few, if any, such lines exist in nature. There is, however, a class of structures from which the original length can be estimated. These are trains of micro-boudins bounded by fractures. The gaps between the broken fragments may be filled with the ductile material surrounding the boudins or they may be filled with vein material. Examples include broken crystals of tourmaline, rutile and arsenopyrite, amphibole, epidote and kyanite, and some forms of rectangular boudins developed in competent layers embedded in a ductile matrix. Broken fossil parts have also been used.

In the Swiss Alps there are a number of localities where abundant belemnites have been stretched in this manner (Beach, 1979). These have been examined extensively, but the techniques apply to many similar structures. The goal is to estimate the stretch which would have occurred in the absence of the rigid inclusion. Two simple methods have been proposed, each giving different results.

In the conventional method (Ramsay, 1967, p. 248; Ramsay & Huber, 1983, p. 93), the initial length  $l$  is taken as the sum of the lengths of the individual fragments and the

final length  $l'$  as the total sum of the individual gaps  $G$  and fragments  $F$  (Fig. 12.16a). For  $N$  gaps and  $N + 1$  fragments, we have

$$G_{sum} = \sum_{i=1}^N G_i \quad \text{and} \quad F_{sum} = \sum_{i=1}^{N+1} F_i. \tag{12.20}$$

The second method involves a minor but important modification (Hossain, 1979). The final length is taken as the distance between the midpoints of the two end fragments and the initial length is the sum of the fragment lengths between these two points (Fig. 12.16b). These lengths can be written as

$$G_{sum} = \sum_{i=1}^N G_i \quad \text{and} \quad F_{sum} = \frac{1}{2} \sum_{i=1}^N (F_i + F_{i+1}). \tag{12.21}$$

This equation for  $F_{sum}$  and the corresponding illustration makes clear that Hossain's method is a straightforward extension of the center-to-center technique used for deformed grains of §12.2.

In both Ramsay's and Hossain's methods the total stretch associated with the inclusion train is then calculated from

$$S = l'/l = 1 + (G_{sum}/F_{sum}). \tag{12.22}$$

**Problem**

- From the following gap and fragment lengths calculate the stretch using the methods of Ramsay and Hossain:  $G_i = 7, 5, 9$  mm and  $F_i = 11, 5, 7, 9$  mm (Fig. 12.16).

**Solution**

1. By Ramsay's method (Eq. 12.20)  $G_{sum} = 21$  mm,  $F_{sum} = 32$  mm and  $S = 1 + 21/31 = 1.65625$ .
2. By Hossain's method (Eq. 12.21)  $G_{sum} = 21$  mm,  $F_{sum} = 22$  mm and  $S = 1 + 21/22 = 1.95455$ .

As can be seen, the stretch calculated by Hossain's method is significantly greater than that obtained by Ramsay's method.

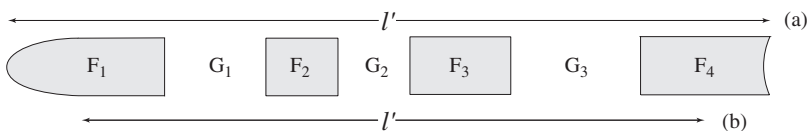


**Figure 12.16** Stretch from boudinage: (a) Ramsay's method; (b) Hossain's method.

Both of these approaches belie the complexity of the physical process of boudin formation. In particular, neither method takes into account the evolutionary sequence of the separation of the fragments which must have occurred.

Before the first fracture, the rigid inclusion can not record any strain. As a consequence, the material adjacent to the inclusion must deform inhomogeneously to compensate for the extension which would have occurred in the absence of the inclusion. Once a fracture forms, a part of the extension will be accommodated by the separation of the fragments and a part, as before, by inhomogeneous deformation near the inclusion contact.

Recognizing that the formation of multiple fragments involves a series of such steps, a third method for estimating the stretch involves an iterative strain-reversal technique and gives even better results (Ferguson, 1981, 1987; Ferguson & Lloyd, 1984; Ford & Ferguson, 1985). Lloyd and Condliffe (2003) describe a computer program which automates the process.

### Steps

1. With  $N$  gaps,  $N$  steps are required to reverse the total stretch. Here  $N = 3$ .
2. The initial and final lengths associated with each gap are given by  $l_i = \frac{1}{2}(F_i + F_{1+i})$  and  $l'_i = G_i + l_i$ . Thus

$$\begin{aligned} l_1 &= 5.5 + 2.5 = 8.0, & l'_1 &= 7.0 + 8.0 = 15, \\ l_2 &= 2.5 + 3.5 = 6.0, & l'_2 &= 5.0 + 6.0 = 11, \\ l_3 &= 5.5 + 2.5 = 8.0, & l'_3 &= 9.0 + 8.0 = 17. \end{aligned}$$

3. The stretch associated with each gap is calculated from  $S_i = l'_i/l_i$  and the gap with the smallest stretch  $S_{min}$  is taken as the final increment of stretch (Fig. 12.17a).

$$\begin{aligned} S_1 &= 15/8 = 1.875\ 00, & S_1^{-1} &= 0.533\ 33, \\ S_2 &= 11/6 = 1.833\ 33, & S_2^{-1} &= 0.545\ 45, \\ S_3 &= 17/8 = 2.125\ 00, & S_3^{-1} &= 0.470\ 59. \end{aligned}$$

4. The gap associated with  $S_{min}$  (which is not always the smallest) is now closed by applying the inverse stretch  $1/S_{min} = 0.545\ 45$  to its length. The other gaps are also reduced by this same factor. There are now  $N - 1 = 2$  gaps and  $N = 3$  fragments (Fig. 12.17b). Relabeling the gaps and fragments, the lengths are now

$$\begin{aligned} l_1 &= 5.5 + 6.0 = 11.5, & l'_1 &= 11.5 + 0.181\ 82 = 11.681\ 82, \\ l_2 &= 4.5 + 6.0 = 10.5, & l'_2 &= 10.5 + 1.272\ 73 = 11.772\ 73, \end{aligned}$$

and the stretches associated with the remaining gaps are

$$S_1 = 11.681\ 82/11.5 = 1.015\ 81, \quad S_1^{-1} = 0.984\ 44,$$

$$S_2 = 11.771\ 73/10.5 = 1.121\ 21, \quad S_2^{-1} = 0.891\ 89.$$

5. With this new  $S_{min}$  the next gap is closed and the other reduced (Fig. 12.17c). The lengths are now

$$l_1 = 11.5 + 4.5 = 16.0, \quad l'_1 = 16.0 + 1.089\ 49 = 17.089\ 49,$$

and the single remaining stretch is

$$S_1 = 17.089\ 49/16 = 1.068\ 09, \quad S_1^{-1} = 0.936\ 25.$$

With this, the final gap is now closed and the belemnite is whole (Fig. 12.17d).

6. The total stretch is the inverse of the product of the inverse stretches at each stage.<sup>4</sup>

$$S = \left[ \prod_{i=1}^N S_i^{-1} \right]^{-1} = \frac{1}{0.545\ 45 \times 0.984\ 44 \times 0.936\ 25} = 1.989\ 13. \quad (12.23)$$

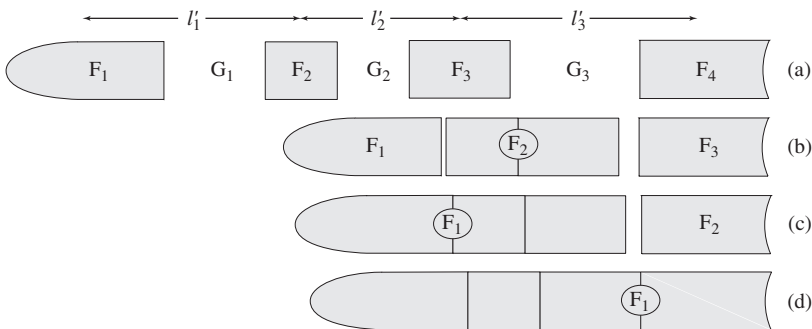


**Figure 12.17** Iterative strain reversal technique (Ferguson, 1981).

Although this method still underestimates the total stretch it gives particularly good results and is the recommended approach. By hand, it does, however, require extra work. Hossain’s method gives nearly as good results if the gap and the fragment lengths are fairly uniform and is just as quick as Ramsay’s approach.

From measured stretches we can determined the state of strain. In two dimensions, there are two cases. If the two stretches and the angles they make with the principal

<sup>4</sup>The symbol  $\prod$  means form the product of the series of all  $N$  items.



directions are known, the principal stretches can be found, otherwise three stretches are needed. The solutions follow the method of Lisle and Ragan (1988). The problem of three stretches is the simpler one and we start with it.

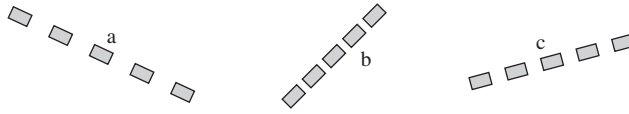


**Figure 12.18** Three idealized stretched belemnites.

**Problem**

- From the three stretched belemnites, determine the principal stretches and their orientations (Fig. 12.18). (Because the gap and fragment lengths are exactly the same in this idealization, the methods of Hossain and Ferguson give identical results.)

**Approach**

- Before undertaking the full construction it is useful to sketch the strain ellipse as a visual check. This is done by assembling the three scaled stretched lines into a rosette (Fig. 12.19a). Because the ellipse is centro-symmetric, each of these radius vectors has an equal and opposite radius vector, and we then have three complete diameters of the ellipse which can then be sketched with a fair degree of accuracy (Fig. 12.19b).

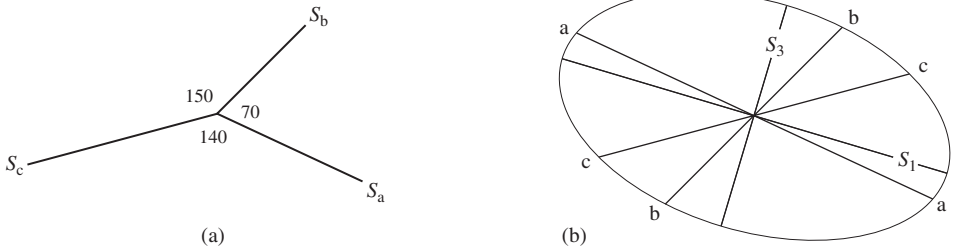


**Figure 12.19** Stretch belemnites: (a) scaled rosette; (b) sketched ellipse.

**Construction**

1. From the three measured stretches, the corresponding reciprocal quadratic elongations are

$$S_a = 2.2 (\lambda'_a = 0.2066), \quad S_b = 1.4 (\lambda'_b = 0.5102), \quad S_c = 1.8 (\lambda'_c = 0.3086).$$

2. Rearrange the three stretch directions into a rosette with arm *c* between arms *a* and *b* (Fig. 12.20a).

3. Draw the vertical  $\gamma'$  axis (but not the horizontal  $\lambda'$  axis) and add three parallel lines at distances equal to the values of  $\lambda'_a$ ,  $\lambda'_b$  and  $\lambda'_c$  using a convenient scale (Fig. 12.20b).
4. Arbitrarily locate the pole  $O_L$  on the intermediate  $\lambda'_c$  line and at this point draw the rosette so that arm  $c$  lies along this same line.
5. Through  $O_L$  draw lines parallel to arm  $a$  to intersect the  $\lambda'_a$  line at  $P'_a$  and parallel to arm  $b$  to intersect the  $\lambda'_b$  line at  $P'_b$ .
6. Points  $O_L$ ,  $P'_a$  and  $P'_c$  lie on the circle, and the perpendicular bisectors of chords  $O_L P'_a$  and  $O_L P'_c$  intersect to locate its center.
7. Through this center now draw the horizontal  $\lambda'$  axis and complete the circle. Measure the intercepts to determine the values of  $\lambda'_1$  and  $\lambda'_3$ .
8. Draw the orthogonal lines  $\lambda'_1 O_L$  and  $\lambda'_3 O_L$  (not shown). These give the orientation of the principal axes relative to the rosette.

### Answer

- The principal quadratic elongations and the corresponding principal stretches are

$$\lambda'_1 = 0.20 \quad (S_1 = 2.24) \quad \text{and} \quad \lambda'_3 = 0.60 \quad (S_3 = 1.29).$$

Note that the  $\lambda'$  coordinate of  $P'_a$  is almost the same as  $\lambda'_1$  (see Fig. 12.20b). The angle between  $\lambda'_1$  and arm  $a$  is  $8^\circ$  measured anticlockwise.

When constructing the rosette at  $O_L$  arms  $a$  and  $b$  may not intersect the two corresponding vertical  $\lambda'$  lines. Then rotate the rosette  $180^\circ$  to reverse the directions of arms and then proceed just as before. In this case the pole  $O_L$  will be below the  $\lambda'$  axis rather than above it.

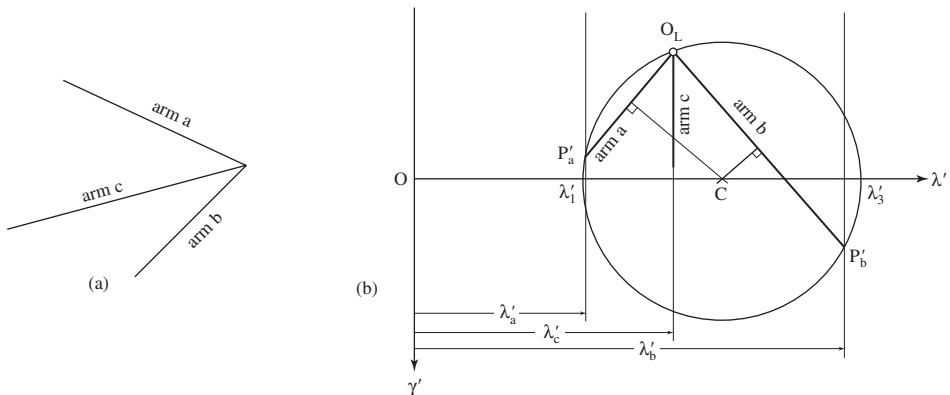


**Figure 12.20** Solution of the belemnite problem: (a) rosette; (b) Mohr Circle construction.

The graphical solution of the problem of two stretches in known angular relation with the principal axes of the strain ellipse proceeds in a similar way, except that an extra step is needed to locate a third point on the circle.

**Problem**

- Two stretched tourmaline crystals are exposed on the plane of schistosity (Fig. 12.21a). A prominent lineation on this plane marks the  $S_1$  direction. Determine the principal stretches.

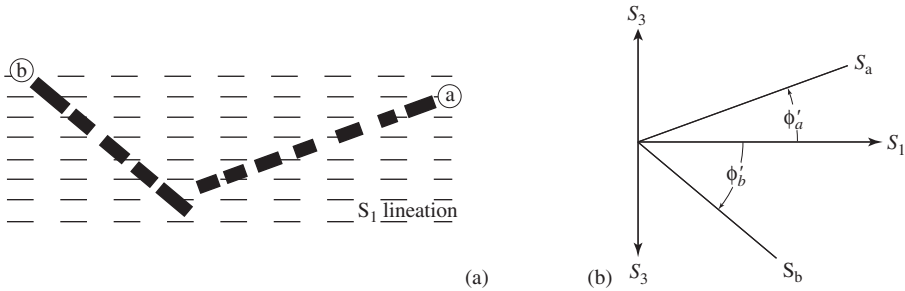


**Figure 12.21** Problem of two stretches: (a) tourmaline crystals; (b) rosette.

**Construction**

1. The two stretches, the corresponding reciprocal quadratic elongations and their orientations relative to the  $S_1$  direction are

$$S_a = 1.7, \quad \lambda'_a = 0.3460, \quad \phi'_a = +20^\circ,$$

$$S_b = 1.4, \quad \lambda'_b = 0.5102, \quad \phi'_b = -40^\circ.$$

2. Construct a rosette representing the two stretches and the principal axes (Fig. 12.21b).
3. Draw the vertical  $\gamma'$  axis and a pair of parallel lines at scale distances equal to the values of  $\lambda'_a$  and  $\lambda'_b$  (Fig. 12.22a).
4. In order to find three points on the circle it is necessary to use the strain rosette twice.
  - (a) First, arbitrarily locate pole  $O_L$  on the  $\lambda'_b$  line and construct the rosette there with arm  $b$  along the  $\lambda'_b$  line. Then draw a line parallel to arm  $a$  to intersect the  $\lambda'_a$  line at  $P'_a$ . This gives two points on the circle (Fig. 12.22a). The  $\lambda'_3$  point on the circle lies on the arm representing the  $S_3$  axis.
  - (b) Second, if this yet to be located  $\lambda'_3$  point were the pole, then the  $S_3$  axis would be vertical (see Fig. 12.10b). From this point arm  $a$  would intersect the circle at point  $P'_a$ . To locate this  $\lambda'_3$  point we simply reverse this construction by making  $O_L = P'_a$  and constructing the rosette there so that the  $S_3$  axis lies along the vertical  $\lambda'_a$  line. Then arm  $a$  intersects the line representing the first  $S_3$  direction to give the  $\lambda'_3$  point. We now add the horizontal  $\lambda'$  axis to the diagram (Fig. 12.22b).
5. The perpendicular bisector of the chord  $P'_aP'_b$  intersects the  $\lambda'$  axis at center  $C$  and the circle can then be completed with  $O_L C = P'_a C$  as radius (Fig. 12.23).

**Answer**

- Measuring the distances of two intercepts gives

$$\lambda'_1 = 0.28 (S_1 = 1.9) \quad \text{and} \quad \lambda'_3 = 0.84 (S_3 = 1.1).$$

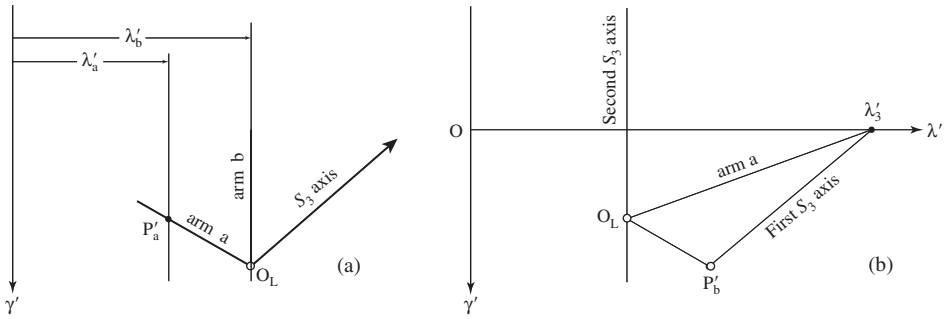


**Figure 12.22** Graphical solution for two stretches: (a) Step 1; (b) Step 2.

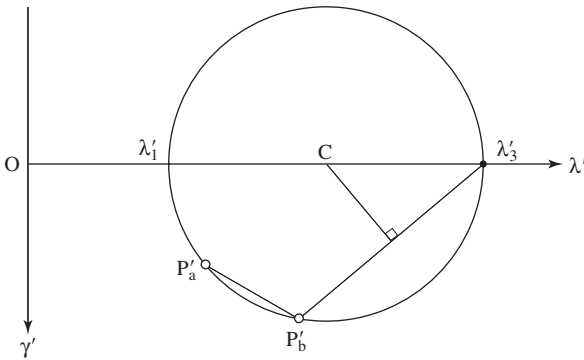


**Figure 12.23** Mohr Circle for two stretches.

In this construction the pole may be located on either of the vertical  $\lambda'_a$  or  $\lambda'_b$  lines. If, as here, it is chosen on the  $b$  line the pole will be on the lower semi-circle, and if on line  $a$  it will be on the upper semi-circle. This method breaks down when the two stretched lines make the same angle with the  $S_1$  direction and lacks sensitivity as this condition is approached.

**12.10 Restoration**

The importance of determining the state of strain lies in the fact that it describes in the most fundamental way the changes in shape and size which occur as the result of homogeneous deformation. Once we have determined the strain ellipse we immediately

know that it was derived from a circle of unit radius. With this information we can then restore any strained object to its initial shape and size.

A simple but important case is the determination of the original thickness of a homogeneously deformed layer. If a material line initially normal to bedding is marked by some physical feature then the associated strain in this single direction could easily be removed. In a few rare situations this may be possible. For example, *Skolithus* is a fossilized worm tube originally normal to bedding surfaces (McLeish, 1971; Wilkinson, *et al.*, 1975). In most cases, however, a more general approach must be used.

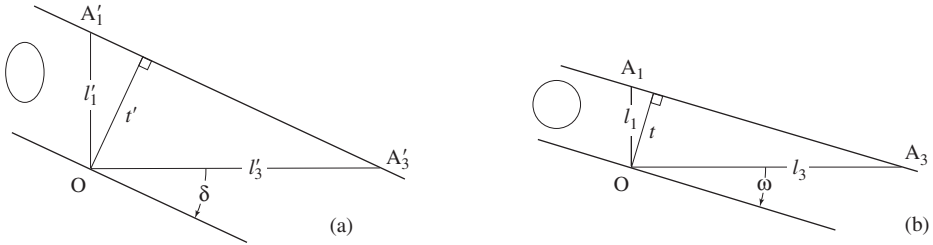


**Figure 12.24** Sedimentary bed: (a) deformed thickness  $t'$ ; (b) restored thickness  $t$ .

**Problem**

- The thickness of a deformed layer is  $t' = 1.30$  m. If the  $S_1$  direction is vertical and  $S_1 = 1.25$ , and  $S_3 = 0.80$  what was the original thickness?

**Method**

1. Arbitrarily locate a point  $O$  on the trace of the inclined lower boundary of the layer. Then draw rays parallel to the principal direction to intersect the upper trace at points  $A'_1$  and  $A'_3$  (Fig. 12.24a).
2. Measure the lengths of the vertical and horizontal segments  $l'_1 = OA'_1$  and  $l'_3 = OA'_3$ . Divide these two lengths by the corresponding principal stretches to give original lengths  $l_1 = l'_1/S_1$  and  $l_3 = l'_3/S_3$ .
3. With these restored lengths  $l_1$  and  $l_2$  locate new points  $A_1$  and  $A_3$  on these same rays (Fig. 12.24b). These fix the relative position of the upper boundary of the layer before deformation, and the perpendicular distance between this trace and point  $O$  is the original thickness  $t$ .

**Answer**

- The thickness of the layer before deformation was  $t = 1.10$  m. It should be especially noted that if the line of measured thickness  $t'$  were unstrained directly the result would be in error because  $t$  and  $t'$  are not generally marked by the same material line. Schwerdtner (1978) described an analytical solution.

Removal of the strain restores not only the initial thickness, but it also removes the inclination due to the strain. Assuming the beds were originally horizontal, this remaining dip is the result of the rotational part of the deformation, hence is equal to the angle of rotation.

For more complicated shapes a more general approach is required. One such application is the restoration of the shape of deformed fossils so that they may be accurately identified (Bambach, 1973; Raup & Stanley, 1978, p. 75). The basic technique, however, applies to any two-dimensional shape.

First, we construct a pair of axes on a drawing or photograph of the deformed object with  $x'$  parallel to the long axis and  $y'$  parallel to the short axis of the strain ellipse (Fig. 12.25a). In this system, the position vectors  $\mathbf{r}'(x', y')$  of points on the outline of the deformed object are determined. This may be done by hand, but it is far easier to record the coordinates with the use a digitizing tablet. Clearly, the more points, the more accurate the description of the deformed object and the more complete the reconstruction can be.

The corresponding position vectors  $\mathbf{r}(x, y)$  in the initial state are related to  $\mathbf{r}'(x', y')$  by the inverse equations (cf. Eq. 12.5)

$$x = x'/S_1 \quad \text{and} \quad y = y'/S_3.$$

With these we then transform these points back to their initial locations and plot the result (Fig. 12.25b).

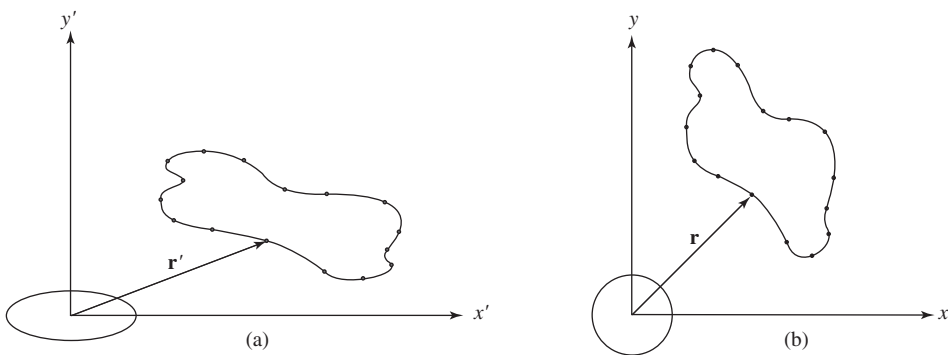


**Figure 12.25** General restoration: (a)  $x'y'$  plane; (b)  $xy$  plane.

If only  $R_s$  is known, the constant-area principal stretches of Eq. 12.19 can be used in this reconstruction of its shape, but if  $\Delta > 0$  it will be too small and if  $\Delta < 0$  it will be too large.

## 12.11 Strain and related tensors

To show how strain and deformation are related, we decompose the deformation tensor  $\mathbf{D}$  into its stretch and rotational components.<sup>5</sup> We do this by viewing the deformation as having occurred in two steps: first, the rotation of the principal axes from their initial to final state followed by the stretch to produce the strain ellipse. We write this sequence as

$$\mathbf{D} = \mathbf{S}\mathbf{R}, \quad (12.24)$$

where the orthogonal *rotation tensor*  $\mathbf{R}$  is applied first, followed by the symmetric *left-stretch tensor*  $\mathbf{S}$  (called this because it is written on the left of  $\mathbf{R}$ ).<sup>6</sup> For computational purposes we need the matrix form

$$\begin{bmatrix} D_{11} & D_{12} \\ D_{21} & D_{22} \end{bmatrix} = \begin{bmatrix} S_{11} & S_{12} \\ S_{21} & S_{22} \end{bmatrix} \begin{bmatrix} R_{11} & R_{12} \\ R_{21} & R_{22} \end{bmatrix}. \quad (12.25)$$

We can perform this decomposition of  $\mathbf{D}$  graphically with the aid of a Mohr Circle construction.

### Problem

- Determine the stretch component of the simple shear deformation

$$\mathbf{D} = \begin{bmatrix} D_{11} & D_{12} \\ D_{21} & D_{22} \end{bmatrix} = \begin{bmatrix} 1 & 0 \\ 1 & 1 \end{bmatrix}.$$

### Procedure

1. Using the convention of Fig. 12.26a, plot the two points

$$p_1(D_{11}, -D_{21}) = (1, -1) \quad \text{and} \quad p_2(D_{22}, D_{12}) = (1, 0)$$

on a pair of coordinate axes labeled  $D_{11}$ ,  $D_{22}$  and  $D_{12}$ ,  $D_{21}$  (Fig. 12.27a).

2. Locate the center  $C$  at the midpoint of diameter  $p_1p_2$  and complete the *off-axis* circle with radius  $p_1C = p_2C$ .
3. The sloping line through points  $O$  and  $C$  intercepts this circle at two points and the lengths of the segments from  $O$  represent the principal stretches  $S_1$  and  $S_3$ .
4. There are two ways of representing the circle representing  $\mathbf{S}$ .

<sup>5</sup>As in §11.7 the same notation common to continuum mechanics is used here: majuscules (upper case letters) for the material description and minuscules (lower case letters) for the spatial description.

<sup>6</sup>A second decomposition is  $\mathbf{D} = \mathbf{R}\mathbf{S}$ , that is, a stretch followed by a rotation. In this case  $\mathbf{S}$  is the *right-stretch tensor*. The ellipses produced by these two stretch tensors are identical but their orientations differ by the rotation. Because the strain ellipse and its orientation are described in the final state which we observe it is convenient to think of the rotation as having preceded the stretch (Elliott, 1970, p. 2234), so the left-stretch tensor is the one we will use.

- (a) A quick way is to draw a second set of axes with the same origin: the  $S_{11}, S_{22}$  axis through the center of the circle and the  $S_{12}, S_{21}$  axis perpendicular to this (Fig. 12.27b). Having removed the rotation, the circle is now *on axis*.
- (b) A more formal way is to rotate the center of the off-axis circle through the angle of rotation  $\omega$  to the horizontal axis and complete the circle as before (Fig. 12.27c).

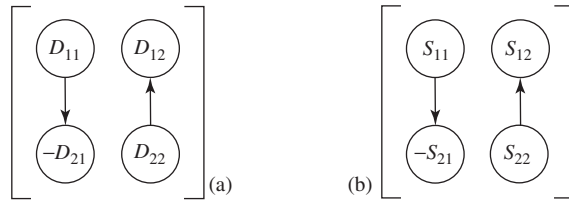


**Figure 12.26** Plotting conventions (after Means, 1992, p. 19): (a) Mohr Circle for **D**; (b) Mohr Circle for **S**.

**Answer**

- Measuring the lengths of the segments  $OS_1$  and  $OS_3$  the principal stretches are  $S_1 = 1.62$  and  $S_3 = 0.62$ . similarly we can determine the coordinates of point  $p_1$  and  $p_2$  which then gives

$$\mathbf{S} = \begin{bmatrix} 1.34 & 0.45 \\ 0.45 & 0.89 \end{bmatrix}.$$

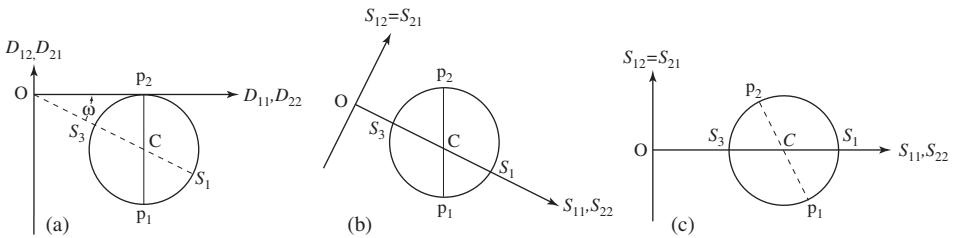


**Figure 12.27** Mohr Circles for **D** and **S**.

We can also find **S** analytically but to do so we first need to form the *inverse* of a matrix. In ordinary algebra if a variable is multiplied by its reciprocal or inverse the result is the number 1. We write this as

$$AA^{-1} = 1 \quad \text{or} \quad A^{-1}A = 1,$$

where  $A^{-1} = 1/A$ . In matrix algebra, the place of 1 is taken by the *unit* matrix **1** (also called the *identity* matrix and represented by the symbol **I**). That is

$$\begin{bmatrix} 1 & 0 \\ 0 & 1 \end{bmatrix} = \mathbf{1}.$$



We then write the product of matrix  $\mathbf{A}$  and its inverse  $\mathbf{A}^{-1}$  in two ways

$$\mathbf{A}\mathbf{A}^{-1} = \mathbf{1} \quad \text{or} \quad \mathbf{A}^{-1}\mathbf{A} = \mathbf{1}.$$

Note that these two results are the same. This is an exception to the general rule – the product of a matrix and its inverse is *commutative*. With the first of these and denoting the unknown inverse matrix  $\mathbf{A}$  by the symbol  $\mathbf{B}$  then

$$\begin{bmatrix} A_{11} & A_{12} \\ A_{21} & A_{22} \end{bmatrix} \begin{bmatrix} B_{11} & B_{12} \\ B_{21} & B_{22} \end{bmatrix} = \begin{bmatrix} 1 & 0 \\ 0 & 1 \end{bmatrix}. \quad (12.26)$$

Performing the multiplication of the two square matrices we obtain four equations containing the four unknown elements of  $\mathbf{B}$

$$\begin{aligned} A_{11}B_{11} + A_{12}B_{21} &= 1, \\ A_{11}B_{12} + A_{12}B_{22} &= 0, \\ A_{21}B_{11} + A_{22}B_{21} &= 0, \\ A_{21}B_{12} + A_{22}B_{22} &= 1. \end{aligned}$$

Solving for these unknowns gives

$$\begin{aligned} B_{11} &= \frac{A_{22}}{A_{11}A_{22} - A_{12}A_{21}}, & B_{12} &= \frac{-A_{12}}{A_{11}A_{22} - A_{12}A_{21}}, \\ B_{21} &= \frac{-A_{21}}{A_{11}A_{22} - A_{12}A_{21}}, & B_{22} &= \frac{A_{11}}{A_{11}A_{22} - A_{12}A_{21}}, \end{aligned}$$

and these  $B_{ij}$  are the required elements of the inverse. With these results, we can quickly form the inverse of any  $2 \times 2$  general matrix  $\mathbf{A}$  in three easy steps.

1. Interchange the elements of the main diagonal  $A_{11}$  and  $A_{22}$ .
2. Change the signs of the off-diagonal elements  $A_{12}$  and  $A_{21}$ .
3. Divide each element by the determinant of  $\mathbf{A}$ .

The full result is

$$\mathbf{A}^{-1} = \frac{1}{\det \mathbf{A}} \begin{bmatrix} A_{22} & -A_{12} \\ -A_{21} & A_{11} \end{bmatrix}. \quad (12.27)$$

Note that if  $\det \mathbf{A} = 0$  then  $\mathbf{A}$  is *singular* and the inverse does not exist.

In this context  $\mathbf{A}^{-1}$  reverses the effect of  $\mathbf{A}$ . As in ordinary algebra, doing and then undoing something is the same as not having done anything to begin with, and the matrix operation of doing nothing is the unit matrix.

To solve Eq. 12.24 for  $\mathbf{S}$ , we *post-multiply* (that is, multiply from the right) both sides by  $\mathbf{R}^{-1}$  giving

$$\mathbf{DR}^{-1} = \mathbf{SRR}^{-1}. \quad (12.28)$$

A positive (anticlockwise) rotation is represented by the orthogonal matrix (see Eq. 7.42)

$$\mathbf{R} = \begin{bmatrix} \cos \omega & -\sin \omega \\ \sin \omega & \cos \omega \end{bmatrix}.$$

Applying the three steps, its inverse is

$$\mathbf{R}^{-1} = \begin{bmatrix} \cos \omega & \sin \omega \\ -\sin \omega & \cos \omega \end{bmatrix}. \quad (12.29)$$

The *transpose* of a matrix is formed by exchanging rows and columns. For  $\mathbf{R}$  this gives

$$\mathbf{R}^T = \begin{bmatrix} \cos \omega & \sin \omega \\ -\sin \omega & \cos \omega \end{bmatrix} \quad (12.30)$$

and we immediately see that the inverse of an orthogonal matrix has a particularly simple form – the inverse and transpose are identical.

$$\mathbf{R}^T = \mathbf{R}^{-1},$$

and we can then immediately write down this particular inverse. We can then write Eq. 12.28 as

$$\mathbf{DR}^T = \mathbf{SRR}^T. \quad (12.31)$$

The product  $\mathbf{RR}^T = \mathbf{1}$  and this means that the two rotations cancel. Just as in ordinary algebra, the unit matrix  $\mathbf{1}$  is usually not written in such expressions. We then have

$$\mathbf{S} = \mathbf{DR}^T. \quad (12.32)$$

We can obtain the angle of rotation directly from the components of  $\mathbf{D}$  from Eq. 11.37,

$$\tan \omega = \frac{D_{21} - D_{12}}{D_{11} + D_{22}} \quad (12.33)$$

and with this angle we can evaluate the elements of both  $\mathbf{R}$  and  $\mathbf{R}^T$ .

**Problem**

- Determine the left-stretch component of the simple shear deformation

$$\mathbf{D} = \begin{bmatrix} 1 & 0 \\ 1 & 1 \end{bmatrix}.$$

**Solution**

1. From Eq. 12.33,  $\tan \omega = 0.5$  or  $\omega = 26.5651^\circ$  and we can then form the matrix for  $\mathbf{R}^T$

$$\mathbf{R}^T = \begin{bmatrix} 0.8944 & 0.4472 \\ -0.4472 & 0.8944 \end{bmatrix}.$$

2. Using this in Eq. 12.32 gives

$$\mathbf{S} = \mathbf{D}\mathbf{R}^T = \begin{bmatrix} 1 & 0 \\ 1 & 1 \end{bmatrix} \begin{bmatrix} 0.8944 & 0.4472 \\ -0.4472 & 0.8944 \end{bmatrix}.$$

3. Performing the multiplication yields

$$\mathbf{S} = \begin{bmatrix} 0.8944 & 0.4472 \\ 0.4472 & 1.3416 \end{bmatrix}. \quad (12.34)$$

We can construct the Mohr Circle for the left-stretch tensor  $\mathbf{S}$  from the components of its matrix representation.

**Problem**

- Draw the Mohr Circle for  $\mathbf{S}$  of Eq. 12.34 and find the principal stretches and their orientation.

**Procedure**

1. Draw a pair of coordinate axes and label the horizontal axis  $S_{11}$ ,  $S_{22}$  and the vertical axis  $S_{12} = S_{21}$ .
2. Using the convention of Fig. 12.26b, plot the two points

$$p_1(S_{11}, -S_{21}) = (0.8944, -0.4472) \quad \text{and} \quad p_2(S_{22}, S_{12}) = (1.3416, 0.4472)$$

using a convenient scale (Fig. 12.11).

3. The intersection of the diameter  $p_1p_2$  and the horizontal axis locates the center  $C$  and the circle can then be completed with  $Cp_1 = Cp_2$  as radius.

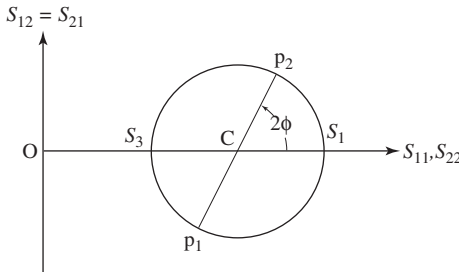


**Figure 12.28** Mohr Circle for  $\mathbf{S}$  by direct plot.

### Answer

- The angle between the  $x_2$  and the  $S_1$  direction is  $2\phi = 64^\circ$  on the Mohr Circle plane or  $\phi = 32^\circ$  on the physical plane and this gives the orientation of  $S_1$  in the deformed state.

From this diagram we can also derive expressions for the principal stretches. Distance  $c$  along the horizontal axis to the center of the circle and radius  $r$  of the circle are given by

$$c = \frac{1}{2}(S_{11} + S_{22}) \quad \text{and} \quad r = \frac{1}{2}\sqrt{(S_{11} + S_{22})^2 + (S_{12} + S_{21})^2}.$$

Then

$$S_1 = c + r \quad \text{and} \quad S_3 = c - r.$$

In three dimensions we can not so easily form the rotation tensor  $\mathbf{R}$  so this method for finding  $\mathbf{S}$  from  $\mathbf{D}$  by first forming  $\mathbf{R}^{-1}$  does not work in three dimensions. There is an alternative approach which also leads to several important insights.

To solve for  $\mathbf{S}$  by this more general method, post-multiply each side by its transpose and apply the *reversal rule* whereby the transpose of a product is equal to the product of transposes in reverse order

$$\mathbf{D}\mathbf{D}^T = \mathbf{S}\mathbf{R}(\mathbf{S}\mathbf{R})^T = \mathbf{S}\mathbf{R}\mathbf{R}^T\mathbf{S}^T. \quad (12.35)$$

Because  $\mathbf{R}\mathbf{R}^T = \mathbf{1}$  the rotations cancel leaving  $\mathbf{S}\mathbf{S}^T$ . By symmetry  $\mathbf{S} = \mathbf{S}^T$  so

$$\mathbf{S}^2 = \mathbf{D}\mathbf{D}^T, \quad (12.36)$$

where  $\mathbf{S}^2$  is the *left Cauchy–Green tensor* (Truesdell, 1991, p. 112). Geometrically  $\mathbf{D}^T$  produces the same ellipse as  $\mathbf{D}$  but rotates the principal axes from the deformed state back to the undeformed state. *Pre-multiplying* (that is, multiplying from the left) by  $\mathbf{D}$  then rotates these principal axes back again to the deformed state and at the same time produces an ellipse whose principal axes are the squares of the principal stretches  $S_1^2$  and  $S_3^2$ . This eliminates the rotation and  $\mathbf{S}^2$  is symmetric. From  $\mathbf{S}^2$  we can then find  $\mathbf{S}$  graphically.

**Problem 2**

- Determine the components of left-stretch tensor  $\mathbf{S}$  directly from the simple shear deformation tensor

$$\mathbf{D} = \begin{bmatrix} 1 & 0 \\ 1 & 1 \end{bmatrix}.$$

**Procedure**

1. Form the product

$$\mathbf{S}^2 = \mathbf{D}\mathbf{D}^T = \begin{bmatrix} 1 & 0 \\ 1 & 1 \end{bmatrix} \begin{bmatrix} 1 & 1 \\ 0 & 1 \end{bmatrix} = \begin{bmatrix} 1 & 1 \\ 1 & 2 \end{bmatrix}.$$

2. As before, plot the points  $p_1(1, -1)$  and  $p_2(2, 1)$  and complete the Mohr Circle for  $\mathbf{S}^2$  (Fig. 12.29).
3. The principal values  $S_1^2 = 2.62$  and  $S_3^2 = 0.38$  are represented by the intercepts on the horizontal axis.
4. Taking the square roots gives  $S_1 = 1.62$  and  $S_3 = 0.62$ . With these construct the Mohr Circle for  $\mathbf{S}$ .
5. On this smaller  $\mathbf{S}$  circle draw a diameter parallel to the diameter  $p_1p_2$  on the larger  $\mathbf{S}^2$  circle. The coordinates of these two points give the components of  $\mathbf{S}$ .

**Answer**

- The coordinates are  $p_1(0.89, -0.45)$  and  $p_2(1.34, 0.45)$ . Therefore the matrix representation of  $\mathbf{S}$  is (compare Eq. 12.34)

$$\mathbf{S} = \begin{bmatrix} 0.89 & 0.45 \\ 0.45 & 1.34 \end{bmatrix}.$$

With  $\mathbf{S}$  we can now find  $\mathbf{R}$ . Pre-multiplying both sides of Eq. 12.24 by  $\mathbf{S}^{-1}$  gives

$$\mathbf{S}^{-1}\mathbf{D} = \mathbf{S}^{-1}\mathbf{S}\mathbf{R}.$$

Because  $\mathbf{S}^{-1}\mathbf{S} = \mathbf{1}$  we have

$$\mathbf{R} = \mathbf{S}^{-1}\mathbf{D}. \quad (12.37)$$

All the results obtained so far are part of the *material description* of a deformation, that is, the independent variables are the material coordinates. In geological applications we must deal with the deformed state, that is, with the spatial coordinates as independent variables.

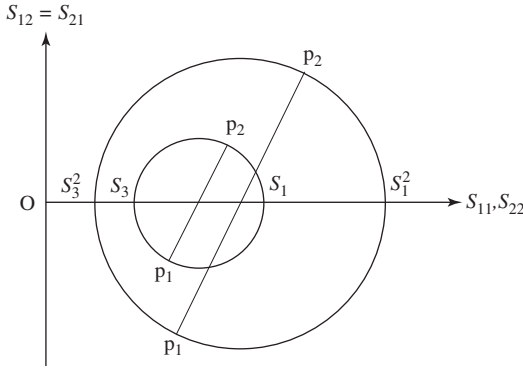


**Figure 12.29** Mohr Circle for  $S^2$  and  $S$ .

The pair of affine transformation equations which relate the particle at spatial point  $p(x_1, x_2)$  back to its initial location at  $P(X_1, X_2)$  is

$$\begin{aligned} X_1 &= d_{11}x_1 + d_{12}x_2 - T_1, \\ X_2 &= d_{21}x_1 + d_{22}x_2 - T_2. \end{aligned}$$

The coefficients  $d_{11}, d_{12}, d_{21}$  and  $d_{22}$  describe the rotation and stretch required to restore the initial configuration, and constants  $-T_1$  and  $-T_2$  describe the reverse translation. In matrix form these two become

$$\begin{bmatrix} X_1 \\ X_2 \end{bmatrix} = \begin{bmatrix} d_{11} & d_{12} \\ d_{21} & d_{22} \end{bmatrix} \begin{bmatrix} x_1 \\ x_2 \end{bmatrix} - \begin{bmatrix} T_1 \\ T_2 \end{bmatrix}. \tag{12.38}$$

This constitutes the *spatial description* of a homogeneous deformation and the essential part of this description of the reverse transformation is the square matrix representing the *inverse deformation tensor*

$$\mathbf{D}^{-1} = \mathbf{d} = \begin{bmatrix} d_{11} & d_{12} \\ d_{21} & d_{22} \end{bmatrix}.$$

Just as before, we can decompose  $\mathbf{d}$  into the product of a reverse rotation and an inverse stretch. The first step involves forming the inverse of both sides of Eq. 12.24 to give

$$\mathbf{D}^{-1} = (\mathbf{SR})^{-1}.$$

Applying another version of the *reversal rule* whereby the inverse of the product of two matrices is the product of inverses in reverse order we then have

$$\mathbf{D}^{-1} = \mathbf{R}^{-1}\mathbf{S}^{-1}.$$

This makes sense because if we take two steps forward and then back-up we must reverse the second step first. We may also write this as

$$\mathbf{d} = \mathbf{r}\mathbf{s}, \tag{12.39}$$

where  $\mathbf{r} = \mathbf{R}^{-1}$  and  $\mathbf{s} = \mathbf{S}^{-1}$ .

As in the previous example, we first determine the inverse stretch tensor graphically with the aid of a Mohr Circle construction.

**Problem**

- Using Eq. 12.36, determine the inverse stretch component of the inverse simple shear deformation

$$\mathbf{d} = \begin{bmatrix} 1 & 0 \\ -1 & 1 \end{bmatrix}.$$

**Procedure**

1. With the same method used in Fig. 12.27, plot the points  $P_1(1, 1)$  and  $P_2(1, 0)$ . With  $C$  at the midpoint of  $P_1 P_2$  complete the off-axis circle (Fig. 12.30a).
2. Just as before there are two ways of drawing the circle for  $\mathbf{s}$ . Either draw a second set of axes with the  $s_{11}, s_{22}$  axis through the center of this circle or rotate the circle to the horizontal axis (Fig. 12.30b).

**Answer**

- The principal inverse stretches are  $s_1 = 1.62$  and  $s_3 = 0.62$  and the  $s_1$  direction makes angle  $2\phi = 58^\circ$  with the  $x_1$  axis.

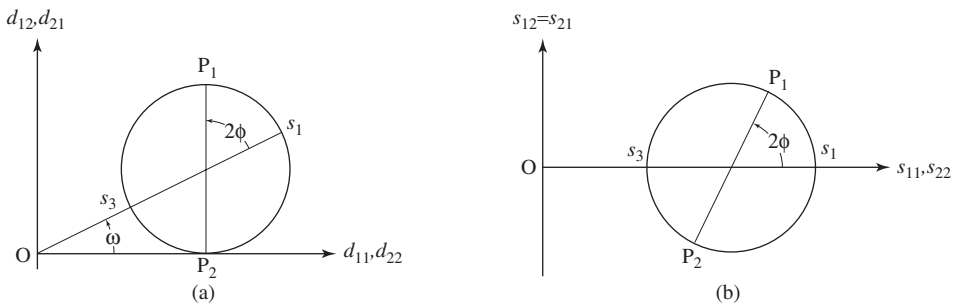


**Figure 12.30** Mohr Circles: (a) inverse deformation tensor  $\mathbf{d}$ ; (b) inverse stretch tensor  $\mathbf{s}$ .

Note that the circles for  $\mathbf{d}$  and  $\mathbf{s}$  have the same radii as the circles for  $\mathbf{D}$  and  $\mathbf{S}$ . This special case arises because there is no area change in simple shear. For more general types of deformation these circles will differ in size.

There is one more strain tensor which is of special interest. Just as in the case of  $\mathbf{D}$  we may also determine the inverse stretch tensor  $\mathbf{s}$  directly from  $\mathbf{d}$ . To do this, first pre-multiply both sides of Eq. 12.39 by its transform:

$$\mathbf{d}^T \mathbf{d} = (\mathbf{r}\mathbf{s})^T \mathbf{r}\mathbf{s}.$$

With the reversal rule

$$\mathbf{d}^T \mathbf{d} = \mathbf{s}^T \mathbf{r}^T \mathbf{r}\mathbf{s}.$$

With  $\mathbf{r}^T \mathbf{r} = \mathbf{1}$  and  $\mathbf{s}^T \mathbf{s} = \mathbf{s}^2$  we have

$$\mathbf{s}^2 = \mathbf{d}^T \mathbf{d}. \tag{12.40}$$

Geometrically, the  $\mathbf{d}$  rotates the axes from the deformed state back again to the initial state. This is followed by  $\mathbf{d}^T$  which rotates the axes back to the deformed state.

Although it will not be obvious,  $\mathbf{s}^2$  is just the *finite strain tensor* which is the main subject of this chapter. So

$$\mathbf{s}^2 = \begin{bmatrix} \lambda'_{xx} & \gamma'_{xy} \\ \gamma'_{yx} & \lambda'_{yy} \end{bmatrix}.$$

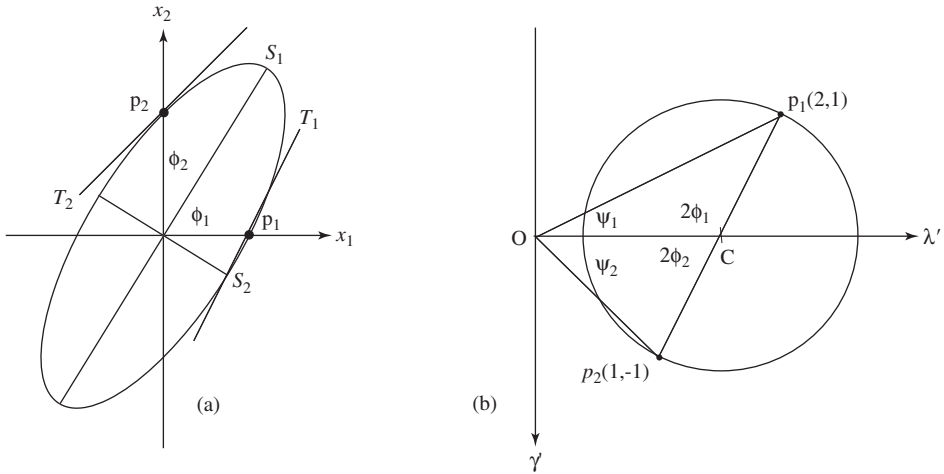


**Figure 12.31** Finite strain tensor: (a) simple shear ellipse; (b) corresponding Mohr Circle.

A comparison of a carefully drawn and scaled ellipse and the corresponding Mohr Circle will demonstrate this fact using the simple shear deformation  $\psi = 45^\circ$  and the tensor

$$\mathbf{s}^2 = \mathbf{d}^T \mathbf{d} = \begin{bmatrix} 1 & -1 \\ 0 & 1 \end{bmatrix} \begin{bmatrix} 1 & 0 \\ -1 & 1 \end{bmatrix} = \begin{bmatrix} 2 & -1 \\ -1 & 1 \end{bmatrix}.$$



## 1. Strain ellipse (Fig. 12.31a):

- (a) The magnitude of the radius vector in the  $x_1$  direction is 0.72 and in the  $x_2$  direction it is 1.00.
- (b) The principal stretches are  $S_1 = 1.62$  and  $S_2 = 0.62$ .
- (c) The  $S_1$  direction makes angle  $\phi_1 = 58^\circ$  with the  $x_1$  axis and  $\phi_2 = 32^\circ$  with the  $x_2$  axis.
- (d) The angle tangent  $T_1$  at point  $p_1$  makes with the  $x_2$  axis is the angle of shear  $\psi = 27^\circ$  and the angle tangent  $T_2$  at point  $p_2$  makes with the  $x_1$  axis is the angle of shear  $\psi = 45^\circ$ .

## 2. Mohr Circle (Fig. 12.31b):

- (a) On a set of  $\lambda'\gamma'$  axes plot points  $p_1(2, 1)$  and  $p_2(1, -1)$  using the convention of Fig. 12.26b.
- (b) Line  $p_1p_2$  is a diameter of the circle with center at  $C$ . The intercepts of the circle represent the values of  $\lambda'_1 = 0.38$  ( $S_1 = 2.62$ ) and  $\lambda'_2 = 2.62$  ( $S_2 = 0.62$ ) (not labeled in the figure).
- (c) From the diagonal elements in the matrix representation of the tensor, the value of  $\lambda'$  associated with the  $x_1$  axis is 2.0000 and with the  $x_2$  axis is 1.0000. The corresponding stretches are  $1/\sqrt{2} = 0.7071$  and 1.0000.
- (d) The  $\lambda'_1$  direction makes angles  $2\phi_1 = 116^\circ$  and  $2\phi_2 = 64^\circ$  with the  $x_1$  and  $x_2$  axes.
- (e) The slope angles of lines  $Op_1$  and  $Op_2$  are the angles of shear  $\psi_1 = 27^\circ$  and  $\psi_2 = 45^\circ$  associated with each coordinate axis.

The underlying reason for the closeness of the strain ellipse and the Mohr Circle for finite strain is the fact that the elements of the tensor are simply the coefficients in the equation of the ellipse. The Mohr Circle is just a graphical way of describing the way the coefficients in the equation of an ellipse vary under transforming the axes.

The equation of an ellipse centered at the origin has two forms. For the case where the ellipse axes coincide with the coordinate axes it is

$$\frac{x^2}{a^2} + \frac{y^2}{b^2} = 1,$$

where  $a = S_1$  and  $b = S_2$  are the lengths of the semi-axes. With the definition of  $\lambda'$  this may also be written as

$$\lambda'_1 x^2 + \lambda'_2 y^2 = 1.$$

This can be written in the form of the matrix equation

$$\begin{bmatrix} x & y \end{bmatrix} \begin{bmatrix} \lambda'_1 & 0 \\ 0 & \lambda'_2 \end{bmatrix} \begin{bmatrix} x \\ y \end{bmatrix} = 1.$$

We then see that the square matrix is just the finite strain tensor in diagonal form. Similarly, the equation of the general ellipse centered at the origin is

$$Ax^2 + 2Bxy + Cy^2 = 1.$$

This too can be written as a matrix equation

$$\begin{bmatrix} x & y \end{bmatrix} \begin{bmatrix} A & B \\ B & C \end{bmatrix} \begin{bmatrix} x \\ y \end{bmatrix} = 1.$$

Here, the square matrix of coefficients is just the finite strain tensor in its general form. Hence

$$\begin{bmatrix} A & B \\ B & C \end{bmatrix} = \begin{bmatrix} \lambda'_{xx} & \gamma'_{xy} \\ \gamma'_{yx} & \lambda'_{yy} \end{bmatrix}.$$

Because  $\mathbf{s}^2$  is symmetric,  $\gamma'_{xy} = \gamma'_{yx}$  and we can write the general equation of the strain ellipse as

$$\lambda'_{xx}x'^2 + 2\gamma'_{xy}x'y' + \lambda'_{yy}y'^2 = 1.$$

With the matrix representation of this tensor, we can also easily find an expression for  $\lambda'$ . We first show how to do this using the diagonal form. In this case, the input is a radius vector of the strain ellipse. The direction cosines of this vector are  $(\cos \phi', \sin \phi')$ , where  $\phi'$  is measured from the  $\lambda'$  axis. Then

$$\begin{bmatrix} \lambda'_1 & 0 \\ 0 & \lambda'_3 \end{bmatrix} \begin{bmatrix} \cos \phi' \\ \sin \phi' \end{bmatrix} = \begin{bmatrix} \lambda'_1 \cos \phi' \\ \lambda'_3 \sin \phi' \end{bmatrix}. \quad (12.41)$$

This output vector is normal to the tangent through point  $P'$  on the ellipse. The expression for  $\lambda'$  is obtained by forming the dot product of this normal vector  $\mathbf{n}$  and the unit vector  $(\cos \phi', \sin \phi')$  giving

$$\lambda' = \begin{bmatrix} \cos \phi' & \sin \phi' \end{bmatrix} \begin{bmatrix} \lambda'_1 \cos \phi' \\ \lambda'_2 \sin \phi' \end{bmatrix} = \lambda'_1 \cos^2 \phi' + \lambda'_2 \sin^2 \phi'. \quad (12.42)$$

This is the projection of the normal vector onto the unit vector in the direction of the radius vector. This is identical to the result of Eq. 12.11 obtained algebraically.

In a similar way, we can also obtain an expression for  $\lambda'$  from the full matrix representing the finite strain tensor. Here the direction cosines of the unit vector are  $(\cos \theta', \sin \theta')$ , where  $\theta'$  is measured from the  $x$  axis.

$$\lambda' = \begin{bmatrix} \cos \theta' & \sin \theta' \end{bmatrix} \begin{bmatrix} \lambda'_{xx} & \gamma'_{xy} \\ \gamma'_{yx} & \lambda'_{yy} \end{bmatrix} \begin{bmatrix} \cos \theta' \\ \sin \theta' \end{bmatrix}.$$

Performing the multiplications and using the equality  $\gamma'_{xy} = \gamma'_{yx}$  yields

$$\lambda = \lambda'_{xx} \cos^2 \theta' + 2\gamma'_{xy} \cos \theta' \sin \theta' + \lambda'_{yy} \sin^2 \theta'. \tag{12.43}$$

The angle between the unit vector  $\mathbf{n}$  normal to the tangent at  $P'$  and the unit radius vector  $\mathbf{r}$  in the direction  $OP'$  is the angle of shear  $\psi$ , and is obtained by the dot product  $\mathbf{n} \cdot \mathbf{r}$ . Then the expression for the associated shear strain  $\gamma'$  can be obtained in exactly the same way used to obtain Eq. 12.16.

**12.12 Exercises**

- Using the circle and ellipse of Fig. 12.32, graphically determine the stretch  $S$  and the angle of shear  $\psi$  associated with a radius making an angle of  $\phi' = +30^\circ$  with the major axis. Check your result with a Mohr Circle construction.

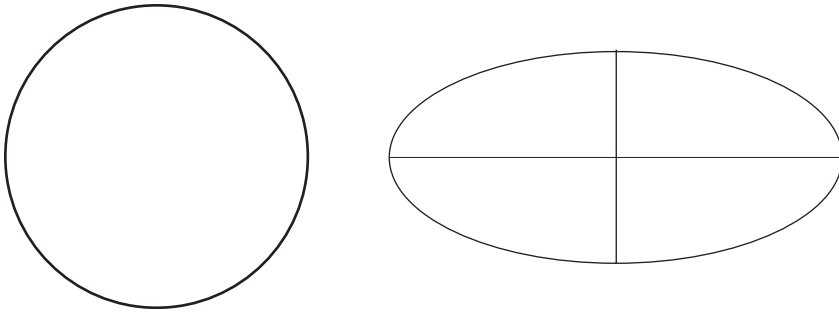


**Figure 12.32**

- Using the collection of deformed two-dimensional pebbles of Fig. 2., estimate the orientation and shape of the strain ellipse.

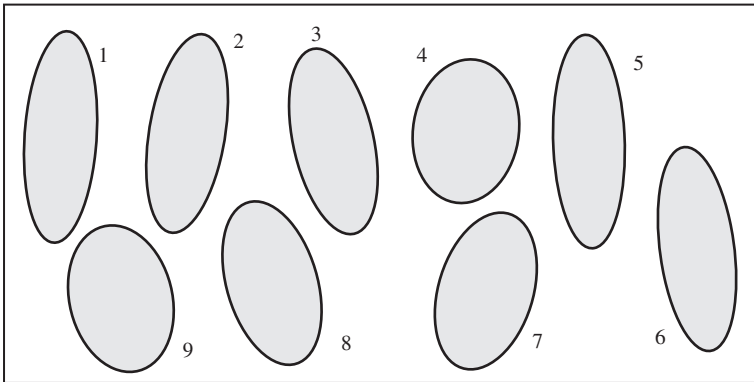


**Figure 12.33**

- Using the collection of deformed brachiopods of Fig. 12.34, estimate the orientation and shape of the strain ellipse using Wellman's method.

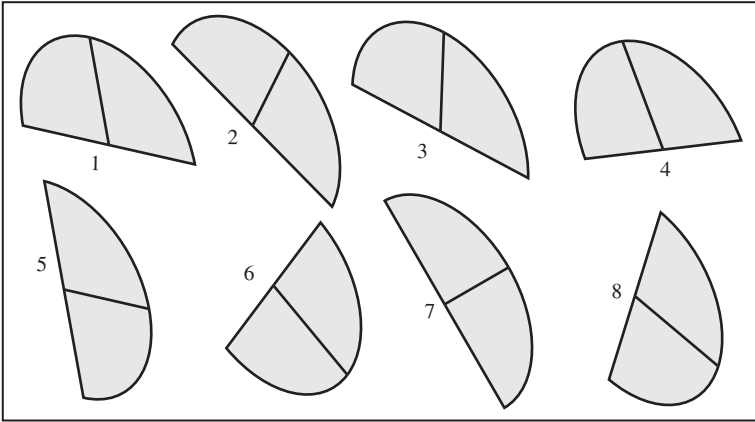


**Figure 12.34**

- With a Mohr Circle construction determine the orientation and shape of the strain ellipse from the two deformed brachiopods of Fig. 12.35.

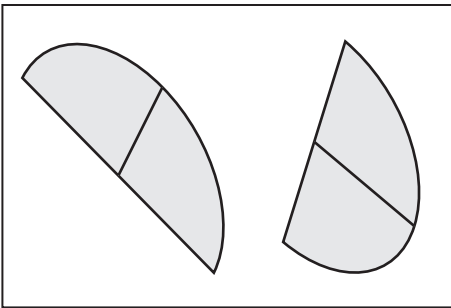


**Figure 12.35**

- With a Mohr Circle construction determine the orientation and shape of the strain ellipse from the deformed shard in of Fig. 12.36.

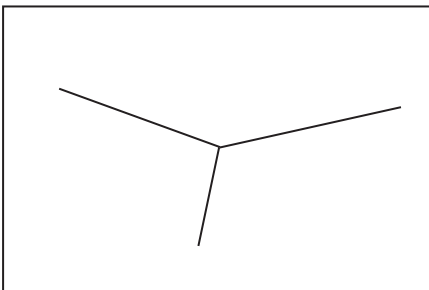


**Figure 12.36**

6. Determine the stretch of the single boudin shown in Fig. 12.37 and Table 12.1 using the methods of Ramsay, Hossain and Fergusson.

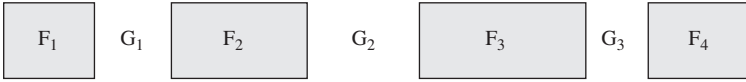


Figure 12.37

Table 12.1

	<i>F</i>	<i>G</i>
1	12 mm	10 mm
2	18 mm	16 mm
3	22 mm	8 mm
4	14 mm	

7. Three stakes were placed on the surface of a glacier to form an equilateral triangle 10 m on a side (Fig. 12.38a). After one year the positions of the stakes were resurveyed (Fig. 12.38b). Determine the strain which accumulated over this time span.

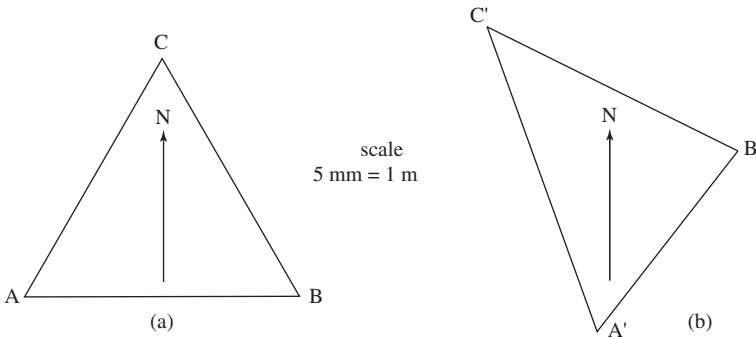


Figure 12.38

# 13

## Flow

### 13.1 Introduction

As we have seen in Chapter 11, the study of deformation is concerned solely with a comparison of a body of rock in its initial and final configurations: the *translation* compares the initial and final places, the *rotation* compares the initial and final orientations, and the *stretch* compares the initial and final shapes and sizes (see Fig. 11.2). No consideration is given to intermediate configurations or to a particular sequence of configurations (Mase, 1970, p. 77).

However, the *motion* or *flow*<sup>1</sup> by which a particular deformed state is attained is also of considerable interest if we are to understand the processes involved in the formation of geological structures. *Kinematics* is the branch of mechanics concerned with the motion of bodies without regard to any associated forces.

In this chapter we first treat the basic elements of a kinematic analysis by describing the measured velocity field in a tectonically active area and the information that can be derived from it. Second, we consider an approach to the more difficult problem of understanding the flow responsible for old structures. Third, by considering the progressive geometrical evolution of structures we can gain some insight into the geometrical nature of geological flow patterns. Finally, after treating some important theoretical matters, we use these results to consider briefly an alternative approach to estimating the time rates of deformation.

### 13.2 Active tectonics

The San Andreas Fault zone of California is one of the most heavily instrumented active structures in the world. For about three decades the velocities of many points through-

<sup>1</sup>Flow, like deformation, is a continuum concept. Thus we may speak of fluid flow, ash flow, debris flow, etc. as long as an appropriate scale is used (see §11.2).

out the zone have been measured using a number of geodetic methods. Since 1986 the preferred approach is the use of the Global Positioning System (GPS). In addition, an extensive network of seismometers is in place. All the data collected by these systems are telemetered to the Scripps Institute of the University of California at San Diego. Figure 13.1 is the resulting velocity map for the southern part of the system.<sup>2</sup> As this map shows the fault zone is several hundreds of kilometers wide and the velocity vectors are essentially parallel. Therefore, to a good approximation, the overall motion is inhomogeneous simple shear flow.

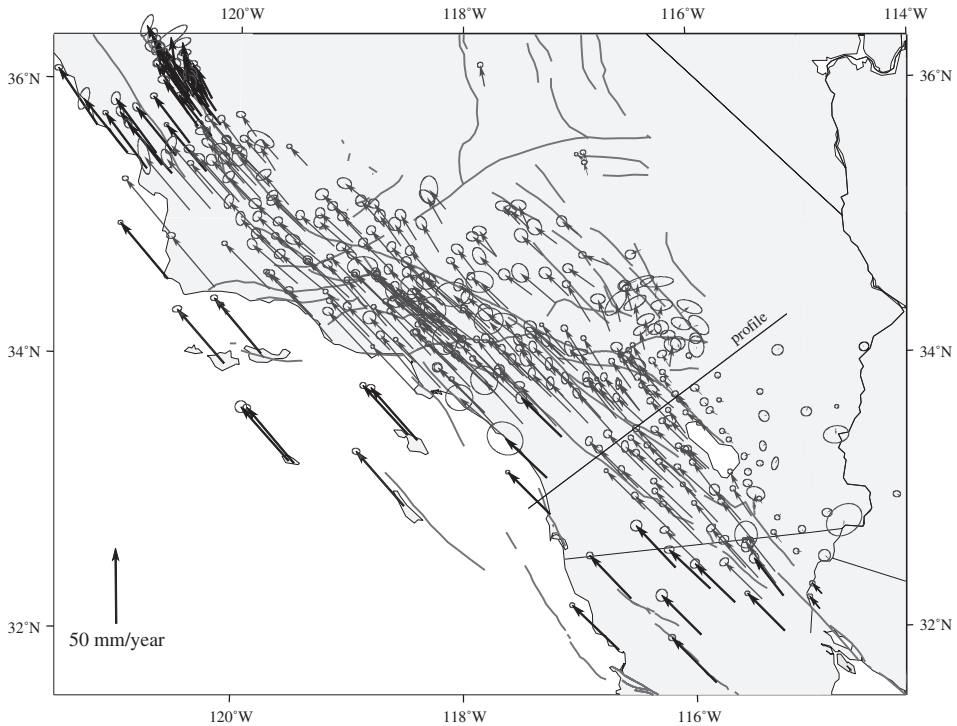


**Figure 13.1** Velocity map of the southern San Andreas Fault zone.

A better appreciation of the velocity distribution can be obtained from a profile across the zone. Figure 13.2 shows such a profile perpendicular to the trend of the vectors along a line just north of the Salton Sea. Table 13.1 gives the data used to construct this profile.

From the velocity profile, we can determine the velocity gradient for the segments between adjacent observation points. Because the profile is approximately linear between Stations 3 and 8 (see Fig. 13.3), and because this also represents the bulk of the velocity variation across the zone, we calculate the average gradient over this interval. This will

<sup>2</sup>For additional details see <http://www.scecdc.scec.org/>

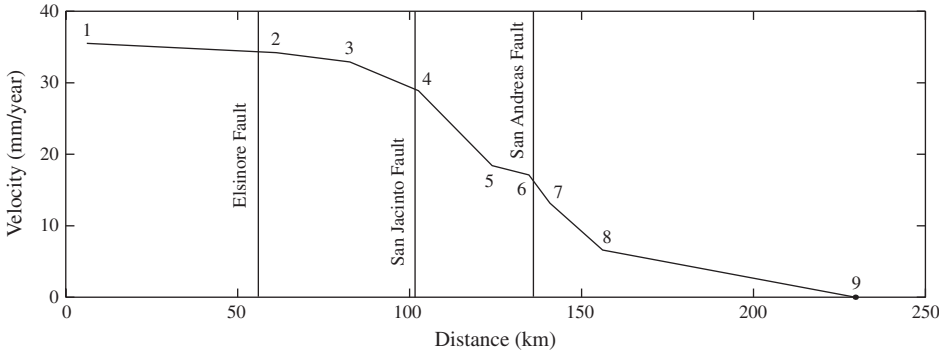


**Figure 13.2** Velocity profile across San Andreas Fault zone.

**Table 13.1** *Velocity profile data*

Station	1	2	3	4	5	6	7	8	9
Distance (km)	6.12	61.22	82.65	102.56	123.98	134.70	140.82	156.12	229.60
Velocity (mm/year)	35.5	34.2	32.9	28.9	18.4	17.1	13.2	6.6	0

give us a feeling for magnitude of the overall velocity gradient. From Table 13.1

$$\Delta d = 156.12 - 82.65 = 73.47 \text{ km} \quad \text{and} \quad \Delta v = 32.9 - 6.6 = 26.3 \text{ mm/year.}$$

To proceed we make two adjustments:

1. We need a common measure of length. Any unit will do, but because the velocities are expressed in millimeters we will adopt this for the distances too.
2. The second is the SI unit of time. For our purposes there are approximately  $3.16 \times 10^7$  s in a year and we will use this figure.<sup>3,4</sup>

We then have

$$\Delta d = (73.5 \text{ km})(10^6 \text{ mm/km}) = 7.35 \times 10^7 \text{ mm.}$$

$$\Delta v = (26.3 \text{ mm/year}) / (3.16 \times 10^7 \text{ s/year}) = 8.32 \times 10^{-6} \text{ mm/s.}$$

Thus the average velocity gradient in this segment is

$$\frac{\Delta v}{\Delta d} = \frac{8.32 \times 10^{-6} \text{ mm/s}}{7.35 \times 10^7 \text{ mm}} = 1.13 \times 10^{-13} \text{ /s.}$$

<sup>3</sup>There are several different measures of the length of a year. One with 365 days is perhaps the most common, but strictly speaking, the *tropical year* (the time between successive spring equinoxes) is a more accurate measure. Its length is 365.242 199 days or 31 556 925.9936 s.

<sup>4</sup>For measuring geological time, however, the recommendations of the North American Stratigraphic Code (A.A.P.G. Bulletin, v. 67, p. 841–875) are commonly used: *kilo-annum* (1 ka =  $10^3$  years), *mega-annum* (1 Ma =  $10^6$  years) and *giga-annum* (1 Ga =  $10^9$  years).



This gradient also expresses the time rate of change of the shear strain  $\gamma$  or

$$\frac{\Delta v}{\Delta d} = \frac{\Delta \gamma}{\Delta t}.$$

As we will see in §13.5, the magnitudes of the time rates of the principal extensions in simple shear are exactly half this, that is,

$$\frac{\Delta e_1}{\Delta t} = +5.65 \times 10^{-14}/\text{s} \quad \text{and} \quad \frac{\Delta e_3}{\Delta t} = -5.65 \times 10^{-14}/\text{s}.$$

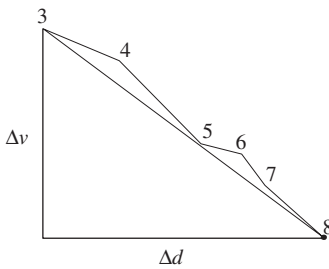


**Figure 13.3** Velocity gradient calculation.

The seismogenic zone of the San Andreas Fault system extends to a depth of about 15 km. Below this there must be a ductile shear zone with essentially the same overall geometry and distribution of strain rates.

Besides measuring the motion associated with active fault zones, the GPS technology can also be used to study the motion in areas of other types of active tectonics, including the motions at plate boundaries and the uplift of orogenic belts.<sup>5</sup>

### 13.3 Ancient tectonics

Even though they are restricted to the earth's surface, the study of the actual motion in tectonically active areas gives important clues about the movements responsible for some of the ancient structures we see in crustal rocks. Unfortunately, there is still the necessity of trying to obtain additional information from a study of the rocks themselves, especially as they bear on structures which formed at depth in the geological past. This is a very difficult task, but there is one promising approach. During synkinematic metamorphism some evidence of the patterns of flow may be preserved in the newly formed mineral grains, and in certain circumstances these features may be dated radiometrically.

An example of such features is the preservation of the history of rotation in porphyroblasts. Garnet grains in schists which commonly display a double spiral of inclusions

<sup>5</sup>For more details see <http://www.unavco.ucar.edu/>

are called *snow-ball* garnets (Rosenfeld, 1970; Passchier & Trouw, 1996, p. 176–182).<sup>6</sup> Christensen, *et al.* (1989) have measured the radial variation in the  $^{87}\text{Sr}/^{86}\text{Sr}$  ratio in a large garnet porphyroblast from the Appalachian Mountain belt of Vermont. From these dates the time interval during which the garnet grew and rotated was found, and it was

$$\Delta t = (10.5 \times 10^6 \text{ years})(3.16 \times 10^7) = 3.32 \times 10^{14} \text{ s.}$$

In this single crystal a sigmoidal spiral of inclusions records a rotation of about 4 rad or  $230^\circ$  (Fig. 13.4). Thus the average rate of rotation was

$$\frac{\Delta\omega}{\Delta t} = \frac{4 \text{ rad}}{3.32 \times 10^{14} \text{ s}} = 1.20 \times 10^{-14} \text{ rad/s.}$$

Assuming simple shear flow, the rate of the shear strain is exactly twice this value or

$$\frac{\Delta\gamma}{\Delta t} = 2.40 \times 10^{-14}/\text{s.}$$

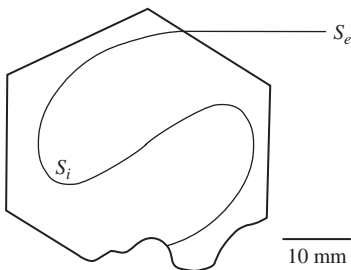


**Figure 13.4** Snow-ball garnet porphyroblast (after Christensen, *et al.*, 1989): the internal schistosity  $S_i$  at the center of the grain has been rotated  $230^\circ$  relative to the external schistosity  $S_e$ .

### 13.4 Progressive deformation

Unfortunately, for most old structures any such time rates are inaccessible to us. We can, however, obtain some important information about the geometrical evolution from a detailed examination of minor structures.

Card-deck models are an especially useful aid to visualizing some of the purely geometrical changes which lead to a final deformed state. An easy and instructive way to appreciate this evolution is to perform the basic circle-to-ellipse experiment by shearing the deck through a series of small increments and watching the geometrical changes as they occur (see Fig. 13.5).

<sup>6</sup>We note that the rotation of such porphyroblasts is currently being hotly debated. Kraus and Williams (2001) give a good review.

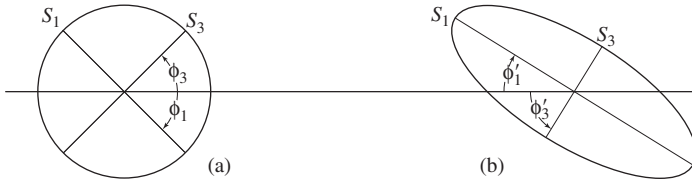


**Figure 13.5** Two stages in progressive simple shear: (a)  $\psi = 0$ ; (b)  $\psi = 45^\circ$ .

A particularly important observation to make during these experiments is the fact that the material lines which mark the axes of the evolving strain ellipse constantly change. This can be easily checked by marking the axes at some intermediate stage (Fig. 13.5b). In the next increment of shear these lines will not mark the axes of the next ellipse. Such flow is *non-coaxial* in nature.

To better appreciate this geometrical evolution, it is useful to plot the changing orientations of these principal axes as a function of the increasing angle of shear  $\psi$ . Figure 13.6a is such a graph where the orientation of  $S_1$  is given by the angle  $\phi'_1$  measured anticlockwise and the orientation of  $S_3$  is given by the angle  $\phi'_3$  measured clockwise from the shear direction.

At small values of  $\psi$  the orientation of the ellipse axes is difficult to determine visually with any accuracy. In particular, it may not be readily apparent that both the  $S_1$  and  $S_3$  axes initially make angles of  $\phi = \pm 45^\circ$  with the shear direction (Fig. 13.5a).

An additional way of tracking this evolution is to graph the changing values of  $S_1$  and  $S_3$  and their ratio  $R_s$ . This clearly indicates how the shape of the strain ellipse evolves in progressive simple shear (Fig. 13.6b).

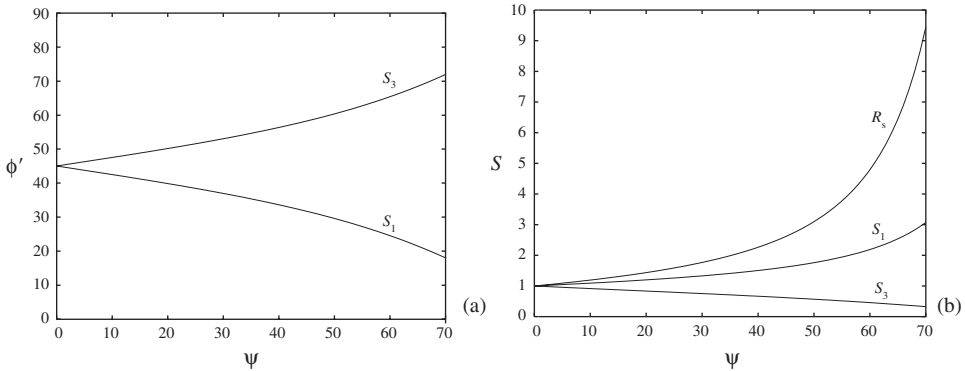


**Figure 13.6** History of principal stretches: (a) orientations; (b) magnitudes.

A graph with  $S_1$  plotted against  $S_3$  is an especially useful aid in visualizing the intermediate stages through which the evolving strain ellipses pass (Fig. 13.7). The initial reference circle is represented by the point  $(S_1, S_3) = (1, 1)$ . As the strain progressively departs from this circle, the evolving ellipses plot on a curve. This curve depicts the

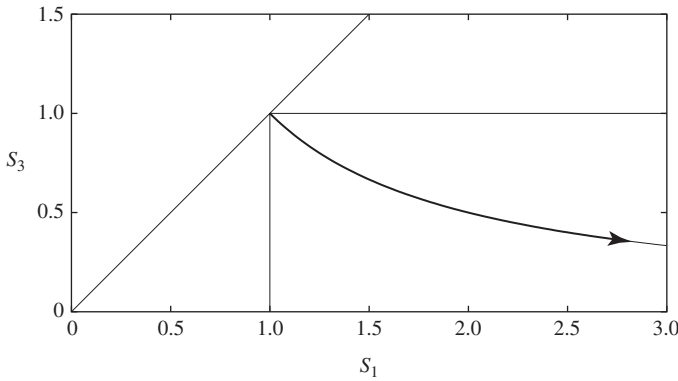


**Figure 13.7** Ellipse graph and constant area strain path.

geometrical evolution and is called the *strain path*. For constant area ellipses, including those resulting from simple shear, the path lies along the hyperbola  $S_1 = 1/S_3$ . This  $\Delta = 0$  path bounds the field of area increase ( $\Delta > 0$ ) above and the field of area decrease ( $\Delta < 0$ ) below.

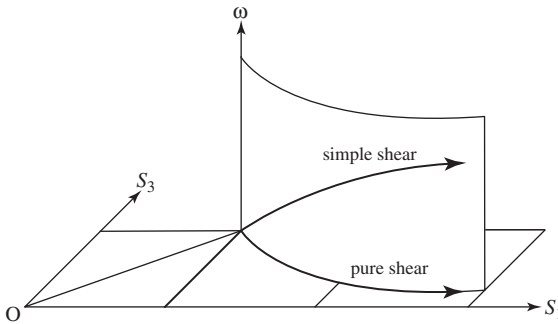


**Figure 13.8** Deformation path.

A more complete history includes the rotation as well as the strain and this can be depicted on a three-dimensional graph (Fig. 13.8). By including the rotation, a curve on this graph represents the *deformation path* for two-dimensional deformations. Paths for constant area ellipses lie on a vertical cylindrical surface through the hyperbolic curve  $S_1 = 1/S_3$ . The constant area path which lies in the plane of  $\omega = 0$  defines the special irrotational deformation *pure shear*. The simple shear path ( $\omega \neq 0$ ) also lies on this cylindrical surface.

It should then be clear that there are many other possible deformation paths which satisfy the constant area condition and which therefore lie on this surface.

The history of the stretch associated with particular lines is also of interest. From Fig. 11.11, the initial and final lengths of a line are given by

$$l = 1/\sin \theta \quad \text{and} \quad l' = 1/\sin \theta'.$$

With these we then have an expression for the stretch associated with any such line in terms of its initial and final orientations

$$S = l/l' = \sin \theta / \sin \theta'. \tag{13.1}$$

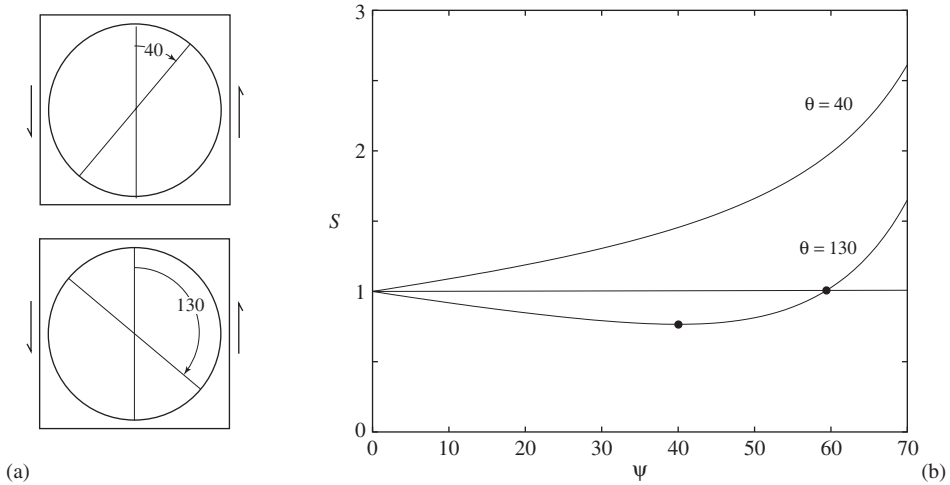


**Figure 13.9** Two typical stretch histories of material lines.

Passive material lines have two distinct types of stretch histories and both can be observed in a card-deck model (Fig. 13.9). If the initial orientation angle  $\theta \leq 90^\circ$  then the stretch history is one of continuous lengthening (see the  $\theta = 40^\circ$  curve). On the other hand, if the initial orientation angle  $\theta > 90^\circ$  the line has a more complex stretch history involving three stages (see the  $\theta = 130^\circ$  curve).

1. At first the line shortens ( $S < 1$ ).
2. When  $\theta' = 90^\circ$  the stretch has its minimum value  $S = S_{min}$ . Thereafter the line lengthens.

(a) The minimum stretch is found by substituting  $\theta' = 90^\circ$  into Eq. 13.1 giving

$$S_{min} = \sin \theta. \tag{13.2}$$

(b) The shear required for this minimum is given by the condition  $\cot \theta' = 0$ . With this in Eq. 11.20

$$\gamma = -\cot \theta = -1/\tan \theta. \tag{13.3}$$

The minus sign is needed because if  $\theta > 90^\circ$ , then  $\tan \theta < 0$ .

(c) For example, if  $\theta = 130^\circ$ ,  $S_{min} = 0.77$  and this occurs when  $\psi = 40^\circ$ .

3. As the line continues to lengthen, it passes through the point where  $S = 1$  and thereafter its length is greater than its initial length  $S > 1$ . This cross-over point occurs when  $\gamma$  has exactly twice the value given in Eq. 13.3 or

$$\gamma = -2 \cot \theta = -2 / \tan \theta. \quad (13.4)$$

In the example, the cross-over point occurs at  $\psi = 59.2^\circ$ .

In the circle-to-ellipse card-deck experiment, the resulting ellipse comprises the *macroscopic view* (see §11.2). A similar situation is common in naturally deformed rocks. If a material line in the  $S_1$  direction is marked by a thin layer of contrasting material, such as a thin quartz vein, then it will likely be elongated inhomogeneously with the development of micro-boudins. Similarly, such a contrasting material line in the  $S_3$  direction will likely be inhomogeneously shortened with the development of micro-folds. These minor structures comprise the *microscopic view*.

These several types of behaviors during progressive simple shear can be clarified by subdividing the original circle (Fig. 13.10a) and the resulting ellipse (Fig. 13.10b) into four pairs of sectors or zones each with a characteristic type of history (Ramsay, 1967, p. 120).

1. *Zone 1* contains the  $S_1$  direction and all lines within this zone increase in length throughout their history. Its boundaries are the two lines of NFLS. This zone is further subdivided into two subzones by the condition  $\theta = 90^\circ$ .
  - (a) *Subzone 1a* contains lines with a history of continuous lengthening. Thin competent bands lying in this sector are stretched, possibly with the development of micro-boudins.
  - (b) *Subzone 1b* contains lines which are initially shortened and then lengthened. Early formed micro-folds may be later stretched, with the possible development of micro-boudins on the fold limbs.
2. *Zone 2*, like Subzone 1b, contains lines with a history of shortening followed by lengthening, but all lines still exhibit a finite shortening. Early micro-folds may be partially disrupted.
3. *Zone 3* contains the  $S_3$  direction and all lines within this sector have a history of continuous shortening. Ptygmatic micro-folds are found within this zone.

### *Pure shear flow*

In contrast, progressive *pure shear* is an example of a constant-area deformation which is irrotational. During the motion which produces this state, the same material lines mark the axes of the evolving ellipse at every stage and this is *coaxial flow*. Pure shear can not be modeled so easily but an approximation can be achieved by squeezing a slab of

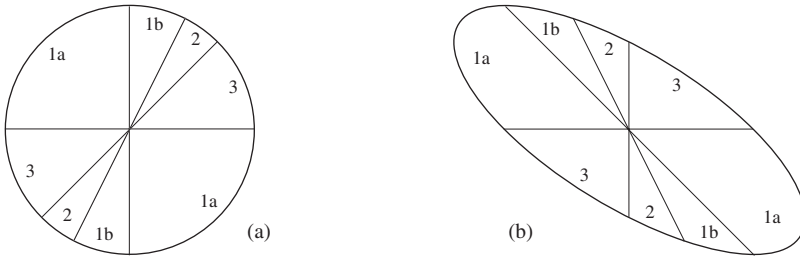


Figure 13.10 Zones in progressive simple shear: (a) before deformation; (b) after deformation.

plasticine in a vise while constraining the top and bottom to prevent thickening. Even without a physical model, however, the distributions of the zones and their histories are simple enough to be readily appreciated. As shown in Fig. 13.11 all the same zones are present and they have the same characteristics (Ramsay, 1967, p. 119). The important difference is their symmetric distribution with respect to the ellipse axes.

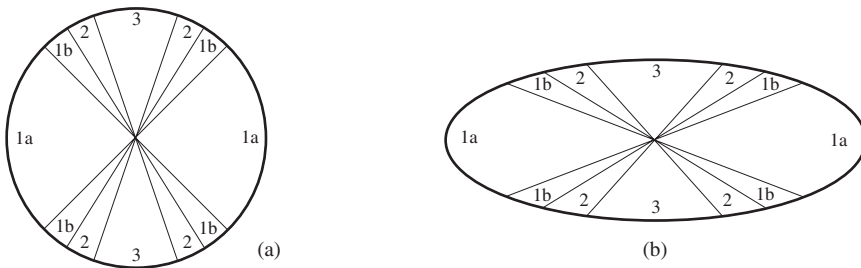


Figure 13.11 Zones in progressive pure shear: (a) before deformation; (b) after deformation.

At the macroscopic scale, every ellipsoid has three planes of symmetry and thus displays *orthorhombic* symmetry. This includes ellipsoids formed by simple shear, pure shear or any other pattern of flow. These planes of two-fold symmetry are the planes of  $S_1S_2$ ,  $S_2S_3$  and  $S_1S_3$ .

Ellipsoids formed by pure shear progressive deformation retain this orthorhombic symmetry at both the microscopic and macroscopic levels. In contrast, during progressive simple shear the microscopic changes reduced the overall symmetry to *monoclinic*. Even more complicated three-dimensional histories may result in *triclinic* symmetry.

The histories, and therefore the distributions of the microstructures, are path dependent. In particular, different rotational histories may give markedly different zonal arrangements and thus also different symmetries. On this basis, *coaxial* and *non-coaxial* flow patterns may be distinguished. Ramsay (1967, p. 114–120) gives an extended discussion, together with excellent photographs of the microstructures which may be associated with these several behaviors.

### 13.5 Kinematics

The motion of a body at an instant in time is described by its associated *velocity field*, another example of a vector field. In the present context, the term *flow* carries the connotation of a continuing motion leading to a deformation. There are two ways of describing such a motion.<sup>7</sup>

1. In the *material* view each particle is labeled with its coordinates  $(X_1, X_2)$  at some initial time. As a particle moves along its *pathline*, the coordinates and the history of the velocity are traced as time passes.
2. The *spatial* view focuses attention on particular points in the body of material as given by its coordinates  $(x_1, x_2)$ .<sup>8</sup> This description specifies the motion at each of these points as a function of time. The flow may be *steady*, that is, the velocities at the spatial points do not change with time, otherwise it is *unsteady*.

Because it is based on the positions of monuments or other markers repeatedly surveyed over time, the San Andreas Fault zone velocity map (Fig. 13.1) and the data on which it is based constitute a material description.

For ancient flows we have no way of obtaining such data. If we are to understand something of the flow patterns responsible for ancient structures we must use the spatial description.

First we must face the vexing matter of whether such flows are steady, even approximately, or not. No geological flow can literally be steady over its entire duration – the motion must, of course, begin and end. However, some flows may closely approximate a steady state for extended periods. The deep shear zone of the San Andreas Fault is a likely example.

Even if the flow is steady, however, the conditions along a pathline will generally not be steady because a particle is constantly being conveyed into a region with a different velocity. Simple shear flow is an exception because the pathlines are parallel to the direction of shear, which is a direction of constant velocity.

On the other hand, many important classes of natural flows are intrinsically unsteady. For example, folding of physically heterogeneous rock bodies with their evolving structural geometries is unlikely to be even approximately steady. For such unsteady conditions, pathline histories will be unsteady both because the pathlines themselves are generally unsteady and because the flow field in this case is itself unsteady.

There are other factors which contribute to unsteady pathlines. Steady flow implies a constant state of stress in combination with constant environmental conditions. However, these condition in general, and pressure  $P$  and temperature  $T$  in particular, commonly

<sup>7</sup>The terms “Lagrangian” and “Eulerian” are commonly used for *material* and *spatial* in kinematics (see also Footnote 1, Chapter 11).

<sup>8</sup>These labels for the material and spatial coordinates differ from those used in Chapter 11, but these are in common usage in continuum mechanics, especially kinematics (Mase, 1970, p. 110).



do not remain constant over time, and the effects of any variations can be measured in metamorphic rocks. The methods, collectively referred to as *geothermobarometry*, are based on the fact that equilibrium mineral assemblages and their chemical compositions depend primarily on the  $P$ - $T$  conditions which existed at the time they formed. Once calibrated with experiments, these chemical details can then be used to calculate  $P$  or  $T$  or both (Spear, 1993). Further, zoned minerals can yield conditions at several points on a rock's  $P$ - $T$  path. If the appropriate minerals are present radiometric dates may also be obtained, yielding  $P$ - $T$ -time paths and these have been widely used to track the history of large-scaled movements in orogenic systems.<sup>9</sup>

The resistance of solids to flow is particularly sensitive to the temperature. Therefore the rate of flow can be expected to increase as a material element moves into a region of higher temperature, and conversely, other things remaining equal.

These are some of the reasons that trying to recover pathline histories is such a problem. In the face of these difficulties a common approach is to *assume* the pathline histories are close enough to being steady that the results have some application. With the present state of knowledge, this may in fact be the only way to proceed, but unfortunately its validity is open to question. More definite answers lie in the future and probably will be based on careful modeling of specific flow environments.

Our task now is to describe the consequences of the motion associated with particle  $P$  currently at spatial point  $p$ . The velocity of this particle is just the rate of change of position with time, that is,

$$\dot{x}_1 = v_1 \quad \text{and} \quad \dot{x}_2 = v_2$$

and at any instant in a deforming body is described by the matrix equation (Means, 1990, p. 955)

$$\begin{bmatrix} v_1 \\ v_2 \end{bmatrix} = \begin{bmatrix} L_{11} & L_{12} \\ L_{21} & L_{22} \end{bmatrix} \begin{bmatrix} x_1 \\ x_2 \end{bmatrix} + \begin{bmatrix} \dot{T}_1 \\ \dot{T}_2 \end{bmatrix}, \quad (13.5)$$

where  $(v_1, v_2)$  are the components of the instantaneous velocity associated with the moving particle and  $(\dot{T}_1, \dot{T}_2)$  are the components of the rate of translation.<sup>10</sup>

The elements of the square matrix are the *rate of deformation tensor*  $\mathbf{L}$  for a small volume of material in the vicinity of the particle. The meaning of the  $L_{ij}$  can be seen by considering the velocities associated with moving particles  $P$  at  $p(x_1, x_2)$  and  $Q$  at  $q(x_1 + dx_1, x_2 + dx_2)$  (Fig. 13.12a). The velocity of particle  $Q$  at  $q$  relative to particle  $P$  at  $p$  is given by the vector  $d\mathbf{v}$  (Fig. 13.12b). We can express the components of  $d\mathbf{v}$

<sup>9</sup>Triboulet and Audren (1988) give a good example of just how complicated the  $P$ - $T$  history can be.

<sup>10</sup>The dots denote the derivative with respect to time.

in terms of the distance between the two points and the rates of change of  $d\mathbf{v}$  in each coordinate directions (Fig. 13.12c). Thus we have

$$\begin{aligned}
 dv_1 &= \frac{\partial v_1}{\partial x_1} dx_1 + \frac{\partial v_1}{\partial x_2} dx_2, \\
 dv_2 &= \frac{\partial v_2}{\partial x_1} dx_1 + \frac{\partial v_2}{\partial x_2} dx_2.
 \end{aligned}$$

We can write these as the matrix equation

$$\begin{bmatrix} dv_1 \\ dv_2 \end{bmatrix} = \begin{bmatrix} \partial v_1/\partial x_1 & \partial v_1/\partial x_2 \\ \partial v_2/\partial x_1 & \partial v_2/\partial x_2 \end{bmatrix} \begin{bmatrix} dx_1 \\ dx_2 \end{bmatrix}. \tag{13.6}$$

The square matrix represents the *velocity-gradient tensor* and it relates the instantaneous relative velocity vector of a particle to the position vector of the spatial point which the particle occupies at that instant. We then have two alternative ways of expressing the components of this tensor.

$$\begin{bmatrix} L_{11} & L_{12} \\ L_{21} & L_{22} \end{bmatrix} \equiv \begin{bmatrix} \partial v_1/\partial x_1 & \partial v_1/\partial x_2 \\ \partial v_2/\partial x_1 & \partial v_2/\partial x_2 \end{bmatrix}.$$

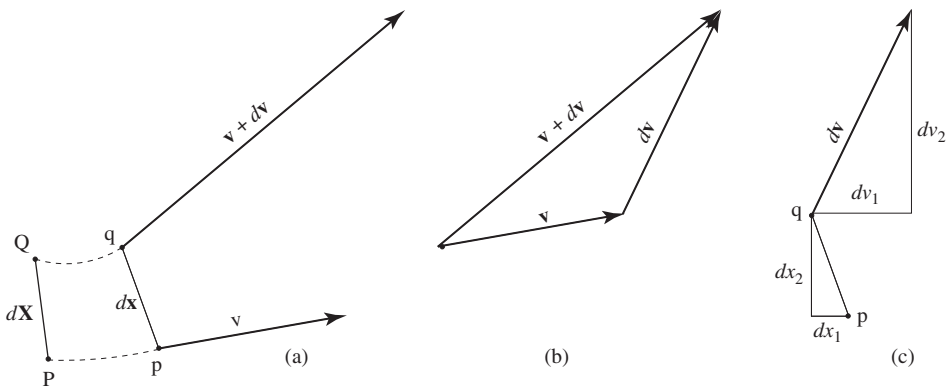


**Figure 13.12** Velocity vectors: (a) two adjacent particles; (b) relative velocity vector  $d\mathbf{v}$ ; (c) velocity gradients.

Again, because it has no effect on the geometry of the deforming body, we neglect the translation rate, and as a result  $(v_1, v_2)$  are now the components of the *relative velocity*. Equation 13.5 now becomes

$$\begin{bmatrix} v_1 \\ v_2 \end{bmatrix} = \begin{bmatrix} L_{11} & L_{12} \\ L_{21} & L_{22} \end{bmatrix} \begin{bmatrix} x_1 \\ x_2 \end{bmatrix}. \tag{13.7}$$

With this expression, we can determine the components of the instantaneous velocity at any point within the homogeneously deforming body. It is particularly easy to find these

velocity components at the points (1, 0) and (0, 1) because they are given directly by the elements of the two columns (see also Fig. 13.13a)

$$\begin{bmatrix} v_1 \\ v_2 \end{bmatrix} = \begin{bmatrix} L_{11} & L_{12} \\ L_{21} & L_{22} \end{bmatrix} \begin{bmatrix} 1 \\ 0 \end{bmatrix} = \begin{bmatrix} L_{11} \\ L_{21} \end{bmatrix} \quad \text{and} \quad \begin{bmatrix} v_1 \\ v_2 \end{bmatrix} = \begin{bmatrix} L_{11} & L_{12} \\ L_{21} & L_{22} \end{bmatrix} \begin{bmatrix} 0 \\ 1 \end{bmatrix} = \begin{bmatrix} L_{12} \\ L_{22} \end{bmatrix}.$$

This is illustrated for sample shear flow in Fig. 13.14a and for pure shear flow in Fig. 13.14b.

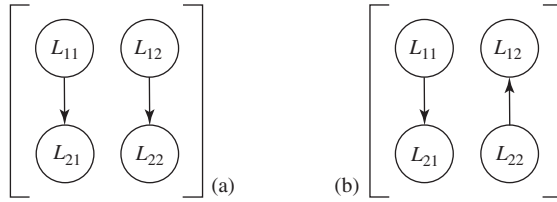


**Figure 13.13** Plotting convention: (a) physical plane; (b) Mohr Circle plane.

Every moving particle in the homogeneously deforming body has associated with it such a relative velocity vector and collectively these constitute the *relative velocity field*.

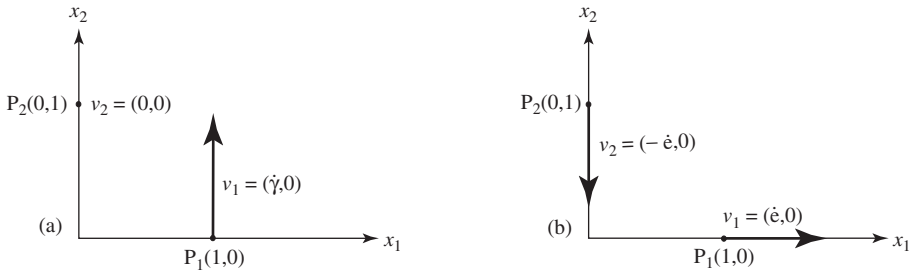


**Figure 13.14** Velocity vectors: (a) simple shear; (b) pure shear.

At any point currently occupied by a particle the motion may be decomposed into a *translating* motion, a *rotating* motion and a *stretching* motion (Truesdell & Toupin, 1960, p. 362). Note carefully the form of these terms: following the sensible suggestion by Means (1990, p. 954) kinematic terms, which refer to instantaneous or continuing motion, are identified with the suffix *-ing* in order to clearly distinguish them from the closely related terms employed to describe the components of deformation.

This tensor describes several related behaviors associated with material lines during flow. The first is the *rate of extension*  $\dot{e} = de/dt$  (where  $e = dl/l$  and  $l$  is the current length), and it is measured in dimensionless units of extension per second. The second is the *rate of rotation*  $\dot{\omega} = d\omega/dt$  which is measured in radians per second.

The principal extension rates are  $\dot{e}_1$  and  $\dot{e}_3$ , and directions in which these occur are the *principal stretching axes*. The rate of area strain  $\dot{\Delta}$  is related to the principal extension rates by

$$\dot{\Delta} = \dot{e}_1 + \dot{e}_3. \quad (13.8)$$

The Mohr Circle for the velocity-gradient tensor is plotted using the same convention as the deformation tensor (Fig. 13.13b). For simple shear flow the tensor is represented by the matrix

$$\mathbf{L} = \begin{bmatrix} 0 & 0 \\ \dot{\omega} & 0 \end{bmatrix}.$$

### Problem

- Draw a Mohr Circle for the following simple shear velocity-gradient tensor

$$\mathbf{L} = \begin{bmatrix} 0 & 0 \\ 0.1 & 0 \end{bmatrix}.$$

### Construction

1. Draw a pair of axes and label the horizontal axis  $\dot{e}$  and the vertical axis  $\dot{\omega}$ .
2. Plot points  $P_1(L_{11}, L_{21}) = (0, 0.1)$  and  $P_2(L_{22}, L_{12}) = (0, 0)$  using a convenient scale (Fig. 13.15a).
3. Locate center  $C$  at the midpoint of  $P_1 P_2$  and draw a circle passing through these two points.
4. The extreme values on the horizontal diameter of this circle represent the directions of the principal extension rates. The magnitudes of these are  $\dot{e}_1 = +0.05$  and  $\dot{e}_3 = -0.05$  per unit of time. The circle is centered on the vertical axis because  $\dot{e}_3 = -\dot{e}_1$ , and therefore  $\dot{\Delta} = 0$ .

The coordinates of any point  $P$  on the circle which makes angle  $2\phi$  with the  $\dot{e}_1$  direction represent the instantaneous rate of extension  $\dot{e}$  and the instantaneous rate of rotation  $\dot{\omega}$  associated with the material line making an angle  $\phi$  with the  $\dot{e}_1$  direction on the physical plane.

The points of intersection of the circle with the  $\dot{\omega}$  axis represent the *lines of no instantaneous stretching*. In simple shear these occur at  $2\phi = \pm 90^\circ$  on the Mohr Circle plane and  $\phi = \pm 45^\circ$  on the physical plane measured from the  $\dot{e}_1$  direction.

Of particular interest is the instantaneous rate at which the two principal axes rotate, and this is represented by the  $\dot{\omega}$  coordinate of the center of the circle. This is the *vorticity*, and we give it the special symbol  $\dot{\omega}$  to distinguish it from the rates of rotation of general lines. In this example,  $\dot{\omega} = 0.05$  radians per unit of time and the sense is positive or anticlockwise.

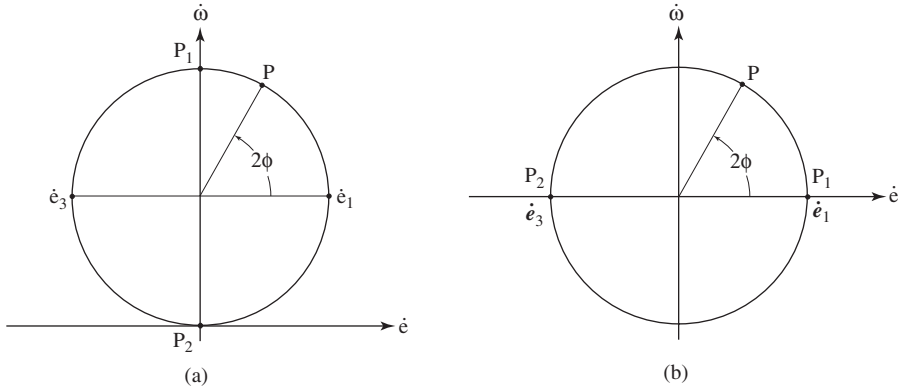


**Figure 13.15** Mohr Circles for **L**: (a) simple shear; (b) pure shear.

The rate of rotation of the axes is just the average rate of rotation of all lines (cf. Fig. 11.13).

For pure shear flow the velocity-gradient tensor is represented by the diagonal matrix

$$\mathbf{L} = \begin{bmatrix} \dot{\epsilon}_1 & 0 \\ 0 & \dot{\epsilon}_3 \end{bmatrix}$$

where  $\dot{\epsilon}_3 = -\dot{\epsilon}_1$  are the principal extension rates. In this case, and generally if the vorticity is zero ( $\dot{\omega} = 0$ ), the velocity-gradient matrix is symmetrical.

**Problem**

- Draw the Mohr Circle for the pure shear velocity-gradient tensor

$$\mathbf{L} = \begin{bmatrix} +0.05 & 0 \\ 0 & -0.05 \end{bmatrix}.$$

**Construction**

1. On a pair of coordinate axes plot points  $P_1(L_{11}, L_{21}) = (+0.05, 0)$  and  $P_2(L_{22}, L_{12}) = (0, -0.05)$  using a convenient scale (Fig. 13.15b).
2. Locate center  $C$  at the midpoint of these two points, which in this case is at the origin.
3. These two points also represent the extreme values of  $\dot{\epsilon}$  and are therefore  $\dot{\epsilon}_1 = +0.05$  and  $\dot{\epsilon}_3 = -0.05$ . Again, the circle is centered on the vertical axis because the rate of area strain  $\dot{\Delta} = 0$ .
4. The circle is also centered on the vertical axis because in pure shear flow the vorticity  $\dot{\omega} = 0$ .

There is no possibility of recovering the detailed history of **L** from features preserved in rocks deformed long ago, but is possible to evaluate the relative importance of the

vorticity for a deformation path or parts of it with the aid of *vorticity gauges* (Passchier & Trouw, 1996, p. 199). To do this it would be helpful to have a way of expressing its importance in purely geometrical terms. The two-dimensional *vorticity number*  $\mathcal{W}$  is just such a parameter, defined as

$$\mathcal{W} = d_V/r,$$

where  $d_V$  is the vertical distance from the center to the horizontal axis and  $r$  is the radius of the circle. This dimensionless number gives the importance of the vorticity relative to the rate of the strain. If  $\mathcal{W} = 0$  the flow is coaxial and the strain rate part of the flow dominates; pure shear flow is an example. Values  $\mathcal{W} > 0$  express the degree to which the flow is non-coaxial. For simple shear flow  $\mathcal{W} = 1$ . Vorticity numbers  $\mathcal{W} > 1$  produce *pulsating* strains (Weijermars, 1997), and these require special circumstances which are probably not common.

Closely related is the *dilatancy number*. This dimensionless number gives the importance of the rate of area change relative to the strain rate. It is defined as

$$\mathcal{D} = d_H/r,$$

where  $d_H$  is the horizontal distance the center is from the vertical axis and  $r$  is the radius of the circle. If  $\mathcal{D} = 0$  the rate of area strain is zero.

We can also separate the strain-rate and vorticity parts directly from the velocity-gradient tensor. To do this we need to form the *transpose* of a matrix. If matrix  $\mathbf{A}$  has components  $A_{ij}$  then the components of its transpose  $\mathbf{A}^T$  are

$$A_{ij}^T = A_{ji}, \quad (13.9)$$

that is, simply exchange rows and columns. Thus the transpose of  $\mathbf{L}$  is

$$\mathbf{L}^T = \begin{bmatrix} L_{11} & L_{21} \\ L_{12} & L_{22} \end{bmatrix}. \quad (13.10)$$

The strain-rate tensor  $\dot{\mathbf{e}}$  and vorticity tensor  $\dot{\mathbf{w}}$  are then given by

$$\dot{\mathbf{e}} = \frac{1}{2}(\mathbf{L} + \mathbf{L}^T) \quad \text{and} \quad \dot{\mathbf{w}} = \frac{1}{2}(\mathbf{L} - \mathbf{L}^T), \quad (13.11)$$

and then

$$\dot{\mathbf{e}} = \begin{bmatrix} L_{11} & L_{12} \\ L_{21} & L_{22} \end{bmatrix} + \begin{bmatrix} L_{11} & L_{21} \\ L_{12} & L_{22} \end{bmatrix} = \frac{1}{2} \begin{bmatrix} 2L_{11} & L_{12} + L_{21} \\ L_{21} + L_{12} & 2L_{22} \end{bmatrix}. \quad (13.12a)$$

and

$$\dot{\mathbf{w}} = \begin{bmatrix} L_{11} & L_{12} \\ L_{21} & L_{22} \end{bmatrix} - \begin{bmatrix} L_{11} & L_{21} \\ L_{12} & L_{22} \end{bmatrix} = \frac{1}{2} \begin{bmatrix} 0 & L_{12} - L_{21} \\ L_{21} - L_{12} & 0 \end{bmatrix}. \quad (13.12b)$$

Then

$$\mathbf{L} = \dot{\mathbf{e}} + \dot{\mathbf{w}}.$$

For simple shear

$$\begin{bmatrix} 0 & 0 \\ \dot{\gamma} & 0 \end{bmatrix} = \begin{bmatrix} 0 & \frac{1}{2}\dot{\gamma} \\ \frac{1}{2}\dot{\gamma} & 0 \end{bmatrix} + \begin{bmatrix} 0 & -\frac{1}{2}\dot{\gamma} \\ \frac{1}{2}\dot{\gamma} & 0 \end{bmatrix}.$$

The matrix representing  $\dot{\mathbf{e}}$  is *symmetric* and the matrix representing  $\dot{\mathbf{w}}$  is *skew-symmetric*.<sup>11</sup>

In terms of the velocity field, each of these parts has a geometrical interpretation. With the same approach we have used several times, we can easily determine the relative velocities at any spatial point: the velocity components associated with point  $p(1, 0)$  are obtained from

$$\begin{bmatrix} v_1 \\ v_2 \end{bmatrix} = \begin{bmatrix} 0 & 0 \\ \dot{\gamma} & 0 \end{bmatrix} \begin{bmatrix} 1 \\ 0 \end{bmatrix} = \begin{bmatrix} 0 \\ \dot{\gamma} \end{bmatrix}.$$

Similarly, the velocity components associated with point  $P(-1, 0)$  are obtained from

$$\begin{bmatrix} v_1 \\ v_2 \end{bmatrix} = \begin{bmatrix} 0 & 0 \\ \dot{\gamma} & 0 \end{bmatrix} \begin{bmatrix} -1 \\ 0 \end{bmatrix} = \begin{bmatrix} 0 \\ -\dot{\gamma} \end{bmatrix}.$$

Thus we have the velocity components for  $\mathbf{L}$  for simple shear (Fig. 13.16a). In this same way, the relative velocities associated with  $\dot{\mathbf{e}}$  (Fig. 13.16b) and with  $\dot{\mathbf{w}}$  (Fig. 13.16c) can be found.

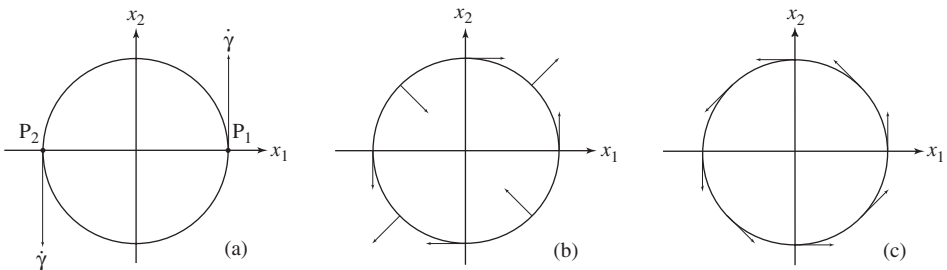


**Figure 13.16** Velocity vectors for simple shear on the physical plane: (a)  $\mathbf{L}$ ; (b)  $\dot{\mathbf{e}}$ ; (c)  $\dot{\mathbf{w}}$ .

<sup>11</sup>Any matrix  $\mathbf{A}$  is symmetric if, for all elements,  $A_{ij} = A_{ji}$  and skew-symmetric if  $A_{ij} = -A_{ji}$ .

At any time  $t$  the relationship between the accumulated deformation as given by the tensor  $\mathbf{D}$  and the velocity-gradient tensor  $\mathbf{L}$  may be summarized by the equation (Elliott, 1972, p. 2624)

$$\mathbf{D} = \int_0^t \mathbf{L} dt.$$

To determine  $\mathbf{D}$  for a specific flow geometry, we must solve this system of *differential equations*.

As we have seen, the deformation-rate tensor for simple shear flow is

$$\mathbf{L} = \begin{bmatrix} 0 & 0 \\ \dot{\gamma} & 0 \end{bmatrix}.$$

The solution of this problem is particularly simple. Assuming steady flow (constant  $\dot{\gamma}$ ) integrating each element in turn yields

$$\mathbf{D} = \begin{bmatrix} C_{11} & C_{12} \\ C_{21} + \dot{\gamma}t & C_{22} \end{bmatrix}$$

where the  $C_{ij}$  are constants of integration; to evaluate these constants we apply the *boundary conditions*. At the initial time  $t = 0$  the deformation is represented by the unit matrix

$$\mathbf{D} = \begin{bmatrix} 1 & 0 \\ 0 & 1 \end{bmatrix}.$$

Therefore the constants  $C_{11} = C_{22} = 1$  and  $C_{12} = C_{21} = 0$  and we then have

$$\mathbf{D} = \begin{bmatrix} 1 & 0 \\ \dot{\gamma}t & 1 \end{bmatrix} = \begin{bmatrix} 1 & 0 \\ \gamma & 1 \end{bmatrix} \quad (13.13)$$

and this result is identical to Eq. 11.37.

The deformation-rate tensor for pure shear flow is given by the matrix

$$\mathbf{L} = \begin{bmatrix} \dot{\epsilon} & 0 \\ 0 & -\dot{\epsilon} \end{bmatrix}. \quad (13.14)$$

This involves two simultaneous differential equations and its solution is more difficult (see Boyce & DiPrima, 1977, p. 105, 304). The result is that the tensor representing the total deformation for steady pure shear at any time  $t$  is given by

$$\mathbf{D} = \begin{bmatrix} \exp(\dot{\epsilon}t) & 0 \\ 0 & \exp(-\dot{\epsilon}t) \end{bmatrix}. \quad (13.15)$$



### 13.6 Deformation rates from structures

One approach to determining the strain rate is to estimate the total time it took the structure to develop and then to calculate an average rate at which the strain must have accumulated. Price (1975) has done this for a wide variety of structural environments (see Fig. 13.17). As an overall view this gives an important perspective but the exercise is fraught with difficulties.

The problem of dating the formation of structures is severe. The most common approach is to bracket the time of development by estimating the age of the youngest deformed strata and the age of the oldest strata which post-date the deformation. The stratigraphic control for these limiting dates is imprecise at best, and subject to large errors at worst.

Further, there is little way of evaluating the nature of the motion between these two bracketing dates. In a simple example the individual folds of a fold train probably develop serially rather than simultaneously. If so, this means that each component fold formed in a fraction of the total available time.

Commonly the total strain associated with a fold is measured by the overall horizontal shortening, but the rate calculated from this shortening is not the strain rate experienced by the material. At any instant the strain rate varies widely at various places in the material making up the fold from a maximum to a minimum, which may be zero.

Further, some common structures have quite complicated histories of progressive deformation. For example, individual buckle folds involve a sequence of three overlapping mechanisms: a preliminary stage of layer-parallel shortening which is a slow process (*A-Folding* in Fig. 13.17), the buckling stage itself is relatively rapid (*B-Folding*) and a final stage of flattening which is again slow (*C-Folding*).

A final difficulty is that the averaging process itself has serious problems (Piffner & Ramsay, 1982, p. 312). To show this we model the progressive stretch of a line by superimposing constant increments of extension  $\Delta e$  for each time step  $\Delta t$ . We can calculate the stretch at any time  $t$  from

$$S = (1 + \Delta e)^n \quad (n = 0, 1, 2, \dots, N).$$

The resulting history is shown graphically by the strongly non-linear curve in Fig. 13.18a. From the total stretch  $S_{total}$  at the final time  $N \Delta t$  we calculate the average rate of extension as

$$\dot{e}_{ave} = \frac{S_{total} - 1}{N \Delta t}.$$

This average is represented by the slope of the line joining points  $(0, 1)$  and  $(N \Delta t, S)$ .

The average rate can also be read off the graph as the length of the vertical line at time  $t = 1$  to the sloping line (Fig. 13.18b). Similarly, the actual rate of extension  $\dot{e}$  is represented by the vertical distance to the exponential curve. As can be seen  $\dot{e}_{ave}$  is much greater than  $\dot{e}$ , thus the averaging approach seriously overestimates the actual strain rate.

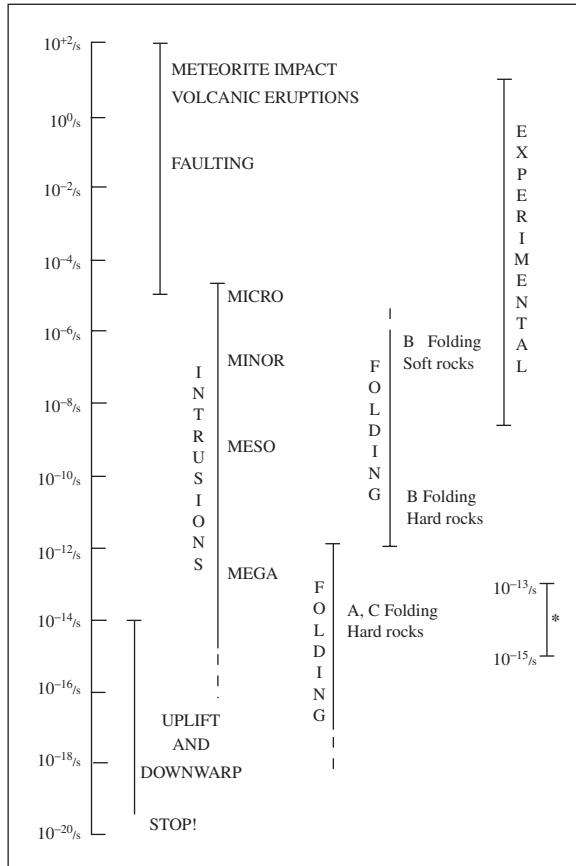


**Figure 13.17** Estimated deformation rates (after Price, 1975, p.574).

In an important contribution Pfiffner and Ramsay (1982) describe an alternative approach which overcomes some of these difficulties.

A large number of finite strain measurements have been made in a wide variety of settings (Pfiffner & Ramsay, 1982, Fig. A1). Many of these can be satisfactorily explained by two-dimensional deformations with volume change. Further, the structural settings in which many of these strained rocks occur also suggests that the deformations were essentially two dimensional. Strains as high as  $\gamma \approx 40$  have been measured in narrow shear zones and in mylonites along thrust planes. In less constrained settings, however, the common strain range is  $R_s = 1-10$ , and these can be characterized as moderate. Because measurements are usually made on objects which are more competent than the enclosing matrix, for example stretched belemnites, these results are usually minimum values. At the lower end of this range, strains at which slaty cleavage appears are characterized by  $R_s \approx 2$ . Below this level, strain is often less easy to detect or measure accurately.

Despite the general difficulty of dating periods of progressive deformation, results obtained from young fold-thrust belts such as the Alps, where the stratigraphic control

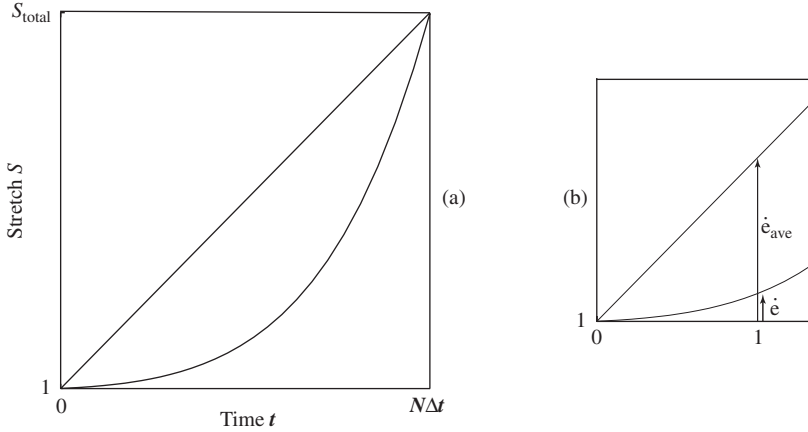


**Figure 13.18** One dimensional deformation: (a) stretch history; (b) details at  $t = 1$ .

is much better, appear to show that total strains accumulate in 1–30 million years. A preponderance of the data suggests a narrower range of 1–5 million years (Pfiffner & Ramsay, 1982, Fig. B1), and it is possible that significant strains associated with individual structures in fold-thrust belts may have accumulated in as short a time as 100 000 years.

Accepting, as a good approximation, that most deformations are essentially two dimensional, it is then likely that the range of associated vorticities, as expressed by the vorticity number, is  $\mathcal{W} = 0-1$ . In other words, simple shear flow (Eq. 13.12) and pure shear flow (Eq. 13.14) bracket most natural deformations.

We can then construct a graph of  $R_s$  vs. time for a realistic range of strain rates assuming steady flow which produce the observed total strains (Fig. 13.19). For flows lasting  $5 \times 10^6$  years strain rates faster than  $10^{-13}$ /s produce very high total strains, as in mylonite zones, or take much less time. Rates slower than  $10^{-15}$ /s lead to very small strains. We can then conclude that for most deformations there is a rather restricted range of strain rates (see the lower right-hand side of Fig. 13.17 where this range is marked with an asterisk). For flows lasting  $10 \times 10^6$  years the conclusions are similar. It is interesting to note that our calculated rates for the San Andreas Fault zone and the Appalachian garnet porphyroblast are within this range.

**13.7 Exercises**

1. Using the data from Table 13.1, calculate the strain rate  $\dot{\epsilon}$  for each of the eight segments across the San Andreas Fault zone.
2. Draw a circle on a card deck and shear the deck through a series of small increments. Observe the stages through which simple shear ellipses pass using the ellipse graph (see Fig. 13.16).

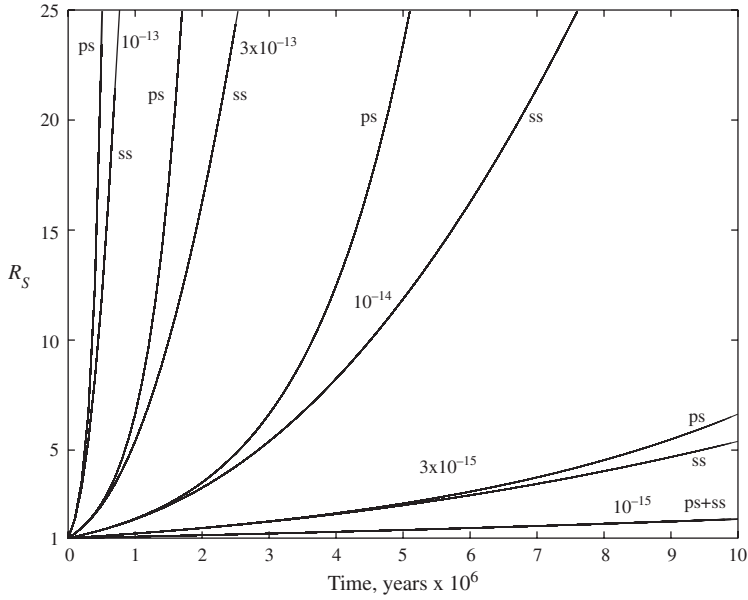


**Figure 13.19** Deformation rates for pure shear *ps* and simple shear *ss* (after Pfiffner & Ramsay, 1982).

3. Add two diameters to the initial circle on the deck making angles  $\theta > 90^\circ$  and  $\theta < 90^\circ$  with the shear direction. Again shear the deck through a series of small increments and observe the histories of the stretch of the two lines (see Fig. 13.9).

# 14

## Folds

### 14.1 Introduction

A *fold* is a distortion of a volume of rock material that manifests itself as a bend or nest of bends in linear or planar elements (Hansen, 1971, p. 8). Many folds involve elements which were originally planar. Sedimentary bedding is the common example, and this is an important case because the geometry of the fold then represents an important indicator of the nature of the deformation. In particular, its features can be correlated with certain aspects of rotation and stretch. However, folds may also develop from originally curved elements, and the problem of relating the features to the deformation is much more severe.

*Folding* occurs when pre-existing elements are transformed into new curvilinear or curvilinear configurations, whatever their original state. Thus folding is just an inhomogeneous deformation which acts on a body of material containing linear or planar elements (see Fig. 11.1). It is worth noting, however, that a deformation which produces a fold in one situation may not in another. Planar or linear elements may be entirely absent from the rock mass, and therefore there is nothing to mark a fold form. It is also possible that initially curved elements might become planar or linear, or that the elements may be so oriented as to remain planar or linear (Ramsay, 1967, p. 473).

In the following sections, a number of relatively simple geometrical properties of folded surfaces are explored. The methods and terminology follow closely the reviews by Fleuty (1964, 1987a) and also Ramsay (1967), and Ramsay and Huber (1987). Turner and Weiss (1963) and Hansen (1971) give many additional details.

### 14.2 Single surfaces

Naturally occurring curvilinear surfaces have a wide variety of forms ranging from comparatively simple, such as shown in Fig. 14.1, to exceedingly complex. The geometry of even a relatively simple curved surface may be quite difficult to describe in detail.

Mathematical methods are also available. Differential geometry deals with the analysis of surfaces and some interesting applications to folds have been made (see Lisle & Robinson, 1995; Bergbauer & Pollard, 2003). Pollard and Fletcher (2005, Chapter 3) give an excellent review of both theory and practice.

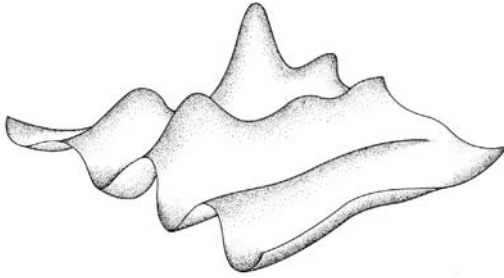


**Figure 14.1** A single curvilinear surface.

Fortunately, it is meaningful to restrict our initial consideration to a much simpler class of surfaces. Many natural folds have shapes which closely approximate the form of cylinders or are made up of approximately cylindrical parts (the folds in Fig. 14.1 become more nearly cylindrical from back to front). A *cylindrical surface* is defined as one which is generated by a line moved parallel to itself in space. The orientation of the generating line is a directional property of the entire surface and has no particular location. In this sense, it is analogous to a crystallographic axis and is called the *fold axis*. An important geometrical feature of cylindrical surface is that its shape can be fully represented in a cross-section drawn perpendicular to the axial direction. This is the *fold profile*.

The trace of a folded surface on the profile plane is a curve and such a curve has several geometrical features which serve to identify certain points on it. The *crest* or high point and the *trough* or low point on the curves are two such features. In three dimensions, each of these points is the intersection of a line and the profile plane. These are the *crest line* and the *trough line*, and they are parallel to the axis. The location of both of these is dependent on the orientation of the folded surface relative to horizontal. On the other hand, the point of maximum curvature, or *hinge point*  $h$ , and the point where the curve changes from concave to convex, or *inflection point*  $i$ , are independent of any reference frame and are, therefore, spatially *invariant*. Such features serve to describe the geometry of cylindrical folds more fundamentally (Fig. 14.2).

Although there are exceptions, hinge and inflection points commonly alternate. In three dimensions such points lie on *hinge lines* and *inflection lines*, and it is convenient to consider a single fold as the portion of the curved surface between the inflection lines on either side of the hinge.

1. If a portion of the profile curve is a circular arc the fold does not have a specific hinge point and it is then arbitrarily identified as the bisector of the circular segment.

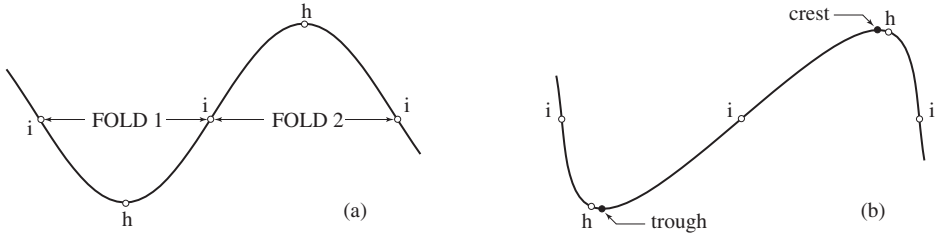


**Figure 14.2** A cylindrical folded surface in profile.

2. Similarly, there will be no inflection point if the transition from concave to convex involves a straight segment; the inflection point is then arbitrarily taken to be the midpoint.

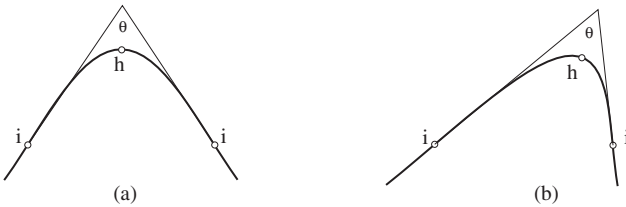


**Figure 14.3** Interlimb angle.

An important character of fold shape is the *interlimb angle*  $\theta$ , defined as the minimum angle between the limbs as measured in the profile plane, or, alternatively, between the lines tangent to the curve at the inflection points (Fig. 14.3). This angle describes the *tightness* of the fold. For general purposes, however, it is often sufficient to categorize the angular relationship between fold limbs with descriptive adjectives. The terms *gentle*, *open*, *close*, *tight*, *isoclinal* and *mushroom (or elastica)* are commonly used. Fleuty (1964, 1987a) suggested that these terms be restricted to specific ranges of interlimb angles (see Table 14.1).

**Table 14.1** *Fold tightness*

Interlimb angle	Descriptive term
180°–120°	Gentle
120°–70°	Open
70°–30°	Close
30°–0°	Tight
0°	Isoclinal
Negative angles	Mushroom

After Fleuty, 1964, 1987a

The terms *hinge zone* and *fold limb* and the distinction between them have been precisely defined in a form which is useful for some advanced purposes (Ramsay, 1967, p. 345). Here, however, a more general meaning is adopted which follows conventional usage (Dennis, 1967, p. 88, 102). The hinge zone is considered to be that portion of the curved surface adjacent to the hinge point and the fold limb to be that part of the surface adjacent to the inflection point. The proportion of the entire curved surface which may be considered to be hinge zone and limb may vary. The extremes occur in chevron folds where the hinge zone is reduced to a point (Fig. 14.4a) and where the folds have the form of linked arcs the limb is represented by the inflection point (Fig. 14.4b). These and intermediate shapes may be described qualitatively as *angular*, *subangular*, *subrounded* or *rounded*.



**Figure 14.4** Limbs and hinge zones.

Symmetry is another invariant feature of cylindrically folded surfaces. Considering only the shape of the surface, every cylindrical fold has at least one plane of symmetry which is perpendicular to the fold axis. If, in addition, a second plane passing through the hinge line and bisecting the interlimb angle is also a plane of symmetry, the fold shape in profile is said to be *symmetric*.

A series of linked folds are symmetric if each member is symmetric and if the pattern is periodic. A consequence is that the two enveloping surfaces are planar and parallel, and the surface containing all the inflection points, or *median surface*, is mid-way between the two enveloping surfaces. These features of symmetric folds make it easy to describe the dimensions of the folds in terms of *amplitude* and *wavelength* (see Fig. 14.5a).

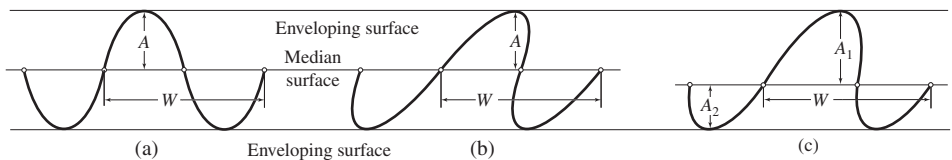


**Figure 14.5** Fold dimensions: wavelength  $W$  and amplitude  $A$ .



With no such plane of symmetry, the fold is *asymmetric*.<sup>1</sup> In the simple case, the line connecting the inflection points may still be the median and dimensions are established just as before (Fig. 14.5b). Or there maybe two separate amplitudes (Fig. 14.5c).

For such folds it is useful to describe the sense of the asymmetry. This is commonly done in terms of *vergence*, or the direction in which an antiformal hinge has been displaced relative to a synformal hinge.

In *overturned folds* or *overfolds* both limbs dip in the same direction and the vergence is in the direction of overturning. If the fold axis is approximately horizontal, the vergence is described unambiguously by giving its azimuth (Bell, 1981). For folds with plunging axes, a useful alternative describes the sense of asymmetry as clockwise or anticlockwise when viewed in a down-plunge direction. The profile curves of Figs. 14.4b and 14.4c show clockwise vergence.

The description of the dimensions of asymmetric folds becomes increasingly involved as the degree of asymmetry increases and more complete schemes have also been suggested (Fleuty, 1964, 1987a; Ramsay, 1967, p. 351; Hansen, 1971, p. 9).

Twiss (1988) introduced an alternative approach to describing and analyzing the shapes of cylindrical surfaces. As a reference standard, a *perfect fold* is defined as a single-hinged, perfectly symmetrical fold with perfectly straight limbs and a hinge zone which is a perfect circular arc (Fig. 14.6). Real imperfect folds are compared against this standard. This involves three parameters.

1. The *aspect ratio*  $P$  is the ratio of the amplitude  $A$  to half the wavelength  $M$  (Fig. 14.6a):

$$P = A/M. \quad (14.1a)$$

With  $P$ , the fold can then be assigned a descriptive term (Table 14.2).

2. The *bluntness* of a fold is a measure of how round or angular the hinge zone is. The *bluntness ratio* is defined as  $B = r_h/r_i$ , where  $r_h$  is the radius of curvature of the hinge zone and  $r_i$  is the radius of the circle tangent to the limbs at the two inflection points (Fig. 14.6b). This bluntness ratio becomes very large for double-hinged and chevron folds. To avoid the resulting awkwardness the *bluntness*  $b$  is used instead.

$$b = \begin{cases} r_h/r_i & \text{if } r_h \leq r_i, \\ 2 - r_i/r_h & \text{if } r_h \geq r_i. \end{cases} \quad (14.1b)$$

With  $b$ , a descriptive term can then be applied (Table 14.2).

3. Fold tightness is expressed by the fold angle  $\phi$ , which is the angle between the two radii of the reference circle through the inflection points (Fig. 14.6b). This is the angle

<sup>1</sup>For Turner and Weiss (1963, p. 122) an asymmetric fold has limbs which dip at different angles, but this is a matter of fold orientation rather than fold shape.

through which the two limbs have been rotated; it is the supplement of the interlimb angle ( $\theta = 180 - \phi$ ). By this definition the angles between the limbs and the median surface are  $\frac{1}{2}\phi$ . There are then two broad fold types: *acute* folds ( $\frac{1}{2}\phi < 90$ ) and *obtuse* folds ( $\frac{1}{2}\phi > 90$ ); *isoclinal* folds are the boundary case ( $\frac{1}{2}\phi = 90$ ). Within these classes descriptive terms can then be applied based on the value of the angle  $\phi$  (Table 14.3).

Table 14.2 Aspect ratio  $P$  and bluntness  $b$

Term	Aspect ratio	Term	Bluntness
Wide	$0.1 \leq P < 0.25$	Sharp	$0.0 \leq b < 0.1$
Broad	$0.25 \leq P < 0.63$	Angular	$0.1 \leq b < 0.2$
Equant	$0.63 \leq P < 1.58$	Subangular	$0.2 \leq b < 0.4$
Short	$1.58 \leq P < 4$	Subrounded	$0.4 \leq b < 0.8$
Tall	$4 \leq P < 10$	Rounded	$0.8 \leq b \leq 1$
		Blunt	$1 \leq b \leq 2$

After Twiss, 1988, p. 609

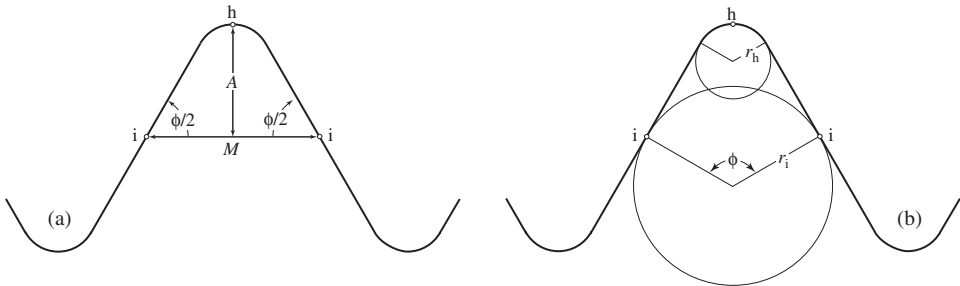


Figure 14.6 Geometry of a perfect fold: (a) aspect ratio; (b) bluntness.

Table 14.3 Fold tightness: folding angle  $\phi$  and interlimb angle  $\theta$

Term		Folding angle	Interlimb angle
Acute	Gentle	$0 < \phi < 60$	$180 > \theta > 120$
	Open	$60 \leq \phi < 110$	$120 \geq \theta > 70$
	Close	$110 \leq \phi < 150$	$70 \geq \theta > 30$
	Tight	$150 \leq \phi < 180$	$30 \geq \theta > 0$
Isoclinal		$\phi = 180$	$\theta = 0$
Obtuse	Fan	$180 < \phi < 250$	$0 > \theta > -70$
	Involute	$250 \leq \phi \leq 360$	$-70 \geq \theta \geq -180$

After Twiss, 1988, p. 609

### 14.3 Relationships between surfaces

Because folds almost invariably involve more than one surface, additional terms and methods are needed to establish the spatial and geometrical relationship between adjacent surfaces. These relationships are also the basis for classifying the shape of folded layers (see §14.6).

The locus of the hinge lines on adjacent surfaces is an important feature of fold geometry, especially from the point of view of field mapping. This discrete surface is often referred to as the *axial plane* or the *axial surface* but it is not directly related to the axis. Indeed non-cylindrical folds may possess such a surface without having an axis. This feature is more appropriately called the *hinge surface* (Fig. 14.7). Preferably *axial plane* should be reserved for the plane parallel to the hinge surface throughout the entire cylindrical fold, as in the phrase *axial plane cleavage* (Oertel, 1962; Donath & Parker, 1964; Fleuty, 1987a). This distinction is not always observed so it is important to understand that the term *axial plane* may be used in two quite different meanings.

In addition to the hinge surface, there is also an *inflection surface*, which is the locus of inflection lines on successive surfaces. Similarly there are *crestal* and *trough* surfaces.

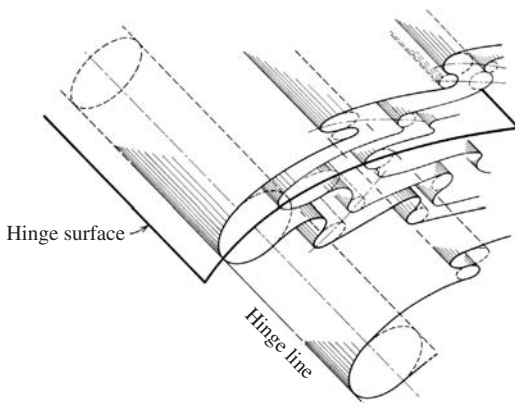


**Figure 14.7** Hinge surfaces of cylindrical folds (after Wilson, 1961, 1982).

### 14.4 Associated structures

Two structures are commonly found in association with folds: *cleavage*<sup>2</sup> and *minor folds* (see also Wilson, 1982; Fleuty, 1987a).

Where folds and cleavage develop synchronously, the usual case is that the cleavage closely approximates the orientation of the hinge surface. The qualification “approximate” is needed because this cleavage commonly displays a fan-shaped pattern, commonly as a *convergent cleavage fan* (convergent here means when traced from the outer

<sup>2</sup>A number of cleavage types have been recognized and named (Dennis, 1967, p. 17–24), but two are particularly important here: slaty or continuous cleavage and spaced cleavage. A comprehensive treatment of field identification of first-generation cleavages is given by Durney and Kisch (1994).

to inner arc) or sometimes as a *divergent cleavage fan* (Ramsay, 1967, p. 405). Cleavage often changes direction abruptly when passing from a layer of one lithology into another.

As a consequence of this axial plane character of the cleavage, there are two additional relationships which are of great importance in the field study of folds.

1. The line of intersection of the cylindrically folded layers and the cleavage is parallel to the hinge line and therefore its orientation gives the axial direction of the fold even without observing a hinge.
2. The angular relationship between the bedding and cleavage as seen in the profile plane allows the antiformal and synformal hinges to be located from a single exposure. At a single outcrop, a sandstone bed is observed to dip due  $40^\circ$  west; the underlying slate with cleavage dips  $80^\circ$  due west (Fig. 14.8). Where are the folds? If the hinge surface is parallel the cleavage, then an antiformal hinge must lie to the east and a synformal hinge to the west. Of course nothing can be said about the size of these folds from a single exposure.

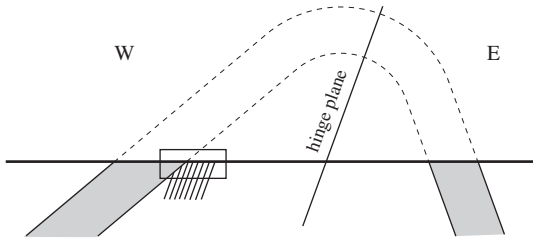


**Figure 14.8** Cleavage–bedding intersections to locate antiforms and synforms.

Cleavage–bedding intersections can be used in still another way. In terms of working out the structure of an area, it is of utmost importance to correctly identify anticlines and synclines. This can be done in a number of ways. If the stratigraphy is well known, it is a simple matter to determine the relative age of the rocks in the core of the fold. If they are older, then the fold is an anticline and if they are not it is a syncline. Another way is through the use of sedimentary structures. As deposited sedimentary rocks are said to *face* upward and in any subsequent attitude they continue to face toward the side that was originally upward and younger. This *direction of younging* can be identified from a study of a variety of sedimentary structures, including cross bedding, graded bedding and ripple marks.

It is useful to extend this concept of facing to the folds themselves. In the case of a normal, upright fold the *structural facing* is upward, and this can be confirmed immediately by determining the direction in which the sedimentary beds of the fold face. Where the folds have overturned limbs, some beds will face downward and some upward and, especially where exposures are sparse, the direction of structural facing may be obscure. However, this direction can be determined unambiguously by an examination of the

beds at the hinges of the folds (Cummins & Shackleton, 1955; Shackleton, 1958; also Holdsworth, 1988).

The direction of structural facing can also be determined at a single outcrop by the application of a simple principle. While the direction of the facing of an individual bed is greatly affected by its local attitude, the component of the facing direction projected onto the axial plane cleavage has a constant direction regardless of the orientation of the bedding (Borradaile, 1976). The situation is illustrated in Fig. 14.9. While the beds of a series of folds have considerable variation in the direction of younging, the component on the cleavage plane is consistently oriented. The identification of the direction of structural facing of folds through the use of sedimentary structures has come to be known as *Shackleton's rule*.

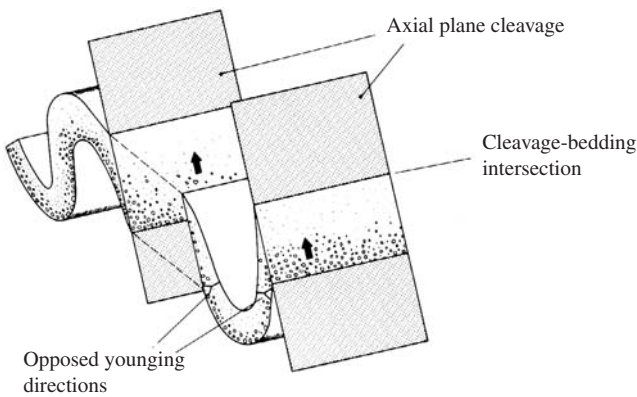


**Figure 14.9** Younging directions on fold limbs have a consistent facing direction on cleavage (from Borradaile, 1976, with permission of Koninklijke Nederlandse Akademie van Wetenschappen).

A profile through a hypothetical area with two phases of folding illustrates the practical importance of this rule. A large, westward closing recumbent anticline has been refolded by smaller, nearly upright antiforms and synforms. The younging directions plotted on the map do not readily indicate the location of the now folded hinge surface of the first fold (Fig. 14.10a). When projected onto the axial plane cleavage of the second folds, however, the directions of the structural facings immediately become apparent, and fall into two groups (Fig. 14.10b). The second phase folds above the first hinge surface face upward, and those below it face downward. In this way, the location of the trace of the hinge surface is identified by the reversals in the facing directions.

This example will also make clear why cleavage–bedding relations alone are insufficient to determine the direction of structural facing, and therefore to allow individual folds to be identified as anticlines and synclines (see Billings, 1972, p. 400f).

Minor folds developed in thin beds may also be used as an aid in working out the structure of an area. It has been observed in many areas that these smaller folds often share axes and axial planes with the main fold, a rule of thumb known as *Pumpelly's rule* (Pumpelly, *et al.*, 1894, p. 158). Such minor folds often show a strong asymmetry with a vergence which is consistently toward the hinges of the antiforms. Such features

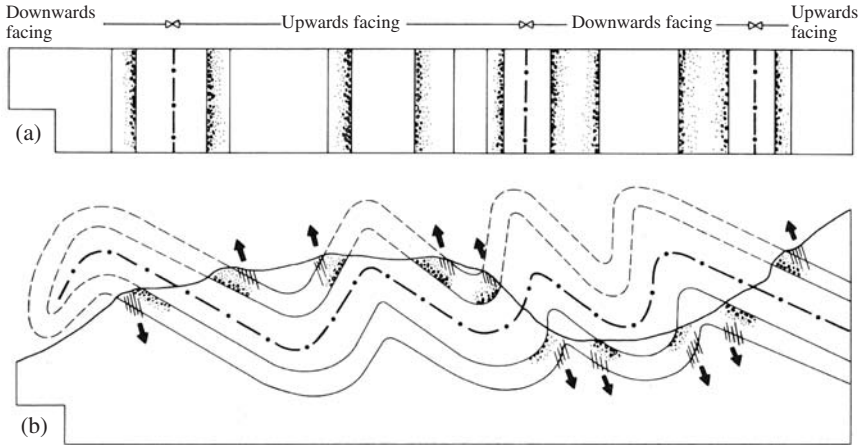


**Figure 14.10** Two phases of folding: (a) map and local younging directions; (b) section to locate the hinge surface of the first fold (after Borradaile, 1976, with permission of Koninklijke Nederlandse Akademie van Wetenschappen).

are useful in identifying large folds when exposures are poor. A short-hand notation has developed to emphasize these relationships. The strongly asymmetric folds on one limb are denoted *Z* folds and those on the other are *S* folds, while the more nearly symmetric folds in the hinge zone are *M* (or *W*) folds (see Fig. 14.11).

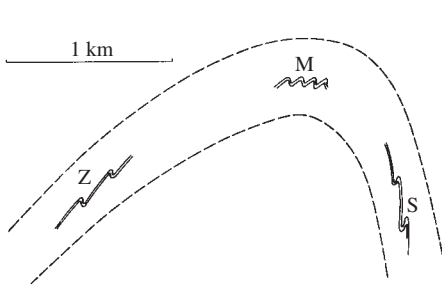


**Figure 14.11** *Z*, *S* and *M* minor folds.

Such minor folds are sometimes referred to as “drag” folds but this is inappropriate for at least two reasons. First, it introduces genetic connotations into what should be a descriptive terminology. Further, the name implies that such folds formed in response to the slipping of the layers past one another producing something like simple shear in the layer containing the small folds by drag. As we have already seen, the shear direction in simple shear is a direction with no finite elongation and yet it is clear that the small folds have indeed shortened in this direction. This makes the concept of drag as a mechanism of folding questionable, though, of course, the shape of small folds once formed by layer-parallel shortening would change shape due to the shear. The most reasonable explanation of Pumpelly’s rule is that the minor folds are small because the layers in which they

form are thin, and they share axes and axial planes with the main folds because the same pattern of deformation is responsible for both (Ramberg, 1987).

As with *all* such empirical rules there are exceptions. For example, the cleavage may not closely parallel the axial plane. This may be the result of superposition of two differently oriented deformations or of a more complex single deformation involving a large rotational component. The term *transected fold* describes this more complex situation (Powell, 1974, p. 1045; Borradaile, 1978). Minor folds may show similar departures from the orientation of the main fold. From a practical point of view the existence of such lower symmetry folds means that these empirical rules must be tested before great reliance is placed upon them.

### 14.5 Fold orientation

The orientation of a cylindrical fold is completely defined by the attitude of the hinge and hinge plane together with a statement of the direction in which the limbs converge at the hinge or *closure*. *Antiforms* close upward and *synforms* close downward. The terms *anticline* and *syncline* are reserved for folds with older and younger rocks, respectively, in their cores. Most anticlines are also antiforms, and all anticlines start their existence as antiforms. It is possible, however, for an anticline to be turned completely over so that it closes downward; such a fold would be described as an anticline in synformal position, or, simply, a synformal anticline. Synclines show similar patterns.

The angles of dip and plunge are also the basis for a descriptive nomenclature. In an effort to standardize usage Fleuty (1964, 1987a) suggested precise limits to a series of traditional terms for both dip and plunge (see Table 14.4). These terms can then be combined to describe the attitude of a fold: for example, a steeply-dipping, gently-plunging fold. Note, however, that because the hinge line is confined to the hinge plane, some combinations of terms are invalid: for example, a gently-inclined, steeply-plunging fold is impossible.

Table 14.4 *Terms describing the attitude of the hinge plane and the hinge line*

Angle	Term	Dip of hinge plane	Plunge of hinge line
0°	Horizontal		
		Recumbent	Horizontal
1°–10°	Subhorizontal		
10°–30°	Gentle	Gently inclined	Gently plunging
30°–60°	Moderate	Moderately inclined	Moderately plunging
60°–80°	Steep	Steeply inclined	Steeply plunging
80°–89°	Subvertical		
		Upright	Vertical
90°	Vertical		

After Fleuty, 1964, 1987a

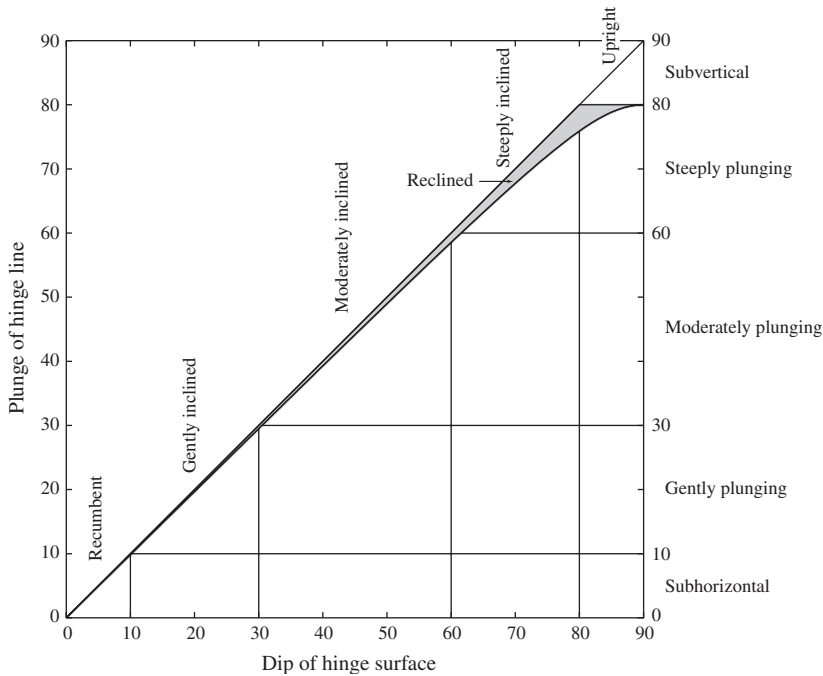


**Figure 14.12** Graph of fold attitudes (after Fleuty, 1964, 1987a; Ramsay, 1967, p. 360).

Folds which close sideways are *neutral* and these require special attention. *Recumbent* applies to neutral folds with both hinge lines and hinge planes within  $10^\circ$  of horizontal. *Vertical* folds have hinge lines and planes within  $10^\circ$  of vertical. Both of these terms are included in the table. These two are end-members in a continuous series of orientations which are termed *reclined*, that is, neutral folds with hinge planes which dip at angles of  $10^\circ$  to  $80^\circ$  and hinge lines which pitch more than  $80^\circ$  in this plane. Because the dip can be greater than  $80^\circ$  and the plunge still less than  $80^\circ$  on this plane required for designation as vertical, it is not practical to place a precise upper limit on the dip of the hinge plane. This minor discrepancy is the result of using the plunge angle in the description of some folds and the pitch in others.

All possible fold orientations are summarized in the graph of Fig. 14.12. The shaded area defines the attitudes of reclined folds; its curved lower boundary gives the plunge of the hinge line with a pitch of  $80^\circ$  on the hinge plane.

The basic weakness of this approach is the result of referring the attitude of the hinge line to a vertical plane through the use of the angle of plunge, even though this plane generally bears no relationship to fold geometry. A classification based solely on dip and pitch could be constructed but would itself have drawbacks, the gravest of which is that pitch is often difficult to measure in the field.

Rickard (1971) devised a simpler approach which avoids this artificial distinction between plunge and pitch, through the use of a triangular diagram (Fig. 14.13).



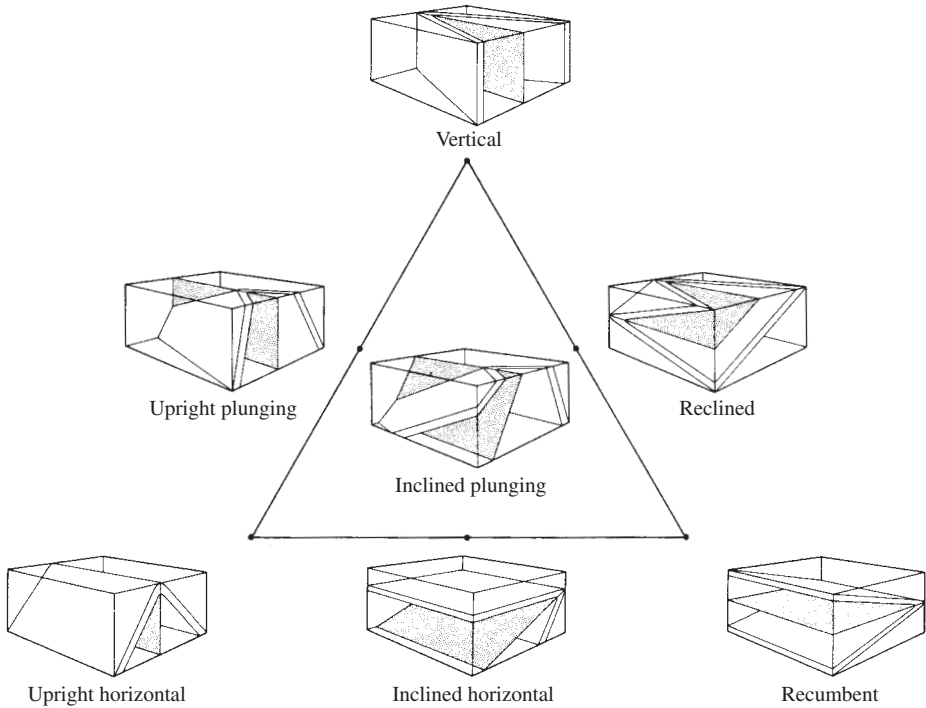


**Figure 14.13** Triangular graph of fold attitudes (after Fleuty, 1964, 1987a; Rickard, 1971).

1. The three special cases are represented by the vertices of the triangle: *upright horizontal folds*, *vertical folds* and *recumbent folds*.
2. The transitions between pairs of these three orientations are represented by the sides of the triangles: *upright plunging folds*, *reclined folds* and *inclined horizontal folds*.
3. General *inclined plunging folds* are represented by the main body of the triangle.

In practice, a special triangular grid is used to classify fold attitudes (Fig. 14.14a). The first step is to represent the fold using an index number: the dip  $D$  of the hinge plane and the plunge  $P$  of the hinge. For example, the fold attitude  $D_{70} P_{50}$  is represented by the point of intersection of the sloping dip lines parallel to the left side of the triangle and the curved plunge lines (see the plotted point on Fig. 14.14a). This point could have also been located by using the pitch angle  $R$ , giving the index  $D_{70} R_{55}$  and using the lines radiating from the vertex of the triangle on the right.

Once this point is plotted, we can then establish the attitude class using the fields delineated on the triangle (Fig. 14.14b). Although the main body of the figure could also be subdivided, it is simpler to name only the special cases with respect to horizontal and vertical. For the more general case, precision is obtained with the use of the index number.

This diagram can also be used to bring out additional details about the folds of an area. If the folds progressively change orientation in some direction, or if some aspect of fold

geometry, such as the interlimb angle, changes with attitude, these variations could be emphasized by a series of points perhaps connected by a curve drawn through them.

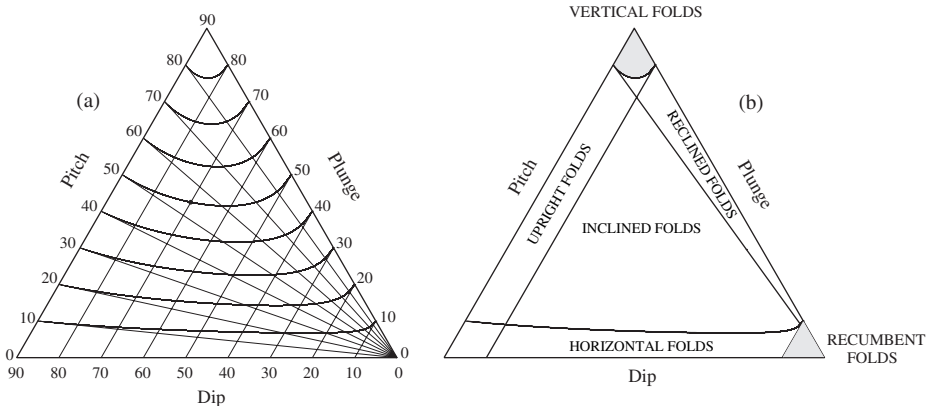


**Figure 14.14** Fold attitudes: (a) plotting grid; (b) classifying fold attitude (after Rickard, 1971).

The value of these several graphical schemes for analyzing and displaying the orientation of folds lies in their comprehensiveness. However, often a simpler approach may suffice. One such approach uses the polar net (Fig. 14.15).

### Technique

1. Plot the attitude of the hinge line. Using the labeled annular fields in the upper part of the diagram, assign the appropriate orientation category.
2. Plot the pole of the hinge plane. Using the labeled annular fields in the lower part of the diagram, assign the appropriate orientation category.

## 14.6 Isogon classification

The geometrical relation between adjacent surfaces is a particularly important aspect of fold shape and it depends on the relative curvature of the two surfaces and the distance between them. A simple and sensitive way of describing this relationship is to construct tangent lines of equal inclination on two surfaces bounding a single layer. The line connecting the points of equal dip is a *dip isogon* (Ickes, 1923; Elliott, 1965; Ramsay, 1967, p. 363). Not only can the resulting patterns aid in distinguishing accurately between different fold forms but the use of isogons also leads to a classification of fold geometry which is both simple to apply and easy to remember, and it is now widely used.

### Construction

1. Obtain a profile of the fold. The most direct and accurate method is to use a photograph taken in the direction of the fold axis. If such a view is not possible, either because of

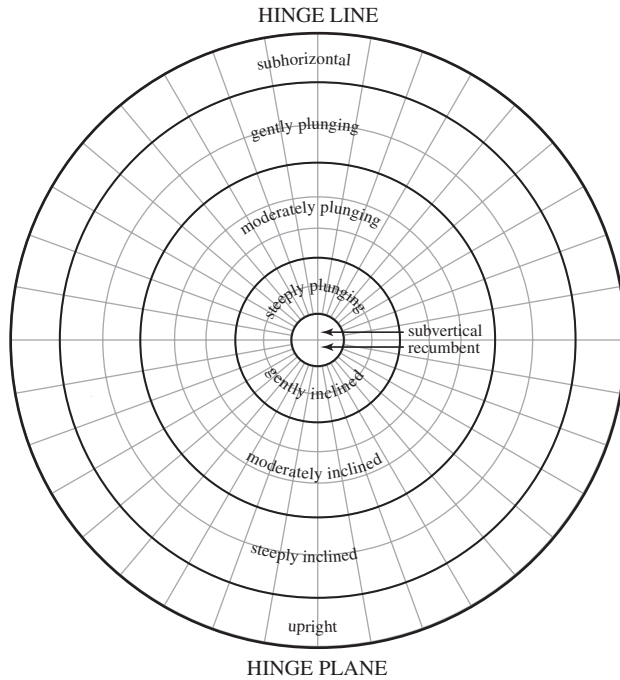


**Figure 14.15** Fold attitude and the Polar Wulff Net (after Lisle & Leyshon, 2004, p. 103).

lack of exposure or large size, the profile view may be constructed from a carefully drawn map (see Chapter 16).

2. On an overlay sheet, carefully trace the curved boundaries of a folded layer.
3. The placement of the specific isogons depends on the orientation of the fold on the profile plane. The pattern of the isogons is, like the shape they reflect, an invariant feature of the fold. It is, therefore, common practice to reorient the fold profile so that a tangent line at the hinge is horizontal ( $\alpha = 0$ ).
4. On each bounding curve draw a tangent inclined at a dip angle  $\alpha$  (Fig. 14.16a). These parallel tangents can be constructed quite easily with the aid of a protractor and a triangle. Marjoribanks (1974) described an instrument which is useful if large numbers of folds are to be analyzed.
5. Connect the two points of equal dip on the two adjacent bounding curves with a straight line; this is an *isogon* (Fig. 14.16a).
6. Repeat at a number of points around the fold. Tangent lines at  $10^\circ$  intervals is often convenient but the choice should be dictated by the actual form of the fold. For purposes of classification, usually there is no need for closely spaced tangent points. Finally, connect the pairs of tangent points (Fig. 14.16b).

Generally the isogons will not be parallel and the degree of departure from parallelism, together with the direction of convergence or divergence, is the basis for a useful geo-

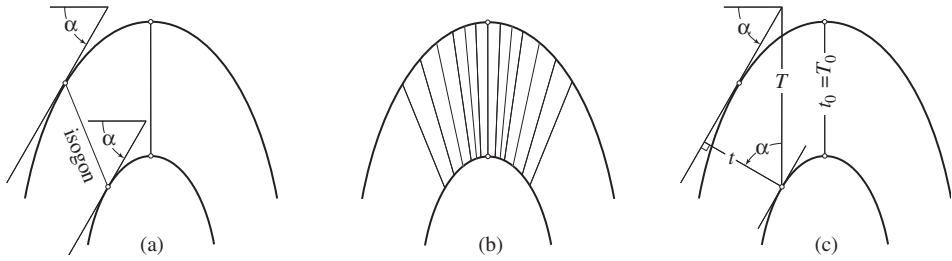


**Figure 14.16** Dip isogons: (a) construction; (b) isogon pattern; (c) thickness variation.

metrical classification (Ramsay, 1967, p. 365). For consistency the inner arc of the fold is taken as the reference point for statements of the direction of isogon convergence. Accordingly, there are then two basic patterns – isogons may *converge* or *diverge*. These can be subdivided into five easily recognizable patterns, including three general and two special cases.

1. *Folds with convergent isogons* (Class 1):

- (a) *Folds with strongly convergent isogons* (Class 1A): the curvature of the outer surface is less than that of the inner, and the smallest distance between the two surfaces occurs along the trace of the hinge surface (Fig. 14.17a).
- (b) *Parallel folds* (Class 1B): the inner surface has a greater curvature than the outer one, but their relationship is such that each isogon is perpendicular to the tangents (Fig. 14.17b). The name is derived from the fact that the distance between the two curves measured along the isogons is constant.
- (c) *Folds with weakly convergent isogons* (Class 1C): the curvature of the inner surface is still greater, but the spacing between the two curves is greatest at the hinge (Fig. 14.17c).

2. *Similar folds* (Class 2): both curves are identical and the isogons are parallel. The name is derived from the fact that the distance between the two curves measured along the isogons is constant (Fig. 14.17d).

3. *Folds with divergent isogons* (Class 3): the curvature of the inner arc is less than that of the outer arc (Fig. 14.17e)

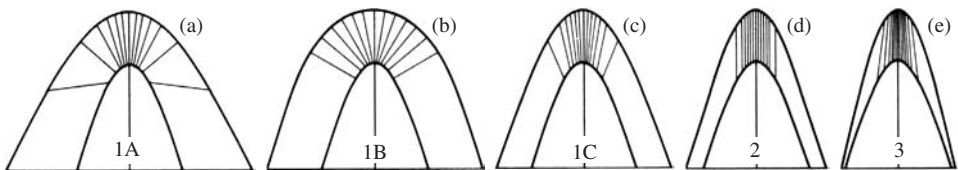


**Figure 14.17** Classification: (a) strongly convergent; (b) parallel; (c) weakly convergent; (d) similar; (e) divergent.

The isogon-thickness classification is now widely used, but its application is not without some limitations (see Lisle, 1997, p. 326 for a review of developments and some further details).

1. The trace of the hinge plane may not be perpendicular to the tangents at the hinge points (Hudleston, 1973, p. 10).
2. There may be places in the folded layer where isogons are not be definable. If the steepest dip on one surface exceeds the steepest dip on the adjacent surface there will be a sector where it is not possible to construct a pair of corresponding parallel tangents and therefore the isogons do not exist here (Ramsay & Huber, 1987, p. 356).
3. Some folds may have parts related to several fold classes (Ramsay, 1967, p. 369–371, 407–410). For example, the opposing limbs of strongly asymmetric folds commonly have different shapes. For even more complex folds single limbs may exhibit several different shapes.

### 14.7 Thickness variation

Fundamentally the isogon patterns reflect the way in which the thickness of the layer varies around the fold. There are two measures of this thickness (Fig. 14.16c).

1. *Orthogonal thickness*  $t$  is the perpendicular distance between pairs of tangent lines drawn at points of equal dip angle  $\alpha$  on the traces of the upper and lower bounding surfaces.<sup>3</sup> In general  $t$  varies with  $\alpha$ , which we express by the symbol  $t_\alpha$ . In order to compare the shapes of folds of different sizes it is convenient to express this measure as a proportion of the orthogonal thickness at the hinge  $t_0$ . Thus

$$t'_\alpha = t_\alpha / t_0, \quad (14.2)$$

where  $t'_\alpha$  is *normalized orthogonal thickness*.

2. *Axial plane thickness*  $T$  is the distance between pairs of tangent lines drawn at points of equal dip angle  $\alpha$  on the traces of the upper and lower bounding surfaces measured parallel to the trace of the hinge plane. In general  $T$  varies with  $\alpha$ , which we express by the symbol  $T_\alpha$ . This may also be expressed as a proportion of the axial thickness at the hinge  $T_0$ :

$$T'_\alpha = T_\alpha / T_0, \quad (14.3)$$

where  $T'_\alpha$  is the *normalized axial plane thickness*.<sup>4</sup>

<sup>3</sup>This corresponds to the definition of thickness for tabular bodies of rock (see §2.1).

<sup>4</sup>These normalized thicknesses are commonly given the symbols  $T'$  and  $t'$  (Ramsay, 1967, p. 360; Hudleston, 1973, p. 6; Lisle, 1997), and we follow this usage. Note, however, that such usage is quite different from the notation for variables in a deformed state or variables for a transformed coordinate system (see also §14.9).

These two measures of thickness are not independent. From Fig. 14.16c

$$t'_\alpha = T'_\alpha \cos \alpha \quad \text{or} \quad T'_\alpha = t'_\alpha / \cos \alpha = t'_\alpha \sec \alpha. \quad (14.4)$$

The detailed thickness variation of every folded layer can be recorded as a curve on a graph of thickness as a function of dip angle. Two different graphs are in use.

1. One is a plot of  $T'/\alpha$  (Fig. 14.18a). Similar folds (Class 2) have constant axial plane thickness and so plot as a horizontal straight line.
2. The other is a plot of  $t'/\alpha$  (Fig. 14.18b). Parallel folds (Class 1B) have constant orthogonal thickness and so plot as a horizontal straight line.

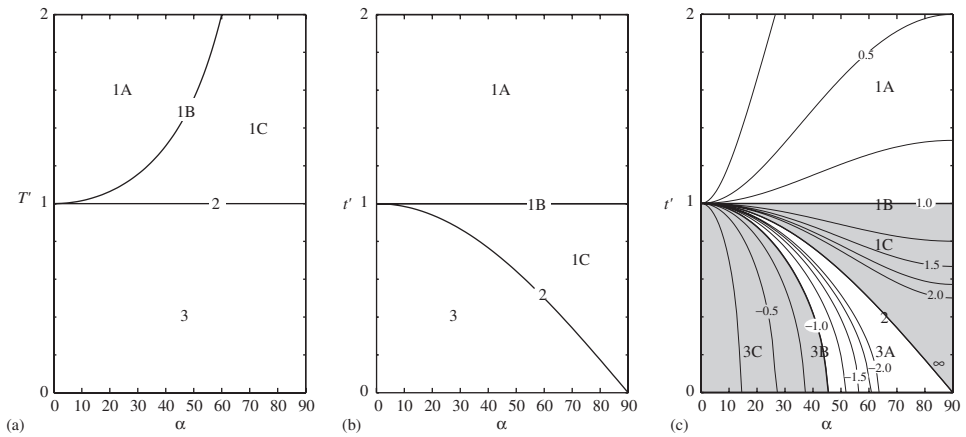


**Figure 14.18** Fold classification and thickness variation: (a) graph of  $T'/\alpha$ ; (b) graph of  $t'/\alpha$ ; (c)  $t'/\alpha$  graph with curves of constant flattening index (after Ramsay, 1967, p. 366; Lisle, 1997).

### 14.8 Alternative graphs

Hudleston (1973) proposed an alternative approach which plots the *isogon angle*  $\phi$  against limb dip  $\alpha$ . As before, the orientation of the fold profile is standardized so that it appears as an upright antiform with the tangent at the hinge horizontal. The angle between the normal to the tangent and an isogon is  $\phi$ ; it is reckoned positive when measured in an anticlockwise sense from the tangent normal (Fig. 14.19a).

The angle of dip  $\alpha$  is taken positive on the right limb and negative on the left. Then the right limb is represented on the right side of the graph and the left limb on the left side (Fig. 14.19b).

A  $\phi/\alpha$  plot yields a curve which characterizes the fold geometry, and at the same time also identifies the class just as the  $t'/\alpha$  plots do. The properties of these classes are also given in Table 14.5.

Table 14.5 *Fold classes based on isogon angle  $\phi$  for positive  $\alpha$*

Fold class	$\phi$
1A	$\phi < 0$
1B parallel	$\phi = 0$
1C	$\alpha > \phi > 0$
2 similar	$\phi = \alpha$
3	$\phi > \alpha$

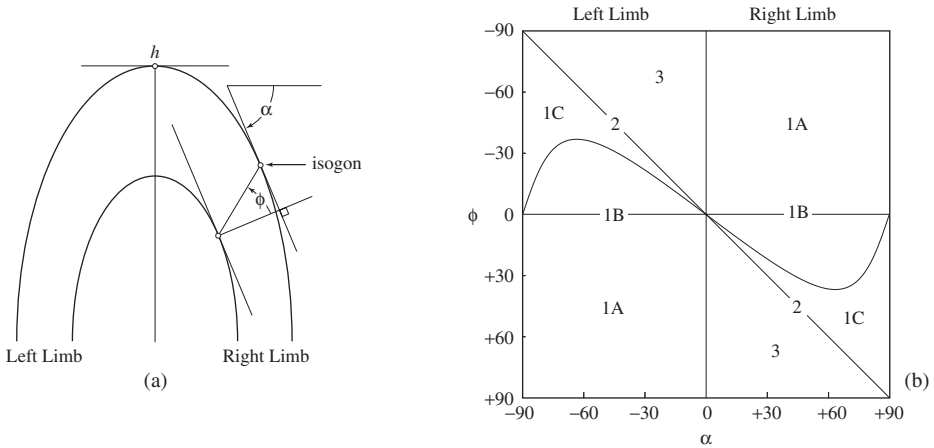


Figure 14.19 Isogon angle: (a) fold and isogon angle  $\phi$ ; (b) graph of  $\phi$  vs.  $\alpha$  (after Hudleston, 1973, p. 7).

The  $t'/\alpha$  and  $\phi/\alpha$  plots have differences, including both advantages and disadvantages (Hudleston, 1973, p. 12–13). The result is that they complement one another in useful ways.

Treagus (1982) adapted Hudleston’s graphical approach to display the variation in cleavage orientation around folded layers (Fig. 14.20a). In this case, the cleavage angle  $\beta$ , defined as the angle between tangent normal and cleavage trace, is used (Fig. 14.20b). Because the cleavage will not, in general, be parallel to the isogons the angle  $\beta$  will be different when measured at the upper and lower boundaries of a folded layer. To be consistent, therefore, one should be picked (in Fig. 14.20b the lower boundary of the layer is used).<sup>5</sup>

The cleavage orientation in several layers with different lithologies can then be displayed as curves on the *cleavage orientation graph* (Fig. 14.20c). From these curves, the patterns can be classed using the same subdivisions as in Hudleston’s graph; these are labeled with roman numerals to distinguish them from the related, but different isogon

<sup>5</sup>We will make important use the cleavage angle  $\beta$  in §14.12.

classes. A folded layer then can be assigned a dual classification, such as 1C/IC or 2/II, or even less simple combinations such as 1C/II.

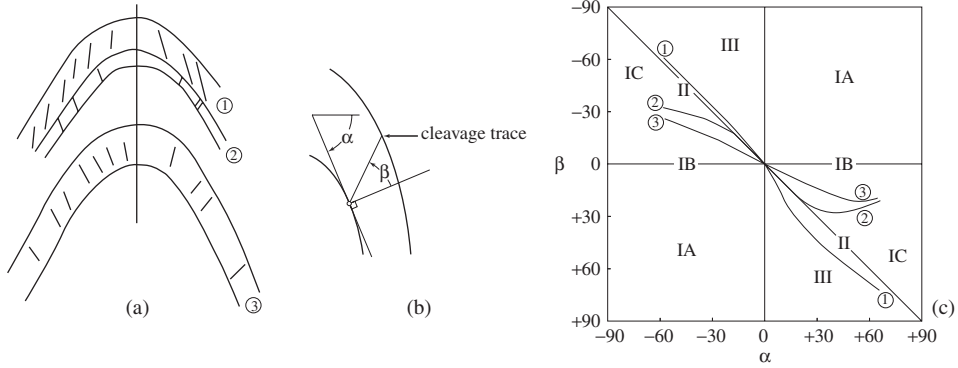


**Figure 14.20** Cleavage angle: (a) folded layers with cleavage; (b) cleavage angle  $\beta$ ; (c) graph of  $\beta$  vs.  $\alpha$  (after Treagus, 1982, p. 56).

### 14.9 Inverse thickness

Lisle (1997) extended and refined Ramsay’s geometrical classification by introducing a polar plot of inverse orthogonal thickness  $1/t'$  against dip angle  $\alpha$ . This plot identifies a diagnostic *pachymetric indicatrix*.<sup>6</sup> Every member of the fold classes can be represented by such an indicatrix (Fig. 14.21).

Each of the two main fold types is represented by a characteristic type of indicatrix: Class 1 folds by *ellipses* and Class 3 folds by *hyperbolas*. Further, the individual members of each of these two indicatrix-based classes can be represented by a single *flattening index* which describes a particular ellipse or hyperbola. This index is based on the equations of the central conics. In order to appreciate the detailed geometrical properties of these figures we first write their equations in canonical form (McLenaghan & Levy, 1996, p. 281),

$$\frac{x^2}{a^2} + \frac{y^2}{b^2} = 1 \quad \text{and} \quad \frac{x^2}{a^2} - \frac{y^2}{b^2} = 1. \tag{14.5}$$

Note that the only difference is that the equation of the hyperbola has a minus sign.

As will be apparent in Fig. 14.21, especially for the elliptical indicatrices, we need to consider each of these two conic sections in different orientations.

<sup>6</sup>Literally, “thickness-measure indicator.”



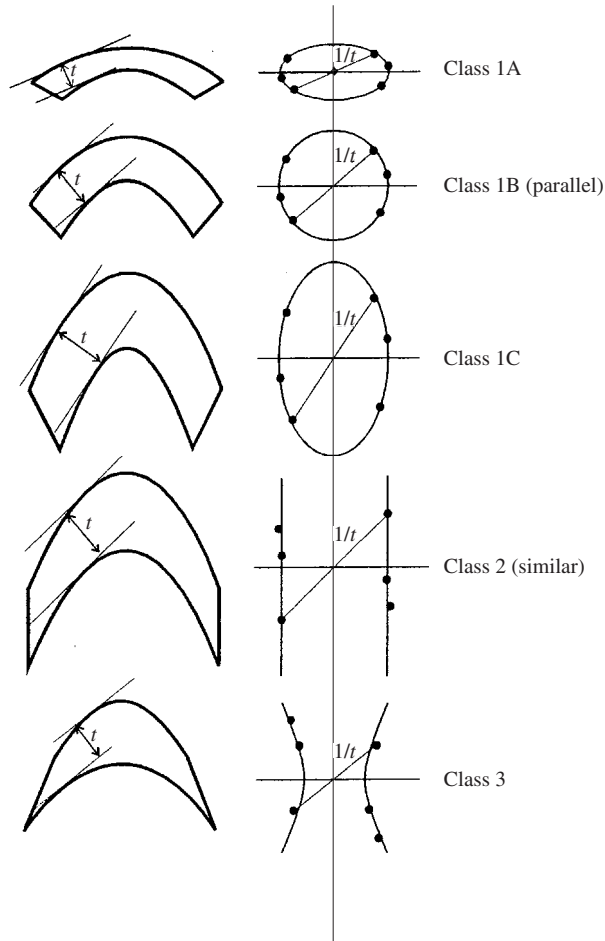


**Figure 14.21** Fold classification based on the pachymetric indicatrix (from Lisle, 1997, p. 326).

1. In the standard orientation:

- (a) The ellipse is characterized by a *major axis* with length  $2a$  which coincides with the  $x$  axis, and a *minor axis* with length  $2b$  which coincides with the  $y$  axis (Fig. 14.22a<sub>1</sub>).
- (b) The hyperbola is characterized by a *transverse axis*  $2a$  which coincides with the  $x$  axis, and the *conjugate axis*  $2b$  which coincides with the  $y$  axis (Fig. 14.22b<sub>1</sub>).

2. In the alternative orientation:

- (a) The ellipse is characterized by the *major axis* with length  $2b$ , which coincides with the  $y$  axis, and the *minor axis* with length  $2a$ , which coincides with the  $x$  axis (Fig. 14.22a<sub>2</sub>),

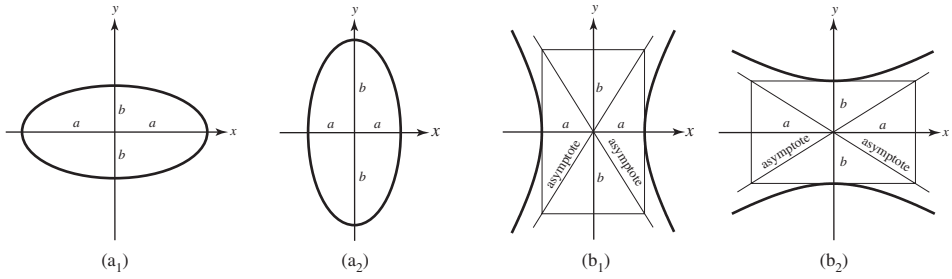


**Figure 14.22** Central conics and their principal axes: (a) ellipses; (b) hyperbolas.

(b) The hyperbola is characterized by the *transverse axis* with length  $2a$  which coincides with the  $x$  axis and the *conjugate axis* with length  $2b$  which coincides with the  $y$  axis (Fig. 14.22b<sub>2</sub>).<sup>7</sup>

We now define a flattening index  $F$  to express the shape and orientation (but not size) of the ellipse in terms of the semi-axes of the ellipse (Fig. 14.22a) or the semi-axes of the hyperbola (Fig. 14.22b)

$$F = \pm b/a, \tag{14.6}$$

where the positive sign denotes an ellipse and the negative sign a hyperbola.

Within each of these two main classes all possible fold geometries can be generated by the flattening of a circle and of an equilateral hyperbola.

1. All possible indicatrices of Class 1 folds can be generated by flattening a circle ( $a = b$ ) horizontally or vertically (Fig. 14.23).
2. All possible indicatrices of Class 3 folds can be generated by flattening an equilateral hyperbola ( $a = b$ ) horizontally or vertically (Fig. 14.24).

In terms of the pachymetric indicatrix the fold classes have the following characteristics.

1. Class 1 folds are characterized by ellipses.
  - (a) Class 1A: the indicatrix is an ellipse has its long axis parallel to the  $x$  direction ( $F < 1$ ).
  - (b) Class 1B: the indicatrix is a circle ( $F = 1$ ).
  - (c) Class 1C: the indicatrix is an ellipse with its long axis perpendicular to the  $x$  direction ( $F > 1$ ).
2. Class 2 or similar folds: the indicatrix is a pair of parallel lines ( $F = \infty$ ).
3. Class 3 folds are characterized by hyperbolas.
  - (a) Class 3A is a new subdivision with  $F < -1$ .

<sup>7</sup>Note that  $a$  and  $b$  are measured along the  $x$  and  $y$  axes in both orientations. For the alternative orientation this is the reverse of the usual convention.

- (b) Class 3B is a new boundary case with  $F = -1$ .
- (c) Class 3C is a new subdivision with  $F > -1$ .

The relationships between these classes and their characteristic values of  $F$  can be summarized with the scale of Fig. 14.25. Note that as  $F$  increases for Class 1C folds they approach the geometry of Class 2 folds but reach this state only when  $F = +\infty$ . Similarly, as  $F$  decreases for Class 3A folds they too approach similar geometry but reach this state only when  $F = -\infty$ . Thus the two parallel lines of the Class 2 indicatrix can be taken as an infinitely flattened circle or an infinitely flattened hyperbola, depending which side of the boundary one considers.

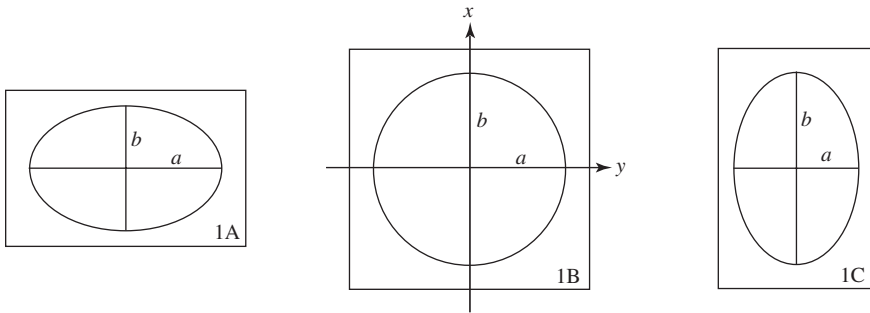


Figure 14.23 Flattened circles.

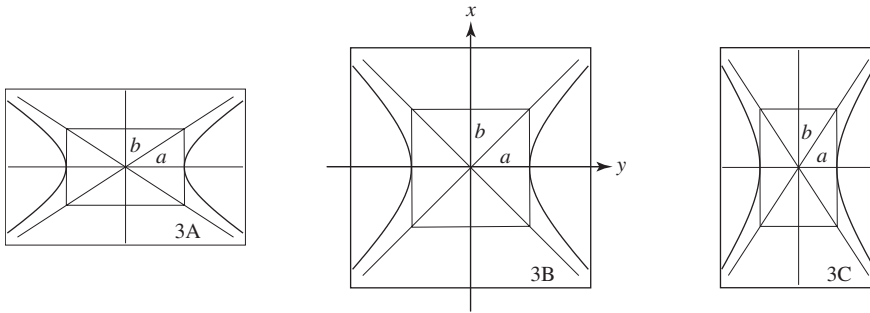


Figure 14.24 Flattened equilateral hyperbolas.

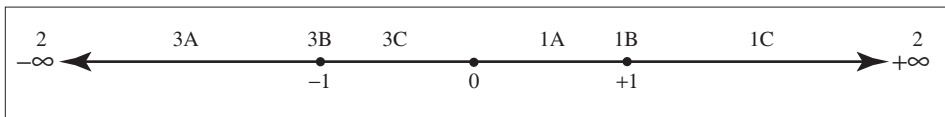


Figure 14.25 Scale of  $F$  values for all fold classes.

For the purposes of the graphical analysis, however, it is more convenient to use the equations of the ellipse and hyperbola expressed in polar coordinates (McLenaghan & Levy, 1996, p. 285–286)

$$r^2 = \frac{a^2 b^2}{a^2 \sin^2 \alpha + b^2 \cos^2 \alpha} \quad \text{and} \quad r^2 = \frac{a^2 b^2}{a^2 \sin^2 \alpha - b^2 \cos^2 \alpha}. \quad (14.7)$$

Again note that the equation of the hyperbola is distinguished by the minus sign.

We now recast these two formulas in a form which applies to measurements of orthogonal thickness  $t$  and the orientation of the angle  $\alpha$ . These in turn lead directly to a useful graphical representation.

1. Because the plot uses the inverse thickness make the substitution  $r = 1/t$  and then invert the equations in order to obtain expressions directly in terms of  $t$ .
2. Setting  $a = 1$ , the index becomes  $F = b/a = b$ .

With these we then have

$$\frac{1}{r^2} = t^2 = \frac{\sin^2 \alpha}{F^2} + \cos^2 \alpha \quad \text{and} \quad \frac{1}{r^2} = t^2 = -\frac{\sin^2 \alpha}{F^2} + \cos^2 \alpha. \quad (14.8)$$

These two expressions differ only in the signs of the first terms on the right-hand sides. They can therefore be consolidated into a single equation by introducing the device  $F^2 = F\sqrt{F^2}$  so that these signs are the same as that of  $F$ . Then with the identity  $\cos^2 \alpha = 1 - \sin^2 \alpha$

$$t^2 = \sin^2 \alpha \left( \frac{1}{F\sqrt{F^2}} - 1 \right) + 1. \quad (14.9)$$

With this result we can then add curves of constant  $F$  to the  $t'/\alpha$  graph (see Fig. 14.18c).

A more direct way of applying this inverse thickness method to the classification of a single folded layer is to plot a few measured  $(1/t', \alpha)$  points on the polar graph and so estimate the form of the pachymetric indicatrix (Fig. 14.26). To normalize the orthogonal thickness Lisle (1997, p. 324, 326) suggests using the *minimum* thickness (for 1A folds) or *maximum* thickness for all the other fold types measured in the vicinity of the hinge.

### 14.10 Best-fit indicatrix

For several reasons, there will always be some uncertainty in the measured angles and thicknesses. First, there are the inevitable measurement errors. Then the fact that natural materials are not perfectly homogeneous means that the states of strain will vary. Finally, we can never be certain that the original thickness of the layer was perfectly uniform. Therefore, an even better way of establishing the geometrical characteristics of a particular fold is to calculate the best-fit indicatrix from a larger number of measurements. This

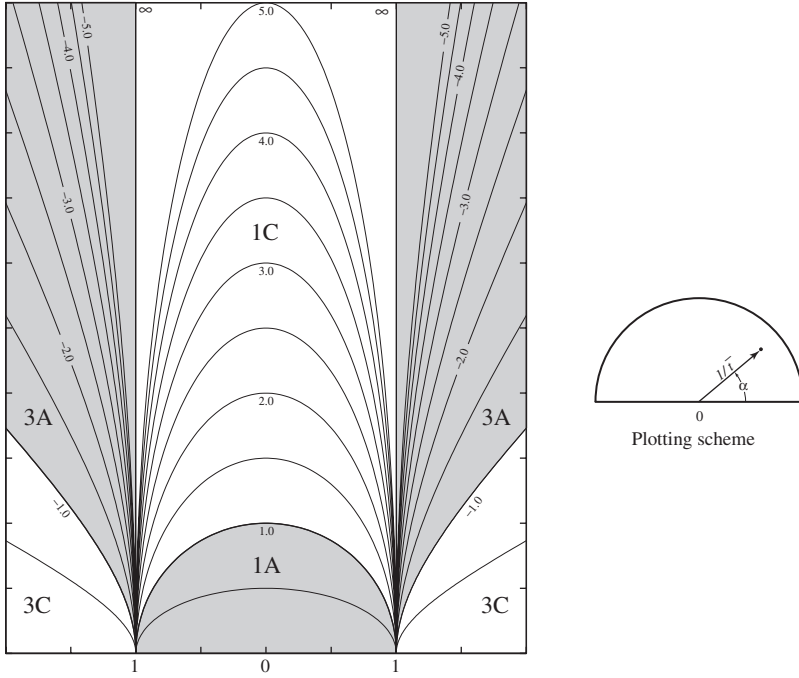


**Figure 14.26** Classification based on polar plot of  $(1/t', \alpha)$ .

not only yields the figure which best represents the fold, but also permits an evaluation of just how good the fit is.<sup>8</sup> The general equation of a conic section (ellipse or hyperbola) with its center at the origin is

$$Ax^2 + 2Bxy + Cy^2 = 1. \tag{14.10}$$

We can evaluate the coefficients  $A$ ,  $B$  and  $C$  by measuring the lengths of several radius vectors or their equivalents. As we have seen, the pachymetric indicatrix uses the inverse thickness  $1/t$  for the magnitudes of these vectors. The components of each such vector are obtained from

$$x_i = (1/t_i) \cos \phi_i, \quad y_i = (1/t_i) \sin \phi_i, \quad (i = 1, \dots, N), \tag{14.11}$$

where  $\phi$  gives the orientation of the tangent relative to an arbitrary set of coordinate axes. If  $N = 3$  then we have three equations with the form of Eq. 14.10, one for each  $(x_i, y_i)$  and we can calculate the exact values of the coefficients  $A$ ,  $B$  and  $C$ .

<sup>8</sup>We give an example of this calculation in the next section.

However, if  $N > 3$  then the system of equations is overdetermined and generally no such exact equation can be found. We then need a way of determining the ellipse or hyperbola which fits these known points best. The controlling equation is

$$r_i = Ax_i^2 + 2Bx_iy_i + Cy_i^2 - 1, \quad (14.12)$$

where the value of each *residual*  $r_i$  is a measure of the departure of the corresponding point from the best-fit curve.

We can also determine the overall best-fit using the *least-squares criterion* and this requires that we minimize the sum of the squares of these residuals. With Eq. 14.12 we write this as

$$\sum_{i=1}^N r_i^2 = \sum_{i=1}^N (Ax_i^2 + 2Bx_iy_i + Cy_i^2 - 1)^2. \quad (14.13)$$

Three conditions must be satisfied for this sum to be a minimum and these are found by differentiating Eq. 14.13 partially with respect to  $A$ ,  $B$  and  $C$  and setting each result to zero. That is,

$$\frac{\partial}{\partial A} \sum r_i^2 = 0, \quad \frac{\partial}{\partial B} \sum r_i^2 = 0, \quad \frac{\partial}{\partial C} \sum r_i^2 = 0. \quad (14.14)$$

Applying these conditions and dividing the first and third results by 2 and the second result by 4 we obtain the three equations

$$\begin{aligned} \frac{\partial}{\partial A} \sum (Ax_i^2 + 2Bx_iy_i + Cy_i^2 - 1)^2 &= \sum (Ax_i^2 + 2Bx_iy_i + Cy_i^2 - 1)x_i^2 = 0, \\ \frac{\partial}{\partial B} \sum (Ax_i^2 + 2Bx_iy_i + Cy_i^2 - 1)^2 &= \sum (Ax_i^2 + 2Bx_iy_i + Cy_i^2 - 1)x_iy_i = 0, \\ \frac{\partial}{\partial C} \sum (Ax_i^2 + 2Bx_iy_i + Cy_i^2 - 1)^2 &= \sum (Ax_i^2 + 2Bx_iy_i + Cy_i^2 - 1)y_i^2 = 0, \end{aligned}$$

and these simplify to

$$\begin{aligned} A \sum x_i^4 + 2B \sum x_i^3y_i + C \sum x_i^2y_i^2 &= \sum x_i^2, \\ A \sum x_i^3y_i + 2B \sum x_i^2y_i^2 + C \sum x_iy_i^3 &= \sum x_iy_i, \\ A \sum x_i^2y_i^2 + 2B \sum x_iy_i^3 + C \sum y_i^4 &= \sum y_i^2. \end{aligned}$$

With the abbreviations

$$\begin{aligned} a &\equiv \sum x_i^4, & b &\equiv \sum x_i^3y_i, & c &\equiv \sum x_i^2y_i^2, & d &\equiv \sum x_iy_i^3, \\ e &\equiv \sum y_i^4, & f &\equiv \sum x_i^2, & g &\equiv \sum x_iy_i, & h &\equiv \sum y_i^2, \end{aligned}$$

we then write

$$\begin{aligned}Aa + 2Bb + Cc &= f, \\Ab + 2Bc + Cd &= g, \\Ac + 2Bd + Ce &= h.\end{aligned}$$

These three are the *normal equations* and we can solve them exactly for the coefficients  $A$ ,  $B$  and  $C$  using Cramer's rule. First the determinant of these equations is

$$\det = \begin{vmatrix} a & 2b & c \\ b & 2c & d \\ c & 2d & e \end{vmatrix} = 2(ace + 2bcd - c^3 - ad^2 - b^2e).$$

Then

$$A = \frac{1}{\det} \begin{vmatrix} f & 2b & c \\ g & 2c & d \\ h & 2d & e \end{vmatrix} = \frac{2(cef + bdh + cdg - c^2h - beg - d^2f)}{\det}, \quad (14.15a)$$

$$B = \frac{1}{\det} \begin{vmatrix} a & f & c \\ b & g & d \\ c & h & e \end{vmatrix} = \frac{(aeg + cdf + bch - c^2g - bef - adh)}{\det}, \quad (14.15b)$$

$$C = \frac{1}{\det} \begin{vmatrix} a & 2b & f \\ b & 2c & g \\ c & 2d & h \end{vmatrix} = \frac{2(ach + bcg + bdf - b^2h - c^2f - adg)}{\det}. \quad (14.15c)$$

We can also determine the goodness of the fit. Equation 14.14 gives the residuals  $r_i$  associated with each measurement (Scheid, 1988, p. 242, 420). Then the overall goodness of fit is given by the *root mean square error*

$$\text{RMS} = \sqrt{\frac{1}{N} \sum r_i^2}. \quad (14.16)$$

In the treatment of the transformation of axes in §7.8 we found the equation of the conic in the transformed coordinates to be (see Eq. 7.58)

$$A'x'^2 + 2B'x'y' + C'y'^2 = 1, \quad (14.17)$$

where

$$A' = A \cos^2 \theta + 2B \sin \theta \cos \theta + C \sin^2 \theta, \quad (14.18a)$$

$$B' = (C - A) \sin \theta \cos \theta + B(\cos^2 \theta - \sin^2 \theta), \quad (14.18b)$$

$$C' = A \sin^2 \theta - 2B \sin \theta \cos \theta + C \cos^2 \theta. \quad (14.18c)$$

As in Eqs. 7.54 it is advantageous to represent this figure by the symmetric square matrix

$$\begin{bmatrix} A' & B' \\ B' & C' \end{bmatrix}. \tag{14.19}$$

If the orientational angle  $\theta$  is such that the  $x'y'$  coordinate axes coincide with a principal axes, the  $x'y'$  term in Eq. 14.17 vanishes and the equation becomes

$$A'x'^2 + C'y'^2 = 1.$$

We can easily find the angle  $\theta$  for this condition by setting  $B' = 0$  in Eq. 14.18b giving

$$(C - A) \sin \theta \cos \theta + B(\cos^2 \theta - \sin^2 \theta) = 0.$$

With the double angle identities

$$\sin \theta \cos \theta = \frac{1}{2} \sin 2\theta, \quad \cos^2 \theta - \sin^2 \theta = \cos 2\theta, \quad \sin 2\theta / \cos 2\theta = \tan 2\theta,$$

and after some manipulation we have

$$\tan 2\theta = \frac{2B}{A - C} \quad \text{or} \quad \theta = \frac{1}{2} \arctan \left( \frac{2B}{A - C} \right). \tag{14.20}$$

Having found angle  $\theta$  which describes the orientation of the coordinate axes which are parallel to the principal axes, we can now determine the values of the coefficients  $A'$  and  $C'$  from Eq. 14.17a and Eq. 14.17c. The matrix representing the conic in this orientation becomes

$$\begin{bmatrix} A' & 0 \\ 0 & C' \end{bmatrix}. \tag{14.21}$$

In the terms of linear algebra, we have *diagonalized* the matrix representing the ellipse or hyperbola.

From this diagonal matrix we can now easily determine the nature of the indicatrix and its orientation by inspection and a few simple calculations.

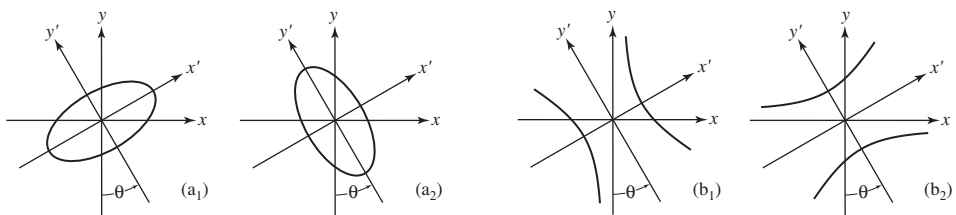


**Figure 14.27** Transformed axes: (a) ellipse; (b) hyperbola.



## 1. Form of the indicatrix:

- (a) If  $A'$  and  $C'$  have the same sign ( $A'C' > 0$ ), it is an ellipse (Figs. 14.27a<sub>1</sub> and 14.27a<sub>2</sub>).
- (b) If  $A'$  and  $C'$  have opposite signs ( $A'C' < 0$ ) it is a hyperbola (Figs. 14.27b<sub>1</sub> and 14.27b<sub>2</sub>).

## 2. Orientation of the indicatrix:

- (a) If  $|A'| < |C'|$  the major axis is parallel to  $x'$  and  $a = 1/\sqrt{|A'|}$ ,  $b = 1/\sqrt{|C'|}$  (Figs. 14.22a<sub>1</sub> and 14.20b<sub>1</sub>).
- (b) If  $|A'| > |C'|$  the major axis is parallel to  $y'$  and  $a = 1/\sqrt{|C'|}$ ,  $b = 1/\sqrt{|A'|}$  (Figs. 14.20a<sub>2</sub> and 14.22b<sub>2</sub>).

We can now calculate the value of the flattening index  $F$  and then with it the geometry of a folded layer is completely specified. The fold class can be determined from the  $t'/\alpha$  graph of Fig. 14.18c or Table 14.6.<sup>9</sup>

Table 14.6 *Fold classes based on the flattening index  $F$*

Fold class	Index
1A	$0 < F < 1$
1B parallel	$F = 1$
1C	$F > 1$
2 similar	$F = \infty$
3A	$-1 < F < -\infty$
3B	$F = -1$
3C	$0 > F > -1$

### 14.11 Determining the flattening index

We now give an example of the calculation of the flattening index  $F$ . In parallel folds the isogons are perpendicular to layer boundaries and all have constant length  $t'_\alpha = t'_0$ . A square is constructed at a typical point  $P$  with sides parallel to the tangents and their corresponding perpendicular isogons (Fig. 14.28a). After homogeneous flattening this square becomes a parallelogram at corresponding point  $P'$  with sides still parallel to the isogons and tangents (Fig. 14.28b).

All such squares in the parallel fold have the same area  $A$ . Because the imposed flattening strain is homogeneous all such parallelograms have the same area  $A'$ . The change in shape of the fold depends on the distortional part of the strain and not on any

<sup>9</sup>Lisle (1997, p. 335–338) lists a BASIC computer program which calculates  $A'$  and  $C'$  and classifies the fold accordingly.

dilatational part. Therefore we take  $A = A'$  and for convenience assign unit areas to both, that is,

$$A = 1 \quad \text{and} \quad A' = t'_{\alpha'}(1/t_{\alpha'}) = 1.$$

From this square and its corresponding parallelogram we have sufficient information to determine a relative stretch in the direction of the tangent. For the square  $l = 1$  and for the parallelogram the length after flattening is  $l' = 1/t_{\alpha'}$ . Thus the stretch is

$$kS_{\alpha'} = 1/t_{\alpha'}, \tag{14.22}$$

where  $k$  is an unknown scale factor. With several such measurements we can now construct the relative strain ellipse for the flattened fold.

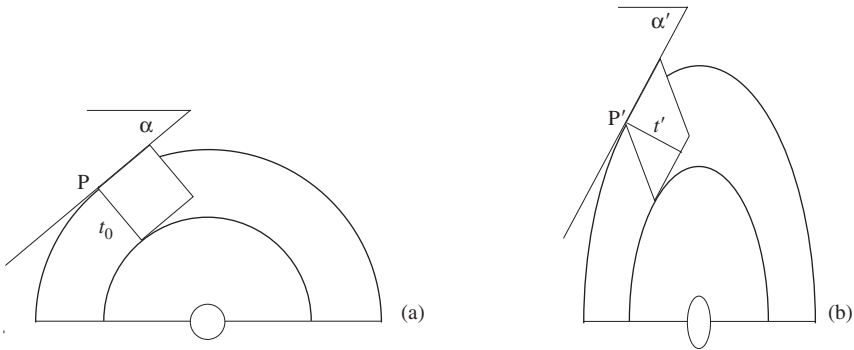


**Figure 14.28** Homogeneous flattening: (a) parallel fold; (b) flattened fold.

**Procedure**

1. At several points around the flattened fold measure the orthogonal thickness  $t$  and the slope angle after flattening  $\alpha'$  of the associated tangent (such as in Fig. 14.28b).
2. The vector with length  $1/t_{\alpha'}$  whose orientation is given by  $\alpha'$  is a radius of the relative strain ellipse.
3. There are several ways of determining the strain from lines of known relative stretch.
  - (a) With three such vectors the strain can be determined with a Mohr Circle construction.
  - (b) With more than three, the best-fit ellipse can be calculated.

**Solution**

- The orientation and principal relative stretches are determined from this strain ellipse. Then the shape of ellipse can be found by calculating the strain ratio

$$R_s = kS_1/kS_3. \tag{14.23}$$

Unlike Ramsay's method which assumes that the  $S_1$  direction is parallel to the axial plane, this method gives the flattening strain whatever its orientation.

### Problem

- From measurements made on a folded layer (Fig. 14.29a) determine the best-fit ellipse.

### Solution

1. From the measured thicknesses calculate the relative stretches at a series of points distributed around the folded layer from  $S = 1/t$ .<sup>10</sup>
2. With Eqs. 14.11 calculate the  $x$  and  $y$  components of each radius vector  $\mathbf{S}$  (see Table 14.7).
3. With Eqs. 14.15 determine the coefficients of the best-fit ellipse. The finite strain tensor is then

$$\begin{bmatrix} A & B \\ B & C \end{bmatrix} = \begin{bmatrix} \lambda'_{xx} & \gamma'_{xy} \\ \gamma'_{yx} & \lambda'_{yy} \end{bmatrix} = \begin{bmatrix} 4.838\ 10 & 0.279\ 76 \\ 0.279\ 76 & 1.277\ 73 \end{bmatrix}$$

By inspection  $\lambda'_{xx} > \lambda'_{yy}$ ; therefore  $S_{xx} < S_{yy}$  and the  $S_1$  direction of the best-fit ellipse is closer to the  $y$  axis than to the  $x$  axis (Fig. 14.29b).

4. The angle the  $S_1$  direction makes with the  $y'$  axis is  $\theta = 4.465\ 62^\circ$ .
5. After a transformation of axes the diagonal matrix representing this tensor is

$$\begin{bmatrix} A' & 0 \\ 0 & C' \end{bmatrix} = \begin{bmatrix} \lambda'_3 & 0 \\ 0 & \lambda'_1 \end{bmatrix} = \begin{bmatrix} 4.859\ 95 & 0 \\ 0 & 1.255\ 88 \end{bmatrix}$$

and  $R_s = S_1/S_3 = \sqrt{\lambda'_3/\lambda'_1} = \sqrt{4.859\ 95/1.255\ 88} = 1.97$ , and this is the flattening index  $F$ . The fold belongs to class 1C.

6. The residuals associated with each measurement are shown in the last column of Table 14.7. The overall goodness of fit is given by  $\text{RMS} = 0.212\ 49$ .

## 14.12 Competence

It has long been appreciated that different rock types deform differently under the same physical conditions. An early attempt to characterize the behaviors of different rock types was to establish the concept of competence (Willis, 1893; also Willis & Willis, 1934, p. 77f), and the basic approach is still widely used. *Competent* rocks tend to resist flow

<sup>10</sup>If the values of  $1/t$  are small (as here) then powers and products will be very much smaller. Possible round-off errors can be avoided by rescaling so that the values are closer to 1 (here we multiply by a factor of 10). This does not affect the final results because we can only obtain the shape as expressed as a ratio, not size of the strain ellipse from these thickness measurements.

Table 14.7 Thickness data (Lisle, 1998, personal communication) and derived values

$i$	$t$ (mm)	$\phi$	$1/t$	$S \times 10$	$x$	$y$	$r$
1	11.0	80°	0.09091	0.90909	0.15786	0.89528	0.22378
2	15.5	69°	0.06452	0.64516	0.23121	0.60231	-0.19993
3	19.0	50°	0.05263	0.52632	0.33831	0.40318	-0.16224
4	21.5	24°	0.04651	0.46512	0.42490	0.18918	-0.03580
5	23.0	-2°	0.04348	0.43478	0.43452	-0.01517	-0.08993
6	19.5	-42°	0.05128	0.51282	0.38110	-0.34314	-0.22005
7	15.5	-62°	0.06452	0.64516	0.30288	-0.56964	-0.23808
8	17.0	-26°	0.05882	0.58824	0.52870	-0.25787	0.36106

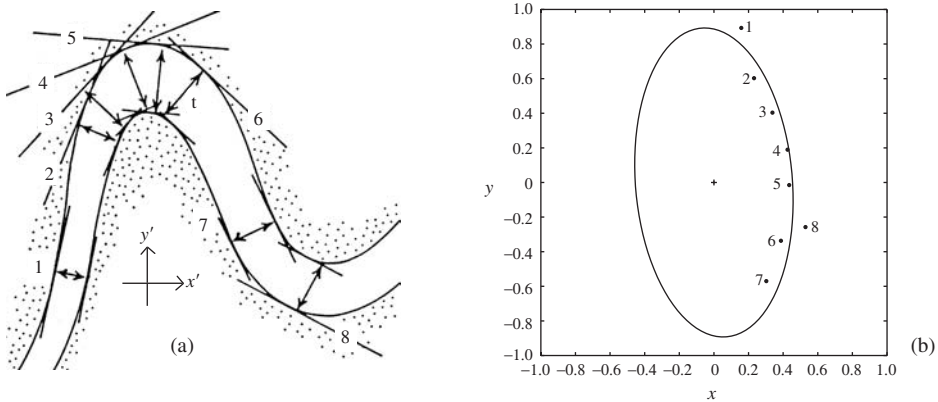


Figure 14.29 Fold classification (Lisle, 1998, personal communication): (a) thicknesses; (b) best-fit ellipse.

and incompetent rocks flow more easily. These distinctions are only relative and some of the meaning is captured by the contrasting pairs of terms: *strong* vs. *weak*, *brittle* vs. *ductile*, *stiff* vs. *soft*.<sup>11</sup>

The most graphic example of such differing behaviors can be seen in a deformed conglomerate containing a variety of pebble rock types in a pelitic matrix: incompetent elements, along with the matrix, are prominently strained whereas competent elements are strained less, or possibly not at all. More particularly, when rocks of different competencies are in contact a variety of structures develop at the interface. Ramsay (1982) gives an extended treatment of such features with many excellent illustrations, as do Talbot and Sokoutis (1992).

From these and other such observations, it is then possible to rank common rock types from the *most* to *least* competent. The position in this ranking depends on chemical

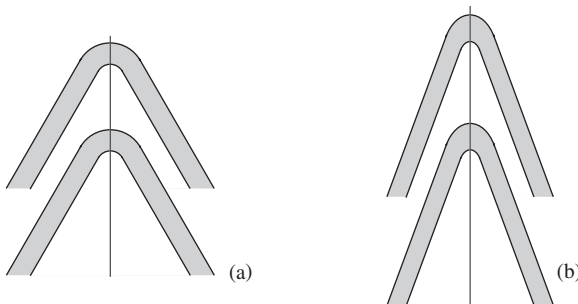
<sup>11</sup>Each of these terms has a technical definition, but we use them here in the everyday semi-quantitative meaning to suggest the broad sense in which the term has been used. Later in this section we will justify a much narrower usage.

Table 14.8 *Common rocks ranked from most to least competent (Ramsay, 1982, p. 117–118)*

Low or very low grade		Greenschist or lower amphibolite facies	
1.	Dolomite	1.	Metabasic rocks
2.	Arkose	2.	Coarse-grained granite and granitic gneiss
3.	Quartz sandstone	3.	Fine-grained granite and granitic gneiss
4.	Greywacke	4.	Banded quartz-feldspar-mica gneiss
5.	Coarse-grained limestone	5.	Quartzite
6.	Fine-grained limestone	6.	Marble
7.	Siltstone	7.	Mica schist
8.	Marl		
9.	Shale		
10.	Halite, anhydrite		

composition and grain size. It also depends on the environmental conditions, particularly temperature, as marked by metamorphic grade, at the time of deformation (Table 14.8).

We are especially concerned here with the effects such differences have on fold geometry. For example, in a multilayered system, competent layers tend to have patterns of isogon class 1B (parallel) whereas incompetent layers tend to have patterns of isogon class 3 (divergent) (see Fig. 14.30a).



**Figure 14.30** Competent (shaded) and incompetent (blank) layers: (a) after folding; (b) after homogeneous flattening.

When rocks of differing competencies are in contact across an oblique boundary, such as on the limbs of a fold, the states of strain in each will also differ, that is, the shape and orientation of the strain ellipses will not be the same in both materials. This is *strain refraction* (Fig. 14.31a).

The most obvious manifestation of strain refraction is a consequence of the fact that cleavage forms parallel to the  $S_1S_2$  plane or close to it and therefore exhibits *cleavage refraction* (Fig. 14.31a). The angles such cleavage planes make with the inclined contact  $\theta_1 > \theta_2 > \theta_3$  implies that the relative competencies of the three lithologies is  $L_1 > L_2 > L_3$ .

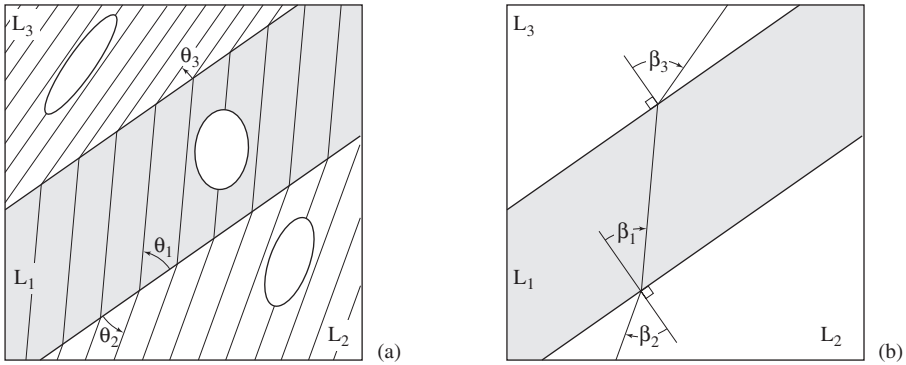


**Figure 14.31** Refracted strain and cleavage: (a)  $S_1$  orientation angles  $\theta_1 > \theta_2 > \theta_3$  (after Ramsay, 1982, p. 113); (b) cleavage angles  $\beta_1 < \beta_2 < \beta_3$ .

If we are to fully understand the role such differences play, we need to know the *flow laws* which describe these several behaviors. To do this it is necessary to experimentally deform rock material under controlled conditions in the laboratory.

The essential problem with this approach is that the strain rates in nature are experimentally inaccessible. As we have seen in §13.6, the rates associated with most natural structures are in the range  $10^{-13}/s$  to  $10^{-15}/s$ . Consider the time  $t$  it takes to produce a modest 10% strain ( $e = 10^{-1}$ ) at the rate  $10^{-8}/s$ , which is still many orders of magnitude faster than typical natural strain rates. The required duration of an experiment is

$$t = \frac{e}{\dot{\epsilon}} = \frac{10^{-1}}{10^{-8}/s} = 10^7 \text{ s} \approx 115.7 \text{ days.}$$

Not only is it difficult to keep the testing apparatus working at high temperatures and pressures for this long, but even if this could be done reliably only three experiments could be completed in a year, and the problem is compounded if larger strains are required. Therefore, experiments are usually performed at strain rates of  $10^{-2}/s$  to  $10^{-7}/s$ . In order to make rocks flow faster in the laboratory, there are two choices (Schmidt, 1982, p. 96):

1. Use a higher differential stress. However, this commonly induces different deformational mechanisms and the results are less applicable to natural structural processes. This in turn limits the application to natural strain rates.
2. Alternatively, perform the experiments at temperature higher than the range expected under natural conditions. The extrapolation of the flow law to lower temperature conditions is less likely to involve different microstructural mechanisms.

Under such conditions, many natural materials typically display *power law creep*. In one dimension, this flow law can be expressed as  $\dot{\epsilon} = f(\sigma^n)$ . In the simplest case  $n = 1$ . Then  $\dot{\epsilon}$  and  $\sigma$  are linearly related (Fig. 14.32), and we have  $\sigma = \mu\dot{\epsilon}$  where the constant of

proportionality is the *coefficient of viscosity*, and its dimension is a pascal second (Pa s). Such behavior is *linear* or *Newtonian*.

More generally  $n > 1$  and the relationship between  $\sigma$  and  $\dot{\epsilon}$  is described by an exponential curve. If the strain rate is steady we can define an effective viscosity as the slope of the curve  $d\sigma/d\dot{\epsilon}$  at a typical point  $P$  (Fig. 14.32a).

More likely, the strain rate varies during the evolution of a structure. Because the natural rates are so slow, the differences over time are probably small, and we may define an effective viscosity as the approximation  $\Delta\sigma/\Delta\dot{\epsilon}$ , which is the average slope in the segment of the curve bounded by the upper and lower rates (Fig. 14.32b).

In either case, it is appropriate to treat competence contrasts as reflecting differences in viscosities, at least as a good approximation. This in turn permits precise rock properties to be specified, and this approach has been used in numerical modeling of a wide range of geological structures and this has significantly extended our understanding the responsible processes (Johnson & Fletcher, 1994).

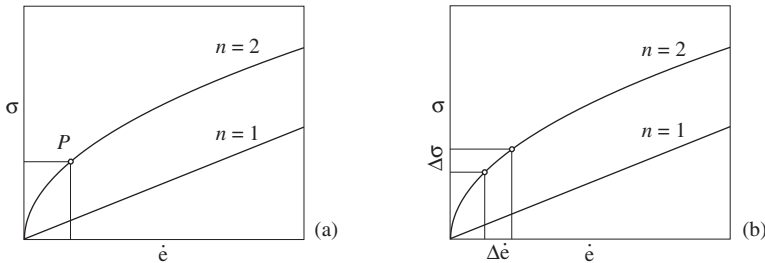


**Figure 14.32** Power laws for  $n = 1$  and  $n = 2$ .

It is also possible to constrain rock viscosities (Talbot, 1999a). Because it is both relatively simple and directly applicable, an instructive case involves the refraction of cleavage as it passes from competent into incompetent layers in a fold (Treagus, 1999).

During flow the rates of shear strain on each side of a bonded contact are controlled by the contrasting viscosities. The final, total shear strains in each material will then also reflect these differences. Thus for each contrasting pair we can then write

$$\frac{\mu_1}{\mu_2} = \frac{\gamma_2}{\gamma_1}, \quad (14.24)$$

where  $\mu_1 > \mu_2$  (henceforth, the terms *competent* and *incompetent* will refer to the materials with greater and lesser viscosity). Note that the magnitude of  $\gamma$  is greater in the material with smaller viscosity, that is,  $\gamma_1 < \gamma_2$ . We can not evaluate the angles of shear directly, but we can measure the angles  $\beta_1 < \beta_2$  which are approximately equal to the corresponding angles of shear  $\psi$  (Fig. 14.31b). We then recast Eq. 14.24 as

$$\frac{\mu_1}{\mu_2} \approx \frac{\tan \beta_2}{\tan \beta_1}. \quad (14.25)$$

We now consider the relatively simple but important process of a single thin isolated layer subjected to a longitudinal compressive load. Under such conditions it will be deflected laterally by *buckling* (Gere, 2001, p. 739). This process can be easily illustrated by applying a load to a short plastic ruler (Fig. 14.33a). In theory a perfectly straight, thin plate or slender column will not buckle so an infinitesimal lateral displacement must be supplied. In practice irregularities or imperfections are always present which serve this function.<sup>12</sup>

A closely related but more relevant experiment is to load a thin elastic sheet of stiff rubber embedded in a block of softer elastic material, such as foam. The deflection of the sheet is affected by a reaction of the embedding medium with the result that now several folds develop (Fig. 14.33b).<sup>13</sup>

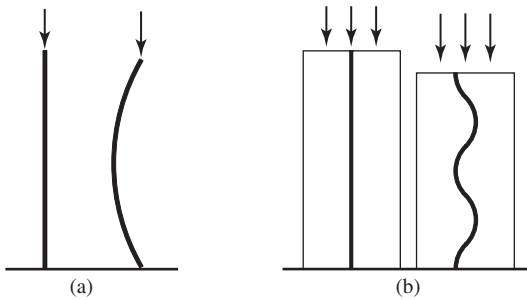


**Figure 14.33** Buckling: (a) isolated slender member; (b) embedded stiff elastic plate.

A similar result is obtained if a thin viscous layer embedded in a less viscous material is shortened (Biot, 1961; Ghosh, 1993, p. 260). It is assumed that initially the layer contains many minute irregularities which can grow in amplitude with the application of a load. Some of these will grow faster than others. A differential equation expressing these deflections as a function of the layer thickness, viscosity and load can then be solved. From this solution, the maximum deflection can then be found, and this then leads directly to the expression for the *dominant* or *characteristic* wavelength  $L$ .

$$L = 2\pi t \sqrt[3]{\frac{1}{6} \frac{\mu_1}{\mu_2}}. \quad (14.26)$$

This expression is valid only for buckles with *infinitesimal amplitude*. For large viscosity ratios the arc length of the buckle remains essentially constant and this length  $L$  is only

<sup>12</sup>Leonard Euler first investigated the buckling of slender members and the terms *Euler buckling* and *Euler critical load* are commonly used to describe aspects of this process (Gere, 2001, p. 478–479).

<sup>13</sup>The mechanics of folding and its mathematical description is a matter for advanced study. Ramsay and Huber (1987, p. 383–404), Ramsay and Lisle (2000, p. 1019–1028) and Ghosh (1993, p. 251–294) give good overviews of the subject including the derivations of some of the controlling equations and numerous references. For large-scale folds gravity becomes an important additional component (Ramberg, 1981). Our goal here is to illustrate the fact that geometry gives important clues to the nature of the physical processes at the time of fold formation.



slightly greater than the initial wavelength which is taken as its measure. This expression allows the viscosity ratio to be estimated from the measured value of  $L/t$ . Experiments have verified the validity of this result for such materials (Biot, *et al.*, 1961).<sup>14</sup>

For smaller viscosity ratios buckling is preceded by a stage of homogeneous layer-parallel shortening (Fig. 14.34). Sherwin and Chapple (1968) modified Biot’s equation to take this additional behavior into account giving

$$L = 2\pi t \sqrt[3]{\frac{1}{6} \frac{\mu_1}{\mu_2} \frac{S_1^2 + 1}{2S_1^4}}. \tag{14.27}$$

Note that if  $S_1 = 1$ , that is, no initial shortening, this reverts to Eq. 14.26. This expression could also be used to estimate the viscosity ratio if the strain were known, but unfortunately this is rarely possible.

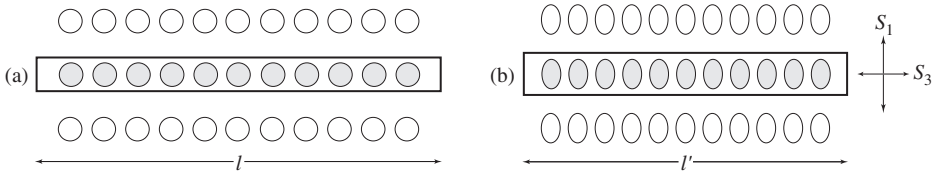


**Figure 14.34** Homogeneous layer-parallel shortening.

Once initiated, the bending continues with the result that *finite-amplitude* folds develop, that is, the amplitude  $A$  increases and the conventional wavelength  $W$  decreases (see Fig. 14.5).

The contributions of buckling and initial layer-parallel shortening to the final fold form can sometimes be evaluated. Because the component of homogeneous shortening depends on the viscosity contrast, a folded competent layer, such as quartz sandstone in shale, will have a larger  $A/W$  ratio, while folds developed in a less competent layer, such as siltstone in the same shale, will have a smaller  $A/W$  ratio – the component of homogeneous shortening is effectively hidden in the siltstone and thus the folds appear to have been shortened less even though the bulk deformation is the same for both. In the limit, where the contrast is very small or zero, there may be no fold at all.

As we have seen in §14.9, the homogeneous flattening of just two basic forms is capable of generating a wide range of fold geometries which are uniquely denoted by the flattening index. Generally these fold types are not, nor were they meant to be, descriptions of real physical processes. For example  $F = \infty$  has no physical meaning. We refer to this as *geometrical flattening*.

<sup>14</sup>Mancktelow (2001) has revisited the problem of single-layer folds from an entirely different perspective.

Largely on these same geometrical grounds flattening has also been proposed as a third and final physical stage in fold evolution (Ramsay, 1967, p. 434; Ramsay & Huber, 1987, p. 353).<sup>15</sup> Such a homogeneously flattened multilayered fold is illustrated in Fig. 14.30b.

There are, however, serious difficulties (Treagus, 1983, p. 366; 1997, p. 357f). The phenomenon of cleavage refraction demonstrates that the viscosities of two contrasting materials, which control the rates at which each deform, play an important role in fold evolution. Therefore late flattening can not be homogeneous in both competent and incompetent layers at the same time. This is *physical flattening*.

This restriction does not apply to a single embedded competent layer and it is therefore physically meaningful to consider the late flattening of a fold with initial parallel geometry. The fact that the thickness variation in the final fold can be represented by an ellipse demonstrates that in this limited case flattening is a valid physical process.

In a series of finite-difference computer models of the progressive folding of a single embedded layer, Chapple (1968) found that the process involved two important stages. At first, incompetent matrix material flowed to fill the space in the core of the growing fold. As the fold tightened this material then started to be extruded. This change occurred when the limb dip was about  $60^\circ - 65^\circ$  (or when the interlimb angle was about  $50^\circ - 60^\circ$ ).<sup>16</sup> In the earlier stage the trace of the  $S_1 S_2$  planes displayed an antifanning (divergent cleavage fan) pattern while in the later stage it displayed a fanning (convergent cleavage fan) pattern. Also, the longitudinal stress in the limbs of the fold changed from compressive (implying limb-parallel shortening) to tensile (implying limb-parallel lengthening). It seems reasonable then to assign to these sequential stages the more conventional terms:

1. *Active folding*: the general buckling deformation of the embedded layer, including the associated strain of both layer and adjacent medium, together with the bodily rotation of the limbs of the developing fold.
2. *Physical flattening*: the flattening deformation of the previously formed fold, including the continuing bodily rotation of the limbs with a consequent decrease in the interlimb angle.

If the transition from the first to second stage which occurs at a limb dip of about  $60^\circ$  is a general one, then final folds with near-vertical limbs present a problem. Such a rotation of the limbs by flattening strain requires a very large strain ratio and would be accompanied by a dramatic thinning of the steep limb. This suggests that already steep limbs are additionally steepened by bodily rotation. To the degree that this occurs, the flattening index then underestimates the total physical flattening.

Figure 14.35a shows a member of a train of small, isoclinal pygmy folds developed in a competent layer embedded in slate. From the best-fit ellipse for ten measured points

<sup>15</sup>The stages of layer-parallel shortening, folding and flattening are labeled A, B and C in Fig. 13.17.

<sup>16</sup>The reason for these contrasting behaviors is that the volume of the space in the core of the fold, as represented by its cross-sectional area, increases in the early stage and decreases in the later stage. The exact transition point likely depends on the detailed shape of the folded layer.

Table 14.9 Data for a ptygmatic fold

<i>i</i>	<i>t</i>	$\phi$	<i>S</i>	<i>x</i>	<i>y</i>
1	8.2	0°	0.12195	0.12195	0.00000
2	8.0	-10°	0.12500	0.12310	-0.02171
3	7.9	+20°	0.12658	0.11895	0.04329
4	7.3	-30°	0.13699	0.11863	-0.06849
5	7.2	+40°	0.18889	0.10640	0.08928
6	6.4	-50°	0.15625	0.10044	-0.11969
7	6.3	-60°	0.15873	0.07937	-0.13746
8	5.8	-70°	0.17241	0.05897	-0.16202
9	5.6	-80°	0.17857	0.03101	-0.17586
10	4.8	90°	0.22083	0.00000	0.20833

(Fig. 14.35b), the flattening index is  $F = 1.59$ . The associated  $RMS = 0.074$ , which indicates quite a good fit. Note however that point No. 10 representing the layer-parallel stretch of the vertical limb is a prominent outlier. Figure 14.35c is the ellipse recalculated using the other nine points: now  $F = 1.45$  and  $RMS = 0.029$  and the fit is even better.

The limb-parallel stretch of the vertical limb is about 14% greater than the stretch in this same direction associated with the second ellipse. This is consistent with the results of Chapple’s model experiments.

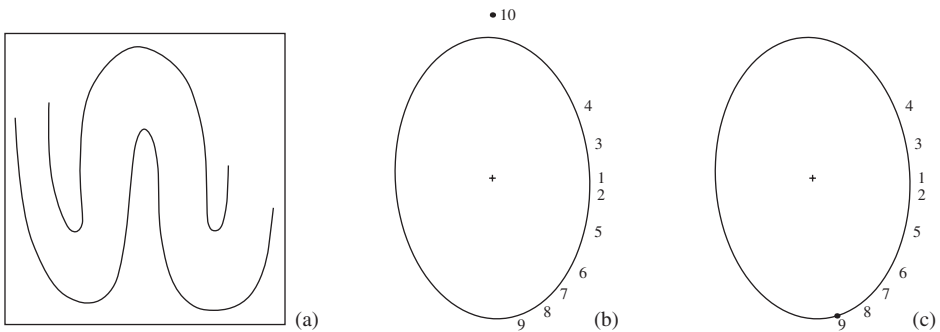
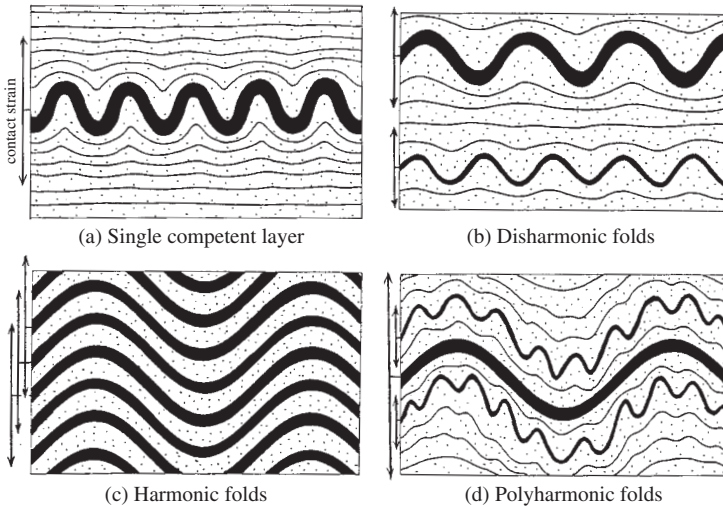


Figure 14.35 Small ptygmatic fold: (a) fold form; (b) first best-fit ellipse; (c) second best-fit ellipse (after Ramsay & Huber, 1987, p. 393).

The analysis of the behavior of multilayered systems is made difficult by a number of factors (Ramsay & Huber, 1987, p. 405–406). Of particular importance are the variations in the thickness and competence of the component layers making up the system, and whether the contacts between layers are bonded or allow slip. All this leads to considerable

physical and analytical complications with the result that the geometry of such systems can not be unambiguously interpreted.<sup>17</sup>



**Figure 14.36** Contact strain and folded multilayers (from Ramsay & Huber, 1987, p. 406 with permission of Elsevier).

We can however adapt our results from folds developed in single embedded layers in the general way (Ramsay & Huber, 1987, p. 405f). The growth of a fold displaces the adjacent material, an effect termed *contact strain*. Theoretically, this strain vanishes only at an infinite distance from the folded layer, but the effects die away quite rapidly so that at a distance beyond about half of the initial wavelength (or  $L/2$ ) they are small enough that they can be neglected for most purposes (see Fig. 14.36a).

If two or more competent layers are present, but the spacing between them is greater than this zone of contact strain, then the geometry of the folds in each will develop independently (Fig. 14.36b). There will then be no necessary relationship between the geometry of these two sets, and these are called *disharmonic folds*.

On the other hand, if the spacing of the layers is smaller so that the zones of contact strain overlap, then *harmonic folds* develop (Fig. 14.36c). Finally, if thin competent layers lie within the zone of contact strain of thicker layers, there will be a partial connection between the folds sets (Fig. 14.36d). These are *polyharmonic folds*.

<sup>17</sup>In a series of papers Hans Ramberg has treated the complex interaction of these physical factors in considerable detail (for a summary and references see Ramberg, 1981).

### 14.13 Exercises

1. Given the dip  $D$  of the hinge plane and the plunge  $P$  or pitch  $R$  of the hinge line in Table 14.10, classify the orientation of the fold using Table 14.4, Figures 14.12, 14.13 and 14.14.

Table 14.10 *Attitude of hinge plane and hinge line*

No.	$D, P, R$	No.	$D, P, R$
1	$D(90), P(0)$	6	$D(65), P(40)$
2	$D(0), R(0)$	7	$D(85), P(80)$
3	$D(20), P(20)$	8	$D(65), P(50)$
4	$D(10), P(5)$	9	$D(85), P(40)$
5	$D(40), P(20)$	10	$D(90), R(90)$

2. Using the fold profile depicted in Fig. 14.37, construct the dip isogons for layers A, B and C and classify the form of each folded layer.

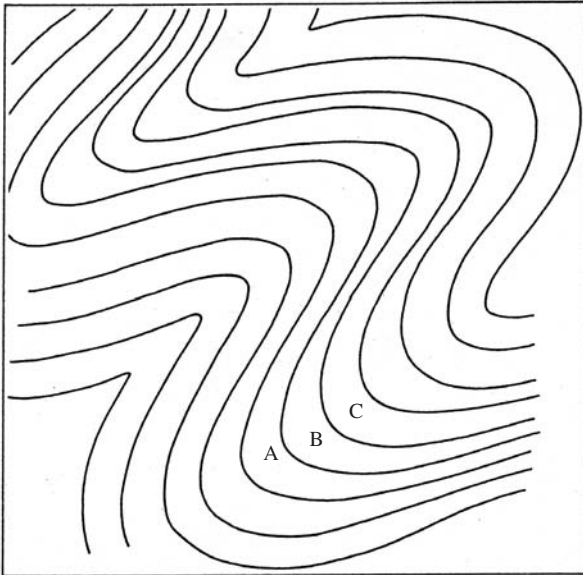


**Figure 14.37** Dip isogon problem.

# 15

## Parallel folds

### 15.1 Introduction

In some folds the thicknesses of layers remain essentially uniform with the result that they display constant orthogonal thickness. Such folds are *parallel*. They commonly have gentle to close shapes and are typically developed in well-bedded sedimentary rocks. There are two end-member shapes (see Fig. 14.4):

1. Rounded forms have smoothly curved limbs and broad hinge zones.
2. Angular forms have straight limbs and narrow hinge zones.

We seek ways of reconstructing both types of such folds in profile from field data. Here we consider only the case of horizontal folds, that is, folds whose profile planes are vertical. The methods will not work for plunging folds and the additional steps required to construct their profiles are treated in Chapter 17.

### 15.2 Rounded folds

First, we treat the case of smoothly rounded folds, sometimes referred to as *concentric folds*.

The requirement of strict constant orthogonal thickness within a folded layer or packet of layers severely limits the states of strain which can exist in parallel folded layers. There are two mechanisms involved: shear and extension.

Some insight into possible states can be obtained by considering simple models. Once again we resort to a deck of thin cards. To produce a fold hold the deck with both hands and press inward on the ends (it helps to give the center of the deck a slight upward nudge with the thumbs). The deck *buckles* and a pronounced rounded form develops (Fig. 15.1a). This combination of layer-parallel simple shear and bending is called *flexural-slip folding*.

The reason that slip dominates is that the card deck is strongly *anisotropic*. The resistance to shear parallel to the cards is small while the resistance to shear in other directions

is very much greater. Clear evidence of such *bedding-plane slip* is found in some naturally occurring folds where veins or dikes are offset across bedding planes and by polished and striated or fibrous-coated bedding surfaces.

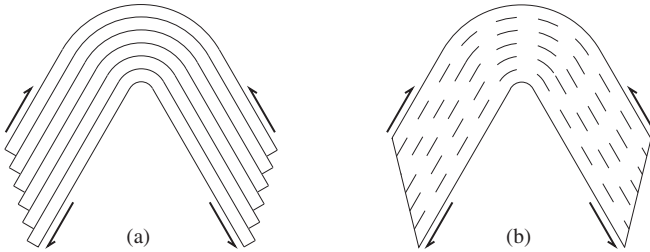


**Figure 15.1** Model folds: (a) flexural slip; (b) flexural flow.

Donath and Parker (1964, p. 48) introduced the idea that competent layers may deform by *flexural flow*, that is, like a card deck with vanishing thin cards (Fig. 15.1b). Ramsay (1967, p. 391; Ramsay & Huber, 1987, p. 446f) discussed this mechanism in some detail. However, it requires that such a layer be sufficiently anisotropic to deform in a manner analogous to the simple shear of a card deck.

Using a finite-element model, Hudleston, *et al.* (1996) explored the role of such anisotropy in the folding of a single embedded layer. Using a local coordinate system with  $x$  parallel to the plane of anisotropy the composite flow law is given by

$$\sigma_{xx} = \mu_N \dot{\epsilon}_{xx} \quad \text{and} \quad \sigma_{xy} = \mu_S \dot{\epsilon}_{xy},$$

where  $\mu_N$  is the viscosity for the shortening rate due to the normal stress  $\sigma_{xx}$  and  $\mu_S$  is the viscosity for the shear rate due to the shear stress  $\sigma_{xy}$ . The degree of anisotropy is then expressed by the ratio  $A = \mu_N / \mu_S$ .

To produce a fold which closely approximated the geometry of pure flexural flow required that  $A > 50$ . Because the anisotropy in naturally occurring layers is unlikely to have a magnitude greater than  $A \sim 10$ , the folding of an isolated competent layer by flexural flow is an unlikely mechanism.

Hudleston, *et al.* (1996) also modeled the folding of a simple system composed of five layers of equal thickness, three competent layers separated by two incompetent layers with the same viscosity as the adjacent matrix material. The *effective value* of  $A \sim 25$ . Under these conditions the resulting fold was essentially parallel, but with a different pattern of internal strain. The competent layers remained nearly parallel. The incompetent layers were more strongly sheared than predicted by the flexural flow process. However, the average taken across any competent–incompetent pair was very close to the prediction for flexural flow.

In nature the material properties of the layers in a fold are quite unlike a deck of cards and these differences have an important influence on fold geometry. In particular, the bending of a competent layer must be accompanied by strain distributed within the layer.

This strain, in turn, affects the local thicknesses of the constitutive layers. Following Ramsay (1967, p, 397–402) we model these changes in a simple way.

### Thickness and strain

Consider a rectangular element within the layer of width  $l$  whose long dimension equals the total thickness of the layer (Fig. 15.2a). At the instant buckling begins, the boundary of the layer at the outer arc is infinitesimally extended and the boundary at the inner arc is infinitesimally contracted. Between these two different states there is a continuous variation in the layer-parallel strain. The result is that there is a surface of no distortion called the *infinitesimal neutral surface* located along the center line of the layer. This subdivides the rectangle into two equal parts, each with a partial thickness  $t$ .

As buckling progresses the changes in tangential lengths continue and the initial rectangle is transformed into the sector of the annulus of a circle. There is now a curved *finite neutral surface* which is no longer at the center of the layer (Fig. 15.2b). The length of the arc along the trace of this surface is equal to the same initial length  $l$ .

The length of a circular arc of radius  $r$  is given by  $l = r\theta$ , where  $\theta$  is the angle subtended by the arc. A more useful form of this is

$$\theta = l/r \quad (\theta \text{ in radians}). \quad (15.1)$$

The fractional part of a circle represented by a sector is given by the ratio  $\theta/2\pi$ . Substituting the expression for  $\theta$  from Eq. 15.1 gives

$$\frac{\theta}{2\pi} = \frac{l}{2\pi r}. \quad (15.2)$$

The length of any other arc, compared with  $l$ , is

$$l' = l + \Delta l, \quad (15.3)$$

where  $\Delta l$  is the change in length and is positive above and negative below the neutral surface. The radius of curvature of these is given by  $r + \Delta r$ , where  $\Delta r$  is also positive above and negative below the neutral surface.

We are particularly interested in the arcs bounding the reference element. For these  $\Delta r$  is the partial thickness of the layer after buckling. We label these  $t'$ . Accordingly, the radius of curvature of each of these arcs is  $r + t'$ . Again  $\Delta r = t'$  is positive above and negative below the neutral surface.

The area of a circle is  $\pi r^2$ , and the area of a sector of this circle is obtained by multiplying by the fraction of the circle  $\theta/2\pi$  (see Eq. 15.2) giving

$$\frac{\theta}{2\pi} \pi r^2 = \frac{\theta}{2} r^2.$$



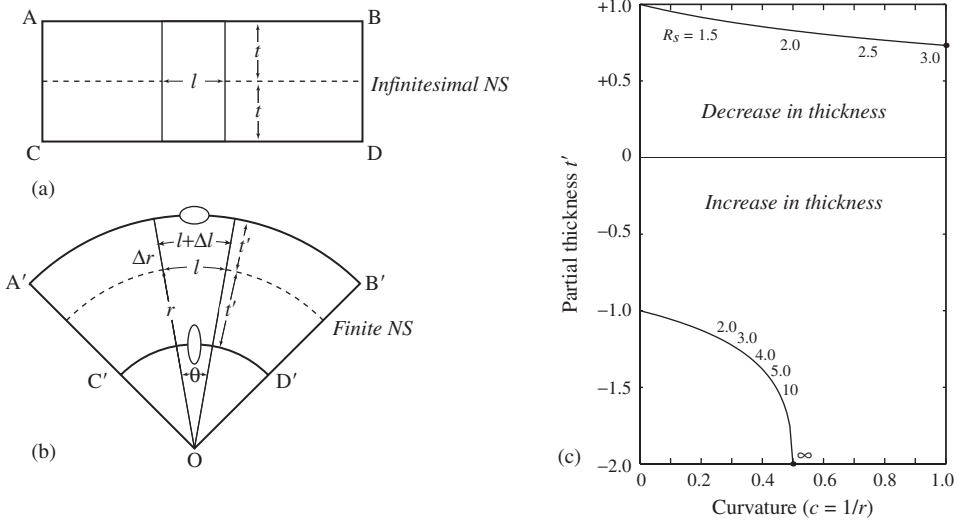


**Figure 15.2** Buckled layer: (a) initial state; (b) final state; (c) changes in partial thicknesses.

The area of an annulus of two concentric circles of radii  $r_1 > r_2$  is  $\pi r_1^2 - \pi r_2^2$ , so the area of a sector of an annulus is

$$\frac{\theta}{2\pi}(\pi r_1^2 - \pi r_2^2) = \frac{\theta}{2}(r_1^2 - r_2^2).$$

Assuming that area is conserved, the two partial areas are the same before and after buckling. We equate the area in the rectangle (Fig. 15.2a) and the area of the annulus of the sector (Fig. 15.2b). Then using Eq. 15.2 gives

$$lt = \frac{l}{2\pi r} \left[ \pi(r + t')^2 - \pi r^2 \right]. \tag{15.4}$$

Rearranging gives the quadratic equation in  $t'$

$$t'^2 + 2rt' - 2rt = 0.$$

With the quadratic formula, the positive root is

$$t' = -r + \sqrt{r^2 + 2rt}. \tag{15.5}$$

(The negative root has no physical meaning.) For convenience, we assign the magnitude of both initial partial thicknesses equal to one. With this expression we may then determine the change in thickness as a function of the curvature  $c = 1/r$  of the finite neutral surface. Clearly, for the thickness above the neutral surface there is a modest decrease.

In contrast, for thickness below the neutral surface there is a pronounced increase as folding proceeds (Fig. 15.2c).

We may also determine the strain throughout the layer. The lengths of the boundary arcs are given by

$$l + \Delta l = (r + t')\theta$$

With Eq. 15.1 this becomes

$$l + \Delta l = \frac{(r + t')l}{r} = l + \frac{t'l}{r} \quad \text{or} \quad \Delta l = \frac{lt'}{r}.$$

With this, the extension  $e = \Delta l/l$  at the two boundaries is then given by

$$e = t'/r. \quad (15.6)$$

If  $t'$  is positive, this expression gives the principal extension  $e_1$ , and if  $t'$  is negative it gives  $e_3$ . From the condition for constant area

$$S_1 S_3 = (1 + e_1)(1 + e_3) = 1.$$

Solving for both  $e_1$  and for  $e_3$  yields

$$e_1 = \frac{-e_3}{1 + e_3} \quad \text{and} \quad e_3 = \frac{-e_1}{1 + e_1}. \quad (15.7)$$

For  $+t'$ , the principal stretch  $S_1 = 1 + e_1 = 1 + t'/r$

$$(1 + t'/r)(1 + e_3) = 1. \quad (15.8)$$

Thus

$$e_3 = -\frac{t'}{r + t'}. \quad (15.9)$$

From these we can now express the strain ratio at any point within the folded layer as a function of the radius of curvature

$$R_s = \frac{1 + e_1}{1 + e_3} = \frac{1 + t'/r}{1 - t'/(r + t')}. \quad (15.10)$$

Expanding, using the expression for  $t'$  in Eq. 15.5 this reduces to

$$R_s = 1 + 2/r \quad \text{or} \quad R_s = 1 + 2c. \quad (15.11)$$

If  $-t'$ , the orientation of the principal stretches are reversed, and a similar manipulation gives

$$R_s = \frac{1}{1 - 2/r} \quad \text{or} \quad R_s = \frac{1}{1 - 2c}. \quad (15.12)$$

As a result of the bending of such a layer, its outer arc is lengthened and its inner arc is shortened. This, in turn, results in a thinning of the material adjacent to the outer arc and a complementary thickening on the inner arc. These two regions are separated by a surface of no longitudinal strain, called the *finite neutral surface* (Fig. 15.2b). At the initiation of bending the neutral surface lies along the center line of the layer, but it migrates thereafter.

While the changes above and below this surface tend to cancel, there will always be a net increase in the total thickness. The magnitude of the effect depends on the thickness and radius of curvature. If the layer is thin and the radius of curvature large, the change in thickness is small. For example, for a ratio of  $r/t = 10$ , the increase in total thickness is less than 1%, which is probably undetectable in most folds.

We are particularly interested in the states of strain at the inner and outer arcs. Using these expressions we calculate the shapes of the strain ellipses at these points (see Fig. 15.2c). As can be seen, the value of  $R_s$  at the outer boundary is quite modest, while the strain at the inner boundary rapidly approaches infinity.

This drastic increase in strain at the inner arc is a geometrical consequence of the model, but it violates the conservation of mass and is therefore not physically possible. Natural systems must find other ways of deforming and there are several possible alternatives (Ramsay, 1967, p. 400).

1. At some point the curvature at the hinge may cease to increase and as the fold continues to develop the curvature on the limbs will continue to increase with the result that the neutral surface will have nearly constant curvature throughout the fold, and the fold will be parallel with essentially circular shape.
2. The neutral surface may shift toward the inner arc so that the strain on the outer arc may continue to increase.
3. A new mechanism of deformation may develop which will distribute the strain more equably (Kuenen & de Sitter, 1938).
  - (a) Shear planes parallel to the layer boundaries may develop, which would allow “bedding-plane” slip, as has been observed in experiments with soft clay .
  - (b) Extension fractures may develop along the outer arc of the fold as observed in experiments with hard clay.
4. Conjugate shear fractures may form in the core of the fold, which would allow continuing shortening. Such fractures are often seen in natural examples of such folds.

Which of these occur, singly or in combination, depends on the physical properties of the material at the time of folding.

### 15.3 Rounded folds in cross section

The property of constant orthogonal thickness implies that a line perpendicular to the bounding surface of one layer is also perpendicular to the bounding surfaces of layers above and below. This, and the fact that any curve may be approximated by a series of circular arcs, forms the geometrical basis for reconstructing a series of horizontal parallel folds in vertical cross section.

#### Basic technique

Hewett (1920; see Fig. 2.9) was the first to reconstruct the geometry of a part of a parallel fold from dip measurements using circular arcs. Busk (1929) applied the method to the reconstruction of a train of parallel folds.<sup>1</sup> It depends on the elementary proposition that the centers of two tangent circles lie on the straight line which passes through their point of contact and which is perpendicular to the common tangent. In Fig. 15.3 two circles with centers at  $O_1$  and  $O_2$  touch at point  $A$ . Radii  $O_1A$  and  $O_2A$  are both perpendicular to the common tangent at  $A$  and therefore lie on the same line.

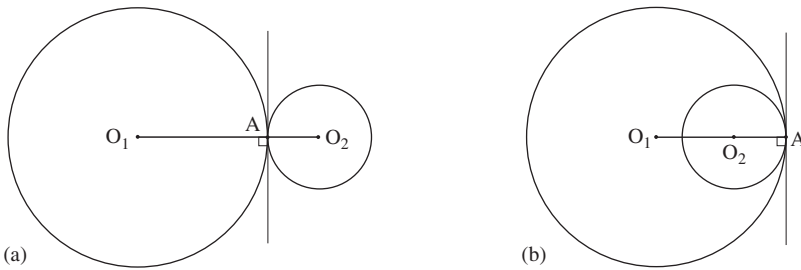


**Figure 15.3** Tangent circles.

The simplest application of this principle is to the problem of constructing the curved traces of the bounding surfaces of a layer between two successive dip lines as plotted on the profile plane.

#### Problem

- Given two measured dip angles at stations  $A$  and  $B$ , draw the circular arc which is tangent to both.

#### Construction

1. Plot points  $A$  and  $B$  in their horizontal and vertical positions using a common scale. At each of these points then draw dip lines at angles  $\delta_A$  and  $\delta_B$  and at each construct dip normals to intersect at point  $O$  (Fig. 15.4).

<sup>1</sup>The method also has application to the reconstruction of any curved surface from dip measurements, such as the slip surface of a landslide (Cruden, 1986).

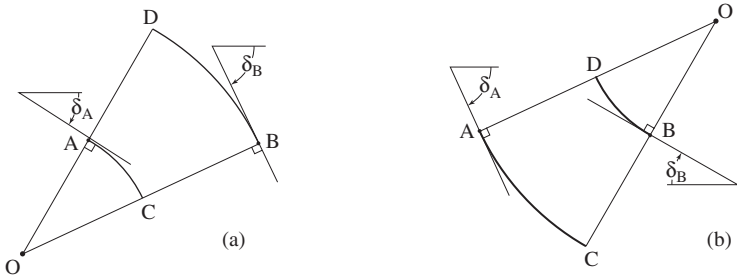


**Figure 15.4** Arcs through two adjacent dips: (a) concave down; (b) concave up.

2. With  $OA$  and  $OB$  as radii and point  $O$  as center draw arcs  $AC$  and  $BD$  which are the traces of the boundaries passing through stations  $A$  and  $B$ . Note that the thickness of the stratum is represented by segments  $AD = BC$  along the dip normals.
3. There are two cases.
  - (a) If the dip increases from  $A$  to  $B$  ( $\delta_A < \delta_B$ ) the circular arcs are concave downward (Fig. 15.4).
  - (b) If the dip decreases ( $\delta_A > \delta_B$ ) they are concave upward (Fig. 15.4b).

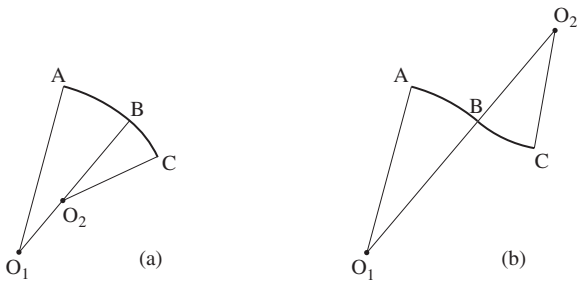


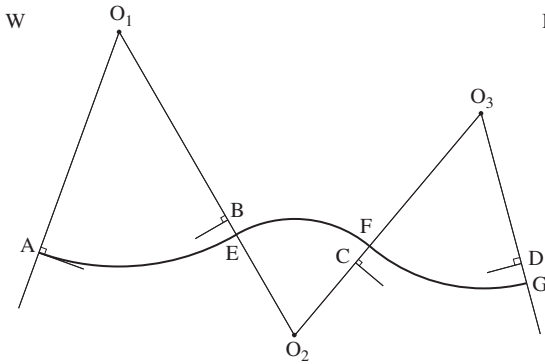
**Figure 15.5** Arcs through three adjacent dips: (a) dips in same direction; (b) dips in opposite direction.

Similarly, a composite arc may be drawn through three adjacent dips at stations  $A$ ,  $B$  and  $C$ . The middle dip may be in the same direction as the other two (Fig. 15.5a) or the middle dip may be in the opposite direction (Fig. 15.5b).

This construction is easily extended to any number of dips by working along the line of section using successive pairs of dips to carry the linked tangent arcs from one dip normal to the next.

**Problem**

- The dips at four stations are, from west to east,  $\delta_A = 20^\circ \text{ E}$ ,  $\delta_B = 30^\circ \text{ W}$ ,  $\delta_C = 40^\circ \text{ E}$  and  $\delta_D = 15^\circ \text{ W}$ . Reconstruct the surface passing through point  $A$ .



E **Figure 15.6** Linked arcs tangent to four dip lines.

**Construction**

1. Plot the distances and elevations of the four stations to scale along the line of section and at each draw the dip line (Fig. 15.6).
2. Draw the normals to the first pair of dip lines at A and B to locate center  $O_1$ . Then repeat for the second pair at B and C, locating center  $O_2$ , and finally the third pair at C and D to locate center  $O_3$ .
3. Draw the three linked tangent arcs starting at A.
  - (a) With  $O_1$  as center and radius  $O_1A$  draw the first arc to locate point E on the B dip normal.
  - (b) With center  $O_2$  and radius  $O_2E$  continue the first arc to locate point F on the C dip normal.
  - (c) With center  $O_3$  and radius  $O_3F$  complete the final arc to locate point G on the D dip normal.
4. The composite curve AEFHG represents the horizon passing through A.

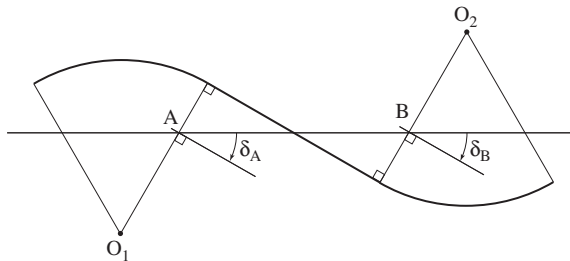


**Figure 15.7** Trace parallel to equal dip lines in same direction.

There are certain situations which require special treatment. If the measured dips at two adjacent stations are equal and in the same direction, the normals will be parallel and the required “arc” will be a straight line (Fig. 15.7).

If the two adjacent dips are not quite the same, the dip normals will intersect at some distance above or below the section. Then the required radius may exceed the expansion of even a beam compass. This may be controlled by working at a smaller scale or the large radius arc may be approximated (Busk, 1929, p. 21).

### Problem

- Given two dip normals which are not far from parallel, draw an arc passing through point  $A$ .

### Construction

1. Project the dip line from  $A$  to locate point  $C$  on the second dip normal (Fig. 15.8). Then draw a line from  $A$  perpendicular to this normal to locate point  $D$ .
2. Bisect  $\angle CAD$  to locate point  $B$  on this second dip normal.
3. Through  $B$  draw a perpendicular line to intersect first dip line  $AC$  at  $F$ .
4. Through  $F$  draw a line perpendicular to  $AB$ . The center  $O$  of the required arc lies on this line well below the section.
5. Sketch an arc through  $A$  and  $B$ , tangent to their respective dip lines and also making a right angle with line  $OF$ .

The validity of this construction lies in the fact that right triangles  $AFO$  and  $BFO$  are congruent, and therefore  $OA$  and  $OB$  are equal.

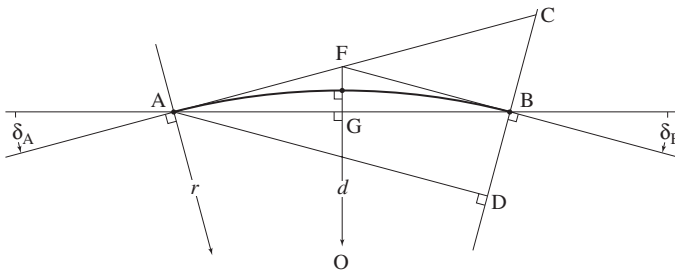


**Figure 15.8** Approximation of large radius arc (Busk, 1929, p. 21).

### Dip interpolation

The fold reconstructed by this method must, of course, be in accordance with the evidence on the ground. If a recognizable horizon is repeated along the traverse, there may be a discrepancy between its observed and reconstructed location. For example, if a recognizable horizon is found at both locations  $A$  and  $B$ , but the conventional reconstruction predicts the location is at  $B'$ , something is clearly wrong (Fig. 15.9).

The usual situation is to adjust the wavelength of the fold to bring it into concordance with the mapped location. There are two types of mismatches.

1. If the dip angles increase along the traverse ( $\delta_A < \delta_B$ ) the arc length must be increased to eliminate the mismatch (Fig. 15.9a).
2. If the dip angles decrease along the traverse ( $\delta_A > \delta_B$ ) the arc length must be shortened (Fig. 15.9b).

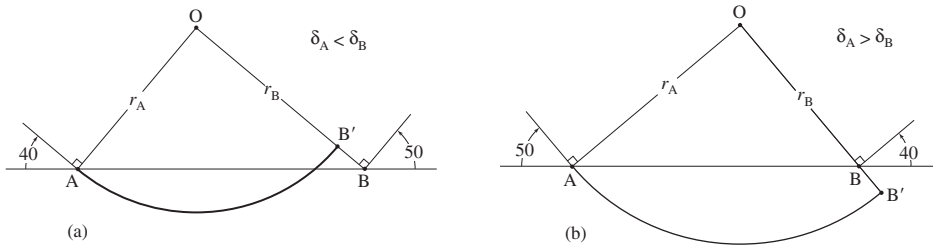


**Figure 15.9** Interpolation required: (a)  $\delta_A < \delta_B$ ; (b)  $\delta_A > \delta_B$ .

Assuming that such a mismatch is not due to change in thickness or faulting, an intermediate dip may be inserted to adjust the actual and predicted position of the marker horizon. This dip may be placed almost anywhere, but in the absence of any additional information it is probably best positioned where the control is poorest, that is, where the difference between adjacent dips is large, or the distance between them is great, or both.

The way this is done is to replace the single circular arc with a pair of linked arcs which have a common tangent at their junction and which satisfies the evidence on the ground.

A method for doing this was given by Busk (1929, p. 26–27), then simplified and extended by Higgins (1962). Owens (2000) discovered that the locus of possible points of common tangency lies on a circular arc. This leads to a completely different way which allows the range of possible solutions to be explored more completely. It is also amenable to an analytical solution.<sup>2</sup>

### Problem

- Given measured dips  $\delta_A = 40^\circ$  at station  $A$  and  $\delta_B = 50^\circ$  at station  $B$  along the line of traverse, construct the trace of the curved surface passing through both  $A$  and  $B$ .

### Construction

1. Plot the outcrop points  $A$  and  $B$  in their correct relative horizontal and vertical locations. Connect these two points with a straight line (Fig. 15.10a).
2. Draw the associated dip lines  $\delta_A = 50^\circ$  at  $A$  and  $\delta_B = 70^\circ$  at  $B$  to intersect at point  $X$ .
3. To locate the center  $K$  of the circular locus of points of common tangency:

<sup>2</sup>For such an analytical/computer solution it is necessary to specify the sense of several angles by adopting a sign convention. For a graphical solution, however, the sense of these angles can be determined by inspection, so they are all treated here as positive quantities.



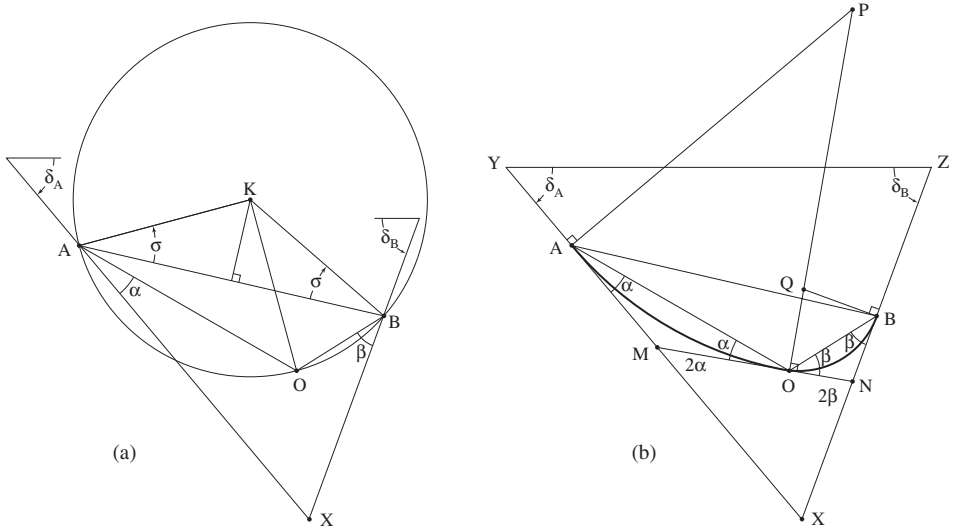


**Figure 15.10** Interpolation (Owens, 2000): (a) point of common tangency; (b) interpolated dip.

- (a) Construct the perpendicular bisector of line  $AB$ .
- (b) Through  $A$  draw a line making an angle  $\sigma$  measured anticlockwise from  $AB$  or through  $B$  clockwise from  $AB$ , where

$$\sigma = 90 - \frac{1}{2}(\delta_A + \delta_B). \tag{15.13}$$

The sense of  $\sigma$  is determined by the rule that  $K$  is above  $AB$  for a syncline (as here), and below  $AB$  for an anticline.

- (c) The intersection of the bisector and either of these two lines is the center  $K$  of the circular arc. Complete the circle with radius  $KA = KB$ .
4. Select a point of common tangency  $O$  on this arc. The location of this point determines the shape of the reconstructed fold: if is near the center of the arc  $AB$  the compound curve will be approximately symmetrical, and if it is significantly closer to either  $A$  or  $B$  it will be distinctly asymmetrical.
  5. Draw line  $AO$ . This line makes angle  $\alpha$  with dip line  $AX$ .
  6. Draw line  $BO$ . This line makes angle  $\beta$  with dip line  $BX$ .
  7. Draw a line at  $O$  making the angle  $\alpha$  with  $AO$ , thus locating point  $M$  on the dip line  $AX$ . Similarly, draw a line at  $O$  making the angle  $\beta$  with  $BO$ , thus locating point  $N$  on the dip line  $BX$  (Fig. 15.10b).
  8. The inclination of straight line  $MON$  is the interpolated dip, and the centers of the two linked tangent arcs can now be established.
    - (a) Construct a line perpendicular to  $MON$  at  $O$ .
    - (b) Construct a line perpendicular to  $AX$  at  $A$  to intersect the normal line at  $O$  at point  $P$ .

- (c) Construct a line perpendicular to  $BX$  at  $B$  to intersect the normal line at  $O$  at point  $Q$ .
- 9. With point  $P$  as center draw a tangent arc with radius  $r_A = PA = PO$ . With point  $Q$  as center draw a tangent arc with radius  $r_B = QO = QB$ .

This method can also be used if the beds at  $A$  and  $B$  dip in the same direction. However, some caution should be observed because the construction inserts a new fold into the cross section.

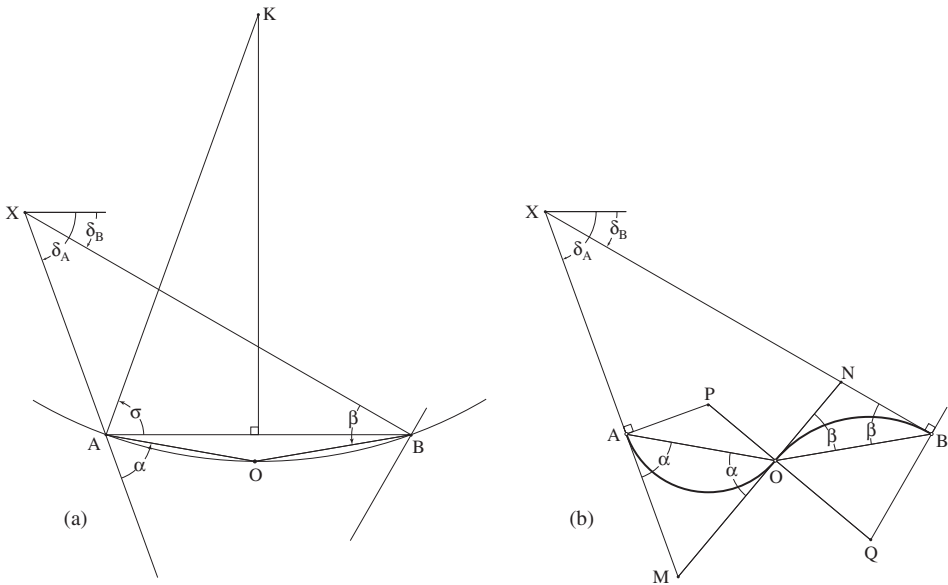


**Figure 15.11** Interpolation (after Owens, 2000): (a) point of common tangency; (b) interpolated dip and resulting compound curve.

**Problem**

- Given measured dips  $\delta_A = 70^\circ$  at station  $A$  and  $\delta_B = 30^\circ$  at station  $B$ , both in the same direction, construct the trace of the curved surface passing through both  $A$  and  $B$ .

**Construction**

1. As before, plot the outcrop points  $A$  and  $B$  in their correct relative horizontal and vertical locations, and connect these two with a straight line (Fig. 15.11a).
2. At each of these points draw the associated dip lines,  $\delta_A = 70^\circ$  at  $A$  and  $\delta_B = 30^\circ$  at  $B$  intersecting at point  $X$ .
3. To locate the center of the circular locus of points of common tangency:
  - (a) Construct the perpendicular bisector of line  $AB$ .

- (b) Draw a line through  $A$  making an angle  $\sigma$  measured anticlockwise from  $AB$  or through  $B$  clockwise from  $AB$ , where

$$\sigma = 90 - \frac{1}{2}(\delta_A - \delta_B). \quad (15.14)$$

4. The intersection of these two lines is the center  $K$  of the circular arc, which in this case is above  $AB$ . Complete the circle with radius  $KA = KB$ .
5. Select a point of common tangency  $O$  on this arc.
6. Draw line  $AO$ . This line makes angle  $\alpha$  with dip line  $AX$ .
7. Draw line  $BO$ . This line makes angle  $\beta$  with dip line  $BX$ .
8. Draw a line at  $O$  making the same angle  $\alpha$  with  $AO$ , thus locating point  $M$  on the dip line  $AX$  and a line at  $O$  making the same angle  $\beta$  with  $BO$ , thus locating point  $N$  on the dip line  $BX$  (Fig. 15.11b).
9. The inclination of straight line  $MON$  is the interpolated dip, and the centers of the two tangent arcs can now be established.
  - (a) Construct a line perpendicular to  $MON$  at  $O$ .
  - (b) Construct a line perpendicular to  $AX$  at  $A$  to intersect the line at  $O$  at point  $P$ .
  - (c) Construct a line perpendicular to  $BX$  at  $B$  to intersect the line at  $O$  at point  $Q$ .
10. With points  $P$  and  $Q$  as centers draw the tangent arcs  $AO$  and  $BO$ .

### General reconstruction

With this collection of techniques we may now reconstruct the form of any folded strata from map data or from a field traverse made expressly for the purpose. In either case, the line of section should be as nearly perpendicular to the strike direction of the dipping beds as possible. In preparing the cross section, it is conventional to orient the line so that its eastern or northern end is on the right-hand side.

Even in simple, well-behaved folds, it is rarely possible to locate a section line exactly normal to all measured strikes, in which case apparent dips in the direction of the section line must be computed before the dip lines are plotted. In addition to the correct locations along the section line, the elevations of these points must also be plotted using the same scale, that is, there must be no vertical exaggeration.

The number of readings exactly on the chosen section line is never enough. Other measurements may be used by projecting them short distances to the line of section. Usually they are projected parallel to the local line of strike, but this may require adjustment if there is a significant angle between the section line and the dip direction; otherwise, projecting strike lines may cross and the dips will then be reversed on the section line from their relative positions in the field. The need to convert to apparent dips and the use of obliquely projected attitudes means that the folds are not strictly cylindrical. This introduces errors and uncertainties which must be kept in mind when interpreting the form of reconstructed folds (see Busk, 1929, p. 19).

**Problem**

- Complete the structure section of the folds at depth for the data of Table 15.1.

Table 15.1 *Structural data*

Station	Dip	Station	Dip
A	20° E	F	25° E
B	10° W	G	75° E
C	45° W	H	50° E
D	10° W	I	20° E
E	0°	J	0°

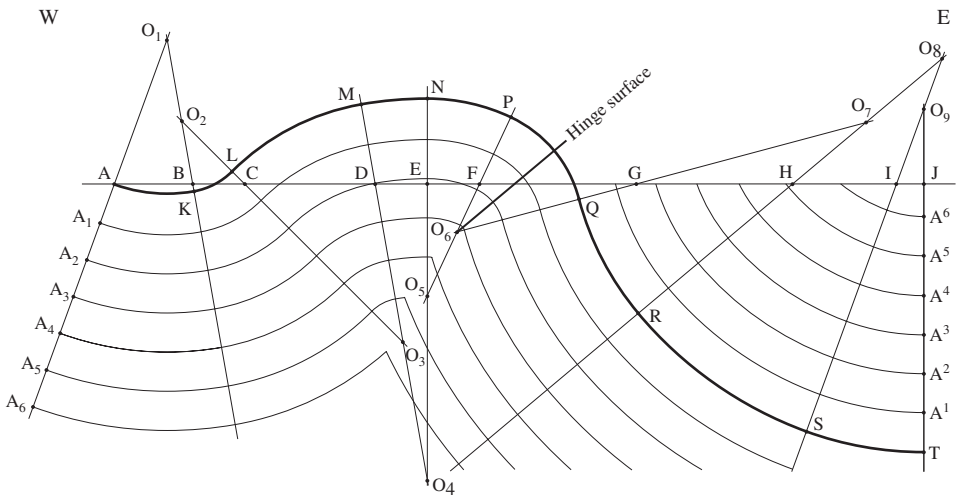


**Figure 15.12** Full reconstruction by tangent arcs showing trace of the hinge surface.

**Construction**

1. At each station, draw the dip normal; pairs of these intersect at centers  $O_1 - O_9$ .
2. Starting with the horizon exposed at point A and using each center in sequence, draw the circular arcs to locate points K–T representing the intersection of this horizon with each dip normal (Fig. 15.12).
3. These may represent the actual thicknesses of known strata or they may be shown schematically with constant thickness (as here).
4. With  $O_1$  as center draw arcs through points  $A_1 - A_3$  to the B dip normal. Using successive centers continue the traces of these contacts.
5. For horizons  $A_4$  and  $A_5$  an adjustment is required. From their intersections with radius  $O_1 O_2$ , the next step would be to continue using center  $O_2$ , but this can not be done because it lies above horizon  $A_4$  and therefore has no control on the shapes of curves below it. The following steps should then be used.

- (a) The  $A_4$  and  $A_5$  arcs should be continued just beyond the  $B$  dip normal.
  - (b) To maintain uniform thickness  $A_4$  and  $A_5$  should be marked off on the  $D$  dip normal. Swinging arcs through these marks back into the core of the anticline produces angular, rather than rounded hinges.
6. To locate the trace of the hinge plane in the asymmetric anticline bisect the angle  $PO_6Q$ .

In many cases, this reconstruction produces acceptable results as confirmed by observations at the surface of the earth, and it improves as the quality and quantity of structural and stratigraphic control increases. There are, however, some important limitations and an awareness of these should aid in constructing and interpreting such sections.

At best, concentric circular arcs can only approximate the natural curves of rounded parallel folds, although once again, the more attitude data available, the closer this approximation will be to reality. A part of the problem arises because each arc segment utilizes only two dip angles.

With the Busk construction, measurement errors or local structural irregularities will propagate throughout the section. Reches, *et al.* (1981) suggested a modification of the basic technique which may help avoid this problem. Several concentric arcs, using a number of adjacent centers, are drawn on an overlay sheet to find the arc which gives the best fit to the structural and stratigraphic data.

Mertie (1947) explored quite a different approach involving no assumptions about the nature of the curvature, and which makes the best possible use of the existing data. The technique involves constructing a curve called an *evolute* which utilizes a number of adjacent dip measurements. Along this curve the center and radius of curvature of the traces of the parallel layers, called *involutives*, vary continuously. The construction of these curves is more involved than drawing tangent arcs and it does not seem to have been widely used. It does represent a useful way of emphasizing just how limited concentric circular arcs are in approximating general curves.

In an additional approach, McCoss (1987) gave a practical explanation of how rotated cubic spline interpolators can be used to construct the form of folded surfaces using a computer-aided approach.

Finally, the appearance of the sharp cusps in the core of the anticline warns us that there is something seriously wrong there. If continued upward the same problem would appear in the cores of synclines. To round off these cusps, as suggested by Badgley (1959, p. 34), is entirely cosmetic and ignores completely the most serious defect of the reconstructions by the Busk technique for the form of the folds at depth – it fails utterly in the cores of the folds!

In order to see what the problem is we attempt to restore the layers to their pre-folding state. We do this by measuring the length of each folded horizon to estimate their original lengths (Fig. 15.13). As can be seen, this reconstruction using tangent arcs results in a considerable loss of material, which is entirely unrealistic.

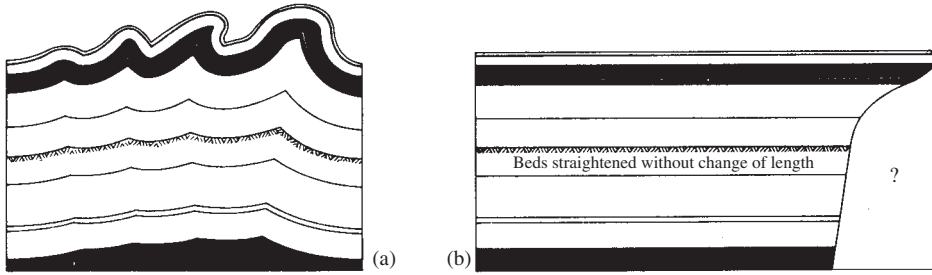


**Figure 15.13** Unequal shortening (after Carey, 1962): (a) reconstruction; (b) restoration (from Carey, 1962). Used with permission of the *Journal of the Alberta Society of Petroleum Geology*.

### 15.4 Balanced cross sections

In the light of these limitations, it would be useful to have some way of testing our reconstruction for internal consistency and geological reasonableness. Here, we briefly describe such a test.<sup>3</sup> By way of introduction we make the following assumptions:

1. The deformation which produced the folds was two dimensional, that is, all changes occurred in the plane of the section.
2. The deformation was isochoric, and as a consequence area in the plane of the section is conserved.
3. The layers which mark the folds originally had constant orthogonal thickness.
4. The fold geometry is essentially parallel throughout.

If area is conserved and bed thickness is constant, it follows that the length of any bed must also remain constant, or nearly so. Because of the requirement of this constancy of bed length, it follows that the length of the traces of each folded surface must be the same from one bed to another. This leads to a simple test of consistency to the reconstructed shape of the parallel folds.

#### Steps

1. Establish a pair of reference lines at either end of the section in regions of no interbed slip. These may be located at the hinges of major anticlines or synclines, or in regions well beyond the fold belt.
2. Measure the length of the traces of selected horizons between the two reference lines. This can be done most easily with a curvimeter.<sup>4</sup> These lines should all be the same length.
3. If the lengths are not the same, the section must show a valid explanation of why they are not.

<sup>3</sup>There is a large and growing literature on the subject. Good overviews are given by Suppe (1985, p. 57–70), Ramsay and Huber (1987, p. 543–559), Marshak and Woodward (1988), De Paor (1988) and Woodward, *et al.*, (1989).

<sup>4</sup>This is a device with a small wheel and dial which measures the length of a curved line.

Sections which pass this test are termed *balanced* (Dahlstrom, 1969a; Hossack, 1979; Elliott, 1983). An important property of such sections, and indeed the principal reason for constructing them is that the amount of shortening represented by the folds can be determined by comparing the original and deformed lengths of the folded traces. Note too that balance is a *necessary*, but not *sufficient* condition for the correctness of the section. That is, if the section does not balance it can not be correct, but even if it does balance it may not be completely accurate.

If this test is applied to the parallel folds reconstructed by Busk's method, it will be found that the bed length is not consistent (Fig. 15.13). The source of most of this discrepancy lies in the cusp-shaped hinges in the cores of the anticlines. Clearly, these reconstructed forms can not represent the actual geometry in the deeper zones even approximately. This means that the mechanism of parallel folding breaks down at depth and that other mechanisms become important. The geometry of these deeper structures can not be predicted from surface data alone. However, the main alternatives can be outlined.

There are two main ways of resolving this difficulty. The first is to introduce one or more *thrust faults* in the core of the fold which accommodates the shortening in order to conserve total bed length. Fault slip and fold shortening may be interchanged (Fig. 15.14a) or faults alone may accomplish the required shortening (Fig. 15.14b).

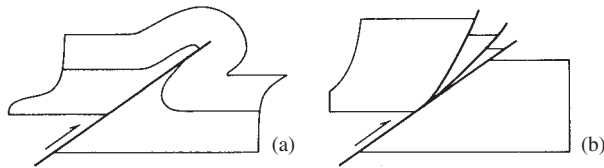


**Figure 15.14** Thrusts in fold cores: (a) accommodation by folding; (b) accommodation by imbricate faulting (from Dahlstrom, 1969a). Used with permission of the National Research Council of Canada.

The second way is to keep the bed length and thickness of the deeper layers as constant as possible. The only way of doing this is by changing the sizes and shapes of the folded layers. This is *disharmony*. An example is shown in Fig. 15.15. The immediate question is then how would the next lower layer be drawn? This leads to the shearing off, or *décollement*.

Often thrusts and fold disharmony occur together. A famous section from the Jura Mountains where the basic concept of the *décollement* was first developed is shown in Fig. 15.16.

Where such a detachment is present we can calculate its depth.

## 15.5 Depth of folding

The position of this basal detachment is determined by the location within the sedimentary sequence of weak layers, such as shale, or in extreme cases, salt and gypsum, or by

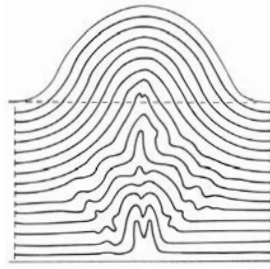


**Figure 15.15** Reconstruction of fold at depth by maintaining original bed length and conserving area (from Goguel, 1952). Used with permission of Mason et Cie.

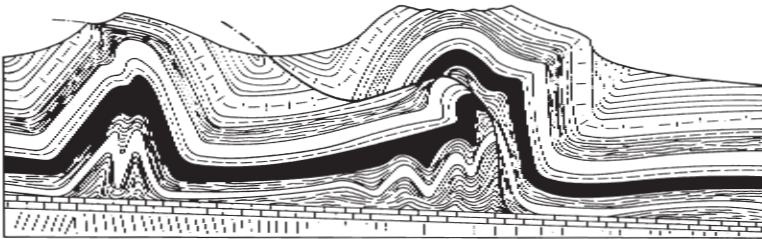


**Figure 15.16** Section through a part of the Jura Mountains (from Buxtorf, 1916).

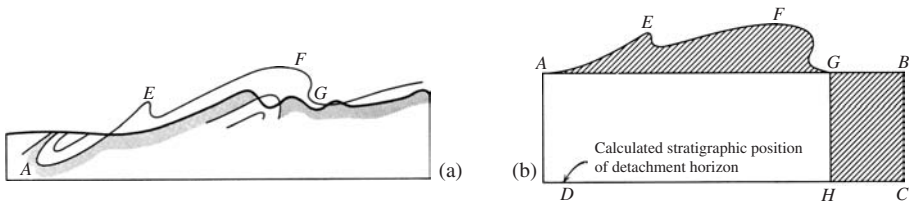


**Figure 15.17** Calculation of depth of folding (from Dahlstrom, 1969b). Used with permission the Bulletin of Canadian Petroleum Geology.

the contact between the sedimentary rocks and the underlying rigid basement unit. In detail the behavior of the lower part of the folded sequence depends on the mechanical properties of the rocks involved. Instead of tightly crumpled folds in the cores of the anticlines, thrust faults may form that root in the décollement zone. These faults may or may not break through to the surface, and if they form early in the folding they themselves may be deformed by continuing folding or by late thrusting.

The effect of folding is to make a packet of rocks thicker and shorter. If volume is conserved in the packet, the amount of material uplifted must exactly equal the decrease due to shortening. Since both the amount of thickening and shortening can be measured on a cross section, the depth of the décollement can be determined (Dahlstrom, 1969b, p. 342).



### Calculation

1. The lateral shortening of a reference horizon between points of no slippage is determined by comparing the bed length measured with a curvimeter, with the lateral distance this horizon occupies in the folded packet. In Fig. 15.17a the bed length measured at the top of the Mississippian Rundle group is  $AEFG = AB$ . The distance  $GB$  represents the actual shortening.
2. The amount of increased area of the thickened packet between the two no-slip reference points is measured with a planimeter.<sup>5</sup>

In Fig. 15.17b, this area lies between the straight line  $AG$  and the trace of the folded reference horizon  $AEFG$ .

3. The depth  $AD$  of folding follows directly from the relationship:

$$\text{Depth} = \frac{\text{area uplifted}}{\text{shortening}}.$$

Note that the area of rectangle  $GBCD$  equals the area measured in step 2.

It should also be noted that when the depth to the basal thrust is independently known, the shortening may be found using this same formula. This is also an estimate of the minimum displacement on the décollement thrust.

This method of estimating the depth of folding has been used with good results in the Jura Mountains where the concept of the décollement originated. However, these results are not without difficulties. How can a packet of sedimentary rocks be deformed in a manner which is independent of the underlying material? Suggestions have been made concerning the possible existence of related structures, such as imbricate slices in the underlying block. Besides raising several additional difficulties, there is now clear and compelling geophysical evidence that in the external zones of at least some mobile fold belts no such sub-décollement structures are present, but the agents responsible for the deformation remain in question.

It should be abundantly clear that parallel folding is a complicated process, and must involve other modes of deformation, including disharmony and shearing off. It does not follow, however, that every group of parallel folds has a single décollement thrust at depth. The necessary adjustments may take place locally and gradually rather than at a single horizon at depth. Many small-scaled examples of detachment structures can be found in the field.

More importantly, in the internal zones of mountain belts, the basement and cover rocks may both participate in the deformation. Synchronous folding and thrusting of the overlying, near-surface rock layers would be a certainty, and these would most likely involve, at least in part, the parallel mode.

<sup>5</sup>See <http://en.wikipedia.org/wiki/Planimeter> and <http://wantasub1.stores.yahoo.net/dip1.html>.

Barnes and Houston (1969) have described a simple example which illustrates the principle involved. In a part of the Medicine Bow uplift in the Northern Rocky Mountains of Wyoming, a Precambrian basement complex is unconformably overlain by Paleozoic and Mesozoic sedimentary rocks. During the Laramide Orogeny, these layers were folded, presumably in response to distributive movement on micro-fractures in the basement unit (Fig. 15.18). Under these circumstances shearing off is not required.

Compton (1966) described a similar example, and he was able to demonstrate actual slip on the closely spaced fractures in a gneissic basement. In this case, up to 3700 m of overlying sedimentary rocks were deformed by folding. An interesting feature is the evidence of disharmony in the upper part of the sequence, particularly in the cores of synclines. Dalstrom (1969b) has shown that in certain instances this upward increase in disharmony may lead to an upper detachment fault.

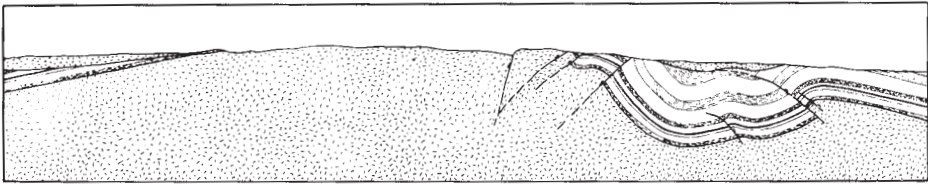


**Figure 15.18** Laramide fold in the Northern Rocky Mountains (from Barnes and Houston, 1969). Used with permission of Contributions to Geology.

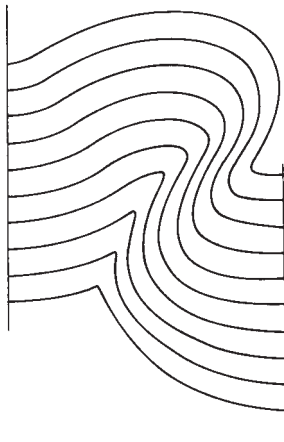


**Figure 15.19** Thinning of the overturned limb (after Busk, 1929, p. 57).

## 15.6 Non-parallel modifications

If non-parallel folds are present, even locally, there may be severe distortions if an attempt is made to force the structural data into a parallel mode.

We have already seen how homogeneous flattening changes the geometry of parallel folds (see §14.11).

There is a limit to how much shortening can be accomplished by the process of parallel folding. Often the result is that, after a certain degree of shortening, parallel folds often become asymmetrical, that is, one limb becomes steeper than the other and may finally become overturned. Although it may occur earlier, thinning is geometrically required at the point of overturning (Busk, 1929, p. 30). The beds of the less steep limb may still be parallel. In terms of the reconstruction by circular arcs, this non-parallelism is proved when correlation of a key horizon and the utilization of certain dip measurements is irreconcilable. The simplest approach is to make the necessary adjustments in the thinner limb by freehand sketching (Fig. 15.19).

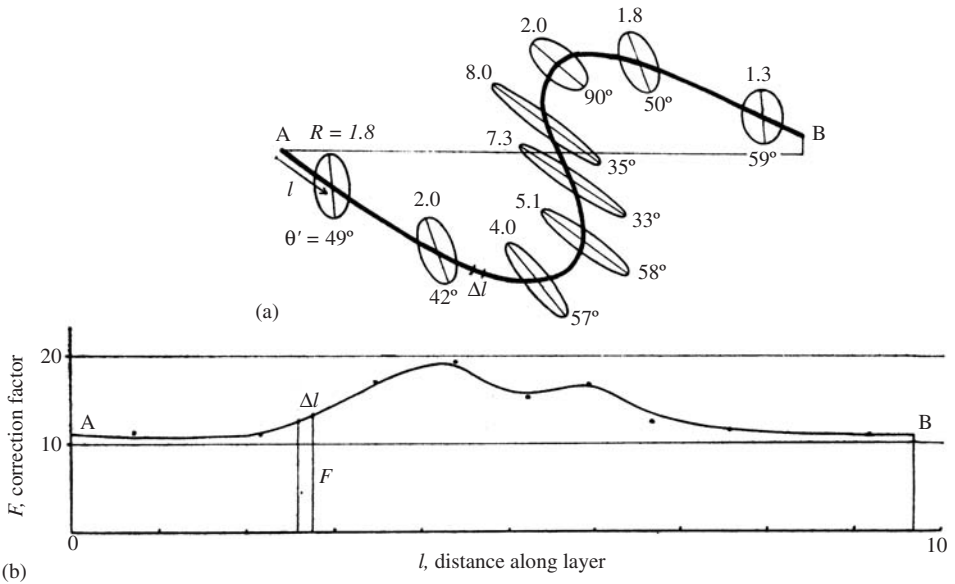


**Figure 15.20** Shortening in a non-parallel fold: (a) folded layer and the strain at several points; (b) graph of the correction factor as a function of distance along the layer (after Ramsay, 1969, p. 61).

We can approximate the original bed length by measuring the length of the curve representing the reconstruction of the uppermost parallel folded layer, as we have done in Fig. 15.13.

However, once a folded layer departs from parallel geometry any estimation of the horizontal shortening becomes more difficult. One reason for such a departure is the homogeneous flattening treated in §14.11. In this case we can separate the folding and flattening strain.

More generally, it is necessary to apply a correction to the deformed length, thus determining the original bed length, and this requires information on the state of strain at as many points in the layer as possible. In Fig. 15.20, an increment  $\Delta l'$  of the deformed

bed is shown, together with the principal stretches derived from measurements. In terms of the original length of this same increment  $\Delta l$  and the extension parallel to the bedding,

$$\Delta l' = S \Delta l \quad \text{or} \quad \Delta l = \Delta l' / S.$$

In other words, to recover the original length of this segment, we must multiply the deformed length by a correction factor  $F = 1/S$ . From Eq. 12.9,

$$F^2 = \frac{1}{S^2} = \frac{\cos^2 \phi'}{S_1^2} + \frac{\sin^2 \phi'}{S_3^2}. \quad (15.15)$$

Because of the problems of determining the full state of strain, it is useful to consider separately the distortion and the dilatation. This can be done by first combining the two terms on the right by using a common denominator, and making the following substitutions

$$R_s = S_1/S_3, \quad 1 + \Delta = S_1 S_3, \quad \cos^2 \phi' = 1 - \sin^2 \phi'.$$

The term  $1/(1 + \Delta)$  can be factored out, leaving

$$F^2 = \left( \frac{1}{1 + \Delta} \right) \left( \frac{1}{R_s^2} + \frac{R_s^2 - 1}{R_s} \right) \sin^2 \phi'.$$

Applying this to Fig. 15.20, where  $R_s = 2.7$  and  $\phi' = 53^\circ$ , gives

$$F = 1.35 \sqrt{1/(1 + \Delta)}.$$

It may be difficult to determine the area strain  $\Delta$ , which will not be zero if the strain has not been plane or if there has been a volume change, or both. This is the same problem faced in the construction of balanced sections, and without further information applying this result generally gives a minimum estimate of the original length, hence a minimum estimate of the shortening.

### Problem

- Given the folded layer of Fig. 15.20a, together with nine determinations of the constant area strain ellipses, find the shortening of the layer.

### Steps

1. Measure the arc length of the deformed layer, and determine the distance from point *A* to the points where the strain is known (after Ramsay, 1969; see Fig. 15.20b).
2. At each locality, calculate the correction factor and plot its value against distance. Draw a smooth curve through these points to give an estimate of the continuous variation of *F* with distance.

- To find the original length of the layer from  $A$  to  $B$ , sum all the  $\Delta l$  to give true original length.

The value of this simple integral is the area under the curve which can be found with a planimeter. The result is 12.8 square units.

### Answer

- The length of the straight line  $AB$  is 6.1 units. The measured arc length around the folded layer is 9.7 units; by removing the strain this is increased to 12.8 units. The shortening is then  $(6.1 - 12.8) = -6.7$  units. Expressed as an extension:  $e = (-6.7/12.8) = -0.52$ . Because the area strain is not known, this is a minimum shortening.

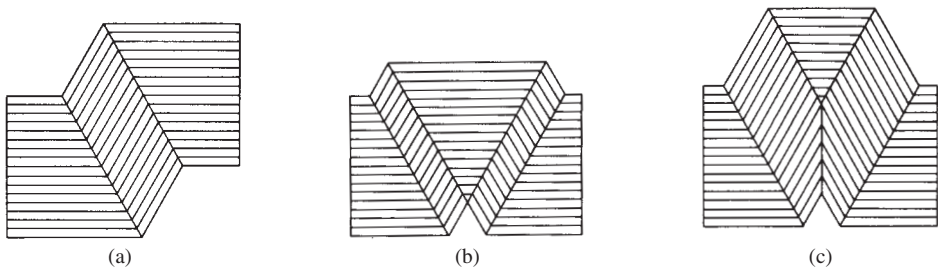


**Figure 15.21** Model angular folds.

## 15.7 Angular folds

Large-scaled folds with relatively straight limbs and narrow hinges have been recognized in many mountain belts: Appalachians (Faill, 1973), eastern Canadian Rockies (Dahlstrom, 1970; Thompson, 1981; Mountjoy, 1992), Jura Mountains (Laubscher, 1977a, 1977b), and elsewhere.

Angular folds are found in some thinly laminated rocks such as shale, slate, phyllite and fine-grained schist.

Similar small-scaled angular folds can also be produced in card decks but the process requires a special mechanical device (Weiss, 1969; Suppe, 1985, p. 336). The problem is that the straight limbs and narrow hinges can not be produced by hand. Further, while the geometry of such angular folds is simple the processes by which they form are not (Twiss & Moores, 1992, p. 248f). We can, however, illustrate the main principles involved. Commonly such model folds take two forms.

- Kink bands* are angular, step-like monoclines between two parallel *kink band boundaries*, which are also the hinge planes (Fig. 15.21a).
- Box folds* are the results of the intersection of conjugate kink bands (Fig. 15.21b).
- With greater shortening, box folds display *chevron* forms (Fig. 15.21c).

The deformation within a kink band is homogeneous simple shear combined with an external rotation. The process, but not the geometry, can be roughly modeled with a simple card-deck experiment: grip the deck firmly at both ends and without rotating the ends, shift the deck into a Z or S shape.

These kink-band type folds are taken as models of the larger-scaled angular folds, and the geometrical features of these models are then used to reconstruct angular folds in cross section.

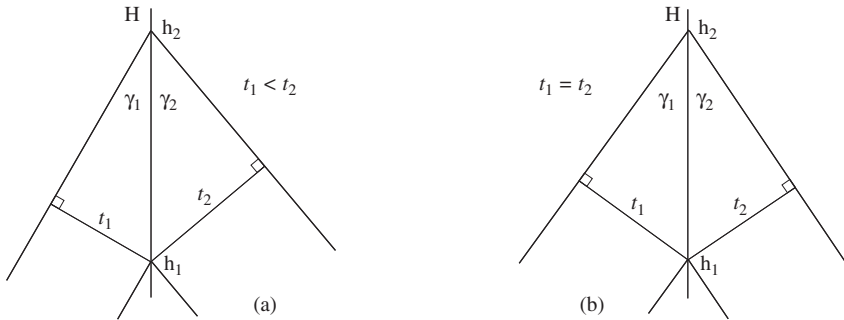


**Figure 15.22** Limb thickness: (a) asymmetric fold; (b) symmetric fold.

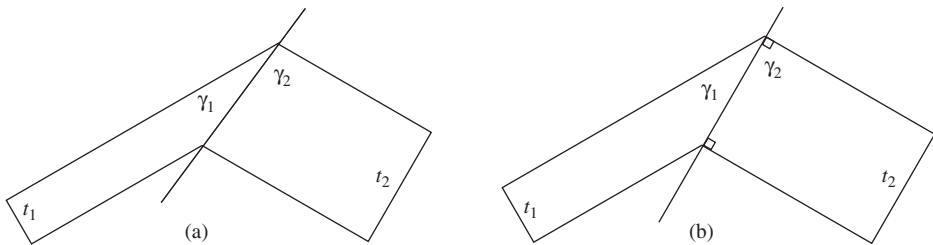


**Figure 15.23** Case of obtuse  $\gamma = 120^\circ$  and small  $R$ : (a)  $R = 0.40$  and  $\gamma_2$  is also obtuse; (b) boundary case when  $R = 0.50$  and  $\gamma_2 = 90^\circ$ .

The shapes of box and chevron folds have two variations. The thickness of a layer on opposing limbs may be the same or it may be different. This variation in orthogonal thickness is closely related to the angles the trace of the hinge plane makes with the limbs (Suppe, 1985, p. 64). This relationship can be used as an aid in reconstructing their shapes in cross section. In Fig. 15.22, the orthogonal thickness of the thinner limb is labeled  $t_1$  and that of the thicker limb is labeled  $t_2$ . The corresponding angles the hinge plane  $H$  makes with these *partial limb angles*  $\gamma = \gamma_1 + \gamma_2$ . Note that the smaller angle is associated with the thinner limb. From the two right triangles involving these sides and angles with common hypotenuse

$$\frac{t_1}{\sin \gamma_1} = \frac{t_2}{\sin \gamma_2} \quad \text{or} \quad \frac{t_1}{t_2} = \frac{\sin \gamma_1}{\sin \gamma_2}. \tag{15.16}$$

That is, the ratio  $R$  of the thicknesses and of the sines of the angles are equal. The interlimb angle  $\gamma = \gamma_1 + \gamma_2$ . This result can be used in two ways.

1. If partial hinge angles are known, the ratio of the limb thicknesses can be found directly from Eq. 15.16. Alternatively, defining  $R = t_1/t_2$  and the total hinge angle we may write

$$R = \frac{\sin(\gamma - \gamma_2)}{\sin \gamma_2}. \quad (15.17)$$

For example, from Fig. 15.23a  $\gamma_1 = 30^\circ$  and  $\gamma_2 = 40^\circ$ . Then  $R = 0.78$ , that is,  $t_1$  is 78% of  $t_2$ .

2. If the interlimb angle and both limb thicknesses are known, then the partial hinge angles can be found. With the identity for the sine of the difference of two angles Eq. 15.17 becomes

$$R = \frac{\sin \gamma \cos \gamma_2 - \cos \gamma \sin \gamma_2}{\sin \gamma_2} = \frac{\sin \gamma}{\tan \gamma_2} - \cos \gamma.$$

Then

$$\tan \gamma_2 = \frac{\sin \gamma}{R + \cos \gamma}. \quad (15.18)$$

Again from Fig. 15.23a,  $R = 0.78$  and  $\gamma = 70^\circ$ . With these values we have  $\gamma_2 = 40^\circ$  and therefore  $\gamma_1 = 30^\circ$ .

In the special and important case, if  $t_1 = t_2$  then  $\gamma_1 = \gamma_2$  and conversely. The trace of the hinge plane then bisects the interlimb angle (Fig. 15.22b).

Equation 15.18 has a minor quirk: if interlimb angle  $\gamma$  is obtuse then  $\cos \gamma$  is negative. For large values of  $R$ , the denominator  $R + \cos \gamma$  will be positive and  $\gamma_2$  will be acute, but if  $R$  is small, then  $R + \cos \gamma$  may be negative with the result that  $\gamma_2$  will be obtuse. For example, if  $\gamma = 120^\circ$  and  $R = 0.40$ , then  $\gamma_2 = -83.4^\circ$  or  $+96.6^\circ$  (Fig. 15.23a).

The boundary between an acute or obtuse angle  $\gamma_2$  occurs when  $R + \cos \gamma = 0$  and then  $\gamma_2 = 90^\circ$  (in Fig. 15.23b  $R = 0.50$ ).

## 15.8 Angular folds in cross section

Geological maps of terranes with angular folds have a characteristic pattern; the angle and direction of dips are nearly the same in parallel bands and change abruptly from one band to the next. These are *dip domains* which are identified in the field. Based on the attitudes in these domains, we wish to develop techniques for reconstructing the angular folds in section.

The reconstruction of such angular folds involves the straightforward projection of lithologic contacts parallel to the domain dips. A crucial step is the location of the hinge points and therefore also the trace of the hinge plane.

**Problem**

- Draw a section depicting the folds shown on the geological map (Fig. 15.24).

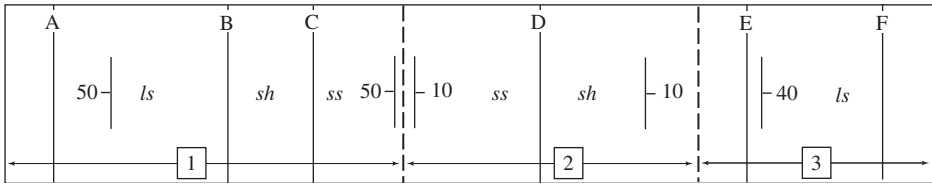


**Figure 15.24** Geological map of angular folds with Domains 1, 2 and 3.

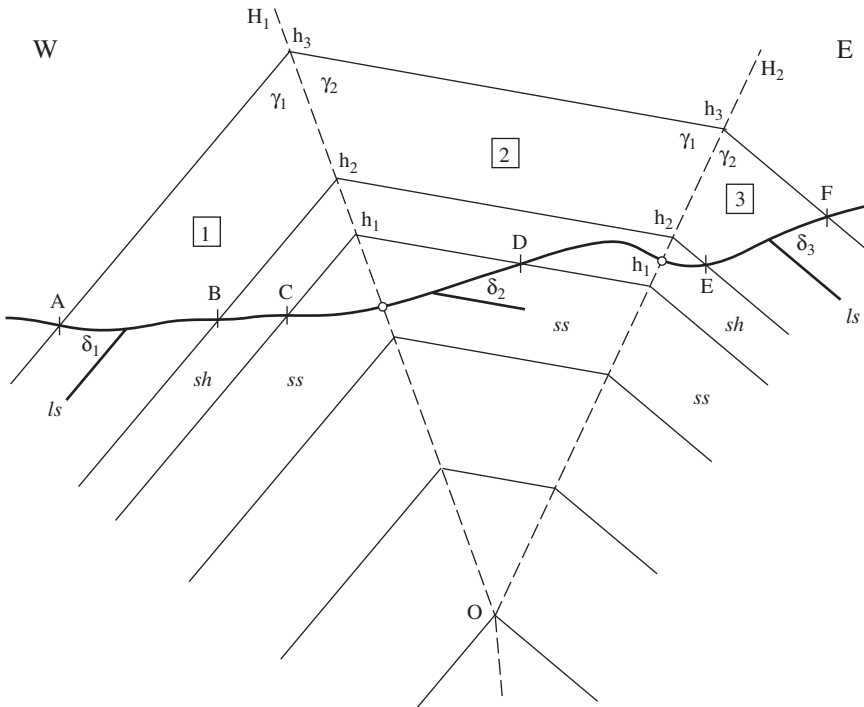


**Figure 15.25** Angular fold with constant limb thickness.

**Construction**

1. Along the line of section plot the contacts between the sandstone, shale and limestone units (points A–F). For each domain a representative dip  $\delta_1 = 50^\circ$  W,  $\delta_2 = 10^\circ$  E and  $\delta_3 = 40^\circ$  E (Fig. 15.25). Add the points representing the domain boundaries.
2. In *Domain 1* project the three contacts A, B and C parallel to  $\delta_1$ .
3. In *Domain 2* project the single contact D parallel to  $\delta_2$ . The intersection with contact C from *Domain 1* fixes hinge point  $h_1$  on on the first hinge plane  $H_1$ . The interlimb angle  $\gamma_{12} = 180^\circ - (\delta_1 + \delta_2) = 120^\circ$ .



4. Add the trace of the hinge plane  $H_1$  by connecting the point representing the domain boundary (shown by a small circle) and point  $h_1$ . This bisects interlimb angle  $\gamma_{12}$  at  $h_1$  so the beds in *Domain 2* have the same thicknesses as in *Domain 1*.
5. In *Domain 3* project contacts  $E$  and  $F$  parallel to  $\delta_3$ . The limestone unit here has the same thickness as in *Domain 1*. Therefore the underlying shale unit must also retain its thickness and its lower contact can be drawn to intersect contact  $D$  from *Domain 2*. This locates hinge points  $h_1$  and  $h_2$  on the second hinge plane  $H_2$  which is added to the section. The interlimb angle here is  $\gamma_{23} = 180^\circ - (\delta_3 + \delta_2) = 150^\circ$ . Again note that  $H_2$  bisects this angle.
6. The remaining contacts can then be added across the three domains.
7. This exhausts the surface stratigraphic data. The reconstruction can be continued at depth using subsurface information, if available, or schematically (as here).
8. Hinge planes  $H_1$  and  $H_2$  intersect at point  $O$  which is the hinge of a chevron fold at the core of the box fold.

In this reconstruction, point  $O$  lies at the center of a series of concentric polygons. As such, it is roughly analogous to the centers of the circular arcs of the Busk construction. As with those centers it also signals a pronounced change in the form of the fold at depth. Because of the angular nature of these forms it is not as obvious but there is a serious problem here, just as there was in the core of the reconstructed rounded folds. This important matter is treated below.

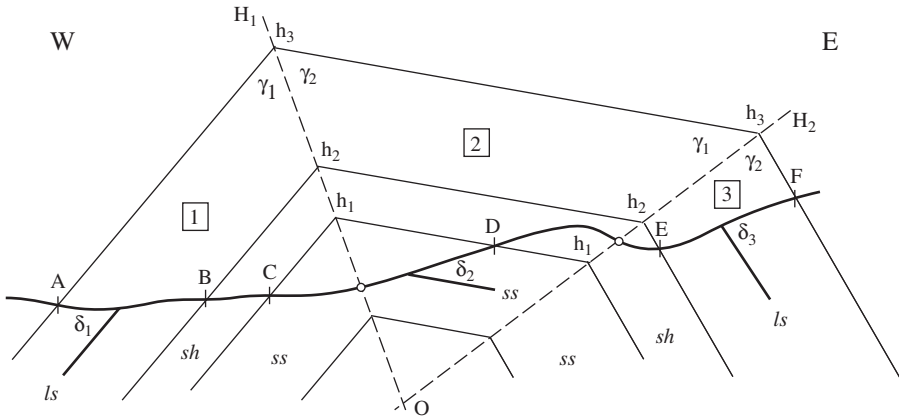


**Figure 15.26** Angular fold with unequal limb thickness.

Angular folds which involve a change of thickness are reconstructed in much the same way. The structure section of Fig. 15.26 is the same as in *Domains 1* and *2* of the previous example. In *Domain 3*, however,  $\delta_3 = 60^\circ$  and here the limestone unit is a third thicker.

### Construction

1. As before, contacts  $A$ ,  $B$  and  $C$  are projected parallel to  $\delta_1$  and  $D$  parallel to  $\delta_2$ . This locates hinge point  $h_1$  on hinge plane  $H_1$ , which can then be drawn in using the point representing the domain boundary.
2. Contacts at  $E$  and  $F$  are projected parallel to  $\delta_3$ . The thickness of the limestone unit in *Domain 1* is 75% of that in *Domain 3*. Increasing the underlying shale bed by a third, complete its lower contact to locate hinge point  $h_1$  on the  $H_2$  hinge plane. The interlimb angle here is  $\gamma = 180^\circ - (\delta_3 - \delta_2) = 130^\circ$ .
3. With  $R = 0.75$  in Eq. 15.18,  $\gamma_2 = 82^\circ$  and therefore  $\gamma_1 = 48^\circ$ . With these angles we then draw  $H_2$  through  $h_1$ , thus also locating  $h_2$  and  $h_3$ .
4. Complete the projections in *Domain 2* by connecting the hinge points on  $H_1$  and  $H_2$ .

Finally, as Suppe (1985, p. 64) points out, the shapes of folds with smoothly rounded forms can be closely approximated by a series of straight line segments. If the attitude data are reasonably complete, the kink method predicts essentially the same fold shape as the method of tangent arcs because the traces of the hinge planes intersect at a center of curvature just as the dip normals do. Because they do not require curves, reconstructions using the kink method are also much easier to produce.

### 15.9 Faults in fold cores

An important advantage of this method of depicting angular folds is that the bed length and area of beds in section can be easily determined. With such information, attempting to restore the pre-fold geometry shows, not surprisingly, that there is a deficiency of mass in the core of the folds just as in the case of the folds with rounded forms. In order to balance the cross sections, some additional structural elements are required. Two figure prominently in resolving the space problems:

1. *Fault-bend folds* (Fig. 15.27a)
2. *Fault-propagation folds* (Fig. 15.27b)

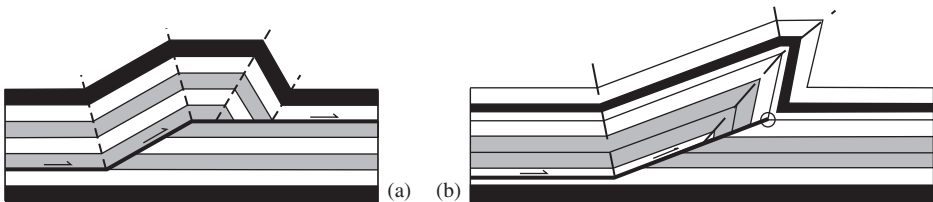


**Figure 15.27** Angular folds and faults: (a) fault-bend fold (after McClay, 1992); (b) fault-propagation fold (after Suppe, 1985, p. 351).

### 15.10 Some problems

Even though it has been a successful interpretive tool, any such representation is, however, a model and models are not reality. Even for a successful model it would be unusual for it to account for every detail. For example, many other folds have straight limbs but curved hinge zones, not angular ones as the model specifies. This is likely due to the fact that the transition from flat to ramp thrusts can not be a sharp angle as the model requires. A more realistic curved transition will produce rounded hinges (Tavani, *et al.*, 2005)

There are other problems which remain unresolved. As can be clearly seen in Fig. 15.27 the limbs of the folds deform by homogeneous layer-parallel simple shear. This is essentially a flexural flow mechanism and as discussed in §15.2 this requires an unrealistic degree of anisotropy. The model also requires that the shear strain must be the same in layers of contrasting competencies and this presents considerable difficulty. Further, the homogeneous thickening or thinning (necessarily accompanied by homogeneous, layer-parallel shortening or lengthening) of all the layers of a fold limb compounds this difficulty. A few carefully chosen strain determinations would help resolve these questions, but such measurements do not seem to have been made. All this suggests that the process of angular folding is more complicated than the model indicates.

### 15.11 Exercises

1. Model a flexural slip fold with a card deck on which a number of small circles have been stamped. Measure the orthogonal thickness, and verify that Eq. 15.4 holds.
2. The data given below were obtained along an east to west transverse. Reconstruct the folds, calculate the depth of folding and invent disharmonic folds or thrusts or both to balance the profile. The area can be determined most simply by superimposing your construction on graph paper and counting squares.

Station	Distance (m)	Elevation (m)	Dip
A	0	650	30° E
B	900	800	41° E
C	2300	850	18° W
D	2550	750	37° E
E	3550	800	44° W
F	4900	1150	5° E
G	5350	1000	69° E
H	6900	650	8° W
I	8000	550	66° W

3. Complete the cross section of angular folds of Fig. 15.28.

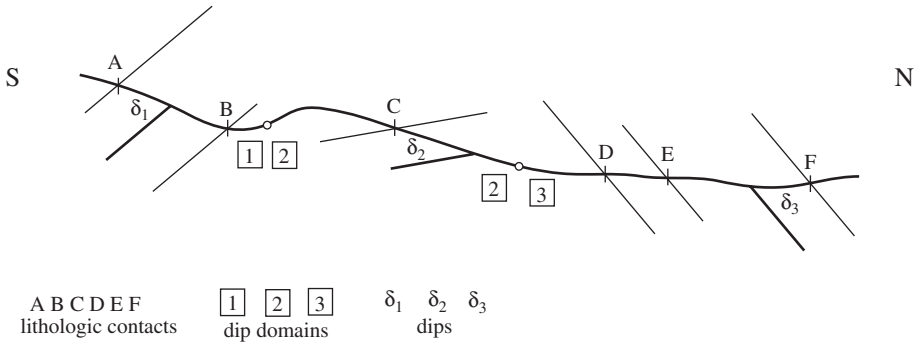


**Figure 15.28** Angular fold problem.

# 16

## Similar folds

### 16.1 Introduction

Several mechanisms for producing similar folds have been proposed (Ramsay, 1967, p. 43; Bayly, 1971; Matthews, *et al.*, 1971). The simplest of these can be illustrated with a deck of cards. A layer is represented by a band drawn on the edge of a deck which is then deformed by inhomogeneous simple shear.

This is called *shear folding*. Because each individual card and the portion of the band marked on its edge remain undistorted during displacement the thickness of the band measured parallel to the shear plane is constant. This is also the axial-plane direction, hence the folded layer has constant axial-plane thickness and parallel isogons, and this is the distinguishing characteristic of Class 2 folds.

In this model folding the band on the edge of the cards plays no mechanical role – it simply reflects the pattern of inhomogeneous shear. This behavior is *passive*. Similarly in nature, a layer subject to shear folding can act only as a passive marker. It can not have mechanical properties which differ significantly from the surrounding material, for if it did there would be a component of bending or buckling and the resulting folds would not be ideally similar. Because rock bodies are commonly composed of contrasting lithologies similar folds are rare. However, they might be expected in rocks which are monomineralic or nearly so. Salt, ice, and dunite are a few rocks where passive bands and streaks of impurities might be distorted into similar folds. They also might occur in rocks which are polymineralic but statistically homogeneous, such as granite. Despite the apparent rarity a number of general lessons can be learned from the geometry of shear folding, and this chapter is devoted to several of them.

### 16.2 Geometry of shear folds

In describing shear folds it is convenient to establish a set of coordinate axes directly related to the geometry of simple shear (see also §11.4). In the models the edge of the

deck is taken to be the  $xy$  plane (Fig. 16.1a). Correspondingly, the shear plane is the  $yz$  plane with the  $y$  axis in the shear direction.

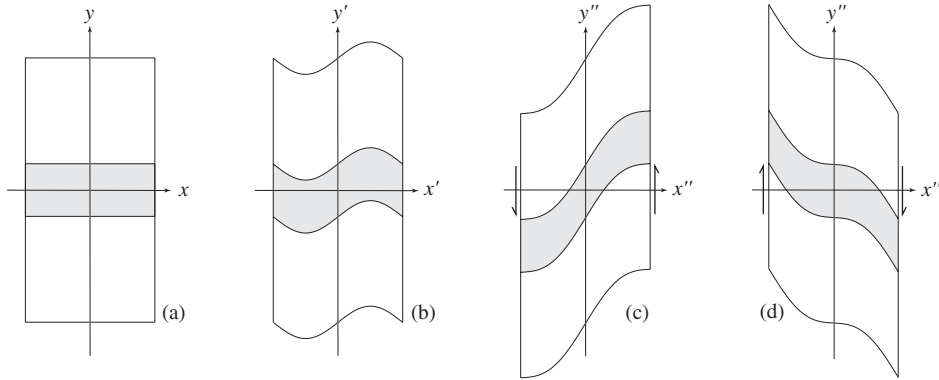


**Figure 16.1** Model folds: (a) initial layer; (b) sinusoidal displacement; (c) positive homogeneous shear; (d) negative homogeneous shear.

There are several cases. If the layer is initially parallel to the  $xz$  plane and if the form of the displacement curve is sinusoidal, then the fold form will also be sinusoidal (Fig. 16.1b). This relationship can be expressed as

$$y' = A \sin x', \tag{16.1}$$

where  $A$  is the amplitude of the displacement curve and, in this special case, also the amplitude of the folds. Other displacement curves will, of course, give correspondingly different fold forms.

In simple shear no change occurs in the  $z$  direction and therefore these folds will be cylindrical with axes parallel to  $z$ . The strain is related to the slope angle of the displacement curve  $\psi$ . In this case the maximum strain occurs at the limb inflection points and minimum strain, which is zero, occurs at the hinge points.

Asymmetric folds may, of course, be obtained by an asymmetric pattern of displacements. We may model this case in a simple way by considering that the shear displacement has two components – an inhomogeneous part to produce the fold and a homogeneous part to destroy symmetry. Starting with the band parallel to  $x$  the deck is deformed in two stages.

1. Impose the sinusoidal displacements to produce a symmetric fold.
2. Superimpose a homogeneous simple shear on the deck which changes this symmetric fold into an asymmetric one. There are two cases: positive shear (Fig. 16.1c) and negative shear (Fig. 16.1d), and the two results are notably different.

The total displacement curve has the form

$$y' = A \sin x' + x' \tan \psi, \tag{16.2}$$

where  $\psi$  is the angle of shear of the homogeneous component. The order of the stages of deformation may be reversed or the components may act simultaneously during a more complex pattern of shear, all with the same result. The geometry of these asymmetric folds brings out three general features.

1. Axial-plane thickness is not necessarily equal to the orthogonal thickness of the original layer.
2. Fold hinge and inflection points do not necessarily coincide with points of maximum and minimum curvature on the displacement curve.
3. Strain distribution is not generally related to fold geometry.

There is, of course, no necessary relationship between the attitude of the layer and the shear direction. If the layer is initially inclined to the  $x$  axis at an angle  $\phi$ , and if, as before, the displacement curve is sinusoidal then the folded layers on the  $xy$  plane will have the form (Ramsay, 1967, p. 426)

$$y' = A \sin x' + x' \tan \phi, \tag{16.3}$$

and the form of the folds is asymmetric. There are two cases:  $\phi > 0$  (Fig. 16.2a) and  $\phi < 0$  (Fig. 16.2b). Note that the results are the same as the folds produced by a combination of inhomogeneous simple shear and a homogeneous component. Hence the cases of initial inclination and component of homogeneous shear can not be distinguished on the basis of fold geometry.

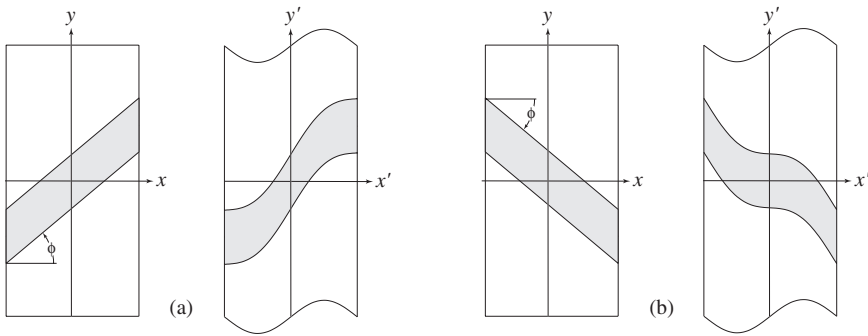


**Figure 16.2** Asymmetric folds: (a)  $\phi > 0$ ; (b)  $\phi < 0$ .

In a special case of two-component shear a symmetric fold may be produced from an inclined layer (Fig. 16.3a). The sinusoidal shear produces an asymmetric fold (Fig. 16.3b). Homogeneous shear then returns the symmetry (Fig. 16.3c).

### 16.3 Single-sense shear

Objections have been raised concerning this shear folding mechanism. First, folds often termed *similar*, but which do not possess the ideal similar geometry, have been shown to

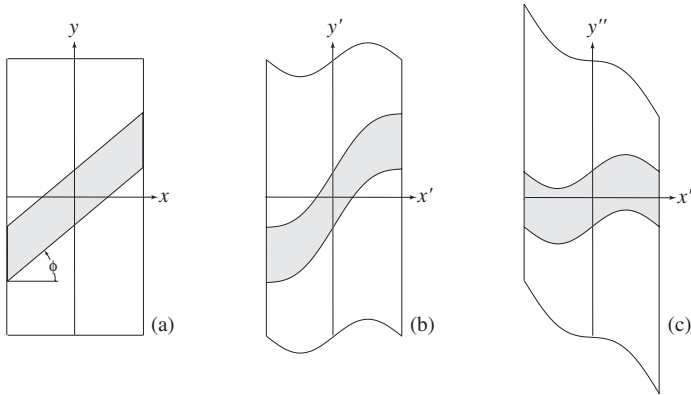


**Figure 16.3** Symmetric fold from asymmetric displacements: (a) initially inclined layer; (b) sinusoidal displacement; (c) homogeneous shear returns symmetry.

result from an entirely different mechanism – the homogeneous flattening of originally parallel folds (see §14.6). This difficulty is avoided by reserving the term for the special class of fold shapes with parallel isogons.

A second objection, and a more serious one, is directed at the mechanical feasibility of the systematic reversal in the sense of shear as required by all the previous examples. However, inhomogeneous single-sense shear is capable of producing well-developed similar folds.

Such single-sense shear can produce such a fold in two distinctly different ways. Crucial is the relationship of the angles  $\phi$  and  $\psi$  to the maximum dip angle of the initial layer. The two cases are the homogeneous shear of a slightly curved layer (Fig. 16.4a) and the slightly inhomogeneous shear of a planar layer (Fig. 16.4b). These can be described by the equation

$$y' = A \sin x' + x' \tan \phi - x' \tan \psi. \quad (16.4)$$

Note that  $\phi$  and  $\psi$  have opposite signs. In a very special but instructive case,  $\phi + \psi = 0$  and the equation reduces to Eq. 16.1, and the fold is sinusoidal. Again, the roles of  $\phi$  and  $\psi$  can not be distinguished from the final fold form alone. More information is required, such as observations of the progressive evolution of such folds (Ragan, 1969b).

## 16.4 Shear folds in three dimensions

In three dimensions, the geometry is more even involved. In shear folds the axial plane coincides with the  $yz$  plane and the hinge line and axis are always parallel to the intersection of the shear plane and the layer being folded. As we have seen, when this intersection is parallel to  $z$  then so too is the axis (Fig. 16.5a).



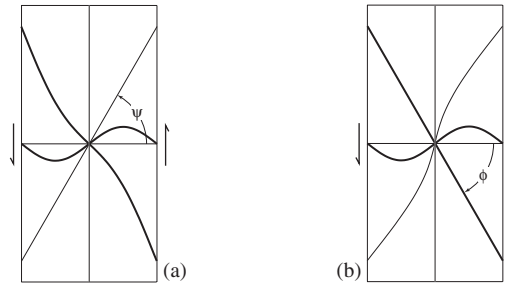


**Figure 16.4** Single-sense shear: (a) homogeneous shear of a slightly curved surface; (b) slightly inhomogeneous shear of a plane.

On the other hand, if the original layer makes an angle  $\beta$  with  $z$ , the fold axis will also be inclined at this same angle and its orientation can not be used to determine the  $z$  direction (Ramsay, 1967, p. 425).

Because the fold axis now plunges, the  $xy$  plane no longer displays the fold in profile and the fold shape will be a subdued version of the displacement curve (Fig. 16.5b). The fold amplitude  $A'$  measured in the now inclined profile plane is related to the amplitude of the displacement curve on the  $xy$  plane by

$$A' = A \cos \beta. \quad (16.5)$$

In the previous two-dimensional cases,  $\beta = 0$  and  $A' = A$ . A limiting case occurs when  $\beta = 90^\circ$  and  $A' = 0$ , that is, when the layer is parallel to  $xy$  no fold develops at all (Fig. 16.5c). These plunging folds may also involve a component of homogeneous shear or be derived from layers which are also inclined to  $x$ .

As these examples show, folds with a variety of symmetries and attitudes can be generated by homogeneous and inhomogeneous shear of variably inclined layers by *forward* modeling. In contrast, we can not separate the role of initial layer inclination and a component of homogeneous shear from the fold geometry alone. To solve this *inverse* problem more information is needed. Knowing the state of strain at a few points within the folded layer would be one way, but unfortunately this is rare.

## 16.5 Superposed folds in two dimensions

Card-deck models can also be used to illustrate the effects of shear folding on previously existing folds. The form of the first folds is drawn on the edge of the card deck (Fig. 16.6a), which is then sheared inhomogeneously (Fig. 16.6b). As a result of this deformation, the originally straight traces of the first hinge surface *HSI* behave in the same fashion as layer boundaries of the previous examples. At the same time, the layer becomes complexly recurved. Two features are noteworthy.

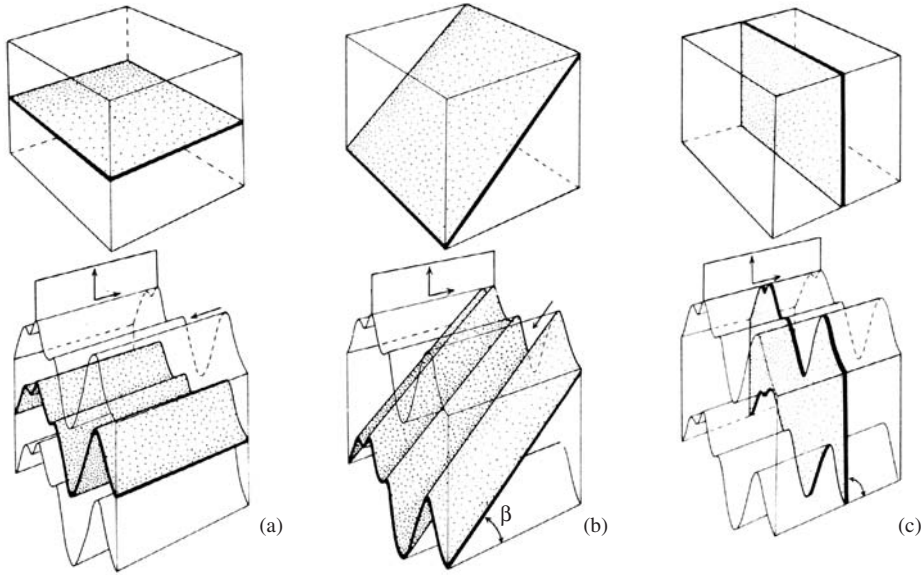


**Figure 16.5** Layer inclined to z axis: (a)  $\beta = 0$ ; (b)  $\beta > 0$ ; (c)  $\beta = 90^\circ$  (from Ramsay, 1967, p. 425–426).

1. Hinge points of the first folds do not coincide with the points of maximum curvature of the second folds.
2. Traces of the hinge surfaces of the second displacement curve *HS2* do not pass through the points of maximum curvature on the limbs of the now twice folded bands, but alternate from one side to the other as it passes from limb to limb.

To concentrate on essentials we have modeled the second folds using a purely cosinusoidal pattern of displacement, but all the previous controls by the initial layer attitude and a homogeneous shear still apply.

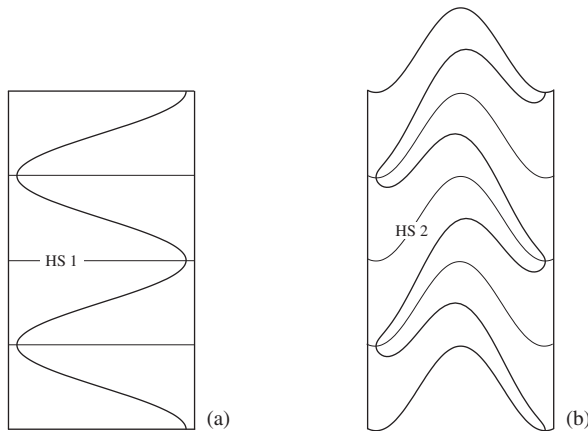


**Figure 16.6** Model of superposed folds: (a) first folds; (b) second folds.

In this experiment, we have necessarily modeled the superposition of shear folds on the card decks in distinct stages. In nature, such folds may, however, form during a single, more complicated pattern of continuous motion. This requires a shift of the early shear direction so that the first folds are cut by the later displacements. Motions of this type can be seen in foam patterns in eddies on the surface of small ponds.

Given such superposed folds, it is possible to unravel an important part of the second deformation using the simple rules of shear folding (Fig. 16.7a).

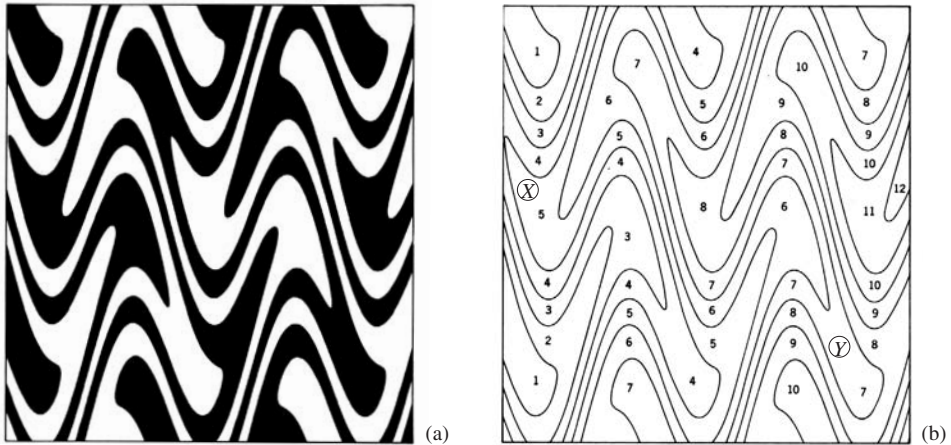


**Figure 16.7** Analysis (after Carey, 1962): (a) fold pattern; (b) tracing and numbering.

### Analysis

1. *Identify the first generation folds:* on a tracing of the folds, number the layers in sequence. If continuity is lost in highly attenuated zones it is usually possible to work around them. If not, a second or even third sequence may be started. Once labeled, special patterns identify the cores of the first folds. For example, at point *X* in Fig. 16.7b the numbers run outward from the core in descending order while at point *Y* they run outward in ascending order. Without relative ages they can not be distinguished, but clearly one of these cores represents a first generation anticline and the other a syncline.
2. *Involuted hinge surfaces of the first folds:* wherever the core layers form an apex, the trace of the folded hinge surface of the first fold *HSI* must pass into the next layer. Since the first hinge points can not be accurately located, the point of maximum curvature is used as a close approximation. Through these points draw in the traces of the first hinge surface using solid, dashed or dotted lines to indicate the degree of confidence in their locations. These traces can then be marked with zeros or cross-bars depending on whether the index numbers rise or fall in the cores.

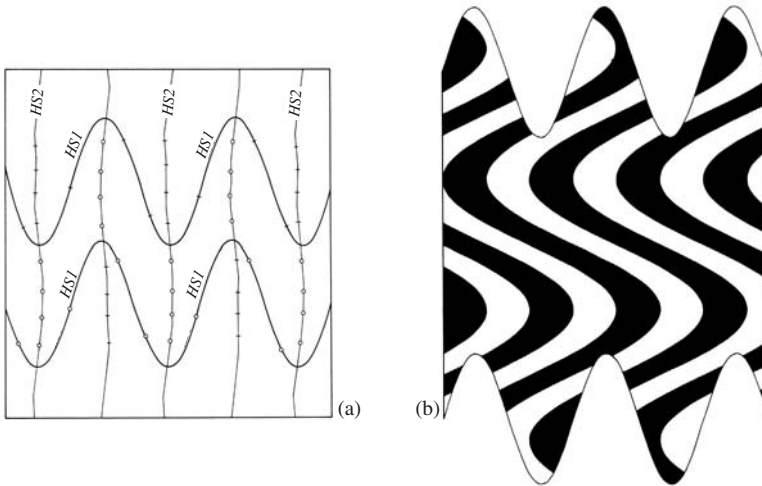


**Figure 16.8** Reconstruction: (a) traces of hinge surfaces; (b) removal of second folds.

3. *Hinge surfaces of the second folds*: a second set of traces can be drawn through the hinge points of the folded limbs. These appear as a series of roughly straight and parallel lines. Using crosses and zeros to mark sequences which rise or fall it will be seen that groups of symbols alternate along these traces. If difficulty is encountered in following the involuted *HS1* traces through strongly attenuated zones or across widely spaced areas, they may be completed using the following clues.
  - (a) Involute *HS1* traces of like sign must join.
  - (b) The sense of curvature of the *HS1* traces must be the same where they cross a particular *HS2* trace, that is, all must be either concave up or down.
  - (c) The folded *HS1* traces cross the straight *HS2* traces only at points where sign changes occur. This fact may also be used to determine the number of *HS1* traces to be inserted across gaps.
4. *The form of the second folds*: collecting all the *HS1* and *HS2* traces and visually averaging both, the displacement curves and the directrix responsible for the second folding can be extracted from the complex pattern (Fig. 16.8a).
5. *Form of the first folds*: the traces of the hinge surface of the first folds are assumed to have been linear. Therefore, the effect of the second folding can be eliminated by shifting the patterns parallel to the displacement curve derived from the original superimposed folds (Fig. 16.8b). This is easily accomplished by a simple construction.
  - (a) Draw a series of closely spaced lines on the original fold pattern parallel to the directrix of the second set of folds.
  - (b) On a tracing sheet, draw a second set of parallel lines with the same spacing.
  - (c) Overlay this sheet on the fold pattern and mark off the points of intersection of the folded points with the first line, and then shift the tracing according to the reverse displacement curve and repeat for a second line. Repeat this for all lines.

The pattern of the first folds can be drawn by connecting points across these guidelines. The first attempt is apt to be somewhat crude. Irregularities due to drafting and positioning errors may be filtered out by repeating the tracing process.

## 16.6 Wild folds

In both theory and concept, this process of superimposing folds upon folds could be repeated any number of times. To model such multiple folds with the aid of card decks would require that the convoluted patterns of earlier experiments be transferred onto a deck with a different orientation relative to the  $y$  direction. Unfortunately, any attempt to perform such an experiment meets with severe practical difficulties which mount beyond the second set. However, such patterns are easily produced by a computer plot. The technique consists simply of adding sine or cosine curves of varying amplitudes and wavelengths alternately along the  $x$  and  $y$  axes. Examples for runs of three and four sets of superposed folds are shown in Fig. 16.9.

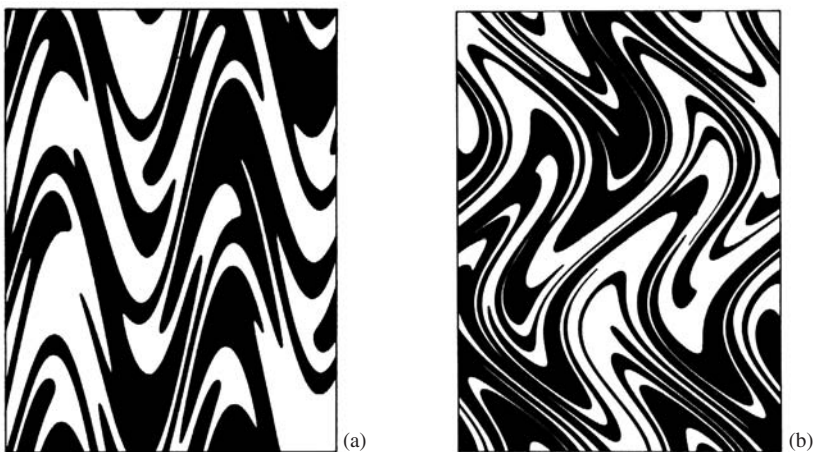


**Figure 16.9** Multiple superposed folds: (a) three sets, (b) four sets.

*Irregular folds* are characterized by irregularities of the axial planes, discontinuities and rapid variations in the thickness of bands (Fleuty, 1964, p. 477). The most disordered types also show a wide variation in the attitudes of hinges and hinge surfaces. Such folds are particularly common in migmatitic gneisses where they give the appearance of stirred porridge (De Sitter & Zwart, 1960, p. 253), sometimes called *wild folds* (Kranck, 1953, p. 59; Berthelsen, *et al.*, 1962). Except for their perfectly periodic character and continuity, certain aspects of these computer-generated patterns are similar to the wild folds found in nature, suggesting that their appearance may be more a matter of complexity than irregularity.

The superposition of multiple folds can also be looked at as physical mixing, a well-known process in chemical engineering where the homogenization of multicomponent

fluids or fluid-like substances is important (Ottino, 1989, 1990, 1992). A characteristic of such motions is that the final result depends in a very sensitive way on the initial conditions. Such motion for which trajectories starting from slightly different initial conditions diverge exponentially are termed *chaotic* (Moon, 1992, p. 434). There are two interesting geological examples which can be observed in the field.

1. In migmatites, because of high temperatures, diffusion is significant and tends to blur the boundaries between layers of different compositions and to obliterate thin layers altogether.
2. Obsidian/pumice rock flows onto the earth's surface at low temperatures and diffusion is negligible and as a result highly deformed inhomogeneities are often preserved in exquisite detail at the scale of millimeters or less.

This process of physical mixing is probably important in homogenizing magma bodies during formation and emplacement and perhaps also in the mantle. For all such motions, inevitable observational errors, however small, render the initial state indeterminate.

### 16.7 Superposed folds in three dimensions

Card-deck models can also be used to illustrate superposed folds in three dimensions. The first folds are represented by a cylindrical surface cut across the deck; deformation of the deck by inhomogeneous simple shear then refolds this surface. Although the method requires special preparations, including the cutting and deforming of the cards, a number of interesting and informative experiments can be performed, and these are well worth pursuing (see O'Driscoll, 1964).

A simple example will indicate the approach and its potential. If a set of upright folds is deformed by a second set of upright folds trending at right angles to the first, a series of domes and basins result (Fig. 16.10). Other angles between the first and second folds can be simulated by first homogeneously shearing the deck in a horizontal direction; the domes and basins are then asymmetrical and en echelon.

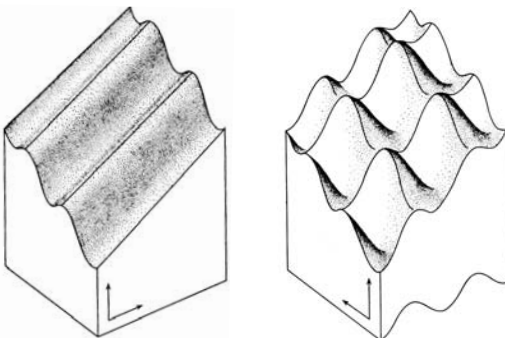


**Figure 16.10** Superposed folds in three dimensions (after O'Driscoll, 1962, p. 166): (a) first folds; (b) second folds.

Because of their similarity to the patterns caused by the intersection of two sets of waves, these are called *interference* patterns. If instead of a single fold surface, the deformation operated on a multilayered block, and if an exposed plane cuts horizontally through the superposed folds, an outcrop pattern of the interference structures is produced. The characteristics of this type of pattern depend on the relative orientation and size of the first and second folds. If, as in the model, the first folds are horizontal and upright, and further, if the sizes of both sets of folds are about the same, the resulting patterns can be described directly in terms of the attitudes of the first folds. Within this framework, several types of patterns can be distinguished.

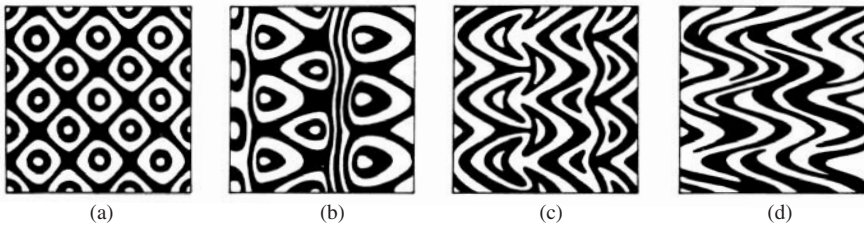


**Figure 16.11** Interference patterns (from Ramsay, 1967, p. 531).

1. If the first folds are horizontal and upright, and the trends of the two folds are perpendicular, the pattern of domes and basins alternates with a high degree of symmetry and regularity (Fig. 16.11a).
2. Inclined first folds are reflected by dome–basin patterns which no longer have simple rounded forms. This reflects the difference in dip on the limbs of the first folds (Fig. 16.11b).
3. Inclined first folds with overturned limbs result in characteristic crescent and mushroom patterns (Fig. 16.11c).
4. If the first folds are recumbent or reclined, and the trends of the two sets are parallel, the patterns do not differ in kind from the two-dimensional patterns so easily modeled with card decks (Fig. 16.11d).

Other relative orientations give patterns which are transitional with these four and many can be illustrated by means of the three-dimensional card-deck experiments as described by O’Driscoll.

A full discussion of interference patterns, together with many excellent illustrations, is given by Ramsay (1967, p. 518f). His classification scheme has been expanded and extended by Thiessen and Means (1980).

A special type of superimposed fold is produced in three dimensions when a body of rock with preexisting folds is cut by a shear zone. Generally, all preexisting lines rotate toward the plane of shear and the convergence of such lines is particularly striking at high shear strains. One especially interesting effect of this involves folds which outside the shear zones show only a slight variation in the orientations of their hinge lines (Cobbold &

Quinquis, 1980; Ramsay, 1980). In contrast, inside the shear zone they show an extreme variation and a *sheath fold* is produced (Fig. 16.12).

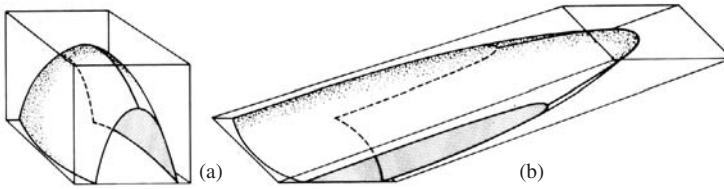


**Figure 16.12** Sheath fold (after Ramsay, 1980, p. 93).

## 16.8 Exercises

1. Print a row of small circles across the end of a card deck and then produce the following types of shear folds:
  - (a) With a band perpendicular to the shear direction (Fig. 16.13a), form a symmetric sinusoidal fold with reverse sense of shear.
  - (b) Add a component of homogeneous simple shear to produce an asymmetric fold.
  - (c) With a band at a small angle to the shear direction (Fig. 16.13b), form a symmetric fold by single-sense shear.

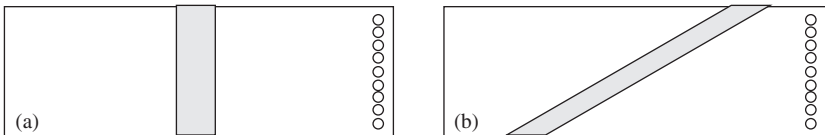


**Figure 16.13** Experimental shear folds.

2. Draw the profile of a similar fold on the edge of a deck of cards with the trace of its hinge surface oblique to the direction of shear. Homogeneously deform the deck to produce a superimposed fold. Note the thickness variation in the now twice-folded layer, the location of the new hinge point and the location of the hinge points of the first fold.
3. Using Fig. 16.14 remove the effects of the *F2* folding to give the form of the *F1* folds. As will soon become apparent, the *F1* folds in this problem are highly regular and it is only necessary to proceed to the point where their form can be confirmed with some confidence rather than attempting a complete and detailed reconstruction.



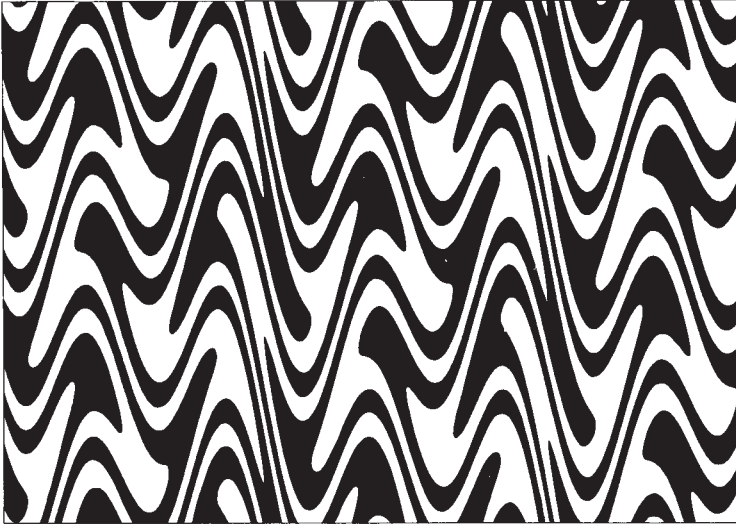


**Figure 16.14** Superimposed folds.

# 17

## Folds and topography

### 17.1 Map symbols

Just as structural planes intersect the earth's surface to give characteristic outcrop patterns, equally distinctive though more complex patterns result from the intersection of folds with the topographic surface. In this chapter we treat some important aspects of the patterns made by folds which are essentially *cylindrical*.

If exposures are good, it is generally possible to locate and measure the attitudes of both the hinge and hinge surface of a fold in the field. On the other hand, if these features can not be directly observed, then the attitude information and the location of the hinge surface must be found using indirect methods.

In any case, the fold is then identified on the map with a line marking the trace of the hinge surface at the earth's surface, together with symbols indicating the attitude of the hinge and hinge surface and the direction of closure (Fig. 17.1).

### 17.2 Outcrop patterns

Horizontal folds have the simplest type of outcrop pattern. On a horizontal exposure plane, the map pattern of such a fold is essentially the sum of the patterns of the inclined limbs, that is, a series of parallel outcrop bands (Fig. 17.2a). If the relative age or correlation of the units, or the attitude at several points is not known, it may not be possible to interpret the pattern as being part of a fold at all. However, once these are known, the existence of a fold becomes clear.

For plunging folds, a converging pattern of the fold limbs is characteristic and unmistakable (Fig. 17.2b). However, on the basis of the pattern alone it is not possible to distinguish antiforms and synforms. Again, if the dip at several points or the direction of plunge is known the type of fold may be immediately determined.

If the horizontal fold is exposed in an area of some topographic relief, the inclinations of the opposing limbs are immediately evident and the interpretation of a fold can be

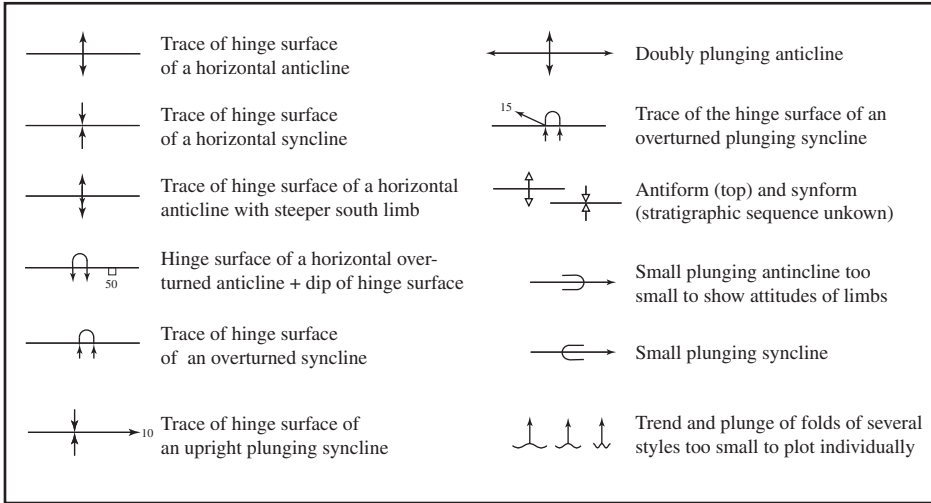


Figure 17.1 Map symbols for folds (after Compton, 1985, p. 373).

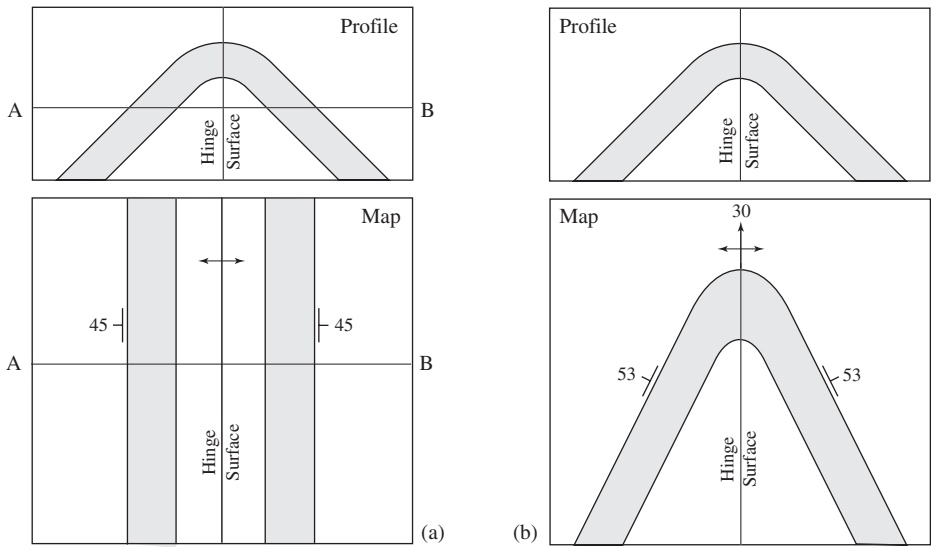
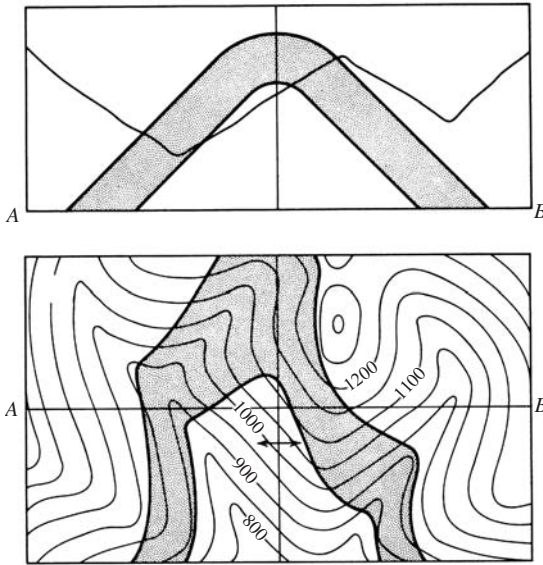


Figure 17.2 Fold profile and map: (a) horizontal upright anticline; (b) plunging upright anticline.

made with some confidence. If the topography is such that a hinge intersects the surface, the existence of the fold becomes obvious (Fig. 17.3).

In all these cases, given attitude data, vertical cross sections could be constructed. However, only if the fold is horizontal does such a section give authentic information about the fold geometry. In all other cases the shape of the folded surfaces, the thickness variations in the folded layers, and the interlimb angles are distorted in vertical sections.

If the aim is to portray the fundamental fold geometry, such vertical sections are useless and must be avoided.



**Figure 17.3** Profile and map of a horizontal upright antiform.

### 17.3 Down-plunge view

By viewing map patterns of tilted, but not folded strata in the down-dip direction an important visual simplification is achieved (Chapter 3). This same approach may be used to even greater advantage in viewing the map patterns of plunging folds. By turning the map, and adopting a view so that the line of sight is in the direction of the plunging fold axis, the profile of the fold is actually seen. As before, the principle is that the distortions at the earth's surface are eliminated by this down-plunge view. This is easily seen in the case of an inclined cylindrical pipe of circular cross-section (Fig. 17.4a). If the pipe is cut horizontally, its trace will be an ellipse on the plane of the map. If this ellipse is then viewed in the direction of its inclined axis, it will again appear circular.

Figure 17.5 shows a geological map of several upright folds plunging due north. In a down-plunge view, antiforms and synforms are simply and directly seen as such. The map pattern also indicates that disharmonic folds are also present and the down-plunge view automatically includes them in their proper place in the structure. In contrast, a vertical section mechanically constructed along a line  $SS'$  would fail to represent the small plications in the cores of the folds.

If the folds are inclined, the correct shape of the plunging folds is seen only if the line of sight is parallel to the fold axis, not when it is parallel to the trace of the hinge surface. As shown on the geological map (Fig. 17.6), the folds plunge due north at  $20^\circ$ . Though

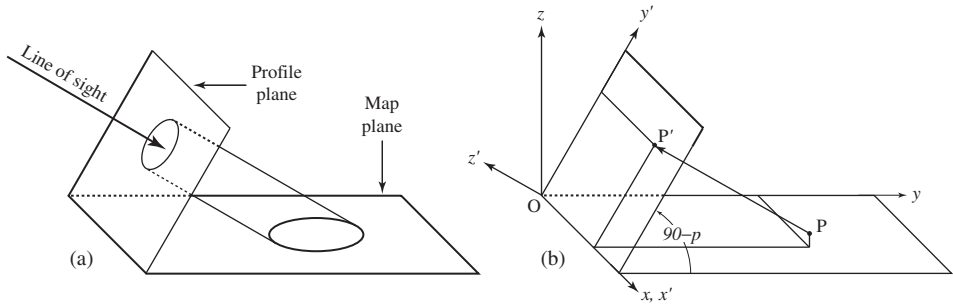


Figure 17.4 Map and profile: (a) map ellipse projected as a circle; (b) map and profile coordinate axes.

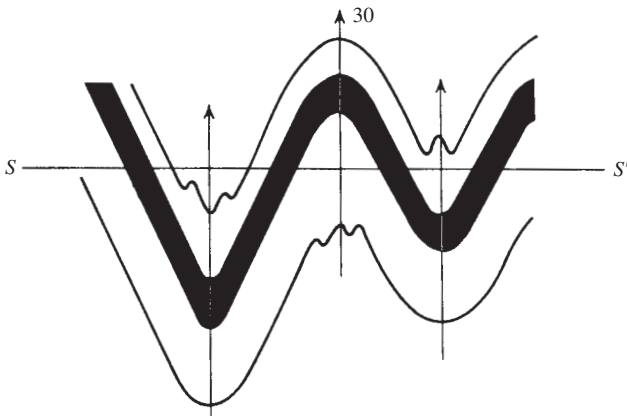
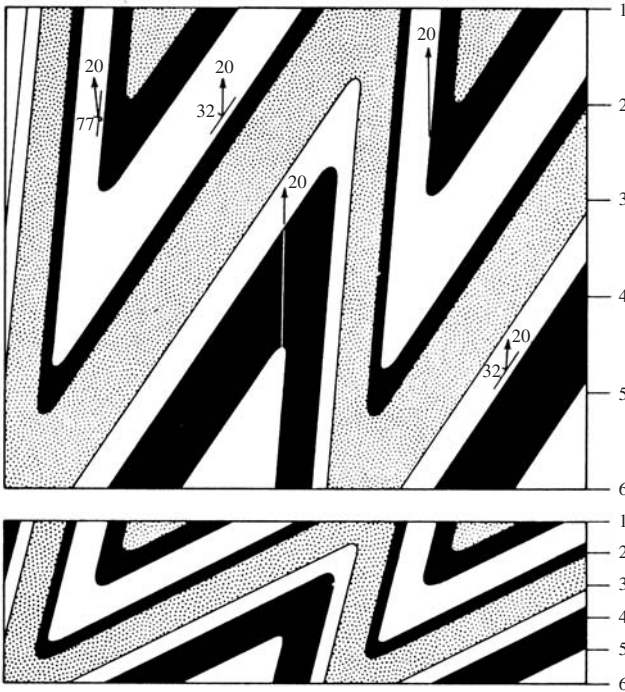


Figure 17.5 Map of upright plunging fold (from Mackin, 1950).

not shown, the surface trace of the hinge surface trends N 15 E and dips steeply to the west. With a line of sight parallel to the fold axis, the true shape of the folded layers is revealed; the result of this view is also shown on the constructed profile. Note carefully that *if* the folds are viewed parallel to the strike of the hinge surfaces, that is, toward N 15 E, the folds falsely appear upright with apparent thinning on the steep eastern limbs of the antiforms.

The down-plunge view reveals another important feature of fold patterns. The folds of Fig. 17.5 have vertical hinge planes, and thus its trace also connects points of greatest curvature of the outcrop pattern, a fact that can be readily seen in the down-plunge view. This coincidence holds *only* when the folds are exposed in an area of negligible relief. If the relief is significant there will, in general, be a discrepancy between the real and apparent hinge points (see Fig. 17.3).

For inclined plunging folds exposed on horizontal plane surfaces, the line connecting the points of greatest curvature of the outcrop pattern and the trace of the hinge surface always depart. The degree of departure depends on the geometrical nature of the folded



**Figure 17.6** Map and profile of plunging inclined folds (from Mackin, 1950).

surfaces, and the effect is compounded by the topographic relief. For similar folds, the two traces are parallel but not coincident (Fig. 17.7a), and for parallel folds the lines are neither parallel nor coincident (Fig. 17.7b). If this relationship seems difficult to accept, a down-plunge view will immediately confirm its validity.

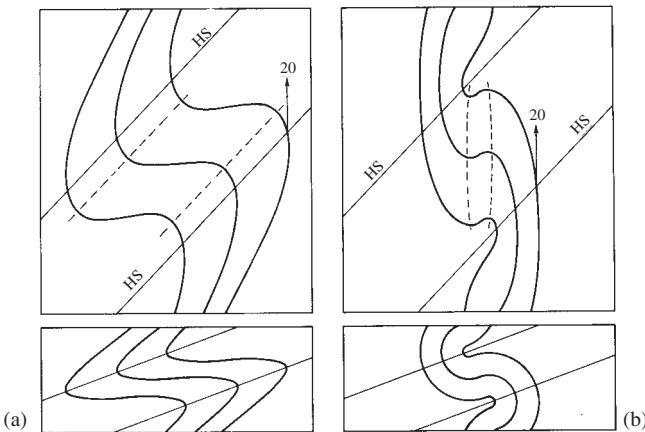


**Figure 17.7** Maps and profiles with trace of hinge surface *HS* (after Schryver, 1966): (a) similar folds; (b) parallel folds.

### 17.4 Fold profile

The true form of cylindrical folds seen in the down-plunge view may also be constructed graphically from a geological map. There are two different, though equivalent, techniques. The first is the more straightforward one, and applies to areas of negligible topographic relief (Wegmann, 1929). It involves constructing the foreshortened map pattern with the aid of a grid.

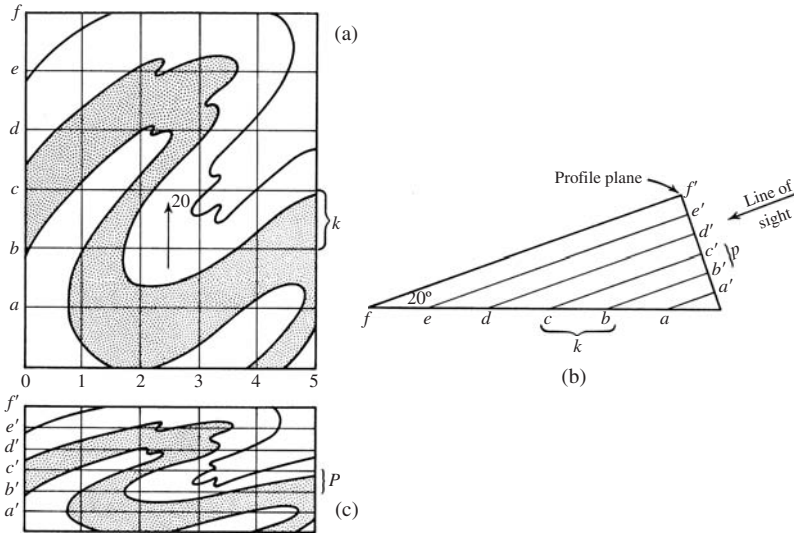


**Figure 17.8** Profile construction: (a) map; (b) profile grid; (c) profile.

#### Construction

1. On the geological map, draw a square grid with one coordinate direction parallel to the trend of the fold axis and with grid spacing  $s$  (Fig. 17.8a).
2. Viewed down-plunge, the spacing of the map grid  $s$  across the line of sight, that is, perpendicular to the trend of the fold axes, remains unchanged (1, 2, 3, ...). Parallel to the axial trend the spacing  $s'$  is given by (see Fig. 17.8b)

$$s' = s \sin p. \tag{17.1}$$

3. A second grid is then drawn representing this down-plunge view: the spacing 1, 2, 3, ... is the same as originally constructed on the map, while  $a', b', c', \dots$  is the foreshortened one  $s'$ .
4. The contacts of the folded layers fold pattern are then transferred from the map grid to the profile grid point by point and the folds then sketched in (Fig. 17.8c).

The resulting profile involves no speculation; no line appears on it that is not also on the map. Contrast this with the construction of a vertical cross section of parallel folds in

which surface attitudes are projected in directions at right angles to the fold axis. Both profiles and vertical sections require the projection of data. For the profile, however, the data are projected parallel to the fold axis, which is a direction of minimum change in cylindrical folds, whereas the vertical section requires projection in the direction of maximum change.

The second technique, using an orthographic construction, is more involved, but it has the advantage of being adaptable to more complex situations (Wilson, 1967).

### Construction

1. Establish folding lines *FL1* parallel and *FL2* perpendicular to the trend of the fold axes, preferably outside the map area (Fig. 17.9a).
2. Establish a vertical section parallel to the fold axes by folding about *FL1*. On this section, the line *OP* represents the profile plane in edge view. A series of selected points on the map are projected perpendicular to *FL1*, thence to *OP* using the angle of plunge, which is here  $20^\circ$ .
3. Folding about *FL2*, these same points are projected from *OP* using circular arcs with point *O* as center.
4. Also project each of the same map points perpendicular to *FL2* to fix their location on the profile plane (see details of the projection of point 1 on the map to  $1'$  on the profile on Fig. 17.9b).
5. After a sufficient number of points have been transferred in this manner, the form of the folds on the profile plane can be completed by connecting appropriate points.
6. The result is an “up-plunge” view, but this can be easily converted to a down-plunge view simply by reversing it.

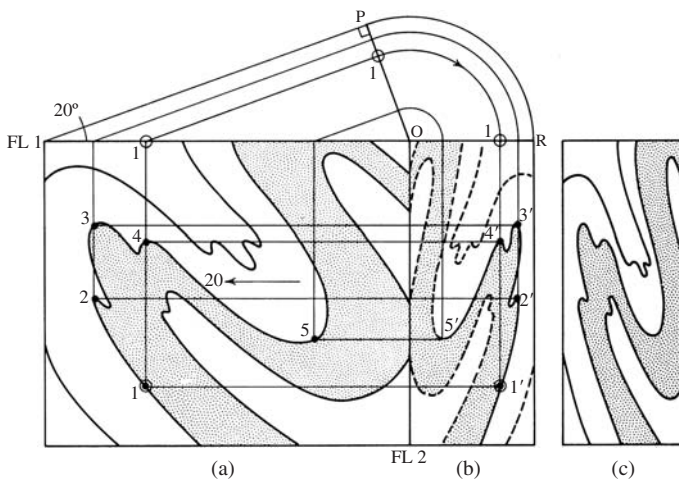


**Figure 17.9** Fold profile by orthographic construction.



The advantage of this procedure over that of the grid method is that a fold profile can also be constructed when the map pattern is influenced by topographic irregularities.

### Construction

1. As before, construct  $FL1$  parallel and  $FL2$  perpendicular to the trend of the plunging folds.
2. Instead of projecting directly to the profile plane via  $FL1$ , the topography must first be taken into account. This is done by adding a series of scaled elevation lines to the edge view using the contour interval of the topographic map (Fig. 17.10). The points on the outcrop traces of the folded surfaces are then projected across  $FL1$  to their corresponding elevation lines.
3. These points are then projected to the profile plane  $OP$ , using the plunge angle. This final projection can be made easier if the use of the circular arcs is avoided. By constructing line  $OB$  to bisect the angle  $POR$ , the points can be projected along the line of plunge directly to this bisector, and then to the profile, thus saving one step (see also Appendix A). The fold profile is sketched as before from points projected from the edge view and from the map.

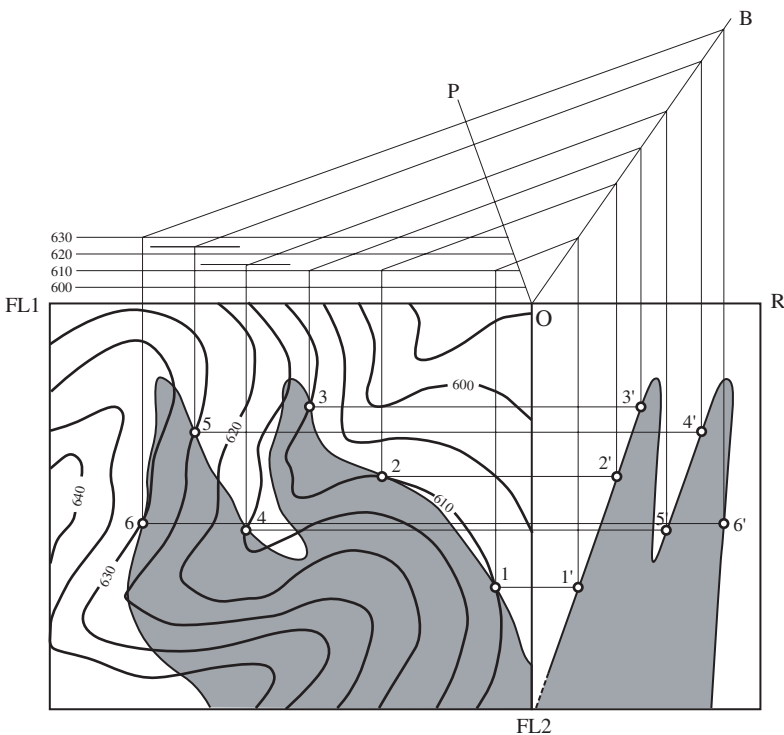


**Figure 17.10** Fold profile from outcrop pattern in an area of topographic relief.

Strictly, the construction of a fold profile requires that the fold axes of the entire area be constant in trend and plunge, or at least have negligible variability. If the axes are not parallel, the folds are not cylindrical, and no single direction of view or projection exists. However, if the plunge angle changes progressively over an area, it is possible to draw an approximate profile, and thus to depict the general fold style. One method is to draw a series of overlapping strip profiles for small areas where the plunge angle is essentially constant, and join them to make a composite section. A second method is to adapt the orthographic construction used above.

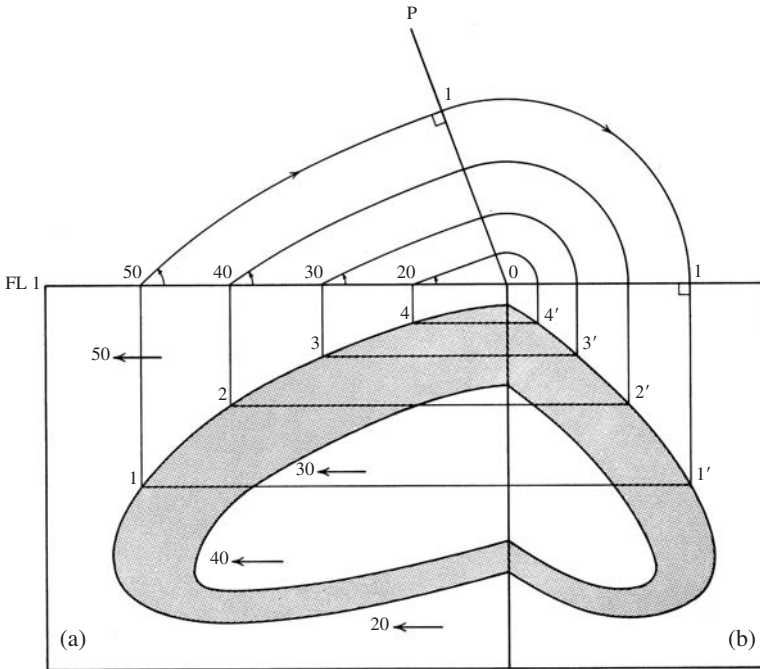


**Figure 17.11** Approximate profile of non-cylindrical fold: (a) map; (b) profile.

**Construction**

1. As before establish folding lines *FL1* and *FL2* (Fig. 17.11a).

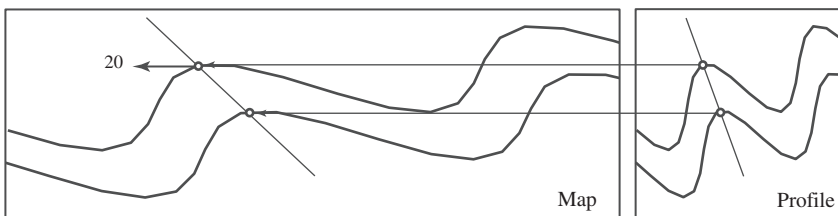


**Figure 17.12** Hinge points and trace of hinge surface on map from profile.

2. Project the data points to *FLI* and for each, plot the associated plunge angle. Using the tangent-arc method of §15.2, curved plunge lines are constructed to project the points to the profile plane.
3. From the map and the edge view *OP*, points are then projected to the profile plane, and the form of the folds is completed by sketching between the control points (Fig. 17.11b).

### 17.5 Hinge and hinge plane

With the true shape of the fold displayed, the hinge points together with the trace of the hinge surface can be added to the profile.

The hinge points can then be projected directly back to the map. In the case of an area of negligible relief, the trace of the hinge surface can then be located (Fig. 17.12). This trace establishes the strike of the hinge plane. Because the plunge of the fold axis is an apparent dip of this plane, the true dip can then also be found.

When topographic relief is involved, however, an alternative approach is needed to determine the attitude of the hinge plane and add its trace to the map (Charlesworth, *et al.*, 1976, p. 58).

The pitch angle the trace of the hinge plane makes on the profile together with the plunge of the fold axis represent two apparent dips, from which the true dip and strike can be found.

With the attitude of the hinge plane known its outcrop trace can then be added to the map using the method of §3.5.

### 17.6 Computer graphs

There is a simple way of obtaining the down-plunge profile directly from the map pattern on a plane surface using available graphical programs (Johnston, 1999). The first step is to obtain a digital image of the fold patterns by scanning the map.

Most drawing programs have a way of transforming objects using a *scaling* tool. The geological map is scanned, rotated and then reduced by rescaling with the factor  $(\sin p)$  100% parallel to the rotated fold trend to produce the profile. We illustrate the method with the same two simple cases.

1. In the special case of folds with attitude  $F(30/000)$  (Fig. 17.13a), the vertical dimension is reduced while leaving the horizontal dimension unchanged. In the case of  $p = 30^\circ$ , in this example it is 50% of the original dimension.
2. The second, more general case involves fold plunging in some other direction, for example  $F(30/330)$ , that is,  $F$  has a bearing of N 30 W (Fig. 17.13b). The map is

rotated  $30^\circ$  in a clockwise direction to bring this trend to “north”. As before, the vertical dimension is reduced by the same factor.<sup>1</sup>

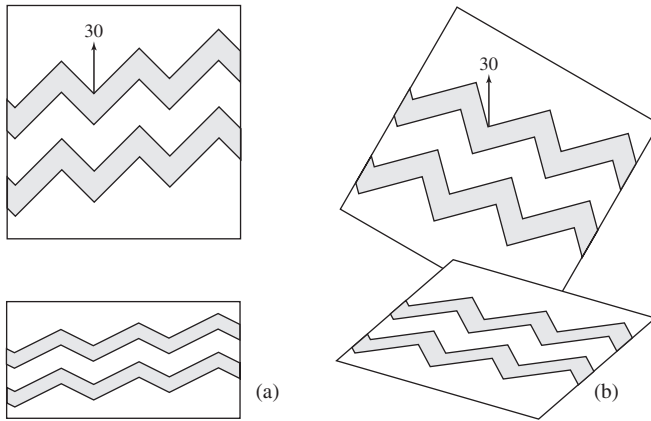


**Figure 17.13** Profiles by computer graphics: (a) Case 1  $F(30/000)$ ; (b) Case 2  $F(30/330)$ .

## 17.7 Transformation of axes

The simple method using computer graphics will not work if the fold pattern involves topographic relief. An alternative method is required. First a file of  $(x, y, z)$  map coordinates of the points on the geological contacts is obtained with the aid of a digitizing table augmented by the elevation of these points. The transfer of these points to the profile can be viewed as a transformation of the coordinates axes (see §7.8). With the expressions for this transformation, the process of depicting the form of the structures on the profile plane can be automated. Several profiles generated in this way have been published (Charlesworth, *et al.*, 1976; Langenberg, *et al.*, 1977, 1988; Kilby & Charlesworth, 1980; Langenberg, 1985).

A variety of coordinate axes could be used, but it is advantageous to follow conventional usage and choose right-handed sets of axes for both the map and profile with a common origin (Fig. 17.4b). The orientations of these axes are

1. Map coordinates:  $+x$  east,  $+y$  north and  $+z$  up.
2. Profile coordinates:  $+x'$  to the right,  $+y'$  upward and  $+z'$  in the up-plunge direction and therefore perpendicular to the plane of the profile.

We illustrate the basic approach using the simple profiles generated by computer graphics. In the first case of Fig. 17.13a, a single rotation about the  $x$  axis by the angle

<sup>1</sup>In Adobe Illustrator click on **Object** on the tool bar, then **Transform** and **Scale**. Click on the non-uniform button and enter 100 in the horizontal box and 50 in the vertical box.

$\omega_x = 90 - p$  transforms the map coordinates into profile coordinates. This is accomplished with the matrix expression involving  $\mathbf{R}_x$  of Eq. 7.38 which transforms any map point in the form of vector with components  $(x, y, z)$  is given by

$$\begin{bmatrix} 1 & 0 & 0 \\ 0 & \cos \omega_x & -\sin \omega_x \\ 0 & \sin \omega_x & \cos \omega_x \end{bmatrix} \begin{bmatrix} x \\ y \\ z \end{bmatrix} = \begin{bmatrix} x' \\ y' \\ z' \end{bmatrix}. \quad (17.2)$$

In this example the elevations are uniform, that is,  $z$  is constant. Any value could be used but here we assign  $z = 0$ . With  $\omega_x = 90 - p = 60^\circ$  the point  $P(x, y, z) = (5, 5, 0)$  (in arbitrary units representing the northeast corner of the square map), is transformed to  $P'(x', y', z')$  with the matrix multiplication

$$\begin{bmatrix} 1.0000 & 0 & 0 \\ 0 & 0.5000 & -0.8660 \\ 0 & 0.8660 & 0.5000 \end{bmatrix} \begin{bmatrix} 5 \\ 5 \\ 0 \end{bmatrix} = \begin{bmatrix} 5.0000 \\ 2.5000 \\ 4.3301 \end{bmatrix}. \quad (17.3)$$

Because the plot is confined to the  $x'y'$  plane of the profile the  $z'$  value is simply ignored. Note that  $x' = x$  and  $y' = \frac{1}{2}y$ , just as in the graphic example (see Fig. 17.14a).

The second, more general case of Fig. 17.13b requires two steps. First, a rotation about the  $z$  axis brings the trend of the fold axes into parallelism with the  $y$  axis. This is accomplished with the matrix expression involving  $\mathbf{R}_z$  of Eq. 7.42, where  $\omega_z$  is the angle between the trend of the fold axes and the  $y$  axis.

$$\begin{bmatrix} \cos \omega_z & -\sin \omega_z & 0 \\ \sin \omega_z & \cos \omega_z & 0 \\ 0 & 0 & 1 \end{bmatrix} \begin{bmatrix} x \\ y \\ z \end{bmatrix} = \begin{bmatrix} x' \\ y' \\ z' \end{bmatrix}. \quad (17.4)$$

Using  $\omega_z = -30^\circ$  gives

$$\begin{bmatrix} 0.8660 & 0.5000 & 0 \\ -0.5000 & 0.8660 & 0 \\ 0 & 0 & 1.0000 \end{bmatrix} \begin{bmatrix} 5 \\ 5 \\ 0 \end{bmatrix} = \begin{bmatrix} 6.8301 \\ 1.8301 \\ 0 \end{bmatrix}. \quad (17.5)$$

The second rotation about  $x$  is

$$\begin{bmatrix} 1.0000 & 0 & 0 \\ 0 & 0.5000 & -0.8660 \\ 0 & 0.8660 & 0.5000 \end{bmatrix} \begin{bmatrix} 6.8301 \\ 1.8301 \\ 0 \end{bmatrix} = \begin{bmatrix} 6.8301 \\ 0.9151 \\ 1.5849 \end{bmatrix}. \quad (17.6)$$

Again note that  $x'' = x'$  and  $y'' = \frac{1}{2}y'$  (see Fig. 17.14b).

Alternatively the total rotation is given by the product matrix  $\mathbf{R} = \mathbf{R}_x \mathbf{R}_z$ , giving

$$\mathbf{R} = \begin{bmatrix} \cos \omega_x \sin \omega_z & -\sin \omega_z & 0 \\ \cos \omega_x \cos \omega_z & \cos \omega_x \cos \omega_z & -\sin \omega_x \\ \sin \omega_x \sin \omega_z & \sin \omega_x \cos \omega_z & \cos \omega_x \end{bmatrix}. \quad (17.7)$$

This gives the same result as with the two-step approach.

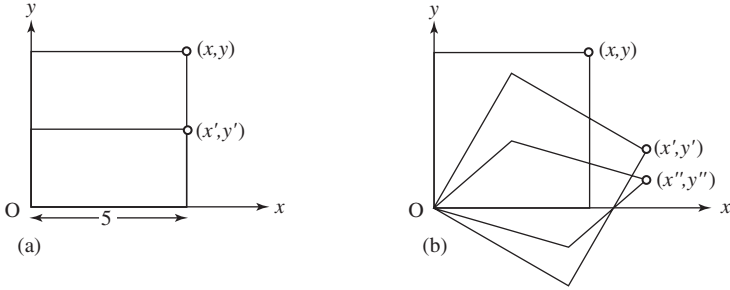


**Figure 17.14** Profile plane by coordinate transformation: (a) Case 1; (b) Case 2.

Note that while both of these simple example problems involved a map plane with constant elevation, the method and equations are completely general and the full coordinates of the map points  $(x, y, z)$  can be used.

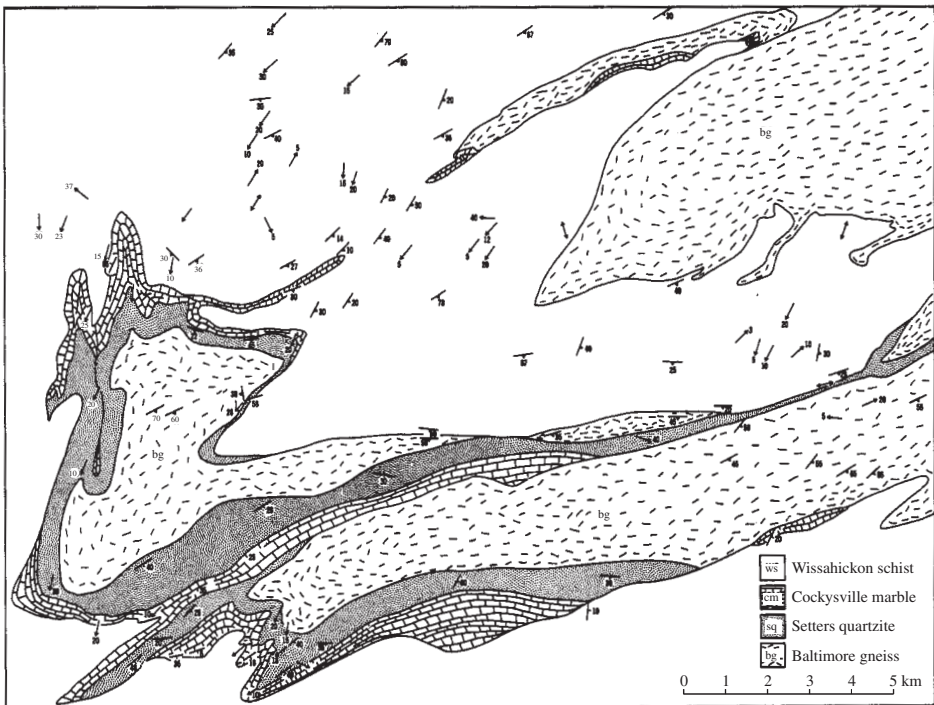


**Figure 17.15** Map of the Coatesville–West Chester District, Pennsylvania (after McKinstry, 1961).

## 17.8 Cautionary note

These methods of constructing fold profiles have been used in Europe for more than 100 years, where they led to a sweeping synthesis of the nappe structure of the Swiss Alps (for a historical review see Christensen, 1963). The validity of these results requires that the folds are cylindrical and that the axial direction has been correctly determined. We return to both these matters in Chapter 18.

The down-structure view as a way of visualizing complex structures on geological maps was described by Bailey and Mackin (1937, p. 189) and Mackin (1950). They first applied the method to a large, poorly exposed structure in the Appalachian Piedmont of western Pennsylvania (a simplified version of the map is shown in Fig. 17.15). If this map is viewed toward 15/245, the structure appears as several gneiss-cored overturned anticlines with severely sheared overturned limbs. McKinstry (1961) and Mackin (1962) debated the validity of this interpretation which crucially depends on whether the structure is truly cylindrical. More recent detailed mapping and geophysical work suggests that the assumption of axial continuity may not hold (Alcock, 1994a, 1994b).

In such circumstances, and especially in the early stages of an investigation, an assumption about the axial continuity and corresponding validity of the down-structure view should probably be considered only a working hypothesis. Further testing is then required.

## 17.9 Exercises

1. The hinge lines of the folds of Fig. 17.16 plunge 30/090. With the aid of a down-plunge view add the appropriate structural symbols for the trace of the hinge plane, including its dip, and the attitude of the hinge lines.

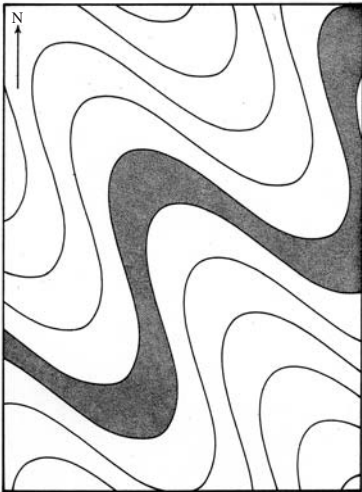


**Figure 17.16** Fold problem.

2. Construct the profile of the shaded layer of these folds.

# 18

## Structural analysis

### 18.1 Introduction

Problems involving the angular relationships between lines and planes may be solved with the methods of descriptive geometry although the advantages of using stereographic projection should now be obvious. However, if certain structural problems are to be solved graphically the use of the stereonet is indispensable. The three-dimensional structural geometry of a rock mass, especially if complex, is one of these. The same basic techniques may also be applied with profit to much simpler situations and this is a convenient way to introduce the method.

### 18.2 S-pole and beta diagrams

In cylindrical folds, the hinge zones may be too smooth to allow accurate field measurement of the attitude of the hinge line or the folds may be too large or incompletely exposed. If attitudes at a number of places on the folded surfaces can be measured, the orientation of the fold axis may be determined by a simple stereographic plot of the data.

#### Problem

- From the following measured dips and strikes on the limb of a fold determine the orientation of the axis.
  1. N 88 E, 16 N
  2. N 68 E, 30 NW
  3. N 60 E, 45 NW
  4. N 41 E, 50 SE
  5. N 35 E, 35 SE
  6. N 20 E, 20 E

#### Methods

1. *Beta diagram*: plot each measured plane as a great circular arc. These intersect at a point called the  $\beta$  axis (Fig. 18.1a).



2. *S-pole diagram* (also called a  $\pi$  diagram): plot the poles of the measured planes. These define a great circle whose pole is the  $\beta$  axis (Fig. 18.1b).

### Answer

- Both give the attitude of the fold axis as 10/049.

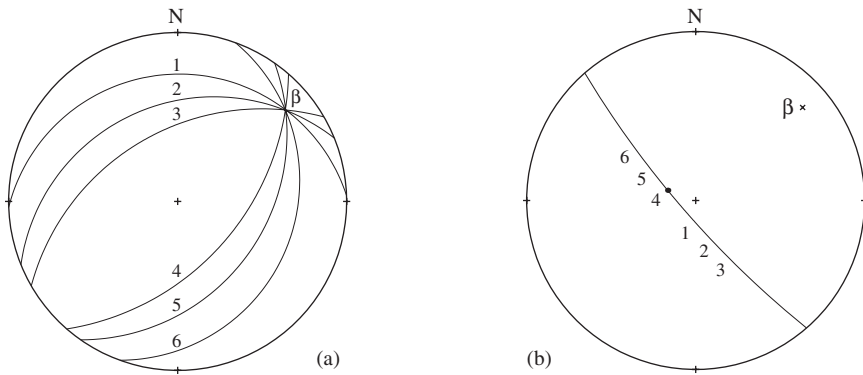


**Figure 18.1** Plot of a fold: (a)  $\beta$  diagram; (b) *S-pole diagram*.

The basis of these methods is the collection of all the measured attitudes at single point. This has both advantages and disadvantages. The obvious advantage is that it allows the orientation of the fold axis to be determined. The disadvantage is that these attitudes are removed from their context on the map. The best of both worlds is always to use the stereographic plots in conjunction with the geological map.

### 18.3 Fold axis and axial plane

The reason for carefully distinguishing between the hinge line and the fold axis may now be appreciated. The  $\beta$  intersection characterizes the relationship of any pair of attitudes and therefore all attitudes. This axis has no specific location in the fold, only orientation. In cylindrical folds, the hinge lines and fold axis are parallel, but they refer to quite different aspects of the fold geometry. In simple cylindrical folds, there is a similar relationship between the planar hinge surface of the fold and the axial plane, and there is an interrelationship between both pairs of features, as an example will illustrate.

### Problem

- From the map of an overturned, plunging anticline, what is the attitude of the axis and the axial plane (Fig. 18.2a)?

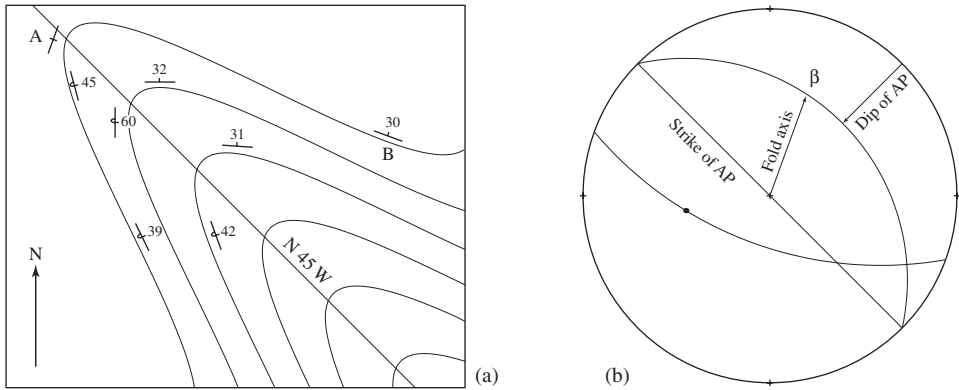


**Figure 18.2** Axis and axial plane: (a) map; (b) stereogram.

### Construction

1. An *S*-pole diagram of the measured attitudes yields the  $\beta$  axis (Fig. 18.2b).
2. With this direction a profile may then be constructed to locate the trace of the hinge surface or it can be seen in a down-plunge of the map.
3. Add to the stereogram the strike of the hinge surface which is also parallel to the axial plane. Because the fold axis is parallel to the axial plane, the axis is, in effect, an apparent dip of that plane. A great circle through  $\beta$  and the strike of the hinge surface fixes the dip of the axial plane.
4. For an overturned fold, the plunge and trend of the fold axis may be estimated from the geological map by inspection.

(a) Its trend parallels the strike of the vertical plane (Point A).

(b) Its plunge equals the dip of the plane whose strike is normal to this plane (Point B).

### 18.4 Equal-area projection

In practice, stereographic plots of lines or planes are never as perfect as in Figs. 18.1b and 18.2b. Inevitable measurement errors as well as the departures from ideal cylindrical geometry all contribute to a scatter of points. If the scatter is small, it is generally possible to visually locate the best-fit point or great circle within acceptable limits, but with only a few points the confidence will be low. A larger sample is then required.

Another problem concerns the visual evaluation of such diagrams. If points distributed uniformly on the lower hemisphere are depicted on the Wulff net, the result will not be uniform (Fig. 18.3a). There is a tendency to cluster at the center of the net and it would falsely appear to have a weak vertical preferred orientation of the lines or poles. The reason is that the grid spacing varies with the vertical angle and the result is that points plot closer together at the center of the net than at the primitive.

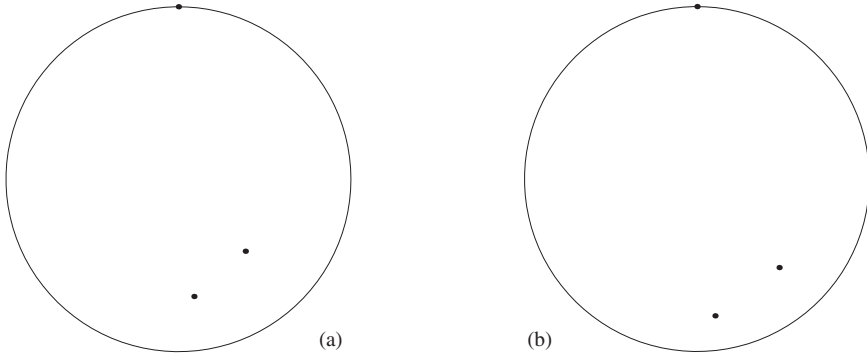


**Figure 18.3** Plot of a uniform distribution: (a) equal-angle net; (b) equal-area net.

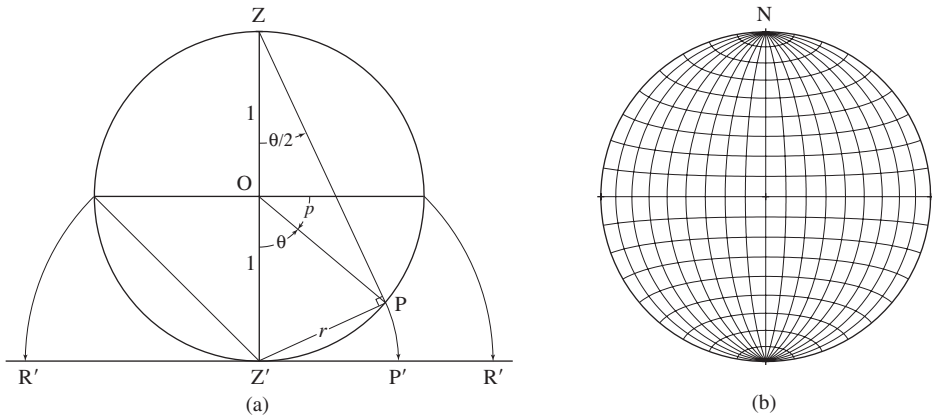


**Figure 18.4** Lambert projection: (a) geometry; (b) equal-area net.

To overcome this problem the *Lambert equal-area projection* is used.<sup>1</sup> As in the case of the stereographic projection, we examine the geometry of this method on a vertical diametral plane through a reference sphere of unit radius. On this section a line with plunge  $p$  makes an angle  $\theta = 90^\circ - p$  with the vertical and intersects the lower hemisphere at a point  $P$  (Fig. 18.4a). The projection of this point onto the horizontal projection plane passing through the nadir point  $Z'$  is found by swinging an arc with radius  $Z'P$  using point  $Z'$  as center. From the right triangle  $ZZ'P$  the radial distance  $r$  from  $Z'$  to any such point  $P'$  is then

$$r = 2 \sin \frac{1}{2}\theta. \tag{18.1}$$

<sup>1</sup>Johann Heinrich Lambert [1728–1777], a self-educated German scientist, made important contributions to physics, astronomy, philosophy and mathematics (he first established the fact that  $\pi$  was irrational). The equal-area projection was part of his contributions to the theory of map construction which are still basic for the modern theory.

In practice it is convenient to reduce the radius of the primitive to be equal to the radius of the sphere, that is, make  $r = 1$  when  $p = 0$  ( $\theta = 90^\circ$ ). By Eq. 18.1 the radius of the primitive  $z'R'$  is then

$$r = 2 \sin 45 = 2(\sqrt{2}/2) = \sqrt{2}.$$

Dividing by the scale factor  $\sqrt{2}$ , we obtain the adjusted version of Eq. 18.1

$$r = (2/\sqrt{2}) \sin \frac{1}{2}\theta = \sqrt{2} \sin \frac{1}{2}\theta. \quad (18.2)$$

With this result, a series of curves may be drawn corresponding to the small and great circle on the Wulff net (Fig. 18.4b). The result is the equal-area net, also called the *Schmidt net*.<sup>2</sup> Equal-area nets of any size can be easily constructed from

$$r = R\sqrt{2} \sin \frac{1}{2}\theta \quad \text{or} \quad r = R\sqrt{2} \sin \frac{1}{2}(90 - p), \quad (18.3)$$

where  $R$  is the desired radius of the primitive.

Now a uniform distribution of lines appears to be uniform in projection (Fig. 18.3b). The technique of plotting and manipulating lines and planes is identical to that used on the Wulff net. The only practical difference is that circles, great and small, do not project as circles.

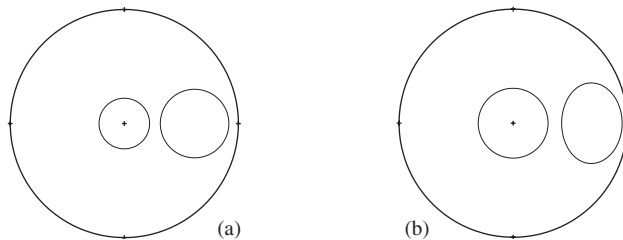


**Figure 18.5** Projection of equal areas: (a) Wulff net; (b) Schmidt net.

The contrasting properties of the equal-angle and equal-area nets are shown in Fig. 18.5. On the Wulff net areas which are equal on the sphere are the same shape but noticeably unequal in size in projection, while areas on the Schmidt net are equal but variably shaped.

When the size adjustment given by Eq. 18.2 or Eq. 18.3 is made, an area on the sphere is no longer equal to the area in projection. However, areas which are equal on the sphere remain equal in projection and this is the important property of the Schmidt net (Sellés-Martínez, 1993).

<sup>2</sup>Named after the German petrologist who used it for this purpose (see Schmidt, 1925).

### 18.5 Polar net

When plotting many points by hand, it is particularly advantageous to use the polar version of the Schmidt net (Lisle and Leyshon, 2004, p. 42). As in the case of the polar Wulff net (Fig. 5.21a), the planes represented by the great circles are now vertical, and the small circles are concentric about the center with radii given by Eq. 18.1 (Fig. 18.6).

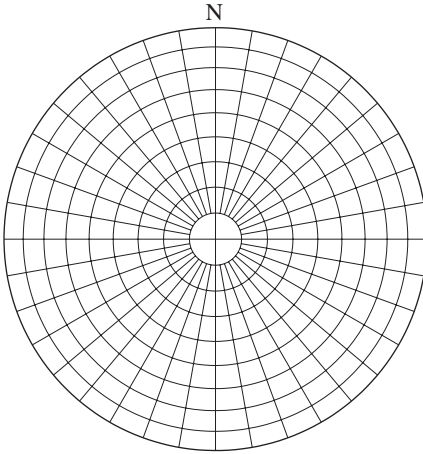


**Figure 18.6** Equal-area polar net.

### 18.6 Equal areas

We now verify that equal areas on the hemisphere are also equal in projection. Following Watson (1988) an element of area on the surface of a sphere of unit radius is  $\sin \theta \, d\theta \, dt$  and an element of area on the horizontal projection plane is  $r \, dr \, dt$  (Fig. 18.7).

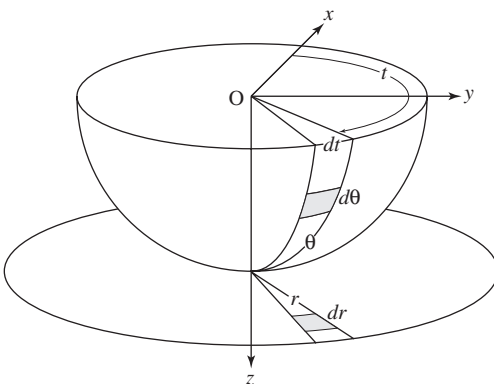


**Figure 18.7** Projection of an element of area.

The method must project the point with coordinates  $(x, y, z)$  on the surface of a unit sphere onto the point with polar coordinates  $(r, t)$  on the plane subject to the condition that areas on the sphere and on the projection plane are equal, that is,

$$\sin \theta \, d\theta \, dt = r \, dr \, dt \quad \text{or} \quad \sin \theta \, d\theta = r \, dr.$$

Then

$$\int \sin \theta \, d\theta = \int r \, dr \quad \text{or} \quad -\cos \theta = \frac{1}{2}r^2 + c.$$

To evaluate the constant of integration we note that the nadir point  $(0, 0, 1)$  must project to the origin on the  $xy$  plane, that is,  $r = 0$  when  $\theta = 0$ . Using these in the above equation gives  $c = -1$ . With these values and after rearranging we have

$$r^2 = 2(1 - \cos \theta). \tag{18.4}$$

The trigonometric identity

$$\sin^2 \alpha = \frac{1}{2}(1 - \cos 2\alpha)$$

may be rewritten as

$$1 - \cos \theta = 2 \sin^2 \frac{1}{2}\theta,$$

where  $\alpha = \frac{1}{2}\theta$ . Using this in Eq. 18.4 gives

$$r^2 = 4 \sin^2 \frac{1}{2}\theta \quad \text{or} \quad r = 2 \sin \frac{1}{2}\theta, \tag{18.5}$$

and this is identical to Eq. 18.1 found graphically. Hence the Lambert construction does indeed result in the projection of equal areas.

## 18.7 Contoured diagrams

Because of the equal-area property we can now be sure that the distribution of points on the Schmidt net truly represents the distribution on the sphere.

However, such scatter diagrams are difficult to evaluate and compare visually. The usual way around this problem is to contour the density of the points on the net. Once the point diagram has been prepared, the densities are counted out, and a variety of graphical methods have been devised to do this (Stauffer, 1966; Denness, 1970, 1972; see also Turner & Weiss, 1963, p. 58f).

By hand, most techniques use a circular counter, usually representing 1% of the total area of the net, to determine the density of points. If the area of the net is  $A = \pi R^2$  and the area of the counter is  $a = \pi r^2$ , then

$$\frac{a}{A} = \frac{\pi r^2}{\pi R^2} = \frac{1}{100} \quad \text{and} \quad \frac{r}{R} = \frac{1}{10}.$$

Accordingly, for a net with radius  $R = 7.5$  cm, a 1% counter has a radius of  $r = 0.75$  cm.

The original and still widely used way of counting is the Schmidt method (Turner & Weiss, 1963, p. 61). The point diagram is superimposed on a grid with spacing of  $R/10$  (Fig. 18.8a). Counting is accomplished with a special tool, called the *Schmidegg counter* (Knopf & Ingerson, 1938, p. 245). In the body of the diagram, the circle at one end of the counter is centered at each grid node and the number of data points within its 1% circle are tabulated. If the counting circle overlaps the primitive, both ends of the tool are used (Fig. 18.8b). The tool can also be used as a free counter to determine the density variation in greater detail.

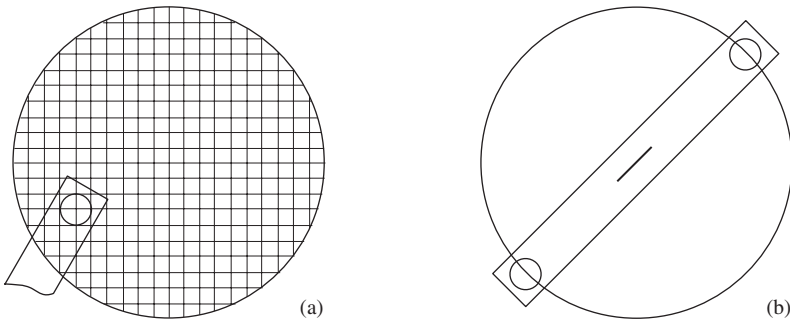


**Figure 18.8** Schmidt method: (a) counting grid; (b) Schmidegg counter.

The alternative graphical method which we used here to introduce the approach is one of the simplest yet devised. It applies reasonably well to all situations and is particularly useful in the field because it is entirely self-contained.

For this method a special counting net is required (Kalsbeek, 1963). The projection area is completely subdivided into small triangles (Fig. 18.9a). In general, six of these triangles form a hexagonal area equal to 1% of the total area. In addition to ease of use, this counting net has the advantage of a fixed relationship between the total number of points and the counted density. Each point is counted three times (except for a small discrepancy caused by the semicircular areas at each end of the six spokes).

**Counting**

1. Superimpose the point diagram and a second tracing sheet on the counting net. At the center of each hexagon, the total number of points within that hexagon is written (see Fig. 18.9b, Point A). For the main body of the diagram there will be numbers at

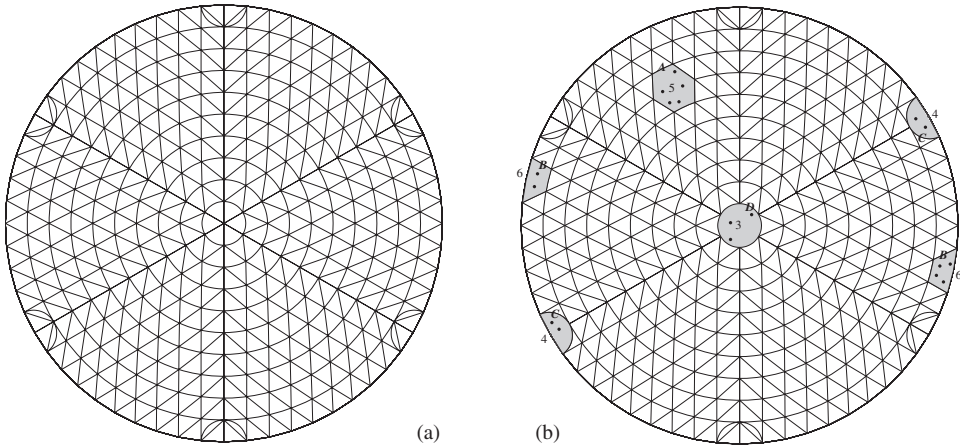


**Figure 18.9** Counting: (a) Kalsbeek net; (b) density determinations.

the center of each overlapping hexagon. For parts of the diagram with no points, the hexagons may be left blank, rather than noting a zero for each.

2. At the circumference of the net, the points in each half hexagon on one side of the net are combined with the complementary half on the opposite side, and this number is written on both sides of the *net* along the primitive (see Point *B*).
3. Points at the ends of the spokes are counted using the complementary half circles (Point *C*). At the very center, the small 1% circle is used (Point *D*).

There is a problem with this or any such manual counting technique. As we have seen, the nature of the Schmidt net is such that the shape of a small circle on the sphere projects as an oval-shaped area which is not constant in shape with inclination. In the past an effort was made to circumvent this problem by using counters of variable shape. This requires much more work and for most purposes it has not been found necessary. Further, the problem is eliminated entirely with computer-generated diagrams.

Following the counting process, the tracing sheet bearing the numerical densities expressed as the number of points per 1% area is removed from the counting net, and contours of equal density are then drawn. To facilitate the comparison of diagrams with different numbers of total points, contours are drawn in percentages of total points per 1% area of the net. Therefore, the numbers posted during the counting process must be converted to percentages. In the special case of exactly 100 points, each number will, of course, also be the required percentage figure. If 50 points are plotted, each point represents 2% of the total, and the posted numbers are doubled, and so forth.

### Contouring

1. Within the main body of the diagram, contours of equal density are drawn as shown at Point *A* of Fig. 18.10a. The position of these contours is easily found by interpolating



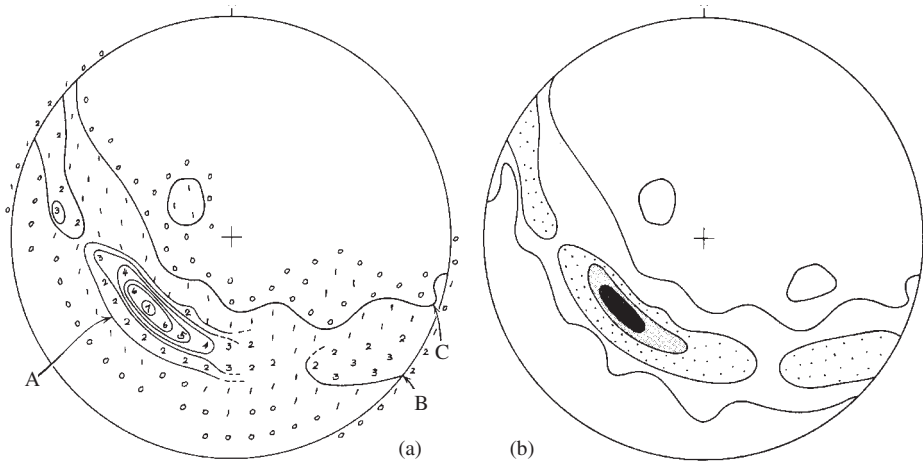


**Figure 18.10** Contouring by hand: (a) counted densities and preliminary contours; (b) completed diagram; contours 2–4–8–12% per 1% area, maximum 14%.

by eye. It is usually easiest to locate the area of greatest concentration and work outward.

2. For contour lines which approach the primitive, the counts along the edge are used. When a contour line intersects the primitive it must reappear exactly  $180^\circ$  opposite (see Point B).
3. When a contour line should be strictly drawn intersecting the primitive, but it is clear that it immediately loops back again, it is permissible to avoid actual contact with the primitive (Point C).
4. When the preliminary contouring is complete, several modifications may be made to improve the appearance of the diagram (Fig. 18.10b):
  - (a) The maximum found during the counting may not be the true maximum of the diagram. The greatest concentration can be found by returning the point diagram to the counting net. Using the central 1% circle as a free counter, shift the diagram around until the largest number of points lies within it.
  - (b) All the contour lines may not be necessary to show the pattern; a maximum of six usually brings out the pattern without producing clutter. For example, if the spacing is very close, intermediate contours may be eliminated. The values of the remaining contours in the final diagram are indicated in the legend in the form 2–4–8–12% per 1% area, maximum 14%.
  - (c) The area of maximum concentration is often blackened. Although usually unnecessary, patterns may be used for the areas of lesser concentration. Particularly effective is the use of stipple patterns graded so that the areas of greater concentration have a denser appearance. Line patterns detract from the visual effect and should be avoided.

In order to convey as much objective data as possible to the reader, it is useful to supply both the point diagram and its contoured equivalent.

### 18.8 Statistics of scatter diagrams

The scatter of points inevitably involves questions of a statistical nature and a variety of techniques are available for extracting information concerning their best fit and confidence (Mardia, 1972; Watson, 1983; Fisher, *et al.*, 1987) but many questions remain. Here we take a more direct, graphical approach to introduce the subject (Vollmer, 1995).

First, does the scatter of points display a meaningful pattern or not? Figure 18.11 shows three scatter diagrams, each with 100 points. A visual comparison shows that they are different and that each has an irregular distribution of points with local clusters and gaps. The contoured equivalents of these would also show these features. Yet each is a random sample taken from a uniform population (Fisher, *et al.*, 1987, p. 59): there is no statistical difference between them. The question then is, when faced with scatter diagrams, how can we determine whether such differences are significant or not?

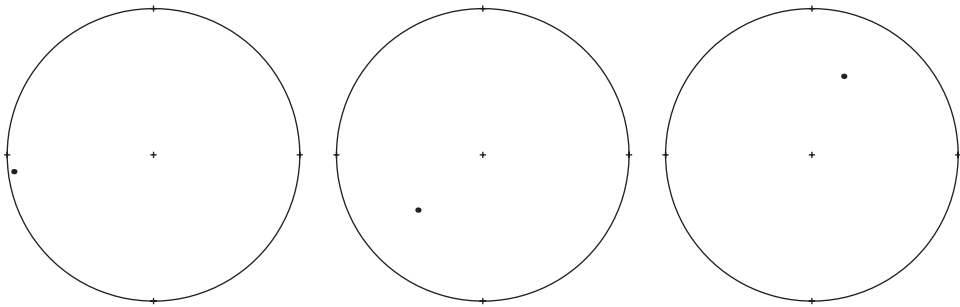


**Figure 18.11** Three random samples from a uniform distribution.

Suppose we have plotted a single point from such a data set. On the equal-area net we then place a circular counter somewhere on the net. There are two possible outcomes of such a single trial – the point will lie within the counter (a success) or it will not (a failure). For a projection of area  $A$  and radius  $R$ , the *probability*  $p$  that the point will lie within a counting circle of area  $a$  and radius  $r$  is

$$p = a/A = r^2/R^2. \quad (18.6)$$

With the 1% counter,  $p = 0.01$ . This circle has an angular radius of  $0.9^\circ$ .

We now complete the point diagram with a total of  $N$  randomly placed points. The expected number of points falling within a counting circle is then described by a binomial distribution (see Walpole & Myers, 1993, p. 128), and the mean  $\mu$  of a binomial distribution is given by

$$\mu = Np. \quad (18.7)$$

The expected number of points  $E$  within the counting circle will be equal to the mean, that is,

$$E = \mu = Np. \quad (18.8)$$

The measure of departure from uniformity is the *standard deviation*  $\sigma$ . For a binomial distribution this is

$$\sigma = \sqrt{Np(1-p)}. \quad (18.9)$$

Kamb (1959) assumed that densities greater than  $3\sigma$  differ significantly from that expected from a random sample of a uniform population. That is

$$E = 3\sigma. \quad (18.10)$$

We now need to determine the size of the counter which will accomplish this. Dividing both sides of Eq. 18.9 by  $Np$  we have

$$\frac{\sigma}{Np} = \sqrt{\frac{1-p}{Np}}. \quad (18.11)$$

From Eqs. 18.7 and 18.10

$$Np = 3\sigma \quad \text{and} \quad \sigma/Np = 1/3.$$

With this in Eq. 18.11 and squaring yields

$$\frac{1-p}{Np} = \frac{1}{9}.$$

Solving for  $p$  then gives

$$p = \frac{9}{N+9}. \quad (18.12)$$

Finally, using this in Eq. 18.6 we obtain an expression for the required radius of the counting circle

$$r = \frac{3R}{\sqrt{N+9}}. \quad (18.13)$$

With this, we now have a way of distinguishing diagrams which have meaningful departures from uniformity. If a diagram contoured with a counter of this size shows greater fluctuations then it is probably not random.

Table 18.1 Angle  $\phi$  as a function of  $k$  and  $N$ 

	$N = 50$	$N = 100$	$N = 150$	$N = 200$
1%	9.0°	9.0°	9.0°	9.0°
$k = 1$	11.4°	8.1°	6.6°	5.7°
$k = 2$	22.2°	15.9°	13.1°	11.4°
$k = 3$	32.1°	23.4°	19.4°	16.9°

Because they are produced with specific structural questions in mind, most diagrams have clearly discernable patterns, even though they also have local, insignificant fluctuations. Distributions which are clearly non-random are no longer described by the binomial distribution. In such cases, the primary benefit of Kamb's criterion is that it reduces the influence of sample size, so that diagrams with differing numbers of points may be compared.

However, Vollmer (1995) also found that  $E = 3\sigma$  tends to over-smooth data sets with stronger concentrations. For these a smaller counter is needed. For data sets with few outlying points, Eqs. 18.12 and 18.13 can be modified by substituting  $k\sigma$  for  $3\sigma$  giving

$$p = \frac{k^2}{N + k^2} \quad \text{and} \quad r = \frac{kR}{\sqrt{N + k^2}} \quad (18.14)$$

where the parameter  $k$  can be subjectively lowered to reduce smoothing and increase resolution for distributions which clearly deviate from uniform.

### 18.9 Computer-generated diagrams

Plotting and contouring of large number of data points is an ideal computer application. Not only is there a great saving of time and effort but the data can be examined quickly in a variety of ways which would not be possible otherwise.

The problem of the varying shape of a circular counter on the Schmidt net is solved by counting on the surface of the hemisphere rather than on the projection plane (Warner, 1969). While this would be difficult by hand, it is actually easier to program the computer to do it this way. The area of a spherical cap on a sphere of unit radius is

$$a = 2\pi(1 - \cos \phi) \quad (18.15)$$

where  $\phi$  is the semi-apical angle of the right-circular cone defining the cap. The area of the hemisphere with unit radius is  $A = 2\pi$ , thus with Eq. 18.6

$$p = a/A = 1 - \cos \phi. \quad (18.16)$$

Solving for  $\cos \theta$  and substituting the expression for  $p$  in Eqs. 18.14 we then have

$$\cos \phi = 1 - \frac{k^2}{N + k^2} = \frac{N}{N + k^2}. \quad (18.17)$$

The density is found by determining the angle between the position vector of a grid node and each data vector using the dot product (see §7.3). If this angle is less than or equal to  $\phi$ , then the count is incremented. From the final nodal data, the contours can then be automatically drawn.

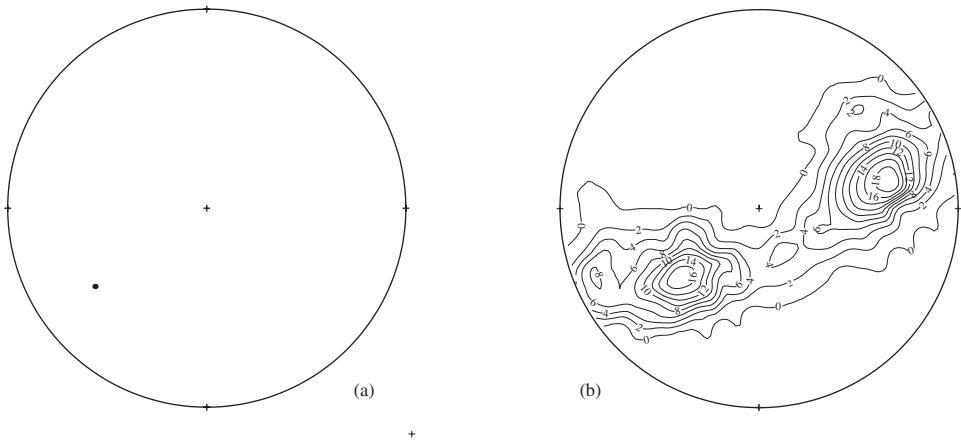


**Figure 18.12** Example of automatic contouring: (a) point diagram; (b) contoured equivalent.

A number of computer programs have been described (see Vollmer, 1995, for a good discussion and earlier references) and several are readily available: Allmendinger (2001), Holcombe (2001), Jacobson (1996), RockWare (2001), Wallbrecher (2005). Recently, Haneberg (2004, p. 43–47) gives a good general description of the basic method using Mathematica.

To illustrate the basic method a short generic program which takes advantage of contouring routines available in the programming language MATLAB<sup>®</sup> is used (Middleton, 2000).

1. Instead of a rectangular grid (Fig. 18.8a), the 331 nodes of the Kalsbeek net are used (see Fig. 18.3b). For each of these nodes:
  - (a) The  $xy$  coordinates relative to the origin at the center of the net and  $+x = \text{east}$  and  $+y = \text{north}$  are calculated.
  - (b) The direction cosines of each unit node vector  $l_N, m_N, n_N$  are found from the plunge and trend of the nodes.
2. From the plunge and trend the direction cosines  $l_D, m_D, n_D$  of each unit data vector are determined.

3. At each node visited in sequence the dot product of the node vector and all of the data vectors are calculated. If the angle between a data vector is less than the angular radius of the counting circle, found with Eq. 18.17, a data point is counted. Finally, the density  $z$  is found by dividing the number of these points associated with a particular node by the total number of data points.
4. To properly count the density associated with nodes at or near the primitive the opposite vectors of data points with small plunge angles are copied into the upper hemisphere.
5. Finally, the field of  $z(x, y)$  values is contoured using MATLAB routines.

Figure 18.12a shows the point diagram and Fig. 18.12b is the contoured equivalent.

### 18.10 Interpretation of diagrams

*Pattern* is the key to interpreting a point diagram and its contoured counterpart. The real equivalents of the ideally perfectly linear and perfectly planar patterns are:

1. A *point maximum* is an axially symmetrical clustering of points about a single direction.
2. A *girdle* is a grouping of points distributed in a band along a great circle.

For folds, we may choose to construct a  $\beta$  diagram which produces a point maximum, or an *S*-pole diagram which produces a girdle pattern. There are several compelling reasons for adopting the latter type of diagram.

1. In the  $\beta$  diagram, the total number of intersections  $N = n(n - 1)/2$ , where  $n$  is the number of individual great circles. As this expression makes clear, the number of intersections rapidly rises as the number of circles increases. For example, if  $n = 100$ , which is not a particularly large sample, then  $N = 4950$ . Such a large number is apt to give the impression of a large sample size and therefore a false sense of confidence in the result. It also involves much more work to produce a  $\beta$  diagram.
2. As a result of inevitable scatter, spurious concentrations of intersections may result. This will be especially true in open folds where the interlimb angle approaches  $180^\circ$  or in tight folds where it approaches  $0^\circ$ . These spurious intersections will not be randomly distributed about a mean position, and they may exceed the number of significant  $\beta$  points (Ramsay, 1964).
3. Perhaps the most important advantage is that the *S*-pole diagram, if based on a representative sample of the attitudes of the structure, gives information on the shape of the folded surface, the interlimb angle and the attitude of the axial plane.

An instructive approach to understanding *S*-pole diagrams is to follow the patterns as they evolve during folding. Consider the cylindrical folding of a single bed. Before folding, the poles of the horizontal layer would plot as a concentration of points at the center of the net (Fig. 18.13a), that is, the poles would cluster about a vertical line. If the diagram were constructed parallel to the profile plane, there would be a point maximum at

each end of a diameter of the net. As the layer is folded about a horizontal axis, the original vertical poles are spread into a fan. In terms of pattern, whether projected horizontally or vertically, the original point maximum spreads into a *partial girdle* (Fig. 18.13b). With further folding, the girdle continues to spread (Fig. 18.14a). Finally, with rotation of the limbs into parallelism, a *full girdle* develops (Fig. 18.14b). Note that the same diagrams would result from either antiforms or synforms.

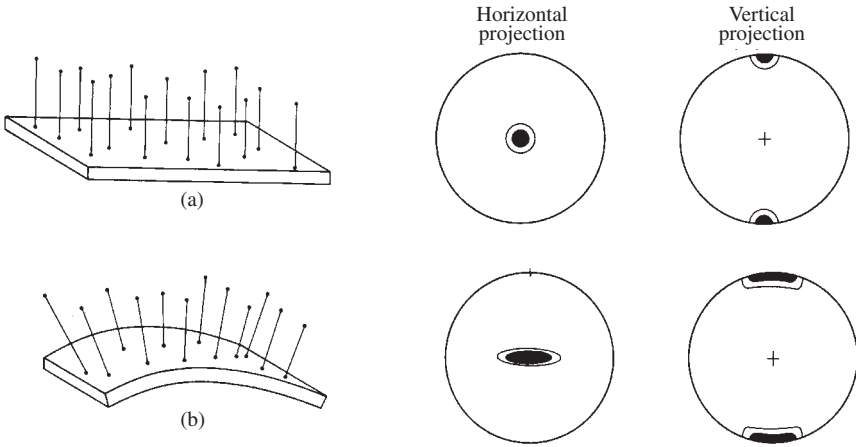


Figure 18.13 S-pole diagrams 1: (a) horizontal layer; (b) layer bent through 45°.

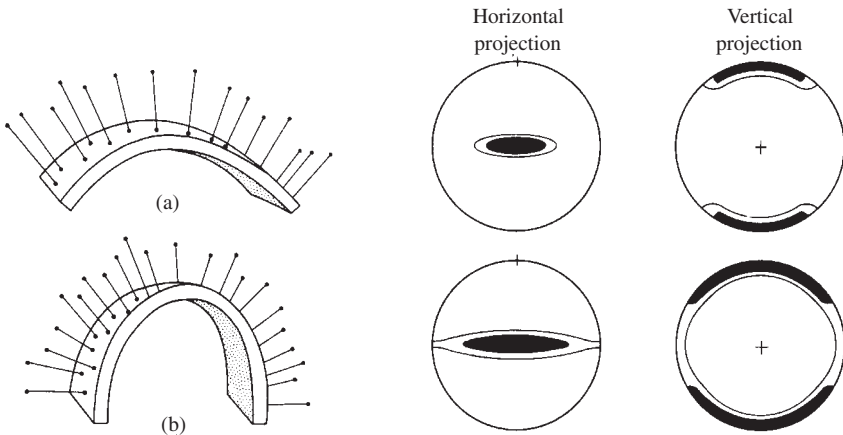
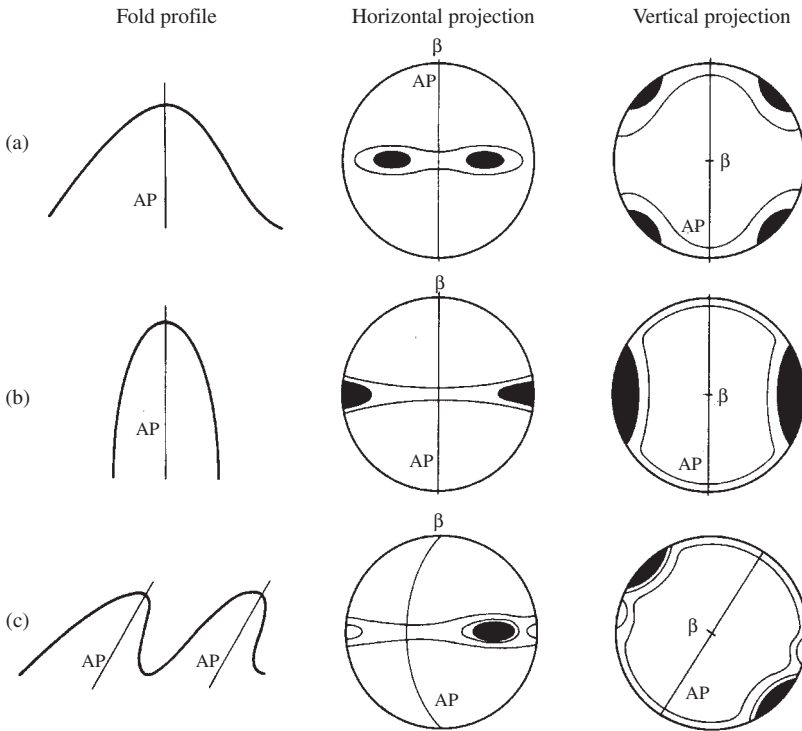


Figure 18.14 S-pole diagrams 2: (a) layer bent through 90°; (b) layer bent through 180°.

If the fold shape is dominated by planar limbs, the S-pole pattern will consist of a point maximum associated with each limb, and the interlimb angle will be the supplement of the angle between these two maxima. On the other hand, if the fold shape is dominated by a uniformly curved hinge zone, the density of points within the girdle will be uniform,

and the interlimb angle will be the supplement of the angle between the two extreme poles in the girdle. Most folds have shapes and patterns between these two extremes.



**Figure 18.15** Patterns: (a) symmetric open fold; (b) symmetric isoclinal fold; (c) asymmetric fold with inclined axial plane.

Note also that symmetric folds have symmetric patterns, both in terms of location and concentration of points (Figs. 18.15a and 18.15b). Conversely, the patterns of asymmetric folds are also asymmetric; for such folds a large number of variations in the patterns are possible. Figure 18.15c illustrates a simple example. The overall shape of the contours is symmetric, but the maxima within the girdle have noticeably different values. The stronger one marks the pole of the dominant limb.

For purposes of introduction, the folds illustrated above are horizontal or upright or both. The axis and axial plane can, of course, have any attitude, and this will be reflected on the diagram. Several plunging and inclined folds are shown in Fig. 18.16.

### 18.11 Superimposed folds

The *S*-pole diagram may also be viewed as a test for the homogeneity of the fold axes in the area being examined. As such, the diagram can be used to decide if, and in what direction, a fold profile can be drawn. On the other hand, the pattern may not be interpretable; the scatter may be such that no clear-cut maximum or girdle is present. Such areas are



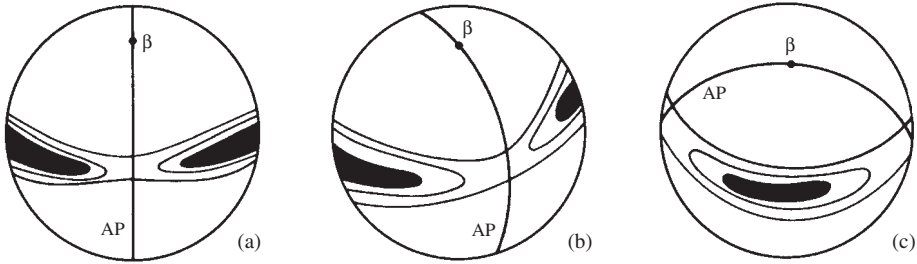


Figure 18.16 Folds with different attitudes of axes and axial planes.

inhomogeneous with respect to axial directions. This will be the general case in rock masses that have undergone two or more episodes of folding.

The approach in areas of polyphase folding is to seek smaller, homogeneous subdivisions for which the data do yield interpretable diagrams. An artificial example will suggest the approach that is used.

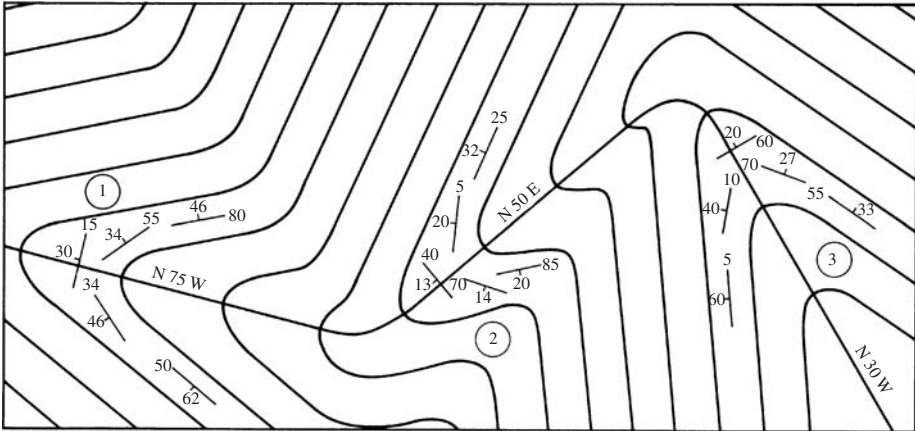


Figure 18.17 Idealized superimposed folds; areas 1, 2 and 3 are recognizable by the straight segments of the apparent traces of the hinge surface.

**Problem**

- From a geological map of an area in which the rocks have undergone two episodes of folding (Fig. 18.17), determine the geometrical relationship between the two sets of folds.

**Analysis**

1. Subdivide the map area into domains, each of which contains structures that are statistically homogeneous, that is, characterized by cylindrical folds. In some cases, these subdivisions may be located by trial and error, or by the recognition of the

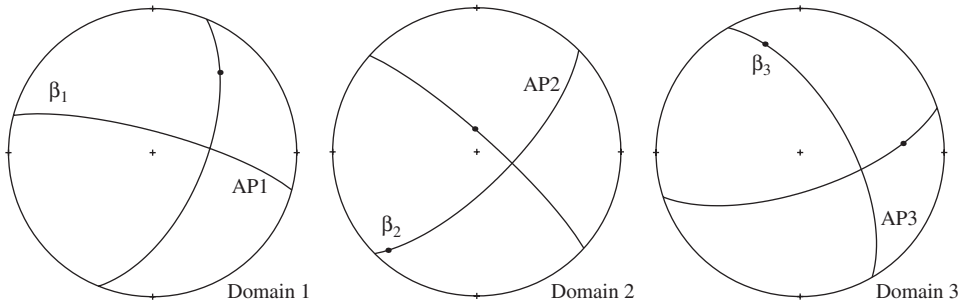


**Figure 18.18** Stereograms of data from domains 1, 2 and 3.

rectilinear nature of the apparent traces of the hinge surfaces, or by other structural evidence.

2. A plot of the data from each domain then yields the orientation of the folds in each homogeneous part of the structure (Fig. 18.18). Changes from one subarea to the next can then be determined by comparing diagrams.
3. Synoptic diagrams are useful in illustrating these variations, and in obtaining information about the second folds. In this example:
  - (a) Beta intersections of the axial planes from the three domains define the axis of the second folds (Fig. 18.19a).
  - (b) The axes of the three domains lie on a single great circle, which indicates a special type of dispersal of preexisting fold axes and linear structures during the second deformation (Fig. 18.19b). This pattern is characteristic of similar folding.

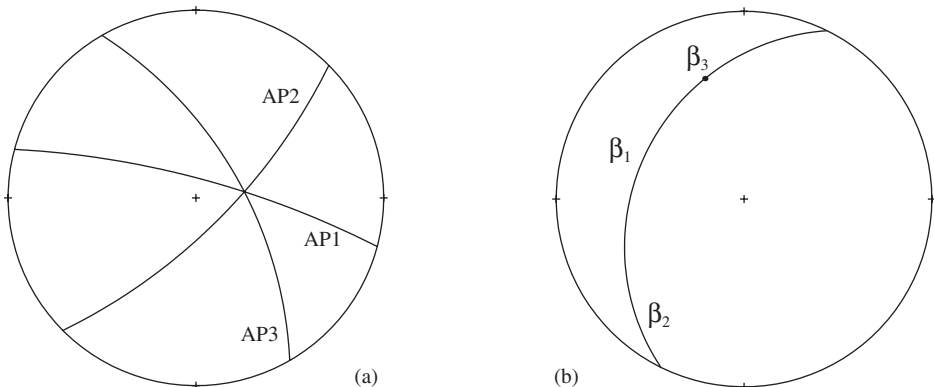


**Figure 18.19** Synoptic diagrams: (a) axial planes; (b) fold axes.

Turner and Weiss (1963, p. 178–179) give an extended and more realistic example of this type of analysis which is well worth examining in detail. Because of problems intrinsic to distinguishing homogeneous domains by eye and by hand, Vollmer (1990)

described a computer program which automatically searches the data base and defines the domains based on the best fit of several indexes and constructs the synoptic diagrams.

In general, results of this type, together with information on the type of folding, permit individual hinge lines to be traced through the superimposed folds (Stauffer, 1968).

### 18.12 Sampling problems

Valid interpretations of point diagrams and their contoured equivalents depend on the data being representative, that is, accurately reflecting the range and relative abundances of attitudes. Because of limited exposure and inability to explore completely the third dimension, it is difficult to justify any particular collection of data as being strictly representative. Usually all that one can do is to conscientiously try to avoid introducing any obvious bias.

To illustrate this sampling problem, we consider a situation which frequently arises when attempting to determine and describe the distribution of discontinuities of various orientations in a rock mass for geotechnical purposes (Terzaghi, 1965; La Pointe & Hudson, 1985). Such planes of weakness include bedding, cleavage and fractures of several types, including faults and joints. Joints are perhaps the most common of these and in the following discussion this term will be used, but the relationships apply to any structural planes whatever their origin.

If the joints are essentially planar and parallel so that they form a *set*, they are said to be systematic. Commonly several sets of systematic joints are present. Joints which belong to no set are often referred to as random joints, and if only random joints are present they are said to exhibit a random pattern (though it is uncertain whether any group of such joints is strictly random in a statistical sense).

To evaluate the relative frequencies of various joint orientations observed at a particular locality, the dip and strike of each joint are measured, and each is then represented

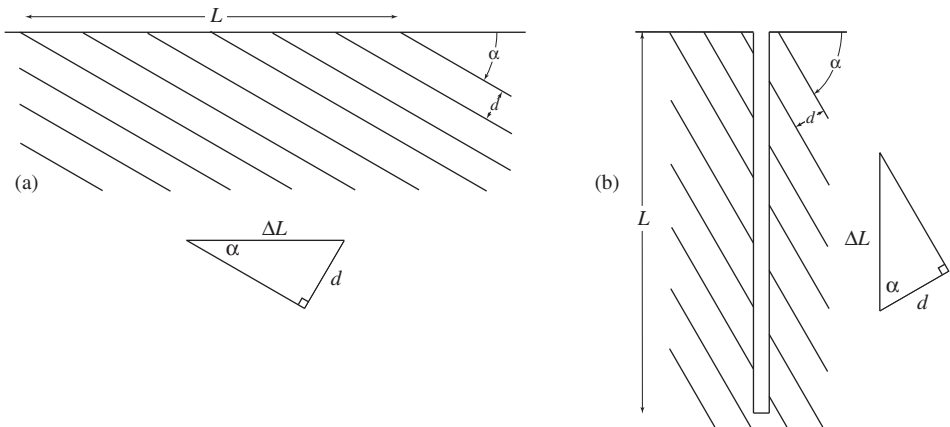


**Figure 18.20** Joints: (a) strike-normal section of a joint set; (b) section of a joint set and drill hole.

on a Schmidt net by its pole. If such a joint survey is carried out in an area where the slopes are sufficiently irregular that exposures with a great variety of orientations are available for examination, the resulting joint-orientation diagram is likely to be a reasonably representative sample of the joints in the area. However, if the investigator must rely on observations made on nearly two-dimensional exposures, the orientation data are unlikely to provide even approximately correct information concerning the abundance of the joints of all sets present at the locality. Figure 18.20a illustrates the effect of the angle  $\alpha$  between exposure plane and members of a joint set. If the average spacing between joints is  $d$ , then from Fig. 18.20b the number of joints  $N_\alpha$  with a particular orientation encountered along a sampling line of length  $L$  will be

$$N_\alpha = \frac{L}{d} \sin \alpha. \tag{18.18}$$

As this equation shows, the number of joint planes  $N_\alpha$  is proportional to (1)  $L/d$ , and (2)  $\sin \alpha$ . An idealized plot of the poles of joints of all possible orientations may be constructed. In such a diagram, the successive contours, starting at the circumference, are the loci of poles of joints which intersect the horizontal surface such that  $\sin \alpha = 0.1, 0.3, 0.5, 0.7, 0.9$  respectively.

Then the relative densities of poles in the zones bounded by these *isogonic* (equal-angle) lines are also shown. As can be seen in Fig. 18.21a, joints with poles near the isogonic line for  $\sin \alpha = 1.0$  (the primitive) will be about 10 times as abundant as poles near the isogonic line  $\sin \alpha = 0.1$ .

The results of a survey from a vertical drill hole exhibit a similar but even more serious deficiency. In this case  $L/d$  is proportional to  $\cos \alpha$  and there is a disproportionately large number of near-vertical poles and very few near the primitive (Fig. 18.21b).

If both surveys were made in the same body of rock, it would be easy to conclude that a joint system developed at depth was quite different than the one observed at the surface, when in fact the differences are due entirely to limitations of the samples.

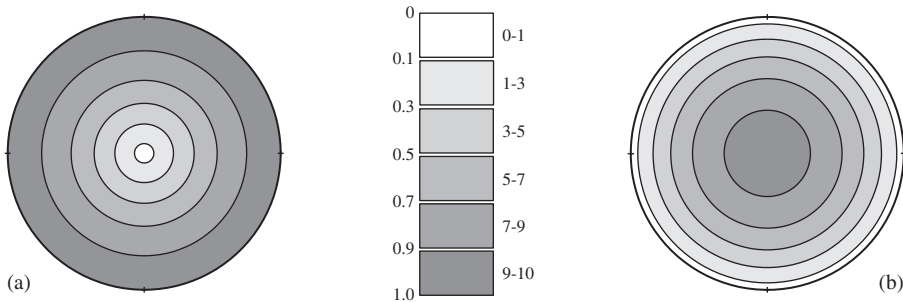


**Figure 18.21** Idealized contoured diagram of the poles of random joints (after Terzaghi, 1965, p. 296): (a) as measured on a horizontal surface; (b) as measured in the core of a vertical drill hole.

The accuracy of such a diagram can be improved by replacing the number of joints  $N_\alpha$  intersected at an angle  $\alpha$ , by a value  $N_{90}$  representing the number of joints with the same orientation which would have been observed on an outcrop surface with the same dimensions intersecting the joints at an angle of  $90^\circ$ , where

$$N_{90} = \frac{N}{\sin \alpha}. \quad (18.19)$$

However, no adequate correction can be made for low values of  $\alpha$  because in real rock the number of intersections is significantly affected by local variations in spacing and continuity if  $\alpha$  is small. Further, no correction whatsoever can be applied if  $\alpha = 0$ . Hence even a corrected diagram fails to indicate the abundance of joints subparallel to the plane of the exposure.

In this illustration, the outcrop surface was assumed to be horizontal, but it should be clear that there will be a *blind spot* in the vicinity of the pole to the exposure plane whatever its attitude. For similar reasons, the results of the survey of joints in a drill core will not adequately sample the joints; the problem is more severe because there is a *blind zone* for joints which are parallel to the drill hole. In both cases, an adequate sample of such planes requires that joints on other exposure planes or in other drill hole directions, and the data so obtained, appropriately weighted, are then combined into a collective diagram (Terzaghi, 1965, p. 298f).

As always, measurement errors will be present in any data set. Yow (1987) has treated the role of such errors in determining the size of the blind zone.

For these same geometrical reasons the measurement of the orientations of planes made on a thin section with a universal stage are subject to bias, called the *Schnitteffekt* (Turner & Weiss 1963, p. 226f).

### 18.13 Engineering applications

As indicated in the previous section, the methods of structural analysis also have wide application to many practical problems in engineering geology where the usual goal is the characterization of the distribution of discontinuities in a rock mass. Lisle and Leyshon (2004, p. 86–93) have a good introduction and Hoek and Bray (1981) give a comprehensive treatment.

Rock slopes may fail in several ways. A simple, but typical problem involves a rock mass containing an inclined planar discontinuity exposed in a road cut (Fig. 18.22a). The question is, will the slope fail by slip on this plane or not? Slip will occur on Plane 1 if it dips more steeply than the angle of friction  $\phi$ .

Alternatively, if a stereographic plot of the pole of the fracture plane lies within a vertical cone with angular radius equal to the angle of sliding friction  $\phi$  it will not slip, and if it lies outside this cone it will (Fig. 18.22b).

Whisonant and Watts (1989) suggested that a point vector plot may be an aid to visualizing the potential sliding condition.

There is an additional factor which must be taken into account. The rock mass bounded by Plane 1 is free to move out of the roadcut – it is said to *daylight*. In contrast, Plane 2 does not daylight because its motion is blocked.

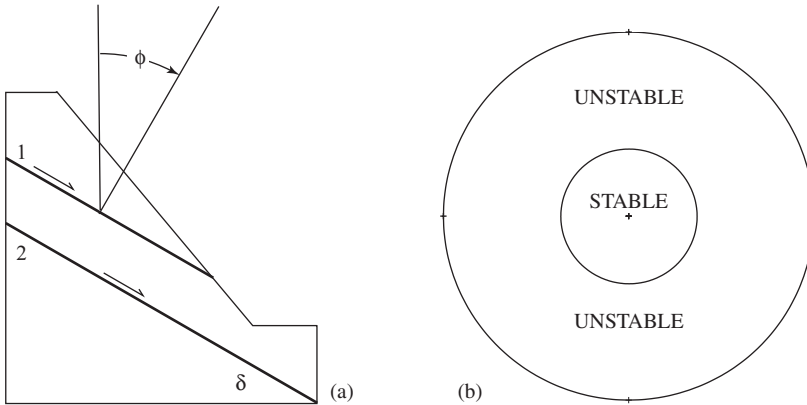


**Figure 18.22** Slope failure: (a) road cut and fracture planes; (b) stereographic plot of the pole of fracture plane.

**18.14 Exercises**

1. The data in Tables 18.2 and 18.3 represent the same fold. construct a beta diagram and an *S*-pole diagram. In both, estimate the attitude of the fold axis.

Table 18.2 *Plunge and trend of dip vectors*

No.	p/t	No.	p/t	No.	p/t	No.	p/t	No.	p/t
1	80/045	3	70/202	5	50/172	7	60/195	9	60/187
2	44/188	4	60/065	6	55/087	8	41/117	10	44/105

Table 18.3 *Plunge and trend of pole vectors*

No.	p/t	No.	p/t	No.	p/t	No.	p/t	No.	p/t
1	10/225	3	20/022	5	40/352	7	30/015	9	30/007
2	46/008	4	40/245	6	35/267	8	49/297	10	44/285

2. Determine the attitude of the fold axis of the folds shown in Fig. 18.23.

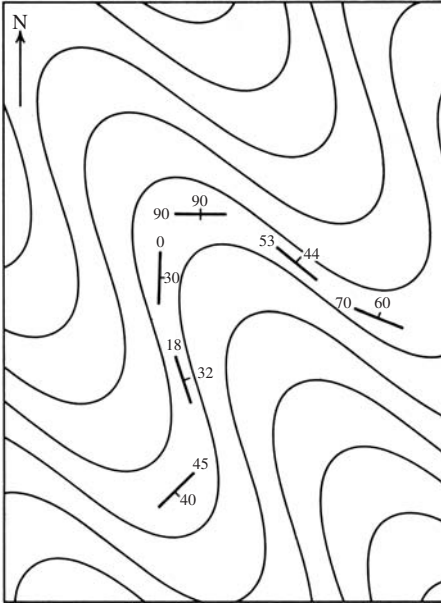


**Figure 18.23** Map of plunging folds.

3. Using the data from Table 18.4 (see also the map in Fig. 18.24) produces a contoured point diagram of pole vectors. Then determine:
  - (a) Trend and plunge of the fold axes.
  - (b) Attitude of the axial plane.
  - (c) Approximate interlimb angle.
  - (d) Sketch the style of the folding.

Table 18.4 *Plunge and trend of pole vectors*

No.	p/t	No.	p/t	No.	p/t	No.	p/t	No.	p/t
1	58/093	11	43/229	21	10/246	31	41/264	41	53/078
2	49/108	12	51/227	22	32/233	32	26/073	42	23/080
3	60/125	13	61/235	23	22/260	33	36/085	43	30/051
4	65/158	14	28/228	24	49/219	34	16/068	44	42/067
5	60/115	15	41/220	25	46/237	35	15/076	45	36/075
6	48/091	16	58/210	26	32/233	36	34/064	46	32/086
7	59/195	17	15/246	27	40/225	37	57/079	47	24/067
8	16/245	18	06/246	28	47/253	38	43/052	48	15/062
9	68/192	19	35/242	29	47/226	39	46/078	49	36/071
10	41/233	20	60/230	30	04/241	40	33/074	50	40/104

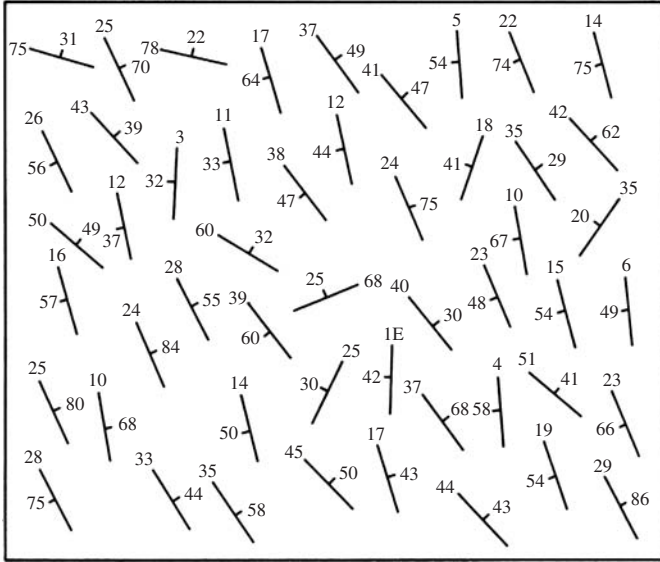


**Figure 18.24** Geological map of a series of folds.



# 19

## Tectonites

### 19.1 Introduction

The term *fabric* includes the complete spatial and geometrical configuration of all the components that make up a rock. It is an all-encompassing term that describes the shapes and characters of individual parts of a rock mass and the manner in which these parts are distributed and oriented in space (Hobbs, *et al.*, 1976, p. 73). These components and their boundaries are *elements* of the fabric. A description of the manner in which these elements and the boundaries between them are arranged in space constitutes a statement of the fabric of the body.

### 19.2 Isotropy and homogeneity

A rock with randomly oriented fabric elements will have the same physical and geometrical properties in all directions, and is therefore *isotropic*. Such rocks are rare in nature. Usually the best that can be said is that a rock mass is approximately isotropic on some specified scale.

If any two identically oriented, equal-volume samples taken from a rock mass are identical in every respect, the mass from which they came is said to be *homogeneous*. At best, some rock masses are only quasi-homogeneous, that is, the proportions of the various mineral components and their distribution are only approximately uniform. Samples from such a mass that are large compared with the grain size will then be statistically indistinguishable, and the mass is said to be *statistically homogeneous*. A region of a rock body which is homogeneous with respect to the orientation or pattern of orientation for a given fabric element is termed a fabric *domain*. In attempting to describe a particular fabric, it is important to insure that the sample is from such a domain.

### 19.3 Preferred orientation

Almost all rocks, including sedimentary, igneous and metamorphic, show some degree of preferred orientation and therefore are *anisotropic*. Such rocks are of considerable interest for the processes of formation and deformation are often recorded by these anisotropic fabrics. Such rocks are termed *tectonites*. These fabrics may be *planar* or *linear*, and they are marked by a preferred orientation of shape or lattice. Some studies include papers by Bjørnerud and Boyer (1996), Bons and Jessell (1996), Lapierre, *et al.* (1996), and Park (1996).

### 19.4 Planar and linear fabrics

At the outcrop or in a hand specimen, planar or linear structures which make up the fabric are visible as traces on the exposure faces. If the structure is simple and well developed, there may be no problem in determining its nature and attitude. However, when the traces are faint, or several different traces are present on the same exposure faces, it may be difficult to tell whether a planar or linear structure is present merely by inspecting several two-dimensional faces. The attitudes of the exposure plane and the traces of fabric on them can be fitted into a three-dimensional picture with the aid of the stereonet.<sup>1</sup>

#### Classification

---

##### 1. Planar structures

- (a) Planar parallelism of planar fabric elements (Fig. 19.1a).
- (b) Planar parallelism of linear fabric elements (Fig. 19.1b).

##### 2. Linear structures

- (a) Linear parallelism of linear fabric elements (Fig. 19.1c).
- (b) Linear parallelism of planar fabric elements (Fig. 19.1d).

##### 3. Composite structures

- (a) Combined structures: two or more planar or linear structures in combination, or both.
  - (b) Complex structures: two fabrics marked by either linear or planar fabric elements only.
    - i Linear + planar fabrics marked by linear elements.
    - ii Linear + planar fabrics marked by planar elements.
- 

<sup>1</sup>Usually only 5–10 measurements are required so that either the Wulff or Schmidt net can be used. We will illustrate both.

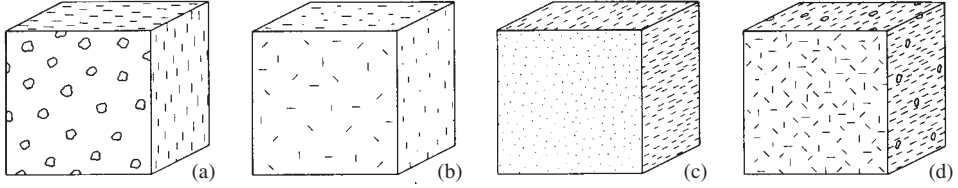


**Figure 19.1** Planar and linear fabrics: (a) planar structure marked by planar elements; (b) planar structure marked by linear elements; (c) linear structure marked by linear elements; (d) linear structure marked by planar elements (from Oertel, 1962).

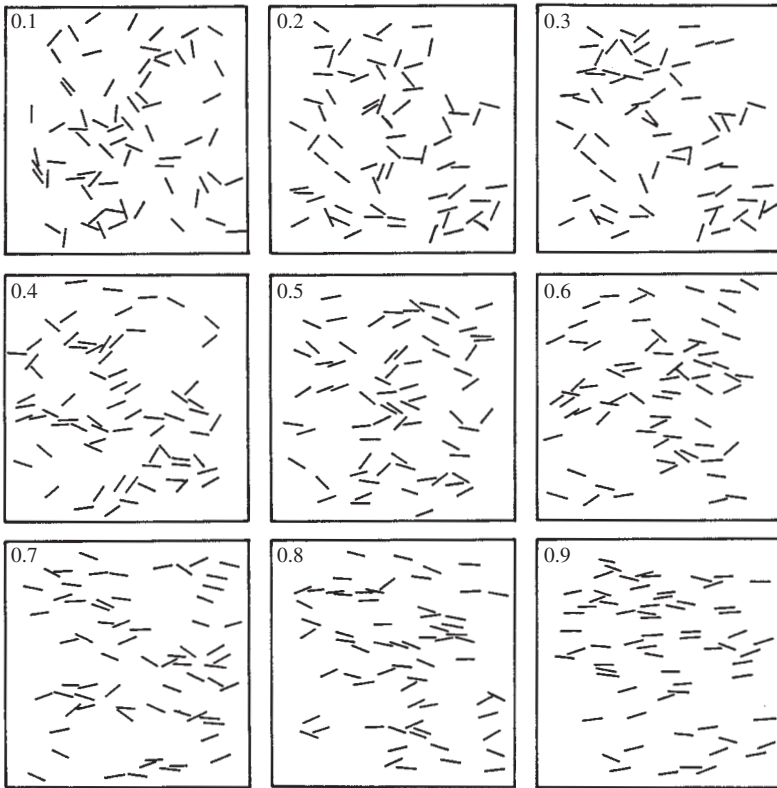


**Figure 19.2** Strength of preferred orientation on a plane (from MacCaskie, 1986, with permission of the *Journal of Geology*).

The description of these fabrics entails the attitude of the planar or linear structure, and the remainder of this chapter is devoted to methods for determining this attitude, but it is also useful to give some information on the overall strength of the alignment of the fabric elements. Commonly terms such as “weak” or “strong” are used, but a more accurate evaluation may be useful. The plots shown in Fig. 19.2 were generated using pseudo-random numbers for mean resultant vectors with a range of  $\bar{R} = 0.1\text{--}0.9$  (see §7.4). These plots can be used to visually estimate the strength of the fabric in the field.

### Planar structures

If a planar structure is present, then each trace may be thought of as an apparent dip of that plane and the method used to find the true dip from two apparent dips may be used. However, more than two points are required to demonstrate that the structure is, in fact, a plane, and the more points that are used the more certain is its existence. If only two points are available, a plane that satisfies the measurements can be found, and this then used to check the results on an exposure face (natural or artificial) perpendicular to the plane.

### Problem

- The attitude data of Table 19.1 represent the measurements taken from five different outcrop faces or from an oriented specimen on which five non-parallel faces have been cut. Determine the attitude of the planar structure.

Table 19.1 *Data for analysis of planar structure*

Face	Strike & dip	Pitch of trace
1	N 40 E, 20 SE	67 S
2	N 46 W, 32 NW	5 N
3	N 68 E, 42 S	75 W
4	N 20 W, 62 W	60 S
5	N 20 E, 46 W	79 N

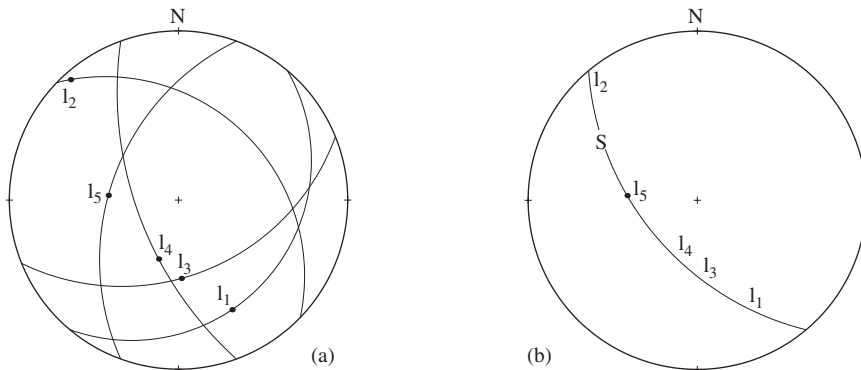


Figure 19.3 Attitude of a planar fabric: (a) data plot; (b) analysis.

### Construction

1. Using the pitch angle plot represent each measured trace as the points  $l_i$  ( $i = 1-5$ ) (Fig. 19.3a). The great circle representing the exposure plane is, of course, used to plot these points but it need not actually be included on the diagram.

- The five points representing these trace points lie on the same great circle  $S$  (Fig. 19.3b). This great circle represents the structural plane defined by the fabric measurements.

### Answer

- The dip and strike of the structural plane  $S$  are N 50 W, 55 SW.

### Linear structures

If the structure is linear, traces will be present on all faces except the one perpendicular to the line (see Figs. 19.1c,d). As shown in Fig. 19.4, a rod-shaped fabric element cut by an oblique exposure plane  $P$  will expose an ellipse. The long axis of this ellipse is an apparent lineation of the true linear structure, that is, the trace marked by the long axis in an orthographic projection of the linear structure onto an exposure face (Lowe, 1946). The true direction of the line lies in the plane  $N$  which is normal to the exposure plane and also contains the trace. Normal planes can be constructed from measurements on exposure faces. The intersection of any two will ideally fix the attitude of the line. In practice more points are needed to confirm the nature of the structure and to increase confidence in the result.

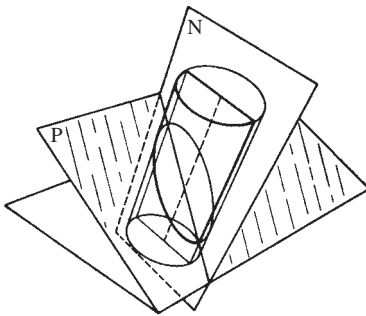


**Figure 19.4** Intersection of exposure plane  $P$  and plane  $N$  normal to  $P$  and containing the fabric trace is parallel to the long axis of the rod-shaped element (Lowe, 1946).

### Problem

- The attitude data of Table 19.2 represent the measurements taken from five different outcrop faces or from an oriented specimen on which five non-parallel faces had been cut. Determine the attitude of the linear structure.

### Construction I

- Plot as a pair of points each fabric trace  $l_i$  and the pole of the corresponding exposure plane  $P_i$  (Fig. 19.5a).
- Add the great circle passing through each pair of these points (Fig. 19.5b).
- These arcs intersect at a point which represents the linear structure  $L$ .

Table 19.2 Data for analysis of linear structure

Face	Strike & dip	Pitch of trace
1	N 12 W, 70 E	19 N
2	N 35 E, 60 W	68 SW
3	N 30 W, 65 W	47 N
4	N 70 E, 80 S	25 SW
5	N 46 W, 18 SW	36 NW

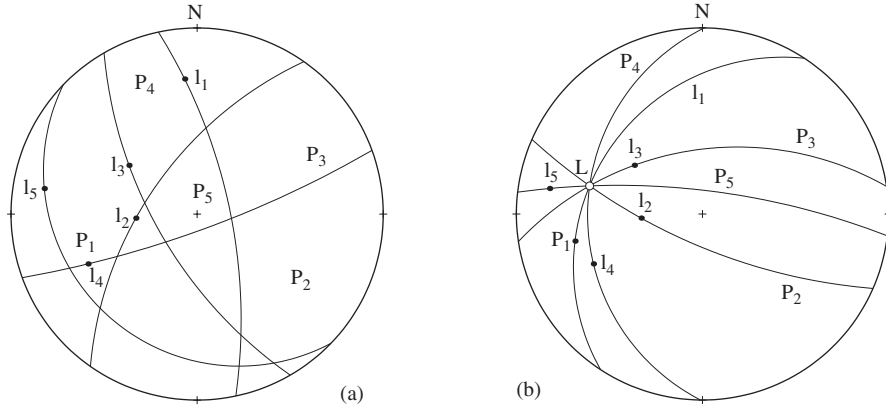


Figure 19.5 Linear structure (method of Lowe, 1946): (a) data plot; (b) analysis.

**Answer**

- The attitude of the linear structure is  $L(26/284)$ .

This method of locating the line of intersection of the  $N$  planes is similar to that used in the  $\beta$  diagram, and has the same disadvantage (see §18.2). As we have seen in §5.9, when planes intersect at small angles, the location of the intersection point is strongly influenced by small variations in the measured angles. In contrast to the idealized data of this example problem, it may be difficult to accurately determine the orientation of the line.

An alternative approach avoids this problem and has the additional advantage of being amenable to numerical treatment.

**Construction II**

1. As before (Steps 1 and 2), plot the pairs of trace points  $l_i$  and the poles of the exposure planes (in Fig. 19.6a these poles are not labeled).
2. Draw the great circle which passes through each pair of points and plot its pole  $P_i$  (note that these constructed poles are *not* the measured poles of the exposure planes).
3. The second set of pole points define a great circle whose pole represents the linear structure (Fig. 19.6b).

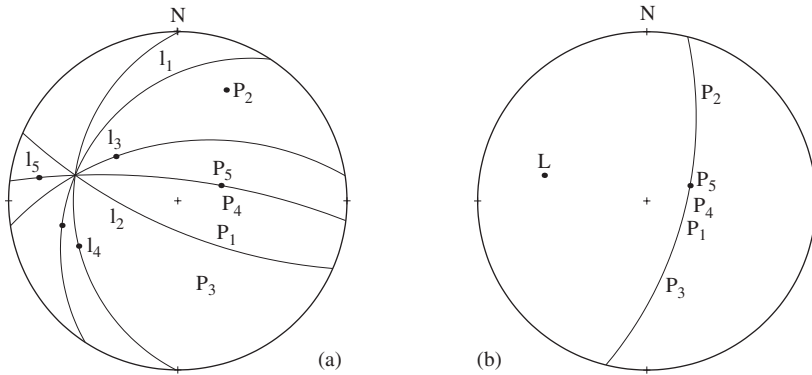


**Figure 19.6** Linear structure (method of Cruden, 1971): (a) data: (b) analysis.

**Table 19.3** *Data from a macro-porphyrritic basalt*

Face	Strike & dip	Pitch of trace
1	horizontal	trend = 106
2	N 12 W, 82 E	45 N
3	N 45 E, 90	44 SW
4	N 23 W, 80 W	46 N
5	N 53 E, 85 SE	50 SW
6	N 46 W, 18 SW	36 NW

Clark & McIntyre, 1951a

**Answer**

- The attitude of this pole *L* is identical to the intersection found by the previous method.

**Problem**

- In these two previous examples, the data were contrived to define exactly a plane and a line. In real life such data will always show a dispersion of points due to imperfectly developed fabric and measurement errors. Table 19.3 contains the data for measurements made of the linear fabric in a basalt.

**Results**

1. The plot using Lowe’s (1946) method of Fig. 19.7a shows a considerable spread of intersections. Locating the mean point *L* presents a problem.
2. In contrast, the plot using Cruden’s (1971) method illustrates the ease in fitting the best-fit great circle and therefore the pole point *L*.

Where two or more fabric traces are present on the exposure faces, these techniques for identifying planar and linear structures and determining their attitude may be combined.

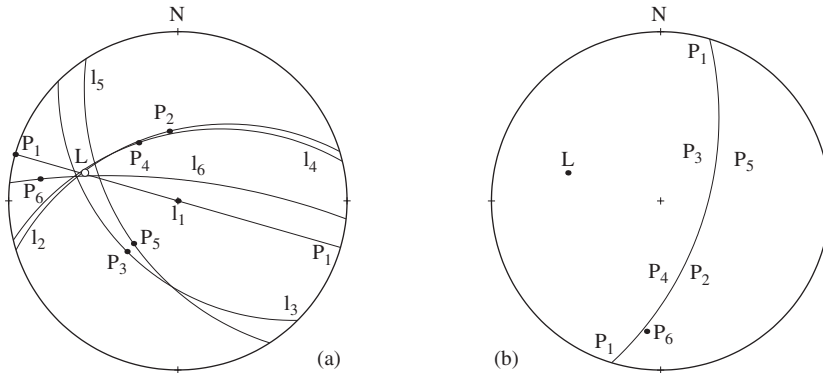


**Figure 19.7** Linear structure (Clark & McIntyre, 1951a): (a) Lowe's plot; (b) Cruden's plot.

### 19.5 Complex structures

In some rocks, fabric elements of just one shape may be arranged to give more than one structure, even though there is only a single trace on an exposure face (Den Tex, 1954). A simple experiment may help to see how this is possible: A parallel alignment of pencils on a table top is analogous to linear structure marked by linear elements (Fig. 19.1b) and a collection of pencils scattered randomly on a table top is analogous to the case of a planar structure marked by linear elements (Fig. 19.1c). If the dispersion of the pencils is now restricted so only orientations within some angle of azimuth, say  $30^\circ$ , are represented, the result is a configuration intermediate between the two end member classes. It possesses both a dominant linear fabric (the still strong alignment) and a subordinate planar fabric (the tendency to spread in a plane). A similar pattern involving planar elements can be generated which is intermediate between Figs. 19.1a and 19.1d.

The geometrical analysis of such fabrics depends on the fact that in a given series of random exposure planes, certain faces will be more favorably oriented for observing the traces of the internal structure than others. Specifically, those exposure planes parallel to a linear structure, and those perpendicular to a planar structure will exhibit the best developed traces. Conversely, those planes perpendicular to the linear structure and those parallel to the planar structure will show no traces at all.

#### *Principal linear, subordinate planar structure*

Such complex structures occur when, for example, linear elements are statistically arranged with linear parallelism, but with a deviation into a plane. The deviation that produces this subordinate structure means that the principal structure can not be as well developed.

Figure 19.8a shows the equal-area plot of the poles  $P$  of exposure planes which contained individual traces  $l$ . Exposure faces oriented so that no trace is visible on them must also be examined, but they are not plotted. For optimum results, the measured



planes should be well distributed in space for this type of analysis to yield a reasonable estimate of the structure.

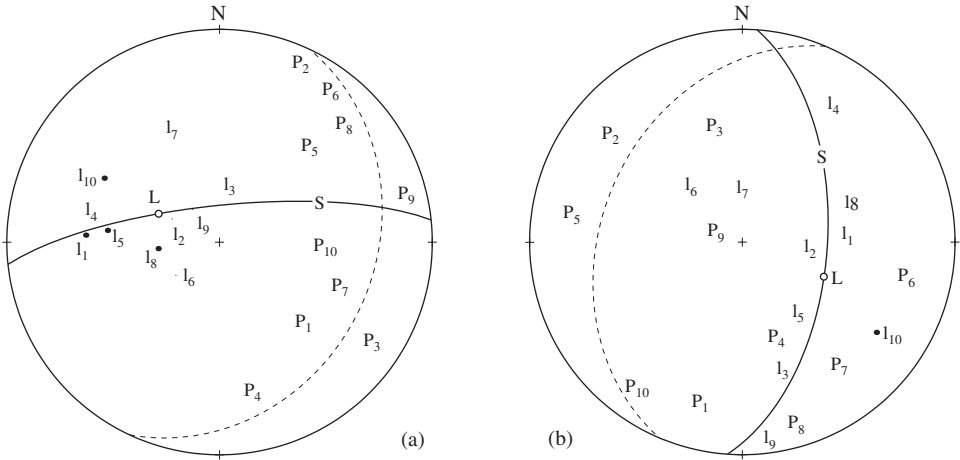


**Figure 19.8** Complex structures (data taken from Figs. 5 and 6 of Den Tex, 1954): (a) principal linear with subordinate planar structure; (b) principal planar with subordinate linear structure.

**Analysis**

1. The  $l_i$  points cluster about a center  $L$  that represents the principal linear structure.
2. The trace points are also spread out along another great circle, which contains six of the ten individual  $l$  points, as well as the center  $L$ . This is the subordinate planar structure.
3. Note the tendency for the poles of the trace-containing exposure planes to be distributed along the great circle  $90^\circ$  from the linear structure  $L$ .

Construction of the linear structure using intersection great circles drawn through the respective poles and traces would have approximated the position of  $L$ , but it could not have detected the spreading that marks the subordinate planar structure.

*Principal planar, subordinate linear structure*

A similarly complex structure may result from planar elements oriented in such a manner as to mark a planar structure, but with deviations that are controlled by a tendency to remain parallel to a line within the plane. Figure 19.6b shows the plot of such a case.

**Analysis**

1. The majority (7 of 10) trace points exhibit a tendency to lie close to a great circle  $S$ .
2. Within  $S$ , there is a tendency for the trace points to cluster around a center  $L$ . The four remaining poles are located approximately  $90^\circ$  from  $L$ . The point  $L$  is, therefore, a subordinate linear structure lying within the principal plane.

3. There is a similar, though less pronounced tendency for the poles  $P$  also to lie along this same great circle. Six of ten poles are less than  $45^\circ$  from  $S$  and are roughly symmetrical with respect to it. The  $S$  plane is therefore the principal planar structure.

### 19.6 $LS$ tectonites

The complex fabrics of the last section are members of a continuous spectrum of fabrics which range from perfectly linear, or  $L$  tectonites, to perfectly planar, or  $S$  tectonites. These are the end members of a general class of  $LS$  tectonites. Intermediate members have intermediate relative strengths of the linear and planar components. A useful way of characterizing fabrics of this spectrum is to note that they generally have three mutually perpendicular planes of symmetry, the plane of  $S$  is one of these and the other two are parallel and perpendicular to  $L$ .

For field identification, it is useful to divide these fabrics into discrete intervals (Flinn, 1965; Schwerdtner, *et al.*, 1977) giving five types:

$$L, \quad L > S, \quad L \approx S, \quad L < S, \quad S \text{ tectonites.}$$

An additional importance of this approach is that it may be possible to correlate the fabric geometry with the shape of the strain ellipsoid.

Other types of fabrics, such as the combined structures, will generally have lower symmetries, either monoclinic or triclinic. These can not be included in the  $LS$  scheme, and their fabric components have to be described separately.

### 19.7 Exercises

- For the following sets of measurements, analyze the data for the structure involved.

Question 1:

Exposure plane	Pitch of trace
N 80 W, 30 N	20 W
N 50 E, 80 N	30 W
Horizontal	N 46 W
N 5 E, 10 S	40 S
N 72 E, 20 S	80 W

Question 2:

Exposure plane	Pitch of trace
N 15 W, 70 E	80 N
N 52 E, 50 SE	40 NE
N 0, 45 E	74 N
N 86 E, 60 S	30 E
N 43 E, 50 W	25 NE
N 52 E, 35 N	14 NE

Question 3:	Exposure plane	Pitch of trace 1	Pitch of trace 2
	N 30 E, 30 W	15 N	85 N
	N 45 W, 20 SW	30 SE	70 SE
	N 20 W, 60 E	52 N	5 S
	N 25 E, 40 E	36 S	28 N
	N 80 W, 70 E	70 E	40 W
	N 50 E, 55 SW	50 SW	15 NE

Question 4:	Exposure plane	Pitch of trace 1	Pitch of trace 2
	N 70 W, 30 S	28 E	80 W
	N 60 W, 10 E	35 E	90
	N 90 W, 20 N	55 E	73 E
	N 20 W, 40 E	26 N	none
	N 15 W, 45 W	45 S	30 N
	N 55 E, 57 SW	85 S	15 N
	N 50 E, 90	20 SW	60 NE
	N 40 W, 30 NE	60 N	35 N

Question 5:	Exposure plane	Pitch of trace
	N 50 W, 50 NE	55 NW
	N 90 W, 30 N	90
	N 20 W, 30 N	27 N
	N 10 W, 70 E	40 N
	N 48 E, 26 NE	46 NE
	N 20 W, 70 E	68 N
	N 32 E, 52 W	38 N
	N 4 E, 70 W	10 N
	N 85 W, 45 N	90
	N 85 E, 65 S	none
	N 20 E, 75 W	60 N
	N 45 W, 20 NE	46 NW
	N 90 W, 52 S	none

# 20

## Drill hole data

### 20.1 Introduction

Exploration of the underground by drilling and the recovery of core samples is an important technique for the geologist, especially in mining, engineering and petroleum projects. Several authors have tackled the geometrical problems which arise (Fisher, 1941; Stein, 1941; Mertie, 1943). In applied projects the identification of fractures is particularly important (Lau, 1983; Kulander, *et al.*, 1990; Sikorsky, 1991). A good overview of many practical aspects of drilling, coring and analysis is provided by Goodman (1976, p. 127–157), and we follow his basic approach.

The information gained from a drilling program depends on the number of holes drilled, the orientation of the holes, the core recovery and the structures seen in the cores. Because drilling is expensive, it is important to extract the maximum information from as few holes as possible.

Inclined holes tend to wander during drilling, especially if long and, at least in part, this is due to rock anisotropy (Brown, *et al.*, 1981). If accurate measurements are needed, down-the-hole survey instruments are lowered along the borehole to measure its plunge and trend at known distances. From this information, the curved path of the hole can then be calculated (Howson & Sides, 1986). Special still or television cameras can also be used.

Our concern here is with the structural information that can be obtained from recovered cores and the basic case involves the attitude of a structural plane. The determination of the true attitude of such a plane is treated in detail. Some of the problems involved in the interpretation of the structure of folded rocks are then outlined.

First, we need a way of describing the orientation of a plane in the recovered core. A plane which is oblique to the drill hole axis intersects a circular core as an ellipse (Fig. 20.1). The major axis of this ellipse marks the local dip line of the plane. This line of dip  $D'$  is easily identified on the core as the low point on the elliptical trace.

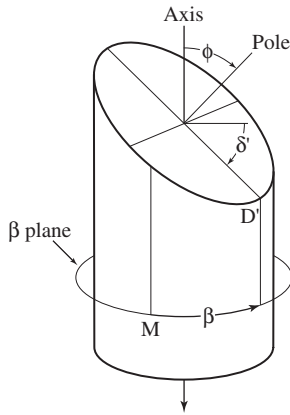


**Figure 20.1** Core with intersecting plane.

To describe the orientation of this plane in the core two angles are needed. Its inclination is given by the local dip angle  $\delta'$ . To specify the local dip direction a reference line is needed, and, as we will see, there are several ways of establishing this. Then the local trend of  $D'$  is measured in the plane normal to the core axis, called the  $\beta$  plane, and is given by the angle  $\beta$  measured from this reference mark  $M$  in a clockwise or anticlockwise sense as viewed in the direction of drilling.

### 20.2 Oriented cores

Special techniques are available which allow the *in situ* orientation of the core to be recovered (Zimmer, 1963; Goodman, 1976, p. 142f). Here we assume that the method of fixing this orientation takes the form of a mark made along the top edge of the inclined cylindrical core parallel to the axis of the hole. Other marking schemes can be converted to this one or the construction easily adapted to other conventions. Almost always exploration holes are drilled downward and all the examples treat this case. In the rare case of a hole drilled upward the various techniques can be easily adapted.

There are two states, each with its own set of geometrical features. One is the core and the plane it intersects and the other is the true attitude of the plane. These two are related by a simple rotation.

The first step is to measure the orientation of the plane in the core given by its inclination  $\delta'$  and its trend  $\beta$ . With these angles, finding the true attitude of the plane is essentially the problem of two tilts in reverse. In plotting the structural plane on the stereonet it is convenient to represent it by its pole and this requires the *core-pole angle*  $\phi = \delta'$ .

#### Problem

- Drill hole  $H(40/030)$  intersects a plane whose attitude is  $D(60/260)$ . What is the orientation of the plane in the recovered core?

### Construction

1. Plot drill hole  $H(60/040)$  and pole  $P(50/060)$  representing the pole of the plane (Fig. 20.2a). As a visualization aid  $D(60/260)$  and the corresponding great circle are useful.
2. Add the reference mark  $M$  on the primitive with the same trend as  $H$  (Fig. 20.2b).
3. About axis  $R(00/120)$  (perpendicular to  $M$ ) rotate  $H$  through angle  $\omega = 30^\circ$  to  $H'$  at the center of the net and  $P$  to  $P'$  along its small circle.
4. Plot  $D'$  representing the local dip line of the plane by counting  $90^\circ$  from  $P'$  and add its great circle representation. The plunge of  $D'$  is the local dip angle  $\delta'$ .

### Answer

- The orientation of the plane in the core is fixed by the local angles  $\delta' = 40^\circ$  and  $\beta = 120^\circ$ .

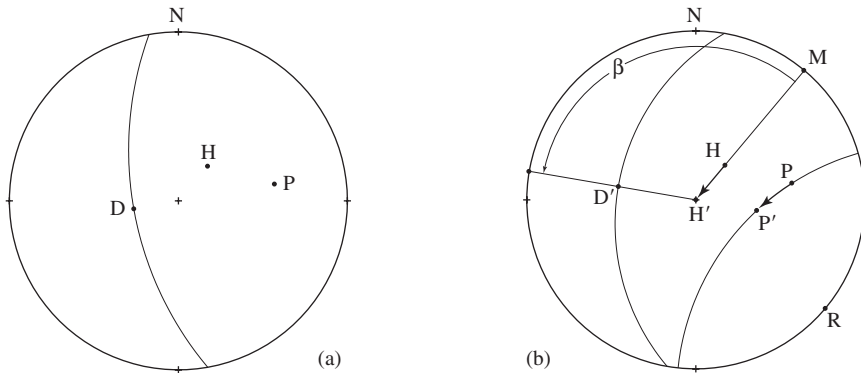


**Figure 20.2** Attitude of plane in oriented core.

The inverse of this type of problem and the more important one is to determine the true attitude of a plane from measurements made on an oriented core.

### Problem

- A drill hole  $H(40/030)$  yielded an oriented core with  $\delta' = 32^\circ$  and  $\beta = 68^\circ$ . What is the true attitude of the plane?

### Construction

1. Plot points  $H'$  at the center of the net representing the local orientation of the core and  $H(40/030)$  the true orientation of the drill hole (Fig. 20.3).
2. On the primitive mark points  $M$  with the same trend as  $H$  and the trend of  $D'$  at  $\beta = 68^\circ$  from  $M$ .
3. Locate  $D'$  using the local dip angle  $\delta' = 32^\circ$ . Plot pole  $P'$  by counting  $90^\circ$  from  $D'$ .
4. As  $H'$  rotates to  $H$ ,  $P'$  rotates to  $P$ , which is the true pole of the plane. The true dip  $D$  and the corresponding great circle can then be added to the diagram.

**Answer**

- The true pole is  $P(44/347)$  and true dip is  $D(46/167)$ . The corresponding strike and dip are N 77 E, 46 SE.

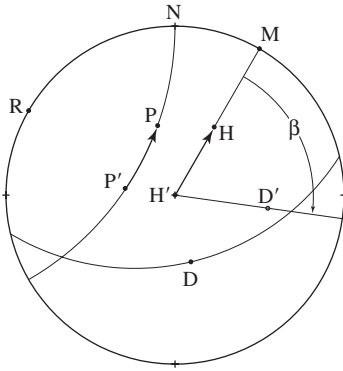


**Figure 20.3** True attitude from an oriented core.

**20.3 Cores without orientation**

Because it adds expense, marking devices are not commonly used during routine drilling. Then, because it is not possible to keep the core from rotating in the drill pipe during recovery, only a limited amount of information is available from a single hole:

1. The plunge and trend of the drill hole.
2. The distance along the hole where the core was taken.
3. The local dip angle of the intersected plane.

In the special case of a vertical hole, the local dip is also the true dip but the true strike is unknown. In this case, we can visualize all the possible orientations by rotating the core at its location at depth through  $360^\circ$ . During this rotation, the structural plane in the core will be everywhere tangent to a right-circular cone. The intersection of this cone with the earth's surface will be a circle. There are two special cases. If the structural plane is vertical, the cone degenerates to a line and if it is horizontal it is a plane. Only in this latter case is the attitude uniquely defined by a single drill hole.

If the drill hole is inclined, the dip angle in the core  $\delta'$  no longer represents the true dip. Again, the true attitude will be tangent to a cone generated by rotating the core about its axis. Depending on the inclination of the drill hole and the attitude of the plane this cone will intersect the earth's surface as an ellipse, parabola or hyperbola.

In such situations, the construction of the appropriate conic section at the earth's surface would permit all possible attitudes to be delimited. This requires drawing the appropriate conic sections accurately and this is not a practical approach.

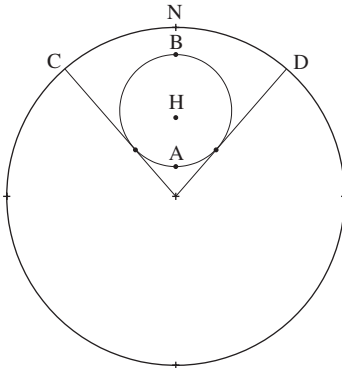


**Figure 20.4** Single rotated core and the locus of all possible poles.

### Problem

- In a core recovered from a hole  $H(40/000)$  a plane has a core–pole angle  $\phi = 30^\circ$ . What can be said of the true attitude of this plane?

### Construction

1. Plot point  $H(40/000)$  representing the inclined drill hole (Fig. 20.4).
2. The pole of the structural plane lies at a constant angular distance from  $H$ , that is, on a small circle with angular radius corresponding to the core–pole angle  $\phi = 30^\circ$ .
3. Locate points  $A(70/000)$  and  $B(10/000)$ . Draw the small circle with radius  $\phi$  about  $H$  (see §6.9).

### Answer

- The two vertical planes tangent to the small circle identify the extreme trends of the poles and their trends  $C$  and  $D$  are  $N\ 41\ W$  and  $N\ 41\ E$ . Points  $A$  and  $B$ , with the maximum and minimum inclinations, give the range of plunges from  $10^\circ$  to  $70^\circ$ .

Without further information, there is no basis of locating the particular point on the small circle which represents the true pole, thus within these limits the true attitude remains unknown. The smaller the small circle, the more limited the range of attitude. If  $\phi = 0$  the circle degenerates to a point and the attitude of the plane is uniquely determined.

Additional information can be obtained from several sources. One possibility is that the true attitude of the plane may be partially known, e.g., the true strike may be known from surface observations.

### Problem

- A drill hole  $H(50/160)$  intersects a bedding plane and its core–pole angle  $\phi = 25^\circ$ . The true strike is known to be  $N\ 40\ E$ . What are the dip possibilities?



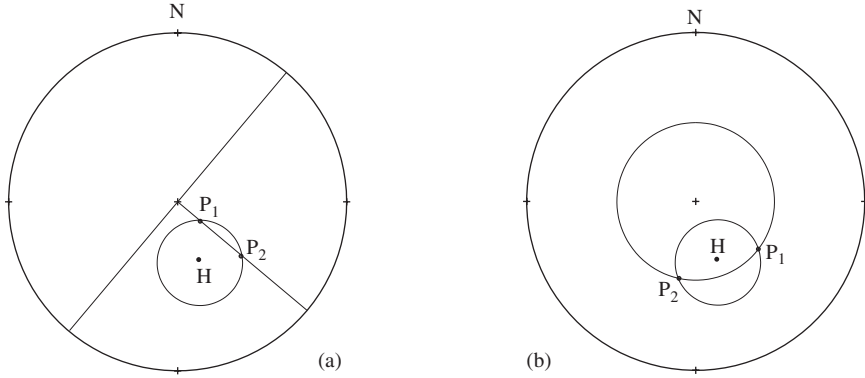


**Figure 20.5** Single hole and partial attitude: (a) strike known; (b) dip known.

**Construction**

1. Plot point  $H(50/160)$  representing the hole and draw a small circle with angular radius  $\phi = 25^\circ$  (Fig. 20.5a).
2. A radius of the net perpendicular to the known strike direction intersects the small circle at  $P_1$  and  $P_2$  and these represent the two possible poles to the bedding.

**Answer**

- Poles  $P_1(70/130)$  and  $P_2(38/130)$  correspond to dip angles of  $30^\circ$  and  $52^\circ$ .

A similar construction based on the known dip angle also yields the possible poles to the planes and the corresponding strike directions can then be determined.

**Problem**

- Drill hole  $H(50/160)$  intersects bedding with core–pole angle  $\phi = 25^\circ$ . The true dip is  $\delta = 50^\circ$ . What are the strike possibilities?

**Construction**

1. Plot point  $H(50/160)$  representing the hole and draw a small circle with angular radius  $\phi = 25^\circ$  (Fig. 20.5b).
2. Points  $P_1$  and  $P_2$  on this small circle with plunge angles equal to the complement of the known dip angle are the possible poles to bedding.

**Answer**

- The strike directions corresponding to  $P_1(40/128)$  and  $P_2(40/194)$  are N 38 E and N 76 W.

## 20.4 Cores with a known plane

Another piece of information can be used if two planes are present in the core and the attitude of one of them is known. The *in situ* orientation of the core can then be fixed and the attitude of the unknown plane determined. As in the case of the oriented core, use is made of the local reference frame to describe the observed relationship between the two planes in the core (Goodman, 1976, p. 143f). An arbitrary line can be used but a simpler approach is to identify the dip direction of the known plane as  $M$ .

### Problem

- Drill hole  $H(70/000)$  intersects both a bed and a fracture. The attitude of the bed is  $D(40/130)$ . Measurements of the plane of the fracture in the core yield  $\phi = 40^\circ$  and  $\beta = 122^\circ$  measured clockwise from  $M$ . What is the true attitude of the fracture?

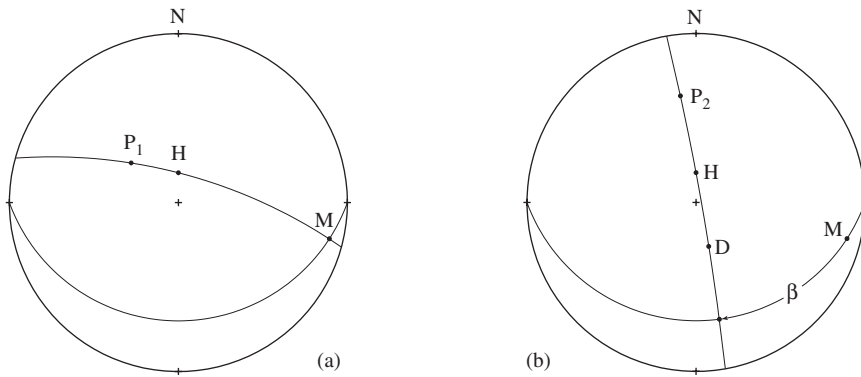


**Figure 20.6** Drill core with known plane.

### Construction

1. Plot the drill hole  $H(70/000)$  and the pole  $P_1(50/310)$  of known bedding (Fig. 20.6a). (Angle  $\phi_1$  between  $H$  and  $P_1$  is not needed.)
2. Draw the great circle whose pole is  $H$  representing the  $\beta$  plane and the great circle through points  $P_1$  and  $H$ . The intersection of these two is the reference mark  $M$  (Fig. 20.6b).
3. From  $M$  count off  $\beta = 65^\circ$  to locate the trend of the true dip line  $D$ .
4. Locate the pole  $P_2$   $\phi = 40^\circ$  from  $H$  along this second great circle. Plot  $D$  of the fracture at  $90^\circ$  from  $P_2$ .

### Answer

- The attitude of the bedding is given by  $P_2(24/346)$  and  $D(66/166)$ . The corresponding strike and dip are N 76 E, 66 S.

### 20.5 Two drill holes

The solution of the problem of two differently oriented drill holes each intersecting a single identifiable plane is obtained by drawing the small circles representing the core–pole cones. The intersections of these circles are possible poles to bedding. There may be two or four solutions.

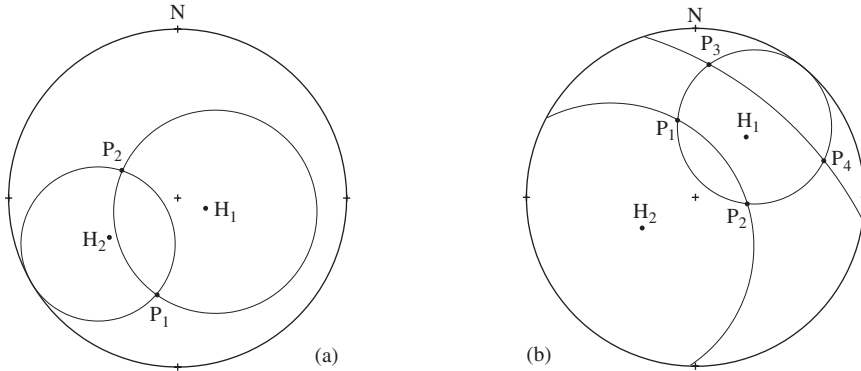


**Figure 20.7** Two drill holes: (a) two attitudes; (b) four attitudes.

#### Problem

- Recovered cores from two inclined drill holes yield the following data on the plunge and trend of each hole and the associated core–pole angle:  $H_1(70/110)$ ,  $\phi_1 = 60^\circ$  and  $H_2(40/240)$ ,  $\phi_2 = 40^\circ$ .

#### Construction

- Plot the points  $H_1(70/110)$  and its small circle with radius  $\phi_1 = 60^\circ$  and  $H_2(40/240)$  and its small circle with radius  $\phi_2 = 40^\circ$  (Fig. 20.7a).
- These two circles intersect at two points  $P_1$  and  $P_2$  which are the two possible poles.

#### Answer

- The attitudes of the poles are  $P_1(29/192)$  and  $P_2(50/296)$ . The corresponding strikes and dips of the planes are N 78 W, 61 S and N 26 E, 50 E.

If a small circle overlaps the primitive, that is, if it extends into the upper hemisphere, there may be additional intersections and it is therefore necessary to construct its opposite (see §6.9 for method).

#### Problem

- Inclined drill holes and their cores yield:  $H_1(40/040)$ ,  $\phi_1 = 40^\circ$  and  $H_2(50/240)$ ,  $\phi_2 = 70^\circ$ .

**Construction**

1. Plot  $H_1(40/040)$  and its small circle with radius  $\phi_1 = 40^\circ$  and  $H_2(50/240)$  and its small circle with radius  $\phi_2 = 70^\circ$  (Fig. 20.7b). The two intersections are  $P_1$  and  $P_2$ .
2. The  $H_2$  circle overlaps the primitive and its opposite supplies two additional intersections  $P_3$  and  $P_4$ .

**Answer**

- The four possible poles to bedding are  $P_1(40/347)$ ,  $P_2(56/097)$ ,  $P_3(7.5/014)$  and  $P_4(18/079)$ .

If the structure of the area is known, even minimally, it may be possible to reduce the several solutions to a single acceptable attitude.

If a recognizable marker horizon is present in both cores it is generally possible to determine the attitude of the structural plane uniquely. The presence of the marker at known distances along each of the holes permits the location of two points on the marker horizon to be found and from these an apparent dip.

**Problem**

- From a single site two holes were drilled.  $H_1(64/000)$  encountered a marker bed at a distance of 19.7 m and the core-pole angle  $\phi_1 = 52^\circ$ .  $H_2(33/270)$  encountered the same marker at a distance of 19.4 m and  $\phi_2 = 55^\circ$ . What is the attitude of the marker bed?

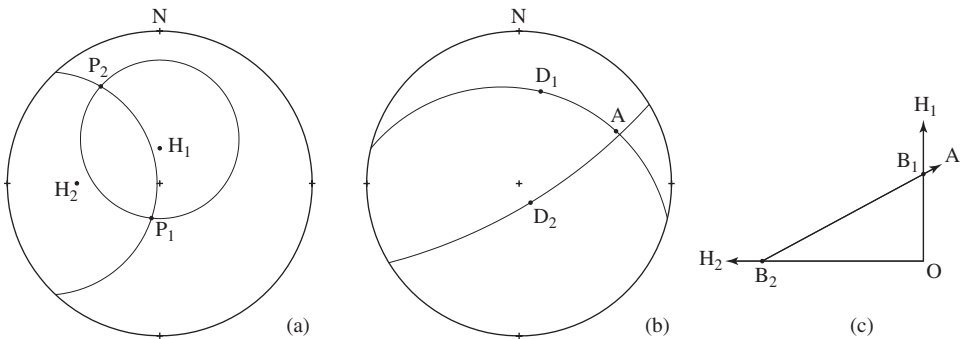


**Figure 20.8** Two holes with marker: (a) stereonet 1; (b) stereonet 2; (c) map.

**Stereographic construction**

1. Plot points  $H_1(64/000)$  and  $H_2(33/270)$ .
2. With  $\phi_1 = 52^\circ$  and  $\phi_2 = 55^\circ$  draw the small circles about each (Fig. 20.8a).
3. The intersections of these circles are possible poles  $P_1(64/193)$  and  $P_2(17/329)$ . The corresponding dips are  $D_1(26/013)$  and  $D_2(73/149)$  (Fig. 20.8b).

### Orthographic construction

1. From a common point  $O$ , plot the trends of the two drill holes in map view (Fig. 20.8c).
2. With the procedures of Chapter 2 locate the points  $X_1$  and  $X_2$  on the plane and their depths  $d_1$  and  $d_2$ .
3. Points  $B_1$  and  $B_2$  are the points along each drill hole  $X_1$  and  $X_2$ . Points  $B_1$  and  $B_2$  are the surface points directly above these two points at depth. Line  $l = B_1B_2$  is then the trend of an apparent dip on the plane. With the difference in the depths  $\Delta d = d_1 - d_2$  the apparent dip is then obtained from  $\tan \alpha = \Delta d/l$ .

### Answer

- The apparent dip is  $A(18/062)$  and this is compatible only with the plane represented by  $D_1$ . The true attitude of the plane is therefore N 77 W, 26 N.

## 20.6 Analytical solution

For the treatment of the data from a few drill holes the graphic approach is quite satisfactory. For the routine analysis of data from an extensive drilling program, an analytical solution is an attractive alternative. Here we derive the solution of the two drill hole problem. Charlesworth and Kilby (1981) give a related treatment.

For each pole common to two intersecting small circles, there are three unknown direction cosines. Correspondingly, three relationships involving these three unknown quantities are required for a mathematical solution. The first is the identity linking the three direction cosines ( $L$ ,  $M$ ,  $N$ ) of the unknown pole of bedding (see Eq. 7.5)

$$L^2 + M^2 + N^2 = 1. \quad (20.1)$$

The other two are obtained from the angle between the pole and the hole and this is given by the dot product of normalized pole and hole vectors  $\mathbf{P}$  and  $\mathbf{H}$  (see Eq. 7.12)

$$\begin{aligned} \cos \phi_1 &= l_1L + m_1M + n_1N, \\ \cos \phi_2 &= l_2L + m_2M + n_2N, \end{aligned}$$

where  $(l_1, m_1, n_1)$  and  $(l_2, m_2, n_2)$  give the orientation of each drill hole. Rearranging gives

$$\begin{aligned} l_1L + m_1M &= \cos \phi_1 - n_1N, \\ l_2L + m_2M &= \cos \phi_2 - n_2N. \end{aligned}$$

Using Cramer's rule, we can express  $L$  and  $M$  in terms of the determinants of these two equations. Thus

$$L = \frac{\begin{vmatrix} (\cos \phi_1 - n_1 N) & m_1 \\ (\cos \phi_2 - n_2 N) & m_2 \end{vmatrix}}{\begin{vmatrix} l_1 & m_1 \\ l_2 & m_2 \end{vmatrix}} = \frac{\begin{vmatrix} \cos \phi_1 & m_1 \\ \cos \phi_2 & m_2 \end{vmatrix} - N \begin{vmatrix} n_1 & m_1 \\ n_2 & m_2 \end{vmatrix}}{\begin{vmatrix} l_1 & m_1 \\ l_2 & m_2 \end{vmatrix}} \quad (20.2a)$$

and

$$M = \frac{\begin{vmatrix} l_1 & (\cos \phi_1 - n_1 N) \\ l_2 & (\cos \phi_2 - n_2 N) \end{vmatrix}}{\begin{vmatrix} l_1 & m_1 \\ l_2 & m_2 \end{vmatrix}} = \frac{\begin{vmatrix} l_1 & \cos \phi_1 \\ l_2 & \cos \phi_2 \end{vmatrix} - N \begin{vmatrix} l_1 & n_1 \\ l_2 & n_2 \end{vmatrix}}{\begin{vmatrix} l_1 & m_1 \\ l_2 & m_2 \end{vmatrix}}. \quad (20.2b)$$

There are five determinants, two in each numerator and one common to both denominators. They are

$$D_1 = m_2 \cos \phi_1 - m_1 \cos \phi_2,$$

$$D_2 = m_2 n_1 - m_1 n_2,$$

$$D_3 = l_1 \cos \phi_2 - l_2 \cos \phi_1,$$

$$D_4 = l_1 n_2 - l_2 n_1,$$

$$D_5 = l_1 m_2 - l_2 m_1.$$

Rewriting Eqs. 20.2a and 20.2b using these symbols and squaring gives

$$L^2 = \frac{(D_1 - N D_2)^2}{D_5^2} \quad \text{and} \quad M^2 = \frac{(D_3 - N D_4)^2}{D_5^2}.$$

Substituting these back into Eq. 20.1 and collecting terms gives

$$(D_2^2 + D_4^2 + D_5^2)N^2 - 2(D_1 D_2 + D_3 D_4)N + (D_1^2 + D_3^2 - D_5^2) = 0. \quad (20.3)$$

The roots of this quadratic are two values of  $N$ , one for each intersection. Using each of these in Eqs. 20.2, we then have two sets of direction cosines, one for each possible attitude of the pole. In the problem of Fig. 20.7a the results are:  $P_1(29.38/192.47)$  and  $P_2(49.91/296.22)$ .

In the case of four possible attitudes, the plunge  $-p$  and trend  $t + 180^\circ$  are used for the opposite small circle to find the direction cosines of the other two poles. In the problem of Fig. 20.7b the results are:  $P_1(39.58/347.14)$ ,  $P_2(55.60/097.01)$ ,  $P_3(7.70/013.92)$ ,  $P_4(17.99/078.84)$ .

### 20.7 Three drill holes

In any situation cores from three drill holes completely fix the attitude of a structural plane. With a marker the attitude can be determined by the simple method of the three-point problem, but its attitude could already have been found with only two differently oriented drill holes. Without a marker, the attitude can be determined by finding the unique pole common to the three core–pole circles.

#### Problem

- Three drill holes have the following orientations and core–pole angles in the recovered core. What is the attitude of the bedding?

$$H_1(60/000), \quad \phi_1 = 51^\circ,$$

$$H_2(50/270), \quad \phi_2 = 67^\circ,$$

$$H_3(55/045), \quad \phi_3 = 38^\circ.$$

#### Approach

- It is a straightforward extension of previous methods to plot the points representing the inclined drill holes and to construct the intersecting small circles representing each of the core–pole cones (Fig. 20.9).

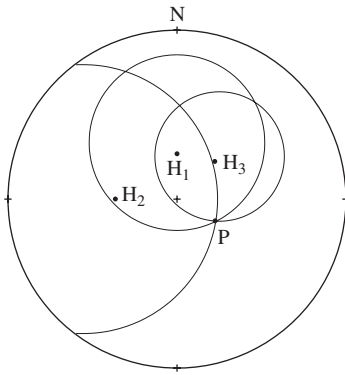


**Figure 20.9** Three drill hole problem.

#### Answer

- The point common to three circles identifies the unique pole, and its attitude is  $P(60/120)$ .

In this contrived problem, the intersecting pairs of small circle are within a degree of each other. In the real world, because of measurement errors and imperfections of natural planes, such accuracy is difficult to obtain. If the intersections are close it is usually possible to make a reasonable estimate the pole’s location. If they are not close, then the

possibility arises that the plane intersected by the three holes does not have a constant attitude. More holes may then be required to determine the structure.

The effort of plotting three small circles, especially if one or more of them overlap the primitive, is time consuming and the analytical approach becomes an attractive alternative. For this problem the analytical results are: for  $H_1$  and  $H_2$   $P(60.38/119.99)$ , for  $H_2$  and  $H_3$   $P(60.46/119.55)$ , and for  $H_1$  and  $H_3$   $P(60.12/119.21)$ . The small differences in these calculated values are not significant.

## 20.8 Interpretation of folds

The deciphering of the structure of folded terranes from drill cores is considerably more difficult. If the wavelength of the folds is large and enough holes are drilled it should be possible to represent the structural geometry by structure contours.

If the beds are sharply folded on a small scale, then each hole will intersect planes with a variety of attitudes. Given certain conditions it may then be possible to determine something of the attitude of these structures. In order to show the basis of the method, consider the following situation. The attitude of the axis of a series of small-scale cylindrical folds is  $F(40/110)$  and these folds are intersected by a drill hole with attitude  $H(36/208)$ . At each point along the recovered core there will be a measurable core–pole angle. For each of these a small circle about the plunging drill hole may be constructed (Fig. 20.10a). Of all these possible circles one is unique. It is the one tangent to the  $S$ -pole great circle, and for this the core–pole angle  $\phi = \phi_{min}$ .

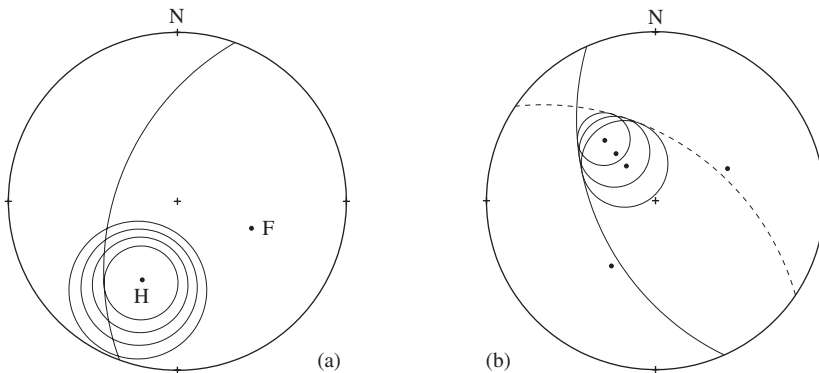


**Figure 20.10** Folded beds: (a) four small circles as possible core–pole cones; (b) two possible fold axes from the  $\phi_{min}$  small circles (after Laing, 1977, p.673–674).

The inverse of this problem, that is, the coring of such folds without knowledge of the fold attitudes, will give the same series of small circles, of which one can be identified as the smallest. Without further information a unique solution is not possible.

One way of obtaining a solution is to examine cores from several differently oriented holes, or, since it is common for drill holes to curve with depth, from an examination of



cores from a number of points along the hole whose variable attitudes are known. If the curve of the deflected drill hole lies in a vertical plane, and the minimum small circles are drawn at a number of points, two great circles may be drawn which are tangent to them. In Fig. 20.10b, such small circles associated with points  $H_1$ ,  $H_2$  and  $H_3$  along the hole are shown. Note that for an additional point  $H_4$  the hole is locally parallel to the  $S$ -pole great circle, or, equivalently, perpendicular to the fold axis and the minimum small circle has degenerated to a point.

In this example, the two possible fold axes have quite different attitudes  $F_1(40/110)$  and  $F_2(40/325)$  and it might be possible to reject the spurious one if the general structural trend of the area is known, even approximately. If, in addition to curving in the vertical plane, a horizontal component of curvature is also present then the bilateral symmetry exhibited by the example of Fig. 20.10b will be destroyed and a unique solution can be obtained.

Other information may also be taken into account. If slaty cleavage is seen in some of the rocks, then two different planes will be present in the cores. Such cleavage often has a reasonably constant attitude which may be known from surface exposures. With the attitude of the cleavage planes known, the attitude of the variable bedding could then be determined at any point using the construction of Fig. 20.5. Further, the intersection of cleavage and bedding could be found, and this related to the fold axis. Details of these and other closely related techniques, together with some important limitations are discussed by Laing (1977). Scott and Berry (2004) and Scott and Selley (2004) have developed a comprehensive system for analyzing folds from drill hole data.

## 20.9 Exercises

1. Two vertical holes are drilled.  $H_1$  cut a marker at a depth of 65 m.  $H_2$ , located 120 m on a bearing of N 30 W, encountered the same marker at 33 m. What is the dip, and what are the strike possibilities?
2. In a vertical drill hole the core–bedding angle is  $20^\circ$ . In a second hole, with attitude 50/045, the core–bedding angle is  $15^\circ$ . What are the possible attitudes of the plane encountered?
3. A vertical hole encountered a marker at 14.8 m, and the core–bedding angle is  $60^\circ$ . A second hole inclined at 30/020 is located 60 m due east. The marker was found at 33.6 m along the drill hole and the core–bedding angle is  $45^\circ$ . What is the attitude of the marker plane?
4. With a recognizable marker horizon why do two differently inclined holes give more information than two parallel holes?
5. Three drill holes intersect a prominent planar structure. From the following information, what is the attitude of this plane?

$$82/217, \phi = 17^\circ, \quad 61/159, \phi = 34^\circ, \quad 50/173, \phi = 30^\circ.$$

# 21

## Maps and cross sections

### 21.1 Geological maps

A variety of structural techniques have been described in previous chapters. In the main, the approach has been one of dissecting the geological map and examining its parts. The map is, however, more than the sum of these geometrical parts, and it remains to consider some of the more collective features.<sup>1</sup>

Properly done, the map is an exceedingly important tool in geology. The graphical picture it gives of the location, configuration and orientation of the rock units of an area could be presented in no other way. Essential as the map is, however, it is not without limitations, and if it is to be of maximum use these limitations must be fully understood. The most important point to realize is that geological maps generally record both *observations* and *interpretation*. In part, the element of interpretation is due to a lack of time and complete exposure; it is almost never possible to examine all parts of an area. If a complete map is to be produced, this lack of observed continuity then requires interpolation between observation points and such interpolation is, to a greater or lesser degree, interpretive.

To distinguish between observation and interpretation several devices may be adopted. Most commonly, special symbols are used to identify several degrees of certainty in the location of lithologic contacts (Fig. 21.1); additional map symbols can be found in Compton (1985, p. 372). The choice of these symbols depends both on the ability to locate the boundaries in the field and on the scale of the map. A common rule of thumb is that a solid line is used if the contact is known and located to within twice the width of the line (Kupfer, 1966). Accordingly, a very thin, carefully drawn pencil line 0.1 mm wide covers 1 m on a 1:10 000 map and is appropriate for a contact known within 2 m

<sup>1</sup>Compton (1985) gives an excellent description of how to effectively present field data in the form of maps and sections.

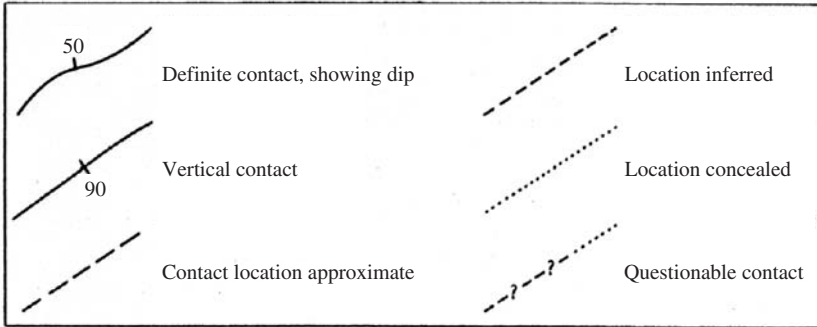


**Figure 21.1** Map symbols for lithologic contacts.

on the ground, and a thin ink line 0.3 mm wide is appropriate for a contact known within 6 m. Clearly, the detail that can be shown on a map is scale dependent.

If contacts are represented by less certain lines, it is important that their inferred locations make geometrical sense; if a contact line crosses a valley it should obey the Rule of Vs according to the inferred attitude. It is quite misleading to show uncertain contacts as if they were all vertical, though many examples of this practice can be found.

Factual and interpretive data may also be distinguished by considering the two aspects more or less separately. An outcrop map is one method of presenting field observations in a more objective way (Fig. 21.2a). Another way of conveying the essential information of an outcrop map, but without actually drawing in the boundaries of the exposed rock masses, is to show abundant attitude symbols, which then serve two functions: to record the measured attitude, and to mark the locality where the attitude can be measured.

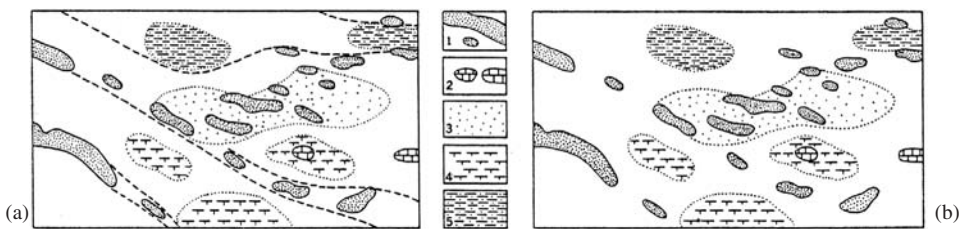


**Figure 21.2** Hypothetical maps. Lithologies: 1, sandstone; 2, limestone; 3, sandy soil; 4, limy soil; 5, clayey soil. (a) Outcrop and soil map showing facies interpretation (after Kupfer, 1966); (b) interpretation as a mélangé; the blocks of sandstone and limestone are shown by outcrops and soils, the clay soil and covered areas are underlain by mélangé matrix (after Hsü, 1968).

However, even an outcrop map or its equivalent can never be entirely objective for several reasons. What constitutes an exposure of rock is itself subject to some interpretation. For purposes of mapping, a thin rocky soil at the top of a low hill might be considered to be an outcrop by a worker in a poorly exposed area. In contrast, a geologist working in mountainous terrain would probably not give such an exposure a second glance because

there are many better exposures. Differences such as these will certainly affect, and may even control the accuracy and completeness of the mapping.

Even with these limitations, it is, of course, important to strive for as high a level of objectivity as possible, and to discuss the difficulties involved in this quest in the text which accompanies the map.

There is another and much more fundamental reason why geological maps are inevitably interpretive. Even the simplest rock mass is extremely complex, and a complete physical and chemical description of a single outcrop could, quite literally, take years and questions concerning the origin of the rock would almost certainly remain. Clearly, such detailed studies are rarely feasible. The question then arises: What observations are to be made and recorded? The process of deciding what is important is guided in at least two ways. First, observations are made which have proven in the past to give results. Routine descriptions of attitude, lithology, visible structures and so forth are an important preliminary stage; some check lists have been published to facilitate this type of field description. However, the creative part of field study involves asking critical questions and then attempting to find the answers. These questions are formulated on the basis of knowledge, intuition and imagination. In this search for understanding, the older, often well-established approaches may actually be a barrier which must be broken through if progress is to be made.

For example, the interpretive aspect of the map of Fig. 21.2a is based on an application of the so-called laws of superposition, original horizontality, original continuity and faunal assemblage (see Gilluly, *et al.*, 1968, p. 92, 103). There are, however, rock bodies composed largely of sedimentary materials which do not obey these laws: a *mélange* is an example (Hsu, 1968). French for *mixture*, the term *mélange* is applied to a mappable body of deformed rocks consisting of a pervasively sheared, fine-grained, commonly pelitic matrix with inclusions of both native and exotic tectonic fragments, blocks or slabs which may be as much as several kilometers long (Dennis, 1967, p. 107). Figure 21.2b is an interpretive map based on the recognition of a *mélange*.

Furthermore, the identification of even well-exposed rock is not always so straightforward that all geologists agree. And, as progress is made, concepts change. The most dramatic way of illustrating these changes is to compare two maps of the same area made at different times. One of the most startling examples, given by Harrison (1963, p. 228), involves a part of the Canadian Shield (Fig. 21.3). The earlier map was made at a time when “granites” were thought to be entirely magmatic in origin. Later, a map was produced after it was realized that metamorphism and metasomatism could produce many of these same rocks. The result is that there is little in common between the two maps. This is an extreme example, but most geological maps still reflect, to a greater or lesser degree, the prejudices of the authors and their times.

As with most things, progress in mapping is an evolutionary process. Each step along the way is, at best, an approximation. These steps, because they are incomplete, necessarily involve some interpretation on the part of the investigator. Just as in the making of

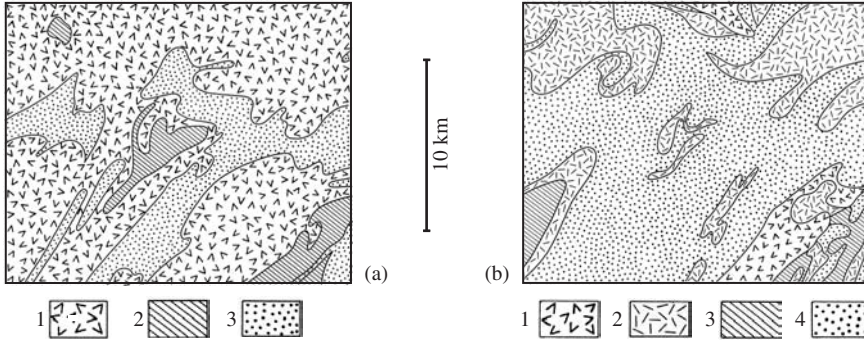


**Figure 21.3** Two maps of same area: (a) map of 1928: 1, granites with inclusions; 2, basic intrusions; 3, metamorphic rocks with granite inclusions; (b) map of 1958: 1, granitic rocks; 2, migmatites with some granite; 3, basic intrusions; 4, metamorphic rocks (after Harrison, 1963).

a geological map, so too does the use of the map as an aid to understanding the structure and history of an area involve several stages of development. The first step does not constitute making structural interpretations, but is rather a repetition of the experience and thinking of the original observer. This step is indispensable in gaining a complete understanding of both the map and the area it represents, and the facility to do this can only be achieved with practice. Two attitudes toward maps greatly increase their usefulness:

1. Regard any geological map as a progress report. Improvement can always be made by further work based on the original mapping, either by the study of new exposures, or a more detailed study using new concepts and techniques.
2. Develop a critical outlook toward the lines and symbols on the map. By refusing to accept them completely, especially those that are clearly interpretive, and by adopting a questioning attitude toward the nature of the various map units and structures, new questions may arise that can be answered directly from the map, or from a visit to the area.

## 21.2 Other types of maps

Lithologic map units, and even different structural elements are often shown in color on geological maps, in combination with the normal symbols printed in black. However, a carefully prepared black and white structural map is often superior to a colored one. On such maps the lithologic units should not be represented by purely geometrical patterns, such as parallel rulings and other such regular patterns. Such patterns fail to express the variously curved lines of strike of the deformed rocks. It is both easier and conveys considerably more information to draw the lines of strike freehand. Further, certain features can be depicted in this way which would be most difficult otherwise. For example, the transition between directionless and foliated rocks can be expressed by a parallel

change in the map pattern. The two contrasting maps of Fig. 21.4 illustrate the value of this approach.

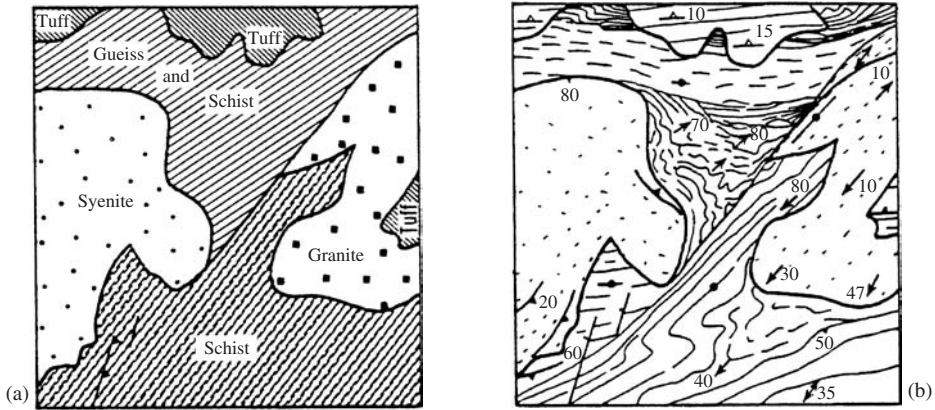


**Figure 21.4** Two black and white structures maps of the same area (from Balk, 1937, with permission of the Geological Society of America).

In addition to surface geological maps, there are a number of other types which may be constructed. Maps may, of course, be drawn wherever rock are exposed, as in a mine. A structure contour map is a type of geological map. Similarly, an isopach map is a geological map, with the zero contour being the underground equivalent of a lithologic contact. An isopach map is also a picture of the structure of the lower boundary of a formation at the time the upper boundary was horizontal. A *paleogeological* map portrays the distribution of rock units immediately below the surface of an unconformity. A worm's eye map is a picture of the unconformity as seen from below; Leversen (1960) gives a number of examples. A *palinspastic* map restores the rock units to their relative positions before structural displacement. Although difficult to draw, such maps are important because they introduce stages of historical development into the description of the geology of an area.

### 21.3 Geological history

After describing the geometry of a rock mass, the next step is to work out the time sequence by which that geometry developed. This concern for history includes both the local chronology, and the dating of these events in terms of the geological time scale. The dating is largely a matter of paleontology and radiometric measurements. The local sequence of events, however, can be worked out without reference to either the geological time scale or to absolute time.

There is a geological feature, not previously discussed, which is of great assistance in dating structures and bracketing periods of deformation. An *unconformity* is a surface of erosion or non-deposition that separates younger from older sedimentary rocks.

There are several important types (Dennis, 1967, p. 159). An *angular* unconformity is characterized by an angular discordance between the two sets of strata (Fig. 21.5a). In contrast, a *parallel* unconformity (also called a disconformity) is marked by an evident break between the two parallel strata (Fig. 21.5b). A non-depositional unconformity is a surface of non-deposition; physical evidence of this surface may not be evident, and paleontologic evidence may be needed to demonstrate the time gap (Fig. 21.5c). A *heterolithic* unconformity (also called a non-conformity) describes the situation where the older rock are non-stratified (Fig. 21.5d).

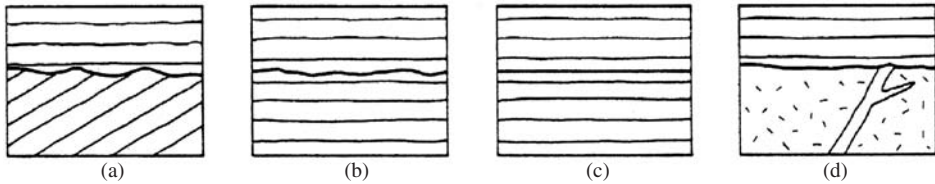


**Figure 21.5** Important types of unconformities: (a) angular unconformity; (b) parallel unconformity; (c) non-depositional unconformity; (d) heterolithic unconformity.

In determining the local chronology it must be kept in mind that several events may have been synchronous; for example, deposition may occur during folding and faulting. A further complication is that a given structure may be the result of several episodes of movement. Nevertheless, though it may be quite involved, the sequence can be worked out using rather simple geometrical relationships. The following criteria are self-evident:

1. Folds are younger than the folded rocks.
2. Faults are younger than the rocks they cut.
3. Metamorphism is younger than the rock it affects.
4. The erosion represented by an unconformity is younger than the underlying rocks and older than the overlying ones. This is strictly true only for a small area; erosion and deposition at widely separated localities may be synchronous.
5. Intrusive igneous rock are younger than the host rocks. This is especially clear where they are in cross-cutting relationships. A similar rule holds for other types of intrusions such as salt domes and sandstone dikes, with the qualification that the act of intrusion is younger though the materials may be older or younger.

An elementary, hypothetical map and the minimum number of events in chronological sequence derived from it illustrates this approach (Fig. 21.6).

## 21.4 Structure sections

One of the problems in reading a geological map is to perceive the structures portrayed on its two-dimensional surface in their proper three-dimensional setting. Several techniques for doing this, especially the powerful down-structure method of viewing maps, have

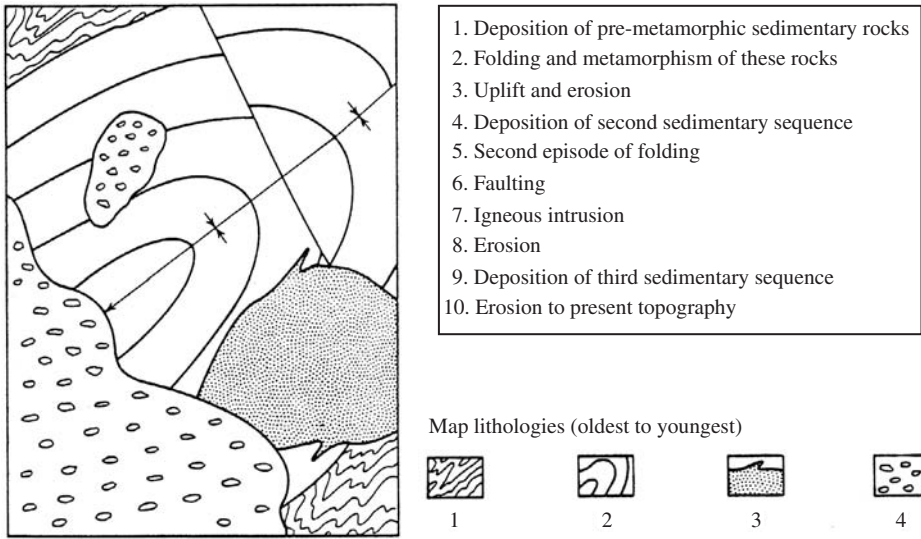


**Figure 21.6** History from a geological map.

been described in earlier chapters. Vertical structure sections, though they have their limitations, are also useful in helping to work out and depict the structural relationships at depth, particularly when the structures are diverse and no single down-structure direction exists. The line of the section is chosen so as to reveal particular geological relationships. The section is oriented so that the right-hand end is its more easterly end or is oriented due north (Compton, 1985, p. 108). Once the location and orientation of the section are fixed, the technique for constructing a vertical section is straightforward and, in general, consists of two parts:

1. The topographic profile along the chosen line of the section.
2. Structural data, such as contacts, attitudes, and so forth, which are added to the line representing the topographic surface and then extrapolated into the underground.

For the topographic profile, the edge of a piece of paper is laid the full length of the chosen section line (Fig. 21.7). Points of intersection of the topographic contours and the section are marked along this edge. Other features, such as the crests of hills or the locations of streams should also be marked, even though a contour line is not present. The elevations of the contours must also be indicated; every contour may be marked, especially if they are widely spaced, or if closely spaced, only those which mark change in slope directions may be used.

A series of elevations lines are then drawn on a second sheet of paper with a spacing equal to the contour interval and plotted at the same scale as the map. The topographic points along the section line are then transferred from the edge of the marked paper, which now represents the line of section, by projecting the contour marks to the corresponding elevation lines, and each of the points so located is joined with a line representing the



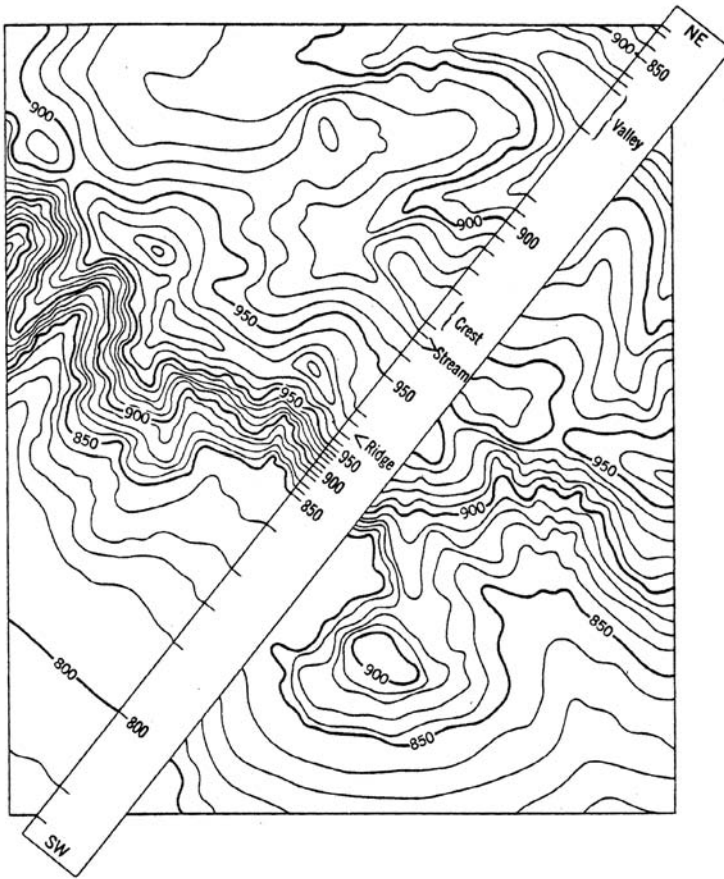


**Figure 21.7** Line of section and topographic profile from a map.

topography. If the spacing of the contour lines is wide, the map may have to be consulted to assist in sketching in topographic details (Fig. 21.8).

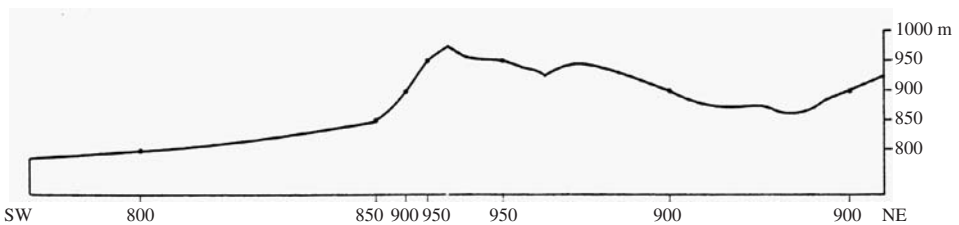


**Figure 21.8** Topographic profile along the line of section.

In constructing this profile, it is easy to exaggerate the vertical dimension by enlarging the vertical scale while keeping the horizontal scale the same. Such an alteration of the vertical scale introduces profound geometrical distortions (see §21.6). Generally, only

unexaggerated sections should be constructed for serious structural work, because only with them are the true geometrical relationships preserved. If more space is required to plot a wealth of structural data, the whole section should be uniformly enlarged (see §21.7).

The second step is to add the structural data to the constructed topographic profile. The various contacts and attitude points can be marked at the same time as the topographic elevations; if there are abundant details which must be transferred it may be less confusing to make two separate plots.

Map data on either side of the section line may be projected to the section; the allowable distance of projection depends on the constancy of the trend of structural features normal to the section line. Where the structures plunge, the map patterns may be projected to the plane of the vertical section with essentially the same construction used for fold profiles. This may also be used to show the structure which existed above the section and has been removed by erosion. When this is complete, all the surface information will have been utilized.

If subsurface information is available, it should then be added. This includes direct geological data on lithologies and contacts obtained from drill holes, and indirect data from geophysical surveys, such as prominent reflection surfaces.

In extrapolating the surface data downward into the underground, several different approaches may be used. In folded sedimentary rocks, making some reasonable assumptions, the form of parallel folds may be reconstructed as rounded or angular forms (see Chapter 14). Even if the plane of the section is not exactly perpendicular to the axes of folds, up- and down-plunge projections may still be used as an aid in depicting the form of the folds.

Lithologic boundaries with no regular features can only be projected downward using the surface attitude; this is only a first approximation and will, at best, be valid only for relatively shallow depths. One example of such an unpredictable boundary is the contact of a discordant intrusive igneous body. Alternatively, such contacts might be shown schematically.

After taking these rather purely geometrical steps, the making of further predictions depends on a thorough understanding of the various processes of folding, thrusting and so forth, and this can only come with experience. As on the geological map, the various lines of the structure section should indicate the degree of certainty in location. Questionable areas should be so indicated or even left blank. The predictions will not everywhere have the same confidence at the same depth. It follows that the lower limit of the structural representation should have an irregular boundary. For example, it might be possible to portray a thousand meters of uniformly dipping sedimentary rocks with reasonable accuracy; on the other hand, the nature of the rocks and structures under a thin sheet of alluvium might be completely unknown.

If structure sections are prepared in black and white, lithologic symbols can be used to indicate the different rock units in much the same manner as with black and white

structure maps. A variety of symbols are used, and several of these are shown in Fig. 21.9; Compton (1985, p. 376–377) gives many more. The meaning of any such symbols used must, of course, be identified on the section, either by labeling the units directly or by including a list in the legend.

In its final form, the section should be labeled with geographical coordinates because knowing the orientation is as important as its location. The line of the section should also appear on the accompanying map. Prominent topographic features should be labeled to assist in orienting the reader. The scale, especially if different from that of the map, is also important.

### 21.5 Other types of sections

A number of variations are possible. Composite sections can be drawn by projecting data to the section plane from some distance, or by combining in one section several different lines that meet at angles. This is generally done to show greater diversity than would be possible along a single, straight line of section.

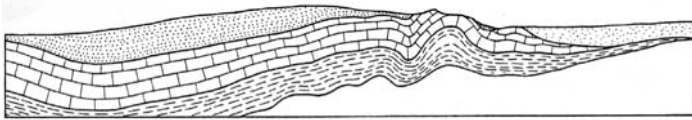
One way of suggesting three dimensions is to use multiple sections. Two groupings are common, but a number of combinations are possible. A *coulisse* diagram is a group of parallel sections drawn and arranged serially to take advantage of some special point of view, such as along the strike of a fault, or in the direction of a fold axis. *Fence* diagrams may be thought of as two intersecting coulisse diagrams giving the appearance of an egg crate.

Time, rather than geographical location, may be the basis for a series of structure sections. As with palinspastic maps, increments of deformation are subtracted from the observed structural geometry, and thus progressively earlier stages in the historical development are illustrated. Figure 21.9 is an abridged version of a famous group of such sections; an examination of the originals and the maps on which they are based is well worth the effort.

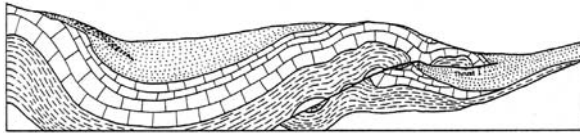
### 21.6 Vertical exaggeration

It is a very common practice to draw cross sections with the vertical scale enlarged relative to the horizontal scale; that is, to stretch the section vertically while leaving the horizontal dimension unaltered (see Suter, 1947). This practice is especially common in sections showing stratigraphic or geomorphic information where more space is needed to plot vertical details or to accentuate certain features which would otherwise be obscure. The result is known as a *vertically exaggerated section*, and the degree of the stretch is defined by an exaggeration factor  $V$

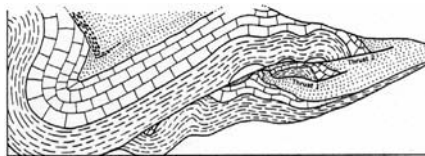
$$V = \frac{\text{vertical scale}}{\text{horizontal scale}}. \quad (21.1)$$



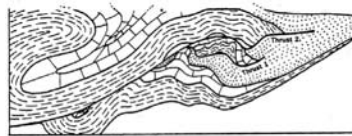
Early folding near margin of sedimentary basin with simultaneous deposition of coarse clastics in marginal trough.



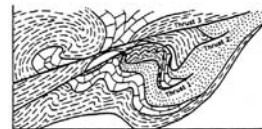
Thrusting and continued folding. Rocks carried toward the trough. Deposition of coarse clastics continues.







Further folding with formation of a new thrust.

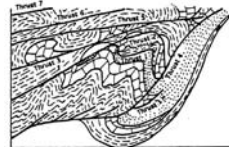


Thrusts are folded as main syncline becomes recumbent.



Involution of the syncline and renewed thrusting.

-  Coarse clastic sediments: sandstones and locally conglomerates
-  Limestone
-  Shale
-  Basement rocks (greenstones, breccia and cherts)



Tightening up of the folds and imbricate thrusting.

**Figure 21.9** Diagrammatic sections showing progressive development of complex folds and thrusts (after Ferguson & Muller, 1949).

For example, if the horizontal scale is 1/50 000 and the vertical scale is 1/10 000, then  $V = 5$ .

Vertically exaggerated sections also arise naturally in a number of situations. For example, seismic profiles plot horizontal distance against return time of the seismic signal. The result is that the section of the reflecting horizons is exaggerated. When using these for structural interpretations special care is required (Stone, 1991).

Largely because of continued exposure to such sections most geologists tend to think in terms of them, and unexaggerated sections often have an “unnatural” appearance. It is therefore vital to understand in detail the geometrical implications of vertical exaggeration. This will both aid in deciding whether to draw such sections or not, and in interpreting the exaggerated sections of others.

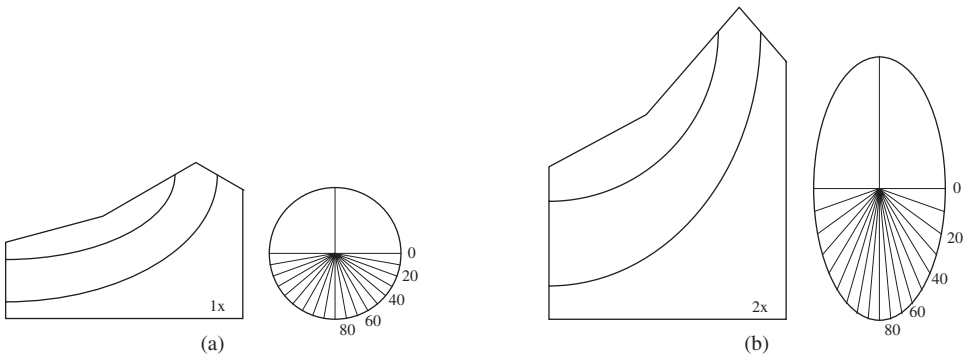


**Figure 21.10** Structure sections: (a) natural section; (b) exaggerated section 2× (after Wentworth, 1930).

As a result of this vertical stretching, both angles of dip and thicknesses are systematically distorted. A useful way of treating these changes is to consider the vertical exaggeration as an artificially introduced strain. For example, vertical exaggeration can be described by a strain ellipse (see Fig. 21.10), and this emphasizes the profound geometrical change which accompanies such exaggeration.

In exaggerating a section, horizontal dimensions are left unchanged and vertical dimensions are multiplied by the exaggeration factor. In Fig. 21.11a, the distance  $w$  is unchanged while the distance  $d$  becomes  $Vd$ . From this geometry, we obtain two relationships.

$$w = d / \tan \delta \quad \text{and} \quad w = Vd / \tan \delta'$$

where  $\delta$  and  $\delta'$  are, respectively, the original and exaggerated dip angles. Equating these two expressions and rearranging we then have

$$\tan \delta' = V \tan \delta. \tag{21.2}$$

In Fig. 21.12 this equation is graphically represented for selected values of  $\delta'$  over a range of exaggeration factors  $V = 1-10$ .

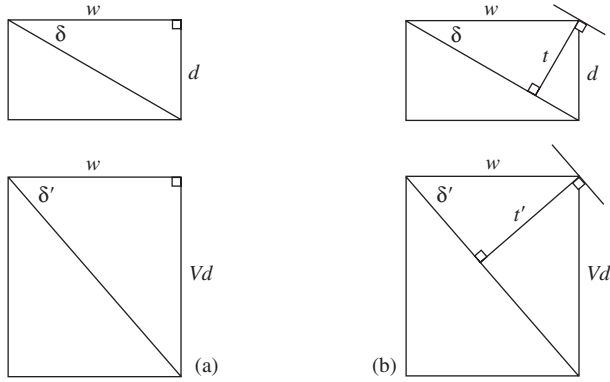


**Figure 21.11** Analytical relationships: (a) exaggerated dip  $\delta'$ ; (b) exaggerated thickness  $t'$ .

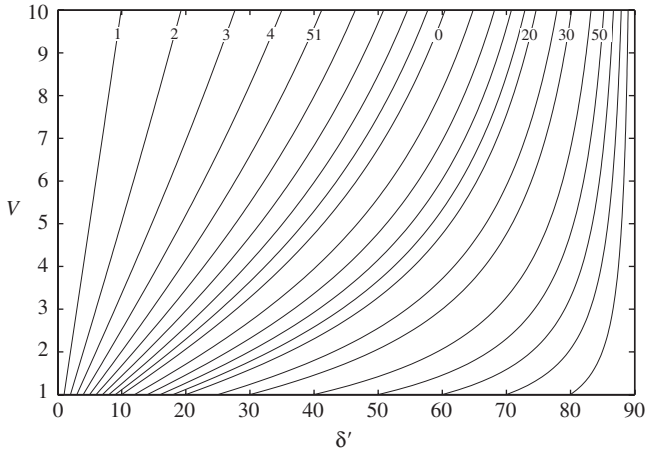


**Figure 21.12** Exaggerated dip angle as a function of vertical exaggeration.

An examination of this graph makes clear the effect of vertical exaggeration on dip (or slope) angles. In general, all angles are steepened, but small angles are affected relatively more, with the result that small differences in inclination are accentuated. It is this property which is of advantage in depicting subtle variations in slope in the presentation of geomorphic information. On the other hand, differences between steep dips are diminished. For example, at  $V = 10$  planes dipping at angles of  $30^\circ$  and  $60^\circ$  appear with inclinations of  $80^\circ$  and  $87^\circ$ . Thus the important distinction between the dips of primary normal and thrust faults is lost and this is a serious disadvantage.

The effect of exaggeration on thickness is also of interest. The basic situation is shown in Fig. 21.11b. From this geometry we obtain expressions involving original thickness  $t$  and exaggerated thickness  $t'$ :

$$w = t / \sin \delta \quad \text{and} \quad w = t' / \sin \delta'.$$

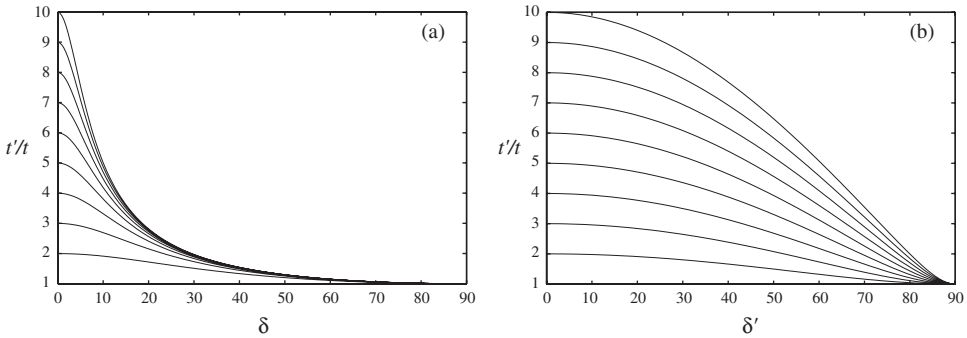


**Figure 21.13** Normalized exaggerated thickness  $t'/t$ : (a) as a function of dip  $\delta$ ; (b) as a function of  $\delta'$ .

Again equating and rearranging, we have

$$\frac{t'}{t} = \frac{\sin \delta'}{\sin \delta}. \tag{21.3}$$

The factor  $t'/t$  is the *normalized exaggerated thickness*, that is, the exaggerated thickness of a layer with true thickness  $t = 1$ . Figure 21.13a gives a graphic representation of this equation for values of  $V = 1-10$ . As can be readily seen,  $t'/t$  varies with the dip. The limiting cases occur when the layer is horizontal and the thickness is multiplied by the exaggeration factor

$$t'_0 = Vt,$$

and when the bed is vertical and its thickness remains unchanged

$$t'_{90} = t.$$

This graph also shows that most of the variations in thickness are confined to a relatively narrow range of shallow dip angles. For example, at  $V = 10$ ,

$$t'_0 = 10 \quad \text{and} \quad t'_{25} = 2.3.$$

Thus a layer of uniform thickness but variable inclination within this range will appear to have approximately a four-fold variation in thickness, and it is easy to see that small real variations in thickness would be masked. Because it spreads out the curves, a more useful plot shows exaggerated thickness as a function of exaggerated dip (Fig. 21.13b).

From these considerations it should be clear that vertically exaggerated cross sections severely distort the form and orientation of geological structures, thus tending to destroy the very information the structure section seeks to show – the true geometrical relationships at depth. Therefore, they should not be used for serious structural work. For those few situations where a vertical exaggerated section may aid a presentation, the

smallest possible exaggeration factor should be used. In addition, there is an important responsibility to keep the reader informed of the degree of exaggeration used. This can be accomplished several ways:

1. Include a bar scale for both the horizontal and vertical dimensions.
2. Give the actual exaggeration factor on the section.
3. Include a protractor of exaggerated dip angles.
4. Include a natural-scale section in addition to the exaggerated one for easy comparison.

The last approach is perhaps the most effective one, but it is quite useful to supply all items. Since exaggerated sections are so common, a natural-scale section should be clearly labeled *no vertical exaggeration*.

There is another subtle distortion which appears when sections of regional extent are drawn as if the earth were flat. Sea level is depicted as a horizontal straight line so that the floors of sedimentary basins appear distinctly concave upward; vertical exaggeration further compounds the distortion. If true sections are drawn, it is, of course, sea level which should appear as a curve and the basin floors more nearly a straight line. This difference in basin geometry has important bearing on the physical properties of basin fill (Price, 1970, p. 15) and on the mechanics of basin evolution (Dallmus, 1958). Again, construct accurate, true-scale sections. Then if there is a genuine reason to distort them do so with caution, and alert the reader of what you have done.

## 21.7 Enlarged sections

Instead of vertically exaggerating a section in order to show abundant details, it is preferable to enlarge both vertical and horizontal dimensions uniformly. With a scanner and graphic software, it is easy to do this for any existing cross section.

There are however times when a completely graphical method is useful. Cluer (1992) described the *method of radial projection*, a simple way of doing this that could be used in the field (Fig. 21.14). This can be used either to plot an enlarged section or to enlarge an existing section. All that is required is the scaling factor defined as

$$F = \frac{\text{profile scale}}{\text{map scale}}. \quad (21.4)$$

### Problem

- With a map scale 1/2000 construct a profile with scale 1/1000 along the section line *AB*.

### Procedure

1. Through points *A* and *B* draw lines at angles of  $45^\circ$  to intersect at a point *O* (Fig. 21.14). Then  $\angle AOB$  is a right angle.
2. Construct the bisector of  $\angle AOB$ . This line intersects *AB* at its midpoint *M*.



3. The scaling factor  $F$  is

$$F = \frac{1/1000}{1/2000} = 2.0.$$

4. Locate point  $M'$  so that  $OM' = F(OM) = 2(OM)$ .
5. Through  $M'$  draw a line perpendicular to  $OM'$  to intersect the extended lines from  $O$  to locate points  $A'$  and  $B'$ . These are the end points of the enlarged section line and  $M'$  is its midpoint.
6. Draw radial lines from  $O$  through control points on the original profile line to intersect the new section line  $A'B'$ .
7. With these new control points the profile is completed just as before using a contour spacing  $F$  times that of the original map or section.

This construction is based on the fact that the pair of isosceles right-triangles  $AOB$  and  $A'OB'$  are similar. Corresponding lengths of such triangles are proportional. By construction  $OM'$  is  $F$  times  $OM$  and therefore  $A'B'$  is  $F$  times  $AB$ , as required.

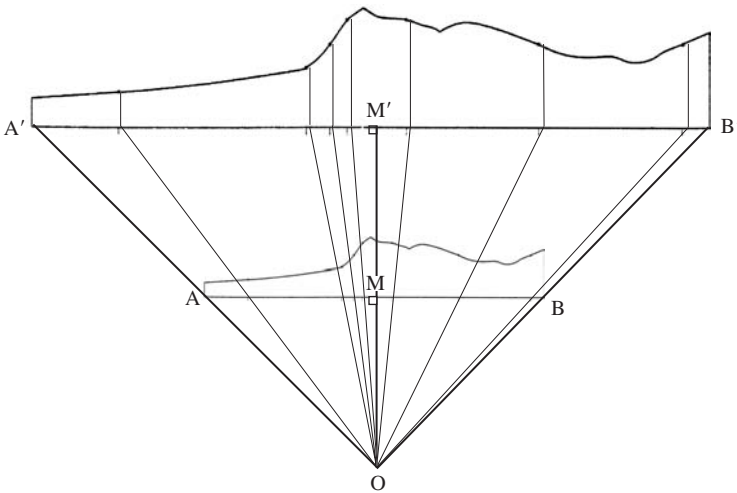


**Figure 21.14** Method of radial projection (after Cluer, 1992).

This construction also may be used to reduce the size of a section, in which case  $F < 1.0$ . Then if line  $A'B'$  is the original section line on the map, length  $OM'$  is multiplied by this scaling factor to give the length of the reduced line  $AB$ . Using the projection point  $O$ , control points are then projected from  $A'B'$  back to  $AB$ .

### 21.8 Exercises

1. Using an available geological map, construct a true-scale cross section showing both topography and structure.
2. With this result, now construct the section with a modest vertical exaggeration.

# 22

## Block diagrams

### 22.1 Introduction

A block diagram is one of the best ways of presenting a wealth of geological information in a compact, three-dimensional form. Almost at a glance, the relationships between the structural data plotted on the visible surfaces of the block can be integrated into a complete spatial picture. The construction of such a diagram entails drawing a scaled block, possibly adding topography to the upper surface, and representing the geological structures on its top and sides.

Such a scaled block may be constructed by the methods of descriptive geometry, but the procedure is fairly involved and time consuming. Fortunately, there are a number of alternatives.

### 22.2 Isometric projection

The unit cube is the basic building block, but a cube of any size differs only by a scale factor. There are several ways to draw such a cube. One of the simplest ways is to use a special isometric graph paper.<sup>1</sup> With this graph paper, the cube is simply traced in. The three front edges of the resulting block intersect at 120° and all have equal lengths (Fig. 22.1a).

The length of the diagonal of the top of the unit cube is  $l = \sqrt{2}$  (Fig. 22.1b). The plunge of the line of sight, which is also an axis of three-fold symmetry, is then given by (Fig. 22.1c)

$$\tan p = 1/l \quad \text{or} \quad p = \arctan(1/\sqrt{2}) = 35.264\ 39^\circ.$$

<sup>1</sup>The term *isometric* applies to a method of projection in three dimensions having three axes equally inclined and all lines drawn to scale (Borowski & Borwein, 1991, p. 311).

On the isometric graph the line of sight is represented by the intersection of the front three edges and it is perpendicular to the page. The scale along each of the edges is equal to  $(\cos p) \times 100\% = 81.4966\%$  of the edge lengths of the original cube.

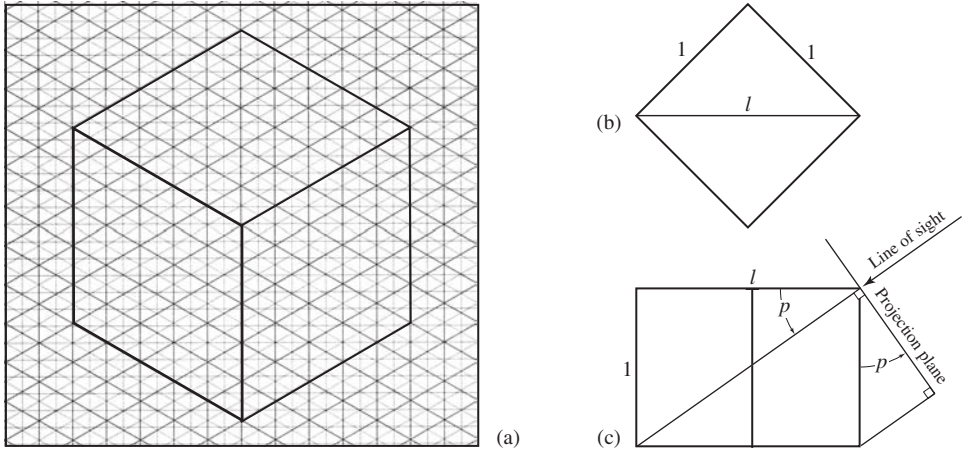


**Figure 22.1** Isometric cube: (a) isometric graph paper; (b) top of unit cube; (c) line of sight.

Isometric projections have a number of useful properties as well as some which require some caution (Lobeck, 1958, p. 120–121):

1. The block has the same scale in the direction of any of the three edges.
2. Distances in other directions are not commensurate with each other unless measured on the two sides of the block.
3. All lines parallel in the object are parallel in projection.
4. All vertical lines in the object are vertical in projection.
5. All angles are distorted, and even two angles lying in the same plane can not be compared unless they have the same orientation.

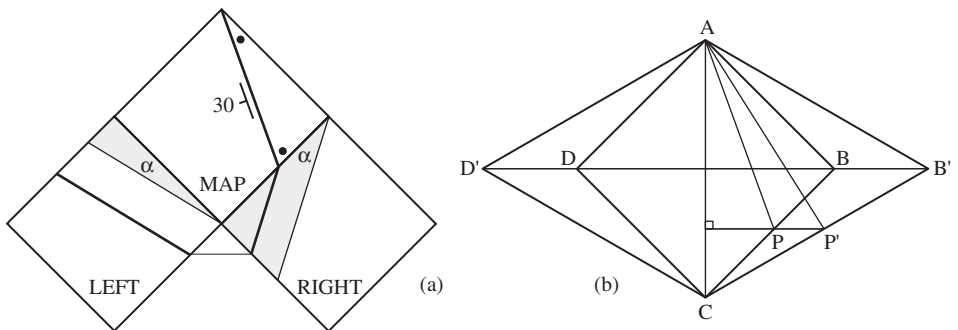


**Figure 22.2** Structural plane: (a) cube faces; (b) strike line in projection (after Phillips, 1971, p. 57).

Having produced an isometric cube, we now need to add the traces of structural planes to its faces (Phillips, 1971, p. 56–59). We start by unfolding the cube in the manner of descriptive geometry to produce an orthographic projection of the cube faces (Fig. 22.2a). The trace of a plane whose attitude is N 20 W, 30 W is added to the map face.<sup>2</sup> The traces of this plane on the two vertical sections are then added using apparent dips. On the right side  $\beta_R = 65^\circ$  and on the left side  $\beta_L = 25^\circ$  (these two angles are marked with black dots in Fig. 22.2a). With Eq. 1.7

$$\tan \alpha = \tan \delta \sin \beta, \quad (22.1)$$

we find that  $\alpha_R = 27.62^\circ$  and  $\alpha_L = 13.71^\circ$ . These are then plotted on the two cube faces (Fig. 22.2a).

Next we need to add these traces to the faces of the cube in projection. For the top face, there is a simple graphical method for doing this (Phillips, 1971, p. 57). Figure 22.2b shows the top of the cube  $ABCD$  and the corresponding rhombus  $AB'CD'$ . The strike is added to the square as line  $AP$ . A line parallel to the common horizontal diagonal through point  $P$  intersects the side of the rhombus at point  $P'$ . Line  $AP'$  is the orientation of the strike line in projection. This strike could just as easily be drawn as a line  $CP$  and constructing line  $CP'$  in the same way.

This construction applies only to strike lines with northerly trends. For strikes with westerly or easterly trends points  $B$  or  $D$  are used. Otherwise the construction is the same.

Now we add the traces of the inclined plane to the sides of the cube (Fig. 22.3). Cube edges  $BC$  and  $CD$  are both five grid units long. From  $5 \tan \alpha_R = 1.6$  grid units point  $M$  is located on the vertical line below  $C$ . Line  $BM$ , which represents the apparent dip on the right face in projection, is added to the projection. Similarly, from  $5 \tan \alpha_L = 1.2$  grid units locate point  $N$  on the vertical line below  $D$ . Line  $CN$ , which represents the apparent dip on the left face, is added to the projection. Triangles  $BCM$  and  $CBN$  represent the shaded triangles of Fig. 22.2a in projection. Using these apparent dip lines, the actual linked segments  $APQR$  can be completed on the three faces of the cube.

As a check, draw a line parallel to the apparent dip line  $BM$  from corner  $A$ ; it should also locate point  $R$ , as it does.

### 22.3 Isometric cube as a strain problem

The view of a plane with a square and circle along an inclined line of sight and the same square and circle appropriately strained homogeneously are formally identical. In §17.6 we used this fact to generate a fold profile by simply distorting the geological map of the

<sup>2</sup>As we have seen in §1.4 measured attitudes always have an associated uncertainty. However, once we decide on a best estimate then the plotting of any derived values should be as accurate as possible. It is for this reason that we retain extra decimal places even though they are not strictly significant.

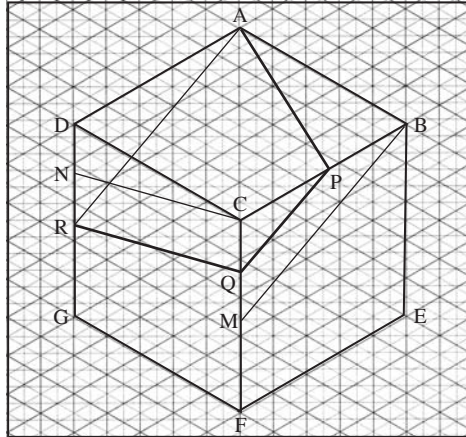


**Figure 22.3** Construction of plane on isometric block (after Phillips, 1971, p.57).

folds. In the present context, this means that two-dimensional strain theory can be used to describe the transformations produced by the method of isometric projections. From Eq. 12.7

$$R_s = \frac{\tan \phi}{\tan \phi'} \tag{22.2}$$

With  $\phi = 45^\circ$  (Fig. 22.4a) and  $\phi' = 30^\circ$  (Fig. 22.4b) we have

$$R_s = \frac{1}{1/\sqrt{3}} = \sqrt{3} = 1.732\ 05 \dots$$

and we can immediately write down the principal stretches which describe this transformation:

$$S_1 = 1 \text{ exactly} \quad \text{and} \quad S_2 = 1/\sqrt{3} = 0.577\ 35 \dots$$

We can now express the relationship between the strike as portrayed on the map and its orientation on the top of the isometric cube. The angle the strike direction makes with the horizontal radius before strain is  $\phi$  (Fig. 22.5a). In projection this angle becomes  $\phi'$  (Fig. 22.5b). Again from Eq. 12.7

$$\tan \phi' = \frac{\tan 70}{\sqrt{3}} \quad \text{or} \quad \phi' = 57.772\ 06.$$

This result is the same found by the graphic method of Fig. 22.2b.

This same approach can also be used to determine the orientation of the trace of the plane on each of the two sides of the cube.

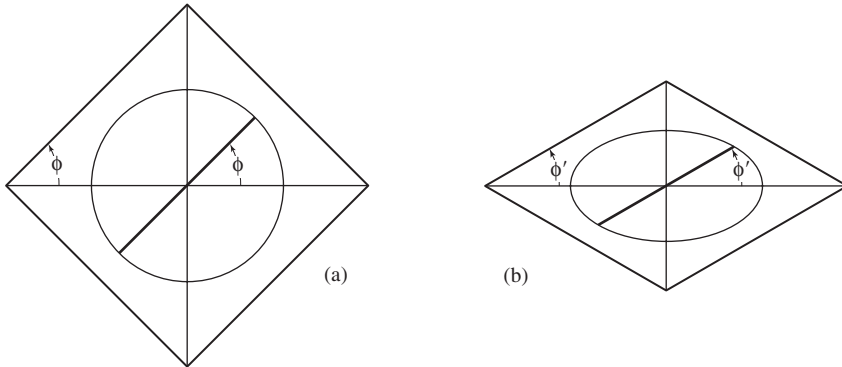


**Figure 22.4** Square to rhombus transformation: (a) before strain ( $\phi = 45^\circ$ ); (b) after strain ( $\phi' = 30^\circ$ ).

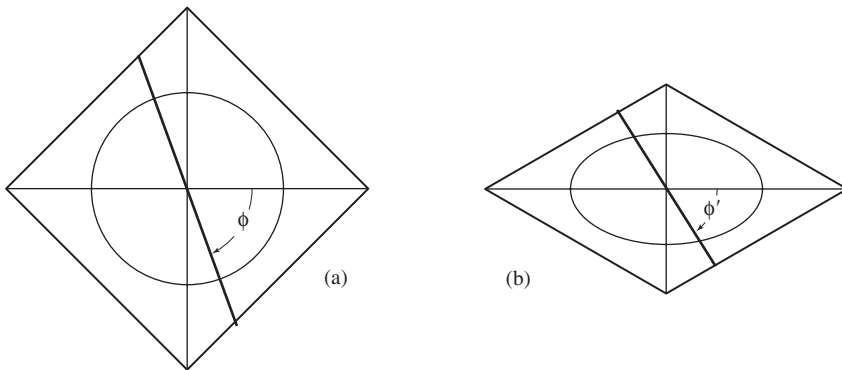


**Figure 22.5** Strike direction on map: (a) before strain ( $\phi = 70^\circ$ ); (b) after strain ( $\phi' = 57.77^\circ$ ).

1. Left side:

- (a) Using the left square of Fig. 22.2a, add a circle and the trace of the plane through its center making an angle  $\phi$  with the vertical diagonal of the square (Fig. 22.6a<sub>1</sub>).
- (b) Homogeneously flatten this square into a rhombus. The trace of the plane now makes an angle  $\phi'$  with this same diagonal (Fig. 22.6a<sub>2</sub>).
- (c) Rotate this rhombus  $30^\circ$  clockwise (Fig. 22.6a<sub>3</sub>).

2. Right side:

- (a) Using the right square of Fig. 22.2a, add a circle and the trace of the plane through its center making an angle  $\phi$  with the vertical diagonal of the square (Fig. 22.6b<sub>1</sub>).
- (b) Homogeneously flatten this square into a rhombus. The trace of the plane now makes an angle  $\phi'$  with this same diagonal (Fig. 22.6b<sub>2</sub>).
- (c) Rotate this rhombus  $30^\circ$  anticlockwise (Fig. 22.6b<sub>3</sub>).

In both cases, the resulting rhombuses together with the traces of the structural plane are the same as found by the graphical method of Fig. 22.3.

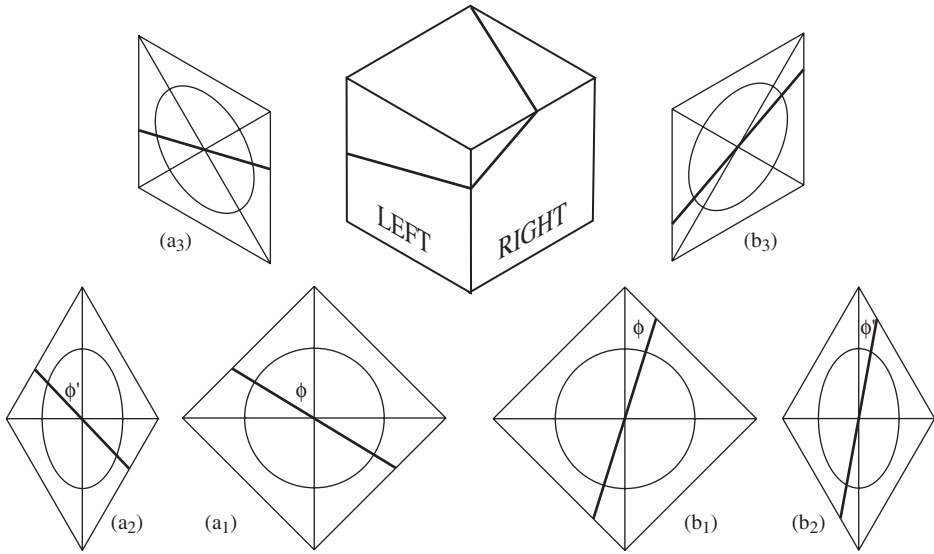


**Figure 22.6** Strain transformation of sides of the cube: (a) left side; (b) right side.

We can also find the orientation of these traces on the sides of the isometric cube by direct calculation.

1. Left side: The required angle  $\phi = 45 - \alpha = 17.38$ . Then

$$\tan \phi' = (\tan \phi) / \sqrt{3} \quad \text{or} \quad \phi' = 58.71.$$

The apparent dip  $\alpha'$  in projection on the left side of the cube is then  $\alpha' = \phi' - 30 = 13.53$ .

2. Right side: In terms of the known apparent dip the required angle  $\phi = 45 - \alpha = 17.38$ . Then

$$\tan \phi' = (\tan \phi) / \sqrt{3} \quad \text{or} \quad \phi' = 10.24.$$

The apparent dip in projection on the right side of the isometric cube is then  $\alpha' = 30 + \phi' = 49.24$ .

### 22.4 Orthographic projection

A more general approach to constructing a cube uses a special *orthographic net*. In both its form and use this net closely resembles the stereonet. The geometrical basis is shown in Fig. 22.7a: point  $P$  on the lower hemisphere is projected orthographically to the diametral plane where it appears as point  $P'$ . The radial distance  $r$  from center  $O$  to  $P'$  is

$$r = \cos p. \tag{22.3}$$

Representations of great and small circles are then constructed in the same manner as in the method of stereographic projection. Here the set of curves related to the great circles are semi-ellipses and the set related to the small circles are straight lines (Fig. 22.7b). Aside from these differences, the method of plotting lines and planes, and performing rotations is essentially the same as before.

It should be noted that because of the closely spaced grid lines near the primitive circle, it is usually easier to count off complementary angles outward from the center of the net than inward from the primitive.

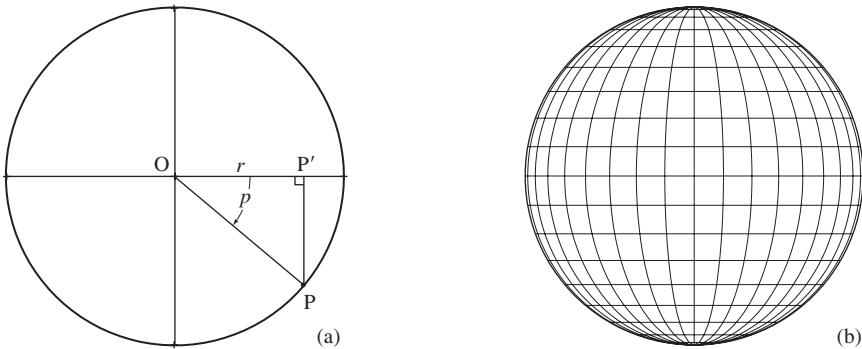


**Figure 22.7** Orthographic net: (a) geometrical basis; (b) resulting net.

## 22.5 General cube

With the orthographic net, a cube in any desired orientation can be constructed. There are two equivalent ways of doing this: (1) by revolving the cube into the desired orientation, and (2) by a direct plot. Because it aids visualization, the first method will introduce the use of the orthographic net.

### Problem

- Construct a cube so that the line of sight plunges 30/320.

### Construction by rotation

1. On an overlay sheet with north marked, draw a square whose sides are equal in length to the radius of the net, located so that the front corner is at the center of the net. In this problem the trend is toward the northwest, so the square is drawn in the northwest quadrant (Fig. 22.8a).
2. Rotate this square so that the line of sight trends due north. Here this requires a clockwise rotation of  $40^\circ$  (Fig. 22.8b).
3. Next rotate the block so that the plunging line of sight is represented by a point at the center of the net. This maneuver is performed in exactly the same way as on the stereonet. First rotate the net  $90^\circ$  so the rotational axis is horizontal. To perform



the rotation, the two upper points move south along the small circles (straight lines) and the center point moves along the vertical diameter a distance equivalent to  $60^\circ$  (Fig. 22.8c).

- The three lines radiating from the center point represent the solid angle made by the front three faces of the cube and each appears correctly foreshortened. The cube is then completed by drawing in the other edges.

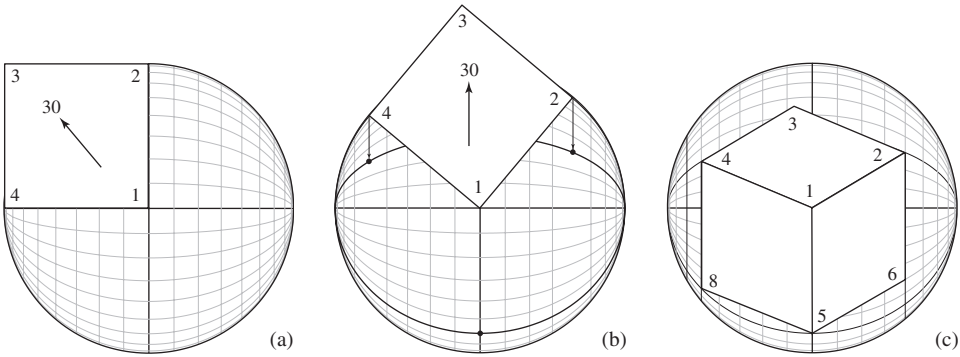


**Figure 22.8** Cube on the orthographic net by rotation (after McIntyre & Weiss, 1956).

**Direct plot**

- In its final position, the top of the cube dips  $60^\circ$  due north (Fig. 22.8c). This inclined plane is represented by the great circle located by counting  $60^\circ$  inward from the primitive or  $30^\circ$  outward from the center to locate the dip vector **D**, which is then traced in (Fig. 22.9a).
- To locate the left corner (point 4) count off  $50^\circ$  anticlockwise from **D** along the great circle. The right corner (point 2) is similarly found by counting off  $40^\circ$  clockwise from **D**. As a check, the angular distance along the arc from points 2 to 4 must be  $90^\circ$ .
- To locate the lower corner (point 5) count off  $60^\circ$  from point 1 southward along the radius of the net. A comparison with the results derived by rotation will show that they are the same. As before, the cube can then be completed (Fig. 22.9b).

At this point, a simple proportional change in the lengths of the three lines representing the front edges of the cube can be made.

**22.6 Computer plot of cube**

There is an alternative way of rotating a unit cube into any desired orientation: the application of the rotation matrices of §7.6. As in the graphic method two steps are required to rotate the line of sight vector into the vertical orientation.

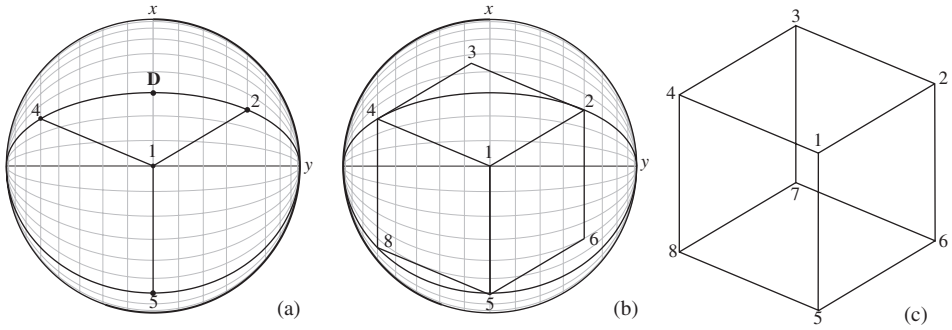


**Figure 22.9** Cube by direct plot: (a) great circle representing the top of the cube; (b) completed cube; (c) computer plot.

1. First rotate the trend of the vector parallel to the  $x$  axis by a rotation about  $z$ . This is given by

$$\mathbf{R}_z = \begin{bmatrix} \cos \omega_z & -\sin \omega_z & 0 \\ \sin \omega_z & \cos \omega_z & 0 \\ 0 & 0 & 1 \end{bmatrix}.$$

2. Then rotate the vector parallel to the  $z$  axis by rotation about  $y$ .

$$\mathbf{R}_y = \begin{bmatrix} \cos \omega_y & 0 & -\sin \omega_y \\ 0 & 1 & 0 \\ \sin \omega_y & 0 & \cos \omega_y \end{bmatrix}.$$

Or the rotation can be accomplished in one step by the single rotation  $\mathbf{R} = \mathbf{R}_y \mathbf{R}_z$ . In expanded form

$$\mathbf{R} = \begin{bmatrix} \cos \omega_y \cos \omega_z & -\cos \omega_y \sin \omega_z & \sin \omega_y \\ \sin \omega_z & \cos \omega_z & 0 \\ -\sin \omega_y \cos \omega_z & \sin \omega_y \sin \omega_z & \cos \omega_y \end{bmatrix}.$$

Table 22.1 *Corners of unit cube of Fig. 22.8a before rotation*

Top	( $x, y, z$ )	Bottom	( $x, y, z$ )
1	(0, 0, 0)	5	(0, 0, 1)
2	(1, 0, 0)	6	(1, 0, 1)
3	(1, -1, 0)	7	(1, -1, 1)
4	(0, -1, 0)	8	(0, -1, 1)

For example, the rotation of the cube of Fig. 22.9b is given by  $\omega_z = +40^\circ$  and  $\omega_y = -60^\circ$ . The  $x, y$  coordinates of each point are then plotted. This is equivalent to projecting the corner points orthographically to the  $xy$  plane (Fig. 22.9c).

### 22.7 Geological structure

The next step is to add the structures to the block faces. Starting with the geological map (Fig. 22.10a) we use the orthographic net to obtain the contacts in projection (Fig. 22.10b).

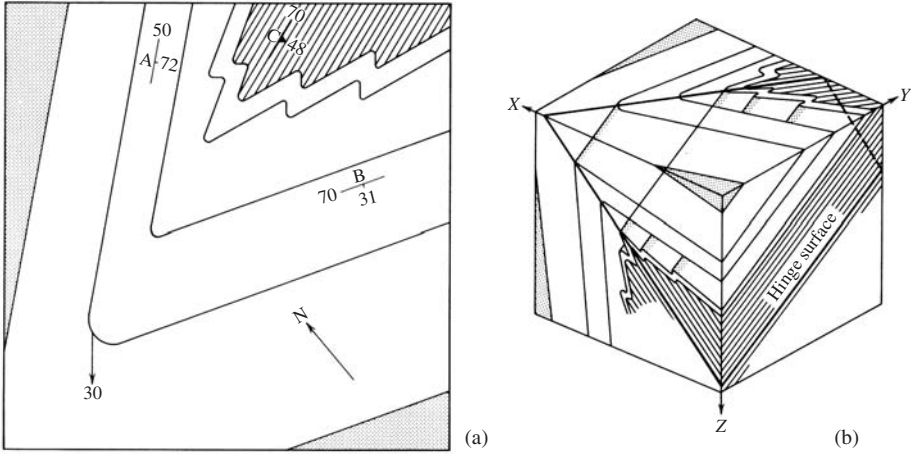


**Figure 22.10** Structural conversion (after Lisle, 1980): (a) geological map; (b) completed block.

By constructing a grid on the geological map and an equivalent foreshortened grid on the parallelogram representing the top of the cube, the geological boundaries are transferred from the map to the top of the cube in much the same manner used in the construction of the fold profile in Fig. 17.8, except here the spacing of both sets of grid lines must be adjusted.

The next step is to determine the orientation of the traces of the various planar structures on the top and sides of the cube, and, if desired, the orientation of lines within the block. The basic approach is to plot the structural data as points on the net and then rotate these points into the cube coordinates.

#### Construction

1. Plot the poles of the bedding at points  $A$  and  $B$  on the limbs of the fold, the pole of the axial plane cleavage at  $C$ , and the plunging hinge line  $F$  exactly in the same way as they would be plotted on the stereonet.
2. Rotate these four points in the same direction and amount as the points  $X, Y$  and  $Z$  were rotated. Note that the point  $F$  moves to the primitive, reappears  $180^\circ$  opposite and continues its rotation (Fig. 22.11a).

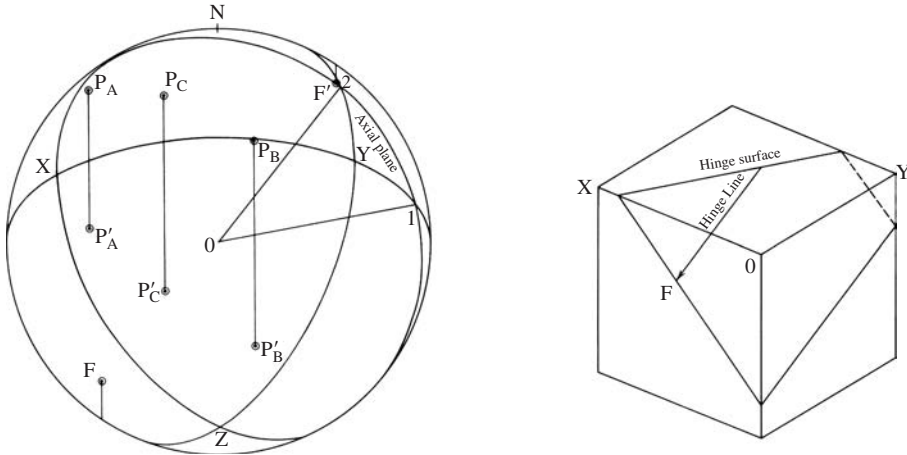


**Figure 22.11** Structural planes: (a) construction on orthographic net; (b) traces transferred to block (after Lisle, 1980).

3. With the new positions of the poles  $A$ ,  $B$  and  $C$ , draw in the three corresponding great circular arcs. Only one of these planes is shown in Fig. 22.11a; it is the arc representing the axial plane cleavage at  $C$ .
4. Draw lines from the center  $O$  to the points of intersection of the structural planes and the three faces of the cube. Again, only one of these is shown on the figure giving the orientation of the traces of the cleavage at  $C$  with the top (point 1) and the front right side (point 2). With these, the traces of planes parallel to  $C$  can be accurately drawn on the top and right sides. Usually the trace can be continued to the third side without further information from the net.
5. The orientation of the hinge line within the block is found by a line from  $O$  to  $F'$ , and the hinge line can then be drawn in from a hinge point on the map (Fig. 22.11b).

The completed block diagram, with the structure on all visible faces, as well as within the block, is shown in Fig. 22.10b.

## 22.8 Orthographic cube as a strain problem

As in the case of the isometric cube, the general orthographic cube may be viewed as a strain problem. The formulation is a bit more involved because the line of sight is no longer an axis of symmetry so each cube face must be treated separately. Therefore, we need an alternative way of determining the shape and orientation of the projection ellipse on each face.

If a unit circle (Fig. 22.12a) is observed along a line of sight inclined to its plane the result is an ellipse (Fig. 22.12b). The length of the ellipse axis perpendicular to the line of sight is unchanged, while the axis in the direction of the line of sight is reduced. You can

actually see this transformation by rotating and tilting the page and viewing the circle obliquely.

The length of the minor semi-axis of this projection ellipse is a function of the angle  $p$  the line of sight makes with the plane of the circle. From Fig. 22.12c

$$S_2 = \sin p, \tag{22.4}$$

hence the strain ratio  $R_s = 1/\sin p$ .

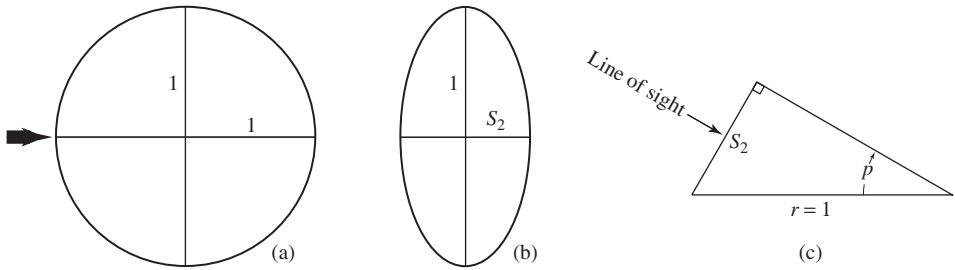


**Figure 22.12** Map face: (a) unit circle; (b) projection ellipse; (c) line of sight and  $S_2$  ( $2\times$  scale).

With this result we know the shape of the projection ellipse for the top of the unit cube of the previous example. Here  $p = 30^\circ$ , so  $S_2 = 0.5$  and as before  $S_1 = 1$ . Applying this strain to the square after the first rotation about the  $z$  axis (Fig. 22.13a), we obtain its shape in orthographic projection (Fig. 22.13b), and this is the same as found graphically with the orthographic net.

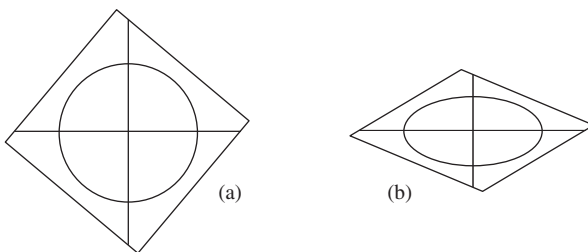


**Figure 22.13** Map face of orthographic cube: (a) after rotation; (b) after strain.

To obtain the shapes of the two side faces several additional steps are needed: determine the angle the line of sight makes with the plane, and the trend of this line on the plane.

1. The angle the line of sight vector  $\mathbf{L}$  makes with the plane of the two side faces is obtained from the dot product of  $\mathbf{L}(p/t) = \mathbf{L}(l, m, n)$  and the pole vectors on the left and right. In the example of Fig. 22.8a, these vectors are simply the two edges of the cube top before rotation. The unit vector in the  $+x$  direction is the pole of the left face

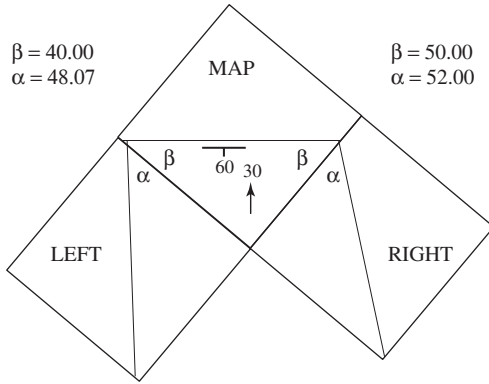


**Figure 22.14** Traces of projection plane on cube faces.

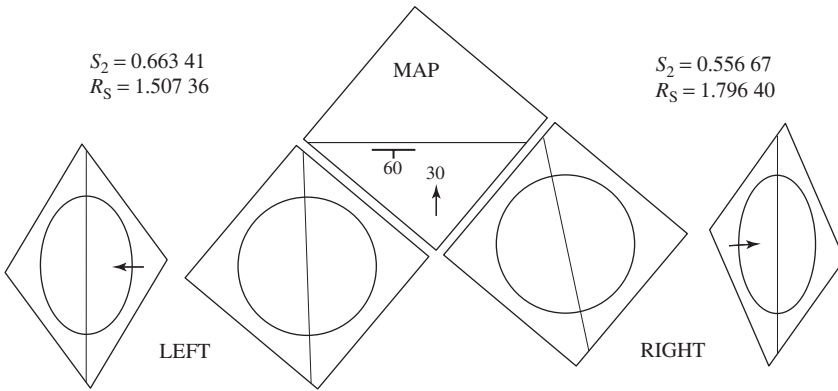


**Figure 22.15** Projection ellipses on left and right cube faces.

$\mathbf{P}_L(+1, 0, 0)$  and the unit vector in the  $-y$  direction is  $\mathbf{P}_R(0, -1, 0)$ . The dot product of two unit vectors is

$$\cos \theta = \mathbf{L} \cdot \mathbf{P}.$$

This gives the angle  $\theta$  between  $\mathbf{L}$  and each of the pole vectors  $\mathbf{P}_L$  and  $\mathbf{P}_R$  in turn. The required angle  $\mathbf{L}$  makes with each plane is then  $90 - \theta$ . With these angles we then can calculate the shape of the projection ellipse using Eq. 22.4. There is a shortcut to calculating this angle between  $\mathbf{L}$  and the plane. Because  $\cos \theta = \sin(90 - \theta)$ , the dot product in this case gives the angle  $\mathbf{L}$  makes with the plane directly. Further, because  $S_2 = \sin(90 - \theta)$ , we have the desired shape of the ellipse without further calculation.

2. The orientation of the major axes of these projection ellipses is established by plotting the traces of the plane of projection on each face, and this simply requires the apparent dips on these faces using Eq. 1.7 (Fig. 22.14).

3. We can then homogeneously strain both these faces (Fig. 22.15). Then as in the isometric case we can determine the orientation of any line in projection using

$$\tan \phi' = \frac{\tan \phi}{R_s}.$$

### 22.9 Topography

If the area has even a small amount of relief, the three-dimensional aspect of the block may be enhanced by adding topography to the diagram. A number of systems for doing this have been devised to adjust map topography systematically to the proportions and scales of the block diagram. The easiest approach method uses a relatively simple graphic method. Given a topographic map, or any part of it, the problem is to show the surface forms on a block in any desired orientation.

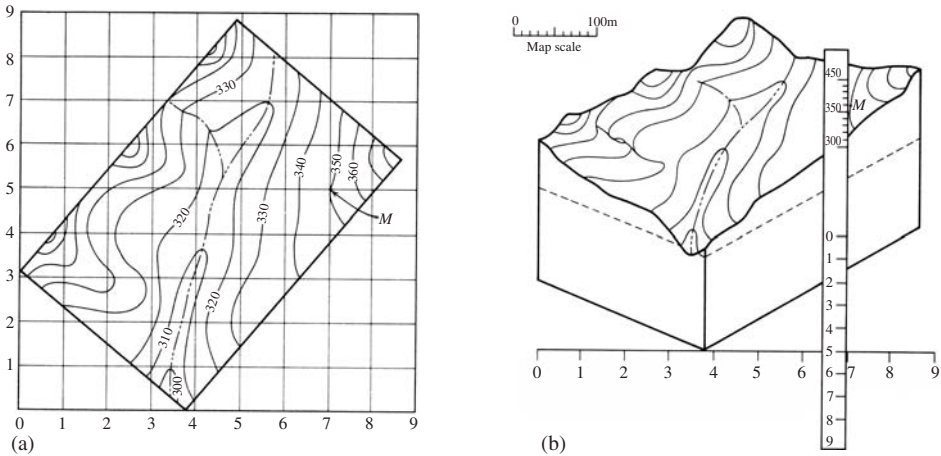


**Figure 22.16** Topography on a block diagram: (a) topographic map with superimposed grid; (b) transferring topographic detail to the block (after Goguel, 1962, p. 119).

#### Construction

1. Draw a square grid on the map with the ordinate in the direction of the proposed line of sight. The grid spacing should be dictated by the amount of detail to be transferred to the block (Fig. 22.16a).
2. Draw a unit cube in the required orientation. Position this cube below the map so that its front corner lies exactly along the line of sight to the corresponding front corner of the map. The cube can then be multiplied to the dimensions of the map by drawing other lines parallel to the line-of-sight line to the outside corners of the map (Fig. 22.16b).
3. The depth of the block depends on the depth of the structure to be shown. In the example, the 300 m level is placed at the top of the unit cube.

4. Along the base of the block reproduce the abscissa scale of the grid and locate it in the correct position with respect to the map grid.
5. From an oblique view, the front-to-back grid spacing is foreshortened; this contracted grid scale is related to the map grid scale by a factor of  $\sin p$ , where  $p$  is the vertical angle which the line of sight makes with the map plane. This corrected scale is plotted along the edge of a strip of paper.
6. The map scale, as measured vertically, is similarly reduced by a factor of  $\cos \beta$ . This new scale is added to the strip.
7. The positions on the block of a series of points, topographic or otherwise, are then located. For example, point  $M$  is at the corner of the horizontal grid number 5 and the vertical grid number 7. On the block, 5 on the corrected grid scale is moved to 7 on the lower abscissa scale, keeping the measuring scale vertical. The elevation of point  $M$  is 350 m, and this height is located on the corrected vertical scale, and the point is then plotted. The procedure is continued until enough points have been located.
8. The topography on the upper surface of the block may be shown with foreshortened contours (Fig. 22.16b).

### 22.10 Modified blocks

In order to show certain features better, a number of modifications may be used. The block may be cut into pieces and the pieces separated to expose its internal parts. Similar cuts may be made to remove corners or variously shaped slices to show other structural details to advantage.

Another way of emphasizing certain features is to dissect the block along a certain structural surface. For example, a complexly folded and faulted stratigraphic horizon could be shown by artificially removing all the overlying material. An excellent example is given by Goguel (1962, p. 134).

Especially in mountainous areas, the presence of topographic relief may hinder rather than aid the presentation, and it may be desirable to eliminate the complications of the outcrop pattern caused by it. This can be accomplished by projecting the structures to a horizontal plane. Any plane can be used, but it is often convenient to use sea level because the topographic contours also use this as datum.

#### Procedure

1. On a transparent overlay sheet, rule a series of closely spaced lines parallel to the trends of the fold axes on the geological map (Fig. 22.17a).
2. Select a series of points on the contact of a lithologic marker. These points should be spaced closely enough to allow the structure to be accurately sketched.
3. Each point is projected to sea level (or other chosen level) by moving it parallel to the trend lines in the direction of the plunge through a distance equal to  $h / \tan p$ , where  $h$  is the elevation of the point and  $p$  is the plunge.



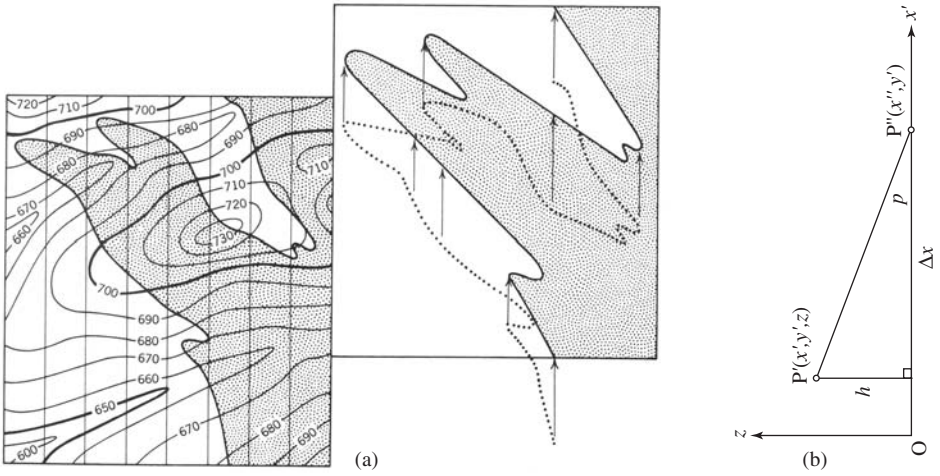


**Figure 22.17** Horizontal outcrop map from geological map: (a) projection of structural data (from Turner & Weiss, 1963, p. 164); (b) geometry of projection.

This procedure can also be viewed as a transformation of coordinate axes. Two steps are required. First, as we have done several times, rotate the geographical coordinate axes about  $z$  so that  $x'$  is parallel to the trend of the fold axes. A typical point  $P(x, y, z)$  relative to the initial axes becomes  $P(x', y', z)$  relative to these new axes (Fig. 22.17b). Point  $P'$  is then projected to the horizontal plane to become  $P''(x'', y'')$ , where

$$x'' = x' + \Delta x \quad \text{and} \quad \Delta x = h / \tan p.$$

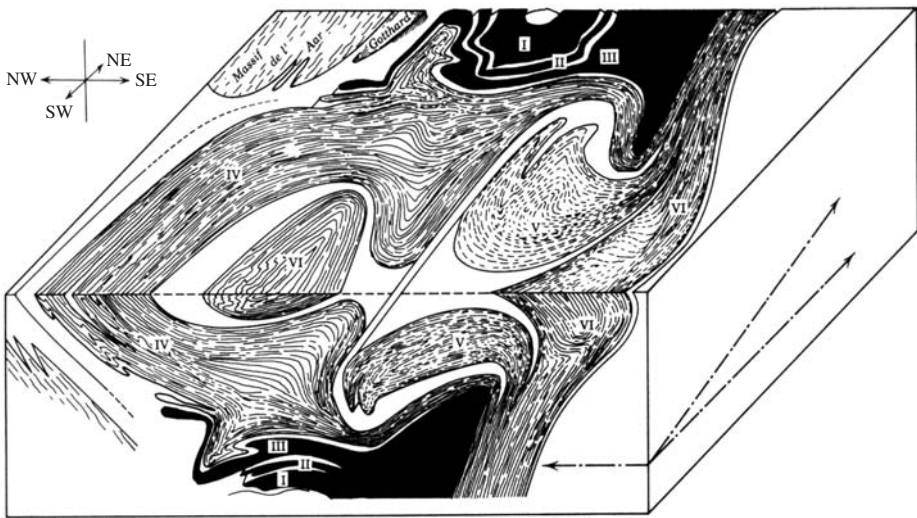


**Figure 22.18** Block diagram showing plunging structures in the Western Alps (from Argand, 1911).

Figure 22.18 is a famous block diagram with an artificially planar upper surface showing the plunging structures of the Pennine Nappes in the Alps. In constructing this diagram, the axial continuity of the cylindrical folds was used as a guide in tracing out the structures on both the top and front of the block.

### 22.11 Exercises

1. Using the map of Fig. 22.19, construct a block diagram using the orthographic method.

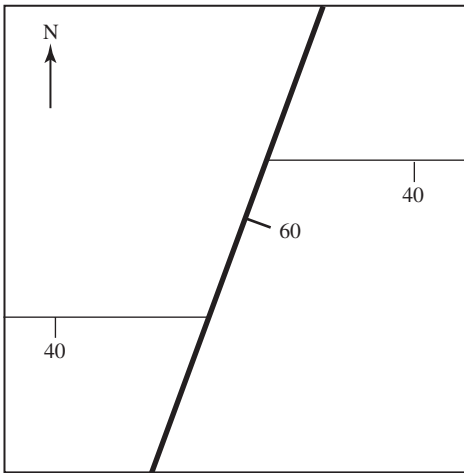


**Figure 22.19**

2. Repeat using the general method.
3. Using an available geological map, construct a scaled block (it is advisable to initially choose a simple structure.)

# Appendix A

## Descriptive geometry

### A.1 Introduction

The emphasis in this book is the geometrical description and analysis of geological structures, especially by graphical means. The basis of much of this is *descriptive geometry*: the art of accurately drawing three-dimensional objects and of graphically solving associated space problems.<sup>1</sup> It is based on the idea of depicting such objects by means of *projections*. Everyday examples of projections are shadows and photographs. Both are the result of projecting various parts of an object to a plane by rays of light. These rays are *projectors* which connect points on the object with the corresponding points on the *image plane*.

By projecting an object to an image plane, a *view* of that object is obtained. Alternatively, a view may be thought of as an actual picture of the object obtained along a line of sight perpendicular to the corresponding image plane.

### A.2 Orthographic projection

The simplest type of projection, and the one used most in engineering as well as for many purposes in geology, is the *orthographic* projection. Orthographic means “drawn at right angles” and refers to parallel *projectors* that are perpendicular to an image plane (Fig. A.1a). The most important property of this projection is that the images of objects appear in their true shape.<sup>2</sup>

<sup>1</sup>The system now called descriptive geometry was developed by the French mathematician, scientist and designer Gaspard Monge [1746–1818].

<sup>2</sup>This method of projection is widely used to produce plans for engineering and architectural projects. In most professional and commercial applications the actual drawings are produced with the aid of Computer Aided Design (CAD) programs. AutoCAD is the de facto standard. Jacobson (1996) describes an add-on to display and analyze geological orientation data. Even more elaborate programs are commonly used in the petroleum industry to combine structural information and seismic data, for example, gOcad (see <http://gocad.org>).

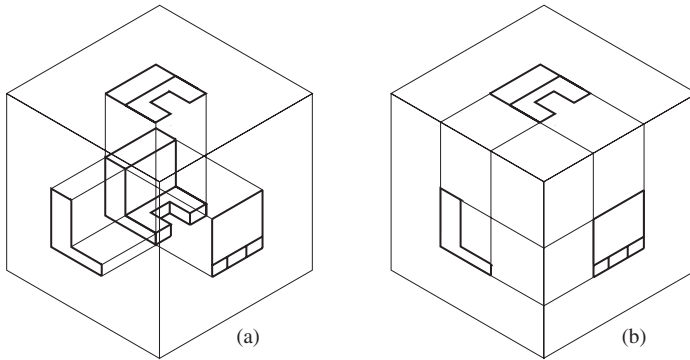


**Figure A.1** Orthographic projection: (a) projectors; (b) projection lines (after Warner & McNeary, 1959).

As in the orthographic projection illustrated in Fig. A.1, it is usually convenient to refer to three separate image planes: a horizontal *Top View* and two vertical planes at right angles, called the *Front* and *Side Views*. Together, these constitute the *principal views*. Other image planes, giving *auxiliary views*, may have any other orientation.

Views are related to the object in two ways: by *projectors* which connect points on the image plane with the corresponding point on the object (Fig. A.1a) or by *projection lines* which connect points on the several views (Fig. A.1b).

In Fig. A.1a a three-dimensional object is projected orthographically to the sides of the cube (Fig. A.2a), and the whole then projected to the plane of the page. In order to show the true shape of the object, it is necessary to obtain a direct or normal view of an image plane. Such a view could be obtained by rotating the cube so that our line of sight is perpendicular to a particular plane of interest. We could obtain direct views of all image planes simultaneously by unfolding the cube, just as one unfolds a cardboard box, so that all the faces lie in a common plane (Fig. A.2b). During this unfolding process, the edges which act as hinges are called *folding lines* (abbreviated *FL*).<sup>3</sup> Any edge may act as a folding line, though most commonly lines that lie in the horizontal plane are used. If auxiliary planes are needed it may be necessary to unfold about other lines, possibly through angles other than  $90^\circ$ .

In practice, of course, the three-dimensional box is never actually constructed nor is the unfolding process so literally followed. All this is by-passed and the required orthographic views are constructed directly. Figure A.2c shows the basic method of construction and the use of lines connecting corresponding points on different image planes. These are the projection lines, and they are perpendicular to the common edges or folding lines.

As can be seen in Fig. A.1b, the projection lines cross the lines of intersection as they pass from one view to another. However, after unfolding, literally or figuratively, there

<sup>3</sup>The term *folding line* seems to have lost favor. We retain it here because it encapsulates a powerful aid in visualizing in three dimensions the data in only two. Simply fold a drawing along a folding line over the edge of a table and *see* the results in three dimensions.

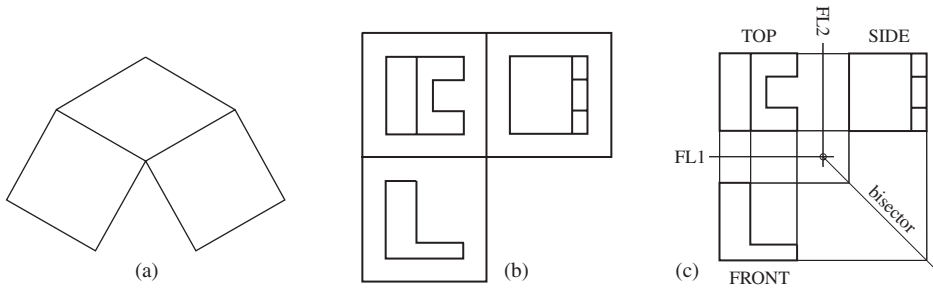


**Figure A.2** Three dimensions to two: (a) unfolding; (b) resulting representation; (c) formal drawing.

is a gap between the Front and Side Views (Fig. A.2c), and we need a way of bridging it. The easiest way is to bisect the right angle between the folding lines. The projection lines from the Front View are then extended to this bisector and then to the Side View.

Any other view can be constructed if two views are given. This is the basis of the orthographic method of solving problems graphically. One simply seeks the particular view, called the *normal* or *direct* view, which shows the required lengths and angles in their true dimensions.

### A.3 Graphical solutions

An important value of the method of descriptive geometry is in developing the ability to visualize geometrical relationships in three dimensions. An important part of this process is to produce clear and accurate drawings. This requires some basic pieces of equipment.

1. Drafting-quality compass.
2. Large-radius protractor.
3. Triangles ( $30^\circ$ – $60^\circ$  and  $45^\circ$ ) of several sizes.
4. Triangular metric and engineers scales.
5. A straight edge (a larger triangle can serve this function).
6. Pencils with reasonably hard lead; Several colored ones are useful.

Graphical solution of problems involving points, lines and planes in a three-dimensional setting can not be absolutely accurate. Limiting factors include the scale and accuracy of the drawing and the skill of the drafter. With a light touch and a sharp pencil it is possible to draw a line as narrow as about 0.1 mm. The intersection of two perpendicular lines is then a small square about 0.1 mm on a side. The maximum error in measuring the distance between two such points is twice this. For other angles the area of intersection is an equilateral parallelogram and the maximum error is even greater. As the width of the line is independent of the scale, the accuracy of a given drawing depends linearly on the scale, other factors being equal. If the scale is doubled, the fractional error is reduced by one-half.

Theoretically, a mathematical solution is capable of absolute accuracy, but no solution can be more accurate than the original data on which it is based. Therefore a graphical solution can be just as accurate as needed if it is within the limits of the numerical observations.

The choice of method, mathematical or graphical, depends on the requirements of the problem and the nature of the observational data. In geology great accuracy is illusive. Thus graphical solutions produced under normal working conditions usually give satisfactory results for most purposes. In addition, the graphical method has one enormous advantage: the actual construction of the various orthographic views is an extremely important aid in visualizing the problem in three dimensions, and in thinking through the sequence of steps which lead to the correct answer. If the graphical method is chosen, the accuracy of any drawing may be improved in a number of ways.

1. Enlarge the drawing. The optimum size is just slightly larger than the data require. This insures requisite accuracy and economy of time.
2. Draw lines as narrow as possible with a hard, sharp pencil using light pressure.
3. Locate intersections using angles as close to  $90^\circ$  as possible.
4. Measure angles with a large-radius protractor.
5. Avoid cumulative errors. Wherever possible measure the total length of a line without lifting the scale for intermediate points.
6. Quality drawing instruments help maintain a higher degree of accuracy. It is especially important that the compass be able to hold its setting.
7. If drawings are to be worked on over a considerable length of time, dimensionally stable materials are advisable. For most purposes, a more practical approach is to complete a construction in as short a working time as possible.
8. Mistakes may be minimized by keeping the actual construction simple and compact, and by labeling all the points on the drawing.

The solution of problems involving lengths and angles can be solved with just two fundamental constructions: the determination of the true length of a line segment and the rotation of a plane figure into any required orientation.

#### A.4 Angles and bisectors

In several of these as well as other constructions we need a method for graphically bisecting angles and lines.

##### *Angle bisector*

1. With point  $O$  as center, and using a convenient but arbitrary radius draw an arc cutting the two sides at points  $P_1$  and  $P_2$  (Fig. A.3a).

- Then with each of these two point as centers draw two arcs with the same radius intersecting at point  $P$ .
- Line  $OP$  is the bisector of angle  $AOB$ .

By construction, the triangles  $OP_1P$  and  $OP_2P$  have corresponding pairs of equal sides and a third side in common. They are therefore *conjugate*. Corresponding angles of conjugate triangles are also equal, that is  $\angle P_1OP = \angle P_2OP$ , as required.

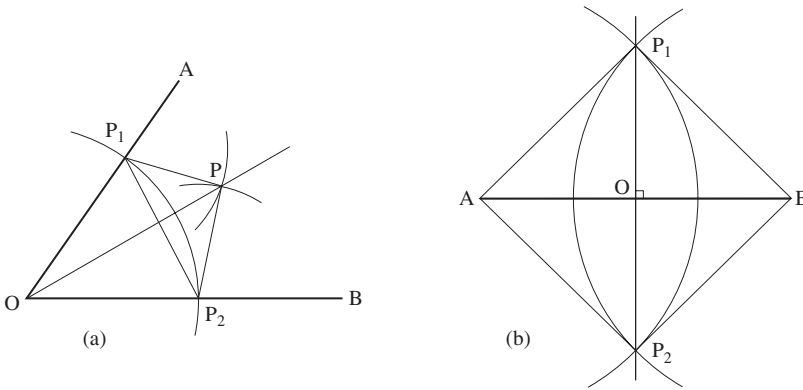


**Figure A.3** Bisectors: (a) angle  $AOB$ ; (b) line segment  $AB$ .

### Line bisector

- With end points  $A$  and  $B$  as centers, draw two arcs intersecting at points  $P_1$  and  $P_2$  (Fig. A.3b).
- Line  $P_1P_2$  intersects  $AB$  at point  $O$ , which is its midpoint. This line has the added virtue of being perpendicular to  $AB$ .

By construction the pair of isosceles triangles  $AP_1B$  and  $AP_2B$  have sides  $AP_1 = BP_1 = AP_2 = BP_2$ . These triangles also share a common side  $AB$ , and they are therefore also conjugate. Also by construction the pairs of angles at  $A$  and  $B$  are equal.

Triangles  $AP_1O$  and  $BP_1O$  have an equal side, share a side and one equal angle and are conjugate. For the same reason triangles  $AP_2O$  and  $BP_2O$  are also conjugate.

Similarly, the pairs of triangles  $AP_1O$  and  $AP_2O$  and  $BP_1O$  and  $BP_2O$  are also congruent. As a result, all four triangles are congruent and the four angles at  $O$  are equal and therefore all are right angles.

It is important to locate the intersection of the arc pairs in these constructions accurately. This requires that they intersect at  $90^\circ$  or close to it. This is easily accomplished by setting the radius to approximately 70% of distance  $P_1P_2$  (Fig. A.3a) or  $AB$  (Fig. A.3b).

### A.5 Projection of a point

The basis of descriptive geometry is the projection of a point to a specified image plane. The idea is to project a point  $A$  in space to, say, the Top View where it is represented by its image  $A_T$  and to the Front View where it is represented by its image  $A_F$  (Fig. A.4a). By rotating the Front View into the plane of the Top View (Fig. A.4b), we now have a representation of all three dimensions on just a two-dimensional composite plane (Fig. A.4c). With this representation, we can easily solve any spatial problem. We can also recover the third dimension at any time from this representation by simply folding the drawing over the edge of a tabletop.

Given any two such views, we can always find the projection of the point on any other view. For concreteness, we start with two given principal views and there are three cases.

1. Project the point to a third principal view (Fig. A.5a),
2. Project the point to a vertical auxiliary view (Fig. A.5b).
3. Project the point to an inclined auxiliary view (Fig. A.5c).

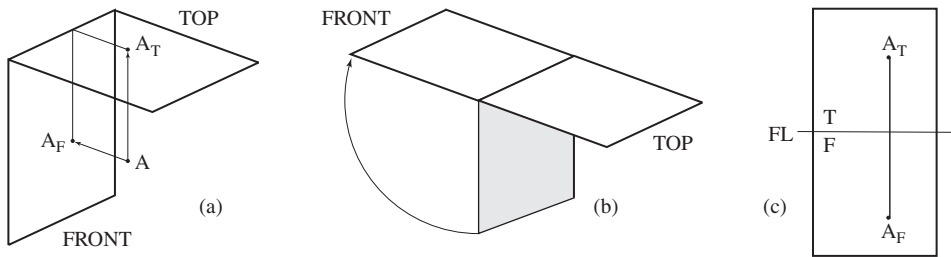


**Figure A.4** Projection of point  $A$ : (a) projection to  $A_T$  and  $A_F$ ; (b) unfolding of the Front View; (c) two-dimensional composite plane (after Steidel & Henderson, 1983, p. 71).

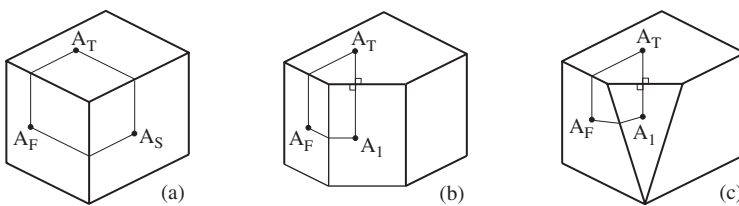


**Figure A.5** Projection of a point: (a) third principal plane; (b) vertical auxiliary plane; (c) inclined auxiliary plane.

#### *Third principal view*

Given two principal views we can always construct the third principal view. The basic method depends on the fact that the image point on any view is located at the intersection of the projection lines from the other two views.



There are two basic ways for locating the image on a third view. The first involves determining a distance. In Fig. A.6a the distance  $D$  from  $FL1$  to image point  $A_F$  in the Front View also represents the distance point  $A$  is below its image point  $A_T$ . Then point  $A_S$  is located on the projection line from the Top View at this same distance. If this distance is determined with a scale, there are two potential errors: first in making the initial measurement and second in plotting this measured distance. A better way is to transfer  $D$  from the Front View to the Side View with a pair of dividers.

The second method constructs intersecting projection lines. In Fig. A.6b image point  $A_S$  lies on the projection line from  $A_T$  and from  $A_F$ . As in Fig. A.2c, the gap between the two vertical views is bridged with the bisector of the angle between  $FL1$  and  $FL2$ . The projection line from  $A_F$  is extended to this bisector parallel to  $FL1$  and then parallel to  $FL2$  to locate  $A_S$  on the projection line from  $A_T$ .

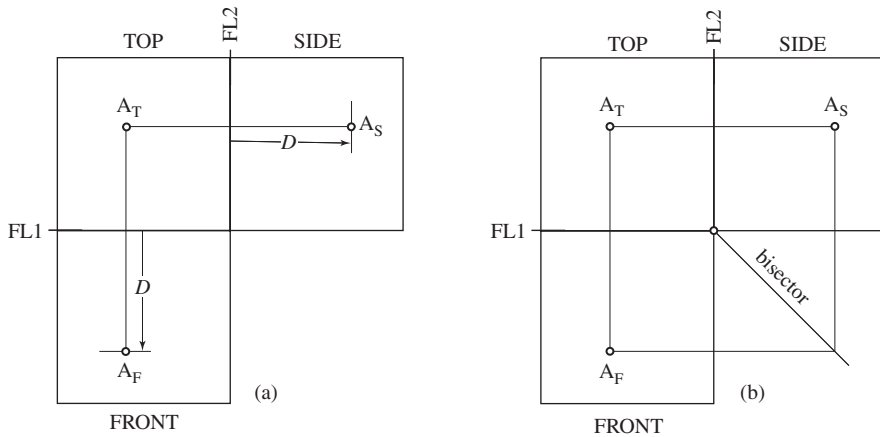


**Figure A.6** Projection of a point to a third principal plane.

### Vertical auxiliary view

The projection of a point to a vertical auxiliary view requires an additional step. The orientation of the required auxiliary plane is specified by the *oblique* folding line  $FL2$ . Thereafter the procedure is the same. Distance  $D$  is the same as in the previous case, which is then transferred to the auxiliary plane and the image point  $A_1$  located on the projection lines from  $A_F$  (Fig. A.7a).

The second method requires the construction of the bisector of the acute angle between  $FL1$  and  $FL2$ . The projection line from  $A_F$  is then extended via this bisector to the projection line from  $A_T$  to locate point  $A_1$  on the auxiliary plane (Fig. A.7b).

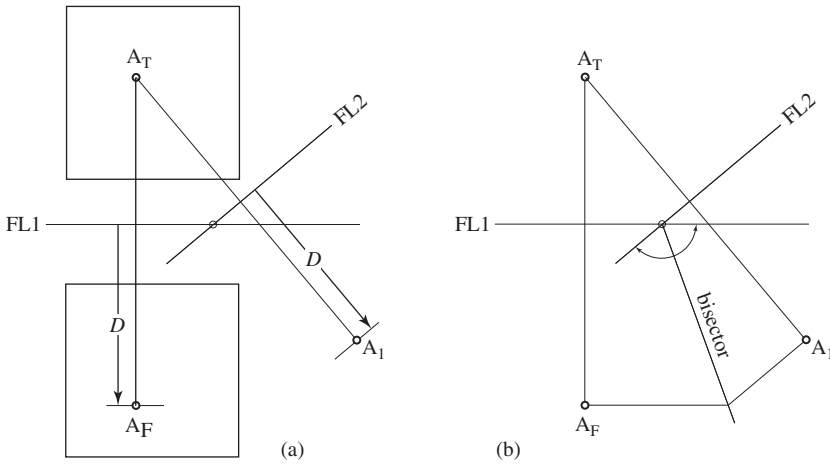


**Figure A.7** Projection of a point to a vertical auxiliary plane.

*Inclined auxiliary view*

The projection of a point to a general auxiliary plane requires yet another step to take into account its angle of inclination, which is taken here to be  $60^\circ$ . The entire construction is usually performed on a single figure but three are used here to make the several steps clearer. As before *FL2* fixes the line of intersection of the auxiliary plane with the Top View. A second folding line *FL3* is then drawn perpendicular to *FL2* (Fig. A.8a).

Use the second folding line to establish a view of the inclined auxiliary plane of the profile. The image point  $A_F$  is projected to it. This locates the image point  $A_1$  on the trace. This point is then projected to the *FL3*, using distance  $D_1$  or intersecting projection lines to locate the point on the required horizontal plane (Fig. A.8b). The final location of image point  $A_1$  is then added to the horizontal representation of the auxiliary view (Fig. A.8c).

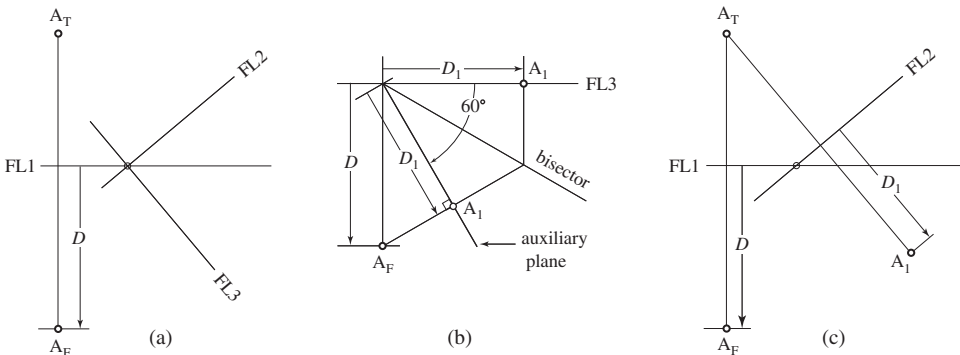


**Figure A.8** Projection of a point to a general auxiliary plane.

### A.6 Projection of a line

The projection of a line segment involves a straightforward application of the previous methods for a single point. We now simply project the two end points individually to the required view.

Using the first method, determine the distances  $D_A$  and  $D_B$  of the image points  $A_F$  and  $B_F$  on the Front View and then transfer these to the Side View to locate the image points  $A_S$  and  $B_S$  (Fig. A.9a).

With the second method, the projection lines from points  $A_T$  and  $B_T$  are extended directly to the Side View and from  $A_F$  and  $B_F$  the Side View via the bisector to locate  $A_S$  and  $B_S$  at the intersections (Fig. A.9b).

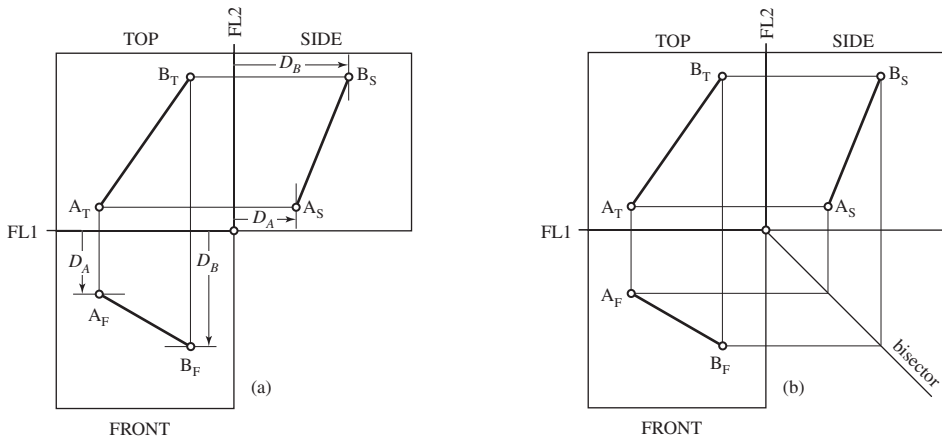


**Figure A.9** Projection of a line to a principal plane.

### A.7 Length of a line

An important special case is the projection of the line segment to the auxiliary plane on which it appears in true length (TL). There are an infinite number of such views, but it is most convenient to choose the vertical plane parallel to the image of the line in the Top View, so we draw  $FL2$  parallel to this trace. The construction of the image on the auxiliary plane is the same as in the previous example.

With the first method, distances  $D_A$  and  $D_B$  are determined on the Front View and then transferred to the Side View (Fig. A.10a).

Using the second method, the projection lines are extended from the Front View to the Side View. In both cases the segment  $A_1B_1$  is the true length (Fig. A.10b).<sup>4</sup>

<sup>4</sup>We now have the *trend* and *plunge* of the line.

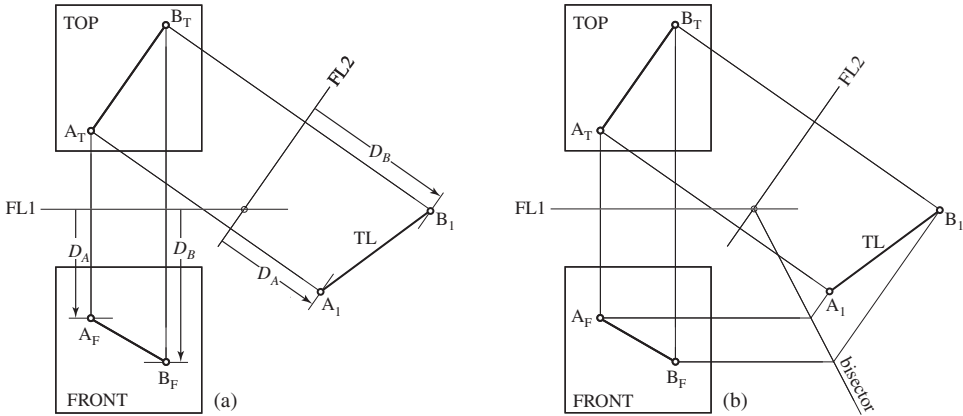


Figure A.10 True length of a line segment.

### A.8 Point view of a line

A final case involves constructing a view of an end or *point view* of a line. We will not often need such a view directly, but it will be used in conjunctions in another construction.

Having obtained the view of the true length of a line segment, draw *FL2* perpendicular to this line and extend the projection lines from the Top and Front Views to this new auxiliary view, using either the dimension *D* (Fig. A.11a) or intersecting projection lines (Fig. A.11b).

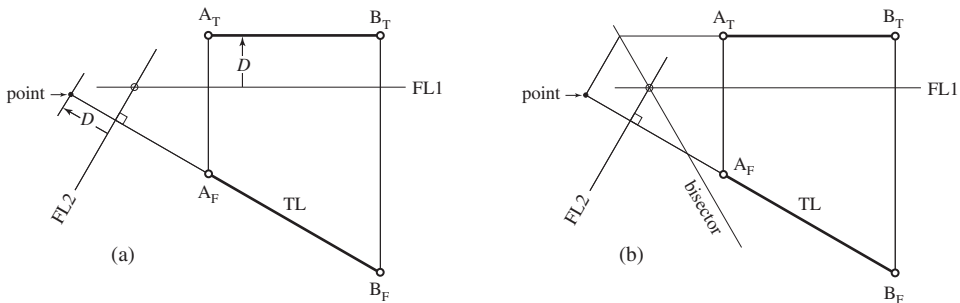


Figure A.11 Point view of a line.

### A.9 Projection of a plane

The next class of projections involves a plane area. The simplest representation of such an element of area is a triangle. Other areas can be built up from a series of such triangles. Just as the projection of a line involved two points, the projection of a plane involves three points.

To illustrate the general method, we choose to project the plane from the Top and Front Views to a vertical auxiliary view.

The first method uses the distances  $D_A$ ,  $D_B$  and  $D_C$  determined on the Front View which are then transferred to the auxiliary view to fix the locations of the image points  $A_1$ ,  $B_1$  and  $C_1$  (Fig. A.12a).

The second method extends the projection lines directly from the Top View and the projection lines from the Front View via the bisector of the obtuse angle between  $FL1$  and  $FL2$  to the auxiliary view (Fig. A.12b).

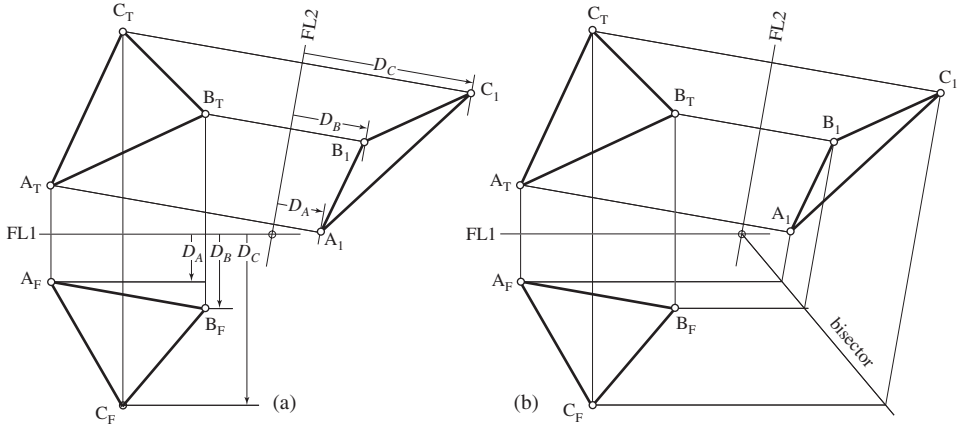


Figure A.12 Projection of a plane.

### A.10 Edge view of a plane

An important special case is the projection of the triangle to the auxiliary view where it appears as in edge view.

The first step is to draw a horizontal line on the Front View from the point of intermediate elevation  $B_F$  to locate point  $B'_F$  on the opposite side (Fig. A.13a). This point is then projected back to the Top View to locate point  $B'_T$ . Line  $B_T B'_T$  appears in its true length. Folding line  $FL2$  is then drawn perpendicular to the line.

Distances  $D_A$ ,  $D_B$  and  $D_C$ , determined on the Front View, are transferred to the auxiliary view. Note that line  $B_T B'_T$  appears in point view.<sup>5</sup>

Alternatively, the points  $A_T, B_T$  and  $C_T$  are projected directly and points  $A_F, B_F$  and  $C_F$  are projected via the bisector to the auxiliary view (Fig. A.13b).

### A.11 Normal view of a plane

The *true shape* (TS) of the plane requires the construction of the normal view, and this in turn requires that a view of the plane in edge view be obtained, as in the previous section

<sup>5</sup>We now have found the *strike* and *dip* of the plane.

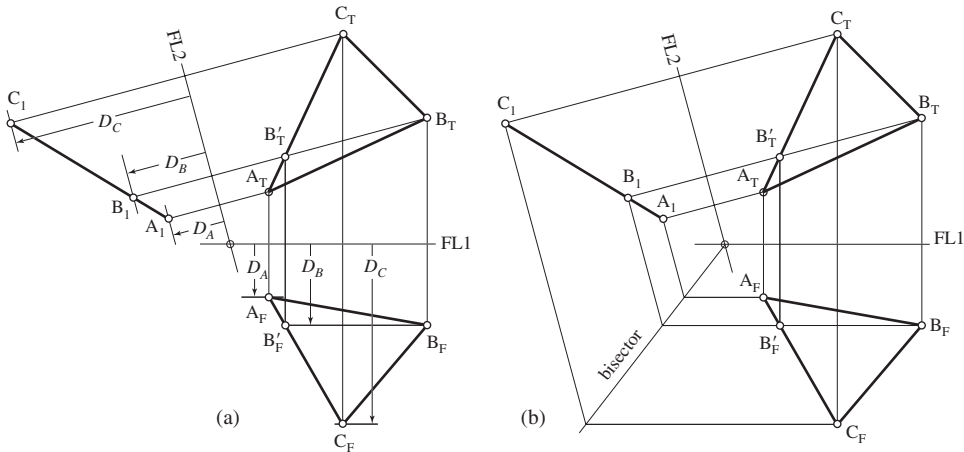


**Figure A.13** Edge view of a triangular element.

(Fig. A.14). Then  $FL3$  is drawn parallel to the trace of the plane in this view. Distances  $D_A$ ,  $D_B$  and  $D_C$  are determined on the Top View and transferred to the required auxiliary view to give points  $A_2$ ,  $B_2$  and  $C_2$ . These are the corners of the triangle in the required view.

In principle, the second method can also be used. In this example, however, there is a problem. When the bisected angle is small, the crossover points on the bisector may be located at some considerable distance. Figure A.14 shows this construction for point  $A$ , where this difficulty is apparent. If the projection lines for points  $B$  and  $C$  were similarly constructed, the figure would be more than double in size. This is usually not practical.

**A.12 Coordinate geometry and vector components**

The final case is to determine the true size (TS) of the triangular element. From two principal views, this requires an auxiliary plane that displays the triangle in normal view.

Our goal has been to describe purely graphical methods for presenting and analyzing points, lines and planes. There are, however, other methods and it is useful to indicate the connection of these with the methods of orthographic projection.

To do this we establish a right-handed Cartesian coordinate system (Fig. A.15a). We can then assign coordinates to image points on the three principal planes:  $A_T(x, y)$ ,  $A_F(y, z)$  and  $A_S(x, z)$ . With any two of these we then have the coordinates of the spatial point  $A(x, y, z)$  (Fig. A.15b).

Similarly, for two points we have  $A(x, y, z)$  and  $B(x, y, z)$ . With these we can then find the equation of the line, and determine associated properties including its orientation and its length.

Finally for three points  $A(x, y, z)$ ,  $B(x, y, z)$  and  $C(x, y, z)$  we can find the equation of the plane and its properties.

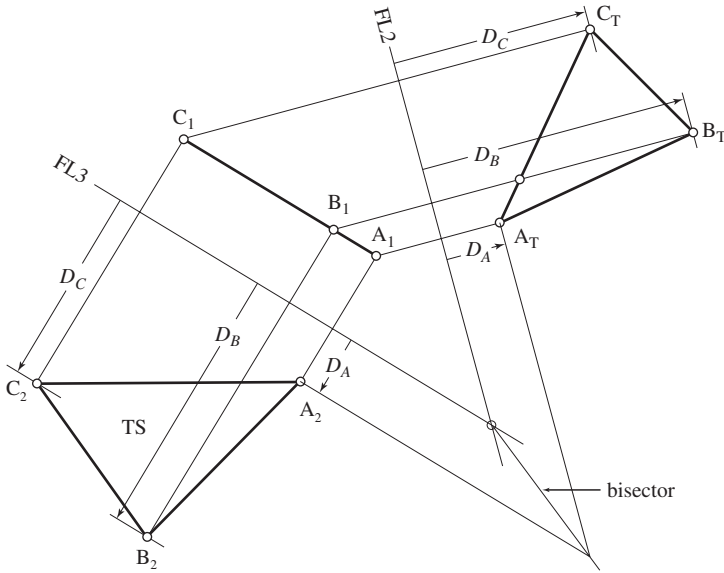


**Figure A.14** Normal view of a triangular element.

In a closely related way, points on the principal image planes can be represented by position vectors  $\mathbf{A}_T(x, y)$ ,  $\mathbf{A}_F(y, z)$  and  $\mathbf{A}_S(x, z)$  (Fig. A.15c). With these we then have the position vector for the points A in three dimensions  $\mathbf{A}(x, y, z)$ .

With a second position vector  $\mathbf{B}(x, y, z)$  we can form the vector from points A to B. Similarly, with a third vector  $\mathbf{C}$  we can find the vector from, say, points A to C. From these two, we can then form the vector dot product to obtain the area of the triangle and cross product to obtain its orientation (see §7.3).

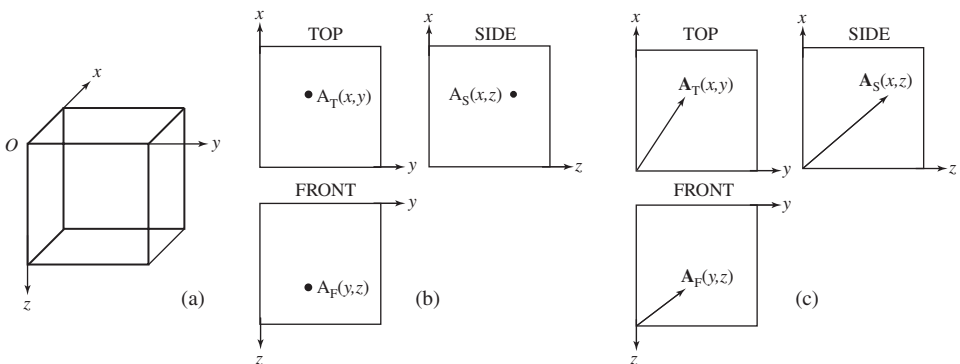


**Figure A.15** Coordinate geometry: (a) coordinate axes; (b) principal coordinate planes; (c) vectors.

# Appendix B

## Spherical trigonometry

### B.1 Introduction

A spherical triangle is a figure on the surface of a sphere bounded by the arcs of three great circles (Fig. B.1a). It has six parts: three *angles*  $A$ ,  $B$  and  $C$  and three opposite *sides*  $a$ ,  $b$  and  $c$ . Each angle is measured by the angle between the two planes whose traces are the intersecting great circles and each side by the angle it subtends at the center of the sphere.

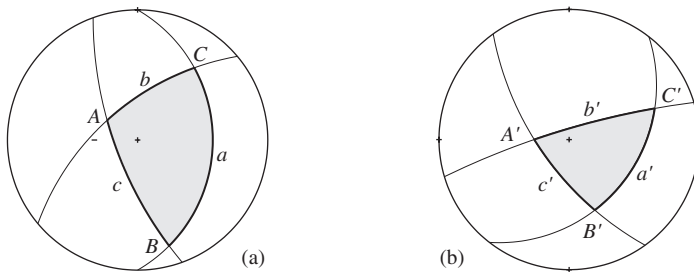


**Figure B.1** Stereogram: (a) general spherical triangle; (b) corresponding polar triangle.

Plane and spherical triangles differ in several ways but there are also some similarities despite the fact that one deals with two dimensions and the other with three. This similarity accounts for much of the power of spherical trigonometry. The Laws of Sines for plane and spherical triangles are

$$\frac{\sin A}{a} = \frac{\sin B}{b} = \frac{\sin C}{c} \quad \text{and} \quad \frac{\sin A}{\sin a} = \frac{\sin B}{\sin b} = \frac{\sin C}{\sin c}.$$

The form of each of these is identical. The only difference is due to the fact that the sides of spherical triangles are measured in angles, not lengths as is the case in plane triangles.



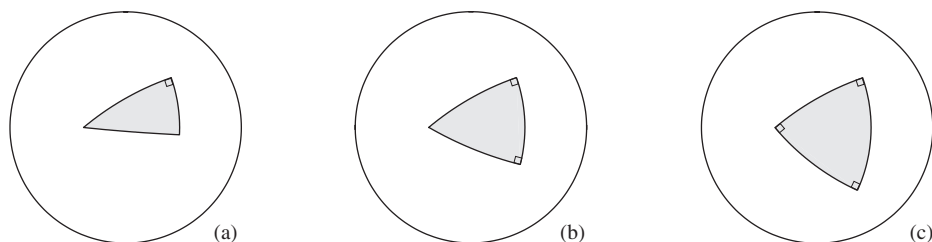


**Figure B.2** Triangles with  $90^\circ$  angles; (a) right-triangle; (b) birectangular; (c) trirectangular.

Spherical triangles arise in many stereographic constructions and for problems involving these spherical trigonometry is an attractive way of obtaining solutions quickly and accurately. Additional background and problems can be found in Higgs and Tunnell (1966) and in Phillips (1971). A number of closely related crystallographic applications are described by Phillips (1963).<sup>1</sup>

## B.2 General properties

Every spherical triangle has a corresponding *polar triangle*, which is formed by locating the poles of each of the three sides of the original triangle  $A'$ ,  $B'$  and  $C'$  and then connecting each pair of these points with the arcs of great circles  $a'$ ,  $b'$  and  $c'$  (Fig. B.1b). These two types of triangles have a number of important properties (Palmer, *et al.* 1950, p. 193):

1. The sum of the sides is less than  $360^\circ$ .
2. The sum of the angles is greater than  $180^\circ$  and less than  $540^\circ$ . A consequence is that any unknown angle can not be found directly from the other two angles.
3. If two angle are equal, the sides opposite are equal, and conversely.
4. If two sides are unequal, the angles opposite them are unequal, and the greater angle lies opposite the greater side, and conversely.
5. The sum of two sides is greater than the third side.
6. If one triangle is the polar of another, then the latter is the polar triangle of the former.
7. The sides and the angles of a spherical triangle are the supplements, respectively, of the opposite angles and sides in the polar triangle, and conversely.

## B.3 Right-spherical triangles

One class of spherical triangles contains a  $90^\circ$  angle. If only one is present it is known as a *right-spherical* or *Napierian triangle*<sup>2</sup> (Fig. B.2a). In special sub-cases, there may be two (Fig. B.2b) or three  $90^\circ$  angles (Fig. B.2c).

<sup>1</sup>The subject seems to have fallen out of general favor; the book by Palmer, Leigh and Kimball (1950) is the most recent on the subject in our library.

<sup>2</sup>John Napier [1550–1617], a Scottish theologian and amateur mathematician, invented logarithms and the decimal point notation, and contributed to the theory of spherical triangles.

The important case involves a single  $90^\circ$  angle. If any two of the remaining five parts are known, any unknown third part can be determined. Ten special cases cover all possible situations and the separate formulas are readily available (Zwillinger, 1996, p. 468). These are not needed, however, because all may be easily formulated with the aid of *Napier's rules*.

1. The *sine* of any middle part is equal to the product of the *tangents* of the two *adjacent* parts.
2. The *sine* of any middle part is equal to the product of *cosines* of the two *opposite* parts.

These rules are easily remembered by noting that the letter *A* occurs in both the words tangent and adjacent, and the letter *O* in both cosine and opposite. The middle, adjacent and opposite parts are easily identified with a simple diagram known as *Napier's device* – a circle divided into five sectors, each containing the value of one of the five parts. Two known parts together with any unknown third part will always be arranged in the compartments so that three parts are all adjacent, or two parts are opposite a third. Figure B.3 shows typical distributions of the middle, adjacent and opposite parts.

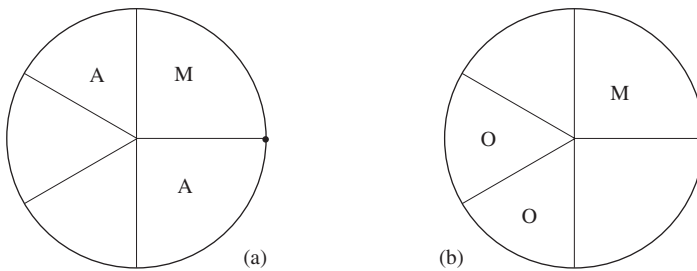


**Figure B.3** Napier's device: (a) middle *M* and adjacent *A* parts; (b) middle *M* and opposite *O* parts.

These five parts of the triangle are labeled 1–5, starting from the right angle (Fig. B.4a). Each time a problem is to be solved, the device is sketched and the value of each known and unknown part is entered in the appropriate sector in cyclical order, starting with the horizontal radius on the right. The values written to the left of the vertical diameter are the complementary angles of the appropriate parts (Fig. B.4b). The order may be taken in either a clockwise or anticlockwise direction so long as the pattern is consistent in both the triangle and the device. We adopt an anticlockwise sense here.

In a closely related case, the triangle may contain a  $90^\circ$  side (Fig. B.5a). The solution of any unknown part is obtained from the corresponding *polar triangle* (Fig. B.5b). In practice, this figure is not actually needed. Starting the numbering scheme from the  $90^\circ$  side, the five parts are entered as before, except that supplementary angles are now used (Fig. B.5c).

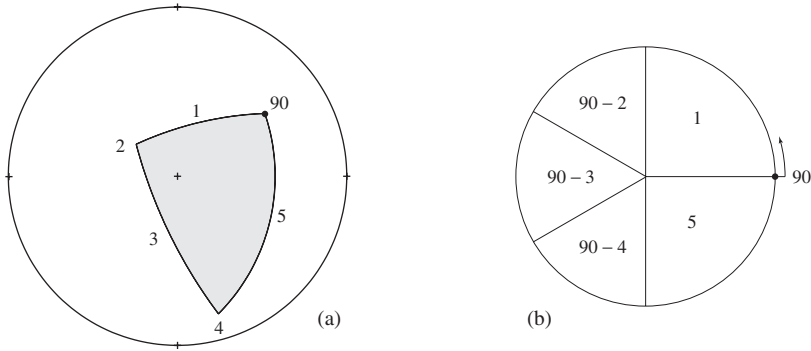


**Figure B.4** Right-spherical triangle: (a)  $90^\circ$  angle; (b) Napier's device.

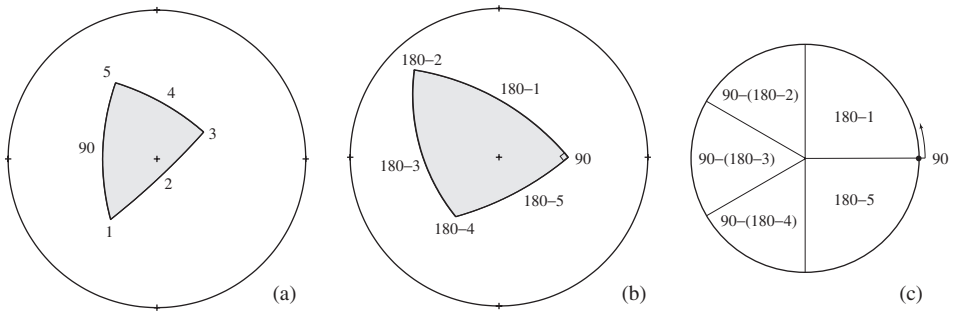


**Figure B.5** Right-spherical triangles: (a)  $90^\circ$  side; (b) polar equivalent; (c) Napier's device.

**Table B.1** *Functions in terms of angles in the first quadrant*

	$-x$	$90 \pm x$	$180 \pm x$
sin	$-\sin x$	$+\cos x$	$\mp \sin x$
cos	$+\cos x$	$\mp \sin x$	$-\cos x$
tan	$-\tan x$	$\mp 1/\tan x$	$\pm \tan x$

The formulas which result from the application of Napier's rules can be simplified by using one of the identities in Table B.1, or the identities for the composite angles

$$\sin[90 - (180 - x)] = \sin(x - 90) = -\cos x, \tag{B.1a}$$

$$\cos[90 - (180 - x)] = \cos(x - 90) = +\sin x, \tag{B.1b}$$

$$\tan[90 - (180 - x)] = \tan(x - 90) = -1/\tan x. \tag{B.1c}$$

### B.4 Examples of right-triangles

The methods of spherical trigonometry can be used both to obtain a numerical result to a specific problem or to obtain a general formula for an entire class of problems.

#### Apparent dip

Given the dip, determine the apparent dip in the direction specified by its structural bearing. This problem was treated in Fig. 1.10 and Eq. 1.5 where the analytical solution was obtained by using plane trigonometry. The solution also applies to the plunge of a line in a plane treated in Fig. 3.3 and Eq. 3.3.

1. Number the elements of the problem (Fig. B.6a): Part 1 =  $\alpha$  (unknown apparent dip), Part 4 =  $\delta$  (dip), and Part 5 =  $\beta$  (bearing). Note that  $\delta$  is assigned to the point of intersection of the two planes; in the usual stereographic construction  $\delta$  is a side of a triangle, not an angle.
2. Sketch Napier's device and enter the values of the corresponding parts: Part 1 =  $\alpha$ , Part 4 =  $90 - \delta$ , and Part 5 =  $\beta$  (Fig. B.6b). Note that Parts 2 and 3 are not used.
3. Applying the first of Napier's rules gives

$$\sin \beta = \tan \alpha \tan(90 - \delta) \quad \text{or} \quad \boxed{\tan \alpha = \tan \delta \sin \beta.} \quad (\text{B.2})$$

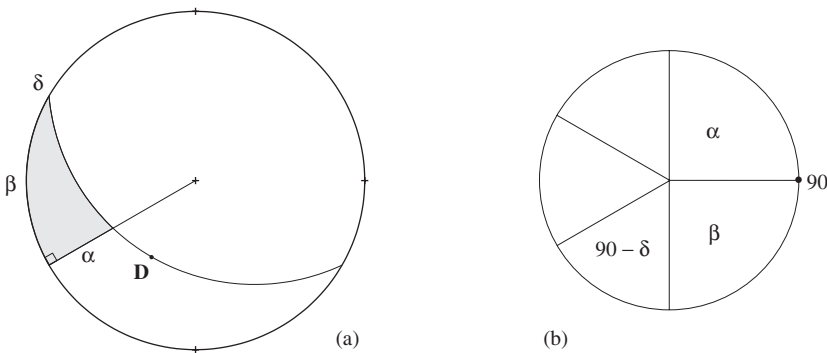


Figure B.6 Apparent dip: (a) stereogram; (b) device.

#### Pitch

Given the dip of a plane and the structural bearing of a line on it, determine the pitch of the line (see also Fig. 3.8 and Eq. 3.4).

1. Label the elements of the spherical triangle (Fig. B.7a): Part 3 =  $r$  (pitch), Part 4 =  $\delta$  (dip), and Part 5 =  $\beta$  (bearing).

2. Sketch the device and fill in compartments for Part 3 =  $90 - r$ , Part 4 =  $90 - \delta$ , and Part 5 =  $\beta$  (Fig. B.7b).
3. Applying Napier's Rule 2 gives

$$\sin(90 - \delta) = \tan(90 - r) \tan \beta \quad \text{or} \quad \boxed{\tan r = \tan \beta / \cos \delta.} \quad (\text{B.3})$$

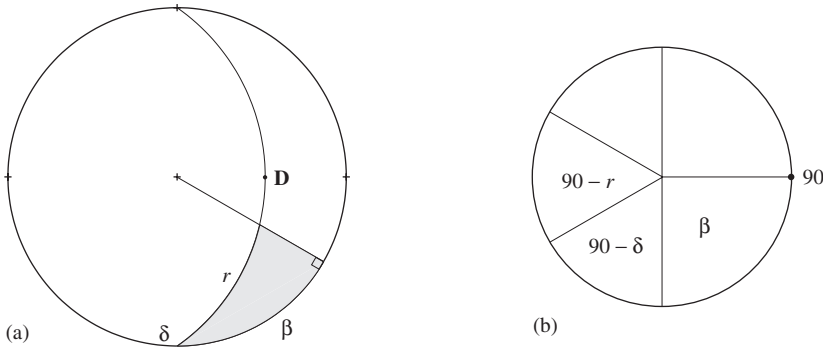


Figure B.7 Pitch: (a) stereogram; (b) device.

*Pitch and plunge*

Given the plunge of a line in a plane determine its pitch.

1. Label the elements of the spherical triangle (Fig. B.8a): Part 1 =  $p$  (plunge), Part 3 =  $r$  (pitch), and Part 4 =  $\delta$  (dip).
2. Sketch the device and fill in compartments for Part 1 =  $p$ , Part 3 =  $90 - r$ , and Part 4 =  $90 - \delta$  (Fig. B.8b).
3. Applying Napier's Rule 1 gives

$$\sin p = \cos(90 - r) \cos(90 - \delta) \quad \text{or} \quad \boxed{\sin r = \sin p / \sin \delta.} \quad (\text{B.4})$$

*Strike error*

Determine the maximum strike error given the dip of a structural plane and the maximum operator error (see Fig. 5.22a).

1. Label the elements of the triangle (Fig. B.9a): Part 2 =  $\epsilon_S$  (maximum strike error), Part 3 =  $\delta$  (dip), and Part 5 =  $\epsilon_O$  (maximum operator error).
2. Sketch the device and fill in compartments for Part 2 =  $90 - \epsilon_S$ , Part 3 =  $90 - \delta$ , and Part 5 =  $\epsilon_O$  (Fig. B.9b).

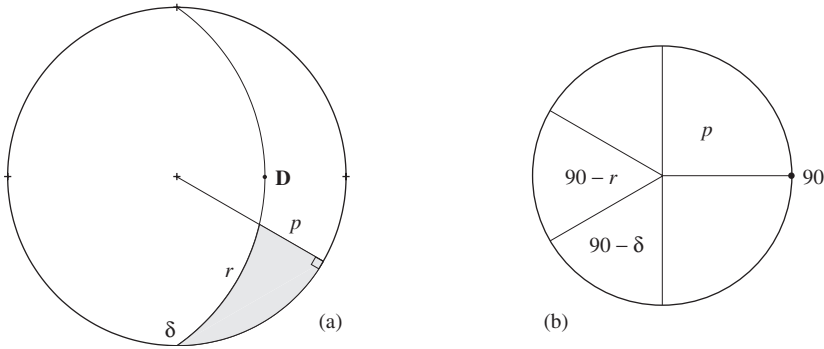


Figure B.8 Pitch and plunge: (a) stereogram; (b) device.

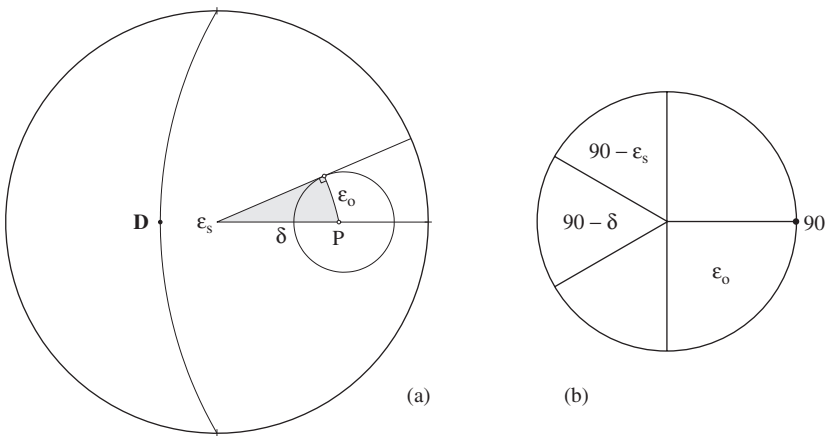


Figure B.9 Strike error: (a) stereogram; (b) device.

3. Applying Napier's Rule 1 gives

$$\sin \epsilon_O = \cos(90 - \epsilon_S) \cos(90 - \delta) \quad \text{or} \quad \boxed{\sin \epsilon_S = \sin \epsilon_O / \sin \delta.} \quad (\text{B.5})$$

*Direction cosines*

For triangles with a 90° side it is sometimes possible to reduce problems to the simpler case of two triangles with 90° angles. The problem illustrated here is the conversion of plunge and trend to direction cosines (compare Fig. 7.3 and Eqs. 7.7).

1. Plot the point representing the plunging line and draw the circular arcs between this point and the three coordinate axes +x, +y and +z. The measured angles along these arcs are the direction angles  $\alpha$ ,  $\beta$  and  $\gamma$  (Fig. B.10a).

2. The spherical triangle whose sides are these direction angles does not contain a  $90^\circ$  element. However, if the trace of the vertical plane containing the line is added to the diagram two right-triangles result.

(a) From Triangle 1 and the corresponding device (Fig. B.10b), by Napier's Rule 2 we obtain

$$\sin(90 - \alpha) = \cos p \cos t \quad \text{or} \quad \boxed{l = \cos \alpha = \cos p \cos t.} \quad (\text{B.6a})$$

(b) From Triangle 2 and, again, Napier's Rule 2 and the corresponding device (Fig. B.10c)

$$\sin(90 - \beta) = \cos p \cos(90 - t) \quad \text{or} \quad \boxed{m = \cos \beta = \cos p \sin t.} \quad (\text{B.6b})$$

(c) Finally from simple geometry

$$\cos \gamma = \cos(90 - p) \quad \text{or} \quad \boxed{n = \cos \gamma = \sin p.} \quad (\text{B.6c})$$

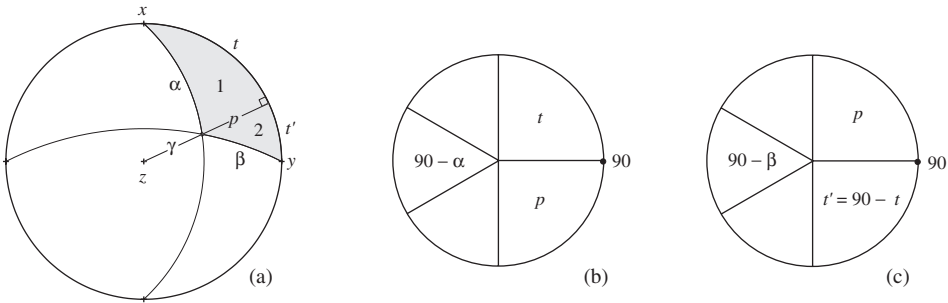


**Figure B.10** Direction cosines: (a) stereogram; (b) first device; (c) second device.

*Intersection errors*

The problem of the maximum error associated with the line of intersection of two planes was treated in Fig. 5.23. The derivation involves the solutions of two separate triangles.

1. First, the triangle with a  $90^\circ$  angle (Fig. B.11a): Sketch a device and enter the values: Part 3 =  $90 - \frac{1}{2}\delta$ , Part 4 =  $90 - B_1$ , and Part 5 =  $\epsilon_O$  (Fig. B.11b). Then Rule 1 gives

$$\sin(90 - B_1) = \tan(90 - \frac{1}{2}d) \tan \epsilon_O.$$

With  $\sin(90 - B_1) = \cos B_1$  and  $\tan(90 - \frac{1}{2}d) = 1 / \tan \frac{1}{2}d$  we have

$$\boxed{\cos B_1 = \tan \epsilon_O / \tan \frac{1}{2}d.} \quad (\text{B.7a})$$

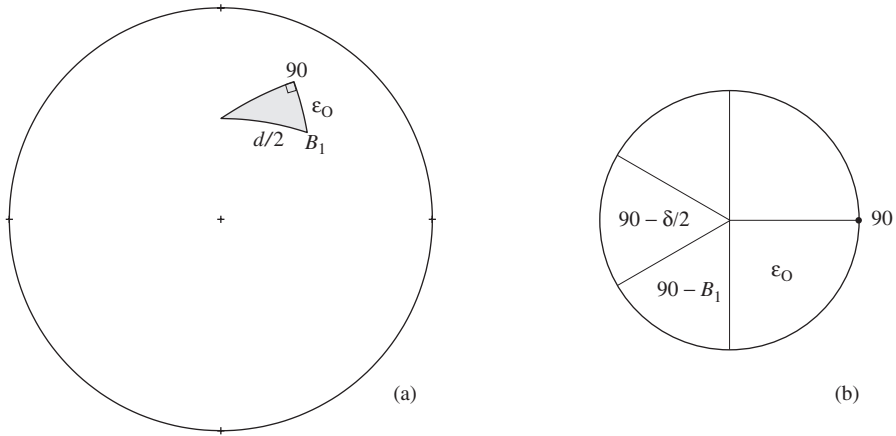


**Figure B.11** Intersection error (first triangle): (a) stereogram; (b) device.

2. Second, the triangle with a  $90^\circ$  side (Fig. B.12a): Sketch a device and enter the values: Part 2 =  $90 - (180 - \epsilon_T)$ , Part 4 =  $90 - [180 - (90 - \epsilon_T)]$ , and Part 5 =  $180 - B_2$  (Fig. B.12b). Then Rule 2 gives

$$\sin[90 - (180 - \epsilon_T)] = \cos(180 - B_2) \cos[90 - (180 - (90 - \epsilon_O))].$$

Making the substitutions

$$\begin{aligned} -\cos \epsilon_T &= \sin[90 - (180 - \epsilon_T)], \\ -\cos B_2 &= \cos(180 - B_2), \\ +\cos \epsilon_O &= \cos[90 - (180 - (90 - \epsilon_O))], \end{aligned}$$

this becomes

$$\boxed{\cos B_2 = \cos \epsilon_T / \cos \epsilon_O.} \tag{B.7b}$$

### B.5 Oblique-spherical triangles

The data may be such that the resulting spherical triangle has no  $90^\circ$  part and it is then termed *oblique*. For such triangles we need three parts to solve for any unknown fourth part. With the scheme used for plane triangles, the three angles are labeled  $A$ ,  $B$  and  $C$  and the three opposite sides  $a$ ,  $b$  and  $c$ .

A number of formulas are available for solving for any unknown part of such triangles, but the following list is sufficient for most purposes. Some derivations are given in Higgs and Tunell (1966) and Palmer, *et al.* (1950), and Zwillinger (1996, p. 469–471) gives a more complete compilation.



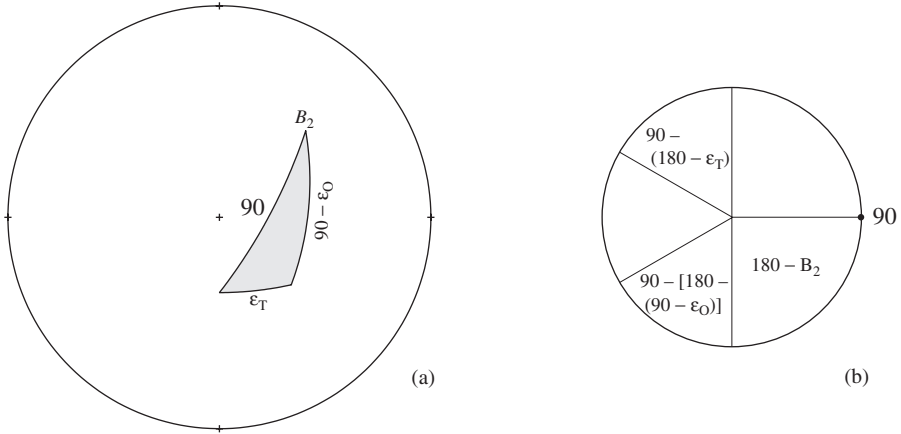


**Figure B.12** Intersection error (second triangle): (a) stereogram; (b) device.

One reason for the large number of formulas is to cover all possible labeling patterns, though it is often simpler to label the known and unknown elements so that just one from the group will do (Fig. B.13). However, the alternative forms serve as a useful way of checking the accuracy of the calculations.

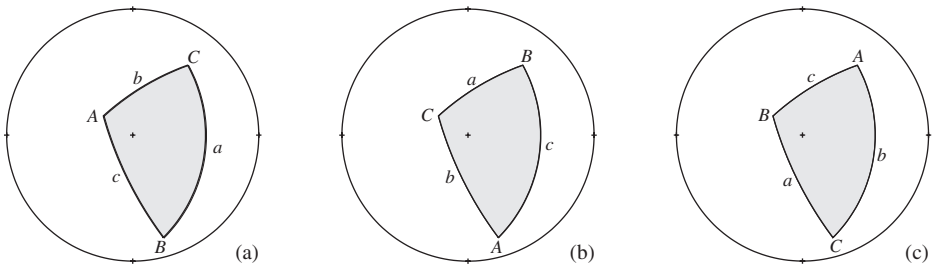


**Figure B.13** Three alternative labeling patterns.

**Law of Sines**

$$\frac{\sin A}{\sin a} = \frac{\sin B}{\sin b} = \frac{\sin C}{\sin c}. \tag{B.8}$$

**Law of Cosines for Sides**

$$\cos a = \cos b \cos c + \sin b \sin c \cos A, \tag{B.9a}$$

$$\cos b = \cos c \cos a + \sin c \sin a \cos B, \tag{B.9b}$$

$$\cos c = \cos a \cos b + \sin a \sin b \cos C. \tag{B.9c}$$

### Law of Cosines for Angles

$$\cos A = -\cos B \cos C + \sin B \sin C \cos a, \quad (\text{B.10a})$$

$$\cos B = -\cos C \cos A + \sin C \sin A \cos b, \quad (\text{B.10b})$$

$$\cos C = -\cos A \cos B + \sin A \sin B \cos c. \quad (\text{B.10c})$$

### Napier's Analogies

$$\frac{\sin \frac{1}{2}(A - B)}{\sin \frac{1}{2}(A + B)} = \frac{\tan \frac{1}{2}(a - b)}{\tan \frac{1}{2}c}, \quad \frac{\sin \frac{1}{2}(a - b)}{\sin \frac{1}{2}(a + b)} = \frac{\tan \frac{1}{2}(A - B)}{\cot \frac{1}{2}C}, \quad (\text{B.11a})$$

$$\frac{\cos \frac{1}{2}(A - B)}{\cos \frac{1}{2}(A + B)} = \frac{\tan \frac{1}{2}(a + b)}{\tan \frac{1}{2}c}, \quad \frac{\cos \frac{1}{2}(a - b)}{\sin \frac{1}{2}(a + b)} = \frac{\tan \frac{1}{2}(A + B)}{\cot \frac{1}{2}C}. \quad (\text{B.11b})$$

In solving oblique spherical triangles, two situations arise. In the first, the distribution of the known elements is such that any unknown part can be obtained unambiguously. In the second, there may be two solutions. In problems involving these cases, there are a variety of ways of obtaining solutions; we illustrate only one way.

#### *Unambiguous cases*

1. Two sides and included angle are known ( $b, A, c$ ): solve Eq. B.9a directly for the unknown side  $a$

$$\cos a = \cos b \cos c + \sin b \sin c \cos A,$$

and all sides are known.

2. Two angles and included side are known ( $B, a, C$ ): solve Eq. B.10a directly for angle  $A$

$$\cos A = -\cos B \cos C + \sin B \sin C \cos a,$$

and all angles are known.

3. All sides are known ( $a, b, c$ ): solve Eqs. B.9 for each of the three unknown angles

$$\cos A = \frac{\cos a - \cos b \cos c}{\sin b \sin c}, \quad \cos B = \frac{\cos b - \cos c \cos a}{\sin c \sin a},$$

$$\cos C = \frac{\cos c - \cos a \cos b}{\sin a \sin b}.$$

4. All angles are known ( $A, B, C$ ): solve Eqs. B.10 for each of the three unknown sides

$$\cos a = \frac{\cos A + \cos B \cos C}{\sin B \sin C}, \quad \cos b = \frac{\cos B + \cos C \cos A}{\sin C \sin A},$$

$$\cos c = \frac{\cos C + \cos A \cos B}{\sin A \sin B}.$$

*Ambiguous cases*

1. Two angles and the side opposite one of them are known ( $a, b, A; a \neq b$ ). There are two solutions if  $a < b$ ; the second is found by replacing  $B$  with its supplementary angle  $\arccos(-\cos B)$ :

(a) Solve Eq. B.8 for unknown side  $B$ ,

$$\sin B = \frac{\sin A \sin b}{\sin a},$$

(b) then the first of Eqs. B.11a for unknown side  $c$ ,

$$\tan \frac{1}{2}c = \frac{\sin \frac{1}{2}(A + B) \tan \frac{1}{2}(a - b)}{\sin \frac{1}{2}(A - B)},$$

(c) and then Eq. B.10c for the unknown angle  $C$ ,

$$\cos A = \frac{\cos c - \sin a \sin b}{\sin a \sin b}.$$

2. Two sides and the angle opposite one of them are known ( $A, B, a; A \neq B$ ). There are two solutions if  $A < B$ ; the second is found by replacing  $b$  with its supplementary angle  $\arccos(-\cos b)$ :

(a) Solve Eq. B.8 for unknown side  $b$ ,

$$\sin b = \frac{\sin a \sin B}{\sin A},$$

(b) then Eq. B.9c for unknown angle  $C$ ,

$$\cos C = \frac{\cos c - \cos a \cos b}{\sin a \sin b},$$

(c) and then Eq. B.10c for the unknown side  $c$ ,

$$\cos c = \frac{\cos C + \cos A \cos B}{\sin A \sin B}.$$

**B.6 Examples of oblique triangles**

Several examples will illustrate how to obtain solutions in both the unambiguous and ambiguous oblique spherical triangles.

### Dihedral angle

Determine the dihedral angle between two intersecting planes (see construction of Fig. 5.18). This problem can also be solved using the dot product of two pole vectors (see §7.3). This is the unambiguous case of two angles and included side.

1. On a stereogram, the two planes are represented by great circles (Fig. B.14). The spherical triangle containing the unknown dihedral angle is formed by arcs of these two circles and the primitive.
2. Label the parts of this triangle so that the unknown angle is  $A$ , the dips of the two planes  $B$  and  $C$ , and the angle between the two strike directions  $a$ .
3. We may solve for angle  $A$  directly by using Eq. B.10a:

$$\cos A = -\cos B \cos C + \sin B \sin C \cos a$$

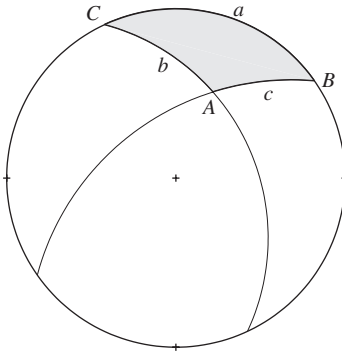


**Figure B.14** Dihedral angle.

### Drill hole problem

Given the plunge and trend of a single drill hole which intersects a plane, the measured core–pole angle in the recovered core, and the known strike of the beds, what is the dip of the plane? This type of problem was treated graphically in Fig. 20.5a. This is the ambiguous case of two angles and a side opposite one of them.

1. On a stereogram, point  $C$  represents the inclined drill hole; a radius of the net through this point and a radius in the dip direction (normal to the given strike) define angle  $A$ . A small circle with radius equal to the core–pole angle  $\phi$  is the locus of all possible poles to the plane.
2. The actual poles of the possible planes are located at the points of intersection of the strike-normal radius and the small circle, labeled  $B_1$  and  $B_2$ . With these two we can then find the possible values of sides  $c_1$  and  $c_2$ . These are the complements of the plunge angles for the two poles.

- (a) First solution (Fig. B.15a): labeling the angle between the two radii  $A$ , the angular radius of the small circle  $a$  and the side between  $A$  and  $B_1$  as  $c_1$ . Find the unknown value by solving Eq. B.8 for  $B$

$$\sin B_1 = \sin A \sin b / \sin a.$$

Then with the first of Eqs. B.11a

$$\tan \frac{1}{2}c_1 = \frac{\sin \frac{1}{2}(A + B_1) \tan \frac{1}{2}(a - b)}{\sin \frac{1}{2}(A - B_1)},$$

and the first possible dip  $\delta_1 = 2 \arctan \frac{1}{2}c_1$ .

- (b) Second solution (Fig. B.15b): the value of the second angle is  $B_2 = \arccos(-\cos B_1)$ . Then the second possible value of side  $c$  is

$$\tan \frac{1}{2}c_2 = \frac{\sin \frac{1}{2}(A + B_2) \tan \frac{1}{2}(a - b)}{\sin \frac{1}{2}(A - B_2)},$$

and the second possible dip  $\delta_2 = 2 \arctan \frac{1}{2}c_2$ .

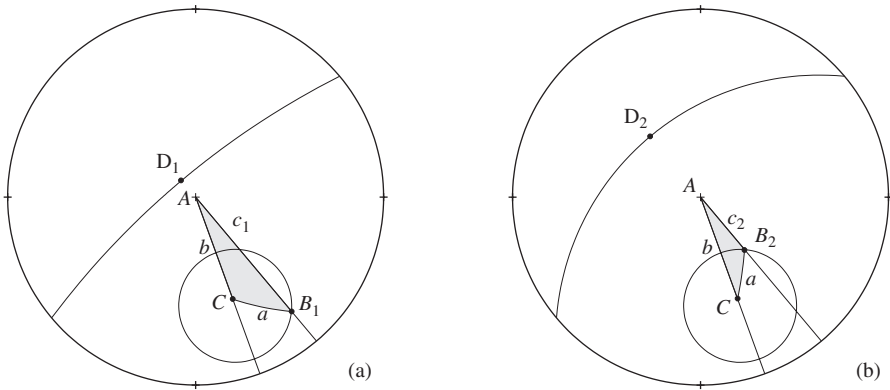


**Figure B.15** Drill hole problem: (a) first solution; (b) second solution.

# References

- Ailleres, L., & M. Campenois, 1994, Refinements to the Fry method (1979) using image processing: *Journal of Structural Geology*, v. 16, p. 1327–1330.
- Alcock, J., 1994a, Simulating the historical process to create laboratory exercises that teach research methods: *Journal of Geological Education*, v. 42, p. 118–124.
- Alcock, J., 1994b, The discordant Doe Run thrust: implications for stratigraphy and structure in the Glenarm Supergroup, southeastern Pennsylvania Piedmont: *Geological Society of America Bulletin*, v. 106, p. 932–941.
- Allmendinger, R.W., 2001, [www.geo.cornell.edu/geology/faculty/RWA/RWA.html](http://www.geo.cornell.edu/geology/faculty/RWA/RWA.html)
- Anderson, E.M., 1951, *The Dynamics of Faulting*: Second Edition, Oliver & Boyd, Edinburgh.
- Angelier, J., 1994, Fault slip analysis and paleostress reconstruction: in P.L. Hancock, editor, *Continental Deformation*, Pergamon Press, Oxford, pp. 53–100.
- Argand, E., 1911, Les nappes de recouvrement des Alpes Pennines et leurs prolongement structuraux: *Beiträge zur geologischen Karte der Schweiz*, nue Folge 31, p. 1–26.
- Aydin, A., & Z. Reches, 1982, Number and orientation of fault sets in the field and in experiments: *Geology*, v. 10, p. 107–112.
- Badgley, P.C., 1959, *Structural Methods for the Exploration Geologist*: Harper & Row, New York.
- Badgley, P.C., 1965, *Structural and Tectonic Principles*: Harper & Row, New York.
- Bailey, E.B., & J.H. Mackin, 1937, Recumbent folding in the Pennsylvania Piedmont – preliminary statement: *American Journal of Science*, v. 33, p. 187–190.
- Balk, R., 1937, *Structural Behavior of Igneous Rock*: Geological Society of America Memoir 5.
- Bambach, R.K., 1973, Tectonic deformation of composite-mold fossil Bivalvia (Mollusca): *American Journal of Science*, v. 273-A, p. 409–430.
- Barnes, C.W., & R.W. Houston, 1969, Basement response to the Laramide Orogeny at Coad Mountain, Wyoming: *Contributions to Geology*, v. 8, p. 37–41.
- Barnes, J.W., 1995, *Basic Geologic Mapping*: Third Edition, Open University Press, Milton Keynes, UK.
- Batchelor, G.K., 1967, *An Introduction to Fluid Dynamics*: Cambridge University Press, Cambridge, 617 p.
- Bayly, M.B., 1971, Similar folds, buckling and great circle patterns: *Journal of Geology*, v. 79, p. 110–118.
- Beach, A., 1979, The analysis of deformed belemnites: *Journal of Structural Geology*, v. 1, p. 127–135.
- Bear, J., & Y. Bachmat, 1984, Transport phenomena in porous media – basic equations: in J. Bear & M.Y. Corapcioglu, editors, *Fundamentals of Transport Phenomena in Porous Media*, Martinus Nijhoff Publishers, Dordrecht, p. 3–61.
- Bell, A.M., 1981, Vergence: an evaluation: *Journal of Structural Geology*, v. 3, p. 197–202.

- Bengtson, C.A., 1983, Easy solutions stereonet rotation problems: *American Association of Petroleum Geologists Bulletin*, v. 67, p. 706–713.
- Bergbauer, S., & D.D. Pollard, 2003, How to calculate normal curvature of sampled geological surfaces: *Journal of Structural Geology*, v. 25, p. 277–289.
- Berthelsen, A., E. Bondesen & S.B. Jensen, 1962, On the so-called wildmigmatites: *Krystalinikum*, v. 1, p. 31–49.
- Bhattacharyya, T., & S. Longiaru, 1986, Ability of the Fry method to characterize pressure-solution deformation – discussion: *Tectonophysics*, v. 131, p. 199–200.
- Billings, M.P., 1972, *Structural Geology*: Third Edition, Prentice-Hall, Englewood Cliffs, N.J.
- Biot, M.A., 1961, Theory of folding of stratified viscoelastic media and its implications in tectonics and orogenesis: *Geological Society of America Bulletin*, v. 72, p. 1595–1631.
- Biot, M.A., H. Odé & W.L. Roever, 1961, Experimental verification of the theory of folding of stratified viscoelastic media: *Geological Society of America Bulletin*, v. 72, p. 1621–1620.
- Bjørnerud, M.G., 1991, Conveying principles of finite strain with standard graphics software: *Journal of Geological Education*, v. 39, p. 23–27.
- Bjørnerud, M.G., & B. Boyer, 1996, Image analysis in structural geology using NIH Image: in D.G. De Paor, editor, *Structural Geology and Personal Computers*, Pergamon, Oxford, p. 105–121.
- Boas, M.L., 1983, *Mathematical Methods in the Physical Sciences*: Second Edition, John Wiley, New York, 793 p.
- Bons, P., & M.W. Jessell, 1996, Image analysis of microstructures in natural and experimental samples: in D.G. De Paor, editor, *Structural Geology and Personal Computers*, Pergamon, Oxford, p. 135–166.
- Borowski, E.J., & J.M. Borwein, 1991, *The HarperCollins Dictionary of Mathematics*: HarperCollins Publishers.
- Borradaile, G.J., 1976, “Structural facing” (Shackleton’s Rule) and the Palaeozoic rocks of the Malaguide Complex near Velez Rubio, SE Spain: *Proceedings of the Koninklijke Nederlandse Akademie van Wetenschappen, Amsterdam, series B*, v. 79, p. 330–336.
- Borradaile, G.J., 1978, Transected folds: a study illustrated with examples from Canada and Scotland: *Geological Society of America Bulletin*, v. 89, p. 481–493.
- Borradaile, G.J., 2003, *Statistics of Earth Science Data: Their Distribution in Time, Space and Orientation*: Springer-Verlag, Heidelberg.
- Borradaile, G.J., & J. McArthur, 1991, Tests of strain analysis by experimental deformation: *Tectonophysics*, v. 185, p. 325–333.
- Bott, M.H.P., 1959, The mechanics of oblique-slip faulting: *Geological Magazine*, v. 96, p. 109–117.
- Boyce, W.E., & R.C. DiPrima, 1992, *Elementary Differential Equations and Boundary Value Problems*: Fifth Edition, John Wiley, New York.
- Boyer, S.E., & D. Elliott, 1982, Thrust systems: *American Association of Petroleum Geologists Bulletin*, v. 66, p. 1196–1230.
- Brown, E.T., S.J. Green & K.P. Sinha, 1981, The influence of rock anisotropy on hole deviation in rotary drilling – a review: *International Journal of Rock Mechanics and Mining Science & Geomechanical Abstracts*, v. 18, p. 387–401.
- Bucher, W.H., 1920, The mechanical interpretation of joints, part I: *Journal of Geology*, v. 28, p. 707–730.
- Busk, H.G., 1929, *Earth Flexures*: Cambridge University Press, Cambridge (republished by William Trusell, New York, 1957).
- Bussell, M.A., 1989, A simple method for the determination of the dilation direction of intrusive sheets: *Journal of Structural Geology*, v. 11, p. 679–687.
- Butler, R.W.H., 1982a, Hanging wall strain: a function of duplex shape and footwall topography: *Tectonophysics*, v. 88, p. 235–246.

- Butler, R.W.H., 1982b, The terminology in thrust zones: *Journal of Structural Geology*, v. 4, p. 239–245.
- Buxtorf, A., 1916, Prognosen und Befunden beim Hauensteinbasis- und Grenchenberg-tunnel und die Bedeutung der letzteren für die Geologie des Juragebirges: *Verhandlungen der Naturforschenden Gesellschaft in Basel*, v. 27, p. 184–254.
- Byerlee, J.D., 1978, Friction of rocks: *Pure and Applied Geophysics*, v. 116, p. 615–629.
- Carey, S.W., 1962, Folding: *Journal of the Alberta Society of Petroleum Geologists*, v. 10, p. 95–144.
- Carroll, R.T., 2003, *The Skeptic's Dictionary*: John Wiley & Sons, New York (see also <http://skepdic.com>).
- Chapple, W.M., 1968, A mathematical theory of finite-amplitude rock-folding: *Geological Society of America Bulletin*, v. 79, p. 47–68.
- Charlesworth, H.A.K., & W.E. Kilby, 1981, Calculating thickness from outcrop and drill-hole data: *Bulletin of Canadian Petroleum Geology*, v. 29, p. 277–292.
- Charlesworth, H.A.K., C.W. Lengenbergs & J. Ramsden, 1976, Determining axes, axial planes and sections of macroscopic folds using computer-based methods: *Canadian Journal of Earth Science*, v. 13, p. 54–65.
- Cheeny, R.F., 1983, *Statistical Methods in Geology*: George Allen & Unwin, London.
- Christensen, J.N., J.L. Rosenfeld & D.J. DePaolo, 1989, Rates of tectonometamorphic processes from rubidium and strontium isotopes in garnet, *Science*, v. 244, no. 4911, p. 1465–1469.
- Christensen, M.N., 1963, Structural analysis of Hoosac Nappe in northwestern Massachusetts: *American Journal of Science*, v. 261, p. 97–107.
- Clark, R.H., & D.B. McIntyre, 1951a, A macroscopic method of fabric analysis: *American Journal of Science*, v. 249, p. 755–768.
- Cloos, E., 1947, Oolite deformation in South Mountain fold, Maryland: *Geological Society of America Bulletin*, v. 58, p. 843–917.
- Cluer, J.K., 1992, A graphic method for projecting topographic profiles to various scales: *Journal of Geology*, v. 100, p. 135–137.
- Coates, J., 1945, The construction of geological sections: *The Quarterly Journal of the Geological, Mining and Metallurgical Society of India*, v. 17, p. 1–11.
- Cobbold, P.R., & H. Quinquis, 1980, Development of sheath folds in shear regimes: *Journal of Structural Geology*, v. 1/2, p. 119–126.
- Compton, R.R., 1966, Analysis of Pliocene-Pleistocene deformation and stresses in Northern Santa Lucia Range, California: *Geological Society of America Bulletin*, v. 77, p. 1361–1380.
- Compton, R.R., 1985, *Geology in the Field*: John Wiley, New York.
- Courant, R., 1936, *Differential and Integral Calculus, Volume II*: Interscience Publishers, New York.
- Courant, R., & F. John, 1965, *Introduction to Calculus and Analysis*: Interscience Publishers, New York.
- Crespi, J.M., 1986, Some guidelines for the practical application of Fry's method of strain analysis: *Journal of Structural Geology*, v. 8, p. 799–808.
- Crowell, J.C., 1959, Problems of fault nomenclature: *American Association of Petroleum Geologists Bulletin*, v. 43, p. 2653–2674.
- Cruden, D.M., 1971, Traces of a lineation on random planes: *Geological Society of America Bulletin*, v. 82, p. 2303–2305.
- Cruden, D.M., 1986, The geometry of slip surfaces beneath landslides: prediction from surface measurements: discussion: *Canadian Geotechnical Journal*, v. 23, p. 94.
- Cruden, D.M., & H.A.K. Charlesworth, 1976, Errors in strike and dip measurements: *Geological Society of America Bulletin*, v. 87, p. 977–980.
- Cummins, W.A., & R.M. Shackleton, 1955, The Ben Lui recumbent syncline (S.W. Highlands): *Geological Magazine*, v. 92, p. 353–363.



- Dahlstrom, C.D.A., 1969a, Balanced cross sections: *Canadian Journal of Earth Science*, v. 6, p. 743–757.
- Dahlstrom, C.D.A., 1969b, The upper detachment in concentric folding: *Bulletin of Canadian Petroleum Geology*, v. 17, p. 326–346.
- Dahlstrom, C.D.A., 1970, Structural geology in the eastern margin of the Canadian Rocky Mountains: *Bulletin of Canadian Petroleum Geology*, v. 18, p. 332–406.
- Dallmus, K.F., 1958, Mechanics of basin evolution and its relation to the habitat of oil in the basin: in L.G. Weeks, editor, *Habitat of Oil*, American Association of Petroleum Geologists, p. 883–931.
- Davis, G.H., & S.J. Reynolds, 1996, *Structural Geology of Rock and Regions*: Second Edition, John Wiley, New York, 776 p.
- Davis, J.C., 2002, *Statistics and Data Analysis in Geology*: Third Edition, John Wiley, New York.
- Davis, R.O., & A.P.S. Selvadurai, 1996, *Elasticity and Geomechanics*: Cambridge University Press, Cambridge.
- Denness, B., 1970, A method of contouring polar diagrams using curvilinear counting cells: *Geological Magazine*, v. 107, p. 55–66.
- Denness, B., 1972, A revised method of contouring stereograms using curvilinear cells: *Geological Magazine*, v. 109, p. 157–163.
- Dennis, J.G., 1967, *International Tectonic Dictionary*: American Association of Petroleum Geologists, Memoir 7, 196 p.
- Den Tex, E., 1954, Stereographic distinction of linear and planar structures from apparent lineations in random exposure planes: *Journal of the Geological Society of Australia*, v. 1, p. 55–66.
- De Paor, D.G., 1980, Some limitations of the  $R_f/\phi$  technique of strain analysis: *Tectonophysics*, v. 64, p. T29–T31.
- De Paor, D.G., 1988, Balanced sections in thrust belts, Part 1: construction: *American Association of Petroleum Geologists Bulletin*, v. 72, p. 73–90.
- De Paor, D.G., 1989, An interactive program for doing Fry Strain Analysis on the Mackintosh microcomputer: *Journal of Geological Education*, v. 37, p. 171–180.
- De Paor, D.G., 1991, A modern solution to the classical three-point problem: *Journal of Geological Education*, v. 39, p. 322–324.
- De Paor, D.G., 1994, A parametric representation of ellipses and ellipsoids: *Journal of Structural Geology*, v. 16, p. 1331–1333.
- Devlin, K.J., 1994, *Mathematics: the Science of Pattern*: Scientific American Library, New York.
- De Sitter, L.U., & H.J. Zwart, 1960, Tectonic development in supra- and infrastructures of a mountain chain: *21st International Geological Congress*, Part 18, p. 248–256.
- Dickinson, W.R., 1966, Structural relationships of San Andreas fault system, Cholame Valley and Castle Mountain Range: *Geological Society of America Bulletin*, v. 77, p. 707–726.
- Donath, F.A., 1961, Experimental study of shear failure in anisotropic rocks: *Geological Society of America Bulletin*, v. 72, p. 985–990.
- Donath, F.A., 1963, Fundamental problems in dynamic structural geology: in T.W. Donnelly, editor, *Earth Sciences: Problems and Progress in Current Research*, University of Chicago Press, Chicago, p. 83–103.
- Donath, F.A., 1964, Strength variation and deformation behavior in anisotropic rocks: in W.R. Judd, editor, *State of Stress in the Earth's Crust*, American Elsevier, New York, p. 281–297.
- Donath, F.A., & R.B. Parker, 1964, Folds and folding: *Geological Society of America Bulletin*, v. 75, p. 45–62.
- Drucker, D.C., 1967, *Introduction to Mechanics of Deformable Solids*: McGraw-Hill Book Company, New York, 445 p.
- Dubey, A.K., 1980, Model experiments showing simultaneous development of folds and transcurrent faults: *Tectonophysics*, v. 65, p. 69–84.

- Dunne, W.M., C.M. Onasch & R.T. Williams, 1990, The problem of strain-marker centers and the Fry method: *Journal of Structural Geology*, v. 12, p. 933–938.
- Durelli, A.J., E.A. Phillips & C.H. Tsao, 1958, Introduction to the theoretical and experimental analysis of stress and strain: McGraw-Hill Book Company, New York.
- Durney, D.W., & H.J. Kisch, 1994, A field classification and intensity scale for first-generation cleavages: *AGSO Journal of Australian Geology & Geophysics*, v. 15, p. 257–295 (see corrections v. 15, p. 539).
- Earl, B.L., 1988, A comment on significant figures and propagation of uncertainty: *Journal of Chemical Education*, v. 65, p. 186–187.
- Elliott, D., 1965, The quantitative mapping of directional minor structures: *Journal of Geology*, v. 73, p. 865–880.
- Elliott, D., 1970, Determination of finite strain and initial shape from deformed elliptical objects: *Geological Society of America Bulletin*, v. 81, p. 2221–2236.
- Elliott, D., 1972, Deformation paths in structural geology: *Geological Society of America Bulletin*, v. 83, p. 2621–2638.
- Elliott, D., 1976, Energy balance in thrusts and deformation mechanisms of thrust sheets: *Proceedings of the Royal Society of London*, v. A2 83, p. 289–312.
- Elliott, D., 1983, The construction of balanced cross-sections: *Journal of Structural Geology*, v. 5, p. 101.
- Elliott, D., & M.R.W. Johnson, 1980, Structural evolution in the northern part of the Moine thrust belt, NW Scotland: *Transactions of the Royal Society of Edinburgh: Earth Sciences*, v. 71, p. 69–96.
- Engelder, T., 1993, *Stress Regimes in the Lithosphere*: Princeton University Press, Princeton, N. J.
- Engelder, T., 1999, Transitional-tensile fracture propagation: a status report: *Journal of Structural Geology*, v. 21, p. 1049–1055.
- Erslev, E.A., 1988, Normalized center-to-center strain analysis of packed aggregates: *Journal of Structural Geology*, v. 10, p. 201–209.
- Erslev, E.A., & Hongxing Ge, 1990, Least-squares center-to-center and mean object ellipse fabric analysis: *Journal of Structural Geology*, v. 12, p. 1047–1059.
- Faill, R.T., 1973, Kink band folding, Valley and Ridge Province, Pennsylvania: *Geological Society of America Bulletin*, v. 84, p. 1289–1314.
- Ferguson, C.C., 1981, A strain reversal method for estimating extension from fragmented rigid inclusions: *Tectonophysics*, v. 79, p. T43–T52.
- Ferguson, C.C., 1987, Fracture and separation histories of stretched belemnites and other rigid-brittle inclusions in tectonites: *Tectonophysics*, v. 139, p. 255–273.
- Ferguson, C.C., & G.E. Lloyd, 1984, Extension analysis of stretched belemnites: a comparison of methods: *Tectonophysics*, v. 101, p. 199–206.
- Ferguson, H.G., & S.W. Muller, 1949, Structural geology of the Hawthorne and Tonopah quadrangles, Nevada: *U.S. Geological Survey Professional Paper* 216, 55 p.
- Ferguson, J., 1994, *Introduction to Linear Algebra in Geology*: Chapman & Hall, London.
- Ferziger, J.H., 1998, *Numerical Methods for Engineering Applications*: Second Edition, John Wiley & Sons, New York.
- Fienen, M.N., 2005, The three-point problem, vector analysis and extension to n-point problem: *Journal of Geoscience Education*, v. 53, p. 257–262.
- Fisher, D.J., 1941, Drillhole problems in the stereographic projection: *Economic Geology*, v. 36, p. 551–560.
- Fisher, N.I., 1993, *Statistical Analysis of Circular Data*: Cambridge University Press, Cambridge.
- Fisher, N.I., T. Lewis & B.J.J. Embleton, 1987, *Statistical Analysis of Spherical Data*: Cambridge University Press, Cambridge.
- Fisher, R.A., 1953, Dispersion on a sphere: *Proceedings of the Royal Society of London*, v. A125, p. 54–59.

- Fleuty, M.J., 1964, The description of folds: *Proceedings of the Geologists Association*, v. 75, p. 461–492.
- Fleuty, M.J., 1974, Slickensides and slickenlines: *Geological Magazine*, v. 112, p. 319–322.
- Fleuty, M.J., 1987a, Folds and folding: in C.K. Seyfert, editor, *The Encyclopedia of Structural Geology and Plate Tectonics*, Van Nostrand Reinhold Co., New York, p. 249–270.
- Fleuty, M.J., 1987b, Slikensides and slickenlines: in C.K. Seyfert, editor, *The Encyclopedia of Structural Geology and Plate Tectonics*, Van Nostrand Reinhold Co., New York, p. 729–731.
- Flinn, D., 1965, On the symmetry principle and the deformation ellipsoid: *Geological Magazine*, v. 102, p. 35–45.
- Ford, M., & C.C. Ferguson, 1985, Cleavage strain in the Variscan Fold Belt, County Cork, Ireland, estimated from stretched arsenopyrite rosettes: *Journal of Structural Geology*, v. 7, p. 217–223.
- Fowler, C.M.R., 1990, *The Solid Earth*: Cambridge University Press, Cambridge.
- Freeman, T., 1991, *Procedures in Field Geology*: Friendship Publications, Columbia, Mo.
- Fry, N., 1979a, Random point distributions and strain measurements in rocks: *Tectonophysics*, v. 60, p. 89–105.
- Fry, N., 1979b, Density distribution techniques and strain length methods for determination of finite strains: *Journal of Structural Geology*, v. 1, p. 221–229.
- Gage, M., 1979, A dilemma in structural mapping: *New Zealand Journal of Geology and Geophysics*, v. 22, p. 293.
- Garland, G.D., 1979, *Introduction to Geophysics (Mantle, Core and Crust)*: Second Edition, W.B. Saunders Company, Philadelphia.
- Gelfand, I.M., & M. Saul, 2001, *Trigonometry*: Birkhäuser, Boston.
- Gere, J.M., 2001, *Mechanics of Materials*: Fifth Edition, Brooks/Cole Thompson Learning, Pacific Grove, Calif.
- Ghaleb, A.R., & N. Fry, 1995, CSTRAIN: a FORTRAN 77 program to study Fry's plots in two-dimensional simulated models: *Computers & Geosciences*, v. 21, p. 825–831.
- Ghosh, S.K., 1993, *Structural Geology: Fundamentals and Modern Developments*: Pergamon Press, Oxford.
- Gill, J.E., 1935, Fault nomenclature: *Royal Society of Canada Transactions*, Third series, v. 35, sec. 4, p. 71–85.
- Gill, J.E., 1941, Normal and reverse faults: *Journal of Geology*, v. 43, p. 1071–1079.
- Gill, J.E., 1971, Continued confusion in the classification of faults: *Geological Society of America Bulletin*, v. 82, p. 1389–1392.
- Gilluly, J., A.C. Waters & A.O. Woodford, 1968, *Principles of Geology*: Third Edition, Freeman, San Francisco.
- Goetze, C., & B. Evans, 1979, Stress and temperature in the bending lithosphere as constrained by experimental rock mechanics: *Geophysical Journal of the Royal Astronomical Society*, v. 59, p. 463–478.
- Goguel, J., 1962, *Tectonics*: Freeman, San Francisco.
- Goodman, R.E., 1976, *Methods of Geological Engineering in Discontinuous Rock*: West Publishing Company, St. Paul, Minn.
- Graham, R.L., D.E. Knuth & O. Patashnik, 1989, *Concrete Mathematics*: Addison-Wesley Publishing Co., Reading, Mass.
- Gretener, P.E., 1981, *Pore Pressure: Fundamentals, General Ramifications and Implications for Structural Geology (Revised)*: American Association of Petroleum Geologists Continuing Education Course Notes Series, No. 4.
- Hafner, W., 1951, Stress distribution and faulting: *Geological Society of America Bulletin*, v. 62, p. 373–398.
- Halliday, D., & R. Resnick, 1978, *Physics, Parts I and II Combined*: Third Edition, John Wiley & Sons, New York.

- Handin, J., 1969, On the Coulomb-Mohr failure criterion: *Journal of Geophysical Research*, v. 74, p. 5343–5349.
- Haneberg, W.C., 1990, A Lagrangian interpolation method for three-point problems: *Journal of Structural Geology*, v. 12, p. 945–948.
- Haneberg, W.C., 2004, *Computational Geosciences with Mathematica*: Springer, Berlin.
- Hanna, S.S., & N. Fry, 1979, A comparison of methods of strain determination in rocks from southwest Dyfed (Pembrokeshire) and adjacent areas: *Journal of Structural Geology*, v. 1, p. 155–162.
- Hansen, E., 1971, *Strain Facies*: Springer Verlag, New York.
- Hansen, W.R., 1960, Improved Jacob staff for measuring inclined stratigraphic intervals: *American Association of Petroleum Geologists Bulletin*, v. 44, p. 252–255.
- Harker, A., 1884, Graphical methods in field geology: *Geological Magazine*, v. 1, p. 154–162.
- Harker, A., 1885, On slaty cleavage and allied rock structures, with special reference to the mechanical theories of their origin: *British Association for the Advancement of Science Report*, p. 813–852.
- Harrison, J.M., 1963, Nature and significance of geological maps: in C.C. Albritton, Jr., editor, *The Fabric of Geology*, Addison-Wesley, Reading, Mass., p. 225–232.
- Herold, S.C., 1933, Projection of dip angle on profile section: *American Association of Petroleum Geologists Bulletin*, v. 17, p. 740–742.
- Hewett, D.F., 1920, Measurement of folded beds: *Economic Geology*, v. 15, p. 367–385.
- Higgins, C.G., 1962, Reconstruction of flexure fold by concentric arc method: *American Association of Petroleum Geologists Bulletin*, v. 46, p. 1737–1739.
- Higgs, D.V., & G. Tunell, 1966, *Angular Relations of Lines and Planes*: Second Edition, W.H. Freeman and Company, San Francisco.
- Hill, M.L., 1959, Dual classification of faults: *American Association of Petroleum Geologist Bulletin*, v. 43, p. 217–221.
- Hill, M.L., 1963, Role of classification in geology: in C.C. Albritton, Jr., editor, *The Fabric of Geology*, Addison-Wesley, Reading, Mass., p. 164–174.
- Hobbs, B.E., W.D. Means & P.F. Williams, 1976, *An Outline of Structural Geology*: John Wiley, New York.
- Hoek, E., & J.W. Bray, 1981, *Rock Slope Engineering*: Third Edition, Institute of Mining and Metallurgy, London.
- Holcombe, R.J., 2001, GEOrient: [www.earthsciences.uq.edu.au/roddh/software/index.html](http://www.earthsciences.uq.edu.au/roddh/software/index.html)
- Holdsworth, R.E., 1988, The stereographic analysis of facing: *Journal of Structural Geology*, v. 10, p. 219–223.
- Hossack, J.R., 1979, The use of balanced cross-sections in the calculation of orogenic contraction: a review: *Journal of the Geological Society of London*, v. 136, p. 705–711.
- Hossain, K.M., 1979, Determination of strain from stretched belemnites: *Tectonophysics*, v. 88, p. 279–288.
- Howson, M., & E.J. Sides, 1986, Borehole desurvey calculations: *Computers & Geoscience*, v. 12, p. 97–104.
- Hsü, K.J., 1968, Principles of melanges and their bearing on the Franciscan-Knoxville paradox: *Geological Society of America Bulletin*, v. 79, p. 1063–1074.
- Hubbert, M.K., 1931, Graphic solution of strike and dip from two angular components: *American Association of Petroleum Geologists Bulletin*, v. 15, p. 283–2862.
- Hubbert, M.K., 1951, Mechanical basis for certain familiar geological structures: *Geological Society of America Bulletin*, v. 62, p. 365–372.
- Hudleston, P.J., 1973, Fold morphology and some implications of theories of fold development: *Tectonophysics*, v. 16, p. 1–46.
- Hudleston, P.J., S.H. Treagus & Labao Lan, 1996, Flexural flow folding: Does it occur in nature?: *Geology*, v. 24, p. 203–206.
- Hudson, J.A., 1989, *Rock Mechanics Principles in Engineering Practice*: Butterworth, London.

- Ickes, E.L., 1923, Similar, parallel and neutral surface types of folding: *Economic Geology*, v. 18, p. 575–591.
- Jacobson, C.E., 1996, SpheriCAD: an AutoCAD program for analysis of structural orientation data: in D.G. De Paor, editor, *Structural Geology and Personal Computers*, Pergamon Press, Oxford, p. 181–193.
- Jaeger, J.C., 1969, *Elasticity, Fracture and Flow*: Third Edition, Methuen, London.
- Jaeger, J.C., & N.G.W. Cook, 1979, *Fundamentals of Rock mechanics*: Third Edition, Methuen, London.
- Johnson, A.M., 1970, *Physical Processes in Geology*: Freeman, Cooper & Company, San Francisco.
- Johnson, A.M., & R.C. Fletcher, 1994, *Folding of Viscous Layers*: Columbia University Press, New York.
- Johnston, S.T., 1999, Squeezing down plunge projections out of graphics packages: *Computers & Geosciences*, v. 25, p. 197–200.
- Jolly, R.J.H., & D.J. Sanderson, 1997, A Mohr circle construction for the opening of a pre-existing fracture: *Journal of Structural Geology*, v. 19, p. 887–892.
- Kalsbeek, F., 1963, A hexagonal net for the counting out and testing of fabric diagrams: *Neues Jahrbuch für Mineralogie, Monatshefte*, v. 7, p. 173–1776.
- Kamb, W.B., 1959, Petrofabric observations from Blue Glacier, Washington, in relation to theory and experiment: *Journal of Geophysical Research*, v. 64, p. 1891–1909.
- Kilby, W.E., & H.A.K. Charlesworth, 1980, Computerized downplunge projection and the analysis of low-angle thrust-faults in the Rocky Mountain Foothills of Alberta, Canada: *Tectonophysics*, v. 66, p. 287–299.
- Kitson, H.W., 1929, Graphic solution of strike and dip from two dip components: *American Association of Petroleum Geologists Bulletin*, v. 13, p. 1211–1213.
- Knopf, E.B., & E. Ingerson, 1938, *Structural Petrology*: Geological Society of America Memoir 6.
- Kottlowski, F.E., 1965, *Measuring Stratigraphic Sections*: Holt, Rinehart & Winston, New York.
- Kranck, E.H., 1953, Interpretation of gneiss structures with special reference to Baffin Island: *Proceedings of the Geological Association of Canada*, v. 6, p. 59–68.
- Kraus, J., & P.F. Williams, 2001, A new spin on ‘non-rotating’ porphyroblasts: implications of cleavage refraction and reference frames: *Journal of Structural Geology*, v. 23, p. 963–971.
- Kretz, R., 1991, The dilation direction of intrusive sheets: *Journal of Structural Geology*, v. 13, p. 97–99.
- Krumbein, W.C., 1939, Preferred orientations of pebbles in sedimentary deposits: *Journal of Geology*, v. 47, p. 673–706.
- Kuenen, Ph.H., & L.U. de Sitter, 1938, Experimental investigation into the mechanics of folding: *Leidse Geologische Mededelingen*, v. 10, p. 217–239.
- Kulander, B.R., S.L. Dean & B.J. Ward, Jr., 1990, *Fractured Core Analysis: Interpretation, Logging, and Use of Natural and Induced Fractures in Cores*: Methods in Exploration Series, No. 8, American Association of Petroleum Geologists.
- Kupfer, D.H., 1966, Accuracy in geological maps: *Geotimes*, v. 10, no. 7, p. 11–14.
- Kutty, T.S., & S. Joy, 1994, RFPHI – a program in TURBOC for the  $Rf/\phi$  diagram method of two-dimensional strain analysis: *Computers & Geosciences*, v. 20, p. 247–263.
- Laing, W.P., 1977, Structural interpretation of drill core from folded and cleaved rocks: *Economic Geology*, v. 72, p. 671–685.
- Lambe, T.N., & R.V. Whitman, 1979, *Soil Mechanics: SI Edition*: John Wiley, New York, 553 p.
- Langenberg, W., 1985, The geometry of folded and thrust rocks in the Rocky Mountain Foothills near Grande Chache, Alberta: *Canadian Journal of Earth Sciences*, v. 22, p. 1711–1719.
- Langenberg, C.W., H.E. Rondeel & H.A.K. Charlesworth, 1977, A structural study in the Belgian Ardennes with sections constructed using computer-based methods: *Geologie en Mijnbouw*, v. 56, p. 145–154.

- Langenberg, W., H. Charlesworth & A. La Rivier, 1988, Computer-constructed cross-section of the Morcles Nappe: *Eclogae geologicae Helvetiae*, v. 80, p. 655–667.
- Lapierre, J., D. Mainprice & W.B. Ismail, 1996, Calculation of rock properties from pole figures using LabView: in D.G. De Paor, editor, *Structural Geology and Personal Computers*, Pergamon Press, Oxford, p. 167–178.
- La Pointe, P.R., & J.A. Hudson, 1985, *Characterization and Interpretation of Rock Mass Joint Patterns*: Geological Society of America Special Paper 199.
- Lau, J.S.O., 1983, The determination of true orientation of fractures in rock cores: *Canadian Geotechnical Journal*, v. 20, p. 221–227.
- Laubscher, H.P., 1977a, An intriguing example of a folded thrust in the Jura: *Eclogae geologicae Helvetiae*, v. 70, p. 97–104.
- Laubscher, H.P., 1977b, Fold development in the Jura: *Tectonophysics*, v. 37, p. 337–362.
- Lee, W., C.L. Mulliss & H.-C. Chiu, 2000, On the standard rounding rule for addition and subtraction: *Chinese Journal of Physics*, v. 38, p. 36–41.
- Levensen, I.A., 1960, *Paleogeological Maps*: Freeman, San Francisco.
- Lisle, R.J., 1980, A simplified work scheme for using block diagrams with the orthographic net: *Journal of Geological Education*, v. 29, p. 81–83.
- Lisle, R.J., 1985a, *Geological Strain Analysis: A Manual for the  $R_f/\phi$  Method*: Pergamon Press, Oxford.
- Lisle, R.J., 1985b, The facing of faults: *Geological Magazine*, v. 122, p. 249–251.
- Lisle, R.J., 1994, Paleostain analysis: in P.L. Hancock, editor, *Continental Deformation*, Pergamon Press, p. 28–42.
- Lisle, R.J., 1997, A fold classification scheme based on a polar plot of inverse thickness: in S. Sengupta, editor, *Evolution of Geological Structures in Micro- and Macro-scales*, Chapman & Hall, London, p. 323–339.
- Lisle, R.J., & P.R. Leyshon, 2004, *Stereographic Projection Techniques for Geologists and Civil Engineers*: Second Edition, Cambridge University Press, Cambridge.
- Lisle, R.J., & D.M. Ragan, 1988, Strain from three stretches – a simple method: *Journal of Structural Geology*, v. 10, p. 905–906.
- Lisle, R.J., & J.M. Robinson, 1995, The Mohr circle for curvature and its application to fold description: *Journal of Structural Geology*, v. 17, p. 739–750.
- Livio, M., 2002, *The Golden Ratio*: Broadway Books, New York.
- Lloyd, G.E., & E. Condliffe, 2003, 'Strain Reversal': a Windows program to determine extensional strain from rigid-brittle layers or inclusions: *Journal of Structural Geology*, v. 25, p. 1141–1145.
- Lobeck, A.K., 1958, *Block Diagrams*: Second Edition, Emerson-Trussell, Amherst Mass.
- Lowe, K.E., 1946, A graphic solution for certain problems of linear structures: *American Mineralogist*, v. 31, p. 425–434.
- MacCaskie, D.R., 1986, Rapid field estimation of the degree of preferred orientation of elongate features: *Journal of Geology*, v. 94, p. 777–778.
- MacDonald, W.D. 1980, Net tectonic rotation, apparent tectonic rotation, and the structural tilt correction in paleomagnetic studies: *Journal of Geophysical Research*, v. 85, p. 3659–3667.
- Mackin, J.H., 1950, The down-structure method of viewing geological maps: *Journal of Geology*, v. 58, p. 55–72.
- Mackin, J.H., 1962, Structure of the Glenarm series in Chester County, Pennsylvania: *Geological Society of America Bulletin*, v. 73, p. 403–410.
- Mancktelow, N.S., 2001, Single-layer folds developed from initial random perturbations: The effects of probability distribution, fractal dimensions, phase, and amplitude: in H.A. Koyi & N.S. Mancktelow, editors, *Tectonic Modeling: A Volume in Honor of Hans Ramberg*: Geological Society of America Memoir 193, p. 69–87.
- Maor, E., 1998, *Trigonometric Delights*: Princeton University Press, Princeton, N.J.
- Mardia, K.V., 1972, *Statistics of Orientation Data*: Academic Press, London.

- Mardia, K.V., & P.E. Jupp, 2000, *Directional Statistics*: John Wiley, Chichester.
- Marjoribanks, R.W., 1974, An instrument for measuring dip isogons and fold layer shape parameters: *Journal of Geological Education*, v. 22, p. 62–64.
- Marshak, S., & N.B. Woodward, 1988, Introduction to cross-section balancing: in S. Marshak & G. Mitra, editors, *Basic Methods of Structural Geology*, Prentice-Hall, Englewood Cliffs, N.J., p. 303–332.
- Mase, G.E., 1970, *Theory and Problems of Continuum Mechanics*: Schaum's Outline Series, McGraw-Hill Book Company, New York.
- Matthews, P.E., R.A.B. Bond & J.J. Van den Berg, 1971, Analysis and structural implications of a kinematic model of similar folding: *Tectonophysics*, v. 12, p. 129–154.
- McClay, K.R., 1987, *The Mapping of Geologic Structures*: Open University Press, Milton Keynes, UK.
- McClay, K.R., 1992, Glossary of thrust tectonics terms: in K.R. McClay, editor, *Thrust Tectonics*: Chapman & Hall, London, p. 419–433.
- McCoss, A.M., 1987, Practical section drawing through folded layers using sequentially rotated cubic interpolators: *Journal of Structural Geology*, v. 9, p. 365–370.
- McIntyre, D.B., & L.E. Weiss, 1956, Construction of block diagrams to scale in orthographic projection: *Proceedings of the Geologists Association*, v. 67, p. 145–155.
- McKinstry, H., 1961, Structure of the Glenarm Series in Chester Country, Pennsylvania: *Geological Society of America Bulletin*, v. 72, p. 557–578.
- McLeish, A.J., 1971, Strain analysis of deformed pipe rock in the Moine thrust zone, northwest Scotland: *Tectonophysics*, v. 12, p. 469–503.
- McLenaghan, R., & S. Levy, 1996, Geometry: in Daniel Zwillinger, editor, *Standard Mathematical Tables and Formulae*: 30th Edition, CRC Press, Boca Raton, Fla., p. 249–330.
- McNaught, M.A., 1994, Modifying the normalized Fry method for aggregates of non-elliptical grains: *Journal of Structural Geology*, v. 16, p. 493–503.
- McNaught, M.A., 2002, Estimating uncertainty in normalized Fry plots using a bootstrap approach: *Journal of Structural Geology*, v. 24, p. 311–322.
- Means, W.D., 1976, *Stress and Strain: Basic Concepts of Continuum Mechanics for Geologists*: Springer-Verlag, New York.
- Means, W.D., 1987, A newly recognized type of slickenside striations: *Journal of Structural Geology*, v. 9, p. 585–590.
- Means, W.D., 1990, Kinematics, stress, deformation and material behavior: *Journal of Structural Geology*, v. 12, p. 953–971.
- Means, W.D., 1992, Rotational quantities in homogeneous flow and the development of small-scale structures: *Journal of Structural Geology*, v. 16, p. 437–445.
- Means, W.D., 1996, *How To Do Anything with Mohr Circles: A Short Course About Tensors for Structural Geologists*: Short Course Workbook, Geological Society of America.
- Meere, P.A., & K.F. Mulchrone, 2003, The effect of sample size on geological strain estimation from passively deformed clastic sedimentary rocks: *Journal of Structural Geology*, v. 25, p. 1587–1595.
- Mertie, J.B., Jr., 1922, Graphic and mechanical computation of thickness of stratum and distance to a stratum: *U.S. Geological Survey Professional Paper 129-C*, p. 39–52.
- Mertie, J.B., Jr., 1940, Stratigraphic measurement in parallel folds: *Geological Society of America Bulletin*, v. 51, p. 1107–1133.
- Mertie, J.B., Jr., 1943, Structural determinations from diamond drilling: *Economic Geology*, v. 38, p. 298–312.
- Mertie, J.B., Jr., 1947, Delineation of parallel folds and measurement of stratigraphic dimensions: *Geological Society of America Bulletin*, v. 58, p. 779–802.
- Middleton, G.V., 2000, *Data Analysis in the Earth Sciences using MATLAB®*: Prentice-Hall, Inc., Upper Saddle River, N.J.

- Middleton, G.V., & P.R. Wilcock, 1994, *Mechanics in the Earth and Environmental Sciences*: Cambridge University Press, Cambridge.
- Moon, F.C., 1992, *Chaotic and Fractal Dynamics*: John Wiley, New York.
- Mountjoy, E.W., 1992, Significance of rotated folds and thrust faults, Alberta Rocky Mountains: in Shankar Mitra & G.W. Fisher, editors, *Structural Geology of Fold and Thrust Belts*, Johns Hopkins University Press, Baltimore, p. 207–223.
- Mueller, B., V. Wehrle & K. Fuchs, 1997, The 1997 release of the World Stress Map (available on-line at [www-wsm.physik.uni-karlsruhe.de/pub/Rel97/wsm97.html](http://www-wsm.physik.uni-karlsruhe.de/pub/Rel97/wsm97.html)).
- Muhuri, S.K., T.A. Dewers, T.E. Scott, Jr. & Z. Reches, 2003, Interseismic fault strengthening and earthquake-slip instability; friction or cohesion?: *Geology*, v. 31, p. 881–884.
- Mulchrone, K.F., & P.A. Meere, 2001, A windows program for the analysis of tectonic strain using deformed elliptical markers: *Computers & Geosciences*, v. 27, p. 1251–1255.
- Müller, L., 1933, Untersuchungen über statistische Kluftrichtung: *Geologie und Bauwesen*, v. 5, no. 4, p. 185–255.
- Mulliss, C.L., & Wei Lee, 1998, On the standard rounding rule for multiplication and division: *Chinese Journal of Physics*, v. 36, p. 479–487.
- Nye, J.F., 1985, *Physical Properties of Crystals*: Revised Edition, Clarendon Press, Oxford.
- O’Driscoll, E.S., 1962, Experimental patterns in superposed similar folding: *Journal of the Alberta Society of Petroleum Geologists*, v. 10, p. 145–167.
- O’Driscoll, E.S., 1964, Cross fold deformation by simple shear: *Economic Geology*, v. 59, p. 1061–1093.
- Oertel, G., 1962, Extrapolation in geological fabrics: *Geological Society of America Bulletin*, v. 73, p. 325–342.
- Oertel, G., 1996, *Stress and Deformation: A Handbook on Tensors in Geology*: Oxford University Press, New York.
- Onasch, C.M., 1986a, Ability of the Fry method to characterize pressure-solution deformation: *Tectonophysics*, v. 122, p. 187–193.
- Onasch, C.M., 1986b, Ability of the Fry method to characterize pressure-solution deformation – reply: *Tectonophysics*, v. 131, p. 201–203.
- Ottino, J.M., 1989, The mixing of fluids: *Scientific American*, v. 260, no. 1, p. 56–67.
- Ottino, J.M., 1990, *The Kinematics of Mixing: Stretching, Chaos, and Transport*: Cambridge University Press, Cambridge.
- Ottino, J.M., 1992, New applications of chaos in chemical engineering: intuition versus prediction: in J.H. Kim & J. Stringer, editors, *Applied Chaos*, John Wiley, New York, p. 143–174.
- Owens, W.H., 2000, An alternative approach to the Busk construction for a single surface: *Journal of Structural Geology*, v. 22, p. 1379–1383.
- Palmer, C.I., C.W. Leigh & S.H. Kimball, 1950, *Plane and Spherical Trigonometry*: Fifth Edition, McGraw-Hill, New York.
- Panozzo, R., 1984, Two-dimensional strain from the orientation of lines in a plane: *Journal of Structural Geology*, v. 6, p. 215–221.
- Panozzo, R., 1987, Two-dimensional strain determination by the inverse SURFOR wheel: *Journal of Structural Geology*, v. 9, p. 115–119.
- Park, Y., 1996, Synkinematic microscopic analysis using NIH Image: in D.G. De Paor, editor, *Structural Geology and Personal Computers*, Pergamon, Press, Oxford, p. 123–134.
- Passchier, C.W., & R.A.J. Trouw, 1996, *Microtectonics*: Springer-Verlag, Berlin.
- Peach, C.J., & R.J. Lisle, 1979, A FORTRAN IV program for the analysis of tectonic strain using deformed elliptical markers: *Computers & Geoscience*, v. 5, p. 325–334.
- Peacock, D.C.P., R.J. Knipe & D.J. Sanderson, 2000, Glossary of normal faults: *Journal of Structural Geology*, v. 22, p. 291–305.
- Pfiffner, O.A., 1981, Fold-and-thrust tectonics in the Helvetic Nappes (E Switzerland): in K.R. McClay & N.J. Price, editors, *Thrust and Nappe Tectonics*, Special Publication No. 9, Geological Society of London, p. 319–327.



- Pfiffner, O.A., & J.G. Ramsay, 1982, Constraints on geological strain rates: arguments from finite strain states of naturally deformed rocks: *Journal of Geophysical Research*, v. 87, p. 311–321.
- Phillips, F.C., 1963, *An Introduction to Crystallography*: Third Edition, John Wiley, New York.
- Phillips, F.C., 1971, *The Use of Stereographic Projection in Structural Geology*: Third Edition, Edward Arnold, London.
- Philpots, A.R., N.H. Gray, M. Caroll, R.P. Steinen & J.B. Reid, 1997, The electronic total station – a versatile, revolutionary new geological mapping tool: *Journal of Geoscience Education*, v. 45, p. 38–45.
- Pincus, H.J., 1956, Some vector and arithmetic operations on two-dimensional orientation variates, with applications to geological data: *Journal of Geology*, v. 64, p. 533–557.
- Pollard, D.D., S.D. Saltzer & A.M. Rubin, 1993, Stress inversion methods: are they based on faulty assumptions?: *Journal of Structural Geology*, v. 15, p. 1045–1054.
- Pollard, D.D., & R.C. Fletcher, 2005, *Fundamentals of Structural Geology*: Cambridge University Press, Cambridge.
- Powell, C. McA., 1974, Timing of slaty cleavage during folding of Precambrian rocks, northwest Tasmania: *Geological Society of America Bulletin*, v. 85, p. 1043–1060.
- Price, N.J., 1966, *Fault and Joint Development in Brittle and Semi-Brittle Rocks*: Pergamon, Oxford.
- Price, N.J., 1970, Laws of rock behavior in the earth's crust: in W.H. Somerton, editor, *Rock Mechanics: Theory and Practice*, Proceedings of the 11th Symposium on Rock Mechanics, American Institute Mining, Metallurgical and Petroleum Engineering, New York, p. 3–23.
- Price, N.J., 1975, Rates of deformation: *Journal of the Geological Society*, v. 131, p. 553–575.
- Priest, S.D., 1985, *Hemispherical Projection Methods in Rock Mechanics*: George Allen & Unwin, London.
- Pumpelly, R., J.E. Wolfe & T.N. Dale, 1894, *Geology of the Green Mountains in Massachusetts*: U.S. Geological Survey Monograph 23.
- Ragan, D.M., 1969a, Introduction to concepts of two-dimensional strain and their application with the use of card-deck models: *Journal of Geological Education*, v. 17, p. 135–141.
- Ragan, D.M., 1969b, Structures at the base of an ice fall: *Journal of Geology*, v. 77, p. 647–667.
- Ragan, D.M., & R.H. Groshong, Jr., 1993, Strain from two angles of shear: *Journal of Structural Geology*, v. 15, p. 1359–1360.
- Ragan, D.M., & M.F. Sheridan, 1972, Compaction of the Bishop Tuff, California: *Geological Society of America Bulletin*, v. 83, p. 95–106.
- Rahm, P.C., 1986, *Engineering Geology*: Elsevier, New York.
- Raleigh, B., & J. Evernden, 1981, Case for low deviatoric stress in the lithosphere: in N.L. Carter, M. Friedman, J.M. Logan & D.W. Stearns, editors, *Mechanical Behavior of Crustal Rocks*, Geophysical Monograph 24, American Geophysical Union, p. 173–186.
- Ramberg, H., 1981, *Gravity, Deformation and the Earth's Crust*: Second Edition, Academic Press, London.
- Ramberg, H., 1987, Drag folds: in C.K. Seyfert, editor, *The Encyclopedia of Structural Geology and Plate Tectonics*, Van Nostrand Reinhold Co., New York, p. 206.
- Ramsay, J.G., 1961, The effects of folding upon the orientation of sedimentary structures: *Journal of Geology*, v. 69, p. 84–100.
- Ramsay, J.G., 1964, The uses and limitations of beta-diagrams and pi-diagrams in the geometrical analysis of folds: *Quarterly Journal of the Geological Society*, v. 120, p. 435–454.
- Ramsay, J.G., 1967, *Folding and Fracturing of Rocks*: McGraw-Hill, New York.
- Ramsay, J.G., 1969, The measurement of strain and displacement in orogenic belts: in P.E. Kent, G.E. Satterthwaite & A.M. Spencer, editors, *Time and Place in Orogeny*, Special Publication No. 3, Geological Society of London, p. 43–79.
- Ramsay, J.G., 1980, Shear zone geometry: a review: *Journal of Structural Geology*, v. 2, p. 83–99.

- Ramsay, J.G., 1982, Rock ductility and its influence on the development of tectonic structures in mountain belts: in K.J. Hsu, editor, *Mountain Building Processes*, Academic Press, London, p. 111–127.
- Ramsay, J.G., 1992, Some geometrical problems of ramp-flat thrust models: in K.R. McClay, editor, *Thrust Tectonics*, Chapman & Hall, London, p. 191–200.
- Ramsay, J.G., & M.I. Huber, 1983, *The Techniques of Modern Structural Geology: Volume 1: Strain Analysis*: Academic Press, London.
- Ramsay, J.G., & M.I. Huber, 1987, *The Techniques of Modern Structural Geology: Volume 2: Folds and Fractures*: Academic Press, London.
- Ramsay, J.G., & R.J. Lisle, 2000, *The Techniques of Modern Structural Geology: Volume 3: Applications of Continuum Mechanics in Structural Geology*: Academic Press, London.
- Raup, D.M., & S.M. Stanley, 1978, *Principles of Paleontology*: Second Edition, W.H. Freeman and Company, San Francisco.
- Reches, Z., 1978, Analysis of faulting in three-dimensional strain field: *Tectonophysics*, v. 47, p. 109–129.
- Reches, Z., D.F. Hoexter & F. Hirsch, 1981, The structure of a monocline in the Syrian Arc System, Middle East – surface and subsurface analysis: *Journal of Petroleum Geology*, v. 3–4, p. 413–425.
- Reches, Z. & D.A. Lockner, 1994, Nucleation and growth of faults in brittle rocks: *Journal of Geophysical Research*, v. 99, p. 18159–18173.
- Redmond, J.L., 1972, Null combination in fault interpretation: *American Association of Petroleum Geologists Bulletin*, v. 56, p. 150–166.
- Rich, J.L., 1932, Simple graphical method for determining true dip from two components and for constructing contoured structural maps from dip observations: *American Association of Petroleum Geologists Bulletin*, v. 16, p. 92–95.
- Rickard, M.J., 1971, A classification diagram for fold orientation: *Geological Magazine*, v. 108, p. 23–26.
- Rickard, M.J., 1972, Fault classification – discussion: *Geological Society of America Bulletin*, v. 83, p. 2545–2546.
- Robinson, G.D., 1959, Measuring dipping beds: *Geotimes*, v. 4, p. 8–9, 24–27.
- RockWare, 2001, [www.rockware.com](http://www.rockware.com).
- Rondeel, H.E., & F. Storbeck, 1978, Errors in geological compass determinations of the attitude of planar structures: *Geologische Rundschau*, v. 68, p. 913–919.
- Rosenfeld, J.L., 1970, *Rotated Garnets in Metamorphic Rocks*: Geological Society of America, Special Paper 129.
- Rutter, E.H., 1986, On the nomenclature of mode of failure transition in rocks: *Tectonophysics*, v. 122, p. 381–387.
- Schedl, A., & B.A. van der Pluijm, 1988, A review of deformation microstructures: *Journal of Geological Education*, v. 36, p. 111–121.
- Scheid, F., 1988, *Theory and Problems of Numerical Analysis*: Second Edition, Schaum's Outline Series, McGraw-Hill Book Co., New York.
- Schmid, S.M., 1982, Microfabric studies as indicators of deformation mechanisms and flow laws operative in mountain building: in K.J. Hsu, editor, *Mountain Building Processes*, Academic Press, London, p. 97–110.
- Schmidt, W., 1925, Gefügestatistik: *Tschermak's Mitteilungen*, v. 38, p. 392–423.
- Scholz, C.H., 1988, The brittle-plastic transition and the depth of seismic faulting: *Geologische Rundschau*, v. 77, p. 319–328.
- Scholz, C.H., 2002, *The Mechanics of Earthquakes and Faulting*: Second Edition, Cambridge University Press, Cambridge.
- Schroeder, M.R., 1991, *Fractals, Chaos, Power Laws: Minutes from an Infinite Paradise*: W.H. Freeman and Company, New York.

- Schryver, K., 1966, On the measurement of the orientation of axial planes of minor folds: *Journal of Geology*, v. 74, p. 83–84.
- Schwerdtner, W.M., 1978, Determination of stratigraphic thickness of strained units: *Canadian Journal of Earth Science*, v. 15, p. 1379–1380.
- Schwerdtner, W.M., P.J. Bennett & T.W. Janes, 1977, Application of L-S fabric scheme to structural mapping and paleostrain analysis: *Canadian Journal of Earth Science*, v. 14, p. 1021–1032.
- Scott, R.J., & R.F. Berry, 2004, A new method for obtaining and quantifying the reliability of structural data from axially-oriented drill core using a fabric of known orientation: *Journal of Structural Geology*, v. 26, p. 643–658.
- Scott, R.J., & D. Selley, 2004, Measurement of fold axes in drill core: *Journal of Structural Geology*, v. 26, p. 637–642.
- Screven, R.W., 1963, A simple rule of V's of outcrop patterns: *Journal of Geological Education*, v. 11, p. 98–100.
- Sellés-Martínez, J., 1993, A common misinterpretation of the equal-area properties: *Journal of Structural Geology*, v. 15, p. 1261–1353.
- Seymour, D.B., & C.A. Boulter, 1979, Tests of computerised strain analysis by the analysis of simulated deformation of natural unstrained sedimentary fabrics: *Tectonophysics*, v. 58, p. 221–235.
- Shackleton, R.M., 1958, Downward-facing structures of the Highland Border: *Quarterly Journal of the Geological Society of London*, v. 113, p. 361–392.
- Sheridan, M.F., & D.M. Ragan, 1976, Compaction of ash-flow tuffs: in G.V. Chilingarian & K.M. Wolf, editors, *Compaction of Coarse-grained Sediments, II*, Elsevier Scientific Publishing Company, Amsterdam, p. 677–713.
- Sherwin, J.-A., & W.M. Chapple, 1968, Wavelengths of single layer folds: A comparison between theory and observation: *American Journal of Science*, v. 266, p. 167–197.
- Sibson, R.H., 1974, Frictional constraints on thrust, wrench and normal faults: *Nature (Physical Sciences)*, v. 249, p. 542–543.
- Sibson, R.H., 1981, Fluid flow accompanying faulting: field evidence and models: in D.W. Simpson & P.G. Richards, editors, *Earthquake Prediction: An International Review: Maurice Ewing Series 4*, American Geophysical Union, p. 593–603.
- Sikorsky, R.I., 1991, A diagram for interpreting orientation data for planar features in core: *Journal of Structural Geology*, v. 13, p. 1085–1089.
- Simpson, C., 1988, Analysis of two-dimensional strain: in S. Marshak & G. Mitra, editors, *Basic Methods of Structural Geology*, Prentice-Hall, Englewood Cliffs, N.J., p. 333–359.
- Simpson, C., & S.M. Schmid, 1983, An evaluation of criteria to deduce the sense of movement in sheared rocks: *Geological Society of America Bulletin*, v. 94, p. 1281–1288.
- Smith, D.P., 1994, The sphere as a tool for teaching statistics: *Journal of Geological Education*, v. 42, p. 412–416.
- Spear, F.S., 1993, *Metamorphic Phase Equilibria and Pressure-Temperature-Time Paths*: Mineralogical Society of America Monograph, Washington, D.C.
- Sprenke, K.F., 1992, Analytic geometry formulas and computer routines for stereonet problems: *Journal of Geological Education*, v. 40, p. 109–115.
- Srivastava, H.B., 1995, Two dimensional strain estimation from weakly deformed rocks: *Annales Tectonicae*, v. 9, p. 3–6.
- Stauffer, M.R., 1966, An empirical-statistical study of three dimensional fabric diagrams as used in structural analysis: *Canadian Journal of Earth Science*, v. 3, p. 473–498.
- Stauffer, M.R., 1968, The tracing of hinge-line ore bodies in areas of repeated folding: *Canadian Journal of Earth Science*, v. 5, p. 69–79.
- Steidel, R.F., Jr., & J.M. Henderson, 1983, *The Graphic Languages of Engineering*: John Wiley, New York.
- Stein, H.A., 1941, A trigonometric solution of the two-drillhole problem: *Economic Geology*, v. 36, p. 84–94.

- Stein, S., & M. Wysession, 2003, *An Introduction to Seismology, Earthquakes, and Earth Structure*: Blackwell Publishing, Malden, Mass.
- Stone, D.S., 1991, Analysis of scale exaggeration on seismic profiles: *American Association of Petroleum Geologists Bulletin*, v. 75, p. 1161–1177.
- Suppe, J., 1983, Geometry and kinematics of fault-bend folding: *American Journal of Science*, v. 283, p. 684–721.
- Suppe, J., 1985, *Principles of Structural Geology*: Prentice-Hall, Englewood Cliffs, N.J.
- Suter, H.H., 1947, Exaggeration of vertical scale of geological sections: *American Association of Petroleum Geologists Bulletin*, v. 31, p. 318–339.
- Talbot, C.J., 1999, Can field data constrain rock viscosities?: *Journal of Structural Geology*, v. 21, p. 949–957.
- Talbot, C.J., & D. Sokoutis, 1992, The importance of incompetence: *Geology*, v. 20, p. 951–953.
- Tauxe, L., & G.S. Watson, 1994, The fold test: an eigen analysis approach: *Earth and Planetary Science Letters*, v. 122, p. 331–341.
- Tavani, S., F. Storti & F. Salvini, 2005, Rounding hinges to fault-bend folding: geometrical and kinematic implications: *Journal of Structural Geology*, v. 27, p. 3–22.
- Taylor, J.R., 1997, *An Introduction to Error Analysis*: Second Edition, University Science Books, Sausalito, Calif.
- Tearpock, D.J., & R.E. Bischke, 1991, *Applied Subsurface Geologic Mapping*: Prentice-Hall, Englewood Cliffs, N.J.
- Ten Haaf, E., 1959, Graded beds of the northern Apennines: Thesis, University of Groningen.
- Terzaghi, R.D., 1965, Sources of error in joint surveys: *Géotechnique*, v. 15, p. 287–304.
- Tewksbury, B.J., 1996, Using graphics programs to help students understand strain: in D.G. De Paor, editor, *Structural Geology and Personal Computers*, Pergamon Press, Oxford, p. 57–73.
- Thiessen, R.L., & W.D. Means, 1980, Classification of fold interference patterns: a reexamination: *Journal of Structural Geology*, v. 2, p. 311–316.
- Thompson, R.I., 1981, The nature and significance of large ‘blind’ thrusts within the northern Rocky Mountains of Canada: in K.R. McClay & N.J. Price, editors, *Thrust and Nappe Tectonics*, Geological Society of London, Special Publication No. 9, p. 449–462.
- Thomson, W., & P.G. Tait, 1867, *Treatise on Natural Philosophy*, vol. 1, Oxford, England.
- Threet, R.L., 1973a, Classification of translational fault slip: *Geological Society of America Bulletin*, v. 84, p. 1825–1828.
- Threet, R.L., 1973, The down-dip method of viewing geological maps to obtain sense of fault separation: *Geological Society of America Bulletin*, v. 84, p. 4001–4004.
- Tikoff, B., & H. Fossen, 1996, Visualization of deformation: computer applications for teaching: in D.G. De Paor, editor, *Structural Geology and Personal Computers*, Pergamon Press, Oxford, p. 75–96.
- Tolson, G., & F. Correa-Mora, 1996, Manipulation of orientation data using spreadsheet software: in D.G. De Paor, editor, *Structural Geology and Personal Computers*, Pergamon Press, Oxford, p. 237–243.
- Townend, J., & M.D. Zoback, 2000, How faulting keeps the crust strong: *Geology*, v. 28, p. 399–402.
- Treagus, S.H., 1981, A simple-shear construction from Thomsom & Tait (1867): *Journal of Structural Geology*, v. 3, p. 291–293.
- Treagus, S.H., 1982, A new isogon-cleavage classification and its application to natural and model fold studies: *Geological Journal*, v. 17, p. 49–64.
- Treagus, S.H., 1983, A theory of finite strain variation through contrasting layers, and its bearing on cleavage refraction: *Journal of Structural Geology*, v. 5, p. 351–368.
- Treagus, S.H., 1987, Mohr circles for strain, simplified: *Geological Journal*, v. 22, p. 119–132.
- Treagus, S.H., 1999, Are viscosity ratios of rocks measurable from cleavage refraction?: *Journal of Structural Geology*, v. 21, p. 895–901.

- Triboulet, C., & C. Audren, 1988, Controls on  $P$ - $T$ - $t$  deformation path from amphibole zonation during progressive metamorphism of basic rocks (estuary of the River Vilaine, South Brittany, France): *Journal of Metamorphic Geology*, v. 6, p. 117–133.
- Truesdell, C., 1954, *The Kinematics of Vorticity*: Indiana University Press, Bloomington.
- Truesdell, C.A., III, 1991, *A First Course in Rational Continuum Mechanics, Volume 1 General Concepts*: Second Edition, Academic Press, Boston.
- Truesdell, C., & R. Toupin, 1960, The classical field theories: *Encyclopedia of Physics*, v. III/1, p. 226–793.
- Turcotte, D.L., 1997, *Fractals and Chaos in Geology and Geophysics*: Second Edition, Cambridge University Press, Cambridge.
- Turcotte, D.L., & G. Schubert, 1982, *Geodynamics: Applications of Continuum Physics to Geological Problems*: John Wiley & Sons, New York.
- Turner, F.J., & L.E. Weiss, 1963, *Structural Analysis of Metamorphic Tectonites*: McGraw-Hill, New York.
- Twiss, R.J., 1988, Description and classification of folds in single surfaces: *Journal of Structural Geology*, v. 10, p. 607–623.
- Twiss, R.J., & E.M. Moores, 1992, *Structural Geology*: W.H. Freeman and Company, New York.
- Vacher, H.L., 1989, The three-point problem in the context of elementary vector analysis: *Journal of Geological Education*, v. 37, p. 280–287.
- Vacher, H.L., 1998, Computational geology 1: Significant figures!: *Journal of Geoscience Education*, v. 46, p. 292–295.
- Vacher, H.L., 2000, Computational geology 12: Cramer's rule and the three-point problem: *Journal of Geoscience Education*, v. 48, p. 522–532.
- Vacher, H.L., 2001a, Computational geology 14: The vector cross product and the three-point problem: *Journal of Geoscience Education*, v. 49, p. 72–82.
- Vacher, H.L., 2001b, Computational geology 16: The Taylor series and error propagation: *Journal of Geoscience Education*, v. 49, p. 305–313 (see correction v. 49, p. 396).
- Vacher, H.L., 2001c, Computational geology 17: The total differential and error propagation: *Journal of Geoscience Education*, v. 49, p. 386–396.
- Verhoogen, J., F.J. Turner, L.E. Weiss, C. Wahrhaftig & W.S. Fyfe, 1970, *The Earth*: Holt, Rinehart & Winston, New York.
- Vistelius, A.B., 1966, *Structural Diagrams*: Pergamon Press, Oxford.
- Vollmer, F.W., 1990, An application of eigenvalue methods to structural domain analysis: *Geological Society of America Bulletin*, v. 102, p. 786–791.
- Vollmer, F.W., 1995, C program for automatic contouring of spherical orientation data using a modified Kamb method: *Computers & Geosciences*, v. 21, p. 31–49.
- Waldron, J.W.F., & K.D. Wallace, 2007, Objective fitting of ellipses in the center-to-center (Fry) method of strain analysis: *Journal of Structural Geology*, v. 29, p. 1430–1444.
- Wallbrecher, E., 1986, *Tektonische und gefügeanalytische Arbeitsweisen: graphische, rechnerische und statistische Verfahren*: Ferdinand Enke Verlag, Stuttgart, Germany.
- Wallbrecher, E., 2005, Fabric8: [www.geolsoft.com](http://www.geolsoft.com).
- Walpole, R.E., & R.H. Myers, 1993, *Probability and Statistics for Engineers and Scientists*: Fifth Edition, Macmillan, New York.
- Warner, J., 1969, FORTRAN IV program for construction of pi-diagrams with the Univac 1108 computer: Computer Contributions, Lawrence, Kansas.
- Warner, F.M., & M. McNeary, 1959, *Applied Descriptive Geometry*: Fifth Edition, McGraw-Hill, New York.
- Watson, G.S., 1983, *Statistics on Spheres*: John Wiley, New York.
- Watson, G.S., 1988, The computer simulation treatment of directional data: *Recent Researches in Geology, Geological Survey of Canada*, v. 12, p. 19–23.
- Weaver, J.D., 1975, Slickensides and slickenlines: *Geological Magazine*, v. 112, p. 400–408.

- Wegmann, C.E., 1929, Beispiele tektonischer Analysen des Grundgebirges in Finnland: *Bulletin de la Commission géologique de Finlande* no. 87, p. 98–127.
- Weijermars, R., 1997, Pulsating oblate and prolate three-dimensional strains: *Mathematical Geology*, v. 29, p. 17–41.
- Weinberger, R., A. Agnon, H. Ron & Z. Garfunkel, 1995, Rotation about an inclined axis: three dimensional matrices for reconstructing paleomagnetic and structural data: *Journal of Structural Geology*, v. 17, p. 777–782.
- Weiss, L.E., 1969, Flexural-slip folding of foliated model materials: in A.J. Baer & D.K. Norris, editors, *Research in Tectonics*, Geological Survey of Canada, Paper 68-52, p. 294–357.
- Wellman, H.G., 1962, A graphic method for analysing fossil distortion caused by tectonic deformation: *Geological Magazine*, v. 99, p. 348–352.
- Wentworth, C.K., 1930, The plotting and measurement of exaggerated cross-sections: *Economic Geology*, v. 25, p. 827–831.
- Wernicke, B., & B.C. Burchfiel, 1982, Modes of extensional tectonics: *Journal of Structural Geology*, v. 4, p. 105–115.
- Whisonant, R.C., & C.F. Watts, 1989, Using dip vectors to analyze structural data: *Journal of Geological Education*, v. 37, p. 187–189.
- Wilkinson, P., N.J. Soper & A.M. Bell, 1975, Skolithos pipes as strain markers in mylonites: *Tectonophysics*, v. 28, p. 143–157.
- Williams, G.D., & T.J. Chapman, 1979, The geometrical classification of noncylindrical folds: *Journal of Structural Geology*, v. 1, p. 181–185.
- Williams, P.F., L.B. Goodwin & S. Ralser, 1994, Ductile deformation processes: in P.L. Hancock, editor, *Continental Deformation*, Pergamon Press, Oxford, p. 1–27.
- Willis, B., 1893, The mechanics of Appalachian structure: *U.S. Geological Survey, Thirteenth Annual Report*, Part 2, p. 212–281,
- Willis, B., & R. Willis, 1934, *Geologic Structures*: Third Edition, McGraw-Hill Book Company, Inc., New York.
- Wilson, G., 1961, Tectonic significance of small scale structures and their important to the geologist in the field: *Annales de la Société Géologique de Belgique*, v. 84, p. 423–548.
- Wilson, G., 1967, The geometry of cylindrical and conical folds: *Proceedings of the Geologists Association*, v. 78, p. 179–210.
- Wilson, G., 1982, *Introduction to Small-scale Geological Structures*: George Allen & Unwin, London [revision of Wilson, 1961].
- Wise, D.U., D.E. Dunn, J.T. Engelder, *et al.*, 1984, Fault-related rocks: Suggestions for terminology: *Geology*, v. 12, p. 391–394.
- Woodcock, N.H., 1976, The accuracy of structural field measurements: *Journal of Geology*, v. 84, p. 350–355.
- Woodward, N.B., S.E. Boyer & J. Suppe, 1985, *An Outline of Balanced Cross-sections*: Studies in Geology 11, Department of Geological Sciences, University of Tennessee, Knoxville.
- Yow, J.L., Jr., 1987, Blind zone in the acquisition of discontinuity orientation data: *International Journal of Rock Mechanics and Mining Science & Geomechanical Abstracts*, v. 24, p. 317–318.
- Yu, H., & Y. Zheng, 1984, A statistical analysis applied to the  $R_f/\phi$  method: *Tectonophysics*, v. 110, p. 151–155.
- Zimmer, P.W., 1963, Orientation of small diameter drill core: *Economic Geology*, v. 28, p. 1313–1325.
- Zoback, M.L., 1992, First and second order patterns of stress in the lithosphere: The World Stress Map Project: *Journal of Geophysical Research*, v. 97, p. 11703–11728.
- Zoback, M.L., M.D. Zoback, J. Adams, *et al.*, 1989, Global patterns of tectonic stress: *Nature*, v. 341, p. 291–298.
- Zwillinger, D., 1996, *Standard Mathematical Tables and Formulae*: Thirtieth Edition, CRC Press, Boca Raton, Fla.

# Index

- abnormal pressures 259
- absolute uncertainty 46
- acceleration 198
- active folding 406
- active tectonics 346
- acute folds 374
- adjacent parts 566
- affine transformation of plane 290
- ambiguous cases 575
- Amontons's law 241, 259
- amplitude 372
- analytical solutions 15
- ancient tectonics 349
- angle bisector 554
- angle of internal friction 248
- angle of rotation 277
- angle of shear 272
- angle of static friction 242
- angles 564
- angular folds 372, 433
- angular forms 410
- angular unconformity 523
- anisotropic rocks 263
- anisotropy 263, 410, 494
- anticline 379
- anticlockwise rotation 109, 188
- anticlustering 302
- antiforms 379
- Appalachian Piedmont 467
- apparent dip 1, 568
- apparent dip vector 21
- apparent plunge 59
- apparent rotation 285
- apparent thickness 30, 36
- arctan function 134
- area of parallelogram 140
- area strain 282
- area stretch 282
- arithmetic mean 7
- aspect ratio 373
- asymmetric folds 373, 442
- "at a point" 199
- attitude 1
- AutoCAD, 551
- auxiliary plane 267
- auxiliary views 552
- average density 274
- average rotation 284
- axes 130
- axial plane cleavage 375
- axial plane 375
- axial-plane thickness 385, 443
- axial surface 375
- azimuth 1
  
- balanced cross sections 426
- "beach balls" 267
- bearing 1
- bedding-plane slip 411
- best-fit indicatrix 392
- beta diagram 468
- beta plane 505
- biaxial stress 206
- blind spot 489
- block 165
- block diagram 534
- bluntness 373
- boundary conditions 364
- bow and arrow rule 180
- box folds 433
- branch faults 182
- breakouts 255
- brittle 240
- brittle–ductile 251
- brittle–plastic 251
- broad forms 306, 365
- buckles 410
- buckling 365, 404
  
- c* surfaces 289
- Canadian Shield 520
- card-deck models 272
- Cartesian stress components 201
- Cauchy's formula 233
- Cauchy–Green tensor 336
- change in length 311
- change in orientation 310
- change of right angle 312
- characteristic equation 234, 238
- characteristic roots 234

- characteristic wavelength  $L$  404  
 chevron forms 433  
 circle 286  
 circular distributions 143  
 circular normal 146  
 cleavage 375  
 cleavage front 308  
 cleavage orientation 387  
 cleavage orientation graph 387  
 cleavage refraction 401  
 clinometer 4  
 clock arithmetic 145  
 clockwise rotation 109, 188  
 clockwise-up convention 314  
 close fold 371  
 clustering 302  
 coaxial flow 354, 355  
 coaxial superpositions 285  
 coefficient of dynamic friction 241  
 coefficient of internal friction 248  
 coefficient of static friction 241  
 coefficient of viscosity 403  
 cohesive shear strength 248  
 column matrices 135, 137  
 compass 4  
 competence 399  
 competent rocks 399  
 complex structures 500  
 composite sections 527  
 computer graphs 463  
 concentric forms 410  
 cone of rotation 109  
 confining pressure 240  
 conjugate angles 555  
 conjugate axis 389, 390  
 conjugate radii 321  
 conjugate shear fractures 252  
 constant area ellipses 352  
 contact strain 408  
 continuous medium *or* continuum 275  
 continuum boundary 275  
 continuum mechanics 275  
 contours of equal density 476  
 contractional fault 165  
 conventional tilt correction 119, 155  
 conventional triaxial test 240  
 convergent cleavage fan 375  
 convergent isogons 384  
 converging pattern 454  
 coordinate geometry 157  
 coordinate system 131  
 core recovery 504  
 core-pole angle 505  
 cores with known plane 510  
 cotangent method 17, 65  
 coulisse diagram 527  
 Coulomb criterion of shear failure 247  
 Coulomb–Terzaghi criterion 261  
 Cramer’s rule 163, 395, 514  
 crest 370  
 crest line 370  
 critical outlook 521  
 critical questions 520  
 cross product 136, 139  
 crystallographic axis 370  
 cubic equation 238  
 cylindrical surface 370  
 daylight 490  
 deck of cards 272  
 décollement 427  
 décollement thrust 429  
 decomposition 331  
 deformation path 352  
 deformation tensors 290  
 deformed bodies 269  
 deformed fossils 304  
 deformed grains 302  
 deformed pebbles 306  
 deformed trilobite 316  
 degrees of certainty 518  
 del 161  
 depth 30  
 depth of folding 427  
 depth to plane 43  
 derivative 47  
 descriptive geometry 551  
 detachment fault 190  
 deviatoric stress 223  
 dextral faults 166  
 dextral shear 273  
 diagonal form 204  
 diametral plane 88  
 differential stress 243  
 differentials 47  
 dihedral angle 101, 576  
 dilatancy number 362  
 dilation of dikes 195  
 dip 2  
 Dip and strike from geological map 76  
 dip domains 435  
 dip interpolation 419  
 dip isogon 382  
 dip notation 3  
 dip slip 166  
 dip vectors 20  
 direct view 169, 553  
 direction angles 132  
 direction cosines 131, 570  
 direction of younging 376  
 directional derivative 161  
 disconformity 523  
 discrepancy 6, 8  
 disharmonic folds 408  
 disharmony 427  
 displacement field 269  
 displacement vector 269, 298  
 distance to plane 44  
 divergent cleavage fan 376  
 divergent isogons 384  
 domain 493  
 domal structure 183  
 dominant linear fabric 500  
 dot product 136, 153, 230, 242, 312, 545  
 down-dip view 73, 172  
 down-plunge view 456, 459  
 down-structure 172  
 downward inclination 92



- “drag” folds 378
- drill hole problem 576
- drill hole survey instruments 504
- drilling 504
- ductile 240
- ductile regime 250
- ductile shear zone 349
- ductility 251
- duplex 181
  
- eccentric angle 226
- echelon faults 165, 183
- edge view 32
- edge view of plane 561
- effective stresses 222
- effective value 411
- eigenvalues 233
- eigenvectors 233
- Einstein summation convention 233
- elements 493
- ellipses 388
- ellipsoid 264
- engineering geology 489
- enlarged sections 532
- epicenter 267
- equal-angle net 92
- equatorial stereographic net 92
- equilibrium mineral assemblages 357
- error 5, 8
- error propagation 46
- Euler angle 118
- Euler axis 118
- “Eulerian” 270
- evolute 425
- exaggerated dip angles 529
- expansion by cofactors 139
- extension 185, 186, 270
- extension fractures 240, 253
- extensional fault 165
- external forces 199
- external rotation 278
  
- fabric 493
- facing 194
- fault 165
- fault-bend folds 438
- fault-bend folds 184
- fault-drag folds 184
- fault plane 267
- fault-propagation folds 438
- fault zone 165, 183
- faunal assemblage 520
- fence diagrams 527
- finite neutral surface 412, 415
- finite strain tensor 340
- finite-amplitude folds 405
- finite-element model 411
- first order patterns 255
- Fisher distribution 149
- flats and ramps 185
- flattening 365
- flattening index 388, 397
- flexural flow 411
- flexural-slip folding 410
  
- floor thrusts 181
- flow 346, 356
- flow laws 402
- fluctuation F, 308
- fold 369
- fold attitudes 380
- fold axis 370, 469
- fold hinge 443
- fold limb 372
- fold profile 370
- folded layer 40
- folding line 11, 552
- folding 369
- folds with divergent isogons 384
- folds with strongly convergent isogons 384
- folds with weakly convergent isogons 384
- footwall 165
- force 198
- forward model 287
- forward modeling 272
- forward problems 118, 251
- fractional uncertainty 46
- free body 204
- frictional equilibrium 255
- frictional resistive force 241
- front view 552, 556
- full girdle 483
  
- garnet porphyroblast 350
- general two-dimensional stress 208
- gentle fold 371
- geological history 522
- geological structure 543
- geometrical flattening 405
- geothermobarometry 357
- giga-annum 348
- girdle 482
- golden ratio 283
- gradient of  $h$ , 161
- gradient vector 162
- graphical method 554
- great circle 88, 89
- Griffith cracks 250
  
- hangingwall 165
- Hartmann’s rule 252
- Heim’s rule 257
- heterolithic unconformity 523
- high-angle faults 168
- hinge faults 188
- hinge line 370, 469
- hinge point 370, 463
- hinge surface 463
- hinge zone 372
- home position 93
- homogeneous 271, 493
- homogeneously deformed 271
- hoop stresses 255
- horizontal axis 110
- horizontal components 185
- horse 181
- hydraulic fractures 255

- hydrostatic component 223  
 hyperbolas 388  
 hypocenter 267
- identity matrix 332  
 image plane 551  
 imbricate structure 181  
 implied absolute uncertainty 15  
 implied uncertainty 15  
 inclination 1  
 inclined auxiliary view 558  
 inclined axes 116  
 inclined drill hole 42  
 inclined horizontal folds 381  
 inclined plunging folds 381  
 incompetent rocks 399, 403  
 infinitesimal amplitude 404  
 infinitesimal neutral surface 412  
 inflection lines 370  
 inflection points 370, 443  
 inflection surface 375  
 inhomogeneous deformation 269  
 inhomogeneous simple shear 441  
 interference patterns 451  
 internal forces 199  
 “internal friction” 250  
 internal rotation 278  
 International System of Units 16  
 interpretation of folds 516  
 intersecting planes 64  
 intersection errors 571  
 intersection vector 67, 142  
 invariant properties 234  
 inverse deformation tensor 338  
 inverse matrix 333  
 inverse problem 118, 251, 287, 289  
 inverse thickness 388  
 involutes 425  
 irregular folds 449  
 isochoric deformation 282  
 isoclinal fold 371  
 isogon 383  
 isometric graph paper 534  
 isometric projection 534  
 isotropic 302, 493
- Jacob’s staff 31  
 Jura Mountains 428
- Kalsbeek net 476  
 kilo-annum 348  
 kinematics 346, 356  
 kink bands 433  
 klippe 179
- L* tectonites 502  
 Lagrangian 270  
 Lambert equal-area projection 471  
 latent roots 234  
 law of Cosines for Angles 573  
 law of Cosines for Sides 573  
 Law of Sines 573  
 Laws of Sines 564  
 laws of superposition 520
- layer-parallel shortening 365  
 least-squares criterion 394  
 left separation 169  
 left slip 166  
 left-lateral faults 166  
 left-slip faults 166  
 left-stretch tensor 331  
 length of line 559  
 limiting equilibrium analysis 243  
 line 57  
 line bisector 555  
 line of sight 72  
 line vectors 67  
 linear elastic fracture mechanics 250  
 linear extrapolation 82  
 linear fabrics 494  
 linear interpolation 77  
 linear structures 497, 498–500  
 lines of no finite longitudinal strain  
   (NFLS) 278  
 lines of no instantaneous stretching 360  
 listric normal fault 190  
 listric thrusts 181  
 lithostatic 257  
 low-angle faults 168  
*LS* tectonites 502
- macroscopic view 274, 354  
 major axis 389  
 map coordinates 464  
 map lithologies 524  
 map symbols 2, 3, 58, 455, 519  
 margin of error 8  
 mass 198  
 material coordinates 269, 309  
 material description 270, 291, 337  
 material displacement gradient tensor 300  
 material view 356  
 matrix 331  
 maximum differential stress 258  
 maximum observer error 106  
 maximum operator error 9, 105  
 maximum strike error 9, 105  
 maximum trend error 69, 106  
 mean direction 145  
 mean normal stress 223  
 mean resultant length 147  
 measured stretches 321  
 median surface 372  
 mega-annum 348  
 mélange 520  
 method of cofactors 158  
 method of radial projection 532  
 micro-boudins 354  
 micro-folds 354  
 microscopic view 274, 354  
 migmatites 450  
 migmatitic gneisses 449  
 minor axis 389  
 minor folds 375  
 mistake 5  
 mixing 449  
 modified Griffith criterion 250  
 modular arithmetic 145

- Mohr Circle 294, 360  
   for finite strain 314  
   for stress 210  
   plane 210  
 monoclinic symmetry 355  
 motion 346  
 mushroom fold 371
- nabla 161  
 nadir point 92  
 Napier's Analogies 574  
 Napier's device 566  
 Napier's rules 566  
 Napierian triangle 565  
 narrow forms 286, 306, 307  
 negative angles 279  
 neutral folds 380  
 Newtonian flow 403  
 NFLS, 278, 280  
 no vertical exaggeration 532  
 nodal planes 267  
 non-coaxial flow 355  
 non-coaxial superposition 285, 351  
 non-conformity 523  
 non-depositional unconformity 523  
 normal component 200  
 normal equations 395  
 normal faults 251  
 normal pressure 259  
 normal separation 169  
 normal slip 166  
 normal view of plane 553, 561  
 normalize 131  
 normalized axial plane thickness 385  
 normalized exaggerated thickness 531  
 normalized orthogonal thickness 385  
 null combination 171
- oblique faults 264  
 oblique horizontal traverse 33  
 oblique slip 167  
 oblique-spherical triangles 572  
 observations and interpretation 518  
 observed apparent dips 25  
 obsidian/pumice rock 450  
 obtuse folds 374  
 off-axis circle 331  
 offset line 195  
 on-axis circle 332  
 open fold 371  
 open fractures 261  
 opposite parts 566  
 opposite 92, 112, 125  
 orientational angle 310  
 oriented cores 505  
 origin of lines 315  
 origin of normals 218, 315  
 origin of planes 218  
 original continuity 520  
 original horizontality 520  
 orthogonal rotation tensor 331  
 orthogonal thickness 385  
 orthographic construction 460  
 orthographic net 539  
 orthographic projection 10, 539, 551  
 orthorhombic symmetry 355  
 outcrop map 519  
 outcrop pattern 72, 454  
 outcrop trace 84  
 outcrop width 30, 33  
 outliers 6  
 overburden pressure 254  
 overcoring 255  
 overfolds 373  
 overthrust 168, 179  
 overturned folds 373
- pachymetric indicatrix 388  
 paleogeological map 522  
 palinspastic map 522  
 parallel folds 384, 410  
 parallel isogons 444  
 parallel lines 79  
 parallel unconformity 523  
 parallelogram rule 134  
 parametric equations 226  
 partial limb angles 434  
 particle 269  
 passive behavior 441  
 pathline 356  
 Pennine Nappes 550  
 percentage uncertainty 46  
 perfect fold 373  
 permissible volume 275  
 physical flattening 406  
 physical plane 210  
 piercing points 178  
 pitch 57, 568  
 pitch and plunge 569  
 pitch of line 61  
 pivotal faults 188  
 planar fabrics 494, 496  
 planar structure 496  
 Plane 1  
 plane in compression 200  
 plane in tension 200  
 plane stress 204  
 plotting techniques 93  
 plunge 57  
 plug and chug 15  
 plunge of line 59  
 plunging folds 454  
 point maximum 482  
 point view of line 560  
 polar net 104  
 polar triangle 565, 566  
 pole 97, 315  
 pole for normals 218  
 pole for planes 218  
 pole vector 141  
 polyharmonic folds 408  
 pore fluid factor 259  
 pore fluid pressure 259  
 pore pressure 222  
 positive angles 278  
 positive plunge angles 133  
 positive rotations 151  
 positive trend angles 133

- post-circle broad form 286, 307  
 post-multiply 334  
 power law creep 402  
 pre-circle broad form 286, 307  
 pre-multiplying 336  
 primitive 89  
 principal axes 277  
 principal diameters 93  
 principal directions 203  
 principal extension rates 360  
 principal extensions 349  
 principal stresses 203, 209  
 principal stretches 277  
 principal stretching axes 360  
 principal views 552  
 probability 478  
 products of vectors 136  
 profile coordinates 464  
 progress report 521  
 progressive deformation 350  
 projection lines 552  
 projections 551  
   line 559  
   plane 560  
   point 556  
 projectors 551, 552  
 propagated uncertainty 48  
 ptygmatic micro-folds 354  
 Pumpelly's rule 377  
 pure shear flow 367  
 pure shear stress 207  
 pure shear 297, 352  
  
 ramp 185  
 random error 6  
 random samples 478  
 rate of area strain 360  
 rate of deformation tensor 357  
 rate of extension 359  
 reciprocal quadratic elongation 311  
 reclined folds 380, 381  
 recumbent folds 380, 381  
 related tensors 331  
 relative displacement 288, 291  
 relative displacement vector 272  
 relative uncertainty 46  
 relative velocity 358  
 relative velocity field 359  
 representative elementary volume 275  
 residual 394  
 restoration 328  
 resultant length 147  
 resultant vector 145, 147  
 reversal rule 336, 338  
 reverse separation 169  
 reverse slip 166  
 revolve 114  
 right lateral faults 166  
 right separation 169  
 right slip 166  
 right to left 152  
 right-hand rule 149  
 right-spherical triangle 565  
 right-stretch tensor 331  
  
 rigid rotation 109  
 rock mass 275  
 rock slopes 489  
 rollover anticline 185  
 roof thrusts 181  
 root mean square error 395  
 root mean square 9  
 rotating motion 359  
 rotation 346  
 rotation matrices 541  
 rotational faults 188  
 rotational problems 154  
 rotations 149  
 round down 16  
 round up 16  
 rounded folds 372  
 rounded forms 410  
 rounding off 16  
 row matrix 137  
 row times column multiplication 137, 150, 153  
 row times column rule 229  
 Rule of Vs 74, 519  
  
 S surfaces 289  
 S tectonites 502  
 sample standard deviation 8  
 sampling problem 487  
 San Andreas Fault zone 346  
 S-C fabrics 289  
 scalar or dot product 21  
 scaling tool 463  
 scatter diagrams 474  
 Schmidegg counter 475  
 Schmidt net 472  
 Schnitteffekt 489  
 seismicity 256  
 seismogenic zone 259  
 seismograph records 266  
 semi-brittle 240  
 sense of rotation 188  
 separation 165, 168  
 Sequential rotations 114  
 set 487  
 Shackleton's rule 377  
 shear folding 441  
 shear fractures 240  
 shear strain 279  
 shear zone 165, 287  
 shearing component 200  
 sheath fold 452  
 shift 184  
 side views 552  
 sides 564  
 similar folds 384, 441  
 similar triangles 78  
 simple shear flow 367  
 simple shear 272, 276  
 single-sense shear 444  
 singular 333  
 sinistral faults 166  
 sinistral shear 273  
 skew-symmetric 363  
 slickenfiber 176  
 slickenlines 176

- slickenplanes 176
- slickenside 176
- slickensteps 176
- slickenstriae 176
- slickenstructures 176
- slickenzone 176
- slip 165
- slip event 262
- small angle intersection 78
- small circle 89
- small circles 124
- snow-ball garnets 350
- sole thrust 182
- spatial coordinates 269, 309
- spatial description 270, 338
- spatial view 356
- spatially invariant 370
- spherical distributions 147
- spherical normal 149
- spherical projection 88
- spherical triangle 564
- S-pole diagram 469
- standard state 257
- static equilibrium 198
- steady flow 356
- stereogram 89
- stereographic projection 88
- stirred porridge 449
- stored elastic strain energy 262
- strain 276, 544
- strain distribution 443
- strain ellipse 276
- strain parameters 313
- strain path 352
- strain ratio 278
- strain refraction 401
- strain rosette 316
- strain tensors 331
- strain-rate tensor 362
- stress 201, 205, 206
- stress drop 262
- stress ellipse 224
- stress ellipsoid 264
- stress inversion 266
- stress matrix 201, 203
- stretch 270, 346
- stretch history 353
- stretching motion 359
- strike 1, 2
- strike error 569
- strike-normal 32
- strike notation 2
- strike-slip 267
- strong fabrics 495
- structural bearing 1
- structural facing 376
- structural contours 84
- structure contours 66, 82
- structure sections 523
- subangular fold 372
- subordinate planar fabric 500
- subrounded fold 372
- sum in quadrature 52
- sum of vectors 134
- superimposed deformations 284
- superimposed stress states 215
- symmetric fold 372
- symmetric matrix 363, 372
- syncline 379
- synforms 379
- synkinematic metamorphism 349
- systematic error 6
- systematic joints 487
- Taylor series 53
- “tectonic rafts” 266
- tectonites 494
- tensor notation 232
- tensors of second rank 229
- Terzaghi’s relationship 223
- Texas Sharpshooter Fallacy 6
- The World Stress Map* project 255
- thickness 30
- thickness in drill holes 41
- thickness measurements 32
- three drill holes 515
- three-point problem 24, 80, 157
- thrust 168
- thrust faults 251, 427
- tight fold 371
- tightness 371
- tilted fault block 190
- top view 552, 556
- topographic contours 84
- topographic profile 524
- topography 547
- torque 198
- total station 24
- trace 234
- traction 199
- trajectories 288
- transected fold 379
- transformation of axes 213
- transformed axes 396
- translating motion 359
- translation 346
- translation rate 358
- translational faults 166
- transpose matrices 293
- transpose 334, 362
- transverse axis 389, 390
- trend 1, 57
- triclinic symmetry 355
- trough 370
- trough line 370
- true dip 1
- true dip vector 21
- true length 559
- true shape 561
- turntable 109
- two drill holes 511
- two tilts 121
- two-dimensional scalar field 161
- unambiguous cases 574
- uncertainty 5, 8, 46
- unconformity 522
- uniaxial stress 205

- uniform translation vector, 291
- unimodal 147
- unimodal distribution 144
- unit base vectors 131
- unit matrix 332
- unit shear 279
- unknown scale factor 317
- unsteady flow 356
- upright horizontal folds 381
- upright plunging folds 381
  
- vector analysis 160
- vector field 161
- vector operator symbol 161
- vector processor 150, 291
- vector processors 229
- vectors 130
- velocity field 356
- velocity gradient 347
- velocity-gradient tensor 358
- velocity profile 347
- vergence 373
- vertical auxiliary view 557
  
- vertical axis 110
- vertical exaggeration 527
- vertical folds 381
- vertical hole 507
- vertically exaggerated section 527
- visualize 553
- von Mises distribution 146
- vorticity 360
- vorticity gauges 362
- vorticity number 362
- vorticity tensor 362
  
- wavelength 372
- weak fabrics 495
- wild folds 449
- window 179
- Wrench faults 251
- Wulff net 92
  
- yield point 250
  
- zenith point 88
- zoned minerals 357